UNIVERSIDAD DE CANTABRIA

ESCUELA DE DOCTORADO DE LA UNIVERSIDAD DE CANTABRIA
DOCTORADO EN INGENIERÍA CIVIL

TESIS DOCTORAL

ANÁLISIS DE LA FRACTURA DE ROCAS ENTALLADAS BAJO DIFERENTES CONDICIONES DE CARGA Y DE TEMPERATURA MEDIANTE CRITERIOS LOCALES

- - - - - -

PhD THESIS

FRACTURE ASSESSMENT OF NOTCHED ROCKS UNDER DIFFERENT LOADING AND TEMPERATURE CONDITIONS USING LOCAL CRITERIA

Presentada por: **JON JUSTO URRUTIA**

Dirigida por: **Prof./Dr. JORGE CASTRO GONZÁLEZ**
Prof./Dr. CÉSAR SAGASETA MILLÁN

Santander, 2020

"No amount of experimentation can ever prove me right; a single experiment can prove me wrong."

"Con ninguna cantidad de experimentos se podrá demostrar que estoy en lo cierto; un solo experimento puede demostrar que estoy equivocado."

Albert Einstein

Acknowledgments

I would like to express my deepest and most sincere appreciation to all those people without whom I would not have been able to complete this doctoral thesis, specially to Jorge Castro González, director of this research, due to his endless effort, support, advices and trust. Likewise, I would also like to thank César Sagaseta Millán, co-director of my thesis, for his supervision and guidance. They have managed to transmit me with their motivation and professionality at all times.

I would like to extend these acknowledgements to all members and friends of the Geotechnical Group of the University of Cantabria, for their support and collaboration, in one way or another, throughout these years. Particularly, Javier de la Fuente, Eduardo Gútiez and Fernando del Puerto, the technicians of the Geotechnical research group, and Alvaro Lagüera, Ainhoa Jaurrieta, Estaban González, Civil Engineering students, deserve special gratitude for their help with the never-ending laboratory work. Likewise, I am also very grateful to Miguel Ángel Sánchez Carro, from the Applied Geology Group of the University of Cantabria, and Javier Escanciano, Civil Engineering student, who dealt with the thin section preparation and the corresponding petrographic analyses in the Geology laboratory. Special thanks to Sergio Cicero González, from the Group of Materials Science and Engineering of the University of Cantabria, for his help and masterclasses on the field of fracture mechanics, as well as to Heinz Konietzky, Director of the Geotechnical Institute of Rock Mechanics of TU Bergakademia Freiberg in Germany, for giving me the chance to collaborate and learn from their expertise in numerical analysis of rock mechanics during my three-month internship in their department.

Additionally, I would like to thank Ane Abando, Kepa Alonso and Santiago Ijalba for the opportunity to work with them in the company Cimentaciones Abando S.A. while working, in parallel, on the PhD. I would not have made it through this doctoral thesis without their flexibility and patience. The knowledge and practical perspective

acquired with them in the field of geotechnical works perfectly complements and strengthens my theoretical background.

Last but not least, I would like to thank my friends and family, specially my parents and brother, for their moral support and encouragement over these years. They probably do not know to what extent they have helped me to stay motivated and eager to get this work done.

Funding

This doctoral thesis is framed within a National Plan Project (Ref.: BIA2015-67479-R) under the name of "The Critical Distance in Rock Fracture", funded by the Spanish Ministry of Economy and Competitiveness and by the European Regional Development Fund (ERDF). The following webpage arises from this National Plan Project: https://rockfracture.unican.es/en/

This research work is also part of the project "Characterization of the fracture process in rocks for geothermal applications", funded by the Department of Universities and Research, Environment and Social Policy of the Government of Cantabria.

Finally, the three-month internship at TU Bergakademie Freiberg in Germany, necessary for the International Doctorate Mention, was partially funded by a short-term research grant given by the German Academic Exchange Service (DAAD) of the German Government.

Awards

The following recognitions emerge from the present doctoral research work:

- First prize in the contest "Your Thesis in 3 minutes" organized by the EDUC (Doctoral School of the University of Cantabria), in the Engineering and Architecture category, for a three-minute video explaining the research topic of my Thesis: https://www.youtube.com/watch?v=V4iE6nK3G10
- Recognition for the best investigation career in the research line "Ground, Materials and Structures in Civil Engineering" by the EIDEIC 2018 (International Meeting of PhD students in Civil Engineering) organized by the University of Cantabria.
- Selected by the Spanish Society of Soil Mechanics and Geotechnical Engineering (SEMSIG) as one of the two Spanish delegates for the European Young Geotechnical Engineering Conference (EYGEC) that took place in Graz, Austria (2018).

Resumen

Las rocas suponen muy probablemente el material más común en el mundo de la construcción, y a su vez, el estudio de su comportamiento es uno de los campos con mayor incertidumbre asociada. La amplía casuística de tipos de litologías, la heterogeneidad de las rocas a diferentes escalas o la presencia de defectos de diferente índole, son consecuencia del historial geológico al que se han visto sometidas a lo largo de milenios. Esto hace de las rocas un material particularmente complejo, por lo que la mecánica de rocas supone una rama del conocimiento muy activa y en continuo desarrollo. La comprensión integral del comportamiento de las rocas a diferentes escalas y bajo diferentes condiciones tensionales y térmicas implica un alto grado de interés en varios ámbitos de la ingeniería, como por ejemplo la ingeniería civil (e.g., estudio de laderas, cimentaciones, excavaciones en roca), ingeniería subterránea (e.g., análisis de túneles, minería) o ingeniería de la energía (e.g., explotaciones de gas y petróleo, depósitos de residuos nucleares, gasificación del carbón, energía geotérmica).

Uno de los principales aspectos que caracterizan las rocas desde un punto de vista mecánico, es su comportamiento a rotura predominantemente frágil. Los materiales frágiles o cuasi-frágiles como las rocas muestran un comportamiento no lineal muy limitado previamente a producirse el fallo. Por lo tanto, la propagación de las fisuras es inestable y se produce la fractura de forma súbita y repentina. Esta condición resulta de especial interés en cualquier ámbito de la ingeniería, pues puede conducir a fallos catastróficos en macizos rocosos agrietados y estructuras sin previo aviso. Por ello, en mecánica de rocas, predecir la rotura es una de las mayores preocupaciones, existiendo una demanda generalizada para el desarrollo y validación de nuevas herramientas y metodologías específicas que permitan analizar y predecir la fractura de rocas de manera precisa y, preferiblemente, sencilla.

De forma general, la resistencia a tracción en rocas es comparativamente más baja que la resistencia a compresión o cortante, por lo que está ampliamente aceptado que los fenómenos de propagación

de fisuras en rocas se encuentran principalmente dominados por modos de carga de apertura/tracción (modo I). Este aspecto resulta especialmente importante bajo la presencia de defectos, ya que estos pueden generar concentraciones de tensiones localizadas y conducir a una rotura prematura e inesperada. Desde un punto de vista de la integridad de la roca, la presencia de defectos es inevitable, puesto que las rocas son materiales indiscutiblemente discontinuos a todas las escalas (desde poros, bordes de grano o microfisuras a escala microscópica, hasta diaclasas, discontinuidades o incluso perforaciones a escala macroscópica).

Los criterios de rotura más básicos asumen que todos los materiales son perfectamente homogéneos, isótropos y libres de defectos, en cuyo caso una muestra se romperá cuando la tensión supere la resistencia última del material. Sin embargo, esto no suele ocurrir en la realidad, observándose una significativa reducción de la resistencia general del material bajo la presencia de defectos. Surge así la mecánica de la fractura, la cual contempla la presencia y tipología de defectos en la evaluación de la resistencia a rotura de un material. Independientemente de su origen, la presencia de estos defectos en la roca juega un papel fundamental en los procesos de iniciación de la fractura. Sin embargo, resulta importante diferenciar entre defectos tipo fisura, aquellos con un radio teóricamente nulo, y los defectos tipo entalla, aquellos con un radio finito. Probablemente como herencia de los comienzos del desarrollo de la mecánica de la fractura, tradicionalmente ha existido una tendencia generalizada de abordar los análisis de rotura desde un enfoque conservador, asumiendo que todos los defectos se comportan como defectos tipo fisura. Sin embargo, hoy se sabe que estos últimos desarrollan campos tensionales más elevados que los defectos tipo entalla, produciéndose así una mayor concentración de tensiones en el frente de una fisura que en el frente de una entalla. A medida que el radio de la entalla aumenta, la concentración de tensiones se disipa, y esto es lo que se conoce como el efecto entalla. Por lo tanto, caer en la hipótesis de que un defecto con un tamaño de radio significativo se comporta igual que una fisura afilada conlleva diseños y predicciones de rotura excesivamente conservadores en muchos casos prácticos y pone en manifiesto la necesidad de realizar análisis específicos en cada caso.

Para el análisis de fractura de componentes entallados existen dos tipos de enfoques: el enfoque global y el enfoque local. El primero de ellos establece que la fractura se produce cuando el factor de intensidad de tensiones en entallas (K_ρ) alcanza un valor crítico (K_ρ^c) que solo depende del material y del radio de entalla (ρ). Este enfoque es por lo tanto análogo al propuesto por la mecánica de la fractura elástico-lineal tradicional para componentes fisurados, en los que la fractura se produce cuando el factor de intensidad de tensiones en fisuras alcanza la tenacidad a fractura del material (bajo condiciones de carga modo I, $K_I = K_{IC}$). Sin embargo, la falta de soluciones analíticas para la definición de K_ρ hacen que el uso de este método esté actualmente muy limitado. Por el contrario, los criterios de fractura locales se basan en el campo tenso-deformacional alrededor del frente de la entalla, pudiendo analizar valores de una determinada variable, como pueden ser tensiones o energía de deformación, en un determinado punto, a lo largo de una determinada distancia o en un determinado volumen alrededor del defecto. En base a ello, se han desarrollado numerosos criterios de fallo para la predicción de rotura de componentes entallados, entre los que destacan actualmente por su mayor uso el Modelo de Zona Cohesiva (MZC), el criterio de Mecánica de Fractura Finita (MFF), el criterio de Densidad de Energía de Deformación (DED) o la Teoría de las Distancias Críticas (TDC), entre otros. Todos estos criterios de rotura han sido ampliamente utilizados para la evaluación de la fractura bajo diferentes condiciones de carga y materiales como aceros y polímeros, por ejemplo. Sin embargo, sus contribuciones en el ámbito particular de la mecánica de rocas son muy escasas y su aplicabilidad y validación en este campo aún requiere de una investigación más exhaustiva. Probablemente, la falta de desarrollo de estas metodologías en esta rama de la mecánica es debida, en gran medida, al alto grado de heterogeneidad de las rocas frente a otro tipo de materiales, lo que hace de ellas un material poco atractivo para la validación de este tipo de herramientas en el ámbito de la mecánica de la fractura. Además, la obtención de conclusiones robustas se complica como consecuencia de la dispersión de los resultados, que es relativamente mayor que en el caso de materiales más homogéneos.

Por ello, tratando de dar respuesta a la demanda de herramientas y metodologías específicas para el análisis y predicción la fractura de rocas, en el presente trabajo de tesis doctoral se pretende estudiar y validar la aplicabilidad de la TDC y el criterio DED en el ámbito de la mecánica de rocas, destacando sus ventajas y limitaciones en este tipo de materiales. Para ello, se han estudiado 6 tipos de rocas de variada litología, a saber, una arenisca Floresta, una caliza Moleanos, un mármol Macael, un mármol de Carrara, una caliza oolítica y un granito, con el objetivo de cubrir una amplia casuística de rocas y poder sacar conclusiones generalizables. Las cuatro primeras rocas se han analizado en la campaña de laboratorio que se enmarca en la presente tesis doctoral, mientras que las dos últimas forman parte de un estudio anterior de Cicero et al. (2014) del que se han aprovechado los resultados.

En primer lugar, se ha analizado la fractura de roca bajo condiciones de carga de modo I en base a la TDC, considerando diferentes radios de entalla en forma de "U", desde 0.15 mm hasta 15 mm, con el objetivo de caracterizar el efecto entalla. Este análisis se ha extendido posteriormente a modos de carga mixtos de tracción y cortante (I+II), empleando la misma tipología y tamaño de radios de entalla. Como alternativa a la TDC, se ha realizado el mismo estudio de fractura en modo I empleando un enfoque energético basado en el criterio DED. Todos estos análisis se han desarrollado tanto a temperatura ambiente como a temperaturas más elevadas de hasta 250ºC, rango de temperaturas habituales en proyectos de índole geotérmica, por ejemplo. Se trata, por lo tanto, de un trabajo de tesis doctoral con una alta componente experimental. En total, se han llevado a cabo 300 ensayos Brasileños, 120 ensayos de compresión uniaxial, 882 ensayos de flexión en cuatro puntos sobre probetas prismáticas con radios de entalla variable y 395 ensayos de flexión en tres puntos con radios de entalla y posición de la carga variable, todos ellos bajo diferentes condiciones de temperatura. Del mismo modo, se han tomado 290 lecturas de dilatación térmica y se han realizado 158 análisis de lámina delgada mediante microscopía óptica. En base a la campaña de ensayos realizada, se ha estudiado la influencia de la temperatura en los principales parámetros de la roca (i.e., resistencia a tracción, σ_u; tenacidad a fractura, K_{IC};

resistencia a compresión, σ_c; módulo de Young, E; coeficiente de Poisson, v), tratando de estudiar la extrapolación potencial de la TDC y el criterio DED a condiciones de temperaturas moderadas.

La TDC utiliza la mecánica de fractura elástico-lineal y un parámetro denominado distancia crítica (L). Este parámetro depende directamente de la tenacidad a fractura (K_{IC}) y de la resistencia a tracción de la roca (σ_u), de acuerdo con la siguiente expresión:

$$L = \frac{1}{\pi}\left(\frac{K_{IC}}{\sigma_u}\right)^2 \qquad (1)$$

Entre las diferentes metodologías incluidas en la TDC, el método del Punto (MP) y el Método de la Línea (ML) son las más extendidas por su sencillez. Tanto el MP como el ML ofrecen, a priori, resultados similares y ambos son estudiados en el presente trabajo. Sin embargo, de cara a las predicciones de fractura, el análisis llevado a cabo en este trabajo se centra principalmente en el ML. El primero de ellos, el MP, establece que se produce la rotura cuando la tensión a una determinada distancia ($L/2$) del frente de la entalla alcanza la resistencia a tracción, mientras que el ML establece que se produce la rotura cuando la tensión promediada a lo largo de una determinada distancia ($2L$) desde el frente de entalla alcanza la resistencia a tracción de la roca. Así, las siguientes expresiones describen los criterios de fallo para el MP y el ML, respectivamente:

$$\sigma(L/2) = \sigma_u \qquad (MP) \qquad (2)$$

$$\frac{1}{2L}\int_0^{2L} \sigma(x)dx = \sigma_u \qquad (ML) \qquad (3)$$

Tomando como base la TDC, la interpretación del efecto entalla se lleva a cabo a través del concepto de tenacidad a fractura aparente (K_{IN}). Por definición, la tenacidad a fractura (K_{IC}) de un material mide la resistencia del mismo a la propagación de una fisura, por lo que corresponde a una situación fisurada con un radio teóricamente nulo, o

al menos suficientemente pequeño para no desarrollar ningún efecto entalla. En esencia, el análisis de fractura de componentes entallados se equipara al análisis de componentes fisurados pero considerando la tenacidad a fractura aparente en lugar de tenacidad a fractura estrictamente real. La TDC propone soluciones analíticas que relacionan K_{IN} y K_{IC} a través de la distancia crítica (L) y el radio de entalla (ρ), basándose en la distribución de tensiones en el frente de entalla propuesta por Creager & Paris (1967) y en los criterios de fallo definidos en las *Ecuaciones (2)* y *(3)* para el MP y ML, respectivamente:

$$K_{IN} = K_{IC}\frac{(1+\rho/L)^{3/2}}{1+2\rho/L} \qquad (MP) \qquad (4)$$

$$K_{IN} = K_{IC}\sqrt{\rho/4L+1} \qquad (ML) \qquad (5)$$

Estas expresiones analíticas corresponden a modo I de carga, donde las tensiones se evalúan en el plano bisector de la entalla. Sin embargo, el análisis bajo modos de carga mixtos (I+II) no resulta tan directo. El plano crítico sobre el que se analizan las tensiones y se aplican los criterios de fallo definidos en las *Ecuaciones (2)* y *(3)* gira en función de la influencia del cortante (modo II), de tal forma que este plano es perpendicular a la máxima tensión principal. La falta de soluciones analíticas para modos de carga mixtos hace necesario el empleo de modelos numéricos para la definición del campo tensional y el plano crítico. Una vez definido dicho plano para un determinado grado de mixicidad, la aplicación de las *Ecuaciones (2)* y *(3)* para la evaluación de la fractura es directa y se procede de manera análoga al modo I de carga.

A diferencia de la TDC, el criterio DED establece que las condiciones de rotura se alcanzan cuando la densidad de energía de deformación media ($\overline{W}$) promediada sobre un determinado volumen de control en el frente de entalla alcanza un valor crítico (W_c) que depende únicamente del material:

$$\overline{W} = W_c \qquad (6)$$

El volumen de control sobre el que se promedia la densidad de energía de deformación se transforma en un área de control (Ω) bajo condiciones de deformación plana. Esta área sólo depende del material analizado a través de un determinado radio (R_0) que, para entallas en forma de "U" como las analizadas en el presente trabajo, se define con la siguiente ecuación:

$$R_0 = \frac{(1+v)(5-8v)}{4\pi}\left(\frac{K_{IC}}{\sigma_u}\right)^2 \qquad (7)$$

En base a este enfoque energético, Lazzarin & Berto (2005) desarrollaron la siguiente expresión para la evaluación de la fractura de componentes entallados en forma de "U":

$$W_C = 0.785 \cdot H(v, R_0/\rho) \cdot \frac{\sigma_{max}^2}{E} \qquad (8)$$

Esta expresión se basa en el criterio de fallo definido en la *Ecuación (6)* y relaciona la tensión máxima (σ_{max}) en el frente de entalla en condiciones de rotura con un parámetro H que depende del material, a través del coeficiente de Poisson, y del cociente entre el radio que define el área de control y el radio de entalla (R_0/ρ). Por lo tanto, una vez conocido el parámetro H, se puede proceder a la predicción de la carga de rotura por medio de la estimación de la tensión máxima que la produce (por ejemplo, mediante la distribución de tensiones propuesta por Creager & Paris, 1967). En el presente trabajo de tesis doctoral se proponen y comparan diferentes métodos para la aplicación de la *Ecuación (8)*, desde la opción más sencilla de emplear valores tabulados de H y las correspondientes extrapolaciones en los casos que sea necesario, hasta la evaluación de H o el promedio de densidad de energía de deformación ($\overline{W}$) mediante análisis numéricos.

En base a los resultados obtenidos, tanto la TDC como el criterio DED ofrecen predicciones de fractura razonables dentro de un rango de $\pm$20% con respecto a la carga de rotura experimental (rango empleado habitualmente en mecánica de la fractura como referencia de predicciones razonables). La precisión de los resultados obtenidos se

mantiene incluso a temperaturas de hasta 250ºC, habiéndose observado un comportamiento predominantemente lineal para este rango de temperaturas en la mayoría de los casos estudiados. Por lo tanto, se puede asumir que el uso le mecánica de la fractura elástico-lineal en la que tanto la TDC como el criterio DED se basan es válido a priori. Como excepción, destaca el caso del mármol de Carrara, que muestra un comportamiento no lineal incluso a temperatura ambiente y, en consecuencia, las predicciones de fractura obtenidas son sensiblemente peores.

Por otro lado, bajo condiciones de carga en modo I, las predicciones de rotura obtenidas tanto con la TDC como con el criterio DED se basan en la distribución de tensiones propuesta por Creager & Paris (1967), la cual es teóricamente válida solo para entallas estrechas y largas con una longitud sensiblemente mayor que su radio. Sin embargo, se ha podido observar que, en general, las predicciones obtenidas son razonables incluso para las entallas de mayor tamaño fuera del ámbito de uso teórico de Creager & Paris (1967). Como alternativa a su solución analítica para la definición del campo tensional en el frente de entalla, se han comparado dichas predicciones de fractura con otras realizadas mediante campos tensionales obtenidos numéricamente. La mejora de los resultados observada no justifica la mayor carga de trabajo necesaria para realizar las predicciones, por lo que el empleo de Creager & Paris (1967) se considera adecuado en el rango de entallas analizado (si bien las entallas de mayor radio se encuentran en el límite).

De igual modo, se ha validado la TDC para la evaluación de la fractura de rocas con entallas tipo “U” bajo modos de carga mixtos I+II, incluso a temperaturas de hasta 250ºC, siempre y cuando se observe un comportamiento predominantemente elástico-lineal. La interpretación de los resultados de modo mixto (I+II) a través de la TDC permite caracterizar la distancia crítica para diferentes grados de mixicidad, empleando la ley de tensiones correspondiente al plano crítico en cada caso. Para ello, resulta necesario el empleo de análisis numéricos.

En general, la TDC y el criterio SED ofrecen predicciones de fractura similares, especialmente cuando se calibra el valor crítico de la densidad de energía de deformación (W_c) para absorber las posibles pequeñas no linealidades del comportamiento de las rocas a tracción. Una de las

principales ventajas del criterio DED es que la densidad de energía de deformación se puede evaluar numéricamente mediante sencillos análisis de elementos finitos y con mallas relativamente gruesas. Además, una vez tabulados los valores del parámetro H, la fractura se puede evaluar de forma directa sin necesidad de análisis numéricos. Esta metodología también permite considerar términos de segundo orden y efectos tridimensionales, si bien estos aspectos se encuentran fuera de los objetivos del presente trabajo. Una de las principales desventajas del criterio DED frente a la TDC es la necesidad de caracterizar los parámetros deformacionales (E, ν) mediante ensayos de compresión uniaxial con medición de deformaciones, usando galgas extensométricas por ejemplo. Desde un punto de vista práctico, la diferencia de los resultados obtenidos con ambas metodologías no justifica la carga adicional de trabajo que implica el criterio DED. La complejidad y coste añadido de medir en módulo de Young y el coeficiente de Poisson a temperaturas por encima de 70ºC es substancial debido al empleo de galgas, adhesivos y cables especiales.

Con respecto a la TDC, su principal ventaja radica en que, una vez definido el valor de la distancia crítica (L) de un determinado material, el análisis de fractura de cualquier componente hecho con dicho material es prácticamente directo. En el caso de las rocas, la distancia crítica es del orden de unos pocos milímetros. Dependiendo de la metodología considerada a la hora de obtener este parámetro, el valor de la distancia crítica obtenida varía ligeramente (e.g., cálculo directo mediante expresión analítica, mejor ajuste de ensayos experimentales de acuerdo con el MP o el ML, mediante análisis numéricos). Sin embargo, de cara a las predicciones de fractura, las consecuencias de las diferencias de L observadas son limitadas, dado que L se encuentra dentro de la raíz cuadrada en las ecuaciones analíticas correspondientes al MP y al ML (*Ecuaciones (4)* y *(5)*).

Teniendo en cuenta la importancia del parámetro L en el análisis correspondiente a la TDC, el significado físico real de este parámetro resulta de especial interés. Existe cierto debate entre la comunidad científica al respecto. Sin embargo, parece claro que la distancia crítica guarda relación con el tamaño de grano. En el caso concreto de las rocas estudiadas, se observa que, aproximadamente, la distancia crítica es

ligeramente mayor que diez veces el tamaño de grano. Con el objetivo de indagar más en este aspecto, se ha estudiado mediante análisis numéricos con elementos discretos la influencia del tamaño de grano en la iniciación de la fractura y en la distancia crítica. Se concluye de este análisis que, efectivamente, existe cierta relación lineal entre el tamaño de grano y la distancia crítica. A partir de los modelos numéricos, se ha obtenido una correlación de 1:1 entre ambos parámetros. Sin embargo, es importante señalar que esta relación debe ser únicamente entendida en términos cualitativos, puesto que las simulaciones numéricas llevadas a cabo son una simple idealización de un problema real (granos bidimensionales, fractura intergranular) de una roca también idealizada (roca cristalina no porosa, isotrópica y con tamaño de granos uniformes).

Como cabía esperar, el efecto entalla resulta claro y significativo tanto en los resultados experimentales de los ensayos de flexión en cuatro y tres puntos como en los resultados numéricos obtenidos a partir de elementos discretos. En todos ellos, se observa como la tenacidad a fractura aparente aumenta con el radio de entalla a partir de un determinado tamaño. Esto implica que la resistencia a la propagación de la fisura aumenta con el tamaño del defecto al producirse una menor concentración de tensiones y, por tanto, la resistencia global del componente también aumenta. Se observa también que por debajo de un determinado radio de entalla (del orden de la distancia crítica de cada material), el efecto entalla es prácticamente despreciable, pudiendo asumirse que en esos casos los defectos tipo entalla se comportan de manera similar a los defectos tipo fisura. Nuevamente, el mármol de Carrara supone una excepción. En este caso no se observa ningún efecto entalla claro, probablemente como consecuencia del comportamiento no lineal. Por otro lado, la temperatura parece no tener influencia en el efecto entalla de las rocas, observándose que la tenacidad a fractura aparente aumenta de forma similar independientemente de la misma.

Para la correcta aplicación de la TDC y el criterio DED a diferentes temperaturas, se ha analizado también la influencia de ésta sobre las principales propiedades mecánicas de las rocas. Así, se han distinguido dos mecanismos principales: en aquellas rocas con porosidad significativa, se observa un incremento de la resistencia a tracción y la tenacidad a fractura aparente hasta una cierta temperatura crítica. Este

incremento de la resistencia está asociado al cierre parcial de los poros y microfisuras preexistentes como consecuencia de la dilatación de los granos durante las primeras fases del calentamiento. Sin embargo, una vez alcanzada una cierta temperatura, la dilatación progresiva y diferencial de los granos genera nuevas microfisuras que conllevan una disminución de la resistencia. Por este motivo, en el caso de las rocas sin porosidad y, por tanto, sin espacio interior para la dilatación de los cristales o los granos, se observa una clara disminución de la resistencia desde el inicio del calentamiento. Se concluye que, en el rango de temperaturas analizado, el comportamiento global de la roca se encuentra fuertemente condicionado por los micromecanismos producidos, no habiéndose observado cambios aparentes en la composición microstructural.

En definitiva, la validación de la TDC y el criterio DED en el ámbito de la mecánica de rocas, ofrece dos herramientas de fácil uso para la predicción y evaluación de la fractura en este tipo de materiales de forma precisa. Ambas metodologías requieren únicamente parámetros fácilmente estimables mediante ensayos estandarizados y habituales en la caracterización de las rocas, como son la resistencia a tracción y la tenacidad a fractura, y en el caso del DED, también los parámetros deformacionales (E, ν). Su aplicabilidad ha sido demostrada incluso a temperaturas de hasta 250ºC en aquellos casos con un comportamiento predominantemente elástico-lineal. Por lo tanto, ambas metodologías suponen dos herramientas con un gran potencial para el estudio y diseño más ajustado de problemas ingenieriles en los que la fractura de rocas juega un papel fundamental, permitiendo así el desarrollo de proyectos en el ámbito de la mecánica de rocas con soluciones más eficientes, con una mayor fiabilidad y un menor coste asociado.

Abstract

Rocks are probably one of the most commonly used materials in construction and, in turn, the study of their behaviour is one of the fields with the greatest uncertainty. The wide casuistry of lithologies, the heterogeneity of the rocks at different scales or the presence of different types of defects, are a result of the geological history they have undergone over millennia. This makes rocks a particularly complex material. Consequently, rock mechanics is a very active branch of knowledge in continuous development. A comprehensive understanding of rock behaviour at different scales and under different stress and thermal conditions is of interest in many engineering fields, such as civil engineering (e.g., study of slopes, foundations, rock excavations), underground engineering (e.g., tunnelling, mining) or energy engineering (e.g., oil and gas extractions, nuclear waste disposals, coal gasification, geothermal energy).

One of the main aspects characterizing a rock from a mechanical point of view is their predominantly brittle fracture behaviour. Quasi-brittle materials like rocks display very limited non-linear behaviour before failure and, therefore, crack propagation is unstable and leads to sudden fast fracture. This condition is a major issue of interest in many practical rock engineering applications, as it can lead to catastrophic failure in cracked rock masses and structures. For this reason, predicting failure is a major concern in rock mechanics, and there is a general demand for the development and validation of new tools and specific methodologies that allow the analysis and prediction of rock fracture in a precise and, preferably, simple way.

In general, the tensile strength of rocks is significantly lower than the compressive or shear strength. Consequently, it is widely accepted that crack propagation phenomena in rocks are mainly dominated by tensile/opening loading modes (mode I). This aspect is especially important in the presence of defects, since they generate localized stress concentrations and lead to premature and unexpected failure. From a rock integrity point of view, the presence of defects is unavoidable, since

rocks are undeniably discontinuous materials at all scales (from pores, grain boundaries or microcracks at the microscale, to joints, discontinuities or even perforations at the macroscale).

The most basic failure criteria assume that all materials are perfectly homogeneous, isotropic, and free of defects. Under these conditions, failure will occur when the stress exceeds the ultimate strength of the material. However, this is not what happens in reality, since a significant global strength reduction is generally observed in the presence of defects. This is why fracture mechanics arise, which considers the presence and typology of defects for the assessment of the fracture resistance of any material. Regardless of their origin, the presence of these defects in rocks plays a key role in the fracture initiation processes. However, it is important to distinguish between crack-type defects, those with a theoretically null radius, and notch-type defects, those with a finite radius. Probably inherited from the early development of fracture mechanics, there was a traditional trend to address fracture analyses from a conservative perspective, assuming that all defects behave as crack-type defects. However, today it is known that crack-type defects develop more demanding stress fields than notch-type defects. Thus, higher stress concentrations will arise at the front of a crack than at the front of a notch. As the notch radius increases, the stress concentration dissipates, and this is what is it is known as the notch effect. Proceeding on the assumption that a defect with a significant radius behaves as a sharp crack entails overly conservative designs and failure predictions in many practical situations, which highlights the need for specific analyses in each case.

Two different approaches are usually considered for the fracture assessment of notched components: the global and the local approach. The first one states that fracture occurs when the notch stress intensity factor (K_ρ) reaches a critical value (K_ρ^c) that only depends on the material and on the notch radius (ρ). This approach is analogous to that of the traditional linear-elastic fracture mechanics for cracked conditions, in which fracture occurs when the stress intensity factor of a crack reaches the fracture toughness of the material (under mode I loading conditions, $K_I = K_{IC}$). However, the use of this approach is rather limited due to the lack of analytical solutions for the definition of K_ρ.

By contrast, local failure approaches are based on the stress-strain field close to the notch tip, and may use values of a given variable (e.g., stress, strain energy, etc.) at a particular point, or values along a certain line or surrounding volume. Based on this, many fracture criteria have been proposed in fracture mechanics for predicting the onset of failure of notched samples. Among them, the most widespread methods at the moment are the Cohesive Zone Model (CZM), the Finite Fracture Mechanics (FFM), the Strain Energy Density (SED) criterion, and the Theory of Critical Distances (TCD). All the aforementioned criteria have been extensively applied for the fracture assessment of different materials under varied loading and failure conditions. However, the fracture analyses of notched components in the particular field of rock fracture mechanics are scarce and their applicability and validation in this field still requires further research. Probably, the lack of development of these methodologies in this branch of mechanics is caused by the relatively large scatter of the experimental results as a consequence of the higher degree of heterogeneity of rocks compared to metallic or polymeric materials, for example. These conditions make rocks less attractive materials (compared to other homogeneous materials) for the validation of the fracture methodologies and also make more difficult the obtention of robust conclusions.

Thus, this work aims to respond to the general demand for specific tools and methodologies for assessment of rock fracture of notched components, leaving aside the over-conservative application of ordinary fracture mechanics that have been traditionally used to deal with this problem. To do so, it is intended to study and validate the applicability of the TCD and the SED criterion in the field of rock mechanics, highlighting their advantages and limitations in this type of materials. In particular, the focus is placed on the fracture behaviour of six different rocks, namely a Floresta sandstone, Moleanos limestone, Macael marble, Carrara marble, Oolitic limestone and Biotite granite, under the presence of U-notch type defects and under different loading and temperature conditions. The first four rocks on the list were tested in the laboratory campaign performed within the framework of this doctoral thesis, while the last two rocks correspond to a previous work carried out by Cicero et al. (2014), from which the fracture data has

been reused. In any case, the six studied rocks comprise a wide casuistic of rock lithologies that enable to obtain robust conclusions about the applicability and limitations of both the TCD and the SED criterion.

Firstly, rock fracture under mode I loading conditions has been analysed based on the TCD, considering different U-shaped notch radii (varying from 0.15 mm to 15 mm) in order to characterize the notch effect. This analysis has subsequently been extended to mixed tensile and shear loading conditions (mode I+II), using the same type and size of notch radii as for mode I analyses. As an alternative to TCD, the SED criterion has also been used for mode I fracture analyses, which is an energy-based approach. Likewise, all the fracture analyses have been performed both at room temperature and at higher temperatures of up to 250ºC, which is a common temperature range in geothermal projects, for example. Therefore, this work has a strong experimental component. In total, 300 Brazilian tests, 120 uniaxial compression tests, 882 four-point bending tests on SENB specimens with variable notch radii and 395 three-point bending tests with variable notch radii and loading positions have been carried out, all of them under different temperature conditions. Similarly, 290 thermal dilatation readings and 158 thin section analyses have been performed. Based on the accomplished laboratory campaign, the influence of temperature on the main rock parameters was studied trying to explore the prospective extrapolation of the TCD and the SED criterion to high temperature conditions. In particular, the tensile strength (σ_u), the fracture toughness (K_{IC}), the compressive strength (σ_c), the Young's modulus (E), the Poisson's ratio (ν) and the thermal expansion were analysed in this work.

The TCD is a local failure criterion that consists of a group of methods with some common features, as the use of linear-elastic fracture mechanics for fracture assessment and the use of a material characteristic parameter with length units called the critical distance (L). This parameter depends on the fracture toughness (K_{IC}) and the tensile strength (σ_u) of the rocks according to the following expression:

$$L = \frac{1}{\pi}\left(\frac{K_{IC}}{\sigma_u}\right)^2 \qquad (1)$$

Among all the existing methodologies within the TCD, the Point Method (PM) and the LM (LM) are the most straightforward and widely used methods. Both the PM and the LM are applied in this work and offer relatively similar results. However, for the fracture prediction results, the focus is placed on the use of the LM. The simplest approach, the PM, states that failure occurs when the stress at a certain distance from the notch tip ($L/2$) reaches the tensile strength of the rock, while the LM states that failure occurs when the average stress over a certain distance from the notch tip ($2L$) reaches the tensile strength. Thus, the following expression define the failure criteria according to the PM and the LM, respectively:

$$\sigma(L/2) = \sigma_u \qquad (PM) \qquad (2)$$

$$\frac{1}{2L}\int_0^{2L} \sigma(x)dx = \sigma_u \qquad (LM) \qquad (3)$$

Based on the TCD, the interpretation of the notch effect is performed through the study of the apparent fracture toughness (K_{IN}). By definition, the fracture toughness (K_{IC}) of a material represents residual strength of a cracked component to crack propagation. Thus, K_{IC} stands for a cracked situation with a theoretical null radius or, at least, with a sufficiently small radius not to develop any notch effect. In essence, fracture analysis of notched components is equated to a situation in a cracked component, where the apparent fracture toughness is considered instead of the strictly real fracture toughness. The TCD proposes analytical solutions that relate K_{IN} and K_{IC} through the critical distance (L) and the notch radius (ρ), based on the stress distribution function at the notch tip proposed by por Creager & Paris (1967) and on the failure criteria established in *Equations (2)* and *(3)* for the PM and the LM respectively:

$$K_{IN} = K_{IC}\frac{(1+\rho/L)^{3/2}}{1+2\rho/L} \qquad (PM) \qquad (4)$$

$$K_{IN} = K_{IC}\sqrt{\rho/4L+1} \qquad (LM) \qquad (5)$$

These analytical expressions correspond to mode I loading conditions, where the stresses are evaluated in the notch bisector plane. However, the analysis under mixed mode (I+II) loading is not straightforward. The critical plane over which stresses are assessed and the failure criteria defined in *Equations (2)* and *(3)* are applied rotate according to the influence of the shear forces (mode II), in such a way that the critical plane is perpendicular to the maximum principal stresses. The lack of analytical solutions for mixed mode loading conditions makes it necessary to use numerical models for the definition of the stress fields and the critical plane. Once that plane is defined for a certain degree of mixicity, the application of *Equations (2)* and *(3)* for the fracture assessment is straightforward and the procedure is analogous to that of mode I loading conditions.

Unlike the TCD, the SED criterion establishes that failure conditions are achieved when the mean strain energy density ($\overline{W}$) averaged over a given control volume at the notch tip reaches a critical value (W_c) that only depends on the material:

$$\overline{W} = W_c \tag{6}$$

The control volume over which the strain energy is averaged becomes a control area (Ω) under plane strain conditions. The size of this area only depends on the material through a certain radius (R_0) that, for U-shaped notches as those studied in this work, is given by the following equation:

$$R_0 = \frac{(1+\nu)(5-8\nu)}{4\pi}\left(\frac{K_{IC}}{\sigma_u}\right)^2 \tag{7}$$

Taking as a basis this energy-based approach, Lazzarin & Berto (2005) developed the following expression for the fracture assessment of U-shaped notched components:

$$W_C = 0.785 \cdot H(\nu, R_0/\rho) \cdot \frac{\sigma_{max}^2}{E} \tag{8}$$

Equation (8) is based on the failure criterion defined by *Equation (6)* and relates the maximum stress (σ_{max}) at the notch tip at failure with a parameter H. This parameter depends on the material through the Poisson's ratio, and on the ratio between radius defining the control area and the notch radius (R_0/ρ). Thus, once the H parameter is known, the fracture load can be predicted by estimating the maximum stress that produces it (using the stress distribution function proposed by Creager & Paris, 1967, for example). In this doctoral work, different methods are proposed and compared for the application of *Equation (8)*, from the simplest option of using tabulated values of H and the corresponding extrapolations when necessary, to the numerical evaluation of H or the average strain energy density ($\overline{W}$).

Based on the obtained results, both the TCD and the SED criterion offer reasonable fracture load predictions within a range of ±20% with respect to the experimental failure load (this range is commonly used in fracture mechanics as a reference for reasonable predictions). The precision of the results is maintained even at temperatures of up to 250ºC. At this temperature range, predominantly linear behaviour has been observed in most of the studied cases. Therefore, it can be assumed that the use of linear-elastic fracture mechanics, in which both the TCD and the SED criterion are based, is valid a priori. As an exception, the case of Carrara marble stands out, which shows a non-linear behaviour even at room temperature and, consequently, the fracture predictions obtained are significantly worse. On the other hand, under mode I load conditions, the failure predictions obtained with both the TCD and the SED criterion are based on the stress distribution proposed by Creager & Paris (1967), which is theoretically only valid for long and narrow notches with a length significantly larger than its radius. However, it has been observed that, in general, the predictions obtained are reasonable even for the largest notches beyond the theoretical application range of Creager & Paris (1967). As an alternative to their analytical solution for the definition of the stress field at the notch tip, the analytically obtained fracture predictions have been compared with others derived from numerically obtained stress fields. The improvement in the observed results does not justify the workload increase required to make the predictions. Thus, the use of Creager & Paris (1967) is

considered adequate in the range of analysed notches (although the largest notches are somehow in the limit).

On the other hand, the application of the TCD for the fracture assessment of rocks with U-shaped notches and subjected to mixed mode (I+II) loading conditions has also been validated, even at temperatures up to 250ºC, as long as a predominantly linear-elastic behaviour is observed. The interpretation of the mixed mode (I+II) results by means of the TCD allows the critical distance for different degrees of mixicity to be characterised, using the stress field at the corresponding critical plane. However, to do so, numerical analyses are required.

In general, the TCD and the SED provide similar failure load predictions, especially when the critical strain energy density (W_c) is calibrated to absorb the small non-linearities of the tensile stress-strain behaviour. One of the main advantages of the SED criterion is that the strain energy density can be easily evaluated numerically through finite element analyses by using coarse meshes, and, although it is not the purpose of this work, it permits to take into account higher order terms and three-dimensional effects. Besides, once the H function is tabulated numerical analyses are no longer required and failure load predictions can be directly performed. By contrast, the main disadvantage compared to the TCD is that additional tests are required (i.e., uniaxial compression tests with strain gauge measurements), since the deformational parameters are needed. Based on the results, differences in the fracture load predictions obtained by the SED criterion and the TCD do not justify the additional workload involved by the SED approach. Indeed, the workload and cost of measuring the Young's modulus and the Poisson's ratio at temperatures above approximately 70ºC is substantial because special (and more expensive) strain gauges, adhesives and wires are required. Additionally, the complexity of performing the uniaxial compression tests at high temperatures compared to those at room temperature is also remarkable.

With regards to the TCD, the main advantage is that, once the critical distance (L) of a certain material is defined, it is straightforward to perform fracture assessments of any component made of that material. In the case of rocks, the critical distance is of the order of a few millimetres. Although slight variations are observed in the values of

L depending on the used method for its calculation (i.e., direct calculation with the analytical expression, best adjustment of the PM, best adjustment of the LM, numerical approach), the consequences of those differences are rather limited when performing fracture load predictions, as L is square rooted in the analytical solutions of both the PM and the LM (*Equations (4)* y *(5)*).

Based on the importance of the critical distance for the fracture analyses according to the TCD, the actual physical meaning of this parameter is a major issue of interest. This is still a matter of debate among the scientific community. However, L seems to be linearly related to the grain size of the rock. In the particular case of the studied rocks, it is observed that, approximately, the critical distance is slightly larger than ten times the grain size. Aiming to go deeper into this issue, the influence of grain size on the fracture initiation and critical distance has been numerically studied by means of Discrete Element Method (DEM). It is concluded from this analysis that, indeed, there is a certain linear relationship between grain size and critical distance. From the numerical models, a 1:1 correlation between both parameters has been obtained. However, it is important to note that this relationship should only be understood in qualitative terms, since the numerical simulations carried out are a simple idealization of a real problem (two-dimensional grains, intergranular fracture) of an already idealized rock (non-porous crystalline rock, isotropic and with uniform grain size).

As expected, the notch effect has proven to be evident and substantial in all the experimental results of the four-point and three-point bending tests as well as in the discrete numerical results. In all of them, it is observed how the apparent fracture toughness increases with the notch radius from a certain notch size. This implies that the resistance to crack propagation of a notched component increases with the size of the defect, as a lower stress concentration occurs. Consequently, the overall resistance of the component also increases. It is also observed that below a certain notch radius (of the order of the critical distance of each material), the notch effect is almost negligible, and it can be assumed that, in these cases, notch-type defects behave in a similar way to crack-type defects. Again, the Carrara marble is an exception, as no clear notch effect is observed, probably as a consequence

of the non-linear behaviour of this rock. On the other hand, there does not seem to be any change in the notch effect of the rocks with temperature, as the tendencies of the apparent fracture toughness against notch radius curves remain approximately parallel and only the absolute values change.

For the correct application of the TCD and the SED criterion at different temperatures, the influence of temperature on the main rock parameters has also been analysed, and two main mechanisms have been distinguished: in those rocks with significant porosity, an increase of the tensile strength and apparent fracture toughness is observed up to a certain critical temperature. This increase in strength is associated with the partial closure of pre-existing pores and microcracks as a consequence of the expansion of the grains during the initial heating phases. However, once a certain temperature is reached, the progressive and differential expansion of the grains generates new microcracks that lead to a decrease of the strength. For this reason, in the case of those rocks without porosity and, therefore, without internal space for the expansion of crystals or grains, a clear decrease of the strength is observed from the onset of the heating process. It can be concluded that, for the analysed temperature range, the global behaviour of rocks is strongly conditioned by the internal micromechanisms, and no apparent changes have been observed in the microstructural composition.

With all this, the validation of the TCD and the SED criterion in the field of rock mechanics offers two easy-to-use tools for accurate fracture predictions and evaluations in this type of materials. Both methodologies only require parameters that can be easily estimated through standardized tests (common for rock characterization), such as the tensile strength and fracture toughness, and in the case of SED criterion, also the deformational parameters (E, ν). Its applicability has been demonstrated even at temperatures of up to 250ºC in those cases with a predominantly elastic-linear behaviour. Therefore, both methodologies demonstrate a great potential for the study and more adjusted designs of engineering problems in which rock fracture plays a key role. They both allow the development of projects in the field of rock mechanics with more efficient solutions, with greater reliability and lower associated cost.

- Contents -

Chapter III – Experimental program

Chapter IV – Results and discussion

Appendix B - Apparent fracture toughness and fracture predictions with the PM

Appendix C - Results of the four-point bending test numerical models

- List of figures -

Chapter I – Introduction

Chapter II – State of the art

Chapter III – Experimental program

Chapter IV – Results and discussion

Chapter V – Discrete element analyses

Appendix B – Apparent fracture toughness and fracture predictions with the PM

- List of tables -

Chapter II – State of the art

Chapter III – Experimental program

Chapter IV – Results and discussion

Chapter V – Discrete element analyses

Appendix A - Experimental results

Appendix A.1. – Brazilian test results

Appendix A.2. – Uniaxial compression test results

Appendix A.3. – Four-point bending test results

Appendix A.4. – Three-point bending test results

Appendix A.5. – Thermal expansion measurements

Appendix C – Results of the four-point bending test models

- List of acronyms -

3PB	Three-Point Bending
3PBT	Three-Point Bending Test
4PB	Four-Point Bending
4PBT	Four-Point Bending Test
AM	Area Method
ASFE	Absorbed Specific Fracture Energy
ASTM	American Society for Testing and Materials
BBM	Block-Based Method
BC	Brazilian-type Compression
BEM	Boundary Element Method
BGD	Basic Geotechnical Classification
BT	Brazilian Test
CB	Chevron Bend
CBM	Continuum Based Method
CCCD	Centre-Cracked Circular Disc
CCNBD	Cracked Chevron Notched Brazilian Disc
CHILE	Continuous, Homogeneous, Isotropic and Linearly Elastic
CTOD	Crack Tip Opening Displacement
CZM	Cohesive Zone Model
DCA	Discrete Crack Approach
DCM	Digital Comparator Measurements
DDA	Discontinuous Deformation Analysis
DEM	Discrete Element Method
DIANE	Discontinuous, Inhomogeneous, Anisotropic and Not-Elastic
DT	Direct Tension
EFEM	Embedded Finite Element Method
EGS	Enhanced Geothermal System

EPFM	Elasto-Plastic Fracture Mechanics
FDM	Finite Difference Method
FE	Finite Elements
FEA	Finite Element Analyses
FEM	Finite Element Method
FFM	Finite Fracture Mechanics
FPZ	Fracture Process Zone
FVM	Finite Volume Method
HBM	Hottinger Baldwin Messtechnik
ICM	Imaginary Crack Method
ISRM	International Society of Rock Mechanics
LEFM	Linear Elastic Fracture Mechanics
LM	Line Method
LVDT	Linear Variable Differential Transformer
MM	Meshfree Method
MTS	Maximum Tangential Stress
MTSN	Maximum Tangential Strain
NATM	New Australian Tunnelling Method
NC	No Cooling
NMM	Numerical Manifold Method
NSIF	Notch Stress Intensity Factor
PD	Peridynamics
PM	Point Method
RMR	Rock Mass Rating
RQD	Rock Quality Designation
RSR	Rock Structure Rating
SCB	Semi-Circular Bend
SED	Strain Energy Density
SEM	Scanning Electron Microscope
SENB	Single Edge Notched Bend
SGM	Strain Gauge Measurements
SR	Short Rod
TCD	Theory of Critical Distances
TML	Tokyo Measuring Instrument Lab.
UCS	Unconfined (or uniaxial) Compressive Strength
UCT	Unconfined (or uniaxial) Compression Test
VM	Volume Method
WC	With Cooling
XFEM	Extended Finite Element Method

- List of symbols -

LATIN

$2a, 2b$	Dimensions of the major and minor axes of an elliptical crack
a	Crack or notch length
a_0	Initial crack length
a_1	Real coefficient of the analytical potential functions
a_{ICM}	Imaginary crack length
a', b'	Best-fit constant parameters for the rational function of H
A	Area
A, B	Material constant parameters
b	Thickness of the specimen
b_{min}	Minimum critical thickness of the specimen
C'	Material constant
d	Microstructural distance
D	Diameter
e	Maximum edge length of the zones within the Voronoi polygons
e_o	Voltage output
E	Young's modulus (or elastic modulus)
E_e	Exciting voltage
E_0	Initial Young's modulus
E_1	Mode I total strain energy density over the control area
$E_{50,PSM}$	Tangent Young's modulus at 50% of the peak load under plane strain conditions
E_r	Expended energy
$E_{s,50\%}$	Secant Young's modulus at 50% of the peak load
$E_{t,50\%}$ (or E_{50})	Tangent Young's modulus at 50% of the peak load

$f_{ij} \cdot g_{ij}$	Angular functions by Filippi et al. (2002)
$f_{ij}^{I}(\theta), \xi_i^{I}(\theta)$	Mode I characteristic orientation functions
$f_{ij}^{II}(\theta), \xi_i^{II}(\theta)$	Mode II characteristic orientation functions
F_a	Applied force
F (or $F_{failure}$)	Failure load
F_{EXP}	Experimentally obtained failure load
F_i	Crack initiation load
F_{PRED}	Predicted failure load
F_{SED}	Predicted failure load according to the SED criterion
F_{TDC}	Predicted failure load according to the TCD
$F(2\alpha)$	Opening angle dependent parameter in the SED expression for blunt notches
$\widetilde{F}_\lambda, \widetilde{G}_\mu, \widetilde{M}_{\lambda\mu}$	Beltrami's (1885) relationships for the total strain energy criterion
G	Energy release rate
G_c	Critical energy release rate
G_0	Shear modulus
h	Height of the specimen
H	Function in the SED expression for blunt notches
H^*	Function H in the case of mixed mode loading
I_1	Mode I function in the SED expression for sharp V-notches
$I_\lambda, I_\mu, I_{\lambda\mu}$	Integrals in the application of SED to blunt notches
jc, jd, jf, jt	Joint cohesion, dilatation angle, friction angle and tensile strength
jkn, jks	Joint normal and shear stiffnesses
$jresc, jrf, jrt$	Joint residual cohesion, friction angle and tensile strength
K_0	Bulk modulus
K	Stress Intensity Factor
K_C	Critical Stress Intensity Factor
K_g	Gauge factor
K_I, K_{II}, K_{III}	Mode I, mode II and mode II Stress Intensity Factor
K^u	U-shaped Notch Stress Intensity Factor
K_I^u, K_{II}^u	Mode I and mode II (U-shaped) Notch Stress Intensity Factor
K_I^V	Mode I (V-shaped) Notch Stress Intensity Factor
K_{IC}	Critical mode I Stress Intensity Factor (fracture toughness)
K_{IN}	Critical mode I Notch Stress Intensity Factor (apparent fracture toughness)

K_N	Critical Notch Stress Intensity Factor
K_t	Stress concentration factor
K_ρ	Notch Stress Intensity Factor
k^*	Stress concentration
l	Average edge length of the Voronoi polygons
l_{ch}	Material characteristic length
L	Critical distance
L_o	Span between the supporting rollers in the three- and four-point bending tests
L_{sg}	Length of the strain gauge
m	Distance of the applied load position to the notch bisector plane in the three-point bending tests
M	Geometrical dependent non-dimensional factor
M_b	Bending moment
M_e	Mode mixity
n	Number of iterations in the relaxation process during the generation of the mesh of the numerical models
P	Applied load
P^*	Pair of forces
P	Water pressure
q	Parameter linked to the V-notch opening angle
r	Distance from the crack tip
r, θ	Polar coordinate system
r, θ, z	Cylindrical coordinate system
r_0	Distance between the notch tip and the origin of the polar coordinate system
r_1, r_2	Inner and outer radii in modified tension tests
r_p	Radius defining the size of the FPZ
r_c	Radius vector of the location of failure
r, R	Inner and outer radii in sleeve fracturing tests
R	Energy required to generate a crack surface unit
R_i	Gauge resistance
R_0	Radius of the control area
R_{0_fem}	Radius of the control area considered in the calculation model
$R_1(\theta), R_2$	Radii defining the circular sector of the control area
R^2	Coefficient of determination
S	Strain energy density factor (Sih's parameter)
S_c	Critical value of the strain energy density factor

S, s_i	Spans between outer supporting rollers and inner loading points in four-point bending tests
t	Thickness of Brazilian discs
$\mathrm{u, v, w}$	Strain state according to the cartesian coordinate system
U	Stored strain energy
V	Wave velocity propagation
V	Element volume
V_p, V_s	Primary and Secondary wave velocity propagation
W_F	Work done by applied forces to deform a component
W	Absorbed specific fracture energy
$\overline{W}$	Average strain energy density
W_1	Mode I strain energy density
$\overline{W_1}$	Average mode I strain energy density
W_c	Critical strain energy density
W_c^*	Calibrated critical strain energy density
W_m	Average absorbed specific fracture energy
x, y, z	Cartesian coordinate system
x'	Distance from the point halfway between the notch tip and its centre radius
X_c	Material characteristic distance
X_{ef}	Effective distance
X_m	Distance between the extended horizontal line drawn from the maximum stress and the extension of the line corresponding to Region III in a bi-logarithmic representation of the stress distribution at the notch tip
X_{pz}	Process distance
Y	Geometry dependent non-dimensional factor
z	Lever arm
z_{min}	Smallest width of the zone adjacent to the joint in the normal direction (within Voronoi polygons)

GREEK

2α	V-notch opening angle
α	Constant dependent on the notch radius
α_0	Relative crack length
α_{temp}	Thermal expansion coefficient
β	Degree of multiaxiality
γ	Supplementary angle ($\gamma = \pi - 2\alpha/2$)
δ	Angle from the notch bisector plane
δ^*	Critical plane

ε	Strain
ε_a	Axial strain
ε_d	Diametric strain
ε_H	Horizontal strain
ε_V	Vertical strain
λ_1	Mode I Williams' (1952) eigenvalues for stress distribution at V-notches
μ_1	Mode I exponent in Fillipi's stress equation (Filippi et al., 2002)
ν	Poisson's ratio
ρ	Notch radius
ρ_{fem}	Notch radius considered in the calculation model
ρ_r	Rock density
σ	Stress
σ_0	Inherent strength
$\sigma_1, \sigma_2, \sigma_3$	Principal stresses
σ_c	Uniaxial compressive strength
σ_{ef}	Effective stress
σ_f	Material strength
σ_{ij}	Stress state
σ_{ij}^c	Critical stress state
σ_n	Normal stress
σ_N	Nominal stress
σ_{max}	Maximum stress
$\sigma_r, \sigma_\theta, \sigma_z, \tau_{r\theta}$	Stress state according to the cylindrical coordinate system
σ_{tip}	Stress at the notch tip
σ_u	Ultimate tensile strength
σ_V	Vertical stress
$\sigma_x, \sigma_y, \sigma_z, \tau_{xy}$	Stress state according to the cartesian coordinate system
σ_{Yield}	Yield stress
τ	Shear stress
$\chi_{b_1}, \chi_{c_1}, \chi_{d_1}$	Linearly dependent terms in Filippi's stress equations (Filippi et al., 2002)
ω	Energy density
$\widetilde{\omega}_1$	Auxiliary parameter in Filippi's stress equations (Filippi et al., 2002)
ω_c	Critical energy density
Ω	Control area

- Chapter I -
Introduction

1 INTRODUCTION

Rocks are by far one of the most common materials in many engineering fields such as underground engineering, civil engineering or energy engineering, and, in turn, one of the materials generating the greatest headaches among engineers when analysing rock-related engineering problems, due to their characteristics, peculiarities and the involved uncertainties.

Rocks are inhomogeneous and present a huge variety in composition and mechanical properties, probably with a broader casuistic than any other construction material. Besides, they also present an enormous diversity in the structure and occurrence of discontinuities and defects, and their behaviour when subjected to any action can be deeply influenced by a great amount of external agents such as pressure, temperature, presence of water and a large etcetera.

Reliable and accurate tests to characterise such a complex material are not feasible, or at least very difficult to carry out with today's techniques and tools. Consequently, rock engineering is based mainly on rather limited input data determined from observations and simplified or idealised measurements of the rock mass or intact rock.

In this regard, it is worth mentioning here a citation of Hoek & Brown (1980) that, even if it was asserted 40 years ago, it is still perfectly valid today:

> *"In view of the scarcity of reliable information on the strength of rock masses and of the very high cost of obtaining such information, it is unlikely that a comprehensive quantitative analysis of rock mass strength will ever be possible. Since this is one of the key questions in rock engineering, it is clear that some attempt should be made, whatever information is available, to provide some form of general guidance on reasonable trends in rock mass strength."*
>
> Evert Hoek & Edwin T. Brown (1980)

The quality of the input data determines to a great extent the success and optimization of any engineering design. Proctor (1971) showed that the estimated cost of an underground excavation and drilling depends more upon geological data than does any other type of civil engineering work. The same statement is also claimed by Bieniawski (1984) in the following quotation:

> *"It is extremely important that the quality of the input data matches the design requirements. Obviously, it must be realized that if incorrect input parameters are employed, incorrect design information will result. Speaking in computer jargon, the following expression would be appropriate: 'garbage in, garbage out'."*
>
> Bieniawski (1984)

Although extensive investigation and a proper characterization of rock will generally improve the quality of the geological input data to be applied in evaluations, assessments or calculations of engineering designs, there are always important sources of uncertainty that must be assumed by engineers. Uncertainties can be caused by innate spatial variability of geological formations, where the role of engineer interpretation is crucial, by errors introduced in measuring and estimating engineering properties, often related to sampling and measurements that might not be representative enough, by inaccuracies

caused by modelling physical behaviour, or by omissions of variables that should not be neglected in an analysis. For instance, Einstein & Baecher (1982) remarked that uncertainties in rock mechanics are inevitable and the importance of knowing how to face them:

> *"In thinking about sources of uncertainty in engineering geology, one is left with the fact that uncertainty is inevitable. One attempts to reduce it as much as possible, but it must ultimately be faced. It is a well recognized part of life for the engineer. The question is not whether to deal with uncertainty, but how?"*
>
> Herbert H. Einstein & Gregory B. Baecher (1982)

As a consequence of the foregoing, there is a general demand for the development of simple and accurate tools and methodologies for the assessment of rock fracture behaviour in many engineering fields: simple because of the lack of sophisticated data in many practical situations, unless specific analyses are performed generally with research purposes; and accurate because of the need for optimization of engineering designs in which the excavation and drilling of rock represents one of the most important economic items that can even compromise the viability of a certain engineering project. A comprehensive understanding of rock fracture processes is therefore a major issue of interest in civil engineering (e.g., slopes, foundations, rock excavations, rock cutting processes), underground engineering (e.g., tunnelling, mining, well stability analyses, hydraulic fracturing) or energy engineering (e.g., gas-oil extractions, coal gasification, nuclear waste disposal, geothermal energy).

The fracture initiation is affected to a great extent by the boundary conditions that are not linked to the rock mass or intact rock itself (e.g., external loads, presence of water). However, other microstructural and macrostructural aspects such as rock composition and minerology (e.g., grain size, grain bonding) or the presence of different scale defects (e.g., pores, discontinuities, joints, holes, cracks, notches) also play a key role in the fracture processes. In fact, the brittle condition of intact rocks, their high inherent strength and their low toughness make them a very sensitive material to the presence of any defect.

One of the main aspects characterising a rock from a mechanical point of view is the predominantly brittle fracture behaviour. This condition makes crack propagation within rocks unstable and leads to sudden fast fracture. The main fatal consequence associated with this type of behaviour is the potential catastrophic failure of rock masses and structures without previous warning, which might be prompted by the presence of defects.

From an integrity point of view, these defects act as stress risers, generating stress concentrations in their surroundings, which contributes to crack initiation and propagation. Almost 75 years ago, Terzaghi (1946) already highlighted the importance of defects in rock, even though fracture mechanics is a relatively recently developed branch of knowledge.

> *"From an engineering point of view, a knowledge of the type and intensity of the rock defects may be more important than of the types of rocks which will be encountered"*
>
> Karl Terzaghi (1946)

Fracture mechanics is a discipline dedicated to the study of the critical conditions in front of a defect from which fracture of the material is developed. There are different fracture approaches depending on the kind of stress riser being analysed. In this sense, notch-type defects develop a higher load bearing capacity than crack-type defects, since they generate less demanding stress fields around them. It is a common practice in traditional fracture mechanics to assume a crack behaviour even in the case of notch-type defects. This approach might be sufficiently accurate in cases with relatively small notches but implies overly conservative results in other cases in which the notch effect is not negligible. This over-conservative working assumption is inherited from linear elastic fracture mechanics and highlights the need to develop new precise methodologies for rock fracture assessment and predictions.

Linear elastic fracture mechanics is a fully developed and validated discipline used for the analysis, among other issues, of brittle failure of cracked components. However, this discipline presents certain limitations for the analysis of notched components. Numerous studies

can be found in the last decades aiming to analyse stress fields under notched conditions, to provide failure load predictions, and to extend linear elastic fracture mechanics to notch analyses. Among them, the focus in this work is on the Theory of Critical Distances (TCD) and the Strain Energy Density (SED) criterion, due to their potential and validation in the analysis of different materials like steels or polymers, for example.

Finally, in several underground engineering fields such as coal mining, geothermal energy, nuclear waste disposal or deep rock drilling, the influence of temperature in rock fracture behaviour might not be negligible. The mechanical characteristics of rocks can vary significantly with a moderate increase of temperatures up to approximately 250ºC for example, which is an expected range for conventional high-level radioactive waste disposal (Ramspott et al., 1979) and for conventional or hot fracture rock geothermal energy systems (Ranjith et al., 2012). For instance, projects dealing with the Enhanced Geothermal System (EGS) technology have broadly been developed and spread since the 1970s (McClure & Horne, 2014). In EGSs, hydraulic fracturing is used to improve well productivity and injectivity in conventional geothermal resources where massive rock blocks are found at moderate or relatively high temperatures up to around 250ºC. For this reason, it is important to study the applicability and limitations of the aforementioned methodologies under moderate temperature conditions, aiming to offer suitable methodologies adapted to the particular characteristics common in rock mechanics, such as temperature.

The main objectives of this thesis will be pointed out in *Section 2*, which tries to address the concerns described above in the frame of rock fracture mechanics. *Section 3* collects the list of publications derived from the present research work. Finally, the structure of the present document and the work outline will be described in *Section 4*.

2 OBJECTIVES

This work aims to study the fracture behaviour of rocks under the presence of notched-type defects and under different loading and temperature conditions, as those common in geothermal applications for example. To do so, the applicability of two different methodologies is

studied, the Theory of Critical Distances and the Strain Energy Density (SED) criterion. They are both local failure criteria, but the SED criterion implies an energy-based approach. These methods have been widely validated in the fracture analyses of different materials but their applicability in the particular field of rock mechanics still requires further research. For this reason, the study is focused on six different isotropic intact rocks, all of them with a relatively uniform microstructure, aiming to simplify the analyses and reduce the scatter of the results.

Both the TCD and the SED criterion take as a basis the stress field around the defects and only require basic rock parameters for the assessment of rock fracture predictions, which can be easily determined in the laboratory from simple and standardized tests. This greatly facilitates the application and validation of both methodologies, since complex parameters that might be difficult (or expensive) to be obtained or could lead to important sources of uncertainty are not required.

It is generally accepted that crack propagation phenomena in rocks are mode I dominated. This is caused by the relatively small tensile resistance of rocks that makes them highly sensitive to opening loading (mode I) conditions. For this reason, the applicability of the TCD and the SED criterion under mode I loading condition is studied first in this work. However, rock masses are usually subjected to complex loading conditions and the defects within the rock are randomly orientated. For this reason, in many practical situations, the influence of combined opening-sliding shear deformations (i.e., mixed mode I+II) needs to be studied. Consequently, after validating the use of the TCD and the SED criterion for the mode I loading, the extension of the TCD to mixed mode I+II is also analysed. However, the study of the applicability of the SED criterion under mixed mode loading conditions is left for future research.

Additionally, the influence of temperature is considered as a variable in this research, aiming to validate the applicability of the proposed methodologies under moderate temperature conditions up to 250ºC. To do so, the influence of temperature on the main rock parameters is studied trying to explore the prospective extrapolation of the TCD and the SED criterion to moderate temperature conditions.

Thus, this work aims to respond to the general demand for specific tools and methodologies for assessment of rock fracture of notched components, leaving aside the over-conservative application of ordinary fracture mechanics that have been traditionally used to deal with this problem.

With all this, the specific objectives of this work are summarised and listed below:

- Validation of the TCD for the fracture analysis of U-shaped notched rocks under mode I loading conditions at room temperature and at moderate temperatures up to 250ºC.
- Extension of the TCD for the fracture analysis of U-shaped notched rocks under mixed-mode I+II loading conditions at room temperature and at moderate temperatures up to 250ºC.
- Validation of the SED criterion for the fracture analysis of U-shaped notched rocks under mode I loading conditions at room temperature and at moderate temperatures up to 250ºC.
- Analysis of temperature influence on main rock mechanical parameters within a range of temperatures from 20ºC to 250ºC.
- Analysis of the physical meaning of the critical distance (L) of rocks (key parameter according to the TCD).
- Analysis of the grain size influence on main rock parameters and interpretation according to the TCD, specially on the critical distance (L).

For a clearer picture of the studied subtopics, *Figure I-1* represents a flowchart with the main subjects and the general structure of the performed rock fracture analyses, which are later developed in more detail throughout the document. Basically, after analysing the individual experimental results, their interpretation is performed through the TCD and the SED criterion. In parallel, several discrete numerical analyses are performed, also based in the TCD for the interpretation of the fracture analyses.

The numbers indicated in the flowchart correspond to the published scientific journal papers for each topic, all of them derived from this doctoral thesis work. These numbers are then specified in *Section 3.1.*, indicating the authors, title and journal of the publications.

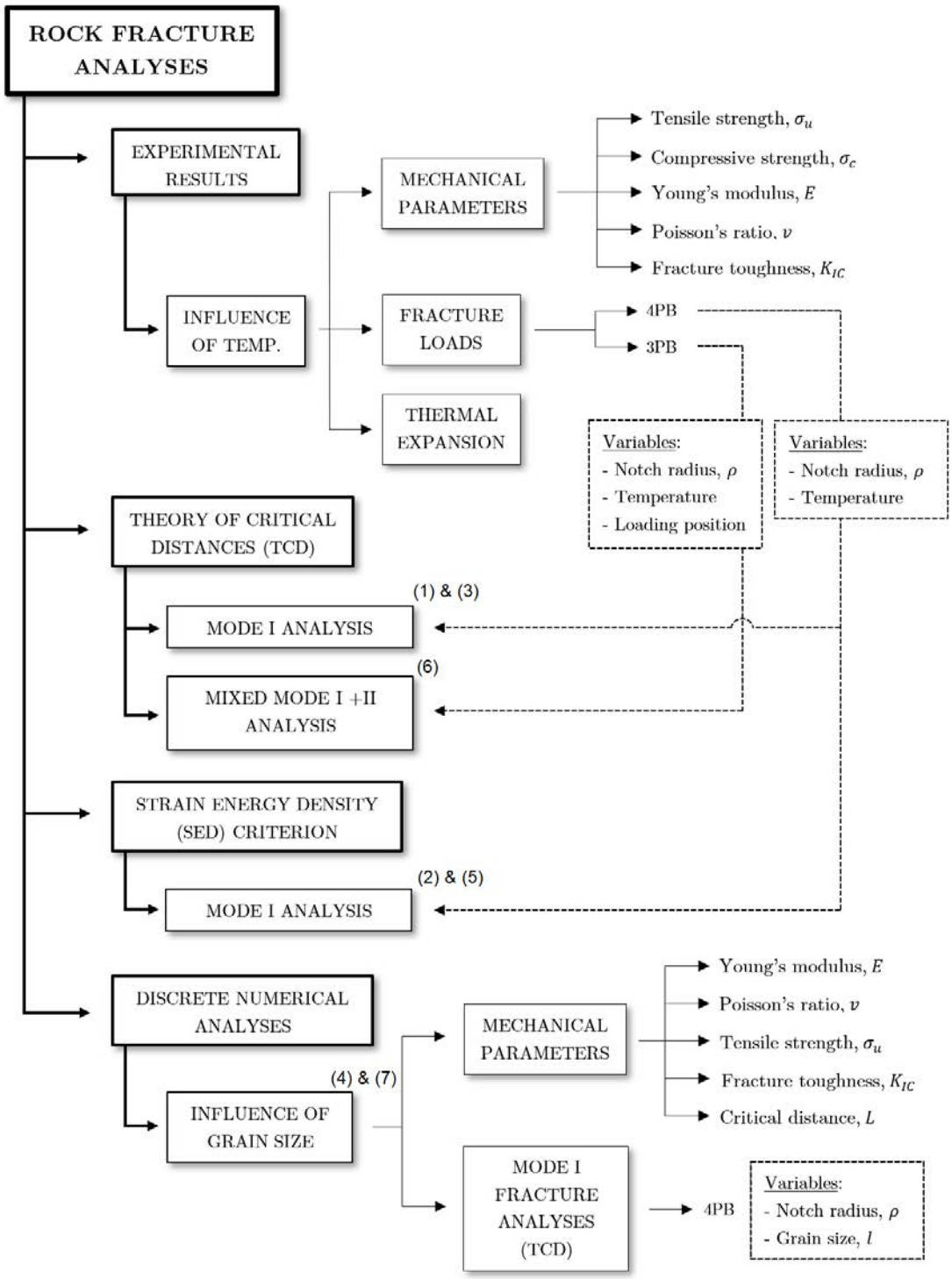

Figure I-1. Flowchart of the main subtopics of the thesis. Each of the indicated numbers correspond to a published scientific journal paper according to the numbering specified in Section 3.1.

3 PUBLICATIONS

A number of publications, including peer-reviewed papers and conference contributions, have arisen from this investigation and related works. These publications are listed below:

3.1 SCIENTIFIC JOURNAL PAPERS

- Justo, J.; Castro, J.; Cicero, S.; Sánchez-Carro, M.A.; Husillos, R. (2017) Notch effect on the fracture of several rocks: Application of the Theory of Critical Distances. Theoretical and Applied Fracture Mechanics, 90:251-258.(1)
- Justo, J.; Castro, J.; Cicero, S. (2018) Energy-based approach for fracture assessment of several rocks containing U-shaped notches through the application of the SED criterion. International Journal of Rock Mechanics and Mining Sciences, 110:306-315.(2)
- Justo, J.; Castro, J.; Cicero, S. (2020) Notch effect and fracture load predictions of rock beams at different temperatures using the Theory of Critical Distances. International Journal of Rock Mechanics and Mining Sciences, 125:104161.(3)
- Justo, J.; Konietzky, H.; Castro, J. (2020) Discrete numerical analyses of grain size influence on the fracture of notched rock beams. Computers and Geotechnics, 125:103680.(4)
- Justo, J.; Castro, J. (2020) Mechanical properties of 4 rocks at different temperatures and fracture assessment using the strain energy density criterion. Geomechanics for Energy and the Environment, 100212.(5)
- Justo, J.; Castro, J.; Cicero, S. (2020) Application of the theory of critical distances for the fracture assessment of a notched limestone subjected to different temperatures and mixed mode loading conditions. *Under review.*(6)
- Justo, J.; Castro, J.; Konietzky, H. (2020) Voronoi based discrete element analyses to assess the influence of the grain size on the apparent fracture toughness of notched rock specimens. *To be submitted.*(7)

3.2 CONFERENCE CONTRIBUTIONS

- Justo, J.; Castro, J.; Cicero, S.; Sánchez-Carro, M.A.; Husillos, R. (2017) Notch effect on the fracture of several rocks: Application of the Theory of Critical Distances. In: International Symposium on Notch Fracture (ISNF 2017), 29th – 31st March, Santander, Spain. 135-142 [Proceedings and Presentation].
- Justo, J.; Castro, J.; Sagaseta, C. (2017) Finite element analyses for fracture assessment on rocks containing U-shaped notches: An energetic continuum approach. In: European Plaxis User's Meeting (EPUM 2017), 18th – 19th May, Schrobenhausen, Germany. [Presentation].
- Justo, J.; Castro, J.; Sagaseta, C. (2018) Application of the Theory of the Critical Distances and the Strain Energy Density criterion for rock fracture prediction at different temperatures. In: Winter School on Geomechanics for Energy and the Environment, 23rd – 25th January, Villars-sur-Ollon, Switzerland. [Presentation].
- Justo, J.; Castro, J.; Cicero, S.; Sánchez-Carro, M.A.; Sagaseta, C. (2018) Comparison between an energetic continuum approach and a local failure criterion for rock fracture predictions. In: European Rock Mechanics Symposium (EUROCK 2018), Geomechanics and Geodynamics of Rock Masses, 22nd - 26th May, Saint Petersburg, Russia. 1203-1208 [Proceedings and Presentation].
- Justo, J.; Castro, J.; Sagaseta, C. (2018) Finite Element Analyses for the fracture assessment of rocks through an energetic approach: application of the SED criterion. In: 26th European Young Geotechnical Engineers Conference (EYGEC 2018), 11th – 14th September, Graz, Austria. 131-140 [Proceedings and Presentation].
- Justo, J.; Castro, J.; Cicero, S.; Sánchez-Carro, M.A. (2018) Influence of temperature on the fracture toughness of several rocks. In: 1st International Symposium on Energy Geotechnics (SEG 2018), 25th – 28th September, Laussane, Switzerland. 352-359 [Proceedings and Presentation].

- Justo, J.; Castro, J.; Sagaseta, C. (2019) Análisis mediante elementos finitos para la evaluación de la fractura de rocas a través de un enfoque energético. Aplicación de la teoría DED. (In Spanish). In: Conferencia anual de la Sociedad Española de Mecánica de Suelos e Ingeniería Geotécnica (SEMSIG 2019), Madrid, Spain. [Presentation].
- Justo, J.; Lagüera, A.; Castro, J.; Miranda, M.; Sagaseta, C. (2019) Influence of temperature on the tensile strength of a limestone and a marble. In: Geotechnical Engineering foundation of the future, XVII European Conference on Soil Mechanics and Geotechnical Engineering (ECSMGE 2019), 1st – 6th September, Reykjavic, Iceland. 1-8 [Proceedings and Presentation].
- Justo, J.; Castro, J. (2019) Application of the theory of critical distances for the fracture prediction of rocks at different temperatures and containing U-shaped notches. In: Rock Mechanics for Natural Resources and Infrastructure Development. 14th International Congress on Rock Mechanics and Rock Engineering (ISRM 2019), 13rd - 18th September, Foz do Iguassu, Brazil. 1242-1249 [Proceedings and Presentation].
- Justo, J.; Castro, J.; Konietzky, H.; (2020) Voronoi based discrete element analyses to assess the influence of the grain size on the apparent fracture toughness of notched rock specimens. In: 54th US Rock Mechanics/Geomechanics Symposium, American Rock Mechanics Association (ARMA 2020), 28th June – 1st July, Golden, Colorado, EEUU. 20-1467 [Proceedings].

4 WORK OUTLINE

This work is framed within the field of "Rock Fracture Mechanics" and, hence, stands for the subdiscipline of "Fracture mechanics" dealing with the particularities of "Rock Mechanics" (*Figure I-2*). Accordingly, Chapter II comprises the state of the art with the review of these two subfields of mechanics, describing the principal aspects necessary for the contextualization of the present work. Firstly, a brief overview on rock mechanics is provided, indicating the main particularities of rocks as a material, their classification systems and some important comments on

rock behaviour. Secondly, a theoretical review on fracture mechanics is provided, including a description of failure modes, failure criteria, analyses of defects (i.e., crack-type defects and notch-type defects) and stress fields around them, and a detailed definition of the two methodologies used in this study (i.e., TCD and SED criterion). Finally, some comments on the use of numerical analyses in rock fracture mechanics are also included.

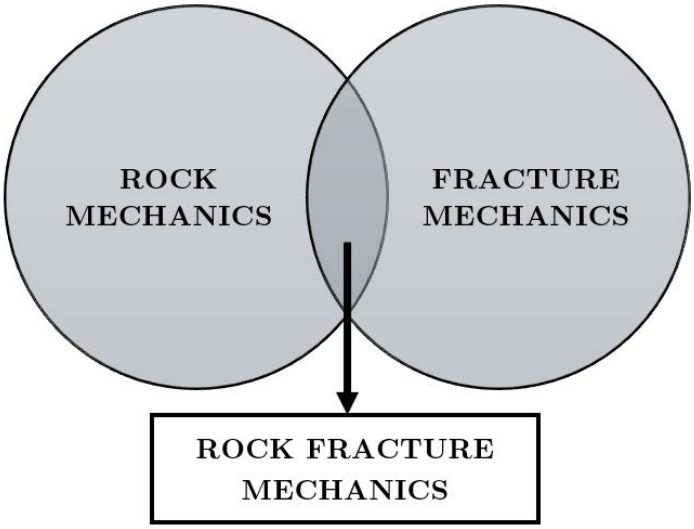

Figure I-2. Conceptual framework of rock fracture mechanics.

Chapter III describes the performed experimental program, providing a full description of the analysed rock materials, which include a broad casuistic of lithologies and characteristics, as well as the tests carried out for the definition of the main rock parameters and for the obtention of the fracture data required for the validation of the proposed methodologies.

Subsequently, Chapter IV provides the analysis of the results and the corresponding discussion. First, the direct experimental results are presented, highlighting the observed trends, and then, the interpretation of the results according to both the TCD and the SED criterion is analysed in detail.

Additionally, Chapter V focuses on the performed numerical analyses based on Discrete Element Methods (DEM), aiming to study the

influence of grain size on the fracture behaviour of an idealised rock and interpreting the results according to the TCD.

Finally, Chapter VI provides the main conclusions of the research and the potential future lines of research that may derive as an extension of the present study.

- Chapter II -
State of the art

As indicated in Chapter I, this work is framed within rock mechanics and fracture mechanics fields. For this reason, the state of the art of each of these two disciplines is developed starting from basic concepts. This way, the present work aims to be self-contained so that it might be of interest for those with a rock mechanics background with scarce knowledge on fracture mechanics and vice versa.

1 ROCK MECHANICS

1.1 INTRODUCTION

The Committee on Rock Mechanics of the Geological Society of America defined 'Rock Mechanics' as the theoretical and applied science of the mechanical behaviour of rocks, being the branch of mechanics concerned with the response of rock to the force fields of its physical environment (Judd, 1964). This definition is rather broad from a scale point of view, as it comprises from the microscale study of the strain mechanisms of mineral crystals subjected to high stresses and temperatures to the macro-scale study of the tunnelling processes, for example. Besides, this branch of mechanics is limited on one extreme with soil mechanics, when rocks are sufficiently weathered or fragmented, and, on the other hand, at depths at which the rocks are no

longer accessible to mining or drilling, it grades into the mechanical aspects of structural geology (Pollard & Fletcher, 2005).

Similarly, the term 'Engineering Rock Mechanics' stands for the particular approach of rock mechanics within an engineering context, rather than in the context of natural processes that occur in the Earth's crust. Thus, when rock mechanics is studied in isolation, there is no specific engineering objective and, for example, the potential collapse of a rock mass is just a mechanical fact. However, rock engineering applies a subjective element to rock mechanics as there is always an engineering objective. Following the same example of the collapsing rock mass, when this is part of a roof of a engineering cavern, there is an adverse engineering connotation, but when the collapse is part of a block caving system in mining, there is a beneficial engineering implication.

Rock engineering problems involve a huge casuistic of rock lithologies that depend on their origin and on the different geological processes that they have undergone over millennia. The group of geological processes define the geological history of a certain area, giving rise to a particular lithology, to a certain series of geological structures and to a characteristic in-situ stress state. These conditions can vary significantly at a regional or local scale, or even within a certain work site. Thus, rocks have a strong heterogeneous component at different scales.

The scale turns out to be an important factor in any rock engineering problem. For this reason, a distinction is normally made between intact rock, that without discontinuities, and the rock mass, with discontinuities. The mechanical properties of an undisturbed rock sample tested at the laboratory may be different from the mechanical properties of the rock mass from which the sample was extracted (see *Figure II-1*).

Rocks are quite different from other structural materials used in civil engineering, at the same time being one of the most common construction materials in the earth's crust. A comprehensive understanding of rock behaviour at different scales is a major issue of interest in many engineering fields such as, for example, civil engineering (e.g., slopes, foundations), underground engineering (e.g., tunneling, mining) or energy engineering (e.g., gas-oil extractions, coal gasification, geothermal energy, radioactive waste disposal).

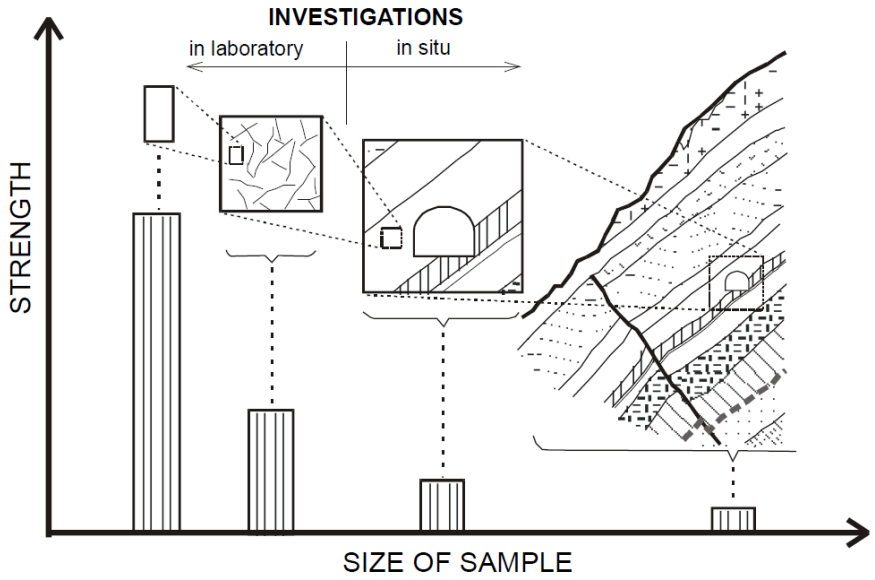

Figure II-1. The scale factor of rock masses and the variation in strength of the material depending on the size of the sample involved (Janelid, 1965).

Given the peculiarities that rocks present as a construction material, there is a general demand for accurate methods to better characterise the rock behaviour under different conditions (e.g., stress states, temperatures) and for practical guidelines to obtain successful and efficient designs to face rock engineering problems. However, the quality of the input data determines to a great extent the accuracy of the derived results, and this data is usually limited, hardly accessible, with a relatively high scatter or not representative enough.

1.2 FROM INTACT ROCK TO ROCK MASS

Intact rock is generally referred to as that from which a specimen can be extracted for a laboratory test, not presenting large scale structural characteristics such as joints, planes, layering and cracks. Most intact rock samples comprise an aggregate of crystals, grains and amorphous particles joined by different cementing materials. The chemical composition of the crystals may be relatively homogeneous, as in the case of some limestones for example, or very heterogeneous, as in a granite. Likewise, they may have uniform or variable sizes and shapes but, in any case, these crystals commonly represent the smallest scale at which the mechanical properties are studied.

Laboratory intact rock specimens usually have dimensions of centimetres and contain a sufficient number of structural particles for them to be considered as roughly homogeneous. The properties of each of the individual particles in such a specimen may differ to a great extent from one particle to another. However, although the individual crystals or grains themselves are generally anisotropic, the interaction between boundaries is sufficiently random so as to endow the specimen with average homogeneous properties. These average properties are not necessarily isotropic due to the processes of rock formation or alteration that might have a preferred orientation.

Moving from intact rocks to a larger scale, the presence of discontinuities define what is called the rock mass (see *Figure II-2*). Although the rock matrix may sometimes emerge healthy in nature, rock masses are usually broken up by joints, bedding planes/layering, foliation and faults, which, from an integrity point of view, can be considered as defects.

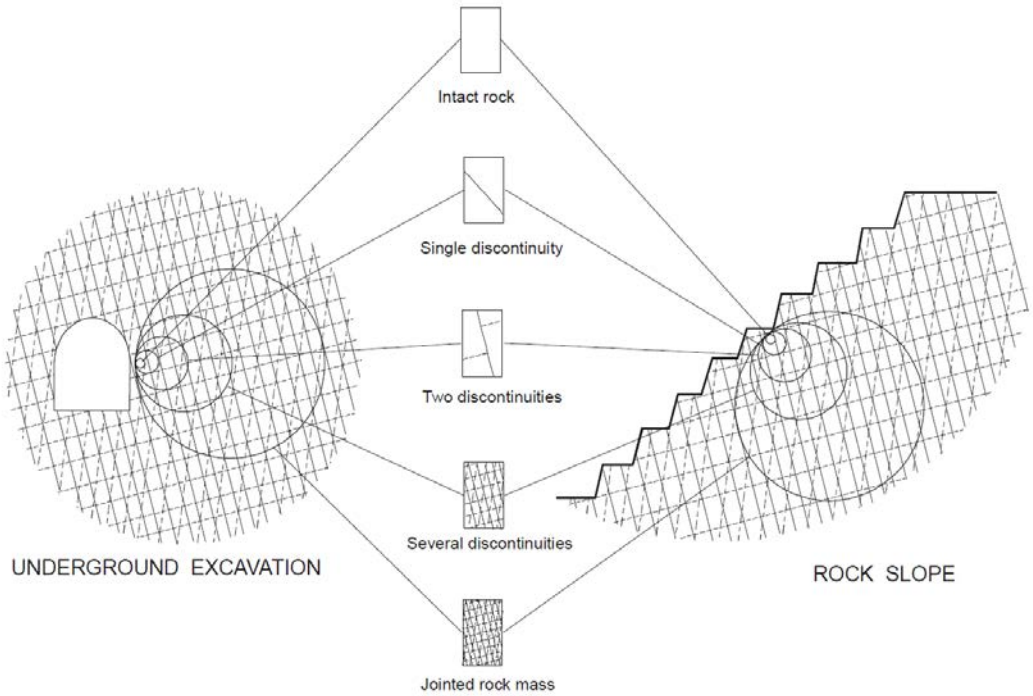

Figure II-2. Various volumes of rock masses involved in a sample, ranging from intact rock to jointed rock mass (Hoek, 1983).

Besides, what on a relatively scale of the rock mass can be considered as an intact rock block, on a laboratory scale can also show different

types of micro-defects such as pores, microcracks, grain boundaries, etc. In the end, the presence of all these defects, no matter their scale and whether they are naturally created or man-made, is irremediable and is part of the heterogeneous nature of rocks.

The importance of the discontinuities and the defects is relative, as it depends on the scale of the studied engineering problem. For example, when the stress state variation caused by any engineering performance affects to a relatively large region compared to the distance between joints (e.g., dam foundations, large underground excavations, etc.), the influence of the joint might not be negligible. However, when the distance between joints is relatively large compared to the dimensions of the work (e.g., drilling holes, well excavations, etc.), the rock behaviour might depend on the inherent properties of the rock matrix.

On the other hand, discontinuities in rock masses are a three-dimensional feature and range in lengths from less than a decimetre to several kilometres. The existing three-dimensional defects interrupt the continuity of the displacements in a rock mass and divide the bedrock into units, volumes or blocks of different scales as those depicted in *Figure II-3*. Where such disturbances are small in relation to the dimensions of a structure in rock, they alter the mechanical properties of the rock mass, but in some cases this mass can still be treated as a continuum. However, where these disturbances have significant dimensions, their effect should not be neglected and they should be treated as part of the structure or as a boundary. Thus, rock engineering problems are usually anisotropic in three dimensions and, in most of the cases, the presence of discontinuities and defects define the macro-scale behaviour of the rock masses.

Based on these conditions, there are generally two ways of thinking about and of modelling the rock mass (Harrison & Hudson, 2000) that can be summarised by two acronyms: CHILE (Continuous, Homogeneous, Isotropic and Linearly Elastic) and DIANE (Discontinuous, Inhomogeneous, Anisotropic and Not-Elastic). The CHILE approach is the simplest form as it assumes an ideal type of a not fractured material, or if it is fractured, the fracturing can be incorporated in the elastic continuum properties. By contrast, the DIANE case studies the nature of the real complex rock mass and this

is modelled accordingly, still often making gross approximations. Rock mechanics started with the CHILE approach and has now developed technics to enable the DIANE approach to be implemented (e.g., discrete numerical analyses). Both approaches have their advantages and disadvantages, and the choice of the modelling technique will depend on the particular circumstances and required information of each rock engineering problem. Regardless the used technique, it must be ensured that the relevant mechanisms and governing parameters related to the problem have been identified, for which the expertise of the engineer is necessary.

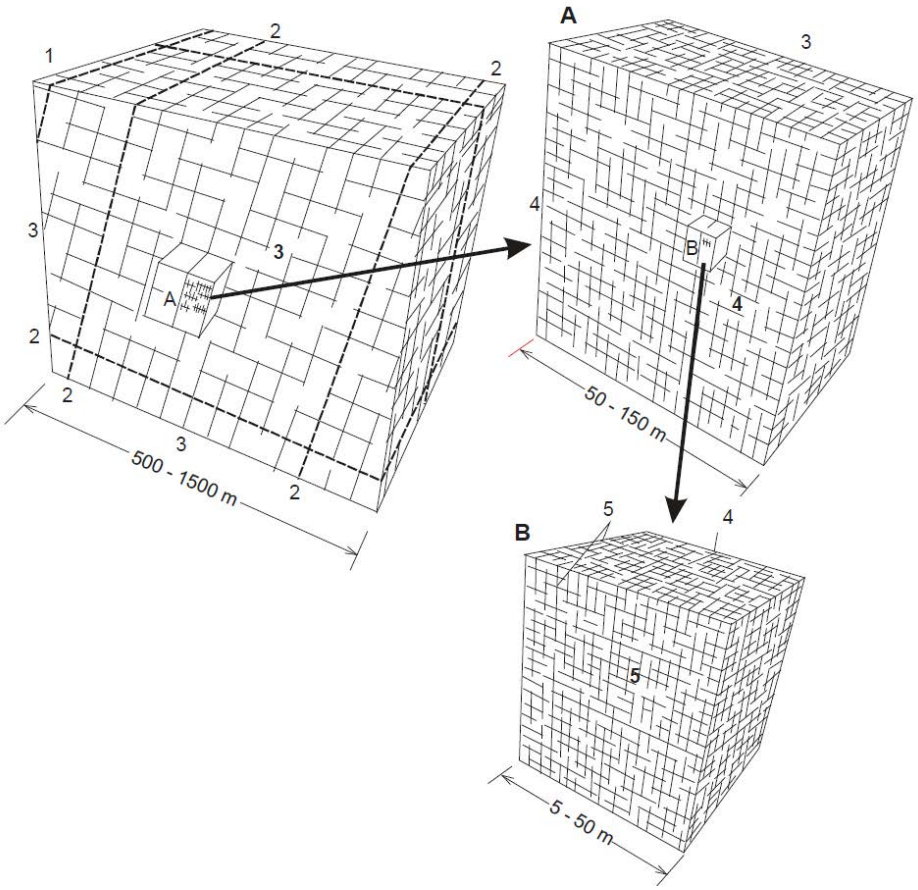

Figure II-3. Simplified representation of various dimensions units or blocks formed by discontinuities of different size (Pusch & Morfeldt, 1993).

1.3 ROCK CLASSIFICATION

Description and classification are the initial steps in an engineering assessment of rocks and rock masses. A complete specification of a rock mass requires descriptive information on the nature and distribution of

both the materials that constitute the mass (i.e., rock, soil, water and air-filled voids) and the discontinuities that divide it (Anon, 1977). The intact rock may be considered as a continuum or polycrystalline solid consisting of an aggregate of minerals or grains, whereas a rock mass may be looked upon as a discontinuous body of rock material. Consequently, a distinction is generally made to classify the intact rock and the rock mass.

1.3.1 Intact rock classification

Intact rock may be described from a geological or engineering point of view. In the first case, the origin and mineral content of the rock are the main issues of interest, together with other aspects such as texture, colour or any change which has occurred since their formation. By contrast, the engineering classification is based on the mechanical properties of the rock usually obtained in the laboratory.

1.3.1.1 Geological classification

From a geological point of view, rocks are generally classified into three basic groups, namely sedimentary rocks, igneous rocks and metamorphic rocks.

1.3.1.1.1 Sedimentary rocks

Sedimentary rocks are formed by the deposition of sediments as a consequence of the weathering of pre-existing rocks or pieces of once-living organisms. This type of rocks usually involve a transport of the sediments, which may occur by various agents, such as water (either in liquid or solid phase), wind or gravity. Consequently, sedimentary rocks often have distinctive layering or bedding. Sedimentation is the collective name for processes that cause mineral or organic particles (detritus) to settle and accumulate or minerals to precipitate from a solution. Depending on the origin of the sediments, different types of deposits can be distinguished, such as detrital deposits, when the sediments are mechanically eroded from pre-existing rocks, chemical deposits, when the sediments are formed by different chemical reactions (e.g., decomposition, precipitation, evaporation), or organic deposits, when the sediments are formed by the action of organisms (e.g., coal, some limestones).

In general, geologists have attempted to classify sedimentary rocks on a natural basis. However, no scheme has found universal acceptance

and different approaches can be found in the literature. One of the first attemps was made by L.V. Pirsson in the book *Rocks and Rock Minerals*, which was first published in 1908. Sedimentary rocks are classified there rather simplistically according to physical characteristics and composition into detrital and nondetrital rocks. Probably, the most important advances on the sedimentary rock classification ocurred in 1948 with the publications of F.J. Pettijohn, R.R. Shrock and P.D. Krynine in the *Journal of Geology*, which are still the basis for all modern discussion on the subject. Basically, three main categories of sedimentary rocks are generally distinguished: Terrigenous clastic sedimentary rocks, carbonate rocks and noncarbonate chemical sedimentary rocks.

- Terrigenous clastic sedimentary rocks are composed of detrital fragments of pre-existing rocks and minerals and are conventionally considered to be equivalent to clastic sedimentary rocks in general. They are also referred to as siliciclastic sedimentary rocks, since most of the clasts are rich in silica. Depending on the clast diameter, this group is generally subdivided into conglomerate and breccia, sandstone, siltstone and mudrock (i.e., shale, claystone and mudstone). Conglomerates and breccias are composed of coarse fragments of pre-existing rock held together by cement or by a finer-grained clastic matrix. Conglomerates are made of consolidated gravel whose clasts are subrounded to rounded, while breccias are consolidated rubble whose clasts are angular or subangular. On the other hand, sandstones are siliciclastic sedimentary rocks that mainly consist of sand-size grains bonded together by interstitial chemical cement or lithified into a cohesive rock by the compaction of the sand-size framework component together with any interstitial primary (detrital) and secondary (authigenic) finer-grained matrix component. Siltstones and mudrocks are composed, respectively, of silt- and clay-size particles.
- Carbonate rocks are chemical sedimentary rocks with, at least in part, a crystalline, interlocking mosaic of precipitated carbonate mineral grains. Limestones and dolomites, with aragonite, calcite and dolomite minerals, are included in this

group. Most carbonates show some textural affinities to the terrigenous clastic sedimentary rocks due to the habitual presence of fossil shell fragment clasts similar to transported quartz or feldspar clasts.

- Noncarbonate chemical sedimentary rocks are less common among the sedimentary rocks and include siliceous rocks (cherts), phosphate rocks (phosphorites), evaporites (rock salt and gypsum, iron-rich sedimentary rocks (iron formations and ironstones), and organic-rich (carbonaceous) deposits in sedimentary rocks (coal, oil shale and petroleum).

Due to the diversity of sedimentary rocks, other aspects such as the texture, fabric or mineralogical and geochemical composition are usually described for a complete characterization.

Texture refers to the size, shape and arrangement of the discrete grains or particles of a sedimentary rock. Two main natural textural groups are generally distinguished among the sedimentary rocks: clastic or fragmental, and nonclastic or essentially crystalline. In the first group, particle size has special interest in the characterization of clastic sedimentary rocks because it provides information on the conditions of transportation, sorting and history of the depositional site. However, in those sedimentary rocks with crystalline texture (e.g., noncarbonate chemical sedimentary rocks), the size of the crystals is controlled by the rate of precipitation and their texture is modified by postdepositional recrystallization processes. Thus, particle size does not provide such valuable information in this case. Particle shape, on the other hand, is usually defined in terms of form, roundness and surface texture for the purpose of identifying the transporting agent and the depositional environment. The particle form refers to the overall shape of particles based on relative length measurements of the longest, shortest and intermediate axes, so that they can be spherical, prismatic or bladelike. The roundness or angularity is a measure of the smoothness of the particles and, finally, surface texture refers to the presence or absence of small markings such as pits, polish or scratches that may occur on grain surfaces.

The fabric of a sedimentary rock controls the rock's porosity and, therefore, the permeability or its ability to hold or transmit fluids such

as oil and water. The orientation, if any, of the particles that make up a sedimentary rock constitutes on aspect of the fabric. Genetically, two main oriented fabrics are usually considered: the primary or depositional orientation, which is produced while the sediment is accumulating, and secondary or deformational orientation, which results from a rotation of the constituent elements under stress or from the growth of new elements during diagenesis. In addition to orientation, the packing also contributes to a rock's fabric. Packing refers to the distribution of grains and intergranular spaces, which can be empty or filled with cement or fine-grained matrix. This parameter is controlled by the grain size and shape and by the degree of compaction of a sedimentary rock, determining the rock's bulk density.

On the other hand, the minerals forming sedimentary rocks are generally divided in two principal types: detrital and authigenic. Detrital minerals, such as grains of quartz and feldspar, survive weathering and are transported to the depositional site as clasts. By contrast, authigenic minerals like calcite, halite and gypsum, form in-situ within the depositional site in response to geochemical processes.

Finally, for a complete description of a sedimentary rock, considerable attention is generally paid to the sedimentary structures at a larger scale. Sedimentary structures include features like bedding, ripple marks, fossil tracks and trails, and mud cracks. These structures are conventionally subdivided based on the mode of genesis. Those produced at the same time as the sedimentary rock itself are called primary sedimentary structures, such as bedding or stratification, graded bedding or cross-bedding. Those structures produced shortly after deposition as a result of compaction and desiccation are called penecontemporaneous sedimentary structures. Mud cracks and load casts, for example, are included in this group. Following the time scale, those sedimentary structures formed well after deposition and penecontemporaneous modification are known as secondary structures (e.g., concretions, vein fillings, stylolites). In any case, all these structures can provide valuable information on the geological history of the rock.

1.3.1.1.2 Igneous rocks

Igneous rocks are formed from the solidification of magma, either below the surface as intrusive or plutonic rocks, or on the surface as extrusive or volcanic rocks:

- Plutonic rocks make up the majority of igneous rocks and are formed from magma that cools and solidifies within the crust, surrounded by pre-existing rock. Under these conditions, the magma cools slowly and, therefore, coarse-grained rocks are formed, such as granite, gabbro or diorite. The mineral grains in such rocks can generally be identified with the naked eye.
- Volcanic rocks are formed at the crust's surface as a result of the partial melting of rocks within the mantle and crust. In this case, the magma is brought to the surface through fissures or volcanic eruptions and solidifies faster than plutonic rocks. Consequently, volcanic rocks are smooth, crystalline and fine-grained, such as basalt.

Apart from the mode of occurrence, igneous rocks are generally classified according to the texture, mineralogy, chemical composition and the geometry of the igneous body, which can provide important information on the conditions under which they were formed.

As in the case of sedimentary rocks, texture refers to the size, shape, orientation and distribution of the mineral grains or crystals of the rock. Textural criteria are especially important to classify volcanic rocks since they will determine whether the volcanic rock is named a tuff, a pyroclastic lava or a simple lava. However, the definition of texture is less important for plutonic rock classification where the majority of minerals are visible to the naked eye. Plutonic rocks also tend to be less texturally varied and less prone to gaining structural fabrics. For this reason, mineralogical classification is most often used to classify plutonic rocks while chemical information is preferred to classify volcanic rocks.

With regards to the mineral composition, feldspars, quartz or feldspathoids, olivines, pyroxenes, amphiboles, and micas are all important minerals in the formation of almost all igneous rocks, and they are basic to the classification of these rocks. The rest of minerals are generally regarded as nonessential in almost all igneous rocks and are called accessory minerals. By contrast, when modal or mineralogical

data cannot be determined due to the small grain size, chemical classification is used based on the alkali and silica contents.

1.3.1.1.3 Metamorphic rocks

Metamorphic rocks are formed from the alteration of pre-existing rocks in response to changing environmental conditions, such as temperature, pressure and mechanical stress, and the addition or subtraction of chemical components. Thus, metamorphic rocks can be derived from sedimentary, igneous or other metamorphic rocks that have suffered a recrystallization as a result of changes in their physical environment. The phenomenon that generates the recrystallization is called metamorphism and comprises changes both in minerology and in the fabric of the original rock.

These alterations can be caused either by the intrusion of hot magma into cooler surrounding rocks, which is called contact metamorphism, or by large-scale tectonic movements that alter the pressure and temperature conditions of the rocks, which is called regional metamorphism. The changing conditions make the minerals within the original rock (known as protolith) react to produce a new mineral assemblage that is thermodynamically stable under the new pressure and temperature conditions. In general, these reactions occur in solid state, although they might be facilitated by the presence of a fluid phase lining the grain boundaries of the minerals. Thus, in contrast to igneous rocks, metamorphic rocks do not crystallize from melting of the host rock.

Protolith compositions and the pressure-temperature conditions may be widely different. Consequently, the diversity of metamorphic rocks is large. Common metamorphic rocks have essentially the same chemical composition as they precursors from which they are formed. For example, common greenschists have essentially the same compositions as basalts, marbles are like limestones, slates are similar to mudstones or shales, and many gneisses are like granodiorites. Thus, the chemical composition of a metamorphic rock closely reflects the primary nature of the original rock.

Metamorphic rocks can be classified with reference to four chemical systems, namely pelitic, calcareous, felsic and mafic:

- Pelitic rocks are derived from mudstone (shale) protoliths and are rich in potassium, aluminium, silicon, iron, magnesium and water, with lesser amounts of manganese, titanium, calcium and other constituents.
- Calcareous rocks are formed from a variety of chemical and detrital sediments such as limestone, dolostone or marl, and are mainly composed of calcium oxide, magnesium oxide and carbon dioxide, with varying amounts of aluminium, silicon, iron and water.
- Felsic rocks can be produced by metamorphism of both igneous and sedimentary protoliths and are rich in silicon, sodium, potassium, calcium, aluminium, and lesser amounts of iron and magnesium.
- Mafic rocks are formed from basalt protoliths and some volcanogenic sediments and contain abundance of iron, magnesium, calcium, silicon and aluminium.

There is a huge amount of literature dedicated to the analysis of rock lithology and classification (e.g., Duncan, 1969). Here, only a general overview of the principal geological classification aspects and considerations have been provided, without the purpose of going into detail. Geological classification of rocks is mainly based on their origin, with reference to texture, fabric, composition or mineralogy. The geological name of a rock might give a rough idea of the expected rock behaviour in a rock engineering problem, due to, for example, the association that can be made between certain types of rock and other in-situ characteristics. The presence of limestone, gypsum and rock salt in a work site, for instance, may provide information about possible dissolution phenomena such as the presence of cavities or enlarged joints. However, from the perspective of engineering rock mechanics, the information provided from a geological approach is generally insufficient. Rocks with the same lithology might present an extraordinarily broad range of mechanical properties. For example, the uniaxial compressive strength of a limestone can vary from 35 to 250 MPa.

Consequently, an engineering classification of rocks based on a mechanical approach is of a major interest for the assessment of any rock engineering problem in general, and for this investigation in

particular, where the fracture behaviour of rocks with different lithologies is studied.

1.3.1.2 Engineering classification

Coates (1964), Miller (1965) and Coates & Parsons (1966) provided the basics for the classification of intact rocks based on mechanical properties obtained in the laboratory. Deere & Miller (1966) presented a modified version of Miller's first work, which is still widely used for rock classification from an engineering perspective. This classification is based on two important properties of the rock: the uniaxial (unconfined) compressive strength (σ_c) and the Young's modulus, this latter modulus being the tangent modulus corresponding to 50% of the peak load ($E_{t,50\%}$). A detailed description of the rock mechanical properties is provided in *Section 1.4*. First, the rock is classified into five categories according to its compressive strength, as indicated in *Table II-1*.

Table II-1. Classification of intact rock based on strength (Deere & Miller, 1966).

Class name	Description	Uniaxial compressive strength, σ_c (MPa)
A	Very high strength	> 225
B	High strength	112-225
C	Medium strength	56-112
D	Low strength	28-56
E	Very low strength	< 28

Only a few types of rocks fall within class A, such as quartzite, diabase, and some dense basalts, among others. Class B comprises most of igneous rocks, the hardest metamorphic rocks, well cemented sandstones, hard shales and most limestones and dolomites. Class C includes shales, porous sandstones and limestones and schist metamorphic rocks. Finally, classes D and E involve weathered rocks and low density and high porosity rocks.

The second parameter considered in this classification system is the Young's modulus. In particular, the modulus ratio is used, which is

defined as the ratio between the $E_{t,50\%}$ and σ_c. Based on this classification three categories are distinguished for high, medium and low modulus ratios, as indicated in *Table II-2*.

Table II-2. Classification of intact rock based on the modulus ratio (Deere & Miller, 1966).

Class name	Description	Relative modulus ($E_{t,50\%}/\sigma_c$)
H	High modulus ratio	> 500
M	Average modulus ratio	200-500
L	Low modulus ratio	< 200

Therefore, using this system for rock classification, two letters are assigned to a rock based on its compressive strength and modulus ratio, in such a way that, for example, BM corresponds to a high strength and medium modulus ratio rock.

It is a common practice to represent the rock in an intact rock classification diagram as those proposed by Deere & Miller (1966). These diagrams represent the uniaxial compressive strength against the Young's modulus in a double logarithmic scale. The strength classes defined in *Table II-1* are represented in the upper part of the diagram and the modulus ratio (*Table II-2*) is derived from the position with respect to two diagonal lines corresponding to 200:1 and 500:1 slopes. In general, those rocks with a compact structure and low or null anisotropy fall within the intermediate region defined by the two diagonal lines. That is, they correspond to an average modulus ratio.

Based on several experimental results, Deere & Miller (1966) tried to define delimited regions within these diagrams for different rock lithologies. *Figure II-4* represents the summary classification diagram of sedimentary rocks. It is observed that most of the limestones and dolomites correspond to strength classes B and C, with few exceptions in classes A and D for very high strength and low strength cases, respectively. Likewise, the region 1 above the 500:1 diagonal corresponds to particular compact limestones and dolomites. By contrast, the envelopes representing regions 2 and 3 corresponding, respectively, to

sandstones and shales, enter the low modulus ratio zone. This is a consequence of the anisotropy generated by stratification and schistosity. Besides, the represented regions 2 and 3 are open at the lower end because several tested samples broke below 7.5 MPa (75 kg/cm^2).

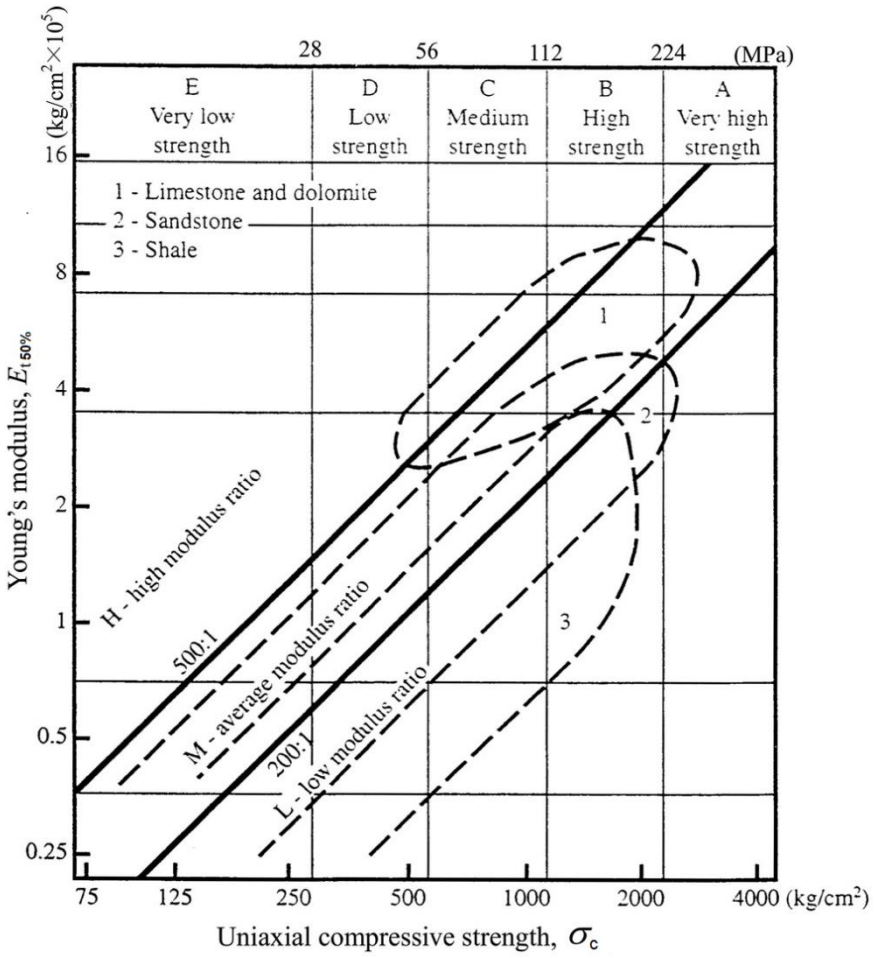

Figure II-4. Classification of intact sedimentary rocks (Deere & Miller, 1966).

Proceeding along the same way, *Figure II-5* represents the summary classification diagram of igneous rocks. Most of igneous rocks correspond to an average modulus ratio (M) with strengths that can vary from very high strength (A) to very low strength (E). Diabase, for example, consists of a dense and uniform rock with fine to medium grain size and is usually classified as AM. Granites also present a relatively low scatter and are typically classified as BM. By contrast, basalts and other

volcanic fine-grain rocks show a higher scatter on the uniaxial compressive strength as a consequence of the broad variety in mineralogy, porosity, grain size and crystalline structure. However, most of the rocks in this last group present medium or higher strengths (C, B, A) and average modulus ratios.

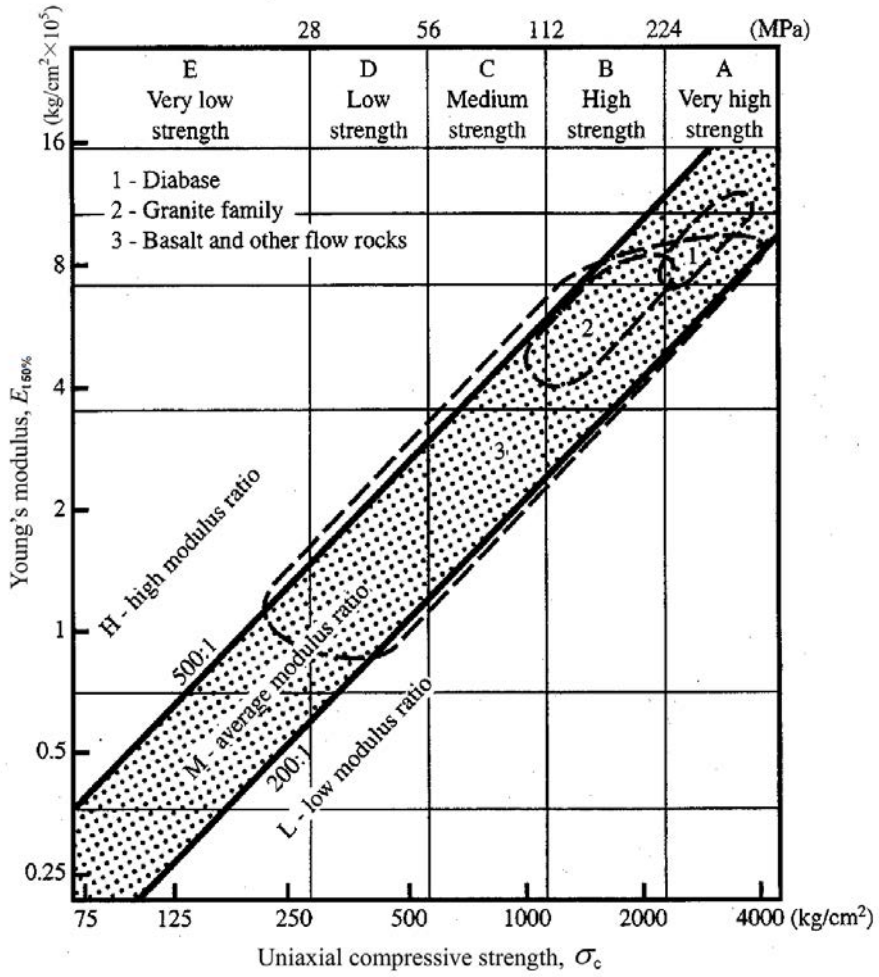

Figure II-5. Classification of intact igneous rocks (Deere & Miller, 1966).

Finally, *Figure II-6* represents the classification diagram for metamorphic rocks. The scatter of the results is higher than in the case of sedimentary and igneous rocks due to the great variation in mineralogy and degree of anisotropy. Most of quartzites are classified as AM, similarly to other dense rocks with compact structure such as diabase and dense basalts. Gneiss are comparable to granites when using this classification system, although they present a slightly lower mean compressive strength and a higher scatter of the modulus ratio as a

consequence of the variation in mineralogy and the effect of schistosity with respect to granites. Region 3 in *Figure II-6* corresponds to marbles. The represented envelope only includes a few number of samples (22 specimens), but it seems to indicate that the modulus ratio in marbles tends to be relatively high. Finally, the schists show a great variability of the results. Region 4a envelopes those schist samples with vertically oriented schistosity or foliation or, in other words, those with a steep foliation angle larger than 45º. The observed high modulus ratios in this region are generally a consequence of the relative low strength caused by the premature failures through the foliation planes with a high dip angle, rather than being an inherent property of the rock itself. On the opposite, those schists with a foliation angle lower than 45º fall within the low modulus ratio zone (region 4b). With this orientation, the compressive strength is not highly affected by the foliation, but the Young's modulus tends to reduce due to the effect of closure of the microcracks parallel to the schistosity plane.

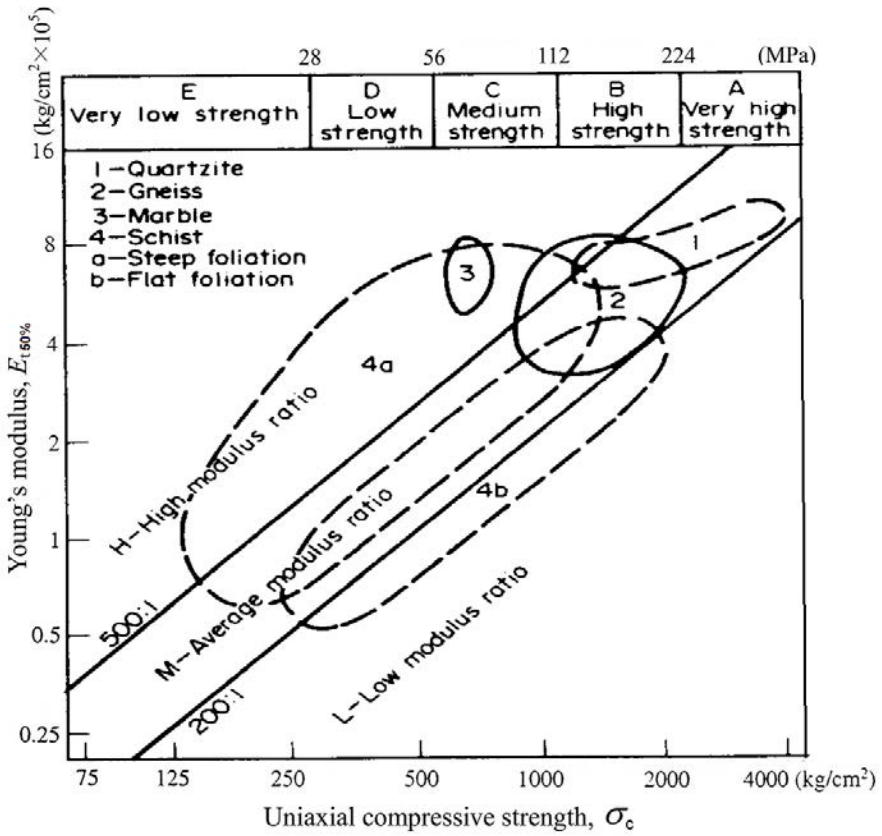

Figure II-6. Classification of intact metamorphic rocks (Deere & Miller, 1966).

This classification system provides valuable information on the behaviour of rocks and is easy to use. It is only based on the uniaxial compressive strength and Young's modulus, which are two essential physical properties in most rock engineering problems. Besides, this classification method somehow encompasses information on the mineralogy, texture, structure and anisotropy of the rock.

Identification of intact rock is reasonably straightforward because lithological descriptions are commonly used. Those descriptions also include some identification parameters, such as texture, fabric or mineralogy and chemical composition. Besides, from an engineering perspective, the uniaxial compressive strength is one of the most common geotechnical parameters to characterize the intact rock. However, the values of rock strength previously mentioned correspond to small rock samples tested in the laboratory. Those laboratory samples are not notably affected by discontinuities and, consequently, the strength and stiffness of a rock mass is generally much lower on a larger scale, as that of engineering problems. For this reason, the characterization and definition of the rock mass is also important in any rock engineering problem.

1.3.2 Rock mass classification

Contrary to intact rock, description of a rock mass is not straightforward. The International Society of Rock Mechanics (ISRM) published in 1978 some recommendations for rock mass description based on the following parameters:

[1] Joint orientation (dip and dip direction)
[2] Joint spacing
[3] Joint persistence
[4] Joint roughness or waviness
[5] Uniaxial compressive strength
[6] Weathering grade
[7] Joint aperture
[8] Joint filling or coating
[9] Water conditions
[10] Number of joint sets
[11] Block size

Among these parameters, only two ([5] and [6]) correspond to the intact rock, one to water conditions or seepage [9] and the other eight refer to joints, which highlights the importance of the discontinuities on the behaviour of a rock mass. In fact, discontinuities are the most important factor governing the deformability, strength and permeability of the rock mass. *Figure II-7* represents the listed parameters. For a detailed description of these parameters, the suggested methods for the quantitative description of discontinuities in rock masses provided by the International Society for Rock Mechanics (ISRM, 1978) is recommended.

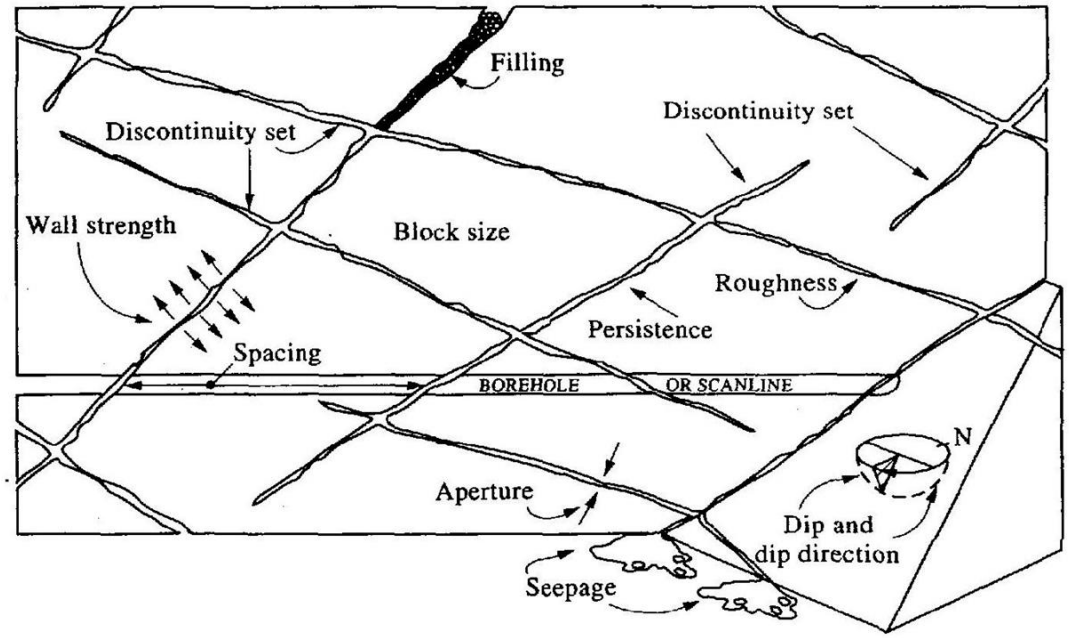

Figure II-7. Parameters for rock mass classification (Hudson & Harrison, 1997).

1.3.2.1 Geomechanics classifications

An important issue in rock mass description and characterization is to select parameters of greatest significance for the actual type of design or construction. There is no single parameter or index, which can fully designate the properties of jointed rock masses. Various parameters have different significance and only if combined can they describe a rock mass satisfactorily (Bieniawski, 1984). According to Lama & Vutukuri (1978), the engineering properties of a rock mass depend far more on the system of geological discontinuities within the rock mass than on the strength

of the rock itself. The amount of joint characteristics gathered in *Section 1.3.2* reveal the importance of joints and discontinuities in rock mass characterization. However, this does not mean that the properties of the intact rock material should be disregarded in the characterization. After all, if discontinuities are widely spaced, or if the intact rock is weak, the properties of the intact rock may strongly influence the gross behaviour of the rock mass. Besides, the properties of the intact rock highly determine the formation and development of new discontinuities. In fact, for some engineering or rock mechanics purposes, such as for example drillability or crushability, the mechanical characterization of intact rock using properties like compressive strength, hardness or anisotropy is of the utmost importance.

In order to simplify the complex reality of rock mass and provide suitable systems or models for its characterization, several classification and design systems have been developed in the past, as those collected in *Table II-3*. These geomechanics classifications are widely used to characterize and quantify the quality of a rock mass. They try to gather, in a systematic way, the knowledge and experience gained from direct observation of the performance of real construction works. To achieve that, they define a quality index of the rock mass based on the estimation of several basic parameters (as those defined above) that are easily evaluated without complex testing. That quality index may empirically be correlated with the strength and stiffness of the rock mass, or directly, with design and construction recommendations for geotechnical structures, such as tunnels, slopes and foundations.

Table II-4 indicates the main rock mass features that are applied and combined by the rock classification systems collected in *Table II-3*. It is observed that most frequently applied parameters in rock design and classification systems are the rock material (rock type, geological name, weathering and alteration, strength), the degree of jointing (joint spacing, block size, RQD) and in-situ stresses. Also characteristics such as orientation of the main discontinuities or joint sets, joint conditions, block shape or jointing pattern, faults and weakness zones, and excavation features (dimension, orientation, etc.) have been considered as important parameters in rock masses, their importance being relative to the studied rock engineering problem.

Table II-3. Main design and rock classification systems (Palmström, 1995).

Name of classification	Form and Type*	Main applications	Reference
The Terzaghi rock load classification system	Descriptive and behaviouristic form Functional type	For design of steel supports in tunnels	Terzaghi, 1946
Lauffer's stand-up time classification	Descriptive form General type	For input in tunneling design	Lauffer, 1958
The new Austrian tunneling method (NATM)	Descriptive and behaviouristic form Tunneling concept	For excavation and design in incompetent (overstressed) ground	Rabcewicz, Müller & Pacher, 1958-75
Rock classification for rock mechanical purposes	Descriptive form General type	For input in rock mechanics	Patching & Coates, 1968
The unified classification of soils and rock	Descriptive form General type	Based on particles and blocks for communication	Deere et al., 1969
The rock quality designation (RQD)	Numerical form General type	Based on core logging; used in other classification systems	Deere & Miller, 1966
The size-strength classification	Numerical form Functional type	Based on rock strength and block diameter; used mainly in mining	Franklin, 1975
The rock structure rating (RSR) classification	Numerical form Functional type	For design of (steel) supports in tunnels	Wickham et al., 1972
The rock mass rating (RMR) classification	Numerical form Functional type	For use in tunnel, mine and foundation design	Bieniawski, 1973
The NGI Q classification system (Q-System)	Numerical form Functional type	For design of support in underground excavations	Barton et al., 1974
The typological classification	Descriptive form General type	For use in communication	Matula & Holzer, 1978
The unified rock classification system	Descriptive form General type	For use in communication	Williamson, 1980
Basic geotechnical classification (BGD)	Descriptive form General type	For general use	ISRM, 1981

*Definition of the following expressions:

Descriptive form:	The input to the system is mainly based on descriptions.
Numerical form:	The input parameters are given numerical ratings according to their character.
Behaviouristic form:	The input is based on the behaviour of the rock mass in a tunnel.
General type:	The system is worked out to serve as a general characterization.
Functional type:	The system is structured for a special application (for example for rock support).

Table II-4. Used parameters in the rock classification systems collected in Table II-3 (Palmström, 1995).

Classification System	1	2	3	4	5	6	7	8	9	10	11	12	13
ROCK													
- Origin, name or type				×				×			×		×
- Weathering	o		■			~					+	×	
- Anisotropy													
ROCK PROPERTIES													
- Unit weight											+	×	
- Porosity											+		
- Rock hardness								×					
- Strength	■	■	■	×			×		×		+	×	×
- Deformability			■	o							+		
- Swelling	o		■										
JOINT CONDITIONS													
- Joint size/length				o				o					
- Joint spacing											×	o	
- Joint wall smoothness									×	×			■
- Joint waviness									×	×			
- Joint filling										×	×		
DEGREE OF JOINTING													
- Block size					×		×						
- Joint spacing/frequency	o	■	■	o		×			×		×		×
- RQD									×	×			
- Number of joint sets										×			
JOINTING GEOMETRY													
- Joint orientation								×	+				
- Jointing pattern											×		
- Continuity		■	■	o	o								
- Structure (fold, fault)	■		■					+					
EXTERNAL FEATURES													
- Water conditions								×	×	×			
- Rock stress conditions	o		■				×		+	×			
- Blasting damage									+				
- Excavation dimensions			■					×	×	×			

Legend
× Well defined input — o Very roughly defined or included
■ Included, but not defined — ~ Partly included (in other parameters)
+ Used as additional information (in RMR as adjusted value)

1. Terzaghi (1946)
2. Lauffer (1958)
3. NATM (1958-75)
4. Patching & Coates (1968)
5. Deere et al. (1969)
6. RQD (1966)
7. Franklin (1975)
8. Wickham et al. (1972)
9. RMR (1973)
10. Q-system (1974)
11. Matual & Holzer (1978)
12. Williamson (1980)
13. BGD (1981)

1.4 ROCK MECHANICAL PROPERTIES

As stated by Evert Hoek in 1986, "The corner-stone of any practical rock mechanics analysis or rock engineering is the geological data base upon which the definition of rock types, structural discontinuities and material properties is based. Even the most sophisticated analysis can become a meaningless exercise if the geological information upon which it is based is inadequate or inaccurate". This statement clearly indicates the importance of rock characterization for use in rock engineering, design and construction. Rock types and structural discontinuities have been already addressed in *Sections 1.3.1* and *1.3.2*, respectively. This section will therefore focus on the last point underlined by Evert Hoek, the rock material properties.

Since rocks are aggregates of mineral grains or crystals, their properties are determined in large part by the properties of their various constituent minerals. In a rock these general properties are determined by averaging the relative properties and sometimes orientations of the various grains or crystals. As a result, some properties that are anisotropic on a submicroscopic or crystalline scale are fairly isotropic for a large bulk volume of the rock. Many properties are also dependent on grain or crystal size, shape, and packing arrangement, the amount and distribution of void space, the presence of natural cements in sedimentary rocks, the temperature and pressure, and the type and amount of contained fluids (e.g., water, petroleum, gases).

Rock properties can be studied from numerous perspectives depending the field of interest. For example, geologists are interested in the radioactive age dating of rocks to reconstruct the origin of mineral deposits; seismologists formulate prospective earthquake predictions using premonitory physical or chemical changes; crystallographers study the synthesis of minerals with special optical or physical properties; exploration geophysicists investigate the variation of physical properties of subsurface rocks to make possible detection of natural resources such as oil and gas, geothermal energy, and ores of metals; solid-state physicists study the magnetic, electrical, and mechanical properties of materials for electronic devices, computer components, or high-performance ceramics; reservoir engineers analyze the response measured on well logs or in the processes of deep drilling at elevated temperature

and pressure; and geotechnical engineers examine the nature and behaviour of the materials on, in, or of which such structures as buildings, dams, tunnels, bridges, and underground storage vaults are to be constructed.

Thus, from an engineering perspective, mechanical properties of rocks are of special interest, as they define their behaviour when subjected to external stresses. These mechanical properties are generally divided into strength properties and elastic (or deformational) properties. Besides, they can be determined either on site using in-situ testing techniques, or in the laboratory. Unless specific research is required for the analysis of a particular rock engineering problem, in-situ tests are rather limited and scarce. The current general trend is to obtain the mechanical properties of rocks through laboratory tests, which require simpler techniques, lower associated costs and are directly performed in samples extracted from rock drill cores. In the following subsection, the main strength (tensile and compressive strength) and elastic properties (Young's modulus and Poisson's ratio) will be reviewed due to their importance in the present study.

1.4.1 Strength properties

1.4.1.1 Tensile strength

It is widely known that rocks have relatively low tensile strength compared to compressive or shear strength. This condition makes rocks especially sensitive to tensile loading, which is the most common failure mechanism. In fact, Hoek (1965) declared that even in compression, at the scale of flaws within the rock, the damage mechanism of crack initiation is the result of tensile stress at the flaw tip.

When tensile laboratory testing methods are employed in standard engineering practice, they are generally governed by the ISRM (1978) and ASTM (2008, 2020) suggested methods. However, other methods of tensile testing can be found in the literature, particularly for research purposes, and can typically be described as either direct or indirect methods depending on how the load is applied to the sample. *Table II-5* collects the most commonly used direct and indirect tensile tests.

Table II-5. Common tensile testing methods.

Test method	Reference
DIRECT TENSILE TESTS	
Split grips for dog-bone shaped specimens	Hawkes & Mellor (1970)
Glued end caps for cylindrical specimens	ISRM (1978); ASTM (2020)
Confined biaxial extension	Brace (1964)
Compression-tension load convert	Gorski (1993)
INDIRECT TENSILE TESTS	
Brazilian tensile tests (BT)	ISRM (1978); ASTM (2008)
Beam three-point bending tests (3PBT)	Franklin & Dusseault (1989)
Beam four-point bending tests (4PBT)	Franklin & Dusseault (1989)
Sleeve fracturing tests	Franklin & Dusseault (1989)
Modified tension tests	Luong (1990)

By definition, the tensile strength is the rupture stress in a pure tensile uniaxial stress state. The ideal test is therefore the direct tensile test, in which the specimen is loaded to failure by a tensile axial force (see *Figure II-8*). It is assumed that under direct tensile conditions the stress state is truly uniaxial and uniform, and therefore the tensile strength is computed as the ratio between the failure load and the specimen cross section. Unfortunately, these assumptions are rarely accurate since stress concentrations at the specimen grips can be responsible for an early failure of the specimen. Moreover, even when failure occurs away from the ends (i.e., in the central part of the specimen), the stress state may be non-uniform throughout the cross section, as small geometrical imperfections or misalignments between specimen and loading frame introduce bending moments.

Direct tensile tests are rarely carried out because of the difficulties preparing the specimens and obtaining reliable results. Consequently, as an alternative to the direct pull test, numerous indirect tests have been devised (as those depicted in *Figure II-9* and *Figure II-10*), which aim to induce tensile failure in a specimen that is otherwise subjected to compressive forces. Continuum mechanics is then used to compute the maximum tensile stress in the specimen at failure, linear elastic behaviour being usually assumed. Although the stress state within the

failing part of the specimen is multi-axial, possibly with the only exception of the four points bending test (4PB), the influence of the other components of the stress tensor, within a failure criterion for tensile strength, is usually not accounted for.

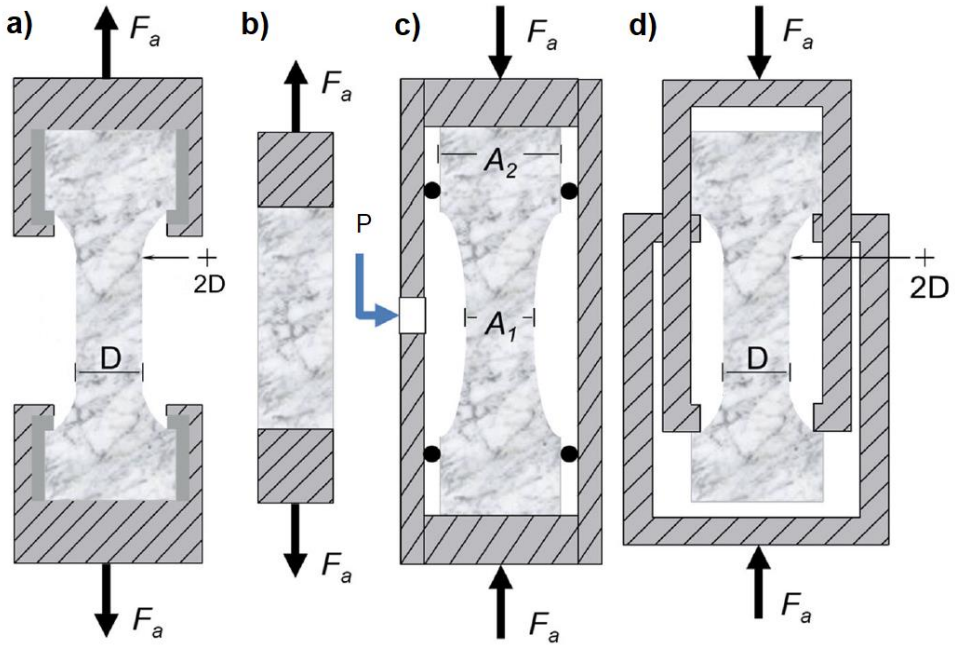

Figure II-8. Direct tensile testing arrangements using (a) split grips for dog-bone shaped specimens, (b) glued end caps for cylindrical specimens, (c) biaxial extension, and (d) compression to tension load converter. F_a is the applied force, D the diameter, A the area, b the thickness and P *the water pressure (Perras & Diederichs, 2014).*

Among the indirect tensile tests, the bending of one dimensional specimens (i.e., bars with circular or rectangular cross section) is very popular in many branches of civil engineering. Three (3PBT) and four (4PBT) points bending tests are adopted as a standard for determining the tensile strength of materials such as natural and artificial building stones, rocks, cement (e.g. ASTM C99:2018, ASTM C880:2018, EN 12372:2006, EN 13161:2008) and consist of loading a simply supported bar perpendicularly to its axis in one and two points, respectively (*Figure II-9b*). The tensile strength is then evaluated by means of applying the well-known Navier's equation to the furthermost fibre from the neutral axis at rupture. It should be pointed out, however, that the validity of this equation has some limitations. In the Saint-Venant solid

the Navier's equation does not apply for sections which are closer than the cross section height to concentrated loads and therefore, from a strict point of view, should not be used for interpreting 3PBT results. On the other hand, if the loaded sections of the 4PBT are sufficiently spaced and the fracture develops in that part of the specimen, then the Navier's equation correctly describes the variation of the normal stress in elastic materials. These theoretical considerations are confirmed also by experimental data; for example Cardani & Meda (2004) have measured the profile of the axial normal strain along the specimen height under the concentrated load of a 3PBT and in the middle section of a 4PBT on Carrara Marble. The data clearly confirm the theory and indicate that if the Navier's equation is used for the 3PBT, the maximum tensile stress is overestimated.

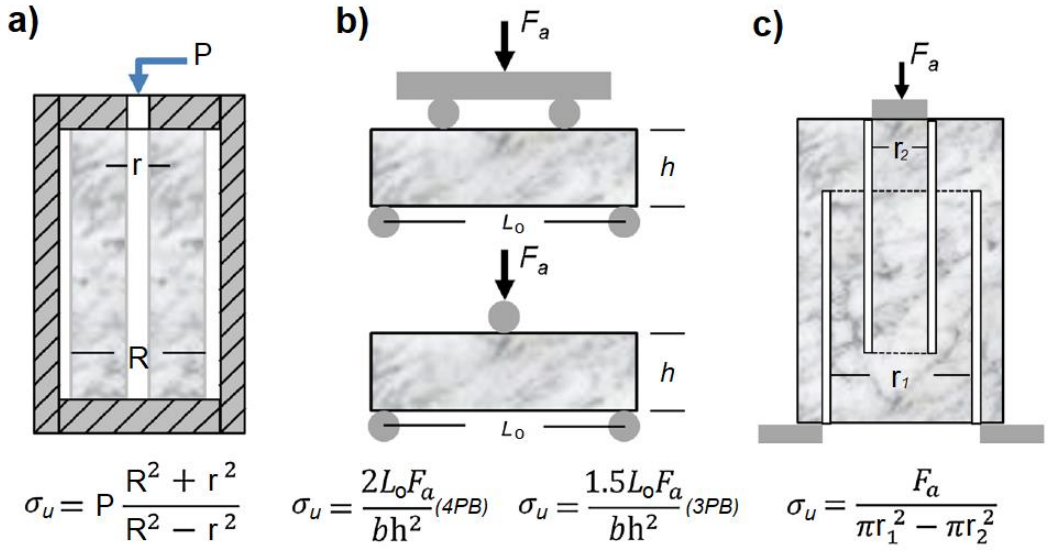

Figure II-9. Indirect tensile testing methods: (a) sleeve fracturing tests, (b) beam bending tests (3PBT & 4PBT), and (c) modified tension tests. F_a *is the applied force,* r *the inner radius (*r_2*),* R *the outer radius (*r_1*),* L_o *the length,* h *the height,* b *the thickness,* P *the water pressure, and* σ_u *the tensile strength (Perras & Diederichs, 2014).*

In the case of the 4PBT, if the loaded sections are sufficiently spaced, the stress state in the central part of the specimen will be uniaxial. However, data in the literature indicate that tensile strength values obtained from 4PBT are generally overestimated (e.g., Jaeger &

Hoskins, 1966; Jaeger, 1967). One of the main reasons explaining these higher estimations is the so-called stress gradient effect and the non-linear behaviour of the rock near bending failure. Large stress gradients imply a small volume of the material being subjected to tensile stress, which reduces the probability of including material flaws in contrast to the direct tests. Likewise, rocks are not perfectly continuous materials and the influence of grain size may also affect stresses at the studied region.

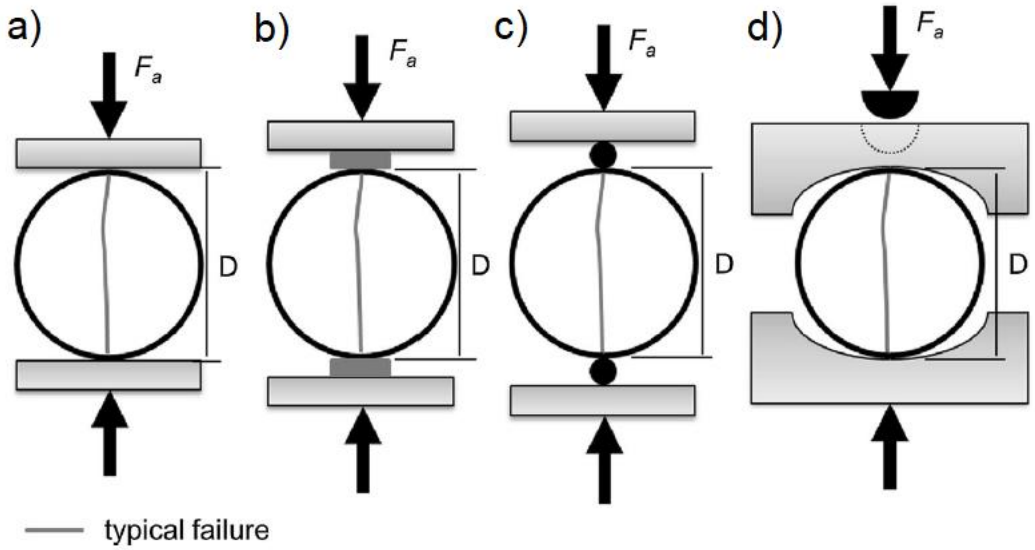

Figure II-10. Typical loading platen arrangements for Brazilian tensile tests (BT) using (a) flat loading platens, (b) flat platens with cushion, (c) flat loading platens with small diameter rods, and (d) curved loading platens. F_a *is the applied force, and* D *the diameter (Perras & Diederichs, 2014).*

The Brazilian test (BT) is one of the most popular tension tests among the scientific community due to the easy preparation of the specimens and the low dispersion of the experimental results (Coviello et al., 2005). It consists of disc-shape specimens diametrically compressed between flat or curved platens, as indicated in *Figure II-10*. The elastic stress fields induced by concentrated (flat platens) and distributed (curved platens) loads differ only in the outer region of the disc, where radial compressive normal stresses tend to infinite for the former case and are equal to the circumferential one (also compressive) in the latter (Hondros, 1959).

The validity of the Brazilian test has been deeply debated in the literature. Colback (1966) presented a detailed discussion based on theoretical arguments and experimental evidence. By using a modified Griffith's fracture theory which takes into account the friction in compressed cracks (McClintock & Walsh, 1962; Hoek, 1964), he showed that fracture would first occur at the disc-platen contact only under concentrated loads, whereas with distributed contact forces an extension fracture would be triggered anywhere in the central third of the disc. He then concluded that Griffith's criterion ensures that the computed tensile stress at failure coincides with the uniaxial tensile strength. Careful experimental investigations conducted on discs covered with a photo-elastic layer and with the use of high-speed photography confirmed the theoretical arguments (Colback, 1966). Primary fracture did occur in the central part of the specimen, provided that the compressive loads were not concentrated and that material flaws were randomly distributed. Secondary and tertiary fractures did only appear subsequently and were associated to the failure of the two halves of the disc. In the opposite case in which primary fracture occurs around the loading points, the tests do not offer reliable tensile strength results and should be therefore discarded.

Figure II-11 shows the comparison between tensile strength values measured by means of the direct pull tests and various indirect tests, including the Brazilian tests. The dashed line indicates equality between direct and indirect tests. It is observed that Brazilian tests provide tensile strength values of the same order of magnitude as direct tests, which are theoretically more accurate. The represented ring tests consist of a variation of the Brazilian tests that were originally developed to overcome the debated issue of the location of the onset of the primary fracture in the Brazilian test by using a hollow disc as a specimen. Experimental results from the literature indicate that the hole drilled in the centre of the specimen forces the fracture to develop in the right location. However, the obtained results consistently and largely overestimate the direct tensile strength and depend on the ratio between inner and outer diameter (Hudson, 1969). Consequently, ring test has fallen into disuse and, therefore, it has not been included in *Table II-5*.

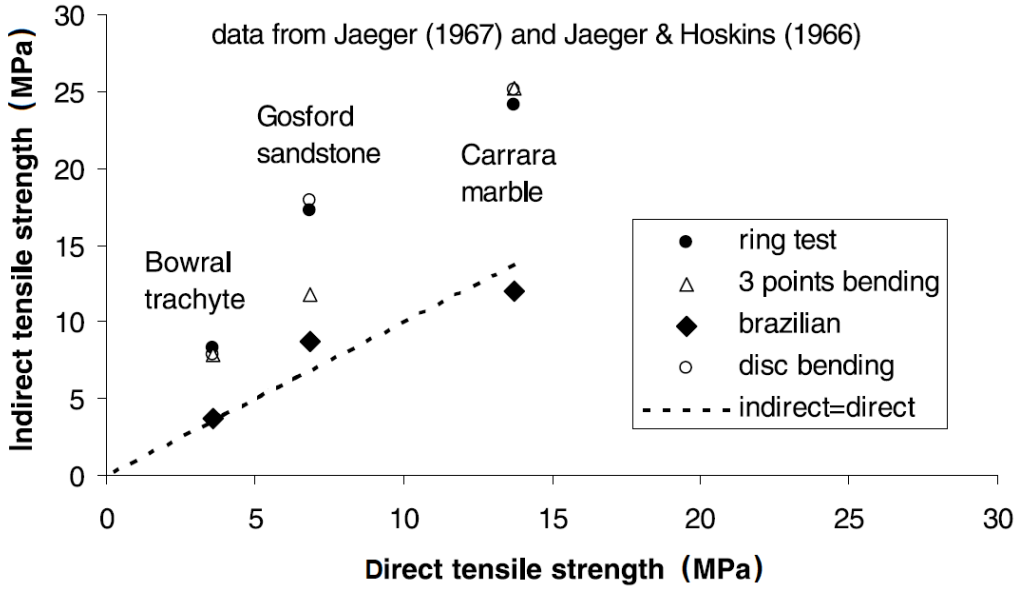

Figure II-11. Comparison between direct and indirect tensile strength values from different tests on three rocks (Jaeger & Hoskins, 1966; Jaeger, 1967).

In tension, damage initiation and peak strength of rocks are roughly coincident due to unstable crack propagation. This means that tensile strength is closely related to the crack initiation processes after which failure follows immediately. Griffith (1921) proposed a theory to describe the formation and propagation of microcracks in solids in two-dimensions, which was centred around micro-flaws within the test sample and thermodynamic principles. Murrell (1963) expanded this theory to three-dimensions. The equations relating the principal stresses (σ_1, σ_3) and tensile strength (σ_u) provided by Griffith and Murrell are, respectively:

$$\sigma_1 = \frac{-8\sigma_u(1 + \sigma_3/\sigma_1)}{(1 - \sigma_3/\sigma_1)^2} \qquad \textit{(II-1)}$$

$$\sigma_1 = \frac{-12\sigma_u(1 + 2\sigma_3/\sigma_1)}{(1 - \sigma_3/\sigma_1)^2} \qquad \textit{(II-2)}$$

The original Griffith theory (1921) was found to reliably predict the fracture initiation stress, however, the concept of crack propagation from a single flaw causing macroscopic failure of a sample was not consistent

with experimental compression results (Hoek, 1965). Diederichs & Kaiser (1999) highlighted that Griffith's theory is a damage initiation threshold over the full range of confining stresses. In the tensile region, crack accumulation and propagation occurs simultaneously with crack initiation, while in compression, crack accumulation and propagation is required (after initiation) to fully fail a crystalline rock sample. This issue will be discussed in *Section 1.4.1.2* for the case of compression tests.

For an unconfined test in which $\sigma_3 = 0$, *Equations (II-1)* and *(II-2)* reduce to $\sigma_1 = -8\sigma_u$ and $\sigma_1 = -12\sigma_u$, respectively. In fact, in the absence of specific tests to determine the tensile strength of a certain rock, it is a common practice to consider that the ultimate tensile strength (σ_u) is approximately 10% of the uniaxial compressive strength.

1.4.1.1.1 Influence of temperature on tensile strength

As mentioned above, the tensile strength of rocks is related to the appearance of microcracks within the intact rock. Thus, the influence of temperature on the tensile strength of rocks is irretrievably linked to their microstructure. The differential thermal expansion of adjacent mineral particles subjected to changes in temperature, and the presence of pores, cavities or microcracks allowing that expansion define the thermal behaviour of rocks. As a consequence of the existing heterogeneity in rock composition, different responses are generally distinguished (see *Figure II-12*).

Extensive research has been conducted to understand the effect of temperature on the tensile strength of rocks due to its interest in many underground engineering fields (e.g., underground coal gasification, enhanced oil recovery, underground nuclear waste disposal, geothermal energy). However, it is important to highlight that, in many cases, the influence of temperature in the mechanical properties of rocks are studied at room temperature after subjecting the rock samples to a thermal treatment or cycle (e.g., Sirdesai et al., 2017; Dongming & Yushun, 2018), while in other cases, somewhat less usual, the tests are performed under temperature control throughout the duration of the tests (e.g., Araújo et al., 1997).

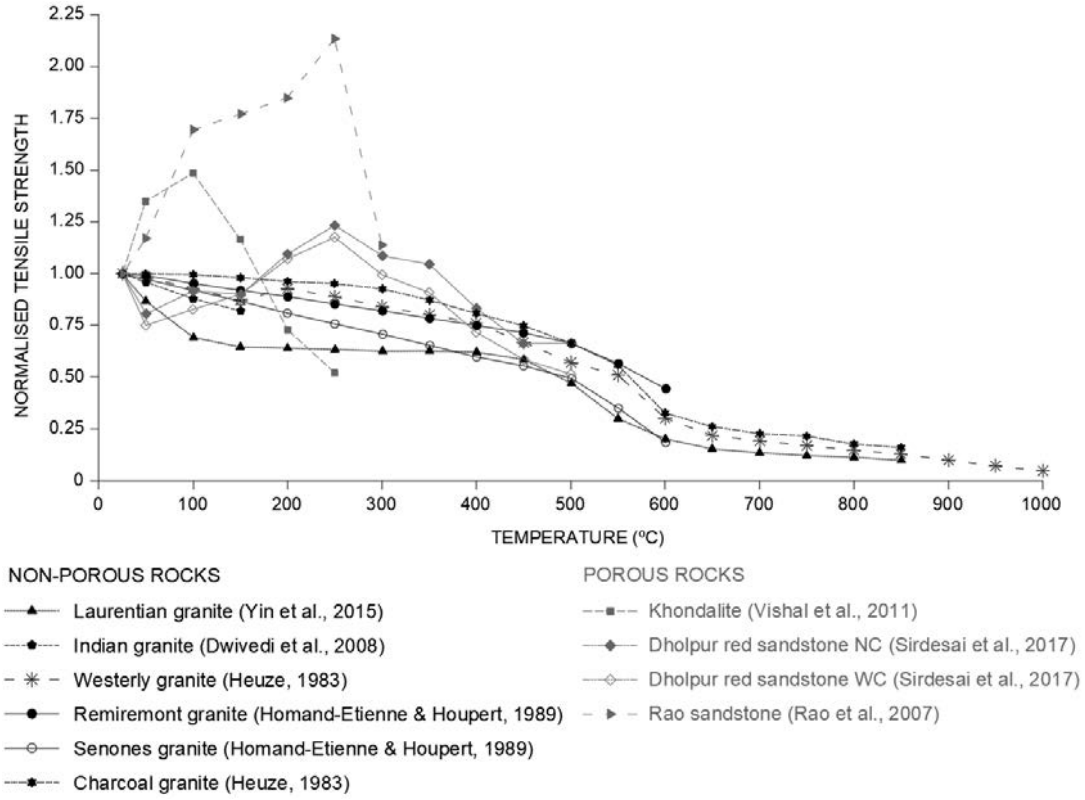

Figure II-12. Comparison between tensile strength at different temperatures for different rocks (adapted from Sirdesai et al., 2017).

Studies of the thermomechanical behaviour of igneous rocks such as granites and basalts, for example, suggest that the tensile strength of the rocks decreases with the increase in temperature (Heuze 1983; Homand-Etienne & Houpert 1989; Dwivedi et al. 2008; Yin et al. 2015). The persistent decrease in the tensile strength of granites and basalts is generally associated with the low porosity and negligible existence of microcracks within these types of rocks. The grains present in these rocks expand at the onset of heating, resulting in the creation of new microcracks as a consequence of differential thermal expansion of the grains with no space for growth. This phenomenon causes a reduction in strength. By contrast, in the case of porous rocks a different trend is generally observed. For example, the tensile strength of khondalitic rocks from southern India was found to increase with temperature up to 100ºC. Further exposure to higher temperatures causes a sharp decrease (Vishal et al., 2011). Rao et al. (2007) reported an increase in the tensile strength of sandstones up to 250ºC. The strength decreases on further thermal treatment. This initial increase in strength is a result of

compaction which occurs due to the expansion of grains. The expansion of grains causes the preexisting pores and microcracks to fill. This phenomenon is of course limited and due to continuous expansion of the grains, new pores and microcracks are created once a critical temperature is reached, which reduce the strength of the rocks. Both phenomena can be seen in *Figure II-12*, where the variation of the tensile strength is represented for several porous and non-porous rocks.

For relatively higher temperatures of the order of several hundred degrees Celsius, the closure or appearance of thermally induced microcracks is no longer the main mechanism defining the strength of the rock. Other mechanisms such partial melting, brittle creep, or chemical and microstructural changes cause a drastic resistance loss of rocks. However, this work will not focus on these mechanisms because they occur at temperatures beyond of the scope of the study.

1.4.1.2 Compressive strength

Before discussing rock compressive strength, *Figure II-13* illustrates the most common loading configurations used in rock compressive strength tests. Among them, the most common tests in engineering applications correspond to triaxial tests, which allow to consider confined conditions, and uniaxial (or unconfined) compression tests. Triaxial tests require a special triaxial cell capable of supporting high pressures, which makes them expensive and laborious compared to uniaxial compression tests. In general, triaxial testing is only considered in those cases in which high confining stresses must be studied (e.g., deep tunnels and excavations), while for shallow works, the analysis is usually limited to the measurement of the unconfined compressive strength (UCS or σ_c). In fact, the focus of rock engineering studies is often on the σ_c, which is a widely correlated parameter used in many rock engineering designs.

The failure of rock in compression is a complex process that involves microscopic failures manifested as the creation of small tensile cracks and frictional sliding on grain boundaries (Brace et al., 1966). Eventually, there is a coalescence of these microscopic failures into a through-going shear plane (Lockner et al., 1991). In brittle rocks sudden failure occurs, with the material essentially losing all of its strength when a through-going shear fault forms. In quasi-brittle rocks presenting small

degree of ductility before failure, however, failure is slightly more gradual. In any case, the strength is defined as the peak stress level reached before macroscopic failure.

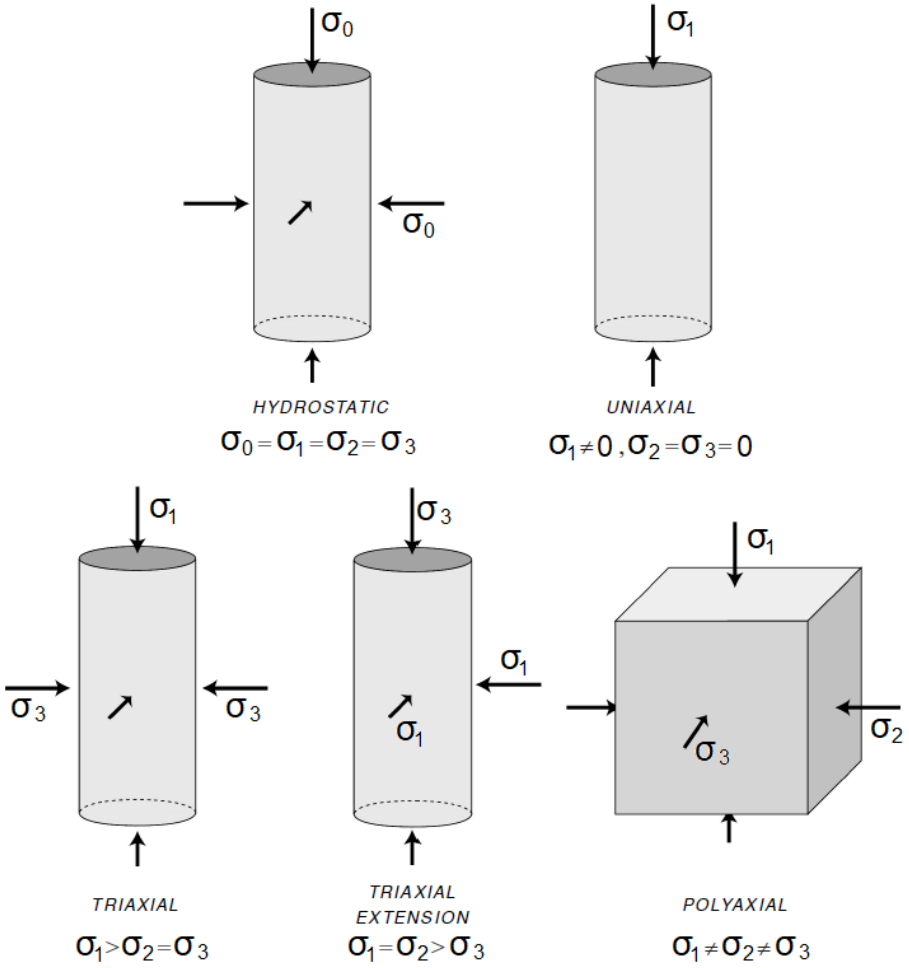

Figure II-13. Most common compressive loading configurations in rock laboratory tests (Zoback, 2007).

Unlike tensile conditions, in compression the peak load does not correspond with crack initiation within the intact rock. This is due to the fact that, at relatively low load level, a lot of microcracks start to develop in a diffuse manner (according to the above mentioned Griffith's theory), but it is not till coalescence takes place that a macroscopic crack arises and final failure occurs. Indeed, crack initiation occurs at a stress level between 30-50% of the peak strength in compression (Brace et al., 1966). Crack initiation represents the first onset of new distributed grain scale cracks within the specimen during testing. The crack initiation

threshold under compression is a robust material property and is mechanistically related to the tensile strength of the rock (Diederichs, 2003). In contrast, the threshold for critical crack accumulation, propagation and interaction (which defines the final failure) is more associated with loading conditions and confining stress. UCS, in turn, is related to testing geometry, loading rate and other influences in addition to the rock properties. Consequently, in order to obtain comparable compressive strength values of different rocks, a unified and standardised testing procedure was proposed by the International Society of Rock Mechanics (ISRM, 1979), where the sample geometry and loading requirements were established.

1.4.1.2.1 Influence of temperature on compressive strength

As interpreted from previous comments, the rock strength is certainly affected by mineral composition, structural and textural characteristics, including porosity, fracturing, the strength of mineral constituents and the nature of the bonding between them. Thus, the same factors determine the strength of rocks at higher temperatures. In parallel to the tensile strength discussion provided in *Section 1.4.1.1*, similar conclusions can be obtained for the case of compressive strength. Under the influence of temperature, depending on the coefficient of thermal expansion of mineral components, an increase of the contact surfaces between particles takes place. This leads to structural changes that have an impact on the strength parameter values and the bulk density of the rock. The rock strength is dependent on the thermal stability of the minerals and their expansion, as well as on the nature of its intergranular contacts, the state of the boundaries between them and the reaction to the resulting stress. On this basis, two main behaviours are generally distinguished as indicated by Dimitriyev et al. (1969): for relative moderate temperature increments, the mineral composition of crystalline rocks remains unchanged, while increasing contact surfaces of the minerals takes place, leading to an increase of rock strength compared to the strength at room temperature. For persistent temperature increments, thermally induced microcracks arise due to differential thermal expansion of adjacent grains and, therefore, strength reduces. By contrast, in other cases a decrease in the rock strength is observed from the onset of heating.

Pinińska (2007) reported that, in addition to mineral composition, an important factor influencing the strength of rock is the grain size and porosity. In fine-grained sandstone and sandstone of low porosity, an increase of compressive strength occurs earlier and is longer than in coarse-grained sandstones of greater porosity. Similar conclusions were obtained by Dengina et al. (1993), who stated that in coarse-grained sandstones, strength decreases more rapidly compared to fine-grained sandstones, in which the decrease of strength takes place more smoothly, as a consequence of intergranular fractures and microcracks passing through the pores in the rocks of coarse graining. Zhi-jun et al. (2009) found that in the case of sandstone, high porosity minimizes cracking due to the expansion of minerals, causing an increase in the density of the rock and its temporary reinforcement. Zhang et al. (2013) also confirmed this phenomenon based on a study on mudstones.

Based on the variation of uniaxial compressive strength with temperature indicated in *Figure II-14* for several rocks, different behaviours are observed depending on the type of rock. In the case of the granite tested by Chen et al. (2012) for example, a continuous decrease of the uniaxial compressive strength is observed from the onset of heating. Up to a temperature of 400ºC its compressive strength falls gently, but a sudden loss of strength is observed in the temperature range from 400ºC to 600ºC. This is probably related to the phase transitions of quartz at 573ºC (Chen et al., 2012). In the case of the marble (Zhang et al., 2009), a small peak is observed at 100ºC, but there is also a general decreasing trend of the compressive strength with temperature. The research on a sandstone performed by Wu et al. (2013) showed an increase in the strength up to 400ºC, after which decreased. Likewise, in the studies of sandstone samples heated to a temperature of 1100ºC conducted by Korzeniowski & Skrzypkowski (2012), the strength of the samples slightly increased at 400ºC and then decreased, with a significant drop after reaching 1000ºC. In the case of the mudstone studied by Zhang et al. (2013), the compressive strength indicates an increase from 90 to 252 MPa, when heated to a temperature of 400ºC. The authors attributed this phenomenon to the evaporation of water and the emission of gases contained in the inner structure of the mudstone. This contributes to reducing sliding between the particles and results in the increase of the strength of rocks. Then, the strength

of the mudstone exponentially decreased down to 70 MPa at 600ºC due to melting and thermal decomposition of minerals, contributing to the formation and the development of new micro-cracks in the structure of the mudstone. Finally, a slightly decreasing tendency with temperature was observed in the limestone analysed by Mao et al. (2009). It was only after exceeding 700ºC that strength rapidly decreased by almost 70% compared to the maximum value obtained at room temperature.

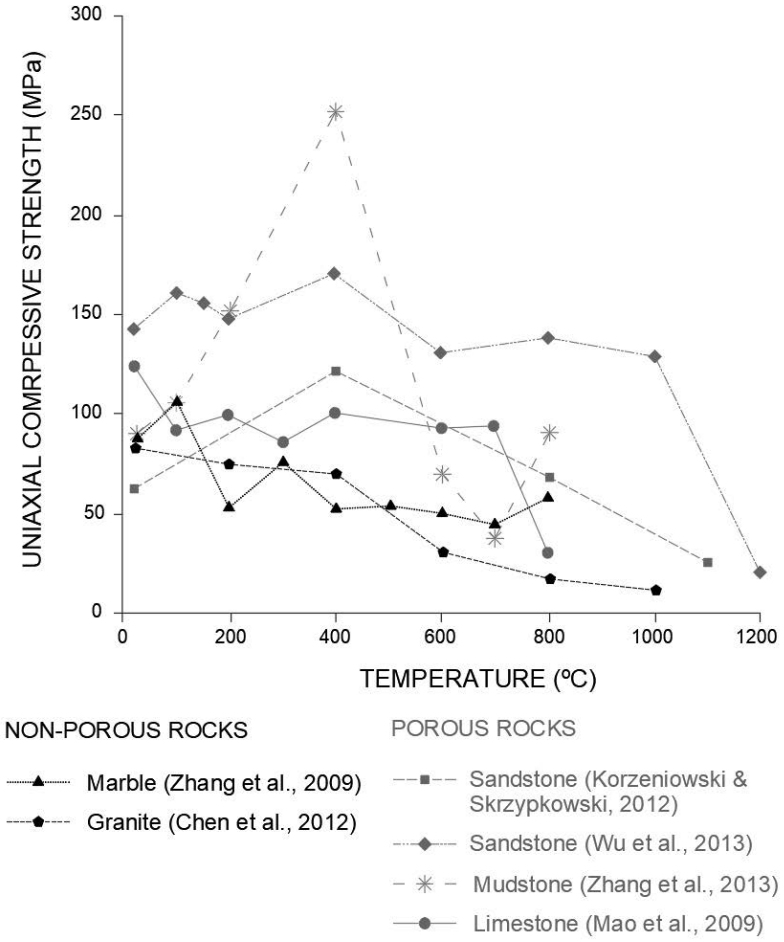

Figure II-14. Variation of compressive strength with temperature for different rocks (adapted from Sygala et al., 2013).

With all this, it seems to be clear that thermally induced micromechanisms (e.g., grain interactions as a consequence of thermal expansion) define the macroscopic changes of the rock strength with temperature. Thus, different trends are generally observed according to the lithology of each rock.

1.4.2 Elastic properties

1.4.2.1 Young's modulus and Poisson's ratio

When a stress (σ) is applied to a material such as rock, the material experiences a change in dimension, volume, or shape. This change, or deformation, is quantified using strains (ε). The mechanisms and character of the deformation of rock can be investigated through laboratory tests, using theoretical models based on calibrated properties of the rock, or by in-situ rock deformation tests performed in the field (e.g., plate load tests, dilatometers, etc.). Except for particular research purposes in which in-situ characteristics are required, the deformational properties of rocks are typically measured in the laboratory. The most common method for studying the deformational properties of rock that define the rock behaviour when subjected to external stresses is by axial compression of cylindrical rock samples. To do so, the same loading configurations as those depicted in *Figure II-13* can be applied. In particular, the uniaxial compression test is probably the most widespread method for determining the deformability of rock materials. The ISRM (1979) provides a full description of the procedure for determining the elastic parameters.

As a first approximation, the uniaxial stress-strain curve of rocks can be idealised to the simplest possible behaviour, in which the strain increases linearly with stress, ending in abrupt failure at a certain critical stress. In this case, a linear-elastic behaviour can be represented by the following equation:

$$\sigma = E \cdot \varepsilon \qquad \textit{(II-3)}$$

The strain (ε) is dimensionless and, therefore, E has the same units as the stress. The latter parameter is called Young's modulus (or elastic modulus). In linear-elastic behaviour, the term 'linear' refers to the mathematically linear relationship between stress and strain. On the other hand, according to continuum mechanics, the term "elastic" means that the strain is a single-valued function of the stress, and does not depend on the stress history or stress path. Thus, for a perfectly linear-elastic material (*Figure II-15a*), at any value of the strain below the failure load, the slope of the curve will be given by $d\sigma/d\varepsilon = E$. An elastic

material may also present a non-linear behaviour (*Figure II-15b*). The stress-strain behaviour of an elastic material during loading is the same as during unloading. According to the definition of the term "elastic", the stress can be expressed as a single-valued function of the strain, but in this case this relation will not be linear ($\sigma = f(\varepsilon)$). As shown in *Figure II-15b*, the slope of the stress-strain curve varies with the stress level (or strain level).

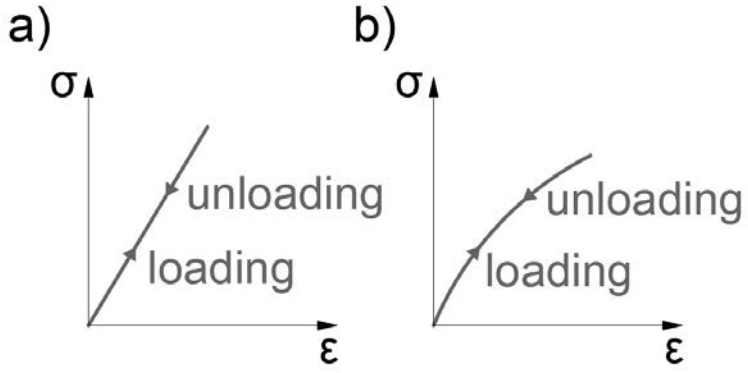

Figure II-15. Schematic representation of stress-strain curves for (a) linear elastic and (b) non-linear elastic behaviour.

As a consequence of these non-linearities, which are more common in soft to medium-strength rocks, the ISRM (1979) suggested different methods for determining the Young's modulus from stress-strain curves, namely the tangent modulus, measured at a fixed percentage of the ultimate strength, the average modulus of the linear portion, or the secant modulus, measured up to a fixed percentage of the ultimate strength (see *Figure II-16*).

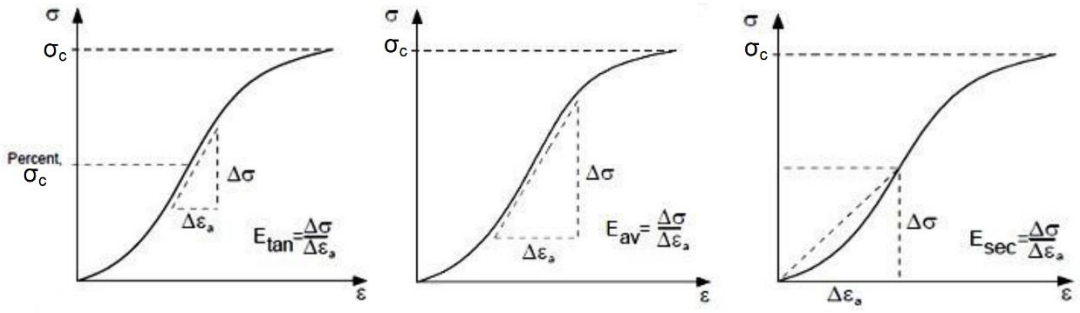

Figure II-16. Different methods for calculating the Young's modulus from stress-strain curves (ISRM, 1979).

Figure II-17 represents the stress-strain curve of a particular rock, indicating the most commonly used typologies of Young's moduli. In general, the slope of the stress-strain curve decreases when increasing the load, with a maximum value at the origin (E_0). For each level of stress (or strain), a tangent or secant modulus (average slope between the origin and each point of the stress-strain curve) can be defined. As a reference modulus, the tangent modulus at a stress level equal to 50% the ultimate strength is commonly used ($E_{t,50\%}$). In fact, in the engineering classification of rocks proposed by Deere & Miller (1966), $E_{t,50\%}$ is the considered elastic parameter (see *Section 1.3.1.2*).

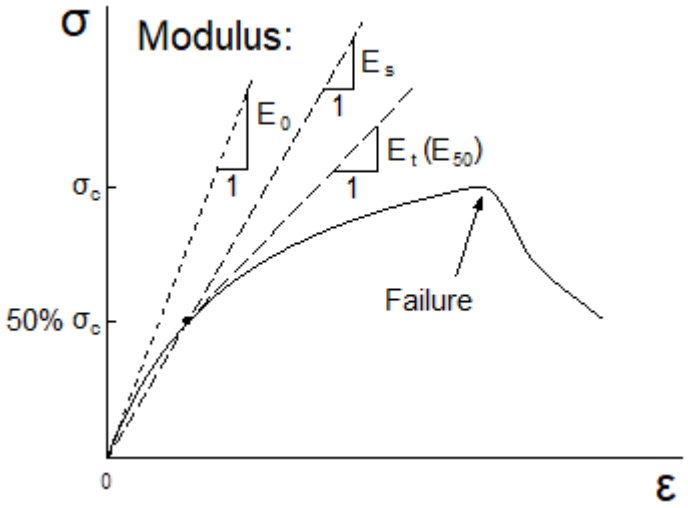

Figure II-17. Representation of Initial (E_0), secant ($E_{s,50\%}$) and tangent ($E_{t,50\%}$) Young's modulus.

For some rocks, the stress-strain curve has an initial interval that is concave upwards, which means that the initial modulus is low and it increases gradually until it reaches a constant value. That initial concavity is caused by the progressive closure of microfractures that were generated by the decompression of the rock sample during its extraction from the ground. This is a typical phenomenon in medium-strength rocks that are easily fissured because of their structure. In particular, the phenomenon notably appears for specimens that are trimmed with their axes perpendicular to bedding planes. In any case, the phenomenon is related to sample extraction and it does not reflect the in-situ behaviour of the rock. For that reason, it should not be considered in the test interpretation.

In order to obtain the stress-strain curves of a certain rock (see *Figure II-18*), the load and the deformations have to be recorder during uniaxial compression tests. The procedure followed in this work for determining the elastic parameters of the analysed rocks is detailed in Chapter III, which deals with the conducted experimental program. Deformations are generally measured using strain gauges, which indirectly measure the strain as the change in an electrical resistance attached to the rock. When the rock slightly reduces its length, the thin electrical conductor is compressed without buckling, and therefore, it will slightly broaden and shorten, decreasing its electrical resistance. It is common to measure the strains both in the axial direction and perpendicularly to the applied load (i.e., vertical and horizontal strains), using two sets of gauges in those directions.

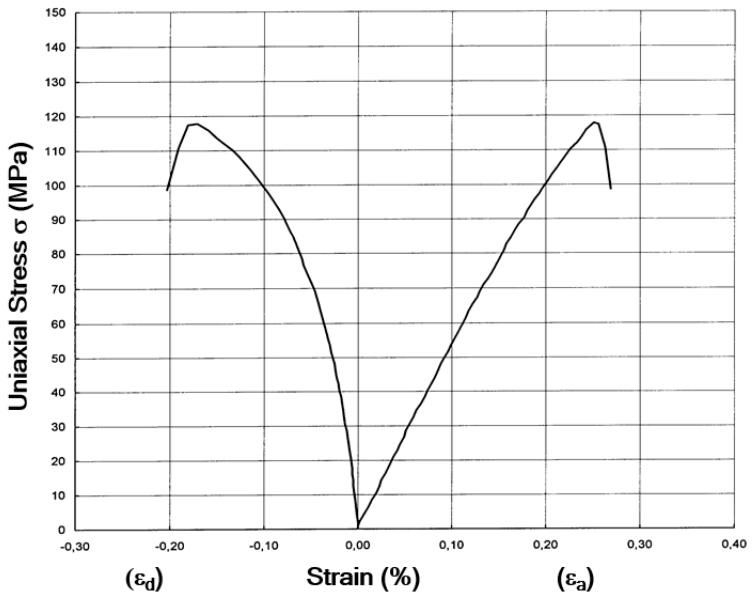

Figure II-18. Typical vertical ($\sigma - \varepsilon_a$) and horizontal ($\sigma - \varepsilon_d$) stress-strain curves obtained in a uniaxial compression test.

Figure II-18 shows the typical stress-strain curves of a cylindrical rock sample subjected to uniaxial compressive load, in which axial (ε_a) and diametric (ε_d) strains are recorded for each stress level. The sign convention indicates that positive normal strains correspond to decreases in the longitudinal dimension of the specimen. By contrast, the diametric strain is negative, which means that the specimen bulges outwards as it

is compressed. The ratio between the lateral and longitudinal strain is widely known as the Poisson's ratio (v):

$$v = -\frac{\Delta\varepsilon_d}{\Delta\varepsilon_a} = -\frac{slope\ of\ axial\ stress - strain\ curve}{slope\ of\ diametric\ stress - strain\ curve} \qquad (II\text{-}4)$$

where the slope of the diametric curve is calculated in the same manner for either of the three ways suggested by the ISRM (1979) for determining E and depicted in *Figure II-16*. Poisson's ratio in this equation has a positive value, since the slope of the diametric curve is negative by the used sign conventions.

With all this, under elastic deformation, the magnitude of the strain response to applied stresses is generally defined using only two elastic constants: Young's modulus (E) and Poisson's ratio (v). However, other different parameters can be provided instead, as for example the shear modulus (G_0), defined as the ratio between the applied shear stress and the distortion (rotation) of a plane originally perpendicular to the applied shear stress, and the bulk modulus (K_0), defined as the ratio between the confining pressure and the fractional reduction of volume in response to the applied hydrostatic pressure. These parameters are correlated with E and v as follows:

$$v = \frac{E}{2G_0} - 1 \qquad (II\text{-}5)$$

$$E = 3K_0(1 - 2v) = 2G_0(1 + v) \qquad (II\text{-}6)$$

As an alternative to the aforementioned procedure for measuring the rock elastic parameters, the velocity of wave propagation can be analysed. That may be done in the laboratory by applying a vibration on one end of a rock specimen and placing a receiver at the other end to measure the arrival time of the vibration (wave). In an infinite elastic continuum, the vibration propagates with two main components: compressive waves (or primary waves, P-waves) and shear waves (or secondary waves, S-waves). Both types of waves travel at different

velocities. The velocity of propagation (V) for each wave depends on the rock density (ρ_r) and the elastic parameters of the rock (E, v). They are given by the following expressions (Siggins, 1993):

$$V_p = \sqrt{\frac{E_0}{\rho_r}\frac{1-v}{(1+v)(1-2v)}} = \sqrt{\frac{G_0}{\rho_r}\frac{2(1-v)}{1-2v}} \qquad \textit{(II-7)}$$

$$V_s = \sqrt{\frac{E_0}{\rho_r}\frac{1}{2(1+v)}} = \sqrt{\frac{G_0}{\rho_r}} \qquad \textit{(II-8)}$$

When this method is used to obtain the elastic parameters, they are usually referred to as dynamic Young's modulus and dynamic Poisson's ratio, to indicate how they are obtained, but, in fact, no difference has been measured between "static" and "dynamic" values, and in this context, it means that they are the E and v values at the very beginning of the stress-strain curve (see *Figure II-17*).

Till now, only elastic deformation has been addressed for the description of rock behaviour. However, certain plasticity may arise in some rocks, especially when they are close to failure. Under these circumstances, rocks could be defined as elasto-plastic materials (even though the influence of plasticity is relatively small in comparison to metallic materials, for example). On the other hand, viscosity introduces another set of material types, such as viscoelastic, visco-plastic or visco-elasto-plastic, but such materials are not the focus of this thesis. Sample stress-strain curves of both linear elastic and elasto-plastic materials are represented in *Figure II-19*. Comparing *Figure II-15b* and *Figure II-19b*, it is observed that both non-linear elastic or elasto-plastic materials deviate from perfectly linear relationship between stress and strain in a similar manner. However, important differences are observed between linear elastic and elasto-plastic behaviours. In the case of elasto-plastic materials, the deviation stems from some damage events in the material, such as closing or opening of small imperfections and cracks in the material (Jaeger et al., 2007). Consequently, the stress-strain curve does

not follow the same path during unloading once a certain stress is reached.

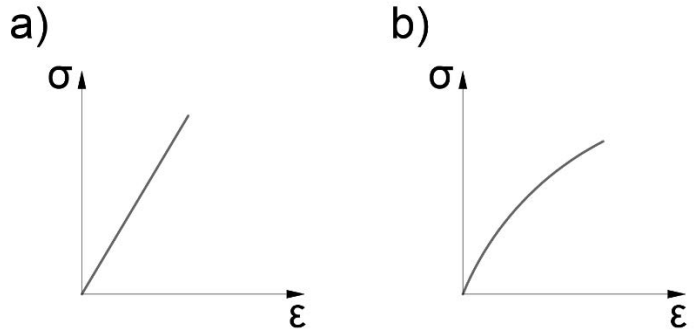

Figure II-19. Schematic representation of stress-strain curves for (a) linear elastic and (b) elasto-plastic behaviour.

A typical rock stress-strain curve follows an initially linear region, followed by a non-linear region, and an eventual sudden failure. This non-linear part is the reason why rock is often described as a 'quasi-brittle' material.

Despite this generality, Miller (1965) classified the stress-strain curves of rocks in six main groups as those observed in *Figure II-20*, based on a laboratory campaign comprising 28 types of rocks. According to Miller's work (1965), type I presents a roughly linear behaviour till sudden failure, which is typical in rocks like basalt, quartzite, diabase, dolomite and hard limestones. Soft limestones or tuff, for example, present an elastoplastic behaviour similar to that indicated in type II. The type III curve, by contrast, is typical in sandstones, granites and some diabase. Metamorphic rocks such as marbles and gneiss, are represented by an S-shaped curve with a highly stepped central region as that depicted in type IV. A similar behaviour is observed in the curve of type V, but with a higher compressibility. This is a typical case of schists loaded perpendicularly to their stratification. Curves corresponding to types III, IV and V are characterized by a concave initial part upwards that becomes steeper when the microcracking or exfoliation surfaces are closed. This initial part is followed by a clearly identifiable linear behaviour, which gradually shows certain degree of plasticity as it approaches failure. Those rocks corresponding to type III, however, present a brittle failure with no plasticity when approaching

the peak load. Finally, some special cases such as rock salt and some evaporites, for example, present a creep behaviour (type VI).

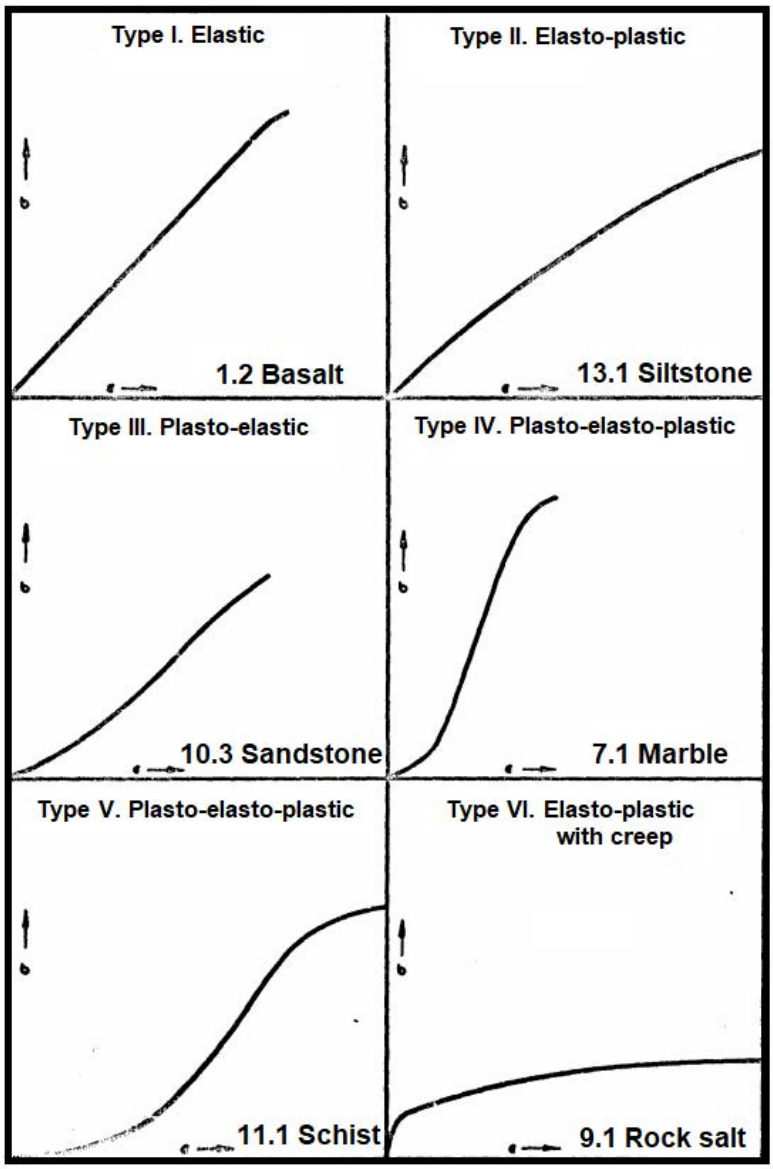

Figure II-20. Typical stress-strain curves for rocks in uniaxial compression till failure (Miller, 1965).

Thus, it is observed that, although as a general criterion it is widely accepted that rocks behave like quasi-brittle materials, certain peculiarities can be distinguished in each case as a consequence of the great variability of existing lithologies. The stress-strain curves provide valuable information of the mechanical behaviour of a certain material before failure and, consequently, its knowledge turns out to be essential for fracture assessments, as will be seen in *Section 2*.

1.4.2.1.1 Influence of temperature on Young's modulus and Poisson's ratio

As happened with the strength parameters of rocks, the elastic parameters are also significantly affected by temperature. Different behaviours have been reported in the literature depending on the rock lithology. However, some common trends can be distinguished.

Several papers can be found in the literature on the performance of uniaxial compression tests on rocks under different temperature conditions. In most of the cases, the rock strength and deformation modulus decrease with increasing temperature, especially beyond a certain temperature (e.g., Dwivedi et al., 2008; Chen et al., 2012). Yang et al. (2017), for example, investigated the strength and thermal cracking of granite under uniaxial compression using thin-section and X-ray micro computed tomography. Their experimental results showed that the tested granite strengthened at 300ºC, and weakened above 300°C. Tullis & Yund (1977) also reported uniaxial compression test results of a granite and showed that both the uniaxial compressive strength and the Young's modulus decreased with increasing temperature.

By contrast, for some rocks, a strengthening effect with increasing temperature is observed (Duclos & Paquet, 1991; Rao et al., 2007), usually involving an increase of the Young's modulus, or in other words, an increase of the stiffness of the rock . This may be related to dissipation of stress concentration at crack tips by increased plasticity (Duclos & Paquet, 1991), or to the closure of pre-existing cracks with thermal expansion (Dmitriyev et al., 1969). Beyond some critical temperature, rocks become weaker with increasing temperature (see Paterson & Wong, 2005, for example) and rock stiffness reduces in parallel while the influence of plasticity becomes more notorious. The mechanisms responsible for this weakening of intact rock with increasing temperature (at relatively high temperature) have been related to thermal cracking and partial melting (Paterson & Wong, 2005), brittle creep (Heap et al., 2009) and chemical transformations (Zhang et al., 2013). In rock types that display strengthening with increasing moderate temperatures, the critical temperature of transition from strengthening to weakening involves a change in the micromechanisms governing the macroscopic

behaviour of the rock. *Figure II-21* shows, as an example, the variation of the Young's modulus with temperature for different types of rocks, which are the same as those depicted in *Figure II-14* to analyse the variation of the uniaxial compressive strength with temperature.

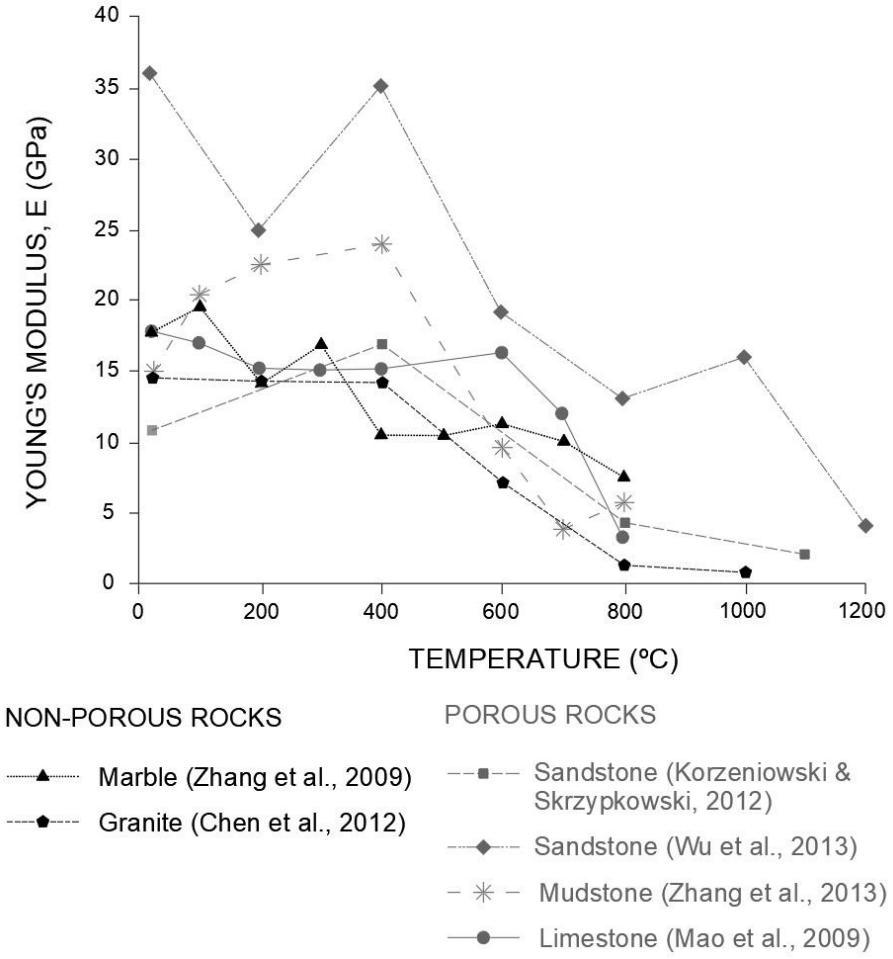

Figure II-21. Variation of Young's modulus with temperature for different rocks (adapted from Sygala et al., 2013).

Figure II-22 shows, as an example, the stress-strain curves of a sandstone subjected to different temperatures up to 950ºC. The region of the curves before failure indicates that up to 400ºC, the curves do not differ in shape and show considerable elastic deformation, presenting similar Young's moduli. In the range of 400-950ºC, the values of the Young's modulus visibly decrease, and at 950ºC important plastic deformations are observed. According to Ranjith et al. (2012), the change of the uniaxially compressed sandstone behaviour from brittle to ductile results from the dehydration of kaolinite, forming part of the

sandstone's binding agent, and from the transformation of goethite into hematite with temperature. The stress-strain curves in *Figure II-22* show that at higher temperatures sandstone exhibits higher values of axial-failure strain. Besides, in accordance with the discussion of the influence of temperature on the compressive strength of rocks provided in *Section 1.4.1.2.1*, the uniaxial compressive strength of the sandstone increases up to 600ºC, after which decreases.

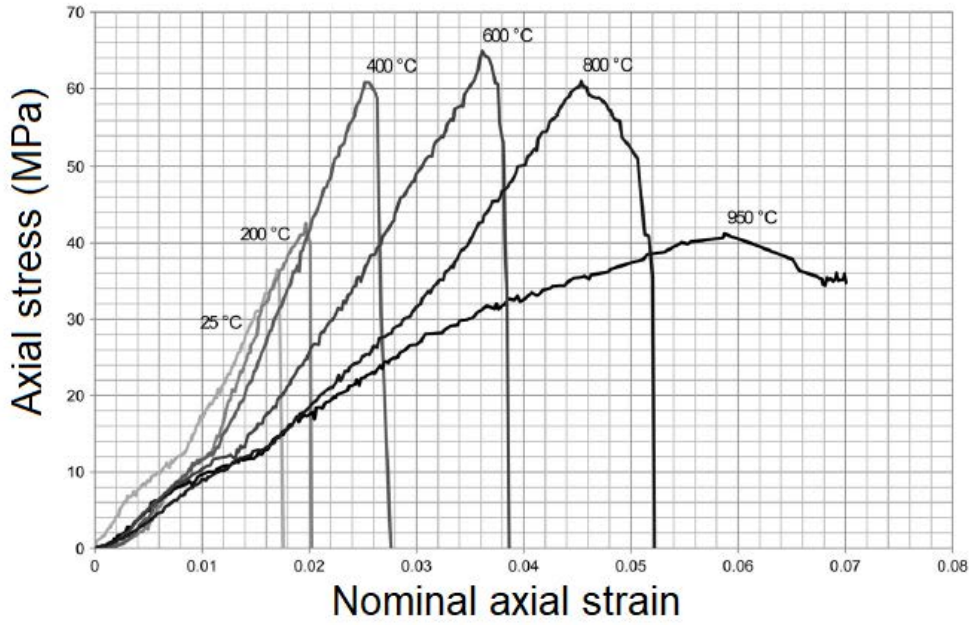

Figure II-22. Stress-strain curves of Hawkesbury sandstone for temperatures varying from 25ºC to 950ºC (Ranjith et al., 2012).

Similar behaviour on another sandstone was reported by Wu et al. (2013), who indicated that sandstones exhibit a predominant elastic behaviour up to approximately 800ºC. On the other hand, in the study of Zhang et al. (2013) performed on mudstone samples at temperatures up to 800ºC (*Figure II-21*), it was shown that chemical changes in the mineral composition of the rock under the influence of temperature cause changes in the shape of stress-strain curves. Up to 400ºC the mineral composition of the mudstone resulted to be stable and the path of the stress-strain curve was not much different from that at room temperature. However, in the temperature range between 600 and 800ºC, the mudstone showed a gradual transition into a ductile behaviour. According to Zhang et al. (2013), this was caused by the

mineral transformation of feldspar, and the dehydration and the transformation of kaolinite into illite. Likewise, Mao et al. (2009) found similar changes in a limestone tested under uniaxial compression from room temperature to 600ºC. Samples heated at higher temperatures and compressed uniaxially deformed in a plastic way.

In general, chemical effects occurring at several hundred degrees Celsius seem to play an important role in brittle to ductile transition of rocks. Significant plasticity degree has been observed at temperatures as low as 100ºC for studies on marble (Zhang et al., 2009), between 250 and 500ºC for studies on sandstone (Rao et al., 2007; Wu et al., 2005; Zhang et al., 2009), 700ºC for studies on limestone (Mao et al., 2009); 750ºC for studies on basalt (Duclos & Paquet, 1991), and 800ºC for studies on granite (Xu et al., 2008, 2009).

All this research data should be understood here in qualitative terms, in order to identify different trends. The absolute stress and strain values may differ significantly even when analysing rocks with a similar lithology. In fact, as highlighted in *Section 1.3.1.2*, according to the engineering classification of rocks proposed by Deere & Miller (1966), important variability of strength and modulus ratio ($E_{t,50\%}/\sigma_c$) are generally found within a certain rock type as a consequence of the broad casuistic of microstructural features.

Finally, a more controversial issue comes up when analysing the influence of temperature on the Poisson's ratio of rocks, since different trends are generally found in the literature with no general agreement. For example, important differences on the Poisson's ratio of granite can be found in the literature, showing in some cases no apparent thermal effect (Heuze, 1983), or an increasing (Xu & Liu, 2000) or decreasing (Yang et al., 2017) trend, probably because of differences in instrumentation, testing methods, calculation methods or the diversity of samples.

In any case, it can be concluded that as a general trend, elastic and quasi-brittle behaviour of rocks tends to exhibit a more ductile behaviour as temperature increases and reaches a certain critical value. However, in most of the cases, rocks can be assumed to behave as quasi-brittle mostly elastic materials for moderate temperatures, although each case should be individually studied.

After this review on rock mechanics, in which the variety of existing rock typologies, their characteristics and peculiarities as a material, and their behaviour (both at room and higher temperatures) have been discussed, the following section focuses on the review of fracture mechanics for the analysis of rock behaviour at failure.

2 FRACTURE MECHANICS

2.1 INTRODUCTION

"Fracture Mechanics" refers to the field within solid mechanics concerned with the study of crack propagation in materials. Although this field was initiated during World War I by the English mechanical engineer A.A. Griffith (1921), it became a mature and established discipline after World War II (Anderson, 2005). Before that, cracks were thought to be small and insignificant nuisances that could never be a threat to large majestic structures like ships and aircraft. However, during the war and for a short time afterwards, many ships and aircrafts failed in sudden, seemingly inexplicable ways. It was eventually determined that the failures were caused by cracks in their metal structures. With this, this branch of knowledge began to gain importance and it was because of disastrous experiences that the study of fracture mechanics was prompted. Thus, fracture mechanics was born in the context of metallic materials. However, this discipline was thereafter developed for all kinds of materials.

Based on the possible stress-strain relations discussed above, two main areas are established in fracture mechanics: Linear Elastic Fracture Mechanics (LEFM), which is applied to brittle materials (e.g., ceramic, glass and some metals with linear-elastic behaviour) that do not exhibit significant plasticity before failure and, on the other hand, Elasto-Plastic Fracture Mechanics (EPFM), associated with high ductility materials with a non-linear behaviour. Rocks are generally studied from LEFM perspective, at least at moderate temperature conditions.

Subsequently, the basics of fracture mechanics will be reviewed, from which different theories and methodologies for the analysis of defects have been developed. Starting from initial and general concepts of fracture mechanics, it is finally intended to arrive at local failure criteria

such as the Theory of Critical Distances and the Strain Energy Density criterion, which are validated in this work for rocks.

2.2 FAILURE MODES

Three types of failure modes are distinguished within the field of fracture mechanics depending on the spatial relationship between the direction of the external load and the crack plane and front (see *Figure II-23*):

- Mode I: Opening mode where the tensile stress is normal to the crack plane.
- Mode II: Sliding mode where shear stress acts parallel to the plane of the crack and perpendicular to the crack front.
- Mode III: Tearing (torsion) mode where shear stress acts parallel to the crack plane and parallel to the crack front.

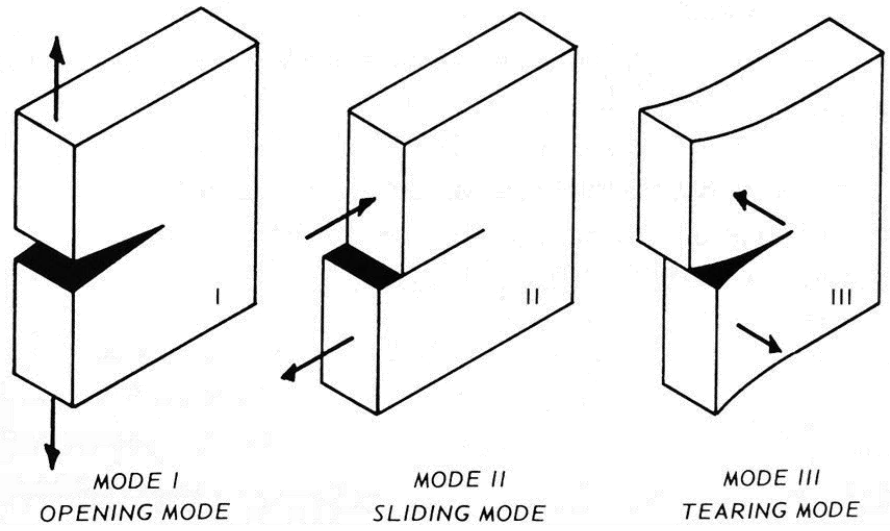

Figure II-23. Schematic representation of failure modes (Ewalds & Wanhill, 1984).

It is generally accepted that crack propagation phenomena in rocks are mode I dominated. This is caused by the relatively small tensile resistance of rocks that makes them highly sensitive to opening loading (mode I). However, rock masses are usually subjected to complex loading conditions and the defects within the rock are randomly orientated. For this reason, rocks are generally subjected to combined loading modes. This work studies mode I and combined opening-sliding shear case (i.e., mixed mode I+II).

2.3 STRESS STATE AROUND DEFECTS

The most basic failure criteria assume that all materials are perfectly homogeneous, isotropic, and free of defects. Under these conditions, failure will occur when the internal stresses exceed material capacity. However, this is not what happens in reality, since a significant global strength reduction is generally observed in the presence of defects. Inglis (1913) is considered the pioneer in the analysis of stress concentration around defects. He first documented and quantified the tendency of stresses to concentrate at material flaws. He based his work on the stress distributions from Love (1906) for two intersecting and deformed bodies, applying these stress distributions to an elliptical crack as that shown in *Figure II-24*.

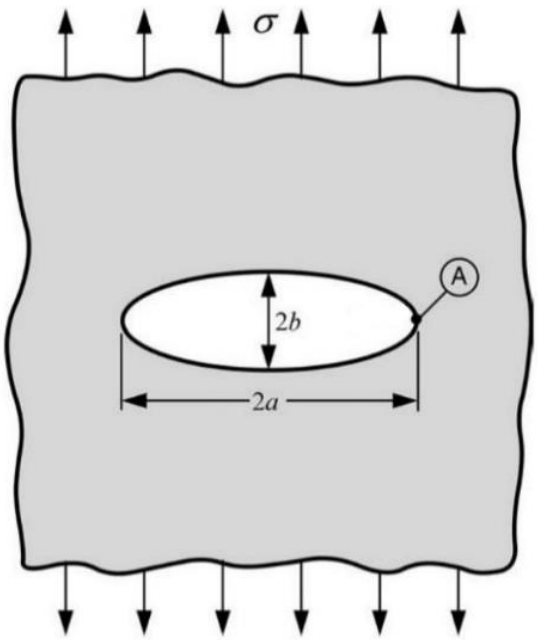

Figure II-24. Schematic representation of an elliptical crack on an infinite plate subjected to uniaxial tension (σ), adapted from (Inglis, 1913).

He found that the material immediately surrounding the crack experienced a stress greater than the far-field applied stress, and that this amplified stress was related to the applied external stress as follows, considering the variables represented in *Figure II-24*:

$$\sigma_A = \sigma\left(1 + \frac{2a}{b}\right) \qquad \textit{(II-9)}$$

Inglis (1913) also found the stress along the minor axis of the elliptical crack to be compressive, and that these stresses decreased in magnitude with distance from the crack. This stress increase at the crack tips would later be termed stress concentration (k^*).

Westergaard (1939) later extended Inglis' crack stress distribution to various bodies. He formulated stress distributions between two circular cylinders, non-circular cylinders, wavy surfaces, ridged surfaces, a crack opened by a wedge and eventually, the classic internal crack initally solved by Inglis (*Figure II-24*). Westergaard (1939) developed a solution for the stress field surrounding a crack that has two advantages over Inglis' (1913) solution. First, Westergaard's solution applies directly to cracks, not to an ellipse that approaches a crack in the limit. Second, the solution is expressed in rectangular coordinates rather than elliptical coordinates. By contrast, it must be noted that his solution applies to an infinite plate in equibiaxial, not uniaxial, tension, as depicted in *Figure II-25*. Nevertheless, it does provide much additional insight into the stress fields surrounding cracks.

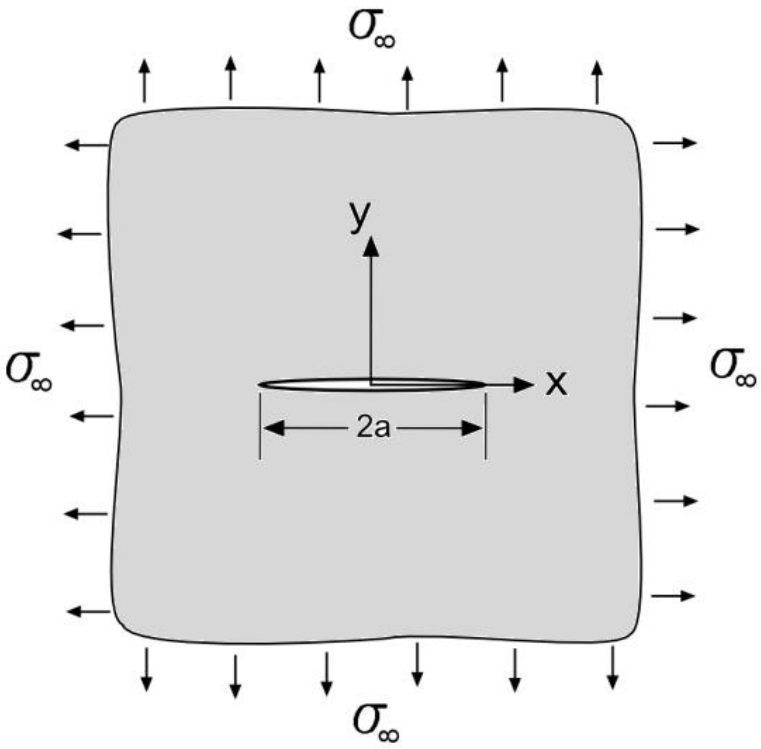

Figure II-25. Schematic representation of a crack in an infinite plate subjected to equibiaxial tension (σ_∞), (adapted from Westergaard, 1939).

Westergaard (1939) found that the material at the ends of the crack (with a length of $2a$) experiences, when subjected to a stress of σ_∞ as shown in *Figure II-25*, a tension equal to:

$$\sigma_y = \frac{\sigma_\infty}{\sqrt{1 - \frac{a^2}{z^2}}} \qquad \textit{(II-10)}$$

where the rectangular coordinates are expressed in complex numbers ($z = x + iy$). This stress distribution reaches a maximum at the crack tip, and decreases with distance away from the crack tip. Thus, the stress intensifying nature of flaws initially pioneered by Inglis (1913) was captured in the resulting stress distribution from Westergaard (1939).

With all this, it is observed that linear-elastic analysis allows to obtain the stress distribution in the front of a crack-type defect from a stress function defined in the complex field. The simplest analytical solution is obtained for an infinite plate with a crack with a length $2a$, under a uniform stress state as that depicted in *Figure II-26*.

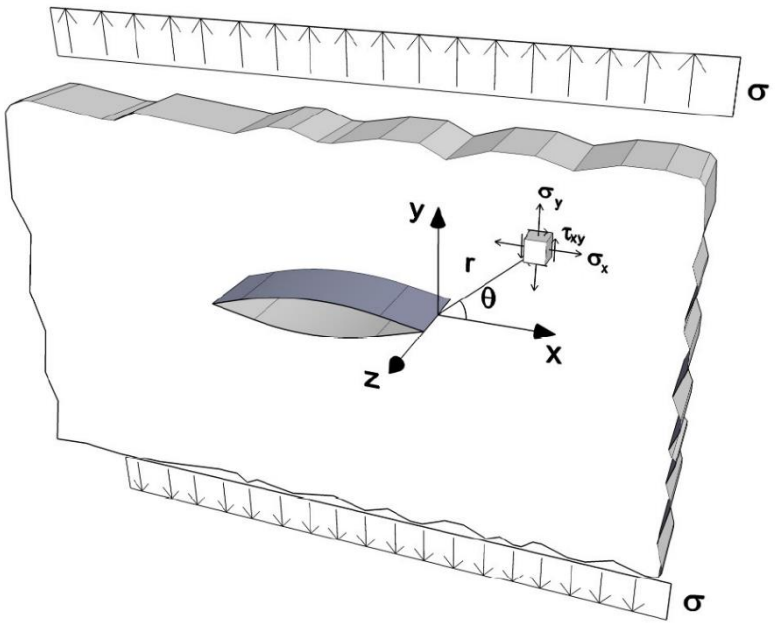

Figure II-26. Stress state in the surroundings of the crack tip (Madrazo, 2013).

This case corresponds to mode I loading conditions. The stress state in the surroundings of the crack tip is given by the following approximate expressions based on Williams' (1957) exact solution:

$$\sigma_x = \sigma\sqrt{\frac{a}{2r}}\left[\cos\frac{\theta}{2}\left(1-\sin\frac{\theta}{2}\sin\frac{3\theta}{2}\right)\right] \qquad (II\text{-}11)$$

$$\sigma_y = \sigma\sqrt{\frac{a}{2r}}\left[\cos\frac{\theta}{2}\left(1+\sin\frac{\theta}{2}\sin\frac{3\theta}{2}\right)\right] \qquad (II\text{-}12)$$

$$\tau_{xy} = \sigma\sqrt{\frac{a}{2r}}\left[\cos\frac{\theta}{2}\sin\frac{\theta}{2}\cos\frac{3\theta}{2}\right] \qquad (II\text{-}13)$$

$$\sigma_z = 0 \qquad (plane\ stress\ conditions) \qquad (II\text{-}14)$$

$$\sigma_z = v(\sigma_x+\sigma_y) \qquad (plane\ strain\ conditions) \qquad (II\text{-}15)$$

Proceeding along a similar path, the strain state in the surroundings of the crack tip can be derived from the following expressions, which establish the displacement at a certain point according to the coordinate system indicated in *Figure II-26*:

$$\mathrm{u} = \frac{\sigma}{2E}\sqrt{\frac{ar}{2}}(1+v)\left[(2k-1)\cos\frac{\theta}{2}-\cos\frac{3\theta}{2}\right] \qquad (II\text{-}16)$$

$$\mathrm{v} = \frac{\sigma}{2E}\sqrt{\frac{ar}{2}}(1+v)\left[(2k+1)\sin\frac{\theta}{2}-\sin\frac{3\theta}{2}\right] \qquad (II\text{-}17)$$

$$\mathrm{w} = -\frac{v}{E}\int(\sigma_x+\sigma_y)\,dz \qquad (plane\ stress\ conditions) \qquad (II\text{-}18)$$

$$\mathrm{w} = 0 \qquad (plane\ strain\ conditions) \qquad (II\text{-}19)$$

where

$$k = \frac{3 - v}{1 + v} \qquad (plane\ stress\ conditions) \qquad \textit{(II-20)}$$

$$k = 3 - 4v \qquad (plane\ strain\ conditions) \qquad \textit{(II-21)}$$

The previous expressions can be expressed as a function of a variable called the stress intensity factor (K, with MPa $\cdot$ m$^{1/2}$ units), which was presented by Irwin (1957) as a key fracture parameter that summarizes the influence of testing geometry, loading, and crack length on the crack tip stress distribution. It expresses the increase in the magnitude of stress near the tip of a crack and the term is a descendant of the stress concentration (k^*) presented by Inglis (1913) almost 50 years earlier.

For the particular case of the infinite plate depicted in *Figure II-26*, which is subjected to mode I loading conditions, the stress intensity factor is as follows:

$$K_I = \sigma\sqrt{\pi a} \qquad \textit{(II-22)}$$

where the subscript stands for mode I case. The stress intensity factor defines the stress and strain state in the vicinity of the crack tip, since it biunivocally defines the stresses and the displacements for each coordinate point (r, θ), except for the singularity at $r = 0$, according to the following expressions:

$$\sigma_{ij}(r, \theta) = \frac{K_I}{\sqrt{2\pi r}} f_{ij}^I(\theta) \qquad \textit{(II-23)}$$

$$u_i(r, \theta) = \frac{K_I}{2E}\sqrt{\frac{r}{2\pi}}(1 + v)\xi_i^I(\theta) \qquad \textit{(II-24)}$$

where $f_{ij}^I(\theta)$ and $\xi_i^I(\theta)$ are mode I characteristic orientation functions, whose value can be deduced by comparison with *Equations (II-11)* to *(II-21)*.

Analogously, there are equivalent expressions that, based on the corresponding stress intensity factors K_{II} and K_{III}, define the stress and displacement states for mode II and mode III loading conditions. For example, under pure mode II conditions the stresses are defined as follows in the vicinity of the notch tip:

$$\sigma_{ij}(r,\theta) = \frac{K_{II}}{\sqrt{2\pi r}} f_{ij}^{II}(\theta) \qquad \textit{(II-25)}$$

with

$$K_{II} = \tau\sqrt{\pi a} \qquad \textit{(II-26)}$$

As observed from the stress intensity factors, the stress state in the vicinity of a defect decreases with the distance from the tip, and it linearly depends on the applied external stress (σ and τ, for mode I and mode II, respectively). It also depends on the square root of a geometric variable characteristic of the dimensions of the defect, such as its length (a). In general, for geometrical conditions different from those represented in *Figure II-26*, the stress intensity factor expression has the following form:

$$K_I = M\sigma\sqrt{\pi a} \qquad \textit{(II-27)}$$

where M is a geometrical dependent non-dimensional factor. Even in the case of simple geometries, the estimation of the stress intensity factor is complex and is generally based on analytical and experimental methods:

- Analytical methods to determine the stress or strain state and, subsequently, the corresponding stress intensity factor value through the application of the theory of Elasticity (for the determination of stress functions in complex variables), supported in numerical techniques such as finite elements.
- Experimental methods, based either on the measurement of the variation in flexibility from which, through energy-based

considerations, the stress intensity factor is determined, or on photoelasticity tests, which define the stress fields for similar geometrical conditions in photoelastic material from which the stress intensity factor is derived.

On the other hand, those expressions relating the stress state and the stress intensity factor indicate that the superposition principle can be applied, because LEFM is assumed. This means that, for a given geometry, the stress intensity factor is equal to the sum of those K values obtained for different loads to which the component is subjected, considering them separately.

The application of these methods has allowed to obtain tabulated values of the stress intensity factor for a wide range of components with geometries and stresses common in engineering problems (e.g., Rooke & Cartwright, 1976; Tada et al., 1985; Murakami, 1987). In the absence of a tabulated solution for a particular problem, the study may be performed by means of any of the existing analytical methods, or by comparison with already solved and tabulated cases, being aware of the approximations made.

2.4 FRACTURE PROCESS ZONE

LEFM correctly describes and predicts fracture behaviour of brittle materials. However, this elastic theory presents a singularity point at the crack tip where the stresses tend to infinite. Going back to the crack tip stress distributions from Inglis (1913) and Westergaard (1939), it is observed that *Equations (II-9)* and *(II-10)* predict an infinite stress at the crack tip. These stresses entail an incongruity between model and actual behaviour, since no material is capable of supporting an infinite stress in reality.

In the mid-20th century, three researchers independently addressed this shortcoming in the existing fracture theory and laid the first notations in Plastic Zone theory. Irwin (1948; 1960), Dugdale (1960), and Barenblatt (1959) postulated that the material closest to the crack tip does not actually contain infinite stresses. This part of the material instead reaches its yield stress, which is a material property, and undergoes plastic deformation. Different names can be found in the literature for this region: Plastic Zone, Process Zone, Cohesive Zone, or Fracture Process Zone (FPZ). This FPZ is developed in rocks as a

consequence of the initiation and coalescence of microcracks in front of the defect tip when increasing the applied load level. This phenomenon is conceptually represented in *Figure II-27*.

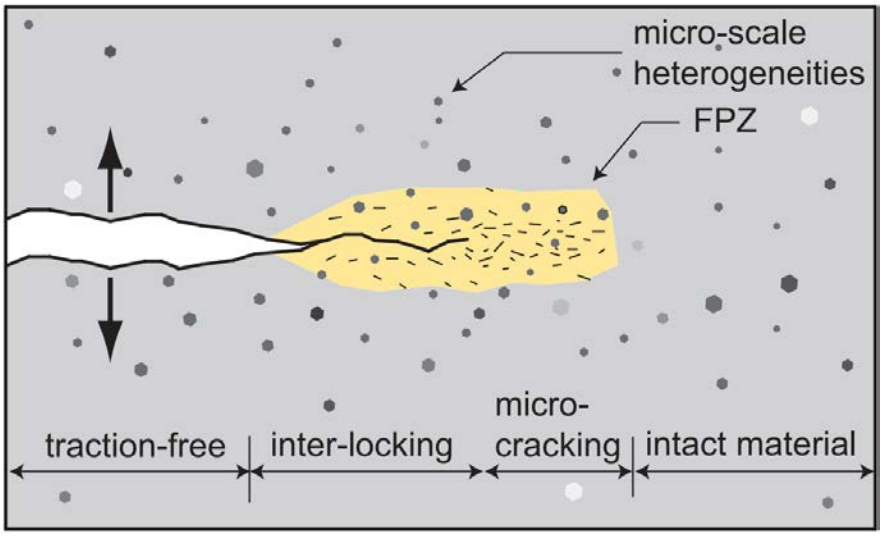

Figure II-27. Schematic representation of microcrack coalescence in the front of the defect tip of a rock-type material (adapted from Labuz et al., 1985).

Since the detection of the FPZ, numerous investigations have been developed for its characterization. From an experimental point of view, four different techniques are generally used for microscale experimental investigation of the FPZ in brittle and quasi-brittle materials: microscopy (e.g., Labuz et al., 1983), interferometry (e.g., Chengyong et al., 1990; Yu & Kobayashi, 1994; Picart et al., 2004), acoustic emission (e.g., Zietlow & Labuz, 1998; Backers et al., 2005; Lin et al., 2009), and ultrasonic pulses (e.g., Labuz et al., 1987; Zang et al., 2000). With the development of finite and discrete element analyses, this issue has also been numerically studied by many authors (e.g., Tarokh & Fakhimi, 2014; Galouei & Fakhimi, 2015). For example, Parisio et al. (2019) studied the characteristics of the FPZ in granite both experimentally and using finite element analyses, and highlighted the importance of dissipative phenomena related to the microcracking and to the size of the FPZ when analysing brittle failure of rocks.

In the case of brittle and quasi-brittle materials, it has been observed that as long as the size of the FPZ is small enough with respect to the

size of the analysed problem (i.e., defect size), LEFM is generally valid and offers good results. In some cases (e.g., Gómez & Torabi, 2018), minor corrections (e.g., using an equivalent linear-elastic stress-strain curve) are considered to somehow correct the effect of the nonlinear region and to provide more accurate fracture assessments. However, in those cases in which the size of the FPZ is relatively large, LEFM is no longer valid and the use of EPFM is necessary, which allows to analyse those fracture situations preceded by large plastic deformations in the vicinity of the defect.

With all this, it can be concluded that the FPZ explains the stress dissipation at the front of the defect tip, which is definitely not infinite.

2.4.1 "Plasticity" at the crack front

Equation (II-23) defines the stresses in the vicinity of the crack (far regions are influenced by boundary conditions of the problem) under mode I loading conditions as those represented in *Figure II-26*. This expression has a singularity at $r = 0$ and, consequently, the theoretical stresses tend to infinite close to the crack tip. Considering the crack plane ($\theta = 0$) the stresses can be rewritten as follows (see *Figure II-28*):

$$\sigma_y\,(\theta = 0) = \frac{K_I}{\sqrt{2\pi r}} \qquad \textit{(II-28)}$$

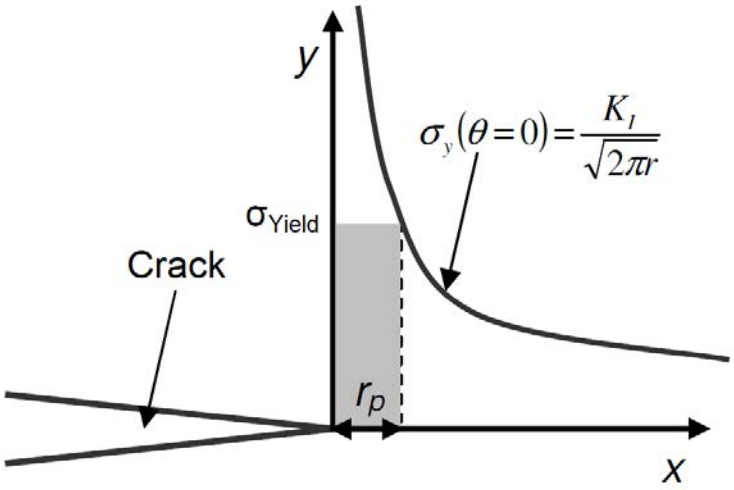

Figure II-28. Stress state in the vicinity of the crack tip.

This theoretical situation with infinite stresses, of course, is not possible and is explained by the presence of a plastic zone at the crack

front (i.e., FPZ). In the case of elasto-plastic materials like steels, the FPZ is characterized by plastic deformations. However, in the case of rock-type materials, the term "plasticity" stands for the appearance of microcracks, but no real plastic deformations are noticeable.

Solving *Equation (II-28)* for the radial distance from the crack tip (r) at which the stress (σ_y) is equal to the material yield stress (σ_{Yield}), the size of the FPZ (r_p) can be derived:

$$r_p = \frac{1}{2\pi}\left(\frac{K_I}{\sigma_{Yield}}\right)^2 \qquad \textit{(II-29)}$$

This formulation of the size of the FPZ was first proposed by Irwin (1960). It must be noted that this expression does not account for the redistribution of stresses that occurs as a result of the material within r_p reaching yield stress values. Thus, r_p potentially underpredicts the actual size of the FPZ. By assuming specimen yielding begins when the stress reaches 88 to 115% of material yield stress, Irwin (1960) found that actual process zone size could range from 80 to 130% of the r_p formulated in *Equation (II-29)*. Thus, r_p provides a reasonable estimate of the process zone size.

Equation (II-29) can be generalized to the whole region around the crack tip. Considering the polar coordinate system indicated in *Figure II-26*, the general expression has the following form that varies for each loading mode:

$$r_p(\theta) = \left(\frac{K}{\sigma_{Yield}}\right)^2 f(\theta) \qquad \textit{(II-30)}$$

As previously indicated, when the size of the FPZ is small ($r_p \ll a$) the application of LEFM is valid for setting fracture criteria. In the case of quasi-brittle materials like the rocks studied in this work, LEFM is used for fracture assessments. By contrast, in those ductile materials where the plastic zone extends significantly around the crack front, the crack growth (and eventual failure) can no longer be justified a process that occurs when the stress intensity factor reaches a critical value, since

this parameter no longer represents the stress conditions in the vicinity of the defect. In this case, new parameters are needed to relate the stress and strain fields. The most commonly used parameters are the Crack Tip Opening Displacement (CTOD) and the J-integral. However, it is not the purpose of this work to go into detail on this topic. For a detailed study of EPFM the works of Janssen et al. (2002) and Anderson (2005) are suggested.

2.5 FRACTURE CRITERIA OF CRACKED COMPONENTS

The presence of defects, no matter whether they are naturally created or manufactured, has proven to be essential to define the critical conditions from which the fracture of a material develops. Regardless of the type of defect being analysed (i.e., crack-type defect or notch-type defect), which will be discussed in *Section 2.6*, they generate stress concentrations in their surrounding area. Under linear elastic conditions, the resultant local stresses are proportional to the external load. Thus, when external load gradually increases the local stresses do it in the same way till critical conditions are reached. This critical situation is achieved when the conditions around the defect are critical to the microstructural reality of the material itself. Local fractures are then produced as a consequence of different micro-mechanisms that determine the defect growth and, eventually, ultimate failure. The critical conditions that lead to the fracture micro-mechanisms are reached for a given stress state (σ_{ij}^{c}) corresponding to a critical stress intensity factor (K_C).

2.5.1 First failure criterion: Fracture toughness of the material

The first fracture criterion in LEFM establishes that a crack will unstably propagate when the stress intensity factor reaches a critical value (K_C). Hereafter, the expressions will be particularized for mode I loading conditions using the corresponding subscript, unless otherwise specified. Thus, this first failure criterion can be expressed as follows under mode I conditions:

$$K_I = K_{IC} \qquad \textit{(II-31)}$$

This critical condition can be accomplished either by an increase of the external stress (σ) or an increase of the crack size (a).

2.5.1.1 Importance of fracture toughness

The fracture toughness is an intrinsic property of any material that represents the residual strength of a cracked component to crack propagation or, in other words, the fracture energy consumption rate required to generate new surfaces. It is a key parameter in cracked and notched fracture analyses as those performed in this work. For this reason, this section summarises the main aspects related to the characterization and evaluation of this parameter.

Under linear elastic conditions and static loads, K_{IC} represents the mode I critical stress intensity factor. This parameter can be obtained based on different testing standards. Among them, the American standard ASTM E-399:2009, which stands for the test method for linear-elastic plane strain fracture toughness of metallic materials, is one of the most widely used, which is, in turn included within the ASTM E-1820:2009 that deals with standard test methods for measurement of fracture toughness. However, together with most developments in the field of fracture mechanics, these standards are focused on metallic materials. Amaral et al. (2008) provided a review of the existing methodologies for the assessment of fracture toughness in rocks. The first recommended techniques for measuring rock fracture toughness were provided by Ouchterlony (1988) and Fowell et al. (1995): a bending technique and a short rod technique as those depicted in *Figure II-29*.

The bending technique propagates an initial crack cut perpendicular to the cylindrical specimen axis, whereas the short rod technique propagates an initial crack cut parallel to the cylindrical specimen axis. Both techniques monitor some form of input energy (either load or displacement) and crack opening. These geometries respond to the traditional limitations that are associated with the extraction and preparation of rock samples, which are generally cylindrical cores obtained from boreholes. However, with the development of technology and new tools that facilitate the preparation of rock specimens, different test configurations and geometries have arisen since then. Most typical methods for measuring the mode I fracture toughness of rocks are gathered in *Table II-6*.

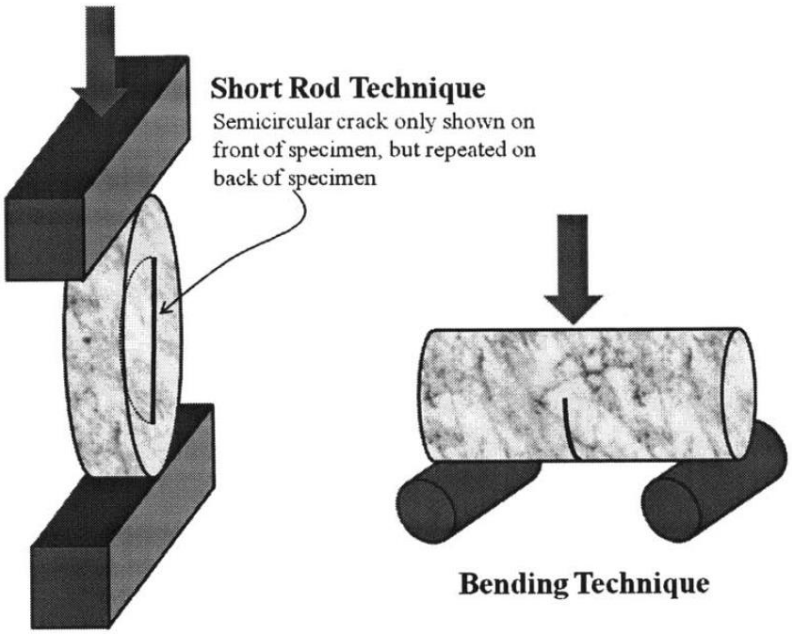

Figure II-29. Basic experimental setup in the short rod and bending techniques (adapted from Ouchterlony, 1988 and Fowell et al., 1995).

Table II-6. Most common methods for measuring the mode I fracture toughness of rocks

Test method	Loading type*
Chevron bend (CB)[1]	3PB
Chevron-notched short rod (SR)[2]	DT
Cracked chevron notched Brazilian disc (CCNBD)[3]	BC
Centre-cracked circular disc (CCCD)[4]	BC
Modified ring[5]	BC
Hollow centre cracked disc[6]	BC
Cracked chevron notched semi-circular bend[7]	3PB
Straight-crack semi-circular bend (SCB)[8]	3PB
Flattened Brazilian disc[9]	BC
Edge-cracked triangular[10]	3PB
Straight notched disc bend[11]	3PB
Edge-cracked bend[12]	3PB & 4PB

Table II-6. (Continued).

*3PB – Three-point bending	*4PB – Four-point bending
*DT – Direct tension	*BC – Brazilian-type compression

[1]Ouchterlony (1988); Funatsu et al. (2015)

[2]Ouchterlony (1988); Wei et al. (2016)

[3]Fowell et al. (1995); Iqbal & Mohanty (2006)

[4]Aliha & Ayatollahi (2009); Akbardoost et al. (2014)

[5]Tutluoglu & Keles (2012)

[6]Amrollahi et al. (2011)

[7]Kuruppu (1997); Chang et al. (2002)

[8]Kuruppu et al. (2014); Ayatollahi et al. (2016)

[9]Keles & Tutluoglu (2011)

[10]Aliha et al. (2013)

[11]Tutluoglu & Keles (2011); Aliha et al. (2015)

[12]Fakhri et al. (2017); Razavi et al. (2018)

Unfortunately, different testing methods usually lead to inconsistent fracture toughness results even for a given rock material (e.g., Aliha et al., 2017). Its importance in the field of rock fracture mechanics makes it a matter in continuous development that attracts considerable research interests (e.g., Muñoz-Ibañez et al., 2020). Probably as a consequence of the wide variety of existing methods and approaches for determining the fracture toughness of rocks, none of them has yet stood out enough to oust the other methodologies, and even those suggested methods by the International Society for Rock Mechanics (ISRM) have been frequently questioned or modified.

The description of the performed laboratory campaign in this work will be detailed in Chapter III. However, it is pertinent to mention here that the edge-cracked bend method has been used in this work based both on three- and four-point bending tests as those depicted in *Figure II-30*.

Assuming a centred load, both test configurations provide pure bending with no shear in the crack section. That is, mode I loading conditions are fulfilled. However, the distribution of shear and bending stresses is different for each case. Four-point bending tests ensure constant bending moment and no shear between the inner loading points, while in three-point bending tests pure mode I conditions are only achieved along the crack section as indicated in *Figure II-31*.

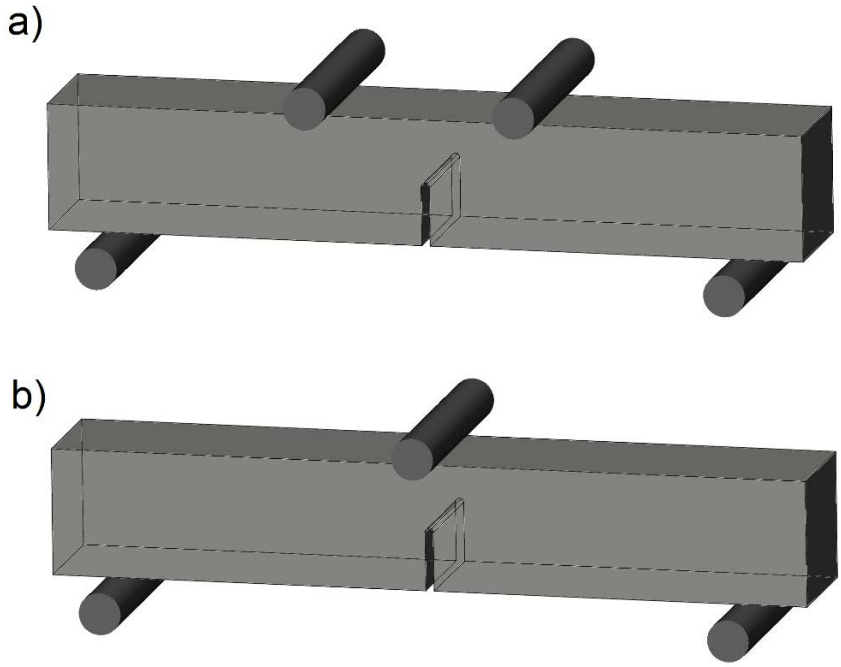

Figure II-30. Illustration of the type of edge-cracked bend specimens assessed in this work under (a) four-point bending and (b) three-point bending conditions.

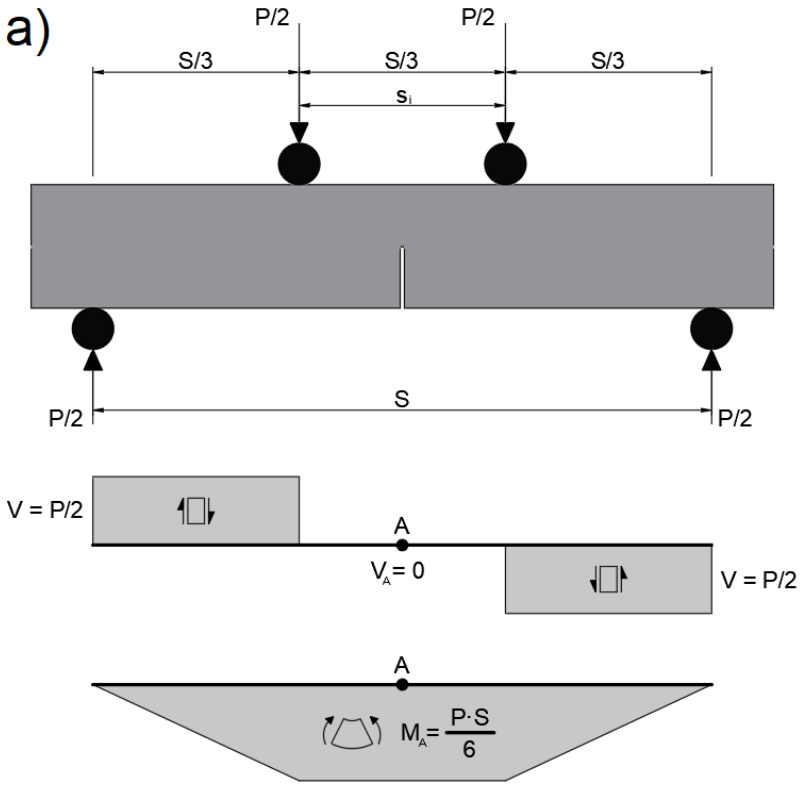

Figure II-31. Shear force and bending moment diagrams of (a) four-point bending and (b) three-point bending test configurations.

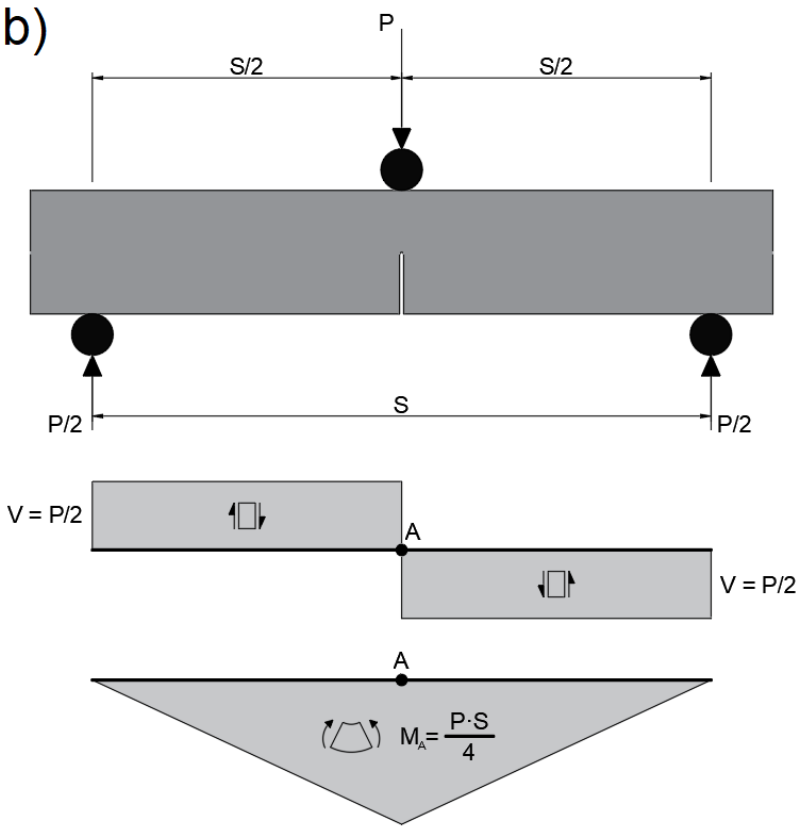

Figure II-31. (Continued).

These edge-cracked bend specimens, from a strict point of view, are indeed edge-notched bend specimens, generally known as Single Edge Notched Bend (SENB) samples. Cracks, by definition, have a null radius ($\rho = 0$), unlike notches, that are characterised by having a finite radius ($\rho \neq 0$). For example, metallic materials do permit fatigue-induced pre-cracking of the samples, but introducing macroscopic real cracks of controlled length into rocks is not possible due to their brittle condition that makes crack propagation unstable. For this reason, in the case of rocks, SENB specimens are actually used, introducing crack-like defects (with sufficiently small notch radius) by means of sharp slots machined into the specimens. Differences between crack-type and notch-type defects will be discussed in *Section 2.6*.

The followed testing procedures for both four-point bending and three-point bending tests respond to the European standards EN 13161:2008 and EN 12372:2006, respectively. In both cases the fracture toughness of the material can be derived from the same analytical expression:

$$K_{IC} = \frac{F}{b\sqrt{h}} Y \qquad \textit{(II-32)}$$

where F is the failure load obtained during the test, b is the specimen thickness (or depth), h is the specimen height and Y is a non-dimensional factor that only depends on the geometry of the specimen. Srawley & Gross (1976) developed the following formulation for determining Y for the case of SENB specimens subjected to four-point bending conditions:

$$Y = \frac{3 \cdot (S - s_i) \cdot \alpha_0^2}{2h \cdot (1 - \alpha_0)^2} X \qquad \textit{(II-33)}$$

with

$$X = 1.99 - \left[\frac{(3.49 - 0.68\alpha_0 - 1.35\alpha_0^2)\alpha_0(1 - \alpha_0)}{(1 + \alpha_0)^2}\right] - 1.32\alpha_0 \qquad \textit{(II-34)}$$

Similarly, Anderson (2005) developed the following formulation for the calculation of Y of the SENB specimens subjected to three-point bending conditions with centred load:

$$Y = \frac{3 \cdot S\sqrt{\alpha_0}}{2h \cdot (1 + 2\alpha_0)(1 - \alpha_0)^{3/2}} X \qquad \textit{(II-35)}$$

with

$$X = 1.99 - \alpha_0(1 - \alpha_0)(2.15 - 3.93\alpha_0 + 2.7\alpha_0^2) \qquad \textit{(II-36)}$$

S and s_i are the spans between the outer supporting rollers and the inner loading points (the latter only for the case of four-point bending tests), as represented in *Figure II-31*. α_0 is the relative crack length defined as the ratio between the initial crack length (a_0) and the total height of the specimen (h). The description of the performed tests and the detailed geometry of the analysed specimens will be provided in Chapter III.

Finally, although the fracture toughness is considered an intrinsic property of the material, there are certain dependencies that should be taken into account when determining its value experimentally, such as the influence of specimen thickness, the loading rate or the influence of temperature.

2.5.1.1.1 Influence of specimen thickness on fracture resistance

Specimens having standard proportions but different absolute sizes involve different fracture resistances. This occurs because the stress states adjacent to the flaw change with the specimen thickness (b) until the thickness exceeds some critical dimension. Once a minimum critical thickness is reached (b_{min}), the value of the critical stress intensity factor becomes relatively constant (K_{IC}) as shown in *Figure II-32*.

Small thickness leads to plane stress conditions, for which the critical stress intensity factor (K_C) is higher than K_{IC}. Thick specimens ($b \geq b_{min}$), by contrast, develop plane strain conditions under which the critical stress intensity factor is constant (K_{IC}). Thus, when talking about material characteristic fracture toughness, the plane strain fracture toughness is meant.

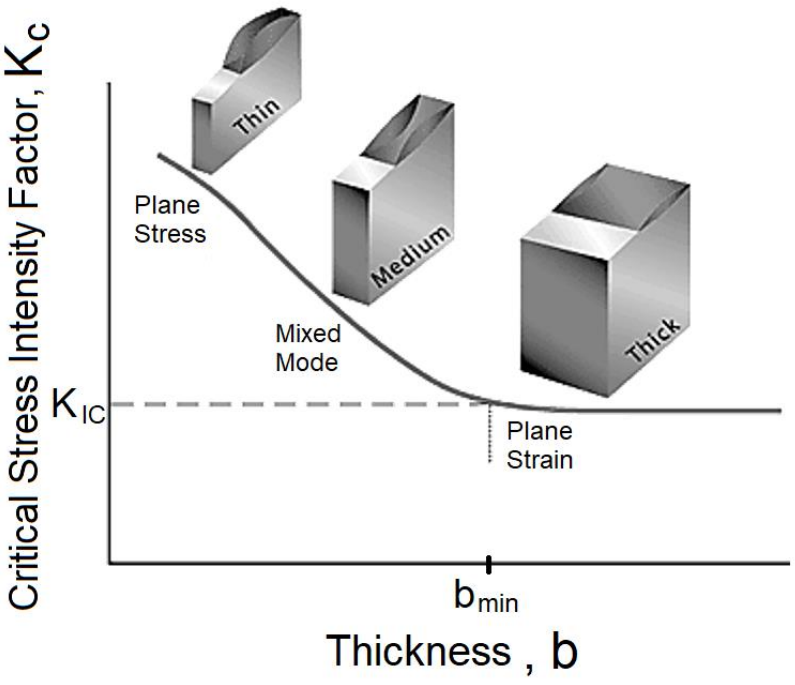

Figure II-32. Influence of specimen thickness on the critical stress intensity factor (Madrazo, 2013).

When an elasto-plastic material with a crack is loaded in tension, the material develops plastic strains as the yield stress is exceeded in the region near the crack tip. The extent of the crack tip plastic zone can vary accordingly if there is a plane strain (large thickness of the specimen) or plane stress (small thickness of the specimen) state (see *Figure II-33*). Material within the crack tip stress field, situated close to a free surface, can deform laterally (in the z direction of *Figure II-33*) because there can be no stresses normal to the free surface. Thus, under plane stress conditions, the stress state tends to be biaxial and the material fractures in a characteristic ductile manner, with a 45º shear lip being formed at each free surface. However, in the case of relatively thick components, the material away from the free surfaces is not free to deform laterally as it is constrained by the surrounding material. The stress state under these plane strain conditions tends to be triaxial and there is zero strain perpendicular to both the stress axis and the direction of crack propagation when a material is loaded in tension. Under plane strain conditions, materials behave essentially elastic until the fracture stress is reached and then rapid fracture occurs.

It is important to remark that, in quasi-brittle materials like rocks, the FPZ is defined by microcracks as indicated above (see *Figure II-27*) instead of plastic strains as those of elasto-plastic materials. Thus, when talking about the plastic zone or the FPZ, this must not be strictly understood as a region with plastic deformations, but as a region where microcracks arise at the crack tip of rock-type materials.

Figure II-33 shows the differences in the stress state of a material around the crack tip both for plane stress and plane strain conditions, defined by their Mohr circles. These differences justify different orientation of the fracture planes, because the maximum shear planes are different for each case. In a real case, due to material constrains, there will be a central part of the crack line under plane strain, followed by an area under intermediate stress and, ultimately, pure plane stress at the outer face, as depicted in *Figure II-34*.

However, as thickness increases the relative influence of the plane strain conditions also increases, generating a decrease of the fracture toughness (see *Figure II-32*). This value of the fracture toughness stabilizes from a certain minimum thickness (b_{min}) onwards. Thus, for

thicknesses larger than that defined by b_{min}, the fracture process is controlled by plane strain conditions. An estimation of this minimum thickness is given by the following expression (Brown & Srawley, 1966):

$$b_{min} = 2.5\left(\frac{K_{IC}}{\sigma_{Yield}}\right)^2 \qquad \textit{(II-37)}$$

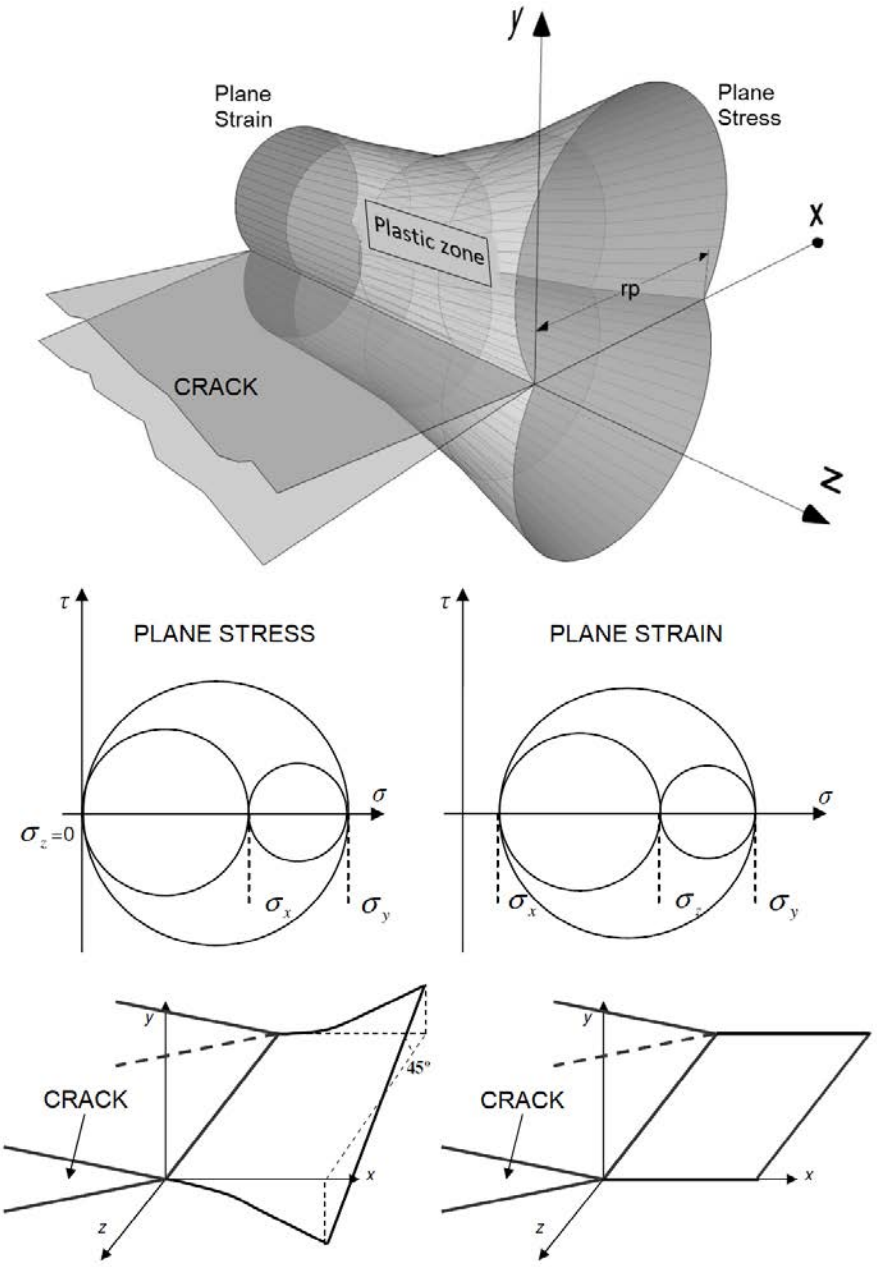

Figure II-33. Schematic representation of plastic zone, Mohr circles and fracture planes under plane stress and plane strain conditions (Madrazo, 2013).

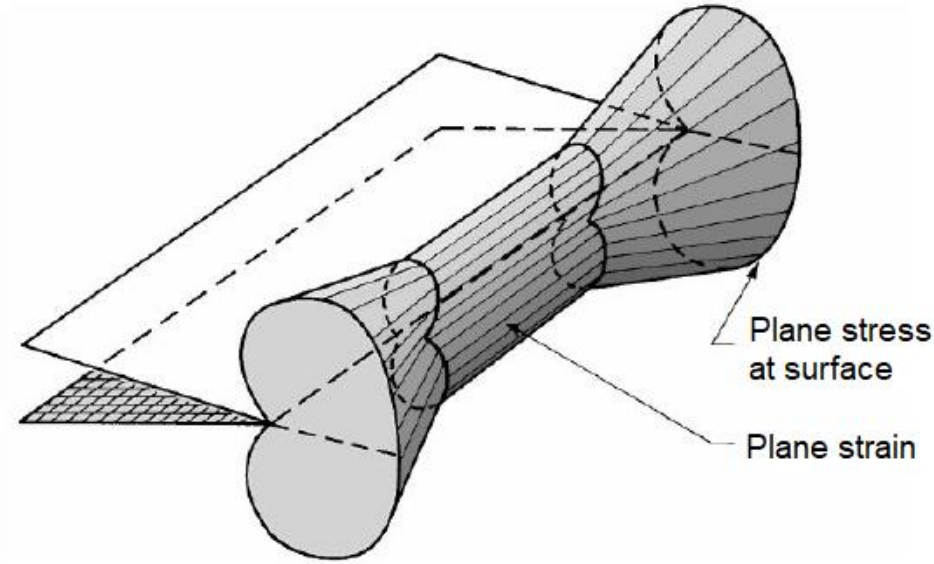

Figure II-34. Through-thickness plastic zone in a plate of intermediate thickness (Janssen et al., 2002).

2.5.1.1.2 Influence of loading rate on fracture toughness

The loading rate of a fracture toughness test significantly affects the resultant material fracture toughness value. K_{IC} decreases when moving from static regime with a low loading rate to dynamic regime with a high loading rate, as represented in *Figure II-35*.

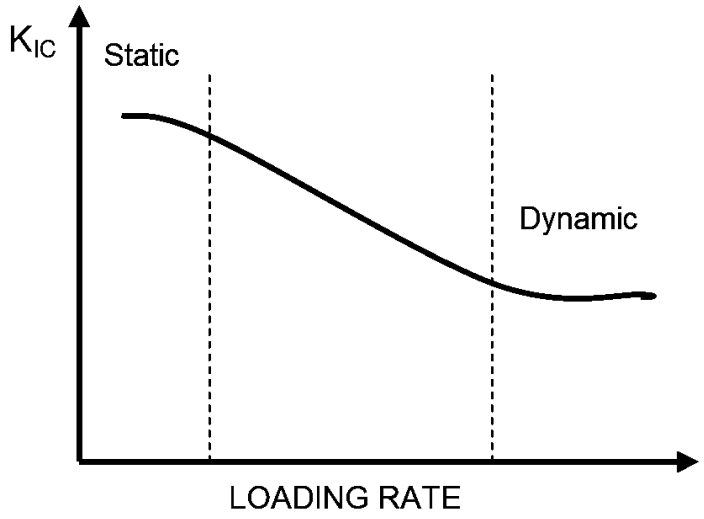

Figure II-35. Influence of loading rate on fracture toughness (Madrazo, 2013).

In general, fracture toughness stands for the static case. In order to guarantee static loading conditions throughout the tests, the European standards EN 13161:2008 and EN 12372:2006 stablish the velocity of the four- and three-point bending tests to a constant loading rate of 0.25±0.05 MPa/s.

2.5.1.1.3 Influence of temperature on fracture toughness

Temperature has a direct effect on the fracture resistance of any material in general, and of rocks in particular (e.g., Mahanta et al., 2016; Feng et al., 2017; Guo et al., 2018). Being able to predict rock fracture under thermal influence is crucial in many underground engineering fields where its effect is no longer negligible (e.g., geothermal extractions, oil-gas exploitations, hydraulic fracturing). Thus, a comprehensive understanding of the effect of temperature on fracture toughness is a major issue of interest in many rock engineering problems. Proof thereof is the large amount of literature dealing with the influence of temperature on the fracture toughness of rocks. Meredith & Atkinson (1985), for example, studied the fracture toughness of a granite and a gabbro and showed that it decreased at temperatures above 100 ºC. The reduction of the fracture toughness of both rocks was caused by the development of micro-cracks induced by differential thermal expansion between adjacent mineral particles. By contrast, Al-Shayea (2000) reported a case of a limestone where the fracture toughness increased at 116ºC by approximately 25%, probably due to the closure of microcracks or pores caused by the thermal expansion. *Figure II-36* represents the variation of mode I fracture toughness with temperature for a broad variety of rock lithologies, collected from different sources.

Similarly to other mechanical properties, different behaviours of the fracture toughness with temperature are distinguished for different lithologies. In some cases, a reduction in the fracture toughness of rocks has been reported at the onset of the heating process, caused by the development of microcracks induced by differential thermal expansions between adjacent mineral particles. By contrast, other studies indicate an increase in the fracture toughness up to a certain temperature. For moderate temperature increments, a strengthening effect can be observed in those cases (Duclos & Paquet, 1991). This could be related

to the partial closure of pre-existing cracks or pores with thermal expansion (Feng et al., 2018) or to the dissipation of the stress concentration at crack tips by increased plasticity (Duclos & Paquet, 1991). These phenomena are obviously limited and beyond a certain critical temperature, the rocks become weaker as a consequence of thermal cracking (Zhang et al., 2009). Besides, in the case of relatively higher temperatures (of the order of several hundred degrees Celsius), an evident resistance loss occurs due to partial melting (Paterson & Wong, 2005) and brittle creep (Heap et al., 2009) of the rocks, even undergoing chemical and microstructural changes (Ranjith et al., 2012).

Thus, it seems evident that the variations in the fracture toughness of the rocks are dominated by micro-mechanisms derived from changes in temperature.

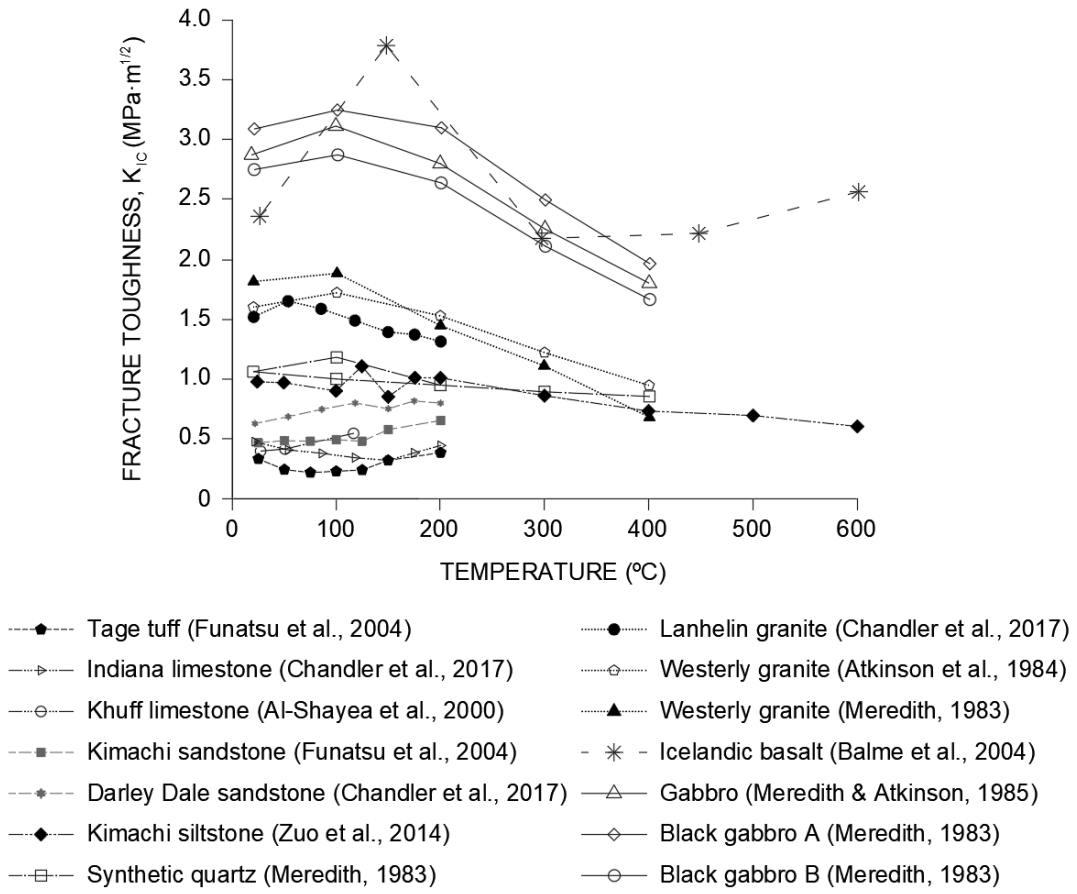

Figure II-36. Influence of temperature on measured mode I fracture toughness of various rocks.

2.5.2 Second fracture criterion: Energy release rate

Griffith (1920; 1924) revolutionized fracture mechanics by considering the fracture of materials from an energy perspective. Based on the previous work of Inglis (1913), he proposed an energy-based fracture criterion that effectively avoided Inglis's infinite-stress prediction at the crack tip, while nevertheless making direct use of his linear elastic solution.

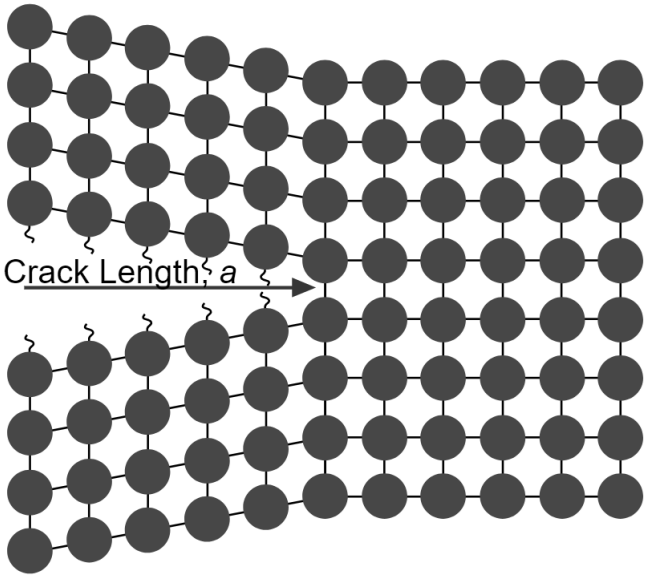

Figure II-37. Illustration of atomic bond breakage along crack growth.

Griffith (1920) compared the work required to break atomic bonds to the strain energy released as a crack grows, considering that in order to break a bond, an amount of work equal to the bond energy must be applied to the system. *Figure II-37* represents a crack that has grown to a length a and in the process has broken several atomic bonds, each requiring a certain amount of work to overcome the atomic bond energy.

Griffith's fracture criterion establishes that a crack will unstably grow when the energy release during the propagation reduces the stored energy of the system. Therefore, the fracture condition can be expressed as follows (Griffith, 1921):

$$\frac{d(W_F - U)}{da} = \frac{dE_r}{da} \qquad \textit{(II-38)}$$

The term on the left represents the energy released per unit length of crack growth, where W_F is the work done by the applied forces to deform the component and U is the strain energy stored in it. The term on the right constitutes the energy expended per unit length of crack growth at material fracture, which presents a resistance quantified by E_r.

When both terms of *Equation (II-38)* are expressed as energy per unit of created crack surface, the term on the left is called the energy release rate (G) and the one on the right is assimilated to the energy required to generate a crack surface unit (R), which is characteristic of the material. Accordingly, the fracture criterion can be expressed as:

$$G = R = G_C \qquad \textit{(II-39)}$$

Thus, the fracture resistance of a material is a function of the energy release rate (G), which depends on the loading conditions and geometry of the component, and its critical value (G_c).

For the particular case of the infinite plate with a crack with a length $2a$ as that depicted in *Figure II-26*, the analytical solution of the energy release rate under plane strain conditions is as follows (Griffith, 1921; Irwin, 1957):

$$G = \frac{\pi \sigma^2 a}{E} \qquad \textit{(II-40)}$$

where E is the Young's modulus of the material.

With all this, a relation between the two characteristic parameters of fracture mechanics, K and G, and the corresponding failure criteria can be stablished. Comparing *Equations (II-40)* and the stress intensity factor defined in *Equation (II-22)* for an infinite plate with the same crack geometry, the following relation is observed between K_I and G (Broek, 1982; Anderson, 2005):

$$G = \frac{K_I^2}{E} \qquad \textit{(II-41)}$$

This expression corresponds to the plane stress situation, while for plane strain the expression is rewritten as:

$$G = \frac{K_I^2(1-v^2)}{E} \qquad (II\text{-}42)$$

2.6 ANALYSIS OF NOTCH-TYPE DEFECTS

2.6.1 Introduction

The application of fracture mechanics in cracks is a well-known and fully established methodology in the analysis of different engineering problems. It is based on the knowledge of the elastic stress field in the front of a sharp crack, which is defined by the stress intensity factor (K_I). Crack propagation is considered to occur when K_I equals a material dependent critical value which, under certain conditions, is called material fracture toughness (K_{IC}). This methodology has been successfully applied to a wide range of situations where the nonlinear micromechanical processes leading to failure are confined within a small region in the vicinity of the crack front. However, there are many situations in which the existing defects are not necessarily sharp. In fact, they can present a considerable blunted geometry.

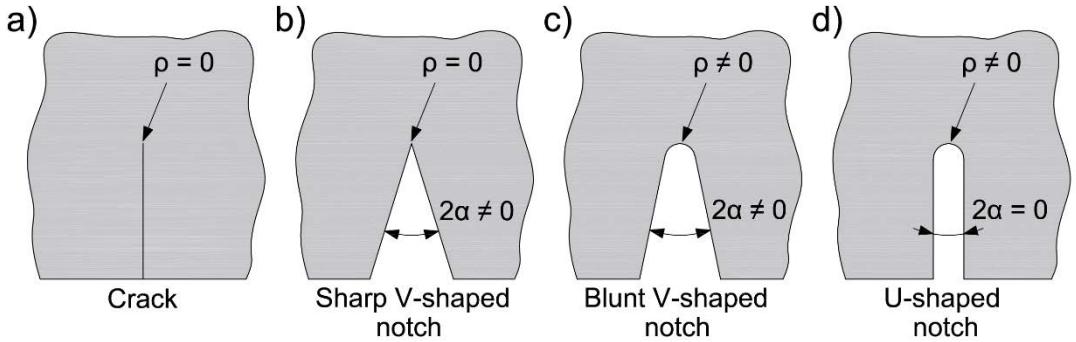

Figure II-38. Classification of defect types: (a) crack, (b) sharp V-shaped notch, (c) blunt V-shaped notch and (d) U-shaped notch.

Notch-type defects develop a higher load bearing capacity than crack-type defects, since they generate less demanding stress fields around them. Several studies can be found in the literature dealing with the stress fields at the notch tip (e.g.; Creager & Paris, 1967; Glinka &

Newport, 1987; Pluvinage, 1998), and all of them suggest a reduction of the stress acting perpendicular to the notch plane. Basically, linear fracture mechanics addresses crack problems or ideally sharp notch problems where the notch radius can be assumed to be roughly equal to zero ($\rho \sim 0$). However, from a strict point of view, every notch has a finite radius and proceeding on the assumption that notches behave like sharp cracks (as considered by traditional fracture mechanics) may be overly conservative in many cases.

According to the general expression of the stress intensity factor based on LEFM and given by *Equation (II-27)*, and assuming that the geometric factor M is a constant for a certain geometry, the product of the square root of the crack size (a) and the applied critical stress is a constant (Williams, 1957):

$$\sigma_c \sqrt{a} = const._1 \qquad (II\text{-}43)$$

However, notch-type defects generate less demanding stress fields. Thus, the previous expression may be rewritten as follows:

$$\sigma_c a^{\alpha} = const._2 \qquad (II\text{-}44)$$

where α is a constant. This notch effect is related to the physical nature of the fracture process (Pluvinage, 1998). For this to occur, certain stress conditions are needed within the material volume or process area. In this case, the traditional maximum stress approaches are often not adequate, in most cases being excessively conservative.

The presence of a notch in a material creates intermediate conditions between those of a material without defects and a cracked material. In some cases, for relatively large and blunt notches, the notch has no effect on the resistant capacity of the material. It would simply involve a section reduction rather than acting as a stress riser. At the other extreme, some sharp and relatively small notches behave as a crack of the same length.

In the field of engineering rock mechanics, apart from those inherent defects of rocks caused by natural sources, notches with different

geometries, sizes and shapes are often created artificially in large rock masses as, for example, for the construction of dams, tunnels, mining excavations, wells, etc. These defects can be generally studied as V-shaped or U-shaped notches, or even as intermediate situations like rounded (blunt) V-notches. For this reason, the influence of the notch geometry (i.e., radius, shape, opening angle and other geometrical aspects) on the fracture behaviour of different components has been widely studied by many authors (e.g., Razumek & Faszynka, 2017; Wu & Tsai, 2017; Chen & Chen, 2018).

2.6.2 Stress distribution at the notch tip

Figure II-39 shows the stress distribution along the bisector of a sharp V-notch plane for the particular case of a specimen subjected to three-point bending conditions (Pluvinage, 1998). The vertical axis represents the dimensionless stress, defined as the local stress divided by nominal stress (σ_{yy}/σ_N), while the horizontal axis represents the dimensionless distance, defined as the distance from the notch tip divided by the defect length (r/a). This distribution can be characterized by two elements: the maximum stress and the stress distribution along the notch plane.

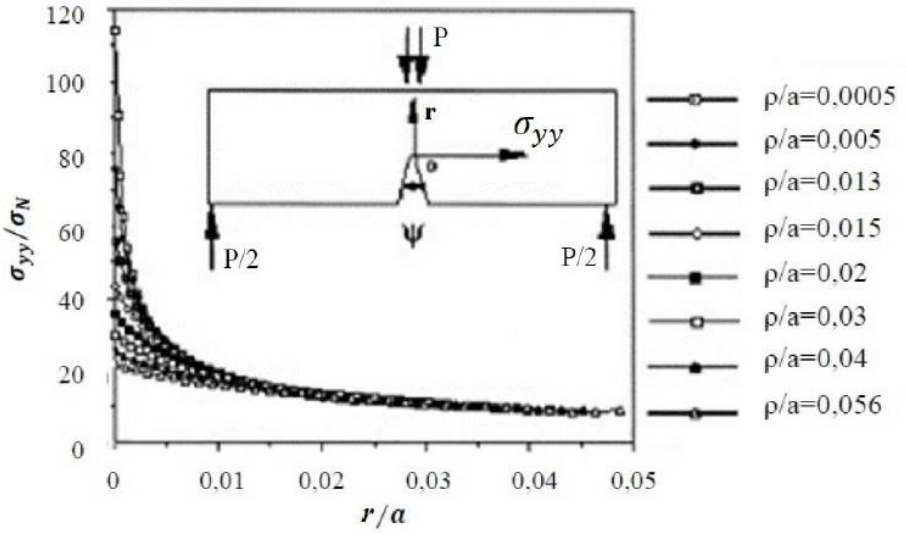

Figure II-39. Influence of notch radius represented as adimensional stress against adimensional distance (Pluvinage, 1998).

Numerous works may be found in the literature providing different models of the stress field at the notch tip along the bisector plane (σ_{yy}).

Table II-7 gathers some of the most widespread stress distribution functions.

Table II-7. Elastic stress distribution functions along the bisector of the notch (adapted from Pluvinage, 1998).

[1]	$\sigma_{yy} = \sigma_N \left[1 + \frac{1}{2}\left(1 + \frac{x}{2}\right)^{-2} + \frac{3}{2}\left(1 + \frac{x}{2}\right)^{-4}\right]$	*(II-45)*
[2]	$\sigma_{yy} = \sigma_{max}\sqrt{\frac{\rho}{\rho + 4x}}$	*(II-46)*
[3]	$\sigma_{yy} = \frac{K}{\sqrt{\pi}}\frac{2(x+\rho)}{(2x+\rho)^{3/2}}$	*(II-47)*
[4]	$\sigma_{yy} = \sigma_{max}\sqrt{\frac{\rho}{\rho + 8x}}$	*(II-48)*
[5]	$\sigma_{yy} = \frac{\sigma_{max}}{3}\left[1 + \frac{1}{2}\left(1 + \frac{x}{2}\right)^{-2} + \frac{3}{2}\left(1 + \frac{x}{2}\right)^{-4}\right]$	*(II-49)*
[6]	Blunt notch: $\sigma_{yy} = \sigma_{max}\left[1 - 2.33\left(\frac{x}{\rho}\right) + 2.59\left(\frac{x}{\rho}\right)^{1.5} - 0.907\left(\frac{x}{\rho}\right)^{2} + 0.037\left(\frac{x}{\rho}\right)^{3}\right]$	*(II-50)*
[6]	Sharp notch: $\sigma_{yy} = \sigma_{max}\left[1 - 0.235\left(\frac{x}{\rho}\right)^{0.5} - 1.33\left(\frac{x}{\rho}\right) + 1.28\left(\frac{x}{\rho}\right)^{1.5} - 0.037\left(\frac{x}{\rho}\right)^{2}\right]$	*(II-51)*
[7]	$\sigma_{yy} = f\sigma_{max}\left[\left(1 + \frac{2x}{\rho}\right)^{-1/2} + \left(1 + \frac{2x}{\rho}\right)^{-3/2}\right]$ $f = 1$ *when* $\frac{x}{\rho} < 0.2$ $f = 1 + \frac{\tan\left(\frac{\pi}{2K_t}\right)}{2.8}\left(\frac{x}{\rho} - 0.2\right)$ *when* $\frac{x}{\rho} \geq 0.2$	*(II-52)*
[8]	$\sigma_{yy} = \sigma_N K_t \sqrt{\frac{\rho}{\rho + 4x}}$ *and* $0 \leq x \leq \frac{\rho}{4}(K_t^2 - 1)$	*(II-53)*

[1] Timoshenko & Goodier (1951)	[5] Usami et al. (1985)
[2] Neuber & Weiss (1962)	[6] Glinka & Newport (1987)
[3] Creager & Paris (1967)	[7] Kujawski (1991)
[4] Chen & Pan (1978)	[8] Bhattacharya & Kumar (1995)

In these expressions of *Table II-7*, σ_N is the nominal stress, σ_{max} is the maximum stress and K_t is a stress concentration factor (not to be confused with the stress intensity factor) defined as the ratio between σ_{max} and the externally applied stress (σ_N), ρ is the notch radius and x is the distance from the notch tip as depicted in *Figure II-40*. According to the expressions of the stress distribution collected in *Table II-7*, unlike the case of cracks, the stress profile of notches present a maximum finite value at the notch tip. Besides, this maximum stress value will decrease as the notch radius increases, as illustrated in *Figure II-40*.

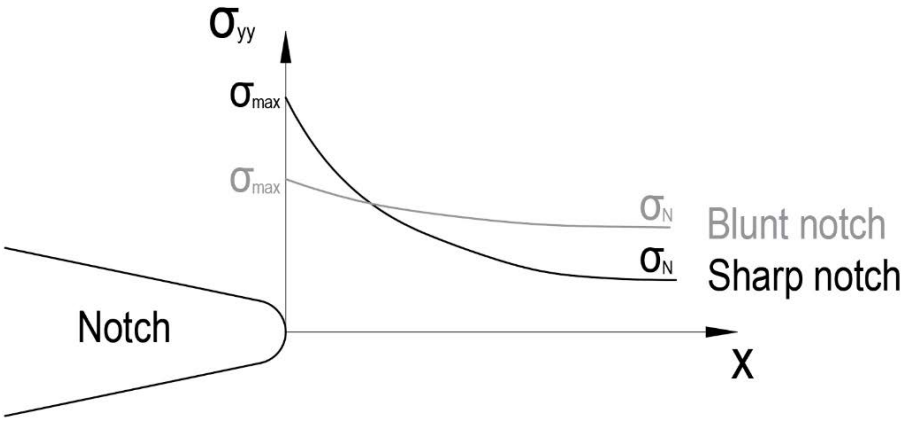

Figure II-40. Stress distribution along the bisector plane of notches with different geometries.

2.6.3 Notch stress intensity factor

The stress distribution at the notch tip can be represented in a bi-logarithmic plot as in *Figure II-41*, with the normal stress along the bisector notch plane divided by the nominal stress (σ_{yy}/σ_N, ordinate axis), and the distance divided by the thickness of the specimen (r/b, abscissa axis).

Figure II-41a shows, in a bi-logarithmic scale, the stress profiles for the particular case of SENB specimens (with different notch radii) subjected to three-point bending conditions (Pluvinage, 1998). Representing any of those curves in a bi-logarithmic form as indicated in *Figure II-41b*, three main regions are distinguished (Pluvinage, 1998):

- Region I: It is the closest zone to the notch tip and corresponds to a nearly constant stress zone. Its value is the product between the elastic stress concentration factor (K_t) and the

stress (σ) in a non-notched situation. X_c is a material characteristic distance, which depends on the microstructure, and X_m represents the distance between the ordinate axis and the intersection point between the extended horizontal line drawn from the maximum stress and the extension of the line corresponding to Region III (see *Figure II-41b*).

- Region II: Transition zone.
- Region III: In this region the dimensionless stress is a potential function of the dimensionless distance:

$$\frac{\sigma_{yy}}{\sigma_N} = C' \left(\frac{r}{b}\right)^{-\alpha} \qquad \textit{(II-54)}$$

where C' is a material constant and α is a constant dependent on the notch radius.

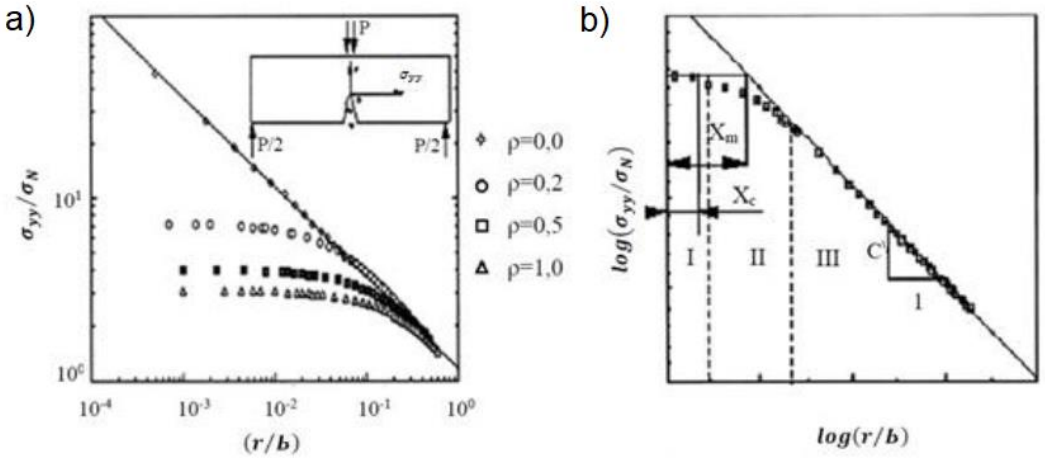

Figure II-41. (a) Stress distribution at the notch tip. Influence of notch radius (Three-point bending specimens); (b) Bi-logarithmic representation of the stress distribution at the notch tip (Pluvinage, 1998).

When r tends to zero ($r \to 0$) the presence of a pseudo-singularity is observed as a function of the distance with the form $r^{-\alpha}$ ($\alpha \leq 0.5$). The stress distribution has the following expression in region III:

$$\sigma_{yy} = \frac{K_\rho}{(2\pi r)^\alpha} \qquad \textit{(II-55)}$$

where K_ρ is the notch stress intensity factor (NSIF), r is the distance from the notch tip and α is a constant that depends on the notch radius (ρ). In the particular case of U-shaped notches, as those analysed in this work, α is approximately 0.5.

2.6.4 Apparent fracture toughness

In the analysis of notched components, the intensity of the stress field is quantified through the NSIF. The NSIF is used not only to describe the stress field in a notch, but also to characterize the apparent toughness of a material (K_{IN}) (Berto & Lazzarin, 2014).

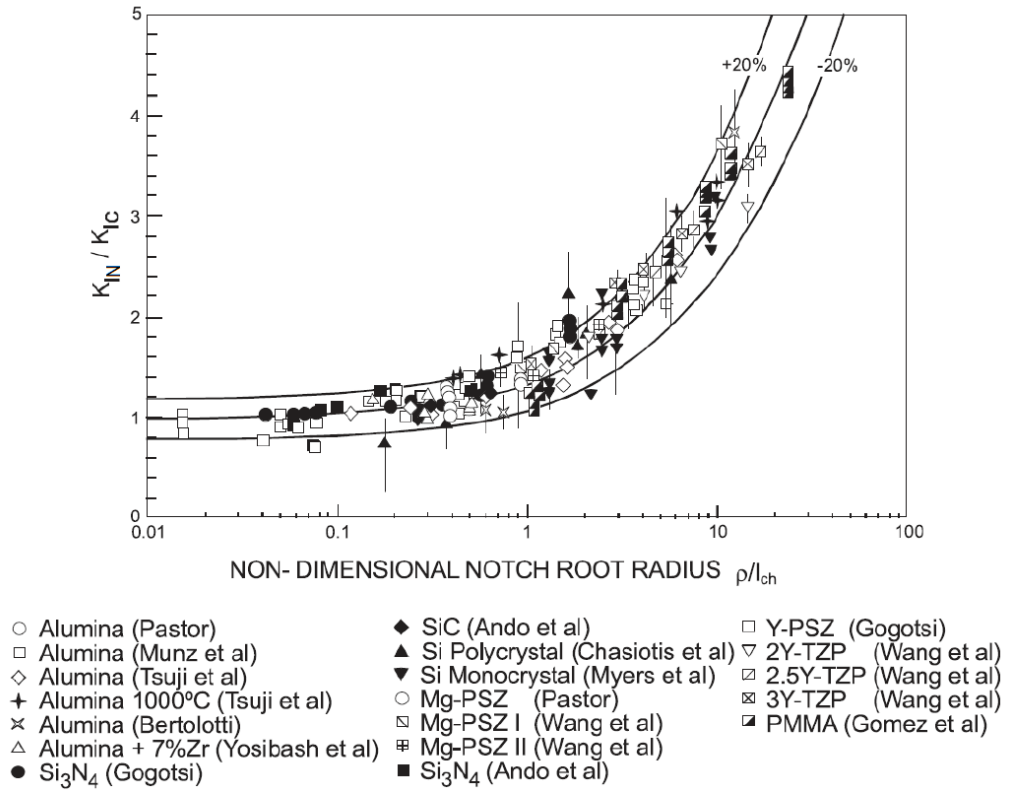

Figure II-42. Variation of apparent fracture toughness (K_{IN}) with notch radius (ρ) of different materials (Berto & Lazzarin, 2014).

By definition, the fracture toughness (K_{IC}) is an intrinsic property of the material that, from a strict point of view, addresses crack problems where the notch radius is equal to zero. However, when the notch radius is large enough to develop a certain notch effect, the resistance to crack propagation increases and, therefore, an apparent fracture toughness (K_{IN}) should be considered instead of the strictly real fracture toughness

(K_{IC}). Thus, the fracture analysis of notched components is equated to a situation in a cracked component where K_{IN} is considered instead of K_{IC}. The apparent fracture toughness somehow considers the influence of the notch effect, as K_{IN} increases with the notch radius as observed in *Figure II-42* for different materials (Berto & Lazzarin, 2014), where the notch radius is normalized with a characteristic length (l_{ch}) that will be addressed subsequently.

2.6.5 Fracture criteria of notched components

Taking as a basis the stress distribution at the notch tip, two types of failure criteria are generally distinguished: global fracture and local fracture criteria. In the case of notches, there is no stress singularity at the tip (unlike cracks), but a maximum stress followed by a pseudo-singularity in which the stress distribution is determined by the NSIF. These are the basic considerations for developing notch fractured mechanics and for determining fracture resistance in materials with notch-type defects.

2.6.5.1 Global fracture criteria

The global failure criterion establishes that failure occurs when the notch stress intensity factor reaches a critical value (K_N), which depends on the material and the notch radius:

$$K_\rho = K_N \qquad \textit{(II-56)}$$

The parameter K_N indicates the fracture resistance of a notched components and has units of MPa · m$^\alpha$. K_ρ defines the stress and strain fields in the vicinity of the notch tip, as shown in *Equation (II-55)*. This approach is analogous to that proposed by linear-elastic fracture mechanics for the analysis of cracks, but its application is very limited because of the lack of analytical solutions for K_ρ (in contrast with the case of K_I, e.g., R6, 2001; BS7910, 2005; FITNET FFS Procedure, 2008) or/and standardised procedures for the experimental definition of K_N (in contrast with the case of K_{IC}, e.g., ASTM E-1820:2009).

2.6.5.2 Local fracture criteria

Concerning local criteria, these are based on the stress-strain field at the notch tip and have more applicability than global criteria from a

practical point of view. Local fracture criteria may use values of a given variable (e.g., stress, strain energy, etc.) at a particular point or values along a certain line or a surrounding volume.

The simplest local failure criterion assumes that the fracture process volume is defined according to a process distance (X_{pz}), which defines the length of the region where local failure occurs (Pluvinage, 1998). At failure, the following parameters reach a critical value:

$$\sigma_{max} = \sigma_c^*;\ X_{pz} = X_c \qquad (sharp\ notch) \tag{II-57}$$

$$\sigma_{max} = \sigma_c^*;\ X_{pz} = X_m(\rho) \qquad (blunt\ notch) \tag{II-58}$$

In the case of cracks or sharp notches where the notch radius tends to zero, the distance X_m (derived from the maximum stress in the singularity zone as indicated in *Figure II-41b*) is smaller than the characteristic distance X_c, which is given microstructural considerations, such as the grain size for example (see *Figure II-43*). In this case, it is the characteristic distance that determines the fracture process, according to the following expression:

$$K_N = \sigma_c^*(2\pi X_c)^{\alpha} \tag{II-59}$$

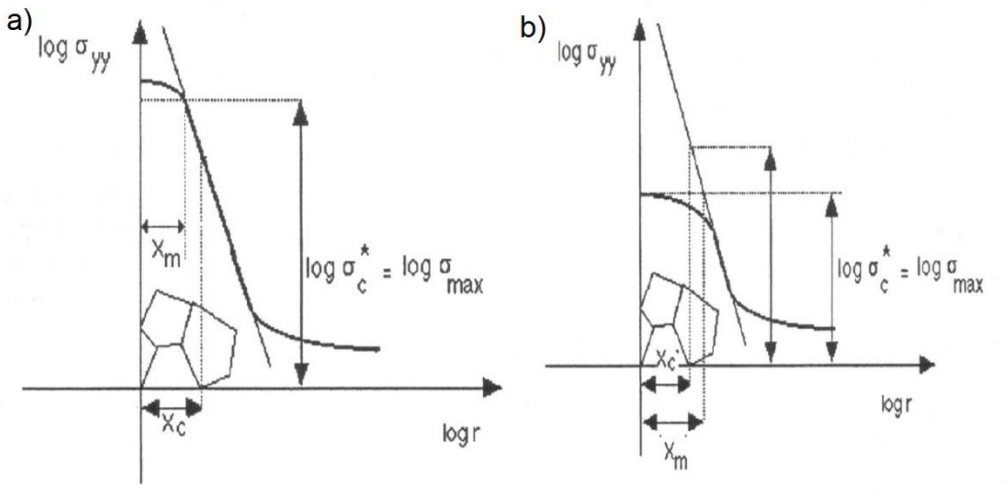

Figure II-43. Stress distribution at the tip of (a) a sharp notch, (b) a blunt notch (Pluvinage, 1998).

By contrast, in the case of a blunt notch $X_m > X_c$, its value depends on the notch radius (ρ):

$$K_N = \sigma_c^* \left(2\pi X_m(\rho)\right)^{\alpha} \qquad \textit{(II-60)}$$

Pluvinage et al. (1999) developed a similar procedure, considering that failure of a notched component occurs when an effective stress (σ_{ef}) along a certain effective distance (X_{ef}) is larger than the material strength ($\sigma_{ef} > \sigma_f$). This effective distance corresponds to the lowest stress gradient point (see *Figure II-44*) located in the transition between regions I and II, and is a linear function of ρ as demonstrated by Kim et al. (2004) and indicated in *Figure II-45*.

Another local failure criterion is called the critical average stress model, which states that failure occurs when the average stress over the effective distance (X_{ef}) reaches the strength of the material (σ_f) (Bao & Jin, 1993; Fenghui, 2000):

$$\frac{1}{X_{ef}} \int_0^{X_{ef}} \sigma(r) dr = \sigma_f \qquad \textit{(II-61)}$$

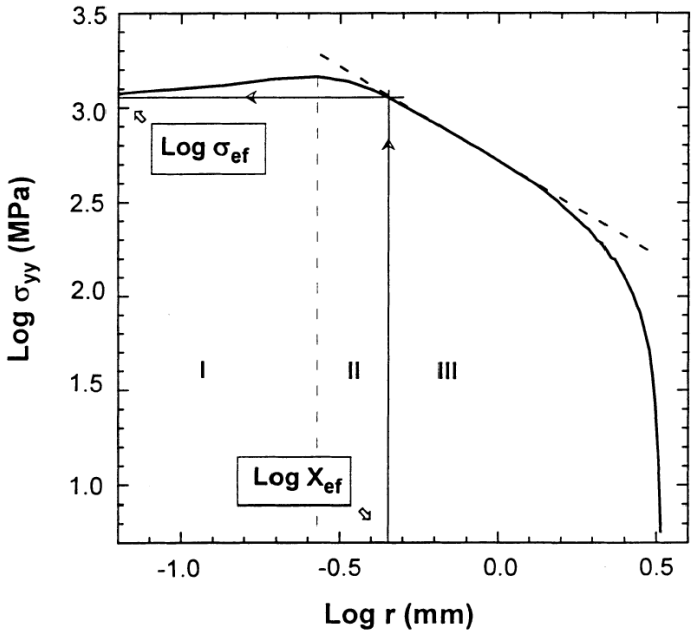

Figure II-44. Bi-logarithmic representation of the stress distribution at the notch tip (Pluvinage et al., 1999).

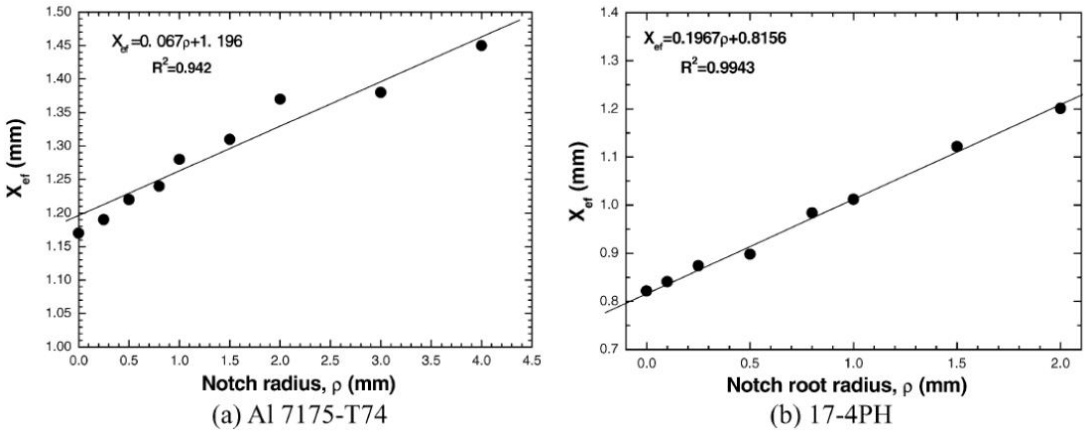

Figure II-45. Relation between effective distance (X_{ef}) and notch radius (ρ) obtained for three-point bending test specimens (Kim et al., 2004).

Proceeding along a similar development as that of the critical average stress model, Elayachi et al. (2005) obtained K_N with the following expression:

$$K_N = \sigma_{ef}(\pi X_{ef})^{\alpha} \qquad \textit{(II-62)}$$

where σ_{ef} is the average stress over the effective distance (X_{ef}). The obtained critical notch stress intensity factor (K_N) can be considered as a value of the fracture toughness of the material, with MPa · $m^{0.5}$ units for the particular case of U-shaped notches where α is approximately 0.5.

Finally, another of the most widely used criteria in the literature is the critical energy density criterion or the Sih criterion (Sih, 1974). This criterion states that failure occurs when the value of the energy density (ω) at a certain distance from the notch tip (X_c) reaches a critical value (ω_c):

$$\omega = \omega_c;\ x = X_c \qquad \textit{(II-63)}$$

All these failure criteria have an obvious solid theoretical base but, in most of the cases, their application in practice is rather limited. This is because of the required use of resistance values such as K_N, for which

there are no standardised characterization procedures, or parameters like the NSIF whose solutions are not known even for common geometries. In other cases, the definition of the calculation parameters such as X_c or σ_f is not fully developed or straightforward. Only the critical average stress criterion seems to provide a clear methodology if σ_f is known. Consequently, apart from the definition of theoretical failure criteria, it is necessary to establish simple methodologies that allow to analyse notched components in a practical way, maintaining the solid theoretical base of the aforementioned criteria.

In this regard, different methodologies have been proposed in fracture mechanics for predicting the onset of failure of notches samples: Gómez et al. (2000) worked on a criterion for brittle and quasi-brittle materials under monotonic loading, based on the Cohesive Zone Model (CZM) proposed in the past by Dugdale (1960) and Barenblatt (1959) to describe stress fields and fracture processes near the defect tip. The CZM has demonstrated to offer good fracture load predictions of notched specimens (e.g., Gómez et al., 2000; Gómez & Elices, 2004). The Finite Fracture Mechanics (FFM) criterion is based on the assumption that the crack grows by finite steps, which are determined by a condition of consistency of both energy and stress requirements (Carpinteri et al., 2008). Likewise, the Strain Energy Density (SED) criterion is an energy-based approach that combines the elementary volume proposed by Neuber (1958) and the local Mode I concept first proposed by Erdogan and Sih (1963). Several publications can also be found on the application of the SED criterion for investigating the fracture behaviour of cracked and notched elements (e.g., Lazzarin & Zambardi, 2001; Torabi et al., 2017). On the other hand, Taylor (2007) collects a group of methodologies named the Theory of Critical Distances (TCD) because they use a material characteristic parameter called the critical distance (L). The TCD was first used by Neuber (1958) and Peterson (1959) but it has been in the last years, with the development of finite element stress analyses, that this theory has been scientifically analysed more in detail (e.g., Taylor, 2007; Susmel & Taylor, 2010). Some other local fracture criteria such as the Maximum Tangential Stress (MTS) criterion (Erdogan & Sih, 1963), the Generalized Maximum Tangential Stress (GMTS) criterion (Smith et al., 2001), the Maximum Tangential

Strain (MTSN) criterion (Chang, 1981), the Extended Maximum Tangential Strain (EMTSN) criterion (Mirsayar, 2015) or the maximum energy release rate (G) criterion (Hussain et al., 1974) are also widely used. In particular, the GMTS, which is an extension of the MTS criterion, states that brittle fracture in notched specimens happens when the value of the tangential stress at a specified critical distance from the notch tip attains a critical value. Thus, this criterion is equivalent to the Point Method of the TCD that will be described in detail in *Section 2.7.3.1.*

All the aforementioned methodologies have been widely applied for the fracture assessment of different materials under varied loading and failure conditions. However, the fracture analyses of notched components in the particular field of rock fracture mechanics are scarce and relatively recent. Aliha et al. (2006), for example, provided good predictions of the mode I and II fracture toughness and angle of fracture initiation of a marble using the generalized MTS criterion, considering the effect of the T-stress. Similarly, Mirsayar et al. (2018) used an extended version of the MTSN to study the brittle fracture of two different marbles under mixed mode I/II. On the other hand, Aliha et al. (2017) and Razavi et al. (2018) worked on the application of an average SED criterion on the fracture behaviour of a marble and a granite, respectively.

Subsequently, both the TCD and the SED criterion will be described in detail, which are the two local fracture criteria whose theoretical frames are evaluated in this work for the fracture assessment of rocks.

2.7 THE THEORY OF CRITICAL DISTANCES

2.7.1 Introduction

In this section, the Theory of Critical Distances (hereafter called the TCD) will be described starting with a historical contextualization, followed by a detailed description of the most important methodologies encompassed by the TCD.

The TCD can be considered as a group of methods with some common features, as the use of LEFM for fracture analyses and the use of a material characteristic parameter called the critical distance (L). Thus, while LEFM only needs one resistance characteristic parameter, the fracture toughness (K_{IC}), the TCD needs two: K_{IC} and L. The TCD

has greatly increased the applications of LEFM, allowing, for example, the performance of failure load predictions and analyses of maximum admissible defects in components with notches or other stress risers of arbitrary geometry, around which elastic analyses of the stress field can be developed (by using Finite Elements, FE, for example).

2.7.2 Historical background

The TCD arises in the 1930's with Neuber's (1936) and Peterson's (1938) works. They were both interested in predicting fatigue failure in notched metallic components. Their ideas were fully developed in the 1950's and were described in two important publications: *Kerbspannungslehre* (in English: Theory of stress in notches) by Neuber (1958) and *Notch Sensitivity* by Peterson (1959).

Neuber (1958) proposed what is known as the Line Method (LM), in which the elastic stress is averaged over a critical distance from the notch tip. However, the main objective of Neuber's idea was not to predict fatigue failure, but to perform a stress analysis. Neuber believed that classic theories for predicting the elastic stresses in bodies were wrong in situations with large curvature radii.

Neuber (1958) argued that materials are not truly continuous, but that the use of continuum mechanics is acceptable since the scale of the problem is larger than any non-homogeneity of the material. It is important to highlight that this statement was referred to the case of the metallic materials being analysed in his work. The solution that Neuber (1958) proposed to the problem of the non-homogeneity of materials was calculating the stresses using the classical theories and then averaging them over a distance equal to the length of a structural particle (Taylor, 2007). This length, as it will be discussed in *Section 2.7.3.2*, is currently assumed to be twice the critical distance ($2L$).

Peterson (1959) knew Neuber's (1958) work but chose a slightly different approach based on the stress at a single point located at a distance of half the critical distance ($L/2$) from the defect tip. This method will be discussed in detail in *Section 2.7.3.1*, which is nowadays known as the Point Method (PM).

One of the main problems that both Neuber (1958) and Peterson (1959) had to face was the definition of the critical distance. Peterson

(1959) speculated that the critical distance could be related to the grain size, but this raised some measurement difficulties. So, the same way as Neuber (1958) did, he chose to determine the value of the critical distance empirically, by adjusting fatigue predictions to experimental data. He observed that for a certain material, the value of the critical distance seemed to be inversely proportional to the strength of the material.

The second problem, derived from the technological limitations of that time, was the precise calculation of the stresses around the defect. Analytical expressions could be used for an approximation of the stress profiles in notches with standard geometries. However, in order to achieve greater precision in the calculations, local stresses were used, since they are basically determined by the defect radius (ρ) and the stress concentration factor (K_t). With this methodology, acceptable precision was achieved, allowing the application of the PM and the LM in a reliable way.

The works of Neuber (1958) and Peterson (1959) were frequently used during the 1960's for the analysis of fatigue problems in metallic materials. In that decade, the PM and the LM were also used for the first time to perform fracture predictions of brittle components, considering the interatomic distance as the critical distance (McClintock & Irwin, 1965; Novozhilov, 1969). A breakthrough in this theory occurred in 1974 with Whitney & Nuismer's work, who analysed fiber-reinforced composite materials. Their proposed methods were called the Point Stress Method and the Average Stress Method, very similar to the PM and LM, respectively. They used them to study the influence of hole dimensions and notch size on static resistance of the material. In addition, these researchers related the PM and the LM with LEFM, which allowed to express the critical distance as a function of the fracture toughness and to relate the critical distances of the two methods ($L/2$ in the PM and $2L$ in the LM). This progress was possible because, at that time, LEFM was already stablished in the field of brittle fracture of cracked materials.

In the 1980's, Kinloch & Williams (1980), with no apparent prior knowledge of Neuber's, Peterson's and Whitney & Nuismer's works, developed a method for the analysis of the blunting effect of cracked

polymers that, basically, was the PM. However, they considered a critical stress parameter (σ_0) different to that of the ultimate tensile stress of the material, and this modification allowed the application of the TCD to be extended to numerous materials.

The TCD, and particularly the PM and the LM, have been applied in different fields as those collected by Taylor (2007), based on experimental data from brittle facture tests in ceramic materials, brittle fracture in metallic materials, or fatigue in polymeric materials. The precision in the fracture predictions offered by the TCD, together with the development of finite element stress analyses in the last decades, have led to an important increase of its use and fields of application. However, despite its simplicity and potential for the analysis of fracture processes as demonstrated for a wide range of materials, scarce work can be found about the application of the TCD in rocks. Lataji (1972) was the first applying the PM in rocks, followed by Ito & Hayasi (1991) and Ito (2008), who successfully applied the PM for the analysis of hydraulic fracturing in a wellbore. Such works have been cited by other authors since then (e.g., Bunger et al., 2010; Shimizu et al., 2011), but the application of the TCD in rocks has not been further developed. This is probably due to the relatively large scatter of the experimental results as a consequence of the higher degree of heterogeneity of rocks compared to metallic or polymeric materials, for example, which makes accurate analysis and the obtention of clear conclusions more difficult. Aiming to fill this gap in knowledge, this work analyses the applicability of the TCD in the field of rock fracture mechanics.

2.7.3 Methodologies within the TCD

The TCD is composed by different methods using the parameter called the critical distance (L) and linear-elastic analyses for fracture assessments. Some of the methods are based on the stress field around the defect tip and, basically, postulate that failure occurs when a distance dependent equivalent stress reaches the inherent strength (σ_0) of the material. This equivalent stress is equal to the maximum principal stress calculated either at a certain distance from the notch tip (Point Method, PM), averaged over a distance (Line Method, LM), over an area (Area Method, AM) or over a finite volume (Volume method, VM). *Figure II-46* illustrates the PM, LM and the AM (the VM considers a

three-dimensional volume) over a stress-distance curve from the notch tip, indicating the critical distance for each method. These methodologies will be later described in detail.

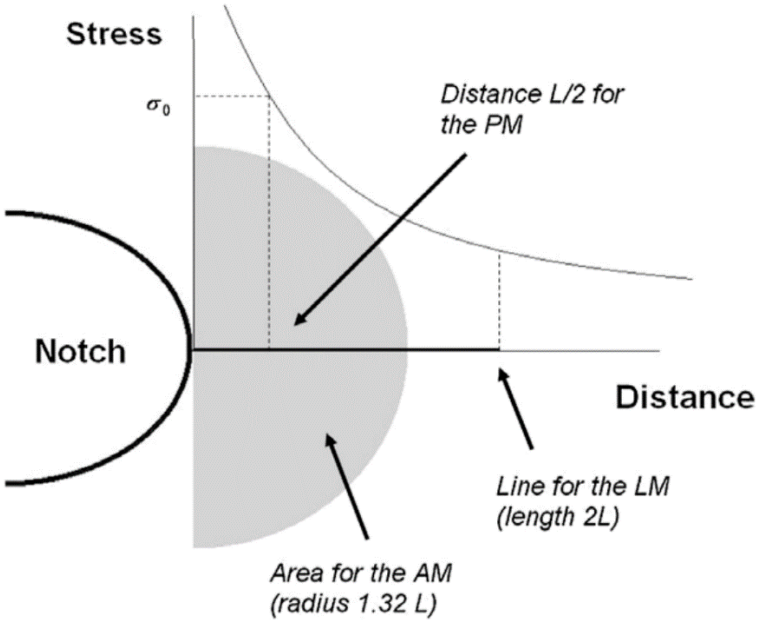

Figure II-46. Illustration of the PM, LM and AM and corresponding critical distance for each method (Shahri & Sandström, 2010).

The PM and LM are theoretically identical for long cracks, and trivially, the two predictions will also be identical for plane tensile specimens. However, there is no guarantee that the predictions will be identical for any other problem and, indeed, they are not (Taylor, 2007). However, as stated by Taylor (2007) and as will be shown in subsequent chapters, the differences between the PM and LM predictions are generally small. Depending on the material analysed, there is some evidence that the accuracy of the PM or LM is related to the operative mechanisms of failure, but in the great majority of cases, the differences between the PM and the LM predictions is so small that both are adequate for describing experimental data that inevitably contains a certain amount of scatter (Taylor, 2007). On the other hand, the AM involves averaging the stresses over some area (or volume when using the VM) in the vicinity of the notch. In this case the analysis is somewhat more complicated, but even so it not difficult to implement such averaging procedures as part of the post-processing of FEA. The

results will obviously depend on the shape of the area or volume chosen (Taylor, 2007).

Other methodologies included within the TCD, such as Finite Fracture Mechanics (FFM) and the Imaginary Crack Method, are based on the stress intensity factor (K) instead of the stress field at the defect tip, but their application is not so straightforward.

The different TCD approaches provide predictions for the apparent fracture toughness (K_{IN}) of notched components. The main parameters affecting these predictions are the fracture toughness (K_{IC}), corresponding to a cracked situation, and the notch radius (ρ). Once the material fracture toughness is known the apparent fracture toughness can be determined as a function of the notch radius. The following expression establishes the critical condition:

$$K_I = K_{IN} \qquad \textit{(II-64)}$$

Where K_I is the stress intensity factor used in fracture mechanics analyses for a crack-type defect with the same length as the notch. Thus, in essence, fracture analysis of notched components is equated to a situation in a cracked component (*Equation (II-31)*) where K_{IN} is considered instead of K_{IC}.

With all this, both the Point Method (PM) and the Line Method (LM), those with the simplest forms, are considered in this work. Although the AM and the VM can also provide valid predictions, these methods are more difficult to use and do not seem to confer any increased accuracy when compared to the experimental data (Taylor, 2007). Consequently, the following subsections provide a detailed description of both the PM and the LM, and some general comments of other methods included within the TCD.

2.7.3.1 Point Method (PM)

The PM constitutes the simplest form of the TCD, and it states that fracture occurs when the tensile stress at a certain distance from the tip equal to $L/2$ reaches the inherent strength of the material (σ_0). Thus, the failure criterion according to the PM can be expressed as follows:

$$\sigma(L/2) = \sigma_0 \qquad \textit{(II-65)}$$

The inherent strength is an intrinsic property of the material. In general, its value is larger than the ultimate tensile strength (σ_u), but in the particular case of brittle and quasi-brittle materials like rocks, where there is a linear-elastic behaviour both at micro- and macro-scales, σ_0 might be assumed to roughly coincide with σ_u (Taylor, 2007). Therefore, *Equation (II-65)* can be rewritten as:

$$\sigma(L/2) = \sigma_u \qquad \textit{(II-66)}$$

Figure II-47 represents the parameters of the TCD, that is L and σ_0, according to the PM.

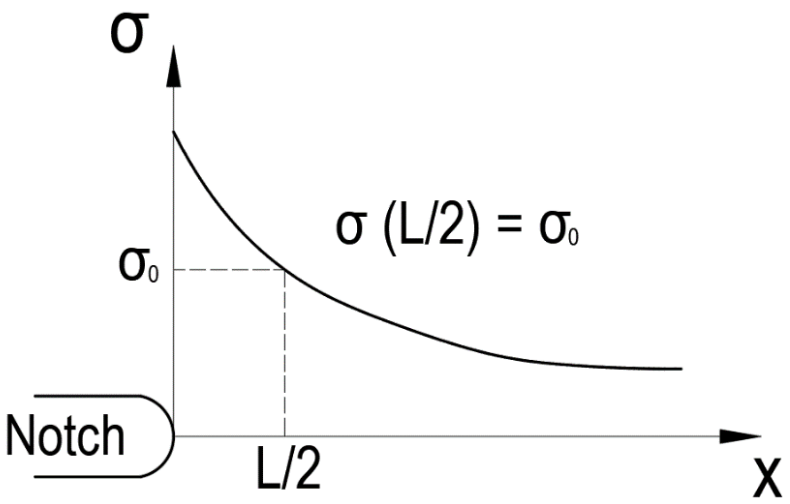

Figure II-47. Graphical representation of the PM on the stress-distance curve along the bisector of the notch plane.

The expression for determining the critical distance can be justified as follows: At failure, the stress intensity factor of a cracked component (K_I) is equal to the fracture toughness of the material (K_{IC}). Thus, based on *Equation (II-22)* and for the particular geometry specified in *Figure II-26*, the failure condition can be expressed as:

$$K_I = \sigma_f \sqrt{\pi a} = K_{IC} \qquad \textit{(II-67)}$$

where σ_f corresponds to the applied external stress at failure. Likewise, the stress field along the bisector plane at that moment, according to *Equation (II-28)*, is:

$$\sigma(r) = \frac{K_I}{\sqrt{2\pi r}} = \frac{\sigma_f \sqrt{\pi a}}{\sqrt{2\pi r}} = \sigma_f \sqrt{\frac{a}{2r}} \qquad \textit{(II-68)}$$

These expressions correspond to mode I loading conditions but can be extrapolated to other failure modes.

Considering the PM in which failure is supposed to occur when the stress at distance equal to $L/2$ reaches the inherent strength of the material (*Equation (II-65)*), the fracture criterion can be expressed as follows, based on *Equations (II-67)* and *(II-68)*:

$$\sigma_f \sqrt{\frac{a}{2(L/2)}} = \frac{K_{IC}}{\sqrt{\pi a}} \sqrt{\frac{a}{L}} = \sigma_0 \qquad \textit{(II-69)}$$

Thus, inverting this equation the expression for the critical distance is obtained, which relates L and σ_0 through the fracture toughness (K_{IC}):

$$L = \frac{1}{\pi} \left(\frac{K_{IC}}{\sigma_0} \right)^2 \qquad \textit{(II-70)}$$

In those cases in which *Equation (II-66)* can be applied (i.e., brittle and quasi-brittel materials), the tensile strength (σ_u) can be experimentally obtained from direct or indirect tensile tests as those mentioned in *Section 1.4.1.1* for the particular case of rocks. Likewise, *Equation (II-70)* can be used to determine the critical distance. To do so, the required fracture toughness value can also be experimentally obtained from standardised tests of cracked components, as those indicated in *Section 2.5.1.1* (e.g., *Table II-6*). Alternatively, σ_0 (σ_u in the case of rocks) and L can also be determined by comparing the stress-distance curves at failure of two specimens with different defect geometries (e.g., by varying the notch radius). According to the PM, the

stress profiles of these two specimens at failure will cut at a point whose coordinates are $(L/2, \sigma_0)$. This last method is especially useful when σ_0 deviates from σ_u, and will be described in *Section 2.7.4.*

Once the TCD parameters are known, the PM allows to perform fracture load predictions of notched components. To do so and to avoid the use of finite element analyses (FEA) in the fracture predictions, the most widespread application of the PM takes as a basis the definition of the stress field at the notch tip proposed by Creager & Paris (1967), which allows to obtain an analytical expression for K_{IN}. The stress field proposed by Creager & Paris (1967) assumes that the stresses at the notch tip are similar to those at a crack tip but displaced a certain distance (half notch radius, $\rho/2$) along the bisector plane of the notch, and is only valid for long and narrow notches:

$$\sigma(r) = \frac{K_I}{\sqrt{2\pi x'}}\left(1 + \frac{\rho}{2x'}\right) \qquad \textit{(II-71)}$$

x' represents the distance from the point halfway between the notch tip and its centre radius. This expression can be rewritten in terms of distance from the notch tip (x), keeping in mind that $x' = x + \rho/2$:

$$\sigma(x) = \frac{K_I}{\sqrt{\pi}} \frac{2(x+\rho)}{(2x+\rho)^{3/2}} \qquad \textit{(II-72)}$$

Considering the PM in which, at failure, $x = L/2$ and $\sigma = \sigma_0$, and stablishing the fracture criterion defined in *Equation (II-64)*, *Equation (II-72)* can be rewritten as follows:

$$K_{IN} = \sigma_0 \sqrt{\pi} \frac{(L+\rho)^{3/2}}{L+2\rho} \qquad \textit{(II-73)}$$

By definition, K_{IN} is equal to K_{IC} in a cracked situation in which the notch radius is equal to zero. Thus, for $\rho = 0$ *Equation (II-73)* is:

$$K_{IC} = \sigma_0 \sqrt{\pi L} \qquad \textit{(II-74)}$$

Finally, combining *Equations (II-73)* and *(II-74)*, the analytical solution for the apparent fracture toughness (K_{IN}) of a notched component according to the PM corresponds to the following expression:

$$K_{IN} = K_{IC} \frac{(1 + \rho/L)^{3/2}}{1 + 2\rho/L} \qquad \textit{(II-75)}$$

With this expression, the apparent fracture toughness of notched components can be calculated as a function of the notch radius, once the critical distance and the fracture toughness of the material are known.

2.7.3.2 Line Method (LM)

The LM states that failure occurs when the average tensile stress over a distance from the defect tip equal to $2L$ reaches the inherent strength of the material (σ_0). In this case, the expression for the fracture criterion is given as:

$$\frac{1}{2L} \int_0^{2L} \sigma(x) dx = \sigma_0 \qquad \textit{(II-76)}$$

Once again, in brittle and quasi-brittle material like rocks, σ_0 can be assumed to coincide with σ_u. Under this condition, *Equation (II-76)* can be expressed as:

$$\frac{1}{2L} \int_0^{2L} \sigma(x) dx = \sigma_u \qquad \textit{(II-77)}$$

This method is illustrated in *Figure II-48*, where it is observed that the area under the stress-distance curve defining the stress profile at failure, which is averaged over a distance equal to $2L$, coincides with the inherent strength of the material.

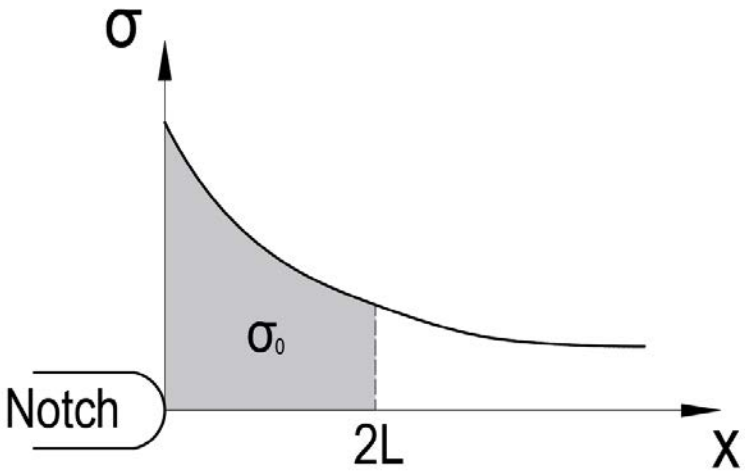

Figure II-48. Graphical representation of the LM on the stress-distance curve along the bisector of the notch plane.

The procedure to get the analytical expression that predicts the apparent fracture toughness according to the LM is analogous to that of the PM. It combines the stress distribution proposed by Creager & Paris (1967) in *Equation (II-72)* with the fracture criterion of the LM indicated in *Equation (II-76)*, considering the failure situation in which *Equation (II-64)* is fulfilled. Thereby, integrating *Equation (II-72)* in the domain defined by *Equation (II-76)* and considering that at failure $K_I = K_{IN}$, the following result is obtained:

$$\sigma_0 = \frac{2K_{IN}}{\sqrt{\pi}} \frac{1}{\sqrt{\frac{\rho}{2} + 2L}} \qquad (II\text{-}78)$$

This expression is rewritten as follows for a cracked situation in which $\rho = 0$:

$$K_{IC} = \sigma_0 \sqrt{\frac{\pi}{2} L} \qquad (II\text{-}79)$$

Similarly to the case of the PM, combining *Equations (II-78)* and *(II-79)*, the analytical expression of K_{IN} according to the LM is:

$$K_{IN} = K_{IC} \sqrt{\rho/4L + 1} \qquad (II\text{-}80)$$

This expression allows to obtain the apparent fracture toughness of a notched component with any notch radius (ρ) according to the LM, once the material fracture toughness and the critical distance are defined.

It is important to highlight that both expressions of the PM and of the LM, i.e., *Equations (II-75)* and *(II-80)*, respectively, are based on Creager & Paris (1967) stress distribution function, which is supposed to be only valid when $\rho \ll a$ and for infinite body dimensions (i.e., sufficiently large not to have any influence of the boundaries).

Both the PM and the LM method offer identical predictions in situations where there is no presence of defects or where the existing defects are crack-type defects. By contrast, under notched conditions, both methods offer certain differences. In any case, these differences are insignificant from a practical point of view (Taylor, 2007).

Figure II-49 shows a comparison between PM and LM predictions for an aluminium alloy (Madrazo et al., 2012). A good agreement with experimental data is observed in both cases, with a small deviation for small notch radii. This is because the PM provides K_{IN} predictions that remain approximately constant up to a critical value of ρ, from which K_{IN} increases. By contrast, the LM shows a continuous increase of K_{IN} with ρ from the beginning.

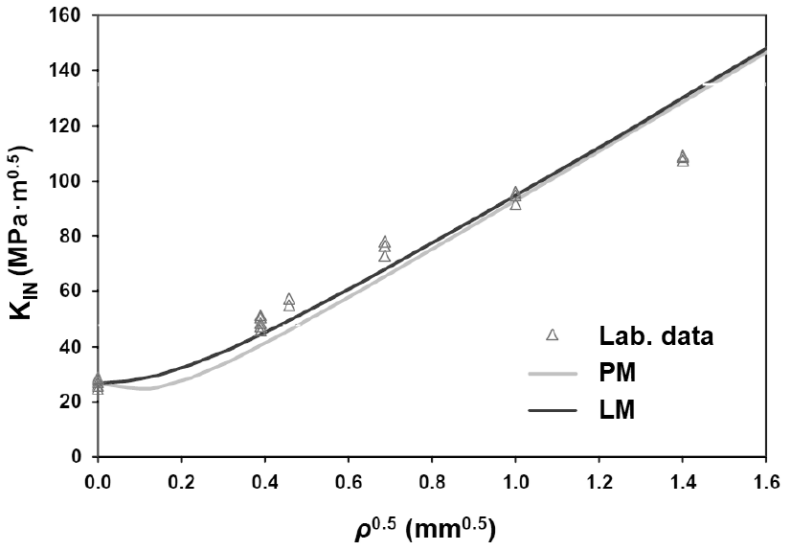

Figure II-49. Comparison between PM and LM predictions on an aluminium alloy (Madrazo et al., 2012).

2.7.3.3 Other methods

As previously commented, there are some other methodologies included within the TCD apart from the PM and the LM. However, the rest of the methods are less attractive from a practical point of view as their use is not so straightforward.

The Area Method (AM) and the Volume Method (VM) are comparable to the already defined LM, but in these cases the stress is averaged over a certain area and volume in front of the notch, respectively. This work is not focused on the use of these methodologies, but as an example, *Figure II-50* illustrates the fracture criterion defined by the AM.

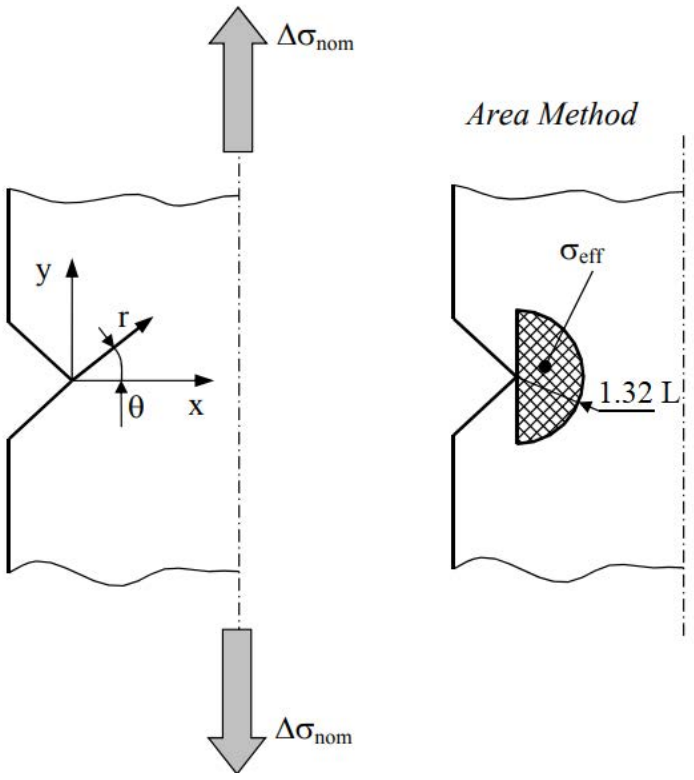

Figure II-50. Schematic representation of the AM of the TCD (Pelekis & Susmel, 2016).

It is observed that defining the stress field along the bisector plane of the notch is no longer enough, but the stress field around the notch is required. When the stress averaged over the area depicted in *Figure II-50* reaches the inherent strength, failure will occur. Thus, based on

the polar coordinate system indicated in *Figure II-50*, the failure criterion according to the AM is expressed as follows:

$$\frac{4}{\pi L^2}\int_0^{\pi/2}\int_0^{L}\sigma(\theta,r)rdrd\theta = \sigma_0 \qquad \textit{(II-81)}$$

Considering the semicircular area centred on the point of maximum stress (*Figure II-50*) and by integrating the stress field ahead of a sharp crack, Bellett et al. (2005) showed that the radius of the semicircular area is 1.32 times L. This solution can be extended for the VM, but this requires the stresses in the three-dimensional space ahead of the notch to be defined. Consequently, its application is rather limited.

On the other hand, the Imaginary Crack Method (ICM) assumes that a crack exists in front of the notch and states that failure occurs when this crack reaches a critical K_I value corresponding to the fracture toughness. Some researchers doubt that this crack is indeed imaginary and defend its physical existence. However, given the theoretical ambiguity, the crack is considered imaginary (Taylor & Kasiri, 2008). This method was independently developed by various groups. First, Haddad et al. (1979) used this methodology for short crack fatigue analyses, Lukas & Klesnil (1978) focused on the study of the notch effect in fatigue analyses, and Waddoups et al. (1971) addressed the notch effect in composite materials. In any case, the methodology arose thanks to the study of the growth of cracks from notches (Smith & Miller, 1977). Two assumptions are made when using the ICM: there is a crack at the notch tip whose length is a_{ICM}, and the propagation of this crack responds to LEFM behaviour. According to this method, the expression of the stress causing failure (σ_f) is given by:

$$\sigma_f = \frac{K_C}{F\sqrt{\pi(a + a_{ICM})}} \qquad \textit{(II-82)}$$

where F is a constant that depends on the geometry of the component. The length of the imaginary crack (a_{ICM}) coincides with L after making

some corrections for the geometry component. This method provides similar results to those of the LM.

Finally, the Finite Fracture Mechanics (FFM) approach has been recently developed and can be considered a variant of the TCD (Seweryn & Lukaszewicz, 2002; Taylor et al., 2005). In this approach, Griffith's energy balance is modified by assuming that crack growth occurs by finite increases in crack length (Δa) rather than conventional analyses that assume infinitesimal defect growth. The resulting failure criterion can be expressed as follows:

$$\sigma_f = \sqrt{\frac{G_c E}{\pi\left(a + \frac{\Delta a}{2}\right)}} = \frac{K_C}{\sqrt{\pi\left(a + \frac{\Delta a}{2}\right)}} \qquad \textit{(II-83)}$$

The results show that the most precise value for this finite propagation is a length of $2L$, which may require corrections based on the geometry. This method provides the same predictions as the LM when the notches are sharp, and similar results for blunt notches (Taylor & Kasiri, 2008).

2.7.4 Analysis methodology and parameters of the TCD

The TCD uses linear-elastic analyses to determine the stress fields around the defects. This procedure might not be realistic in situations where notches (especially in the case of sharp notches) generate stress fields that deviate from elastic behaviour if they are high enough. However, even if linear-elastic analyses are employed under these situations, the TCD provides highly accurate fracture predictions once the corresponding calibration has been performed (Taylor, 2007). Susmel & Taylor (2010) have even shown that the TCD might provide good predictions when working with elasto-plastic stress fields.

Figure II-51 shows an example of the stress analysis performed to a double notched specimen subjected to direct tensile loading (mode I), representing the stress-distance curve along the notch bisector plane. The stresses are obtained using FEA. As observed from the stress-distance curve, the maximum stress occurs at the notch tip and reduces with the distance.

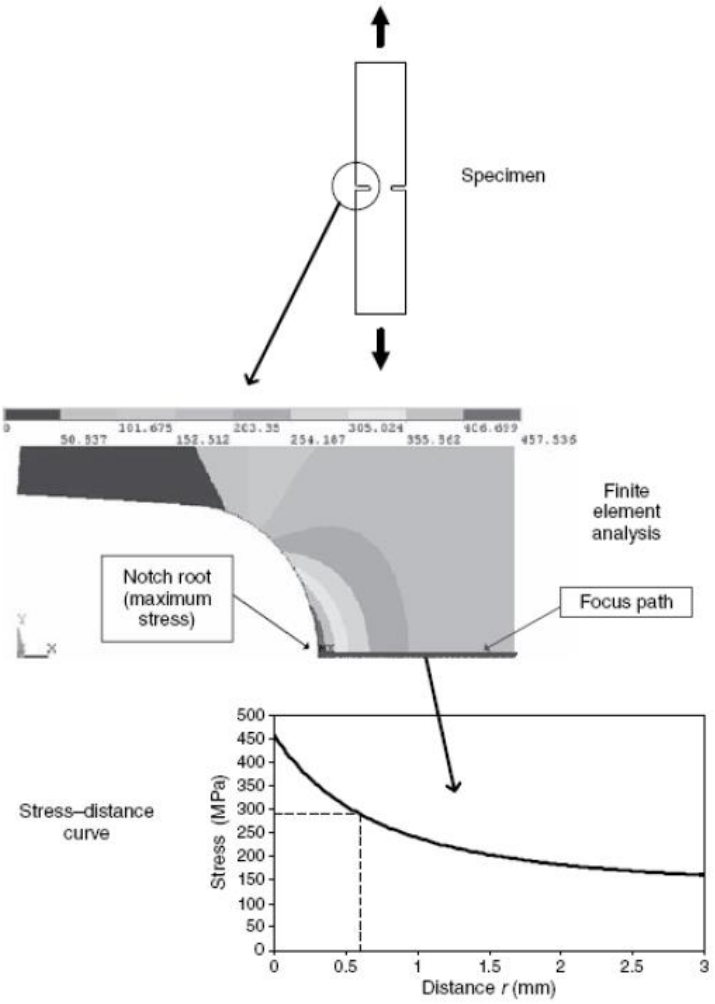

Figure II-51. Example of the application of the PM for the fracture prediction of notched specimens (Taylor, 2007).

In those cases in which the macroscopic behaviour is basically linear but non-linear local processes occur around the defect tip (e.g., relatively large FPZ), σ_0 deviates from σ_u and, therefore, obtaining the critical stress is not straightforward. In this case, the values of the two parameters (i.e., L and σ_0) can be obtained experimentally by testing two specimens with different notch radii (e.g., sharp and blunt notches). As represented in *Figure II-52*, the intersection point of both stress-distance curves (at failure) will correspond to the $L/2$ and σ_0 according to the PM. As it will be shown in this work, this method will be applied using the average values of several tests, given the high variability of rocks that makes it difficult to define a precise value of their mechanical properties.

For a comprehensive understanding of the application of TCD for fracture assessment, the following subsections remark some considerations relating the involved parameters and variables.

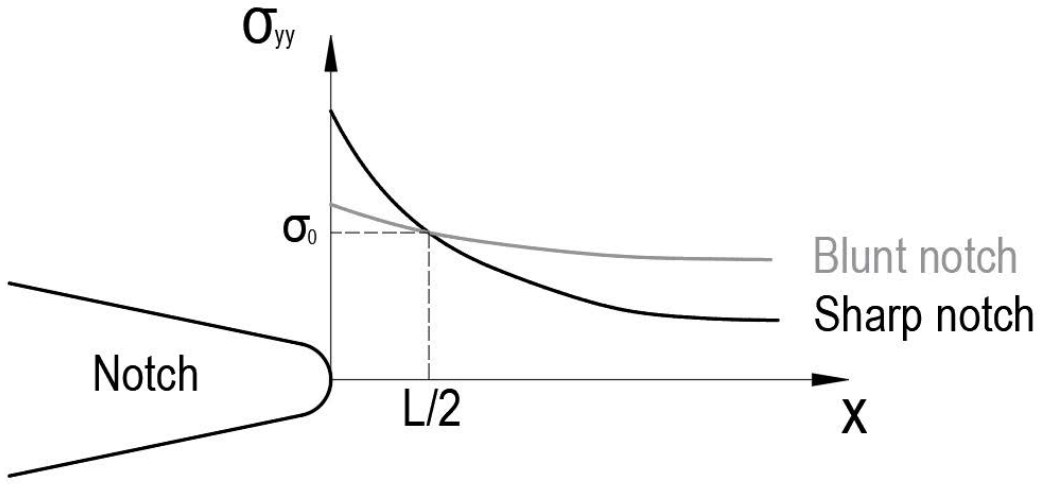

Figure II-52. Scheme of the experimental procedure to obtain the TCD parameters: L and σ_0.

2.7.4.1 Relation between *L* and defect size

As previously mentioned when talking about the importance of scale on rocks, the influence of a defect is relative to the size of the studied engineering problem. In this sense, when the defect is small compared to the critical distance of the material ($a/L \ll 1$), its effect is generally negligible for the analysis of fracture resistance. By contrast, if $a/L \gg 1$ the influence of the defect will gain importance and LEFM provides accurate predictions.

Figure II-53 represents the fracture stress against the defect size, showing that both the PM and the LM provide accurate fracture predictions in the whole range of defect sizes, unlike LEFM that presents certain limitations (e.g., Taylor, 2004).

With all this, knowing the relationship between the defect size and L is useful for analysing fracture behaviour, since it makes possible a rapid evaluation of the relative importance of the defect. It is worth noting that L in *Figure II-53* is around 0.01 mm, while in rocks L is of the order of millimetres (Taylor, 2007).

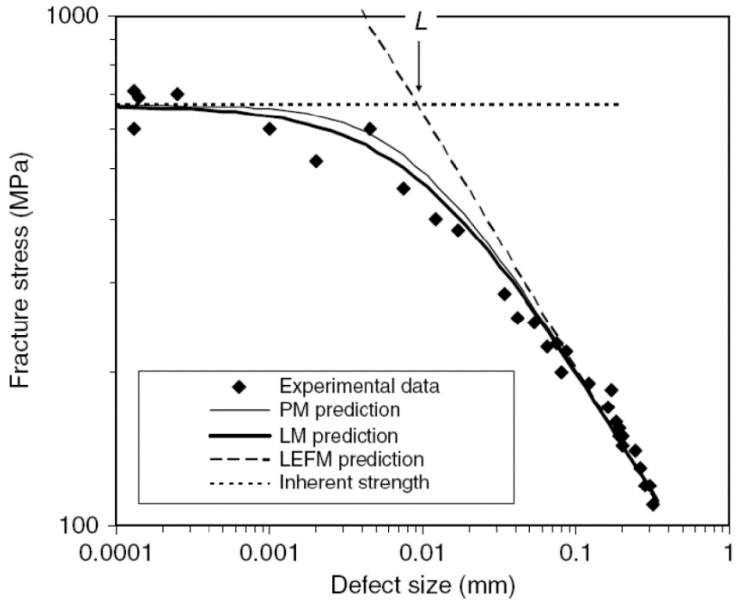

Figure II-53. Experimental results and predictions according to LEFM and the TCD in fracture tests of a ceramic material (Taylor, 2004).

2.7.4.2 Relation between *L* and notch radius

It is observed that notches (or other type of defects) present a crack-type behaviour when the radius (ρ) is smaller than a certain critical value (see *Figure II-54*).

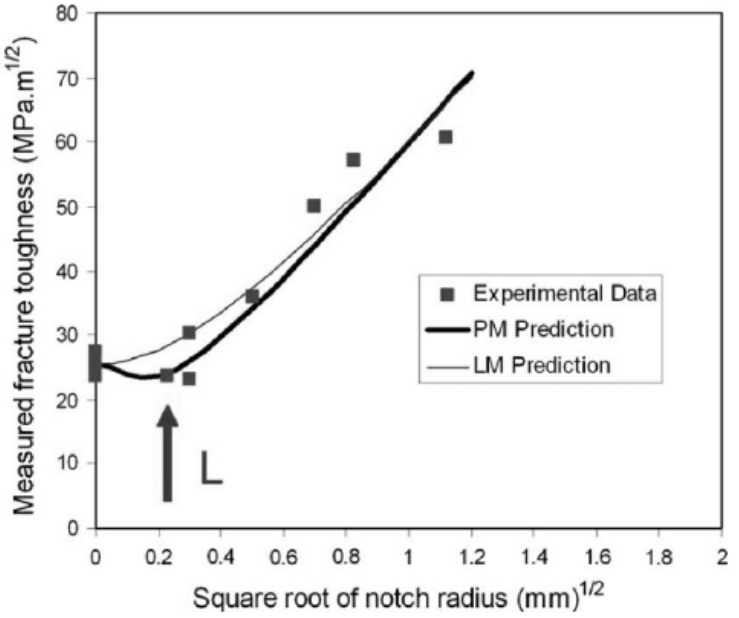

Figure II-54. Experimental results and predictions according to the TCD of the apparent fracture toughness of a metallic material (Hedner, 1987).

According to Hedner (1987), this critical value coincides with the critical distance. Thus, when $\rho/L \ll 1$ the analysis of the notched component is equivalent to the analysis of the same component in a cracked situation. On the other hand, when $\rho/L \gg 1$, the fracture toughness of notched components stabilizes and the problem can be addressed through a stress concentration factor (K_t). In any case, the TCD is able to predict the value of the apparent fracture toughness of notched components as shown in *Figure II-54*.

2.7.4.3 Relation between L and component size

Other length parameters that can be compared with the critical distance are the dimensions of the specimen, mainly the width (h) or the cross section of the component in the direction in which it is expected the crack to grow. This comparison can give rise to situations that are difficult to explain from the physical point of view, as in those cases where L is greater than h. In these cases, TDC would use the stress field of regions beyond the specimen's geometry, which is not possible from a physical perspective. However, the TDC has developed a complex approach for its use in these cases, in which a variable L with the size of the component is considered (Taylor, 2007). The use of this approach is useful in components of reduced dimensions or materials in which the value of the critical distance is large (e.g., sea ice in which the critical distance is of the order of several metres).

2.7.4.4 Relation between σ_0 and σ_u

As stated by Taylor (2007), the magnitude of the inherent strength (σ_0) in unlikely to have any physical significance because it is related to the value of the elastic stress in a region where the actual physical stress is influenced by plasticity, damage and other non-linear effects. However, it is interesting to look at values of the ratio between this stress and the actual failure stress of the material (σ_0/σ_u).

As indicated above, the inherent strength coincides with the ultimate tensile strength ($\sigma_0 = \sigma_u$) in materials with perfect linear-elastic behaviour both at micro- and macro-scales. However, when this condition is not fulfilled, σ_0 presents a higher value than σ_u. For example, for monotonic fracture in polymers and metals σ_0/σ_u values in the range of 2-4 are common, though values outside this range have also

been measured, giving a continuous spectrum of values from 1 up to almost 10.

σ_u is assumed to be the strength of a material containing no defects of any kind. However, this is never achieved in practice, since features such as porosity or inclusions are inevitable and should be considered as an integral part of the material itself. Thus, σ_u is better defined as the strength of a material containing defects which are much smaller than L and so will not be expected to exert any effect. In those materials containing larger defects may develop smaller tensile strengths than this ideal σ_u value, which might be one reason explaining the differences between σ_0 and σ_u in some cases. A common feature of cases where $\sigma_0/\sigma_u > 1$ is the existence of plasticity. The largest values of this ratio are found in metals where plasticity is the main toughening mechanism, and values of unity in the most brittle materials like rocks, where plasticity does not play a significant role (Taylor, 2007).

2.7.5 Analysis methodology under mixed-mode conditions

Susmel & Taylor (2008) reformulated the PM to make it suitable for predicting static failures in notched brittle components subjected to multiaxial loading conditions. They stated that the value of the critical distance is influenced by the loading conditions, in particular the critical distance value changes as the degree of multiaxiality of the stress field damaging the material process zone changes, whereas the inherent material strength is independent. Moreover, they suggested failures to be caused by the propagation of small tensile cracks, whose initial growth occurs on the plane experiencing the maximum normal tensile stress, σ_n (critical plane).

The inherent material strength can thus be always determined under simple mode I loading, in agreement with the Maximum Principal Stress criterion (Albrecht & Yamada, 1977). To properly consider the influence of the degree of multiaxiality on the critical distance value, the maximum (σ_1) and the minimum (σ_3) principal stresses were used by Susmel & Taylor (2008) to define the following stress ratio:

$$\beta(\delta, r) = -\frac{\sigma_3(\delta, r)}{\sigma_1(\delta, r)} \qquad \textit{(II-84)}$$

r and δ stand for the coordinate system depicted in *Figure II-55*. At a given distance (r) from the notch tip, the β value changes as the orientation (δ) of the considered material plane changes. In the same way, for a given δ value, the β ratio changes as the distance from the notch tip (r) increases.

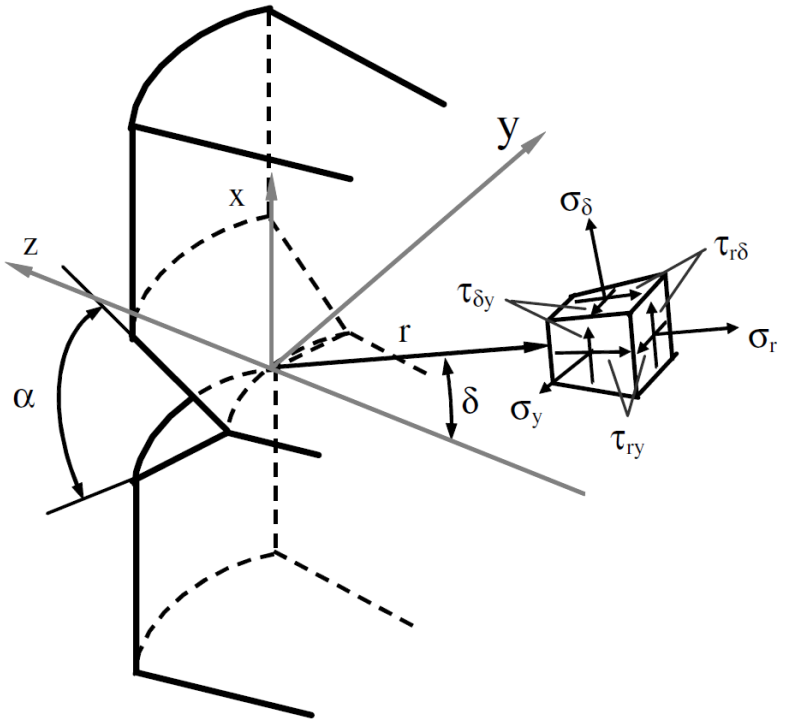

Figure II-55.- Definition of the coordinate system (δ,r) and stress components damaging an elementary material volume in the vicinity of the notch tip (Susmel & Taylor, 2008).

In order to better clarify the way the β ratio varies when calculated on the estimated critical plane, Susmel & Taylor (2008) represented the crack propagation planes of V-notched specimens subjected to mode I (tension) and mode III (torsion) loading conditions (see *Figure II-56*). The hypothesis that the crack propagation plane is the one experiencing the maximum normal stress results in the fact that, under plane stress mode I loading, the critical plane is perpendicular to the applied nominal tensile force and β is constant and equal to zero (see Mohr's circles sketched in *Figure II-56*), whereas, under mode III loading β is equal to unity (as shown by the corresponding Mohr's circles in *Figure II-56*) and the critical plane is at 45º to the specimen axis.

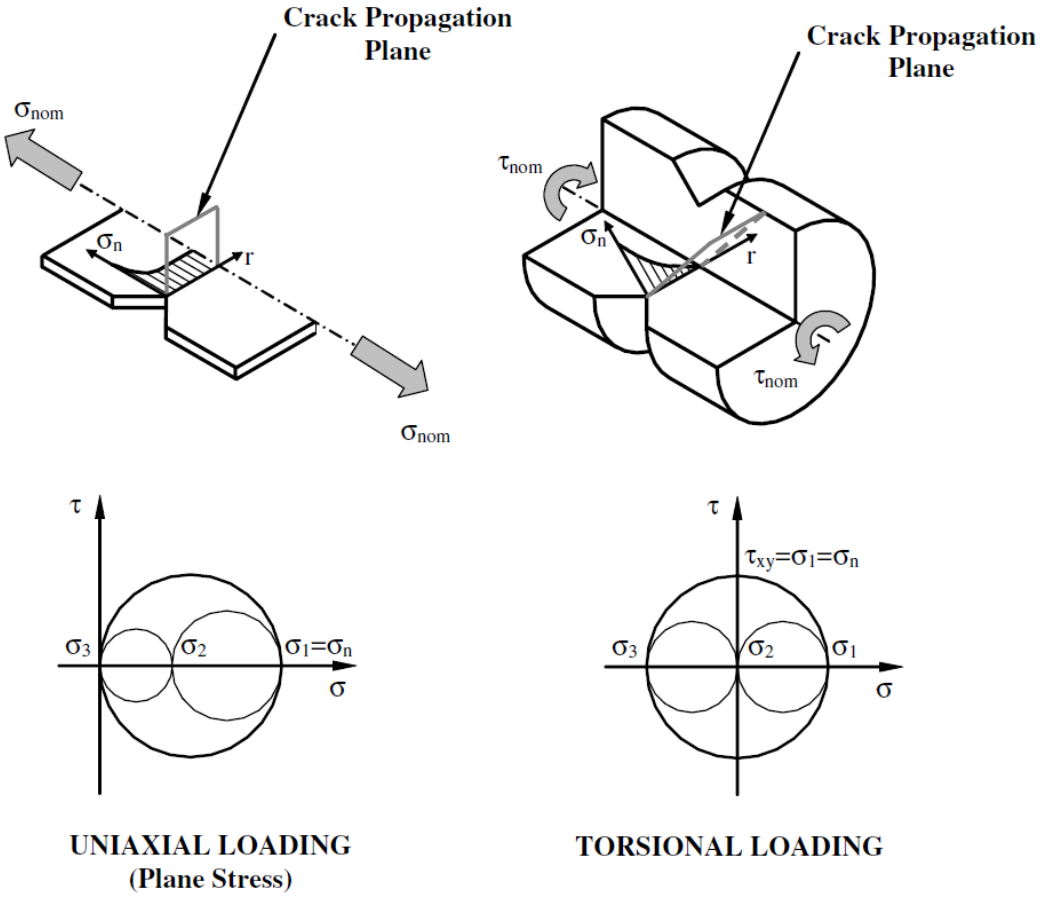

Figure II-56. Crack propagation planes in V-notched specimens under tension (mode I) and torsion (mode III) (Susmel & Taylor, 2008).

After having determined the angle defining the orientation of the critical plane (δ^*), assuming its value is constant, and having assumed that the material linear-elastic behaviour results in a linear dependence between the critical distance (L) and the degree of multiaxiality of the stress field (β ratio) measured along the assumed crack initiation plane, Susmel & Taylor (2008) proposed that the critical distance can be obtained as follows:

$$L\big(\beta(\delta^*, r)\big) = A\beta(\delta^*, r) + B \qquad \textit{(II-85)}$$

where A and B are material constant parameters to be determined by the critical distance value generated under two different β ratios. For example, following the example depicted in *Figure II-56*, A and B can be calibrated by considering the L values generated both under plane

stress pure mode I loading conditions ($\beta = 0$) and under pure mode III loading ($\beta = 1$) conditions. Once A and B are obtained from those two cases, the critical distance for any other mixed-mode (e.g., mode I+III) loading conditions can be calculated, where $0 < \beta < 1$. Analogously, the same procedure can be applied for mixed I+II loading conditions (Susmel & Taylor, 2008).

The procedure for the practical application of the PM under multiaxial loading is illustrated in *Figure II-57*. First, the position of the potential crack initiation point, also known as hot spot, must be located on the component surface (Point C in *Figure II-57*), which is defined as the point experiencing the maximum tensile stress at the notch tip. Usually, this direction is normal to the outer surface of the notch. Then, the linear-elastic stress distribution along the focus path is defined either numerically or using analytical approaches, this focus path being a straight line emanating from the crack initiation point normal to the maximum principal tensile stress. According to the modified PM approach proposed by Susmel & Taylor (2008), failure in a notched brittle component occurs when, at a distance from the notch tip equal to $L(\beta)/2$ ($L(\beta)$ given by *Equation (II-85)*) and measured along the critical path inclined δ^* from the notch bisector line, the maximum tensile normal stress (σ_n) reaches the inherent strength (σ_0), or σ_u for brittle materials.

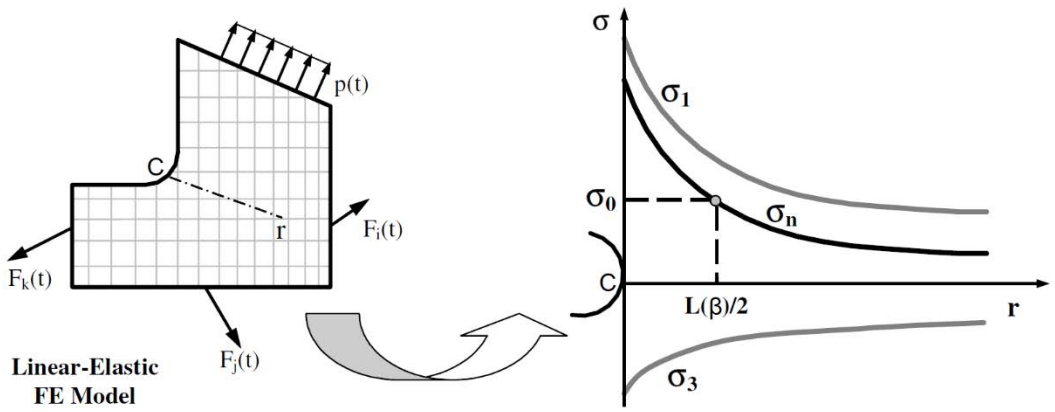

Figure II-57. Schematic representation of the procedure for the application of the PM under mixed-mode loading (Susmel & Taylor, 2008).

In essence, the analysis is exactly the same as that performed for the application of the PM under pure mode I loading conditions, with the difference that the critical plane over which the stresses are studied rotates according to the degree of multiaxiality. *Figure II-58* shows an example of how this plane rotates from mode I to mode I+II loading conditions. Although the proposed methodology was focused on the application of the PM in origin (Susmel & Taylor, 2008), once the critical plane is defined (δ^*), the LM can also be applied over the stress distribution normal to that plane, proceeding as indicated in *Section 2.7.3.2.*

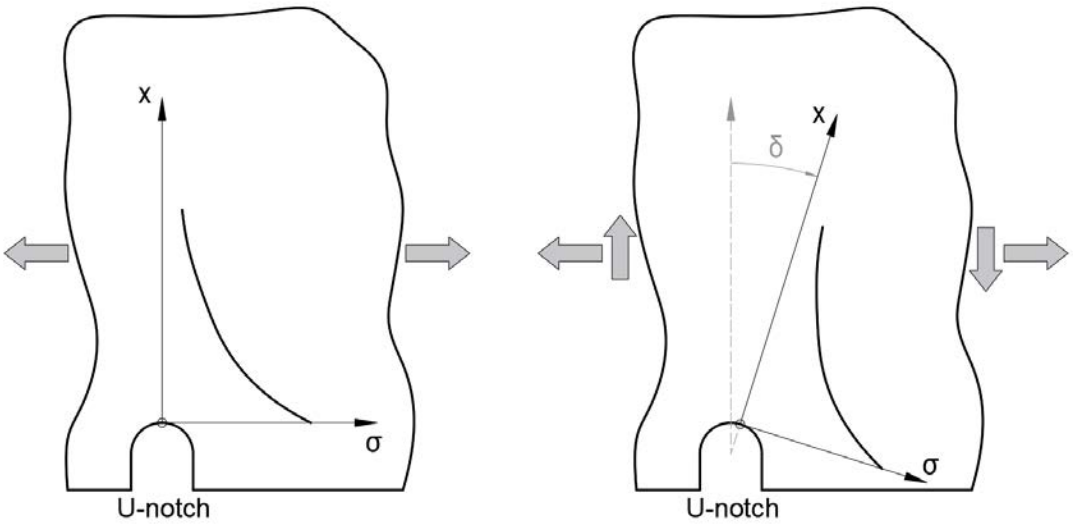

Figure II-58. Schematic representation of the rotation (δ) of the critical plane from mode I loading conditions to mode I+II loading conditions.

Although crack propagation is mainly dominated by mode I, rocks are generally subjected to random loading conditions. For this reason, in many practical situations, the influence of mixed-mode loading conditions needs to be studied. In particular, combined opening-sliding shear deformations (i.e., mixed mode I+II) have special interest in rock fracture mechanics. However, to the best knowledge of the author, the TCD has not been applied yet in the field of rock fracture mechanics under mixed mode loading conditions. For this reason, the applicability of the TCD in rocks subjected to mixed mode I+II is studied in this work.

Negru et al. (2015), based on the concept of the degree of multiaxiality introduced by Susmel & Taylor (2008), proposed the following expression (analogous to *Equation (II-85)*) that links the critical distance with the mode mixity (M_e) to study mixed modes I+II:

$$L(M_e) = AM_e + B \qquad \textit{(II-86)}$$

where A and B are material dependent constant parameters. The dimensionless parameter M_e was first introduced by Ayatollahi & Torabi (2009) to study brittle fracture in U-notched components (as those analysed in this work) under mixed-mode static loading. The expression for the determination of the mode mixity M_e is as follows:

$$M_e = \frac{2}{\pi}\tan^{-1}\left(\frac{K_I^u}{K_{II}^u}\right) \qquad \textit{(II-87)}$$

K_I^u and K_{II}^u being, respectively, mode I and mode II notch stress intensity factors, where the superscript "u" refers to U-shaped notches. Both K_I^u and K_{II}^u are evaluated along the notch bisector, according to Lazzarin & Filippi (2006) generalized proposed formulas:

$$K_I^u = \sqrt{2\pi r}\,\frac{(\sigma_\theta)_{\theta=0}}{1 + r_0/r} \qquad \textit{(II-88)}$$

$$K_{II}^u = \sqrt{2\pi r}\,\frac{(\tau_{r\theta})_{\theta=0}}{1 - r_0/r} \qquad \textit{(II-89)}$$

where (r, θ) are the polar coordinates for a system depicted in *Figure II-59*, and σ_θ and $\tau_{r\theta}$ are the stresses at the distance r from the local origin defined by r_0, which varies with the notch radius (ρ) and with the opening angle (2α). This value will be addressed further in detail, but for the particular case of U-shaped notches, $r_0 = \rho/2$.

Both *Equations (II-88)* and *(II-89)* are extensions of those of Gross & Mendelson (1972) for sharp V-notches and U-notches. However, the

original definitions for the NSIFs given by Gross & Mendelson (1972) are based on Williams' (1952) solution, which matches exactly the stress distributions for ideally sharp V-shaped notches, while *Equations (II-88)* and *(II-89)* are approximate because they are based on the analytical approach proposed by Filippi et al. (2002) to describe the local stress field ahead of rounded V-notches (U-notches being a particular case of rounded V-notches with an opening angle of zero degrees). This approach satisfies the boundary conditions not on the entire free edge but at the notch tip and at a convenient distance from it (Filippi et al., 2002).

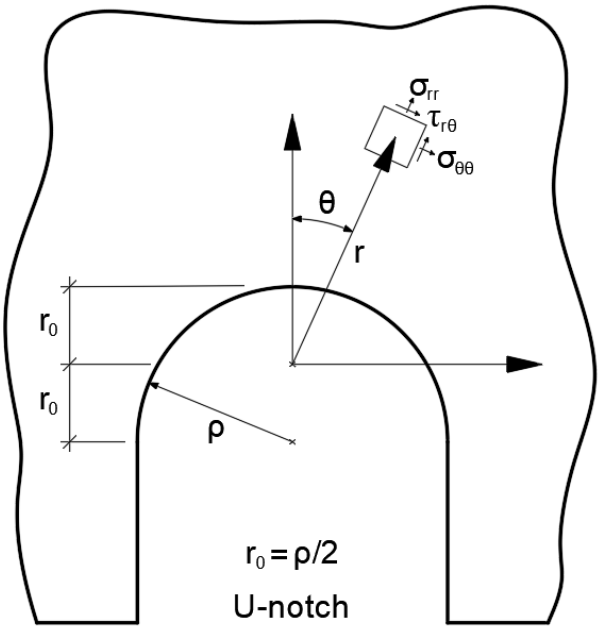

Figure II-59. Polar coordinate system in U-shaped notches.

Thus, *Equations (II-88)* and *(II-89)* are not expected to give a constant value for the NSIFs, but they will rather show an oscillating value ahead of the notch tip as shown in *Figure II-60*. The entity of this oscillation was analysed by Lazzarin & Filippi (2006), who recommended computing the mean values of K_I^u and K_{II}^u over a distance of 0.4 times the notch radius from the notch tip along the bisector, in order to eliminate the weak dependence on the notch tip distance. This proposal has been validated by Lazzarin and Filippi (2006) and by Negru et al. (2015) for notch radii up to 2.5 mm, providing accurate solutions.

However, it will be observed in this work that this proposal is not appropriate for larger notch radii, for which not representative K^u values are obtained using that domain.

Finally, the procedure for the practical application of this approach is the same as that defined by Susmel & Taylor (2008). Once A and B parameters from *Equation (II-86)* are calibrated by considering the L values generated for two different loading mode mixities (M_e), any value of L can be calculated for different mixed-mode loading combinations of components with the same material. That value of L will allow to perform fracture predictions by the application of either the PM or the LM over the critical plane defined above (δ^*).

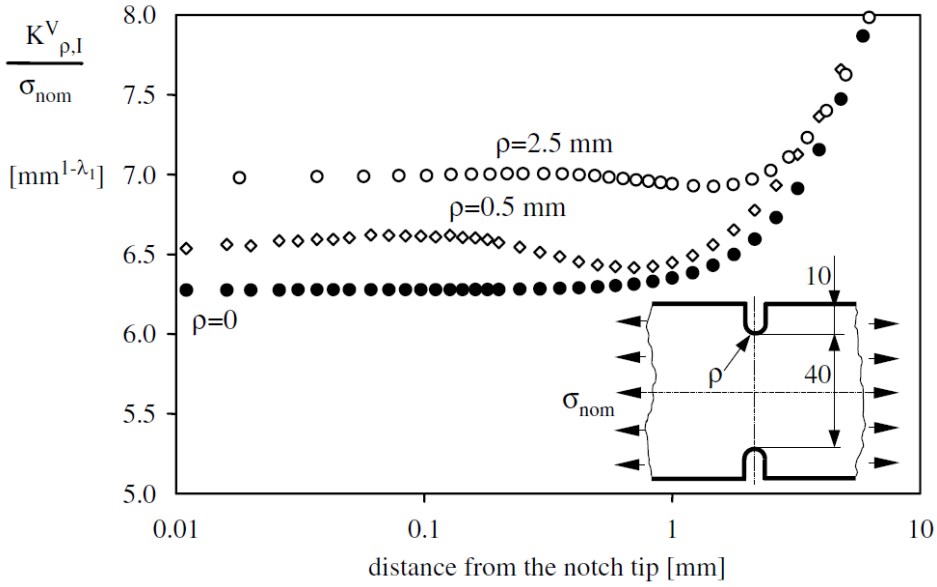

Figure II-60. Plots of $K^V_{\rho I}$ (equal to K^u_I in this case) for some U-notched plates (Lazzarin & Filippi, 2006).

2.8 STRAIN ENERGY DENSITY CRITERION

2.8.1 Introduction

The second local failure criterion used in this work for the fracture assessment of notched rocks is based on the Strain Energy Density (SED) concept, which has been used for many years to formulate failure and fracture criteria for materials exhibiting both ductile and brittle behaviour. The SED of a material is defined as the strain energy per

unit volume, and corresponds to the area under the stress-strain diagram of a material as represented in *Figure II-61*.

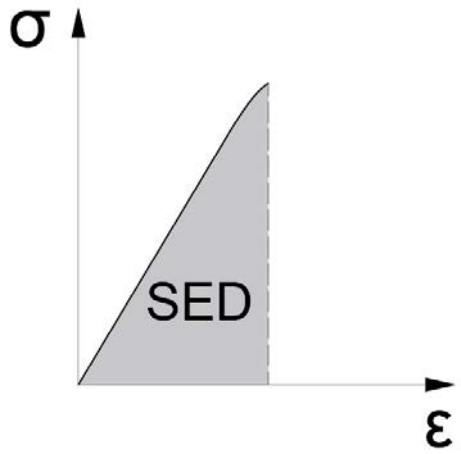

Figure II-61. Definition of the SED in a stress-strain diagram.

Since Beltrami (1885) to nowadays, the SED has turned out to be a powerful tool to assess the static and fatigue behaviour of notched and unnotched components in structural engineering. In fact, different SED-based approaches have been formulated and applied both to static and fatigue loading conditions (e.g., Sih, 1973; Sih, 1974; Kipp & Sih, 1975; Molski & Glinka, 1981; Gdoutos, 1990; Sih, 1991; Ellyin, 1997).

2.8.2 Historical background

Dealing with the strain energy density concept, it is important to contemplate some fundamental contributions by Sih where the concept of "core region" surrounding the crack tip was proposed (see *Figure II-62*). The main idea was that continuum mechanics stops short at a distance from the crack tip, providing the concept of the radius of the core region where the inhomogeneity of the material due to micro-cracks, dislocations and grain boundaries does not allow an accurate analytical solution. The strain energy density factor (S) was defined as the product of the strain energy density by a critical distance from the point of singularity. Thus, Sih's criterion is a point-wise criterion. Failure was thought to be controlled by a critical value of the S factor (S_c), whereas the direction of crack propagation was determined by imposing a minimum condition on S (Sih, 1974; Sih et al., 1974; Kipp & Sih, 1975; Sih, 1991; Sih & Ho, 1991).

A critical value of the strain energy density function can be calculated with the following expression:

$$\left(\frac{dW}{dV}\right)_c = \int \sigma \cdot d\varepsilon \qquad \textit{(II-90)}$$

which has been extensively used since 1965, when it was first determined experimentally for various engineering materials by using plane and notched specimens (Gillemot, 1965; Gillemot, 1976; Sih et al., 1982; Gillemot et al., 1985). The strain energy required for crack initiation in a unit volume of material defined in *Equation (II-90)* is called Absorbed Specific Fracture Energy (ASFE), where W is the energy and V the element volume of the considered material. Measurements of the energy in an infinitely small element (dW) are not possible. However, they can be approximated with sufficient accuracy by calculating the fracture energy over the entire fractured cross section of an unnotched tensile specimen (Gillemot et al., 1985). Thus, the critical value of the strain energy density is an intrinsic property of the material and can be obtained from the area under the stress-strain curve of a tensile test.

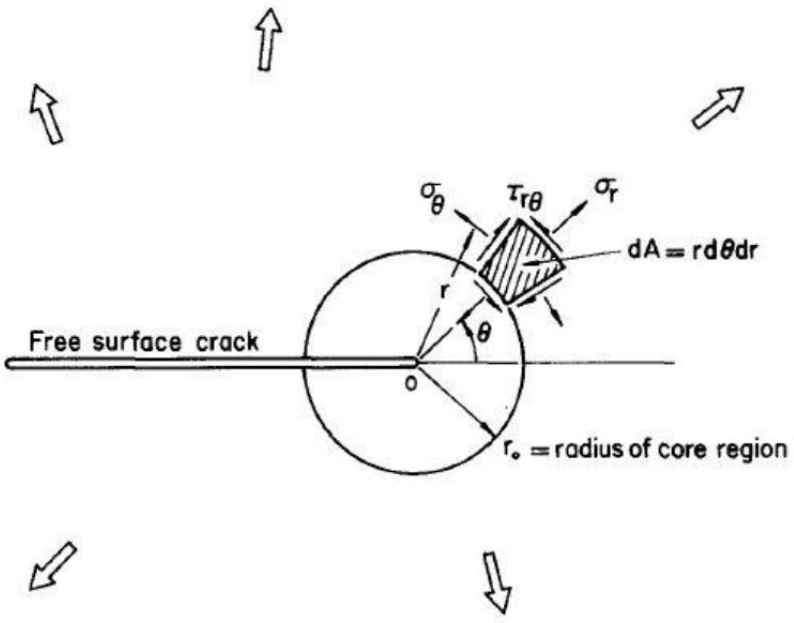

Figure II-62. Definition of the core region (Sih, 1974).

Since distributions of the absorbed specific energy W in notched specimens are not uniform, it was assumed that the specimen fails as soon as a precise energy amount has been absorbed by the small plastic zone at the notch tip. Thus, in the case of notched components, the value of the ASFE represents the average absorbed specific fracture energy (W_m). Notched components loaded under static loads show that the average ASFE (W_m) decreases with increasing the notch sharpness, with the ASFE parameter being plotted as a function of the theoretical stress concentration factor (K_t) as shown in *Figure II-63*.

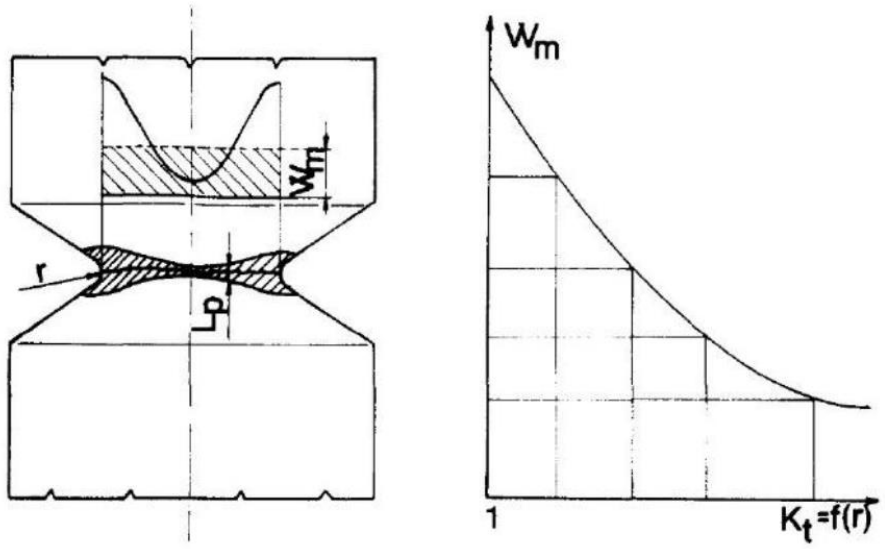

Figure II-63. Definition of the average ASFE (W_m) (Gillemot et al., 1985).

This topic was deeply discussed by Sih (1974), Sih et al. (1974) and Sih (1991), who showed that there was a link between the factor S and the ASFE:

$$S_c = r_c \left(\frac{dW}{dV}\right)_c \qquad \textit{(II-91)}$$

S_c being the critical strain energy density factor and r_c the radius vector of the location of failure. Thus, $(dW/dV)_c$ is equivalent to S_c/r_c.

The strain energy density fracture criterion was refined and extensively summarised by Sih (1991). The theory can account for yielding and fracture, and is applicable also to ductile materials.

Additionally, the concept of strain energy density has also been reported in the literature in order to predict the fatigue behavior of notches both under uniaxial and multi-axial stresses (e.g., Molski & Glinka, 1981; Glinka 1985).

Alternatively to Sih's criterion, which is a point-wise criterion, the averaged Strain Energy Density (SED) criterion was proposed by Lazzarin & Zambardi (2001), which is a local energy-based criterion that combines the so-called elementary volume proposed by Neuber (1958) and the local Mode I concept first proposed by Erdogan & Sih (1963). The average SED criterion states that brittle failure occurs when the mean value of the strain energy density over a control volume (which becomes an area in two dimensional cases) is equal to a critical energy (W_c) that depends on the material. The average SED approach is based both on a precise definition of the control volume and the fact that the critical energy does not depend on the notch sharpness. Such a method was formalised and applied first to sharp, zero radius, V-notches (Lazzarin & Zambardi, 2001; Lazzarin & Zambardi, 2002) and later extended to blunt U-shaped and V-shaped notches under mode I loading (Lazzarin & Berto, 2005; Lazzarin et al., 2009) as well as to welded joints under high cycle fatigue loading (Livieri & Lazzarin, 2005; Berto & Lazzarin, 2009). The control radius of the volume, over which the energy has to be averaged, depends on the ultimate tensile strength, the fracture toughness and the Poisson's ratio in the case of static loads, whereas it depends on the unnotched specimen's fatigue limit, the threshold stress intensity factor range and the Poisson's ratio under high cycle fatigue loads.

The approach has been successfully used under both static and fatigue loading conditions to assess the strength of notched and welded structures subjected to predominant mode I and also to mixed-mode loading (e.g., Lazzarin & Berto, 2008; Lazzarin et al., 2008). The extension of the SED approach to ductile fracture is possible, with a major problem being the definition of the control volume and the influence of the dilatational and distortional components of the strain energy density.

The application of the average SED criterion in materials like steels or polymers has been widely studied by different authors in the last

decades (e.g., Lazzarin & Zambardi, 2001; Lazzarin & Berto, 2005; Cicero et al., 2017), providing accurate results under brittle and ductile conditions. However, despite its huge potential and advantages, its use in more heterogeneous materials like rocks still requires further research. In fact, it was not till 2017 that the applicability of the average SED criterion in rock materials was investigated by Aliha and his co-workers (Aliha et al., 2017), who analysed the fracture of a brittle white marble. This gap in knowledge is probably a consequence of the heterogeneous condition of rocks, which makes fracture analyses more complicated (and therefore less attractive) to be interpreted. Besides, as stated above, the control volume over which the strain energy density is averaged depends on the material. In the case of steels and polymers, the radius defining the control volume ranges from 0.4 μm to 1000 μm. However, rocks present larger sizes of the control volume, which must be taken into consideration in the fracture analysis. This issue will be discussed in detail in this work.

2.8.3 Analytical frame of the SED criterion

In this section, a review of the analytical frame of the SED criterion is provided. Although stresses around a defect were already addressed in *Section 2.3* and, in particular, stress distribution at the notch tip was reviewed in *Section 2.6.2*, a formulation to calculate the stress distribution at the notch that is commonly used to determine the SED is presented here.

Approaches based on strain energy density cannot be used in front of a sharp V-notch since both stresses and strain energy density tend to infinity at $r = 0$. However, if a finite volume is considered in the material close to the notch, whatever its characteristics (blunt notch, sharp notch, crack), the energy always has a finite value. Thus, the question is how to estimate the size of this volume.

Figure II-64 represents the polar coordinate system that will be considered throughout the review of the analytical frame of the SED criterion. It is observed that blunt U-shaped notches are a particular case of V-shaped notches in which the opening angle is zero ($2\alpha = 0$).

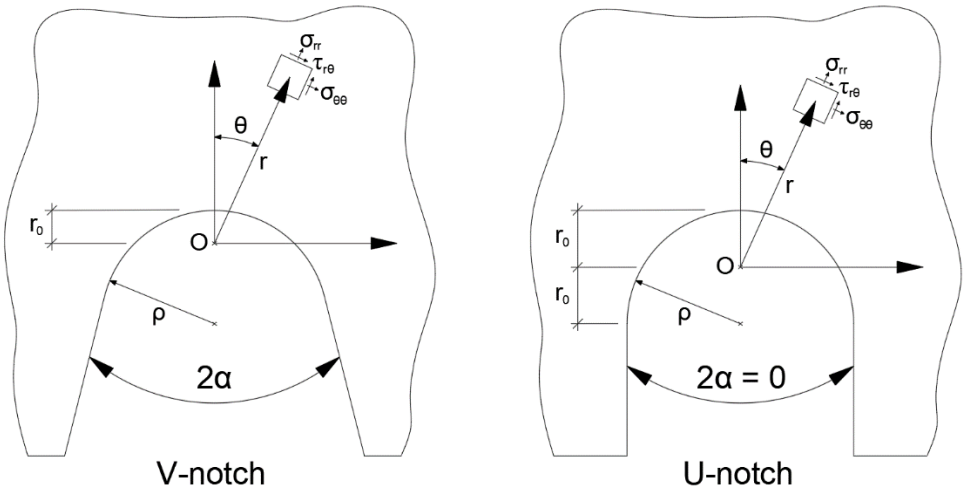

Figure II-64. Polar coordinate system for V-notches and U-notches.

2.8.3.1 Stress distribution in U-notches and V-notches

According to the coordinate system depicted in *Figure II-64* with the origin located at point O, mode I stress distribution (subscript 1 stands for mode I loading conditions) ahead of a V-notch tip is given by the following expression (Filippi et al., 2002):

$$\sigma_{ij} = a_1 \left[f_{ij}(\theta, \alpha) + \left(\frac{r}{r_0} \right)^{\mu_1 - \lambda_1} \cdot g_{ij}(\theta, \alpha) \right] \qquad \textit{(II-92)}$$

where a_1 can be expressed either via the notch stress intensity factor K_I in the case of a sharp, zero radius, V-notch or by means of the elastic maximum notch stress ($\sigma_{tip} = \sigma_{max}$) in the case of blunt V-notches. In *Equation (II-92)*, r_0 is the distance evaluated on the notch bisector line between the V-notch tip and the origin of the local coordinate system. r_0 depends both on the notch radius (ρ) and the opening angle 2α according to the following expression:

$$r_0 = \rho \frac{\pi - 2\alpha}{2\pi - 2\alpha} \qquad \textit{(II-93)}$$

This expression gets its maximum value in the case of U-shaped notches ($2\alpha = 0$), where $r_0 = \rho/2$. The angular functions f_{ij} and g_{ij} are given by Filippi et al. (2002):

$$\begin{Bmatrix} f_{\theta\theta} \\ f_{rr} \\ f_{r\theta} \end{Bmatrix} = \frac{1}{1+\lambda_1+\chi_{b_1}(1-\lambda_1)} \left[\begin{Bmatrix} (1+\lambda_1)\cdot\cos(1-\lambda_1)\theta \\ (3-\lambda_1)\cdot\cos(1-\lambda_1)\theta \\ (1-\lambda_1)\cdot\sin(1-\lambda_1)\theta \end{Bmatrix} + \chi_{b_1}(1-\lambda_1) \begin{Bmatrix} \cos(1+\lambda_1)\theta \\ -\cos(1+\lambda_1)\theta \\ \sin(1+\lambda_1)\theta \end{Bmatrix} \right] \quad \textit{(II-94)}$$

$$\begin{Bmatrix} g_{\theta\theta} \\ g_{rr} \\ g_{r\theta} \end{Bmatrix} = \frac{q}{4(q-1)\left[1+\lambda_1+\chi_{b_1}(1-\lambda_1)\right]} \cdot \left(\chi_{d_1} \begin{Bmatrix} (1+\mu_1)\cos(1-\mu_1)\theta \\ (3-\mu_1)\cos(1-\mu_1)\theta \\ (1-\mu_1)\sin(1-\mu_1)\theta \end{Bmatrix} + \chi_{c_1} \begin{Bmatrix} \cos(1+\mu_1)\theta \\ -\cos(1+\mu_1)\theta \\ \sin(1+\mu_1)\theta \end{Bmatrix} \right) \quad \textit{(II-95)}$$

The eigenfunctions f_{ij} depend only on Williams' eigenvalue λ_1, which controls the sharp solution for zero notch radius (Williams, 1952). The eigenfunctions g_{ij} mainly depend on eigenvalue μ_1, but are not independent from λ_1. Since $\mu_1 < \lambda_1$, the contribution of μ-based terms in *Equation (II-92)* rapidly decreases with the increase of the distance from the notch tip. All parameters in *Equations (II-94)* and *(II-95)* have closed-form expressions (see Filippi et al., 2002) but here, for the sake of brevity, only some values for the most common angles are collected in *Table II-8.*

Table II-8. Characteristic parameters for mode I loading stress distribution (Filippi et al., 2002).

$2\alpha\ [rad]$	q	λ_1	μ_1	χ_{b_1}	χ_{c_1}	χ_{d_1}	$\widetilde{\omega}_1$
0	2.0000	0.5000	-0.5000	1.0000	4.0000	0.0000	1.000
$\pi/6$	1.8333	0.5014	-0.4561	1.0707	3.9707	0.0632	1.034
$\pi/4$	1.7500	0.5050	-0.4319	1.1656	3.5721	0.0828	1.014
$\pi/3$	1.6667	0.5122	-0.4057	1.3123	3.2832	0.0960	0.970
$\pi/2$	1.5000	0.5448	-0.3449	1.8414	2.5057	0.1046	0.810
$2\pi/3$	1.3334	0.6157	-0.2678	3.0027	1.5150	0.0871	0.570
$3\pi/4$	1.2500	0.6736	-0.2198	4.1530	0.9933	0.0673	0.432
$5\pi/6$	1.1667	0.7520	-0.1624	6.3617	0.5137	0.0413	0.288

Under plane strain conditions, the eigenfunctions f_{ij} and g_{ij} satisfy the following expressions:

$$f_{zz}(\theta) = v\left(f_{\theta\theta}(\theta) + f_{rr}(\theta)\right);\ g_{zz}(\theta) = v\left(g_{\theta\theta}(\theta) + g_{rr}(\theta)\right) \qquad (II\text{-}96)$$

whereas $f_{zz}(\theta) = g_{zz}(\theta) = 0$ under plane stress conditions.

2.8.3.2 Average SED criterion

The average SED approach is based on the idea that under tensile stresses failure occurs when the mean strain energy density ($\overline{W}$) over a certain control volume reaches a critical value (W_c) that depends on the material:

$$\overline{W} = W_c \qquad (II\text{-}97)$$

If the material behaviour is ideally brittle, then W_c can be evaluated by using simply the conventional ultimate tensile strength (σ_u), as it directly corresponds to the area under the stress-strain curve of a tensile test:

$$W_c = \frac{\sigma_u^2}{2E} \qquad (II\text{-}98)$$

This expression is only valid for materials exhibiting a sensibly linear-elastic behaviour till failure (i.e., brittle and quasi-brittle materials). However, some attempts can be found in the literature aiming to generalise the SED criterion to non-linear-elastic situations by means of calibrating the critical strain energy (W_c). Cicero et al. (2017), for example, analysed the possibility of extrapolating the SED criterion to non-linear situations. Instead of deriving the critical value of the strain energy density (W_c) from a theoretically linear elastic stress-strain curve, they obtained a corrected critical value (W_c^*) from the value of the average strain energy density ($\overline{W}$) at failure, assuming that $\overline{W}$ is a constant that does not depend on the notch radius.

2.8.3.2.1 Average SED for sharp V-notches

In order to apply the energy-based failure criterion stablished by *Equation (II-97)*, the stress distribution around the notch must be determined to calculate the strain energy density. To do so, *Equation (II-92)* is commonly used. The parameter a_1 of *Equation (II-92)* can be linked to the Mode I notch stress intensity factor by means of the following expression:

$$a_1 = \frac{K_I^V}{\sqrt{2\pi}} \qquad \textit{(II-99)}$$

where, according to Gross & Mendelson's (1972) expression for the NSIF, K_I^V is:

$$K_I^V = \sqrt{2\pi} \lim_{r \to 0} [\sigma_\theta(r,0)] r^{1-\lambda_1} \qquad \textit{(II-100)}$$

In the presence of a notch radius equal to zero (i.e., cracks and sharp V-notches), the distance r_0 is null, and all μ-related terms in *Equation (II-92)* disappear. Then, the elastic strain energy density under Mode I condition becomes:

$$W_1(r,\theta) = \frac{1}{2E} r^{2(\lambda_1-1)} \cdot \frac{(K_I^V)^2}{2\pi} [f_{\theta\theta}^2 + f_{rr}^2 + f_{zz}^2 - 2v(f_{\theta\theta}f_{rr} + f_{\theta\theta}f_{zz} + f_{rr}f_{zz}) + 2(1+v)f_{r\theta}^2] \qquad \textit{(II-101)}$$

The control volume over which the strain energy density is averaged becomes a control area (Ω) under plane strain or plane stress conditions (i.e., two dimensional problems). This area is defined by a circle or a circular sector with a radius (R_0), as indicated in *Figure II-65*.

The control area can be expressed as:

$$\Omega = \int_0^{R_0} \int_{-\gamma}^{+\gamma} r \, dr d\theta = R_0^2 \gamma \qquad \textit{(II-102)}$$

where

$$\gamma = \pi - \alpha \qquad \textit{(II-103)}$$

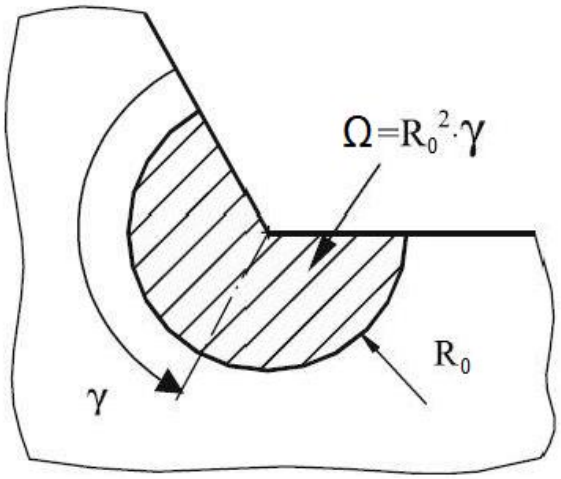

Figure II-65. Control volume (area) for sharp notches (Lazzarin & Berto, 2005).

The total strain energy over the control area (Ω) is then:

$$E_1 = \int_{\Omega} W_1 d\Omega = \int_0^{R_0} \int_{-\gamma}^{+\gamma} W_1(r,\theta) dr d\Omega = \frac{I_1(\gamma)}{4E\lambda_1} (K_I^V)^2 R_0^{2\lambda_1} \qquad \textit{(II-104)}$$

where the integral I_1 is:

$$I_1(\gamma) = \frac{1}{2\pi} \int_{-\gamma}^{+\gamma} [f_{\theta\theta}^2 + f_{rr}^2 + f_{zz}^2 - 2v(f_{\theta\theta} f_{rr} + f_{\theta\theta} f_{zz} + f_{rr} f_{zz}) + 2(1+v) f_{r\theta}^2] d\theta \qquad \textit{(II-105)}$$

Thus, the average value of the elastic strain energy density referred to the control area (Ω) is:

$$\overline{W_1} = \frac{E_1}{\Omega} = \frac{I_1}{4E\lambda_1 \gamma} \left(\frac{K_I^V}{R_0^{1-\lambda_1}} \right)^2 \qquad \textit{(II-106)}$$

Equation (II-106) makes it possible to determine the critical value of the radius (R_0) once the experimental values W_c and K_{IC}^V that provoke the failure under tensile stresses are known. If the critical value of the NSIF is determined by means of specimens with $2\alpha \neq 0$, the critical radius (R_0) can be estimated by means of the expression (Lazzarin & Zambardi, 2001):

$$R_0 = \left[\frac{I_1 \cdot (K_I^V)^2}{4\lambda_1(\pi-\alpha)EW_c}\right]^{1/(2-2\lambda_1)} \qquad \textit{(II-107)}$$

When $2\alpha = 0$, K_{IC}^V equals the fracture toughness K_{IC} and the material critical radius can be derived by *Equation (II-107)* or by the following expressions obtained by Yosibash et al. (2004) for plane strain and plane stress conditions:

$$R_0 = \frac{(1+v)(5-8v)}{4\pi}\left(\frac{K_{IC}}{\sigma_u}\right)^2 \qquad (plane\ strain) \qquad \textit{(II-108)}$$

$$R_0 = \frac{(5-3v)}{4\pi}\left(\frac{K_{IC}}{\sigma_u}\right)^2 \qquad (plane\ stress) \qquad \textit{(II-109)}$$

2.8.3.2.2 Average SED for blunt V-notches

Different from sharp V-shaped notches, in the presence of rounded or blunt V-notches it is possible to link the parameter a_1 of *Equation (II-92)* to the maximum principal stress at the notch tip:

$$a_1 = \frac{\sigma_{tip} r_0^{1-\lambda_1}}{1+\widetilde{\omega}_1} \qquad \textit{(II-110)}$$

where $\widetilde{\omega}_1$ has a closed-form expression (see Filippi et al., 2002) and is defined in *Table II-8* for most common notch opening angles. By using the elastic maximum notch stress, *Equation (II-92)* can be rewritten as follows so as to assess stress at any point in the neighbourhood of the notch tip:

$$\sigma_{\theta\theta}(r,\theta) = \frac{\sigma_{max}}{1+\widetilde{\omega}_1}\left(\frac{r_0}{r}\right)^{1-\lambda_1}\left[f_{\theta\theta} + \left(\frac{r}{r_0}\right)^{\mu_1-\lambda_1} g_{\theta\theta}\right] \quad \textit{(II-111)}$$

$$\sigma_{rr}(r,\theta) = \frac{\sigma_{max}}{1+\widetilde{\omega}_1}\left(\frac{r_0}{r}\right)^{1-\lambda_1}\left[f_{rr} + \left(\frac{r}{r_0}\right)^{\mu_1-\lambda_1} g_{rr}\right] \quad \textit{(II-112)}$$

$$\sigma_{r\theta}(r,\theta) = \tau_{r\theta} = \frac{\sigma_{max}}{1+\widetilde{\omega}_1}\left(\frac{r_0}{r}\right)^{1-\lambda_1}\left[f_{r\theta} + \left(\frac{r}{r_0}\right)^{\mu_1-\lambda_1} g_{r\theta}\right] \quad \textit{(II-113)}$$

The elastic strain energy density is then given by the following expression:

$$W_1(r,\theta) = \frac{1}{2E}\left(\frac{\sigma_{max}}{1+\widetilde{\omega}_1}\right)^2\left\{\left(\frac{r}{r_0}\right)^{2(\lambda_1-1)}\tilde{F}_\lambda + \left(\frac{r}{r_0}\right)^{2(\mu_1-1)}\tilde{G}_\mu + 2\left(\frac{r}{r_0}\right)^{\lambda_1+\mu_1-2}\widetilde{M}_{\lambda\mu}\right\} \quad \textit{(II-114)}$$

where, according to the total strain energy criterion of Beltrami (1885), the following relationships are valid:

$$\tilde{F}_\lambda = f_{\theta\theta}^2 + f_{rr}^2 + f_{zz}^2 - 2v(f_{\theta\theta}f_{rr} + f_{\theta\theta}f_{zz} + f_{rr}f_{zz}) + 2(1+v)f_{r\theta}^2 \quad \textit{(II-115)}$$

$$\tilde{G}_\mu = g_{\theta\theta}^2 + g_{rr}^2 + g_{zz}^2 - 2v(g_{\theta\theta}g_{rr} + g_{\theta\theta}g_{zz} + g_{rr}g_{zz}) + 2(1+v)g_{r\theta}^2 \quad \textit{(II-116)}$$

$$\widetilde{M}_{\lambda\mu} = f_{\theta\theta}g_{\theta\theta} + f_{rr}g_{rr} + f_{zz}g_{zz} - v(f_{\theta\theta}g_{rr} + g_{\theta\theta}f_{rr} + f_{\theta\theta}g_{zz} + g_{\theta\theta}f_{zz} + f_{rr}g_{zz} + g_{rr}f_{zz}) + 2(1+v)f_{r\theta}g_{r\theta} \quad \textit{(II-117)}$$

Considering the control area (Ω) shown in *Figure II-66* for the case of blunt V-notches, the strain energy can be expressed as follows:

$$E_1 = \int_\Omega W_1 d\Omega = \int_{-\bar{\theta}}^{\bar{\theta}} d\theta \int_{R_1(\theta)}^{R_2} W_1(r,\theta) r dr \quad \textit{(II-118)}$$

In a more explicit form, the previous expression takes the following form:

$$E_1 = \frac{1}{2E}\left[\frac{\sigma_{max}\sqrt{2\pi}}{1+\widetilde{\omega}_1}\right]^2 r_0^{2(1-\lambda_1)}\left(I_\lambda + I_\mu + I_{\lambda\mu}\right) \qquad \textit{(II-119)}$$

where

$$I_\lambda = \int_{-\overline{\theta}}^{+\overline{\theta}} \frac{\left(R_2^{2\lambda_1} - R_1(\theta)^{2\lambda_1}\right)}{2\lambda_1}\tilde{F}_\lambda d\theta \qquad \textit{(II-120)}$$

$$I_\mu = (r_0)^{2(\lambda_1-\mu_1)} \int_{-\overline{\theta}}^{+\overline{\theta}} \frac{\left(R_2^{2\mu_1} - R_1(\theta)^{2\mu_1}\right)}{2\mu_1}\tilde{G}_\mu d\theta \qquad \textit{(II-121)}$$

$$I_{\lambda\mu} = 2(r_0)^{\lambda_1-\mu_1} \int_{-\overline{\theta}}^{+\overline{\theta}} \frac{\left(R_2^{\lambda_1+\mu_1} + R_1(\theta)^{\lambda_1+\mu_1}\right)}{\lambda_1+\mu_1}\widetilde{M}_{\lambda\mu} d\theta \qquad \textit{(II-122)}$$

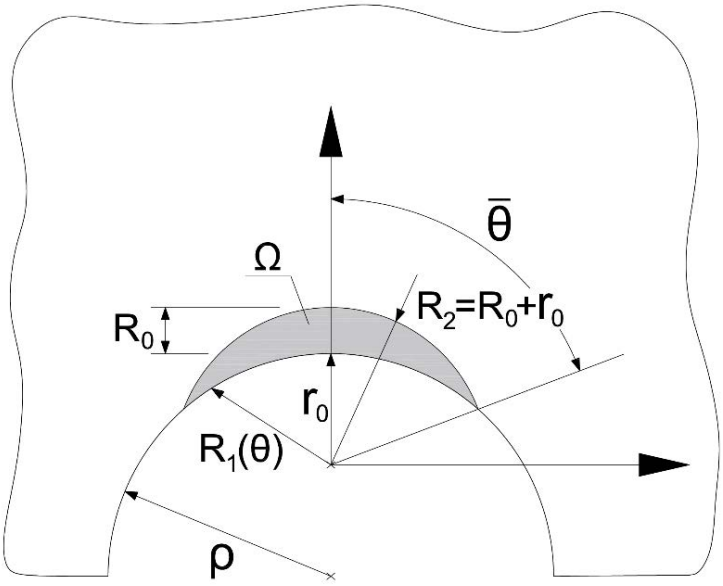

Figure II-66. Control area (Ω) for blunt V-notches.

Equation (II-122) is only valid when the notch angle is different from zero ($2\alpha \neq 0$). Otherwise, in the presence of a U-notch ($2\alpha = 0$), the following expression must be used:

$$I_{\lambda\mu} = 2(r_0) \int_{-\bar{\theta}}^{+\bar{\theta}} ln\left[\frac{R_2}{R_1(\theta)}\right] \widetilde{M}_{\lambda\mu} d\theta \qquad \textit{(II-123)}$$

This integral is always null for $2\alpha = 0$. In general, it is possible to write:

$$I_1 = \frac{1}{2\pi}\left(I_\lambda + I_\mu + I_{\lambda\mu}\right) \qquad \textit{(II-124)}$$

where the introduction of 2π makes I_1 consistent with the expression of the sharp notch case (*Equation (II-105)*). In a synthetic form, the total energy in the control area can be expressed as:

$$E_1 = \frac{1}{2E}\left[\frac{\sigma_{max}\sqrt{2\pi}}{r_0^{\lambda_1 - 1}(1+\widetilde{\omega}_1)}\right]^2 \cdot I_1 \qquad \textit{(II-125)}$$

This expression can be rewritten as follows for the particular case of U-shaped notches ($2\alpha = 0$):

$$E_1 = \frac{1}{2E}\left(\frac{\sigma_{max}\sqrt{\pi\rho}}{2}\right)^2 \cdot I_1 \qquad \textit{(II-126)}$$

Thus, the mean value of the strain energy density is given by:

$$\overline{W_1} = \frac{1}{E}\left(\frac{I_1}{2\Omega}\right)\sigma_{max}^2 r_0^{2(1-\lambda_1)}\left[\frac{\sqrt{2\pi}}{1+\widetilde{\omega}_1}\right]^2 \qquad \textit{(II-127)}$$

where the control area (*Figure II-66*) can be expressed as:

$$\Omega = \int_{R_1(\theta)}^{R_2} \int_{-\bar{\theta}}^{+\bar{\theta}} r \, dr d\theta \qquad \textit{(II-128)}$$

With reference to *Figure II-66*, the integration domain is included between two curves having a different curvature (i.e., R_1 and R_2). R_1 follows the notch edge and then varies with the angle θ. Generally, it should describe the semicircular profile of radius ρ and the two rectilinear segments, up to the intersection with R_2. The latter radius (R_2) has the centre located in correspondence of the polar coordinate system, that is, at the distance r_0 from the notch tip. This distance, as above said, depends on ρ and 2α, being equal to $\rho/2$ in the case of U-shaped notches with $2\alpha = 0$. On the other hand, the distance present between the two radii, evaluated in correspondence of the axis of symmetry, is thought of as coincident with R_0, which depends on the material tensile properties and not on the geometry (*Equations (II-108)* and *(II-109)*). A detailed review on the description and definition of the control area is provided by Lazzarin & Berto (2005). Although the control area is generally defined by a circular sector (*Figure II-66*), this is just a theoretical proposal based on the iso-strain energy density curves close to the notch tip, which can be approximated to circles. However, there is no physical evidence of its actual shape. The circular sector depicted in *Figure II-66* seems to be appropriate in cases where $R_0 \ll \rho$ (e.g., metals), but in the case of rocks the values of R_0 are relatively high as it will be shown in Chapter IV. Some studies based on the FPZ of rocks (e.g., Li & Einstein, 2017), which can be related to the control area, seem to indicate that its shape could be in fact more elongated. However, the physical characterisation of the control area is not the purpose of this work and is proposed as a possible future research line.

In general, the integral I_1 and the area Ω depend on 2α, ρ and R_0. However, I_1 is proportional to $\rho^{2\lambda_1}$ according to *Equation (II-124)*, whereas Ω is proportional to ρ^2. Then, a suitable expression for $I_1/2\Omega$ is:

$$\frac{I_1}{2\Omega}(2\alpha, \rho, R_0) = \frac{1}{\rho^{2(1-\lambda_1)}} \cdot H\left(2\alpha, \frac{R_0}{\rho}\right) \quad \textit{(II-129)}$$

where the function H depends on the notch angle and the ratio between the critical radius and the notch radius. When the control area embraces the semicircular edge of the notch (and not its rectilinear flanks), the average value of SED for the case of blunt V-notches can be expressed in the following form (Berto et al., 2007):

$$\overline{W_1} = F(2\alpha) \cdot H\left(2\alpha, \frac{R_0}{\rho}\right) \cdot \frac{\sigma_{max}^2}{E} \quad \textit{(II-130)}$$

where

$$F(2\alpha) = \left(\frac{q-1}{q}\right)^{2(1-\lambda_1)} \left[\frac{\sqrt{2\pi}}{1+\widetilde{\omega}_1}\right]^2 \quad \textit{(II-131)}$$

Equation (II-130) simplifies to a great deal the fracture analysis of notched components. This analysis can be directly made comparing the critical value of the SED (W_c) with the average SED value ($\overline{W_1}$) over the control area (Ω), as established by the fracture criterion defined in *Equation (II-97)*. Therefore, only some basic mechanical properties of the material (E, ν, σ_u and K_{IC}) and the maximum principal stress at the notch tip (σ_{max}) are needed for fracture assessments, apart from the geometrical aspects of the notch.

Values of the H function are displayed in *Table II-9* for some common notch angles, R_0/ρ ratios and Poisson's ratios. These tabulated values were obtained in origin using numerical analyses of notched components (Lazzarin & Berto, 2005).

Proceeding in the same way, *Table II-10* gathers the values of the H function corresponding to the particular case of U- notches ($2\alpha = 0$), as those studied in this work. In this case, the tabulated values cover a broader range of R_0/ρ ratios and Poisson's ratios.

Table II-9. Values of H function for blunted V-notches (Lazzarin & Berto, 2005).

2α [rad]	R_0/ρ	H			2α [rad]	R_0/ρ	H		
		v=0.3	v=0.35	v=0.4			v=0.3	v=0.35	v=0.4
0	0.01	0.5638	0.5432	0.5194	$\pi/2$	0.01	0.6290	0.6063	0.5801
	0.05	0.5086	0.4884	0.4652		0.05	0.5627	0.5415	0.5172
	0.1	0.4518	0.4322	0.4099		0.1	0.4955	0.4759	0.4535
	0.3	0.3069	0.2902	0.2713		0.3	0.3296	0.3144	0.2972
	0.5	0.2276	0.2135	0.1976		0.5	0.2361	0.2246	0.2115
	1	0.1314	0.1217	0.1110		1	0.1328	0.1256	0.1174
$\pi/6$	0.01	0.6395	0.6162	0.5894	$2\pi/3$	0.01	0.5017	0.4836	0.4628
	0.05	0.5760	0.5537	0.5280		0.05	0.4465	0.4298	0.4106
	0.1	0.5107	0.4894	0.4651		0.1	0.3920	0.3767	0.3591
	0.3	0.3439	0.3264	0.3066		0.3	0.2578	0.2467	0.2339
	0.5	0.2531	0.2386	0.2223		0.5	0.1851	0.1769	0.1676
	1	0.1428	0.1333	0.1226		1	0.1135	0.1079	0.1015
$\pi/3$	0.01	0.6678	0.6436	0.6157	$3\pi/4$	0.01	0.4114	0.3966	0.3795
	0.05	0.5998	0.5769	0.5506		0.05	0.3652	0.3516	0.3359
	0.1	0.5302	0.5087	0.4842		0.1	0.3206	0.3082	0.2938
	0.3	0.3543	0.3372	0.3179		0.3	0.2082	0.1997	0.1900
	0.5	0.2597	0.2457	0.2301		0.5	0.1572	0.1504	0.1427
	1	0.1435	0.1349	0.1252		1	0.1037	0.0988	0.0932

Table II-10. Values of H function for U-notches (Lazzarin & Berto, 2005).

R_0/ρ	v=0.10	v=0.15	v=0.20	v=0.25	v=0.30	v=0.35	v=0.40
0.0005	0.6294	0.6215	0.6104	0.5960	0.5785	-	-
0.001	0.6286	0.6207	0.6095	0.5952	0.5777	-	-
0.005	0.6225	0.6145	0.6033	0.5889	0.5714	-	-
0.01	0.6149	0.6068	0.5956	0.5813	0.5638	0.5432	0.5194
0.05	0.5599	0.5515	0.5401	0.5258	0.5086	0.4884	0.4652
0.1	0.5028	0.4942	0.4828	0.4687	0.4518	0.4322	0.4099
0.3	0.3528	0.3445	0.3341	0.3216	0.3069	0.2902	0.2713
0.5	0.2672	0.2599	0.2508	0.2401	0.2276	0.2135	0.1976
1	0.1590	0.1537	0.1473	0.1399	0.1314	0.1217	0.1110

2.8.3.2.3 Average SED under mixed-mode loading

All the previous SED expressions are thought to be applied under Mode I stress distribution due to direct tensile or bending loads, and not to a generic stress state. The proposal of mode I dominance was suggested first by Erdogan & Sih (1963) when dealing with cracked plates under plane loading and transverse shear, where the crack grows in the direction almost perpendicular to the maximum tangential stress in radial direction from its tip (Erdogan & Sih, 1963).

In the case of sharp V-notches, two different eigenvalues characterise the in-plane stress field under mode I and under mode II loading and this fact does not allow to determine an equivalent NSIF governing the scale effect (Berto & Lazzarin, 2014). The mode I dominance can be directly taken into account by using Sih's parameter S (which is the product of the strain energy density and a convenient distance from the point of singularity) or the SED concept over a material dependent control volume.

In the case of blunt notches under mixed mode loading, the maximum elastic stress is out of the notch bisector line and its position varies along the notch edge as a function of mode I to mode II stress distributions. Thus, under mixed-mode loading, the control area is no longer centred with respect to the notch bisector, but assumed to be rigidly rotated with respect to it and centred on the point where the SED (and the maximum principal stress) reaches its maximum value (Berto et al., 2007; Gómez et al., 2007; Gómez et al., 2008; Berto et al., 2012; Lazzarin et al., 2013). This rotation is shown in *Figure II-67* where the control area is drawn for a U-shaped notch both under mode I loading (*Figure II-67a*) and mixed-mode loading (*Figure II-67b*). In any case, the number of experimental data reported in the literature for mixed-mode fracture analyses is quite limited with reference to prevalent mode II loading conditions, and even more limited for cases where mode I and mode III loading conditions are combined together (Lazzarin et al., 2008).

Dealing with blunt V-notches, the concept of equivalent local mode I, although not exact in principle, can be seen as an accurate engineering approximation for the analysis of components subjected to mixed-mode loading (Berto et al., 2007; Gómez et al., 2008; Gómez et al., 2009; Berto

et al., 2012). In particular, the SED was generalized from mode I to mixed-mode (I+II) under the hypothesis of an equivalent local mode I along the normal line to the notch edge, starting at a point where the principal stress reaches its maximum value (Point P in *Figure II-67b*). The inclined path is perpendicular to the notch surface and starts from the point of the maximum $\sigma_{\theta\theta}$ stress component along the notch profile (Berto & Lazzarin, 2014). When finite element results are compared with the mode I theoretical solution reported by Filippi et al. (2002), the agreement is satisfactory even under prevalent mode II, independently of the notch radius. In parallel, the shear stress component has been verified to be zero, as it happens along the notch bisector under Mode I loading. This observation leads to the conclusion that under mixed mode loading the line normal to the notch edge and starting from the point of maximum principal stress behaves as a virtual bisector line under pure mode I, confirming the applicability of the equivalent local mode I concept.

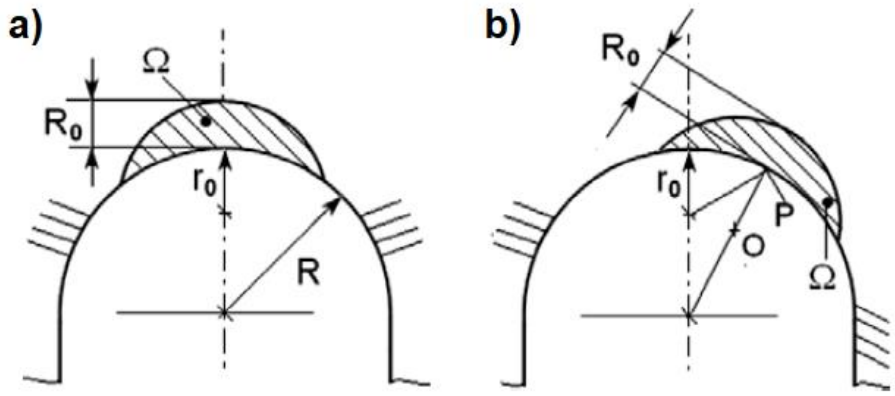

Figure II-67. Critical volume for U-notches under (a) mode I and (b) mixed mode loading (Berto & Lazzarin, 2014).

With all this, analogously to *Equation (II-130)*, which is valid for notches under mode I loading conditions, the following expression can be used for U-shaped notches under mixed-mode loading:

$$\overline{W_1} = H^*\left(2\alpha, \frac{R_0}{\rho}\right) \cdot \frac{\pi\sigma_{max}^2}{4E} \qquad \textit{(II-132)}$$

where σ_{max} is the maximum value of the principal stress along the notch edge and H^* depends again on the normalized radius (R_0/ρ), the Poisson's ratio (ν) and the loading conditions. For different configurations of mode mixity, the function H, analytically obtained under mode I loading, was shown to be very close to H^* (Berto et al., 2007; Gómez et al., 2007; Gómez et al., 2008; Berto et al., 2012; Lazzarin et al., 2013).

As a summary for a clearer justification of the control area (Ω), *Figure II-68* represents numerically obtained iso-strain energy density curves for U-shaped notches under mode I loading conditions (*Figure II-68a*), blunt V-shaped notches (example with $2\alpha = 135º$) under mode I loading conditions (*Figure II-68b*), and U-shaped notch under mode II (shear) loading conditions (*Figure II-68c*). No scale is presented because this figure is only of interest in qualitative terms.

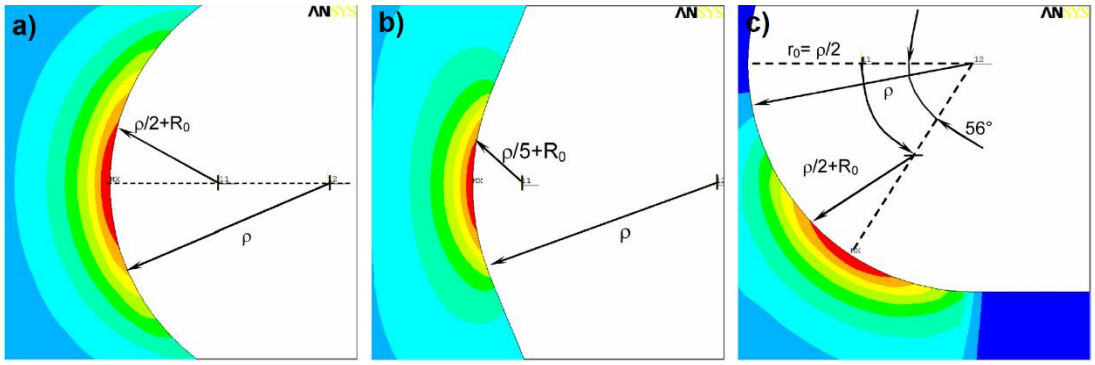

Figure II-68. Iso-strain energy density curves for (a) U-shaped notch under mode I loading, (b) blunt V-shaped notch with $2\alpha = 135º$ *under mode I loading and (c) U-shaped notch under mode II (shear) loading (Berto & Lazzarin, 2014).*

In the case of the U-shaped notch ($2\alpha = 0$) subjected to mode I loading conditions shown in *Figure II-68a*, the centre of the curved lines is approximately located at a distance $r_0 = \rho/2$ with respect to the notch tip, which corresponds to the origin of the local coordinate system. An increase of the radius R_2, due to an increase of R_0, results in a reduction of the strain energy density level. By contrast, in the case of the blunt V-notch with $2\alpha = 135º$ subjected to mode I loading conditions of *Figure II-68b*, the centre of the strain energy density curves is seen to be much closer to the notch tip than in the previous case ($r_0 = \rho/5$).

The greater R_0, the smaller the sensitivity to the notch is. When $\rho = 0$, the radius R_2 coincides with R_0 and becomes independent of the notch opening angle (2α). Finally, in the presence of combined tension and shear loads, the point of the maximum principal tensile stress does not coincide with the notch tip as stated above. The control volume moves as shown in *Figure II-67b*, rotating with respect to the centre of the notch, according to an angle that depends on the ratio between the generalized notch stress intensity factors. An example of the strain energy density contour lines for the case of a U-notch under pure mode II is shown in *Figure II-68c*.

Finally, with reference to mode III loading case, some closed-form expressions for the mean value of the strain energy density in the presence of theoretical parabolic and hyperbolic notches were obtained by Zappalorto and his co-workers (e.g., Lazzarin et al., 2007; Zappalorto & Lazzarin, 2007; Atzori et al., 2010). The analytical results were intended to be the basis for further investigations on the static strength properties of both sharp and blunt notched components under mode III. Taking advantage of some pioneering works (Filon, 1900; Wigglesworth & Stevenson, 1939; Smith 2004), some other recent theoretical developments have been carried out dealing with other notch shapes under linear elastic and elasto-plastic conditions (Zappalorto & Lazzarin, 2009; Zappalorto & Lazzarin, 2010; Zappalorto & Lazzarin, 2011). In any case, with the development of numerical analyses, the SED under mode III can be easily determined by using a commercial finite element programme for example, once the control volume is defined.

In general, the development of numerical analyses has represented a great breakthrough in the field of fracture mechanics and, in particular, for rock fracture analyses, as will be shown in the next section.

2.9 NUMERICAL ANALYSES IN ROCK FRACTURE MECHANICS

Although the use of numerical analyses is not the primary focus of this study, different numerical tools have been used in this work to determine the stress field around defects, as well as to analyse the influence of the grain size on rock fracture assessments. For this reason, a brief review of existing numerical approaches is provided in this section.

As indicated in *Section 1.2*, there are two basic ways of thinking about and modelling rock, considering it as a continuous or a discontinuous material. Although rock is certainly an anisotropic, heterogeneous material, it is commonly modelled in the framework of continuum mechanics, with the disadvantage that this approach does not allow to capture fracture and the associated fracture rock kinematics (at least in a direct way). However, depending on the scale of the discontinuities and the purpose of the studied rock engineering problem, a continuous approach may be a suitable and computationally efficient option, especially when global response is of interest. In this work, for example, Finite Element Analyses (FEA) are used to determine the stress fields around defects.

For detailed fracture analyses of rock masses or rock components, different computational methods and approaches can be found in the literature. Jenabidehkordi (2019) provides a review of most commonly used computational methods for rock fracture analyses and classifies them into three categories:

- Continuum Based Methods (CBMs). As stated above continuum mechanics cannot capture fracture and the associated fractured rock kinematics in a direct way. For this reason, CBMs generally imply hybrid solutions. In general, continuous approaches smear out the crack over a finite width followed by discrete fracture approaches mainly in the context of Galerkin methods, which convert a continuous operator problem (such as a differential equation) to a discrete problem. Thus, the Galerkin methods can be viewed as a separation-of-variables technique used to discretize the problem in space. This technique is not restricted to the finite element method and can theoretically be used also in other discretization techniques such as meshless methods, for example (Jenabidehkordi, 2019). As indicated in *Table II-11*, Finite Element Method and combined Finite Difference - Finite Volume Method are included in this group.
- Discrete Crack Approaches (DCAs). In this case, fracture initiation and propagation is modelled by changing the topology of the domain and cracks have a clearly defined

width. This approach is physically intuitive, but requires tracking of each individual crack, including the concomitant topological changes of the domain. That is, it implies a continuous change in nodal connectivity. Besides, the crack is constrained to follow a predefined path along the element edges. (See *Table II-11*)

- Block-Based Methods (BBMs). These methods model the material or structure through interaction/contact of an assembly of blocks, being able to simulate large displacement of these blocks. The idea behind this class of methods is to bound neighbours of an assembly of blocks to each other using contacts. In fact, all these methods require efficient contact detection models, and the material response is mainly governed by the interaction of the blocks. The macroscopic response is highly sensitive with respect to the shapes, sizes, and distribution of the blocks as well as the contact laws between them. For this reason, calibrating these parameters remains one major challenge of BBMs. The most popular BBM is the Discrete Element Method (DEM), first proposed by Cundall (1971). When using DEM, each particle is represented numerically and is identified with its specific properties (e.g., shape, size, material properties). The DEM allows finite displacements and rotations of these discrete particles as a consequence of the interaction through their contacts, including complete detachment, and recognizes new contacts automatically as the calculation progresses. In this work, DEM is used to study the influence of grain size in rock fracture.

With all this, *Table II-11* collects some of the most widely used computational methods for the analysis of fracture in rocks, sorted according to the categories indicated above.

In this work, both finite element and discrete element analyses are used. FEM is only applied for support calculations and complementary analyses, for which PLAXIS 2D (2017) is used. These analyses are based on basic numerical models and simulations. Thus, a detailed study of the state of the art of finite elements is considered unnecessary and the corresponding comments on the performed numerical models will be

addressed when required. On the other hand, DEM is also applied with the software UDEC v6.00 (Itasca, 2010). Discrete numerical analyses and results are specifically addressed in Chapter V, which includes a detailed description of the method used.

Table II-11. Summary of numerical methods for the analysis of fracture in rocks (adapted from Jenabidehkordi, 2019).

Computational method	Category*
Finite Element Method (FEM)[1]	CBM
Combined Finite Difference – Finite Volume Method (FDM-FVM)[2]	CBM
Element erosion and remeshing[3]	DCA
Embedded Element Methods (EFEM)[4]	DCA
Extended Finite Element Method (XFEM)[5]	DCA
Numerical Manifold Method (NMM)[6]	DCA
Meshfree Methods (MMs)[7]	DCA
Peridynamics (PD)[8]	DCA
Boundary Element Method (BEM)[9]	DCA
Discrete Element Method (DEM)[10]	BBM
Key Block Theory[11]	BBM
Discontinuous Deformation Analysis (DDA)[12]	BBM
Lattice Network Model[13]	BBM

*CBM – Continuum Based Method

*DCA – Discrete Crack Approaches

*BBM – Block-Based Method

[1]Peng (1988); Shangyi et al. (2003)

[2]Selmin (1993); Wheel (1996)

[3]Belytschko & Lin (1987)

[4]Belytschko et al. (1988); Dvorkin et al. (1990)

[5]Belytschko & Black (1999); Dolbow & Belytschko (1999)

[6]Shi (1992); Ma et al. (2010)

[7]Belytschko et al. (1994); Rabczuk & Zi (2007)

[8]Silling (2000)

[9]Simpson et al. (2012); Brebbia & Walker (2016)

[10]Cundall (1971); Cundall (1988)

[11]Shi (1977)

[12]Shi & Goodman (1985)

[13]Mühlhaus et al. (1997); Li et al. (2000)

- Chapter III -
Experimental program

1 INTRODUCTION

The experimental program comprises a broad casuistic of rock lithologies, aiming to prove the suitability of both the TCD and the SED criterion in the fracture assessment of rocks despite the variability in their characteristics and microstructures. The studied rocks are described in detail in *Section 2* of this chapter. Likewise, the experimental program involves an exhaustive and systematic laboratory campaign including several Brazilian tests, uniaxial compression tests with strain measurements, four-point bending tests and three-point bending tests, all of them under different temperature conditions. Thermal expansion measurements and petrographic characterization of the rocks by means of thin-section analyses have also been considered in the performed laboratory campaign. All these tests allow to obtain, not only the basic strength and deformational parameters of the studied rock, necessary for the application of the TCD and the SED criterion, but also important rock fracture data for the validation of the aforementioned methodologies under different loading and thermal conditions, as well as further thermal dilatational and microstructural information that provides interesting conclusions for a better

interpretation of the obtained results. *Section 3* describes in detail the performed laboratory tests.

2 MATERIALS

The accomplished experimental program comprises the study of four rocks with different lithologies, namely a Floresta sandstone, a Moleanos limestone, a Macael marble and a Carrara marble. Additionally, the fracture results of a previous laboratory campaign performed on an Oolitic limestone and a Biotite granite (originally studied by means of the TCD at room temperature by Cicero et al., 2014) have also been considered here, for further validation of the SED criterion. *Figure III-1* shows a picture of each of the six analysed rocks, for which a single-letter code has been assigned for a clear identification along the present document.

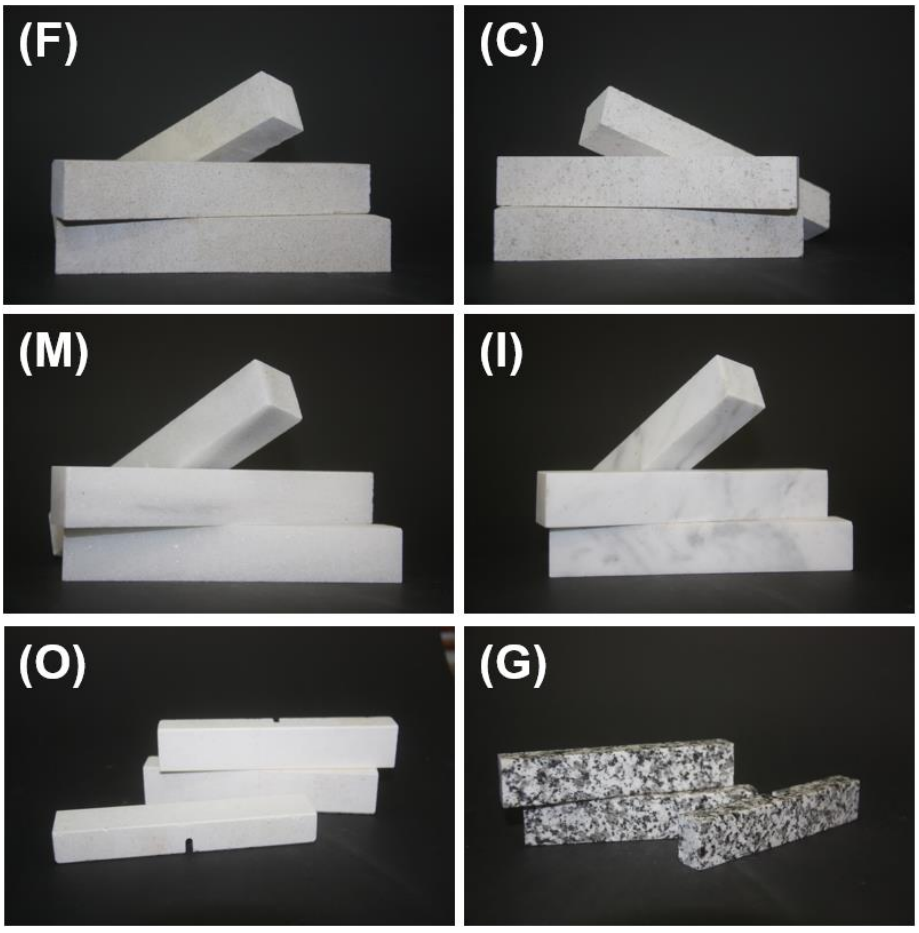

Figure III-1. Images of studied rock specimens: (F) Floresta sandstone, (C) Moleanos limestone, (M) Macael marble, (I) Carrara marble, (O) Oolitic limestone, and (G) Biotite granite.

Aiming to reduce the scatter of the experimental results and to facilitate their analysis and interpretation, the selected rocks are relatively homogeneous, non-altered and isotropic. These materials have been supplied by a regional company specialised in natural stone works, where part of the samples have been prepared.

2.1 FLORESTA SANDSTONE (F)

The studied Floresta sandstone comes from Espluga Calva (Lleida), in the northeast of Spain, and can be classified as a sedarenite. It consists of abundant carbonated grains and quartz (monocrystalline, polycrystalline and chert grains). Carbonates [C] are mainly subrounded, medium size (100-300 μm) and consist of intraclastic grains with mudstone texture, spiritic grains and dolomite. Quartzes [Q] are mainly subrounded and subangular shaped (or occasionally angular), with sizes varying in the range of medium and very fine grains (50-200 μm). Likewise, sparitic crystals [Sp] are abundant with medium to very fine sizes (50-200 μm). Large packing and dissolution voids [V] are common, cement is very scarce and depositional structures are not recognizable, which reduces material anisotropy. An image of the microstructure of the Floresta sandstone is depicted in *Figure III-2*, obtained from the petrographical characterization by means of thin-section analyses using an optical microscope.

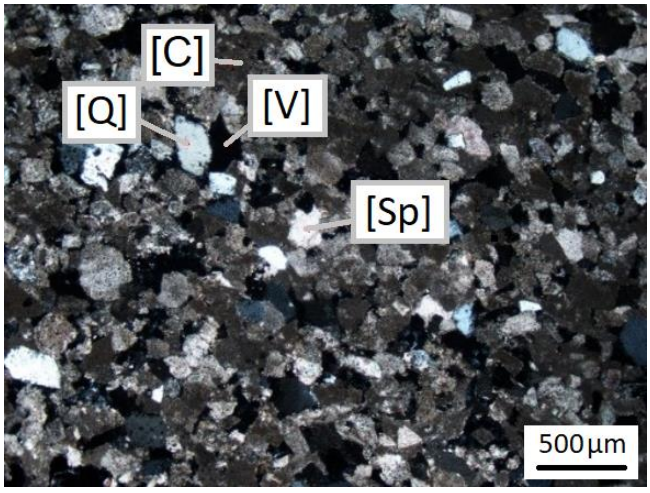

Figure III-2. Optical image of the microstructure of the Floresta sandstone (4x, crossed Nicols).

The Floresta sandstone is a very compact material given its formation by consolidated and restructured quartz sand, with limestone origin cement and with a high porosity of around 16%. For the measurement of porosity, the NIS-Element image visualization software has been used, which allows to identify void areas by HIS colour range. Basically, it recognises the areas where the blue-inked resin used to manufacture the thin-sections has penetrated (see *Figure III-3*).

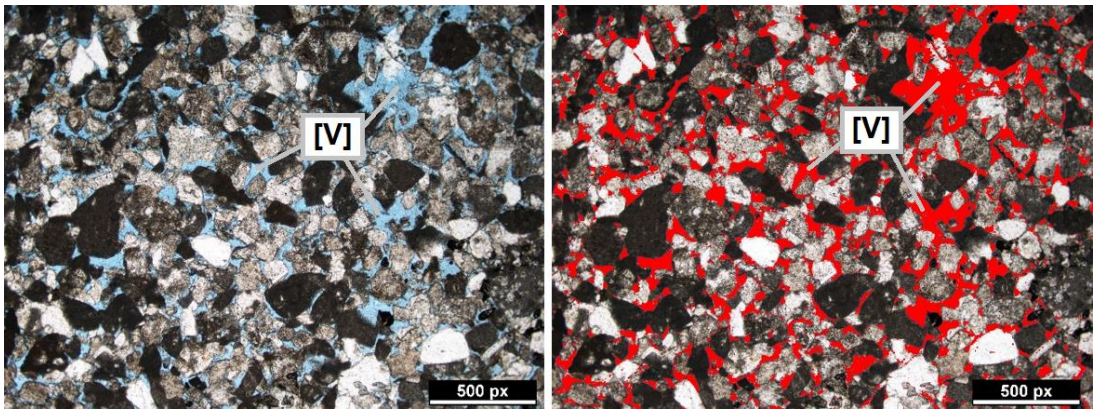

Figure III-3. Identification of voids [V] for porosity measurements.

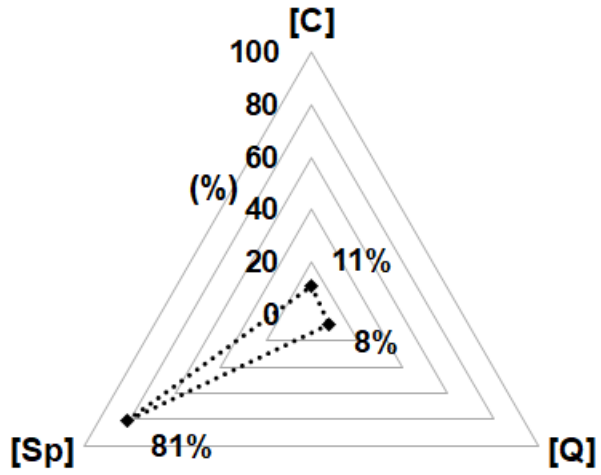

Figure III-4. Percentage of components within Floresta sandstone (F).

Based on the identification and measurements of more than 2000 grains within the Floresta sandstone, it is concluded that sparitic crystals [Sp] are the most abundant component comprising approximately 81% of the grains, followed by carbonates [C] with 11% and, finally, quartz [Q] with 8%. *Figure III-4* summarises the percentage of each component within the Floresta sandstone.

On the other hand, *Figure III-5a* represents the grain size distribution of each of the Floresta sandstone components, as well as of the voids. As a unified criterion for the definition of the size, the length of the maximum axis of the grains and voids have been measured. Additionally, the void distance distribution is also provided in *Figure III-5b*. The results are represented as frequency histograms and as cumulative frequency curves, both of them in percentage.

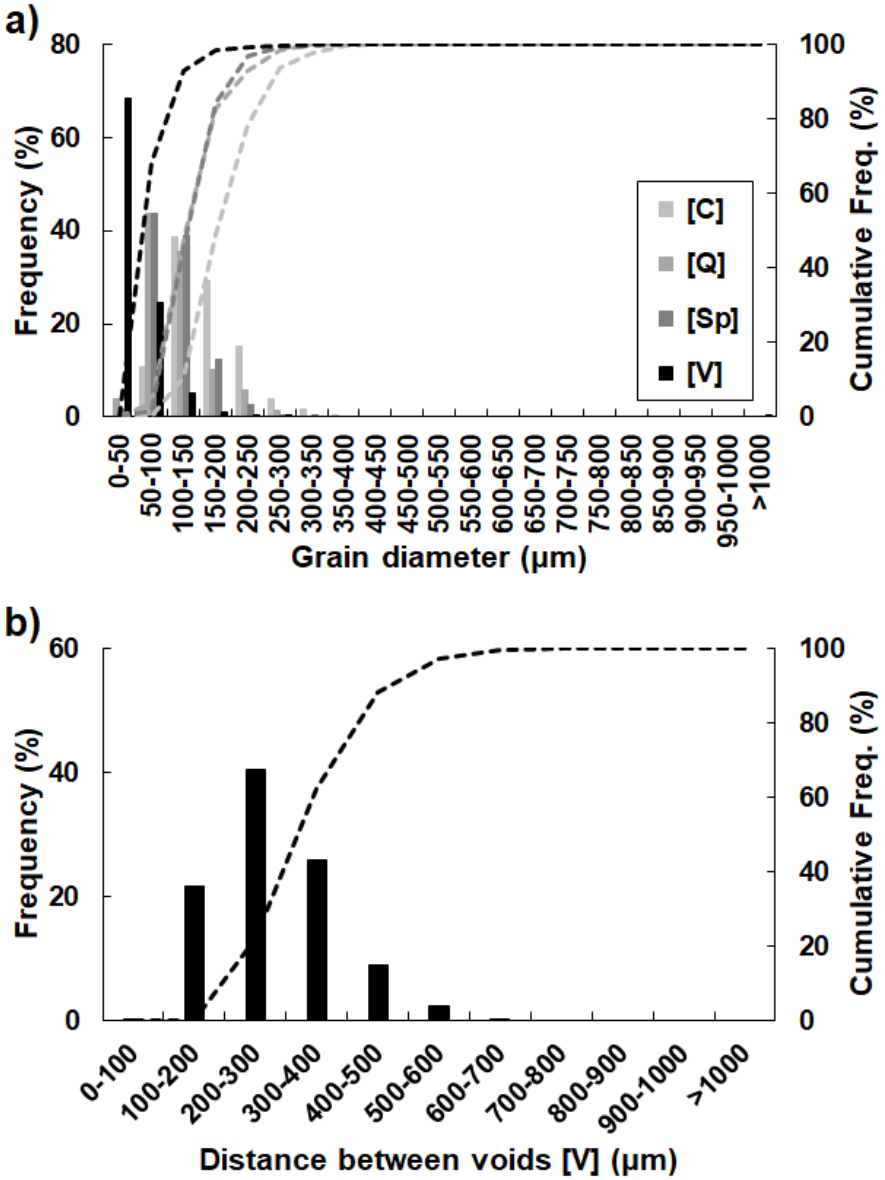

Figure III-5. (a) Grain size distribution and (b) void [V] distance distribution of Floresta sandstone (F).

More than 90% of the voids are between 0-150 μm size, with an approximate average distance between them of around 300-400 μm. Sparitic crystals and quartz offer a very similar grain size distribution as shown in the cumulative size distribution curves of *Figure III-5a*, while carbonates present slightly larger grains on average. *Table III-1* presents some technical data of the analysed Floresta sandstone, including granulometric information such as the mean and median grain size and the sorting coefficient defined as the ratio between the first (Q1) and the third (Q3) quartile. As Q1/Q3 approaches the unity the more uniform the grain size is. The bulk density (EN 1936:2007), open porosity (EN 1936:2007), water absorption (EN 13755:2008) and abrasion resistance (EN 1341:2013) have been directly provided by the supplier.

Table III-1. Technical and granulometric data of the Floresta sandstone (F).

Parameter	Value
Bulk density (kg/m^3)	2320
Open porosity (%)	16.3
Water absorption (%)	4.8
Abrasion resistance (mm)	31
Mean grain size (μm)	116 $\pm$ 45*
Mean [C] grain size (μm)	160 $\pm$ 55*
Mean [Q] grain size (μm)	113 $\pm$ 47*
Mean [Sp] grain size (μm)	111 $\pm$ 40*
Median grain size (μm)	109
Median [C] grain size (μm)	151
Median [Q] grain size (μm)	104
Median [Sp] grain size (μm)	104
Sorting coefficient (Q1/Q3)	0.59
[C] sorting coefficient	0.66
[Q] sorting coefficient	0.57
[Sp] sorting coefficient	0.60

*Standard deviation

2.2 MOLEANOS LIMESTONE (C)

The studied Moleanos limestone is original from Portugal and can be classified as an intrasparitic-pelsparitic limestone (Folk, 1959) or grainstone (Dunham, 1962). It consists of intraclasts, bioclasts, pellets and sparite crystals (see *Figure III-6*). Intraclasts [Intra] correspond to the largest subrounded-rounded shaped grains with sizes mostly varying in the range of coarse sand and microconglomerate (100-500 μm, and sporadically larger than 1000 μm), showing a micritic texture. By contrast, bioclasts [bio] are mainly fragments of bivalves and corals, which occasionally show internal sparitic recrystallization. The most frequent bioclast sizes range from 100-500 μm, depending on the fossilised material, although 2000 μm size bioclasts can be found occasionally. Pellets [Pel] are the dominant allochemical component. The size of the pellets varies in the range of fine to medium sand (100-300 μm) and they always show a micritic internal texture. Sparite crystals [Sp] cement to a great amount the allochemical components, so porosity is significantly lower than in the case of the Floresta Sandstone, namely 6.4%.

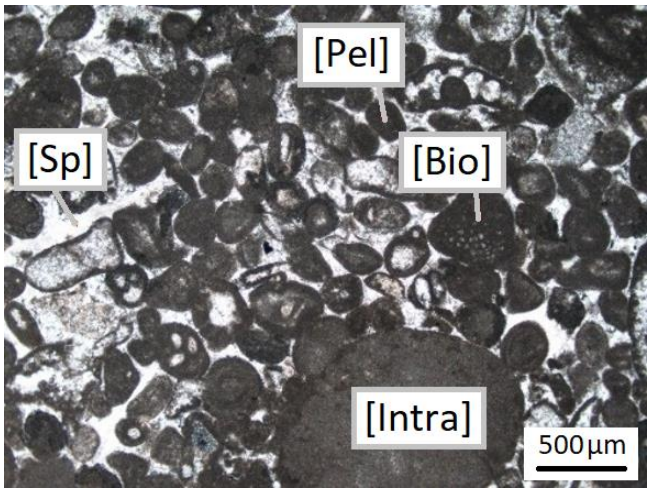

Figure III-6. Optical image of the microstructure of Moleanos limestone (4x, crossed Nicols).

The most abundant components within the analysed Moleanos limestone are pellets and intraclasts, comprising 51% and 43% of the grains, respectively. Bioclasts are less abundant, comprising 6% of the grains as indicated in *Figure III-7*.

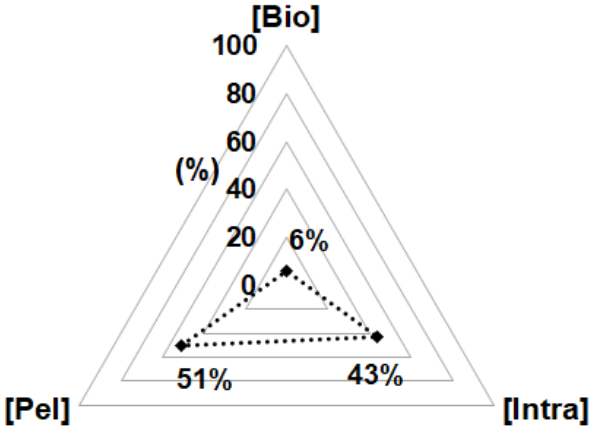

Figure III-7. Percentage of components within Moleanos limestone (C).

From the analysis of more than 4500 grains, the grain size distribution histogram depicted in *Figure III-8* has been derived. Likewise, the cumulative frequency curves have also been represented for each of the components of the Moleanos limestone. It is directly observed that there are significant size differences among the constituent components, being significantly less uniform than the Floresta sandstone.

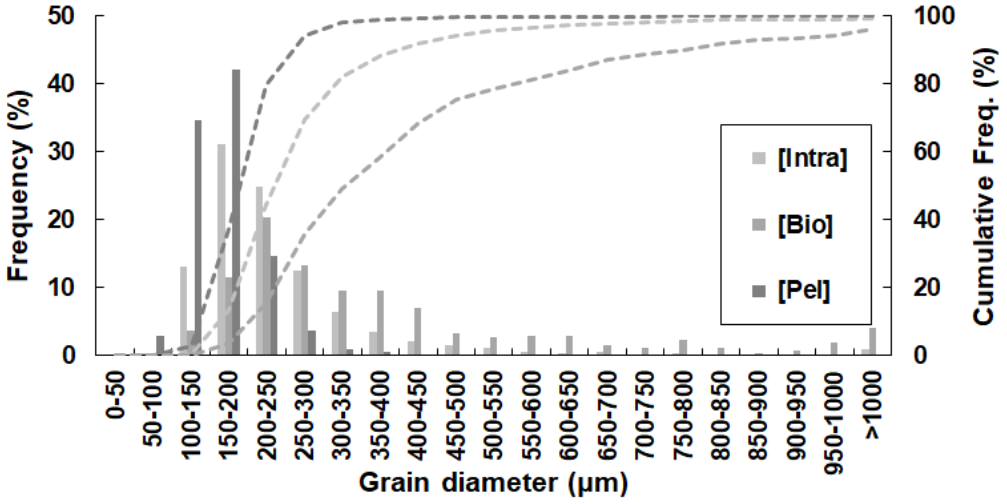

Figure III-8. Grain size distribution of the Moleanos limestone (C).

Table III-2 gathers some technical and granulometric data of the Moleanos limestone. Leaving aside the pellets, the rest of the components present high variability of the grain size, specially the bioclasts.

Table III-2. Technical and granulometric data of the Moleanos limestone (C).

Parameter	Value
Bulk density (kg/m^3)	2500
Open porosity (%)	6.4
Water absorption (%)	2.7
Abrasion resistance (mm)	20
Mean grain size (μm)	218 ± 156*
Mean [Intra] grain size (μm)	248 ± 167*
Mean [Bio] grain size (μm)	410 ± 342*
Mean [Pel] grain size (μm)	170 ± 57*
Median grain size (μm)	183
Median [Intra] grain size (μm)	210
Median [Bio] grain size (μm)	315
Median [Pel] grain size (μm)	162
Sorting coefficient (Q1/Q3)	0.64
[Intra] sorting coefficient	0.63
[Bio] sorting coefficient	0.50
[Pel] sorting coefficient	0.72

*Standard deviation

2.3 MACAEL MARBLE (M)

The studied Macael marble is original from Almería (southeast of Spain) and consists of a white calcitic marble. *Figure III-9* shows the microstructure of the Macael marble obtained from an optical microscope.

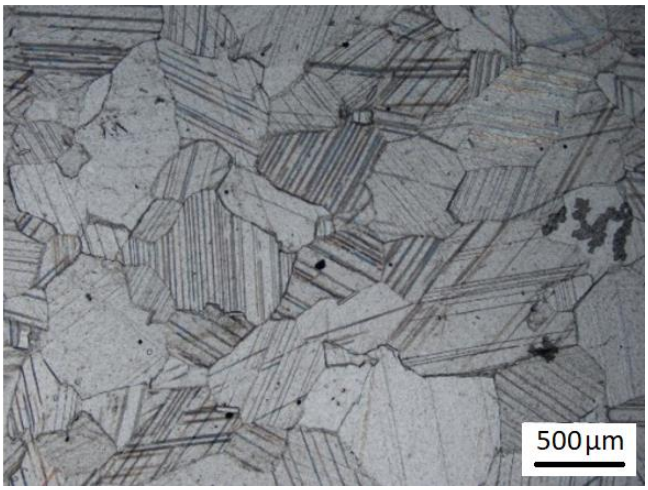

Figure III-9. Optical image of the microstructure of Macael marble (4x, parallel Nicols).

The Macael marble shows a very well developed granoblastic texture with equidimensional idiomorphs leucocratic crystals and null porosity.

Figure III-10 provides an overview of the grain size distribution of the Macael marble. It presents medium size crystals varying from 50 to 1180 μm, obtained from the measurement of more than 4500 crystals.

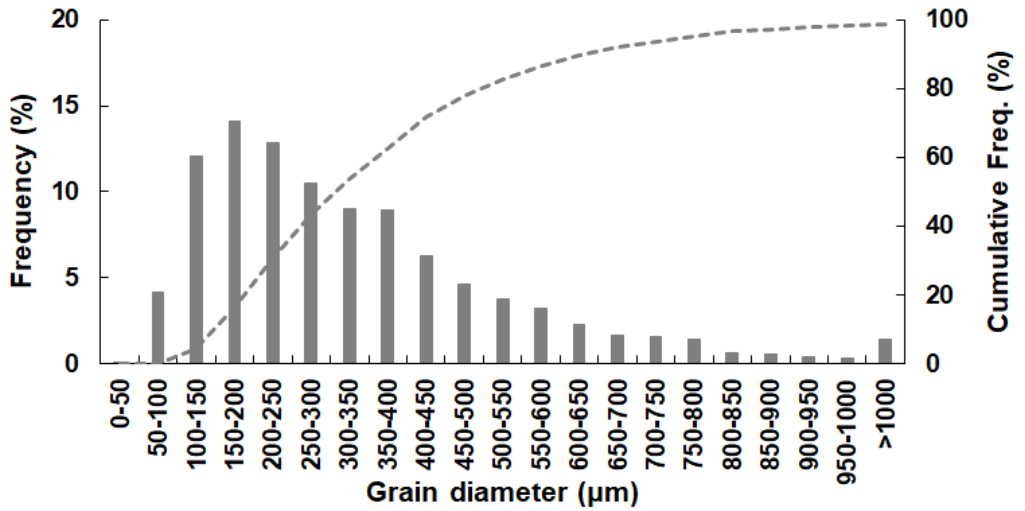

Figure III-10. Grain size distribution of the Macael marble (M).

Finally, *Table III-3* shows, apart from other technical information as in the previous rocks, the mean and median size of the crystals and the sorting coefficient. A significant variability is appreciated in the crystal size when analysing the high standard deviation in comparison with the mean grain size and the low sorting coefficient value, which indicates that grains are not very uniform.

Table III-3. Technical and granulometric data of the Macael marble (M).

Parameter	Value
Bulk density (kg/m^3)	2715
Open porosity (%)	-
Water absorption (%)	0.075
Abrasion resistance (mm)	22.25
Mean grain size (μm)	335 $\pm$ 228*
Median grain size (μm)	282
Sorting coefficient (Q1/Q3)	0.42

*Standard deviation

2.4 CARRARA MARBLE (I)

The last selected rock in the considered experimental program is the Carrara marble (I), from Italy. This rock was chosen because it is an internationally known material that has been widely studied in scientific literature. However, the depletion of the original quarry makes the properties of this marble coming from the surroundings of Carrara vary and, therefore, are not directly comparable.

The studied Carrara marble presents a very similar microstructure to that of the Macael marble, with a well developed granoblastic texture with equidimensional crystals and null porosity, as shown in *Figure III-11*.

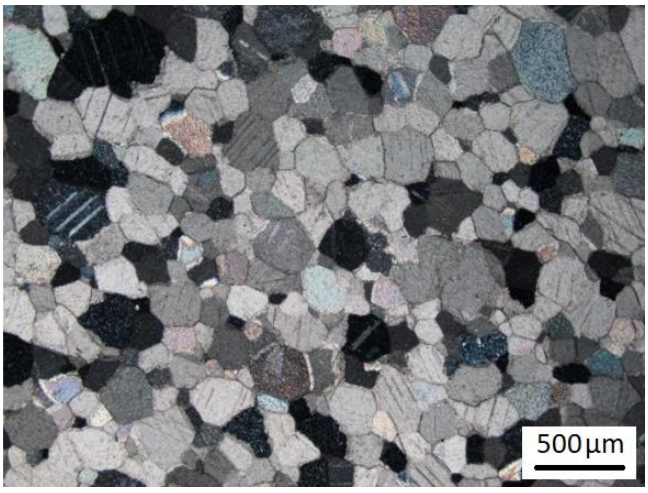

Figure III-11. Optical image of the microstructure of Carrara marble (4x, crossed Nicols).

The main difference between Carrara and Macael marbles is the grain size, which is smaller and better sorted in the case of the Carrara marble (50-350 μm), as observed from the comparison between the grain size distribution curve of *Figure III-12* and that of the Macael marble depicted in *Figure III-10*. More than 4500 crystals have also been measured in this case.

According to the granulometric information gathered in *Table III-4*, the sorting coefficient is significantly larger in the Carrara marble than in the Macael marble, which confirms that the crystals are more uniform in this marble. Likewise, the mean and the median grain sizes are relatively smaller.

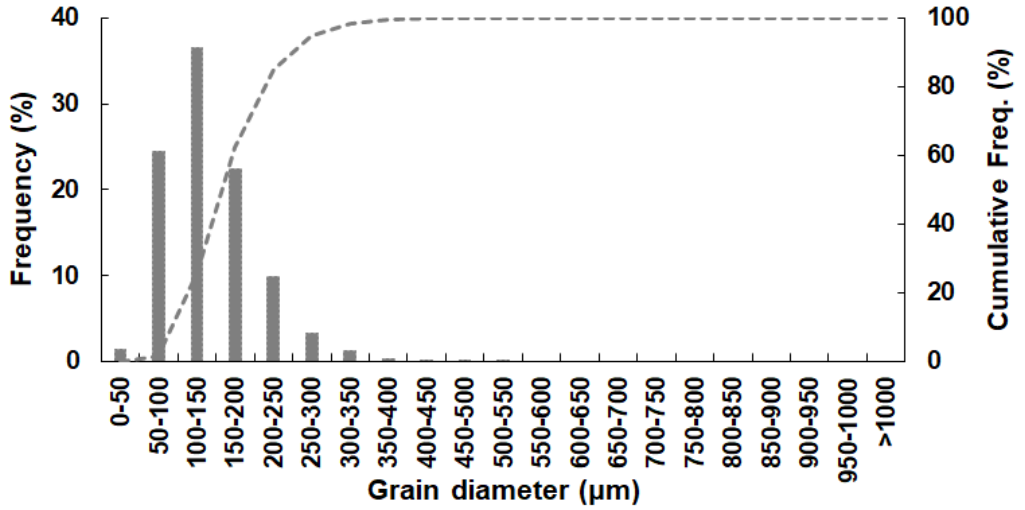

Figure III-12. Grain size distribution of the Carrara marble (I).

Table III-4. Technical and granulometric data of the Carrara marble (I).

Parameter	Value
Bulk density (kg/m^3)	2709
Open porosity (%)	-
Water absorption (%)	0.15
Abrasion resistance (mm)	2.65
Mean grain size (μm)	142 $\pm$ 60*
Median grain size (μm)	132
Sorting coefficient (Q1/Q3)	0.57

*Standard deviation

2.5 ADDITIONAL MATERIALS

Apart from the Floresta sandstone (F), the Moleanos limestone (C), the Macael marble (M) and the Carrara marble (I), which are part of the laboratory campaign framed within this research work, two additional rocks have also been studied here: an Oolictic limestone and a Biotite granite. These two rocks are not part of the performed experimental program but correspond to a previous study by Cicero et al. (2014). A detailed petrographic analysis is not available for the Oolitic limestone and Biotite granite. However, the fracture results and mechanical properties obtained by Cicero et al. (2014) will be used for fracture analyses and will be compared with the rest of studied rocks.

2.5.1 Oolitic limestone (O)

The studied Oolitic limestone is original from Novelda (Alicante), in the southeast of Spain. *Figure III-13* shows the microstructure of this Oolitic limestone.

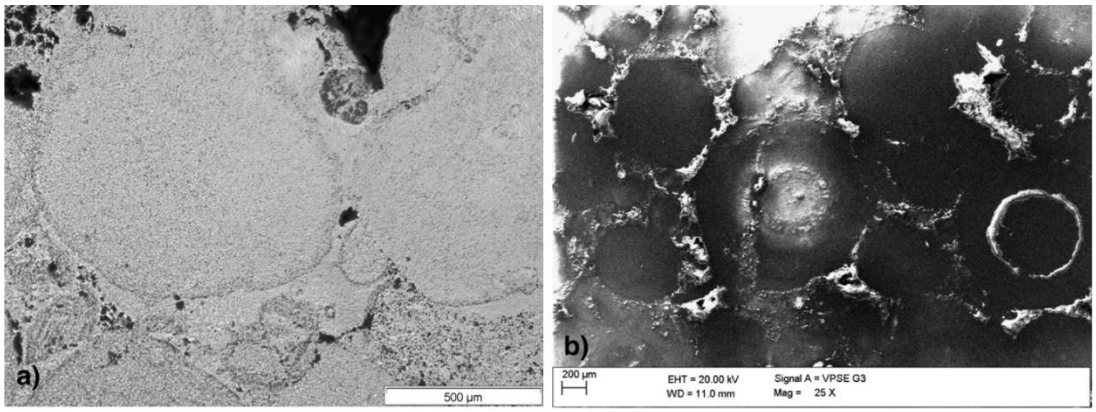

Figure III-13. Microstructure of Oolitic limestone obtained by (a) optical microscopy and (b) SEM (Cicero et al., 2014).

This rock presents a relatively homogeneous microstructure and, based on the water absorption value indicated in *Table III-5*, a similar open porosity of that of the Moleanos limestone is estimated. Finally, this limestone is characterized by having a relatively high average grain size of around 800 μm.

Table III-5. Technical and granulometric data of the Oolitic limestone (O).

Parameter	Value
Bulk density (kg/m^3)	2540
Water absorption (%)	3.01
Abrasion resistance (mm)	22.5
Mean grain size (μm)	800

2.5.2 Biotite granite (G)

Ultimately, the studied Biotite granite also corresponds to the study of Cicero et al. (2014), which is original from Sierra de Guadarrama, from the centre of Spain. *Figure III-14* shows the microstructure of this granite using both optical microscope and Scanning Electron Microscope (SEM).

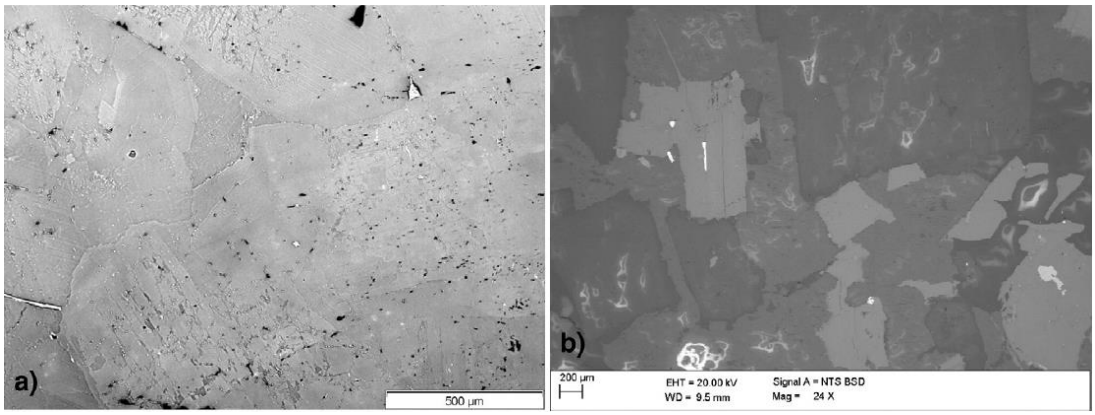

Figure III-14. Microstructure of granite obtained by (a) optical microscopy and (b) SEM (Cicero et al., 2014).

This rock is also highly homogeneous and presents a mean grain size of approximately 1000 μm. As an igneous rock, the granite has negligible porosity. *Table III-6* gathers some technical and granulometric data of the studied granite.

Table III-6. Technical and granulometric data of the granite (G).

Parameter	Value
Bulk density (kg/m^3)	2660
Water absorption (%)	0.18
Abrasion resistance (mm)	19
Mean grain size (μm)	1000

To conclude, *Table III-7* presents a summary of the main technical and granulometric data of each of the studied rocks for a direct comparison between them. Differences in mean grain size are of special interest in this work, since these values will be correlated with critical distance of the rocks. Likewise, porosity also plays a key role and will facilitate a comprehensive understanding of rock behaviour under different temperature conditions, accordingly to the comments on the thermal influence on rock mechanical properties discussed in Chapter II (*Section 1.4*).

Table III-7. Summary of the technical and granulometric data of each of the analysed rocks.

Parameter	(F)	(C)	(M)	(I)	(O)	(G)
Bulk density (kg/m^3)	2320	2500	2715	2709	2540	2660
Open porosity (%)	16.3	6.4	-	-		
Water absorption (%)	4.8	2.7	0.075	0.15	3.01	0.18
Abrasion resistance (mm)	31	20	22.25	2.65	22.5	19
Mean grain size (μm)	116	218	335	142	800	1000
Stand. Deviation (μm)	45	156	228	60		
Median grain size (μm)	109	183	282	132		
Sorting coefficient (Q1/Q3)	0.59	0.64	0.42	0.57		

3 LABORATORY TESTS

This section provides a detailed description of the performed laboratory tests and analyses, namely Brazilian tests, uniaxial compression tests, four-point and three-point bending tests, thermal expansion tests and petrographic characterization by means of thin-section analyses of fractured samples. *Table III-8* introduces a summary of all the performed tests, indicating the number of studied rocks, the number of considered temperature conditions, the repetitiveness of each test and the final total amount. Subsequently, each test type will be described and detailed individually. The four selected rocks correspond to the Floresta sandstone (F), the Moleanos limestone (C), the Macael marble (M), and the Carrara marble (I) described above. Likewise, the considered temperatures vary from 23ºC (room temperature) up to 250ºC and, finally, the repetitiveness of each test aims to provide statistically representative parameters and measurements that contemplate the intrinsic variability of the rocks due to their heterogeneous nature. As a general criterion and generally following the values required by the standards, the number of repeated tests has been set to six, although in some cases the repetitiveness has been increased for verification purposes. On the contrary, in some other tests with less influence on the interpretation of the fracture behaviour of the rocks, a lower repetition has been considered. In total, 300 Brazilian tests, 120 simple compression tests (with strain gauges), 882 four-point bending tests, 395 three-point-bending tests, 290 thermal expansion measurements and 158 thin-section analyses have been performed.

Table III-8. Summary of the performed laboratory tests.

TEST	Nº Rocks	Nº Temp.	Repet.*	**Total**
Tensile splitting (Brazilian) tests	4 (+1)	6	6/12	**300**
Uniaxial compression tests	4	4	6/12	**120**
Four-point bending tests				**882**
without notch	4	6	3/4	90
with $\rho = 0.15$ mm	4	4	6	96
with $\rho = 0.5$ mm	4	4	6	96
with $\rho = 1$ mm	4	4	6	96
with $\rho = 2$ mm	4	4	6	96
with $\rho = 4$ mm	4	4	6/12	120
with $\rho = 7$ mm	4	4	6	96
with $\rho = 10$ mm	4	4	6	96
with $\rho = 15$ mm	4	4	6	96
Three-point bending tests				**395**
without notch	4	1	2/3/4	11
with $\rho = 0.15$ mm	1 (x4)	2	6	48
with $\rho = 0.5$ mm	1 (x4)	2	6	48
with $\rho = 1$ mm	1 (x4)	2	6	48
with $\rho = 2$ mm	1 (x4)	2	6	48
with $\rho = 4$ mm	1 (x4)	2	6	48
with $\rho = 7$ mm	1 (x4)	2	6	48
with $\rho = 10$ mm	1 (x4)	2	6	48
with $\rho = 15$ mm	1 (x4)	2	6	48
Thermal expansion measurements				**290**
with digital comparator	4	12	3/4	150
with strain gauges	4	10	3/4	140
Petrographic characterization				**158**
with $\rho = 0.5$ mm	4	2	6	48
with $\rho = 1$ mm	2	1	1	2
with $\rho = 2$ mm	4	1	3	12
with $\rho = 4$ mm	4	1	12	48
with $\rho = 7$ mm	4	1	3	12
with $\rho = 10$ mm	4	1	6	24
with $\rho = 15$ mm	4	1	3	12

*Repetitiveness: number of repeated tests for statistical validation.

3.1 TENSILE SPLITTING (BRAZILIAN) TESTS

As indicated in *Section 1.4.1.1* of Chapter II, despite being an indirect method, the Brazilian tests are one of the most widespread tensile tests among the scientific community due to the easy preparation of the specimens and the relatively low dispersion of the experimental results (Coviello et al., 2005).

A correct definition of the tensile strength (σ_u) is essential for a proper application of most failure criteria, and in particular, for the application of the TCD and the SED criterion used in this work. First, the critical distance (L), which is a key parameter for fracture assessments of any material according to the TCD, depends on the square of the tensile strength as indicated in *Equation (II-70)*. Likewise, the fracture criteria established by the PM and the LM of the TCD, defined in *Equation (II-66)* and *Equation (II-77)*, respectively, limit the maximum equivalent stress (at a certain point in the PM or averaged over a certain distance in the LM) to the ultimate tensile strength (σ_u) in the case of brittle and quasi-brittle materials like rocks. Similarly, in the case of the SED criterion, the critical strain energy density defined in *Equation (II-98)*, which establishes the fracture conditions, depends on the square of the tensile strength. Additionally, according to *Equation (II-108)* (for plane strain) and *Equation (II-109)* (for plane stress), the area over which the strain energy density is averaged also depends on the square of the tensile strength. This significant dependence of fracture criteria on the tensile strength is not surprising given the sensitivity of rocks to tensile loading conditions.

3.1.1 Sample preparation

The tested samples consist of disc-shaped specimens with a diameter (D) to thickness (t) relation of 2 ($D/t = 2$). Here, 64 mm diameter discs were used, with a thickness of 32 mm. *Figure III-15* shows some pictures of the preparation process of the disc specimens. Basically, long cores were drilled in the laboratory from the supplied rock blocks and cut into slices according to the required dimensions. The sample preparation procedure was exactly the same for those tested at room temperature and at higher temperatures up to 250ºC, each sample being preheated to the target temperature at least 48 hours before testing.

Figure III-15. Preparation of the specimens for the Brazilian tests.

The specific dimensions of each sample were individually measured and visually checked and, in the case of having any appreciable weak plane, the sample was discarded. It was observed that the exact diameter of all the discs varied between 63-64 mm, which has been considered for calculating the tensile strength of each sample.

Likewise, a specific code was assigned to each sample for a correct identification. This code consists of a four-component name that indicates the type of test, the material, the temperature and the number of repetition of the test, in such a way that, for example, "BT-M-T2(NC)-2" indicates the second (2) Brazilian test (BT) of the Macael marble (M) tested at 250ºC (T2) with no cooling before testing (NC). Aiming to identify the influence of the heating methodology, the Brazilian tests have been performed both at constant temperature conditions throughout the test duration (with no cooling, NC) and at room temperature after a thermal treatment (with cooling, WC).

Table III-9 summarises the possible variables considered for the identification code of the Brazilian samples. The material "C2" refers to the same Moleanos limestone (C) coming from a second delivery, for which same extra tests were performed to verify there were no significant differences on the results. In practice, (C2) and (C) are assumed to be the same material, since they have provided the same mechanical properties even though they were extracted from different blocks of the quarry.

Table III-9. Variables of the Brazilian specimen codes.

TEST	MATERIAL	TEMPERATURE		REPETITIVENESS
BT	F	23ºC (T1)		1 7
	C	70ºC (T3)	(NC)**	2 8
	C2*	110ºC (T5)		3 9
	M	150ºC (T4)		4 10
	I	200ºC (T6)	(WC)**	5 11
		250ºC (T2)		6 12

*Moleanos limestone from a second delivery.

** NC (No Cooling) or WC (With Cooling).

3.1.2 Test procedure

The Brazilian tests were performed according to the suggested methods by the ISRM (1978), which are consistent with those stablished by ASTM D3967:2008b. The disc-shape specimens are diametrically compressed by means of curves platens in this case. As reported by Colback (1966) and considering a modified Griffith's fracture theory that takes into account the friction in compressed cracks (McClintock and Walsh, 1962), the distributed contact forces of the curved platens will trigger an extension fracture anywhere in the central third of the disc. By contrast, in the case of the concentrated loads, the fracture would first occur at the disc-platen contact, which can produce misleading results.

The tensile strength (σ_u) can be directly calculated with the following formulation:

$$\sigma_u = \frac{2 \cdot F}{\pi \cdot D \cdot t} \qquad \textit{(III-1)}$$

where F is the failure load, and D and t are the diameter and the thickness of each specimen, respectively.

The experimental configuration of the performed Brazilian tests is depicted in *Figure III-16*, in which P refers to the applied load. The test is performed under displacement control and the load is measured with a pressure cell. As established in the standards (ASTM D3967:2008b), the loading rate was 2.5 mm/min, which ensures reaching failure

between 30 and 60 seconds from the beginning of the test. Besides, the loading shaft is provided with a spherical joint for a correct adjustment of the curved platen on the specimen while guaranteeing that the loading axis remains centred.

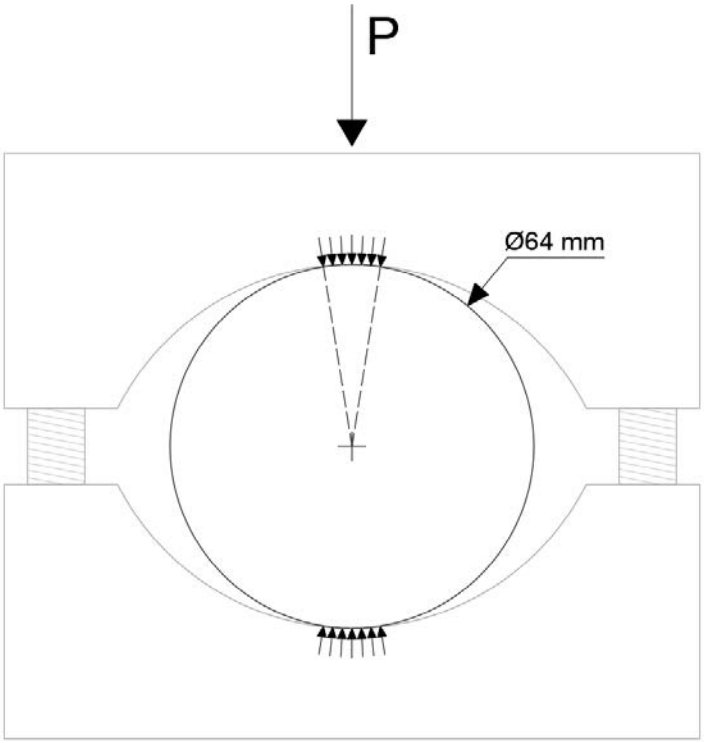

Figure III-16. Schematic representation of the performed Brazilian tests using curved platens.

The followed experimental procedure was the same for those tests performed at room temperature and those at higher temperatures up to 250ºC. Six different temperatures have been considered in this analysis: 23, 70, 110, 150, 200 and 250ºC. As indicated above, approximately half of the specimens were tested at the target temperature under constant temperature conditions, inside an oven adapted to the hydraulic press (*Figure III-17*), while the other half were tested at room temperature after subjecting the specimens to a thermal cycle. *Figure III-17* shows some pictures of the experimental set-up both for room temperature and high temperature tests. In any case, all the specimens were preheated to the target temperature for at least 48 hours before testing, to ensure constant and homogeneous temperature within the sample according to Newton's heating law. The cooled samples were later left at least 24 hours at room temperature conditions before testing.

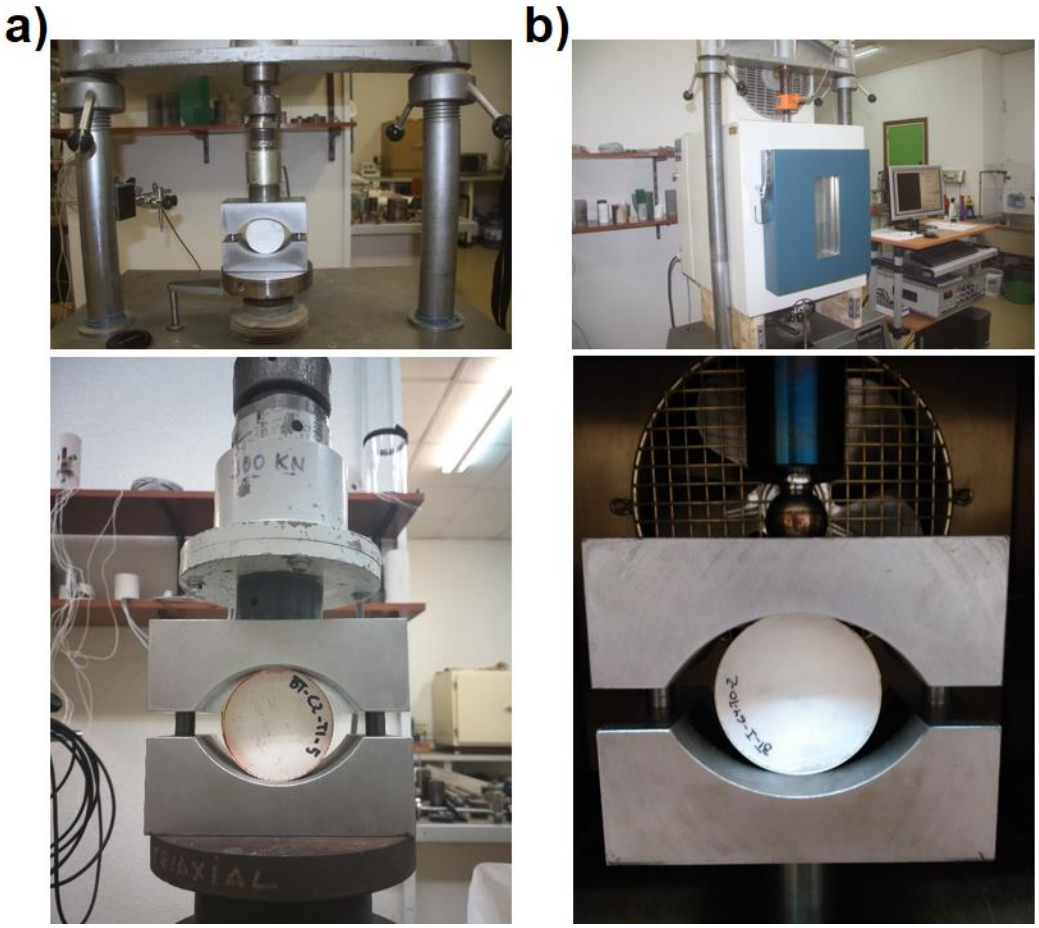

Figure III-17. Experimental set-up of the Brazilian tests performed (a) at room temperature and (b) at high temperatures inside an oven.

All the tested specimens were checked to fail as expected (i.e., along the vertical plane) before being considered valid tests. *Figure III-18* presents some representative specimens after failure, in which failure occurs in the vertical plane along specimen-platen contacts.

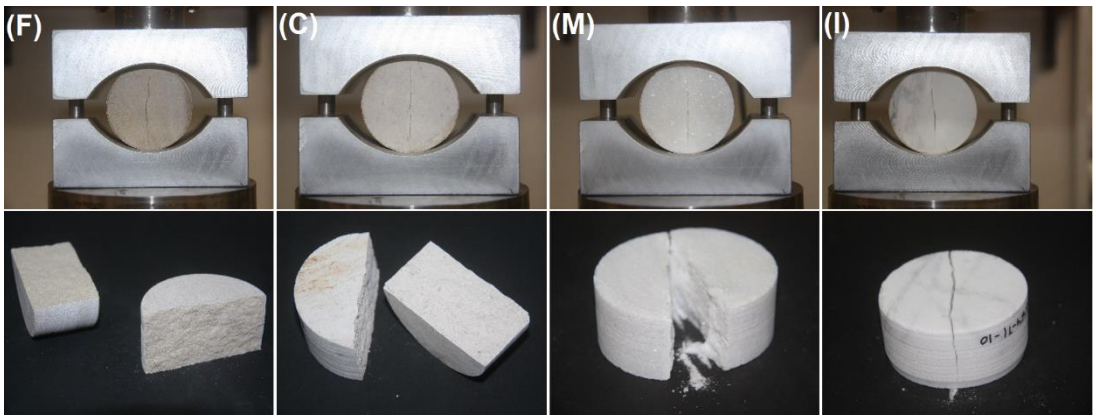

Figure III-18. Some representative Brazilian specimens after failure.

All in all, 300 Brazilian tests have been performed, six for each of the four selected rocks, temperature and testing condition (WC or NC) combinations, except for "T3(WC)" conditions and "C2" material (at room temperature), in which twelve tests have been perform instead for verification reasons. *Appendix A.1* gathers the individual Brazilian test results classified according to the aforementioned code criterion, which will be discussed in the next chapter.

3.2 UNIAXIAL COMPRESSION TESTS

Uniaxial compression tests allow to obtain, when performed with two-directional strain gauges, the deformational parameters (i.e., Young's modulus and Poisson's ratio) of the rock, as well as the uniaxial compressive strength (σ_c). The compressive strength of rocks has no direct influence on the studied fracture criteria as indicated in the TCD and SED criterion descriptions provided, respectively, in *Sections 2.7* and *2.8* of Chapter II. However, it is a widely used parameter in rock engineering designs and its importance for the characterization and classification of the rock is unquestionable. For this reason, uniaxial compressive strength will be analysed together with the rest of basic strength and deformational parameters of the rocks. By contrast, the Young's modulus (E) and Poisson's ratio (v) do have a significant influence on the performed rock fracture assessments when using the SED criterion. These parameters affect the elastic strain energy density (W_1) according to *Equation (II-101)*. The critical strain energy density (W_c) that defines the critical fracture condition is also dependent on the Young's modulus (*Equation (II-98)*), and the area over which the strain energy density is averaged also depends on the Poisson's ratio according to *Equation (II-108)* (for plane strain) and *Equation (II-109)* (for plane stress).

3.2.1 Sample preparation

Traditional uniaxial compression tests use cylindrical rock specimens with a length/diameter ratio between 2.5 and 3. Here, 50 mm diameter and 150 mm length rock specimens have been analysed, using two-directional strain gauges to measure deformations in the longitudinal and circumferential directions. These samples were also extracted from rock blocks like the Brazilian disc specimens although, in this case, a different core drill bit was used with an internal diameter of Ø50 mm

instead of Ø64 mm. Once the samples were extracted, the bottom and upper surfaces of the rock cylinders were polished to make them parallel and ensure a correct stress distribution throughout the rock sample during loading.

The installation procedure of the strain gauges in the rock samples is, in essence, the same for those rocks tested at room temperature and at higher temperatures up to 250ºC: Two facing two-directional strain gauges are placed on the specimen aligned with the directrix, one in front of the other, in such a way that longitudinal and circumferential deformations can be measured during loading. However, since the uniaxial compression tests are performed under constant temperature conditions inside an oven, the components that make up the strain measurement installation (i.e., the strain gauges themselves, the adhesive, the wires and the tin welds) must be able to withstand those temperatures at which tests are carried out. Consequently, certain differences are appreciable in the sample preparation procedure between those samples tested at room temperature and those tested inside the oven at moderate temperatures. These differences will be addressed subsequently while describing the followed strain gauge installation steps (see *Figure III-19*):

[1] Positioning: First, the location on the test specimens where the strain gauges are to be bonded must be determined. Each cylindrical rock sample is instrumented with two opposite two-directional strain gauges (two-element Rosettes), which are located roughly at half height of the specimens. For determining the final position of the strain gauges, it must be considered that the electrical resistors should cover at least 10 grains of the rock and an appropriate surface contact must be ensured. Thus, external pores or macro-grains (e.g., intraclasts in the case of the Moleanos limestone) should be avoided.

[2] Surface preparation: Before bonding, all grease, rust, paint, etc., must be removed from the bonding area to provide a clean and soft surface for an adequate contact and adherence between rock and gauge. To do so, an area somewhat larger than the bonding area has been uniformly abraded using abrasive paper. In the case of porous rocks like the Floresta

sandstone, prior to polishing and cleaning, the surface is covered with a thin film of epoxy resin to fill the external pores. The polishing must then ensure that resin is only acting as a filler for the surface pores while removing the resin surplus. Otherwise, placing the gauge directly on a resin surface and not on the rock surface could lead to inaccurate strain readings. The epoxy resin has only been applied to the Floresta sandstone samples tested at room temperature. For those sandstone specimens tested at higher temperatures the external porosity is filled with several layers of the used adhesive as indicated below.

[3] Fine cleaning: The abraded surface is cleaned with a cloth soaked in a small quantity of chemical solvent such as ethanol, leaving the surface completely free of contamination.

[4] Applying bonding adhesive: Before the prepared surface becomes newly contaminated, the strain gauges are bonded onto the rock surface with special adhesives. Different adhesives have been applied depending on the temperature conditions to which the gauges will be subjected, according to the manufacturer specifications. Firstly, for those samples tested at 23ºC, CN-E adhesive was used (supplied by Tokyo Measuring Instrument Lab. company, TML), which is a single-component (Cyanoacrylate) adhesive featuring high viscosity for bonding strain gauges to porous materials such as concrete and rocks and with a curing time under room temperature conditions of around 40-120 seconds. Secondly, for those tests performed at 70ºC, the Z-70 adhesive was used (supplied by Hottinger Baldwin Messtechnik, HBM), which is a cold curing low viscosity Cyanoacrylate adhesive appropriate for temperatures up to, approximately, 100ºC and with a curing time of around 60 seconds. Finally, those strain gauges subjected to 150ºC and 250ºC were bonded with EP310N (supplied by HBM), which is a low porosity two-component epoxy resin adhesive appropriate for temperatures up to 260ºC. In this case, the curing time depends on the curing temperature, oscillating from 6 hours to 30 minutes. In any case, the adhesive is applied onto the back of the gauge base

and over the surface of the rock sample, ensuring the whole gauge surface is completely bonded. In order to ensure a full bonding of the strain gauges, the external porosity of the Floresta sandstone samples was filled with epoxy resin for those tests performed at 23ºC. However, for the rest of tests performed at higher temperatures, the adhesive specifications suggest covering the rock surface with two or three adhesive layers with a five-minute interval in between.

[5] Curing and pressing: After applying the adhesive, the strain gauges are placed on their position, ensuring the correct alignment of the electrical resistors. A piece of polyethylene sheet is placed directly onto it and pressure is applied to ensure a proper contact and to avoid the appearance of air bubbles. The pressure is uniformly applied throughout the curing time. When using CN-E and Z-70 adhesives for tests performed at 23ºC and 70ºC, respectively, it is enough with the thumb pressure (*Figure III-20*). This process must be done quickly, as the curing process is relatively fast. However, EP310N requires more time and a pressure of 0.1-0.5 MPa while curing inside an oven. For this reason, the pressure was applied in this case by means of metallic clamps that were specifically manufactured with this purpose (*Figure III-20*). The specimens were cured at the target testing temperature in all the cases. Accordingly, the curing time of those samples cured and tested at 150ºC was 3 hours, while it was only 30 minutes for those at 250ºC. For all these latter samples cured inside the oven, the heating and cooling rate was slow enough to avoid thermal sock and the appearance of bubbles.

[6] Gauge leads preparation: After the adhesive has been perfectly cured, the gauge leads (if any) must be raised and cleaned from adhesive surplus to ensure a correct electrical transmission when soldering. The used strain gauge types will be described below, but basically, those used at room temperature include gauge leads to be connected to terminals, while in those strain gauges used at higher temperatures the leadwires are directly welded to gauges, without using gauge leads and terminals.

[7] Bonding connecting terminals: As mentioned in the previous step, this has been only done for those cases corresponding to room temperature tests. The terminals were bonded close to the gauge base (so that gauge leads could be connected), proceeding along the same way as for the gauges (CN-E was used again).

[8] Welding the gauge leads: The gauge leads are welded to the terminals with tin, taking care to prevent excessive tension of the gauge leads.

[9] Welding leadwires: Finally, leadwires are connected to the previously located terminals in the case of the samples tested at 23ºC, and directly to the strain gauges in the rest of cases. The used leadwires in the first case consist of traditional wires while, for those tests at higher temperatures, special wires with fluoropolymer insulation were used. Likewise, traditional tin was used for those tests at room temperature but, for higher temperature conditions, special tin with high lead content was needed.

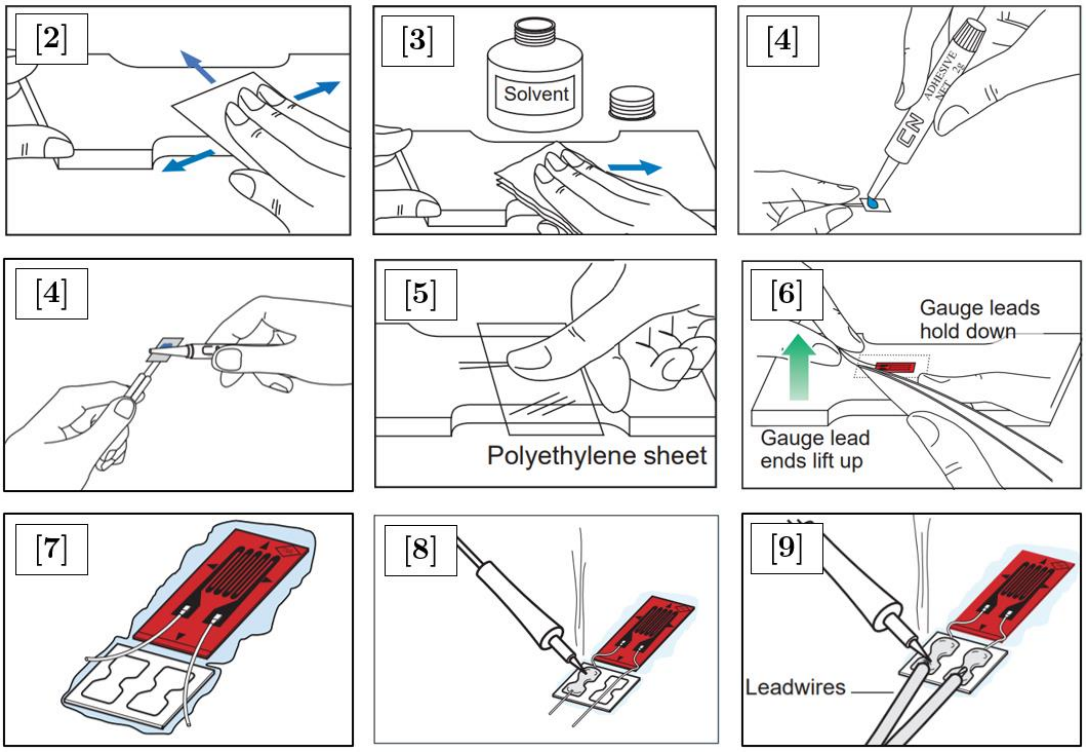

Figure III-19. Illustration of the basic strain gauge installation steps (TML Manual, 2017).

Figure III-20a and *Figure III-20b* show, respectively, some images of the strain gauge installation process for those tests performed at room temperature and at higher temperatures up to 250ºC. As observed, apart from the differences indicated above dealing with the bonding characteristics, different strain gauge typology has been used depending on the temperature conditions to which they will be subjected.

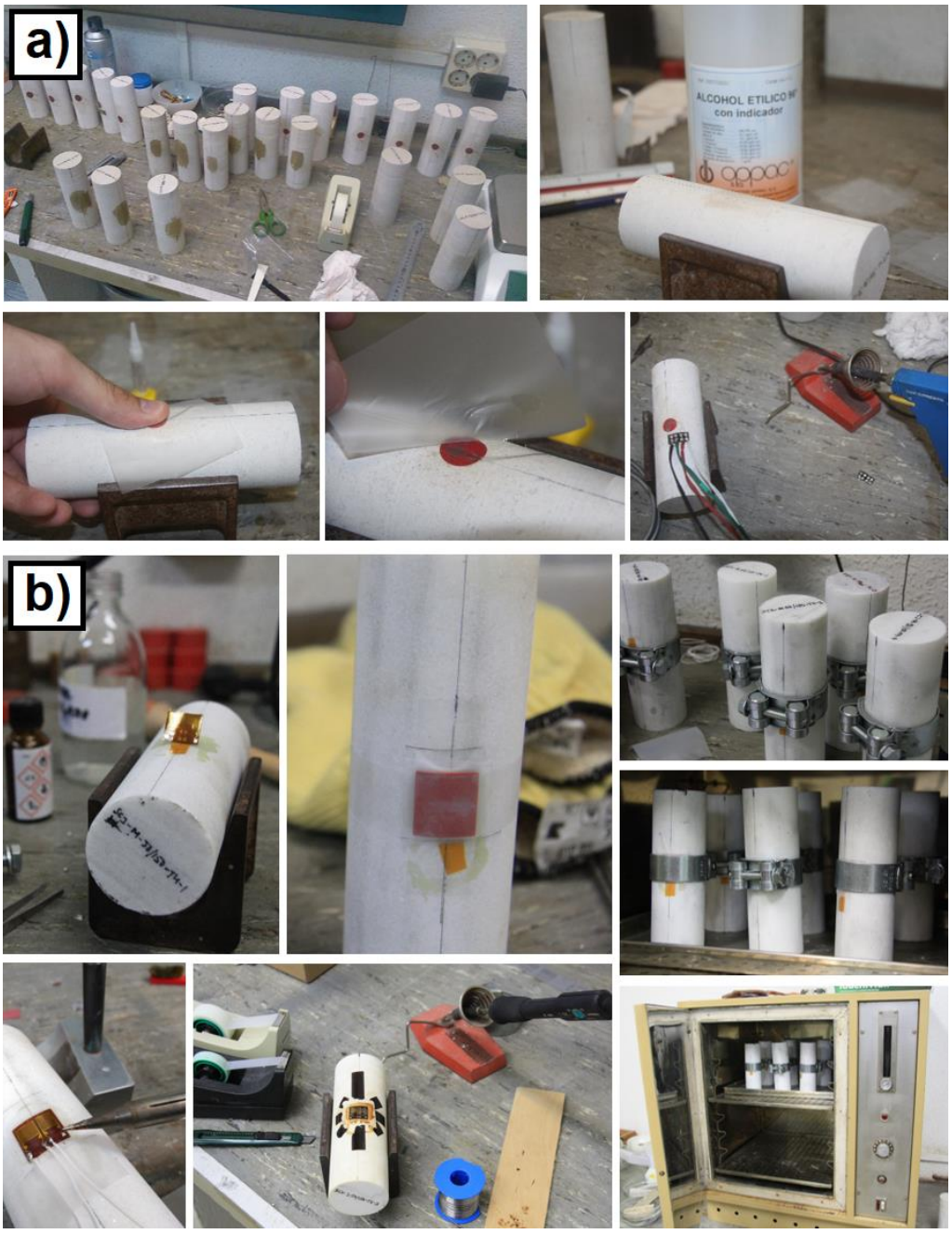

Figure III-20. Strain gauge installation process on the cylindrical rock specimens for the uniaxial compression tests performed at (a) 23ºC and (b) 70, 150 and 250ºC.

Numerous strain gauge typologies can be found on the market. Among them, FCA-6-11 and FCA-10-11 (from TML in Japan) have been used for room temperature uniaxial compression tests and TM11-6 (from HBM in Germany) for high temperature uniaxial compression tests (see *Figure III-21*). Although gauge nomenclature is different for each company, both types of strain gauges are equivalent. The terms FCA and TM refer to "T" rosettes with two-directional (offset by 90º) measurement grids, the number 11 indicates, in all the cases, the self-temperature compensation number and 6 and 10 stand for the gauge length in millimetres. The only difference is that FCA strain gauges use stacked electrical resistors (i.e., measure both strains at a single point), while TM strain gauges measure perpendicular strains at two adjacent points. However, based on the relatively homogeneous materials selected for the research, this issue is expected not to have any important influence on the results.

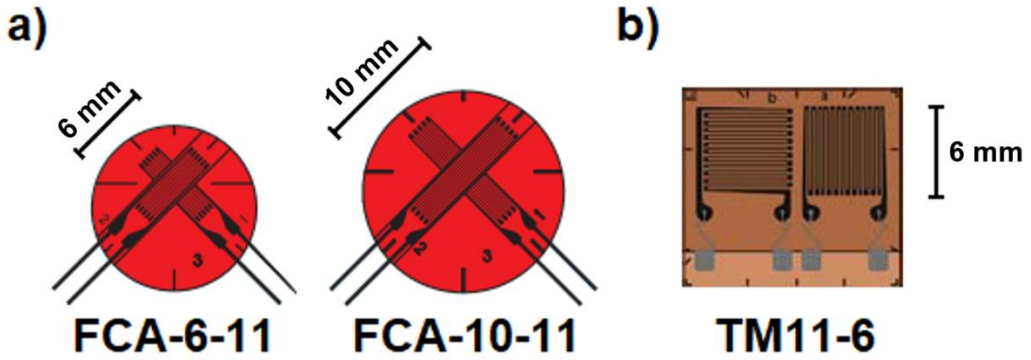

Figure III-21. Schemes of the strain gauge typologies used in the uniaxial compression tests at (a) 23ºC and (b) 70, 150 and 250ºC.

In order to obtain representative strain readings, gauge length must be at least 10 times larger than the mean grain size. Therefore, 6 mm length strain gauges should be enough but, for verification purposes, in those compression tests performed at room temperature, six samples were tested with FCA-6-11 strain gauges and another six samples with FCA-10-11 strain gauges. No appreciable differences were observed on the displacement readings between those with a gauge length of 6 mm and those with 10 mm. Consequently, 6 mm length strain gauges were used also for the rest of the specimens.

As a summary, *Table III-10* gathers some characteristics of the employed strain gauges, as well as the indication of the used adhesive for each case according to what it was described above in the description of the strain gauge bonding process.

Table III-10. Summary data on the used strain gauges.

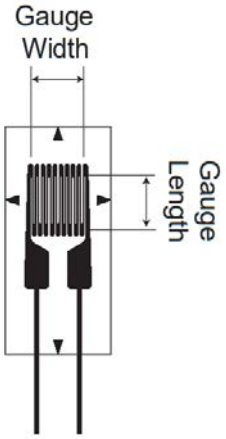

	FCA-6-11	FCA-10-11	TM11-6
Length (mm)	6	10	6
Width (mm)	2.4	2.5	6.3
Resist. (Ω)	120	120	350
Lead wires	Yes	Yes	No
Adhesive 23ºC	CN-E	CN-E	-
Adhesive 70ºC	-	-	Z-70
Adhesive 150ºC	-	-	EP310N
Adhesive 250ºC	-	-	EP310N

As in the case of the Brazilian tests, a specific code was assigned to each specimen for a correct identification. Once again, this code consists of a four-component name that indicates the type of test, the material, the temperature and the repeated number of the test, in such a way that, for example, "UCT-I-T2-4" indicates the fourth (4) uniaxial compression test (UCT) of the Carrara marble (I) tested at 250ºC (T2). In this case, all the tests have been performed under constant temperature conditions at the target temperature, with no cooling before testing. *Table III-11* summarises the possible variables considered for the identification code of the uniaxial compression samples.

Table III-11. Variables of the uniaxial compression specimen codes.

TEST	MATERIAL	TEMPERATURE	REPETITIVENESS
UCT	F	23ºC (T1)	1 7
	C	70ºC (T3)	2 8
	M	150ºC (T4)	3 9
	I	250ºC (T2)	4 10
			5 11
			6 12

3.2.2 Test procedure

The uniaxial compression tests were performed according to the European standards EN 1926:2007 and EN 14580:2006, which define, respectively, how to determine the uniaxial compressive strength, the static elastic modulus and the Poisson's ratio. The cylindrical specimens are uniaxially compressed, generating a theoretically uniform compressive stress along the specimen section. Thus, the compressive strength (σ_c) is a direct output of the test, calculated as the ratio between failure load (F) and the cross section of the specimen:

$$\sigma_c = \frac{F}{\pi \cdot D^2/4} \qquad \textit{(III-2)}$$

where D is the diameter of the specimen. The experimental configuration of the performed uniaxial compression tests is depicted in *Figure III-22*, in which P refers to the applied load. The tests were performed under displacement control with a loading rate of 0.1 mm/min, and the load was measured with a pressure cell.

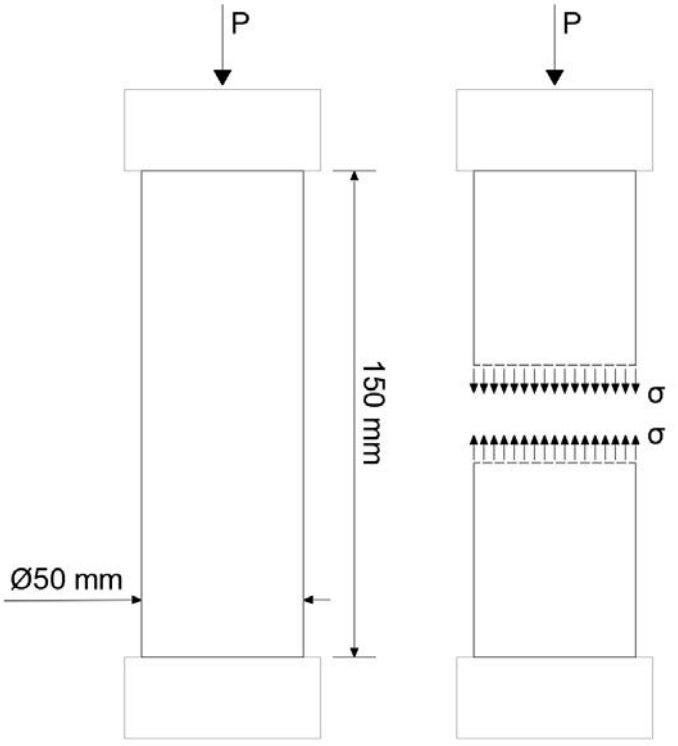

Figure III-22. Schematic representation of the performed uniaxial compression tests.

On the other hand, deformations in the longitudinal and diametric directions were measured by means of strain gauges forming a Wheatstone bridge circuit. It is widely known that strain gauges transform the strains (ε) caused by external loading into a proportional change of electrical resistance (TML Manual, 2017):

$$\varepsilon = \frac{\Delta L_{sg}}{L_{sg}} = \frac{\Delta R_i / R_i}{K_g} \qquad \textit{(III-3)}$$

where ΔL_{sg} is the change in length due to the applied force, L_{sg} is the original length of the strain gauge, ΔR_i is the resistance change of the gauge due to the strain change, R_i is the gauge resistance and K_g is a gauge factor. Normally, this resistance change is very small and requires a Wheatstone bridge circuit (as that represented in *Figure III-23*) to convert the small resistance change to a more easily measured voltage change.

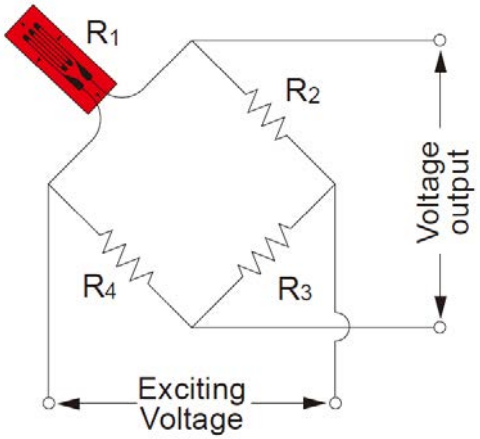

Figure III-23. Schematic representation of the Wheatstone bridge (TML Manual, 2017).

The voltage output (e_o) of the circuit is given as follows:

$$e_o = \frac{R_1 R_3 - R_2 R_4}{(R_1 + R_2)(R_3 + R_4)} \cdot E_e \qquad \textit{(III-4)}$$

where E_e is the exciting voltage and R_i are the gauge resistances, R_3 and R_4 being fixed resistances.

Starting with $R_i = R_1 = R_2 = R_3 = R_4$, the resistance of the active strain gauge changes to $R_i + \Delta R_i$ due to strain. Thus, the output voltage variation (Δe_o) due to strain is given as follows:

$$\Delta e_o = \frac{\Delta R_i}{4R_i + 2\Delta R_i} \cdot E_e \qquad \textit{(III-5)}$$

When $\Delta R_i \ll R_i$,

$$\Delta e_o = \frac{\Delta R_i}{4R_i} \cdot E_e = \frac{E_e}{4} K_g \varepsilon \qquad \textit{(III-6)}$$

Thus, the strain is measured by applying an exciting voltage and reading the output voltage variation due to gauge strains.

With all this, the Wheatstone bridge provides a useful system to obtain accurate measurements of an unknown electrical resistance (and therefore strain) by balancing two legs of a bridge circuit, one leg of which includes the unknown component. Another important advantage is that it allows to compensate thermally induced deformations so that the obtained strain readings refer to those generated by the applied load. In practice, this is done by using a compensation sample, which will be subjected to the same temperature conditions as the tested sample but without any load, as those observed in *Figure III-24*.

Figure III-24 shows some pictures of the experimental set-up of the uniaxial compression tests performed both at room temperature and at high temperatures inside the oven. The testing procedure is exactly the same in both cases, although the used components (i.e., strain gauges, adhesive, wires and welding tin) are different as indicated in *Section 3.2.1.* All the specimens were preheated to the target temperature for at least 48 hours before testing, to ensure constant and homogeneous temperature conditions during the tests. In this case, four different temperatures were studied: 23, 70, 150, and 250ºC. At room temperature, 12 uniaxial compression tests were performed for each rock, while for the rest of temperatures, 6 tests were carried out. Thus, in total, 120 uniaxial compression tests have been performed for this study. *Appendix A.2* gathers the individual uniaxial compression test results

classified according to the aforementioned code criterion, which are analysed in Chapter IV.

Figure III-24. Experimental set-up of the uniaxial compression tests performed at room temperature and at high temperatures inside the oven.

It should be noted that uniaxial compression tests with strain measurements at high temperatures are not conventional tests. Apart from the added complexity of sample preparation, the associated cost of each test is approximately 4-5 times more expensive in those tests performed under high temperature conditions.

Finally, *Figure III-25* presents some uniaxial compression tests after failure. All samples were checked before and after testing in order to discard any possible premature failure as a consequence of weak planes, which was not the case in any of the tests given the material selection.

Figure III-25. Some uniaxial compression specimens after failure.

3.3 FOUR-POINT BENDING TESTS

In order to get a wide fracture database of the studied rocks for the successive fracture analyses, several four-point bending tests have been performed with different U-shaped notch radii and under different temperature conditions. This data is then interpreted by means of the proposed fracture criteria (i.e., TCD and SED criterion) based on the use of the apparent fracture toughness (K_{IN}).

3.3.1 Sample preparation

The used samples consist of parallelepiped 180x30x30 mm size SENB specimens with a U-shaped notch in the middle with a variable radius: 0.15, 0.5, 1, 2, 4, 7, 10 and 15 mm. Besides, the relative notch length (α_0), defined as the ratio between the initial notch length (a_0) and the total height of the specimen (h), has been set to 0.5. Consequently, the largest notch radius is conditioned by the height of the specimen, which, in order to maintain the relative notch length equal in all the samples, cannot be greater than 15 mm.

The samples were externally manufactured with the specified geometry. The quarry rock blocks were cut into slices and, eventually, into prismatic samples using abrasive discs. Then, the sample faces were polished to guarantee parallel surfaces and ensure an adequate geometry precision. Those notches with a radius larger than 1 mm were

manufactured using abrasive discs with semi-circular contour, and the smallest radii, those with 0.15 and 0.5 mm, were produced using rotating diamond wires. In any case, both methods provide U-shaped notches. *Figure III-26* shows some pictures of the preparation process of the SENB specimens used in the four-point bending (and also three-point bending) tests.

Figure III-26. Preparation of specimens for four-point bending and three-point bending tests.

Each specimen dimensions were individually measured and they were visually checked in order to discard any possible sample with weak planes or defects, as well as to identify the real geometry of the samples and notches. The small variations in the relative notch lengths with respect to the theoretical value ($\alpha_0 = 0.5$) as a consequence of the precision of the cutting process were also measured and high confinement conditions were guaranteed in all the samples ($0.45 \leq \alpha_0 \leq 0.55$). As in the case of the Brazilian and the uniaxial compression test samples, all the SENB specimens were also preheated to the target temperature for at least 48 hours before testing.

Figure III-27 shows, as an example, a picture of the SENB specimens (with the studied eight different notch radii) employed in the four-point bending tests.

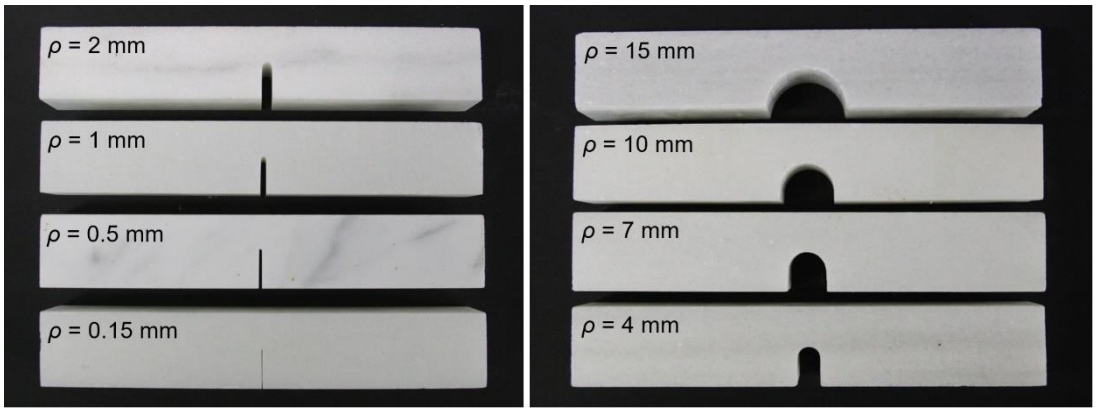

Figure III-27. SENB samples with different notch radii.

A specific five-component code was assigned to each specimen for individual identification, which indicates the type of test, the material, the notch radius (ρ), the temperature and the repeated number of the test, in such a way that, for example, "4PBT-C-015-T3-6" indicates the sixth (6) four-point bending test (4PBT) of the Moleanos limestone (C), with a notch radius of 0.15 mm (015), tested at 70ºC (T3). All the four-point bending tests have been performed under constant temperature conditions at the target temperature (inside an oven), with no cooling before testing. *Table III-12* summarises the possible variables considered for the identification code of the four-point bending test samples.

Table III-12. Variables of the SENB specimen codes for four-point bending tests.

TEST	MATERIAL	ρ (mm)	TEMP.	REPETITIVENESS
4PBT	F	0.15	23ºC (T1)	1 7
	C	0.5	70ºC (T3)	2 8
	M	1	150ºC (T4)	3 9
	I	2	250ºC (T2)	4 10
		4		5 11
		7		6 12
		10		
		15		

3.3.2 Test procedure

The four-point bending tests were carried out according to the European standards (CEN/TS 14425-1:2003 and EN 13161:2008), which define how to determine the flexural strength (and fracture toughness) under the constant moment generated by four-point bending loading conditions (see *Section 2.5.1* in Chapter II). This methodology was first proposed by Srawley & Gross (1976) for ceramic materials, who employed SENB specimens as those used in this work and represented in *Figure III-28*. This configuration ensures constant bending moment and no shear forces between the inner loading points, which guarantees mode I loading conditions. The supporting rollers allow rotation and lateral tilting, which minimise friction between them and the rock surface and reduce possible torsion effects that may arise when opposite faces are not perfectly parallel. Although rolling supports would be desirable according to Ayatollahi et al. (2019) and Bahrami et al. (2020), friction effects between supports and specimens are considered to have a minor influence in this case because of the distance between supporting rollers (namely, 150 mm) and the small displacements prior to failure. Besides, the upper head of the testing device was provided with a spherical joint that allows a greater degree of movement and adjustment, while ensuring that the axis of load application always remains centred.

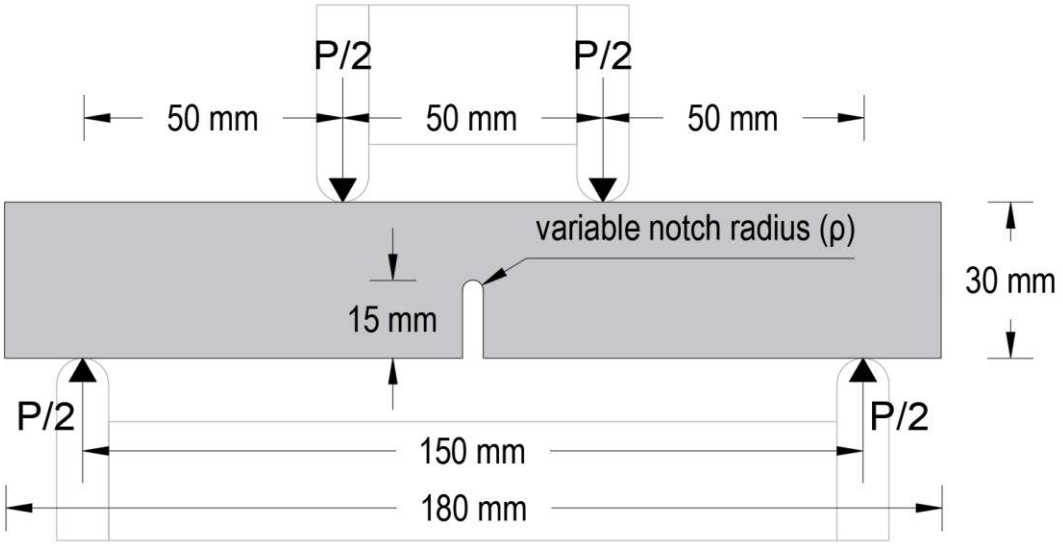

Figure III-28. Schematic representation of the performed four-point bending tests.

Those specimens with the smallest notch radii (i.e., $\rho = 0.15$ mm) are assumed to behave as crack-type defects. Under this hypothesis, the fracture toughness (K_{IC}) for SENB specimens subjected to four-point bending conditions can be calculated with the following formulation initially developed and defined by Srawley & Gross (1976):

$$K_{IC} = \frac{F}{b \cdot \sqrt{h}} Y \qquad \textit{(III-7)}$$

where F is the failure load obtained during the test, b is the specimen thickness, h is the specimen height and Y is a non-dimensional factor that only depends on the geometry of the specimen (see *Equations (II-33)* and *(II-34)*). For the geometry depicted in *Figure III-28*, Y is equal to 10.162. However, for the calculation of the fracture toughness of each rock, the real geometry of the specimens has been considered instead of the theoretical geometry. *Appendix A.3* gathers the individual measurements and results. For the rest of analysed notch radii, which are considered at first instance as notch-type defects, the followed procedure is the same. Thus, *Equation (III-7)* can be rewritten in such a way that an apparent fracture toughness (K_{IN}) is obtained instead of the strictly true fracture toughness:

$$K_{IN} = \frac{F}{b \cdot \sqrt{h}} Y \qquad \textit{(III-8)}$$

The four-point bending tests were performed inside a heat chamber under displacement control with a loading rate of 0.05 mm/min till failure. Constant temperature conditions are guaranteed throughout the duration of the tests. The chamber is coupled to the press in such a way that the loads are transferred to the testing devices through two steel shafts crossing the chamber walls. Four different temperatures have been considered for these tests: 23, 70, 150 and 250ºC. In any case, the testing procedure is the same for all the tests regardless the considered temperature conditions. *Figure III-29* shows the experimental set-up of the performed four-point bending tests both at room temperature and at higher temperatures up to 250ºC inside the oven. Apart from load,

vertical displacement was also recorded in all the tests using a LVDT transducer.

Figure III-29. Experimental set-up of the four-point bending tests performed at room temperature and at high temperatures inside the oven.

Six four-point bending tests have been performed for each rock, temperature and notch radius combination (12 tests in some cases for verification purposes), which implies 792 four-point bending tests in total.

Figure III-30 shows some of the representative fractured specimens obtained from the four-point bending tests for each rock and notch radius. The particular samples shown in *Figure III-30* correspond to the tests performed at 150ºC, but no differences were observed in the trajectories or fracture patterns with temperature. Generally speaking, the cracking process starts at the notch tip and propagates vertically, as expected from pure mode I loading conditions.

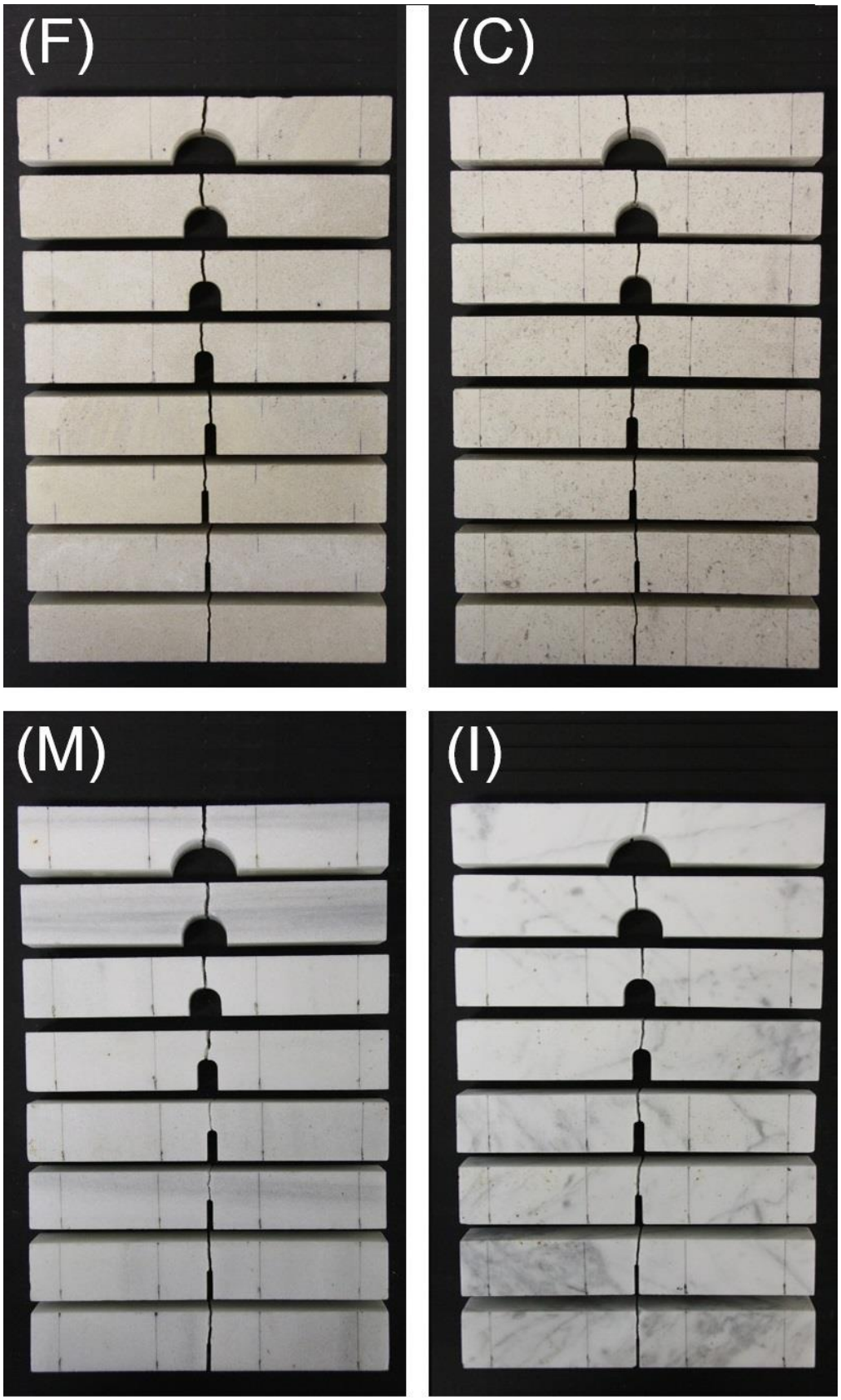

Figure III-30. Some representative fractured SENB specimens of each rock (with different notch radii) obtained from the four-point bending tests performed at 150ºC.

Finally, apart from the 792 four-point bending tests of notched rock samples, 90 extra four-point bending tests were performed without notches, in order to assess the tensile strength of rocks. The used specimens are also 180x30x30 mm size parallelepiped beams, manufactured the same way as those with notches indicated above. Accordingly to the performed Brazilian tests (*Section 3.1*), six temperatures were analysed: 23, 70, 110, 150, 200 and 250ºC, but in this case, the tests were only performed under constant temperature conditions with no cooling. Again, *Table III-13* summarises the possible variables considered for the identification code of the four-point bending tests with no notches.

Table III-13. Variables of the four-point bending (without notches) specimen codes.

TEST	MATERIAL	TEMPERATURE	REPETITIVENESS
4PBT	F	23ºC (T1)	1
	C	70ºC (T3)	2
	M	110ºC (T5)	3
	I	150ºC (T4)	4
		200ºC (T6)	
		250ºC (T2)	

The followed testing procedure was exactly the same as for those specimens with notches. For determining the tensile strength from non-notched samples subjected to four-point bending loading conditions, the European standards (EN 13161:2008) have been followed. For four-point bending tests where the loading span is 1/3 of the support span and for rectangular cross section, the tensile strength (σ_u) is defined as follows:

$$\sigma_u = \frac{F \cdot L_o}{b \cdot h^2} \qquad \textit{(III-9)}$$

where F is the failure load, L_o the span between the supporting rollers, and b and h are the depth and the height of the specimen, respectively. All the individual results can be found in *Appendix A.3* and are studied and interpreted in Chapter IV.

3.4 THREE-POINT BENDING TESTS

As an extension to the four-point bending (mode I) fracture tests, several three-point bending tests with a variable loading position have been performed in order to assess mixed mode I+II loading conditions. These tests were only carried out for the Moleanos limestone (C2), following the European standards (EN 12372:2006) that deal with the determination of the flexural strength under concentrated loads. The Moleanos limestone (C2) correspond to a second delivery but have demonstrated to be equivalent to those first supplied Moleanos limestone (C) specimens. Those three-point bending tests with the centred load are comparable to those performed under four-point bending conditions, as pure mode I loading is satisfied. However, those samples tested with the non-centred load, will develop shear forces (mixed mode I+II) while keeping predominant mode I loading conditions.

3.4.1 Sample preparation

Although the interpretation of the three-point bending test results differ from those of the four-point bending tests, the sample preparation process is the same (*Figure III-26*). *Figure III-31* presents a picture of the tested Moleanos limestone SENB samples, with the same dimensions and notch radii as those corresponding to the four-point bending tests.

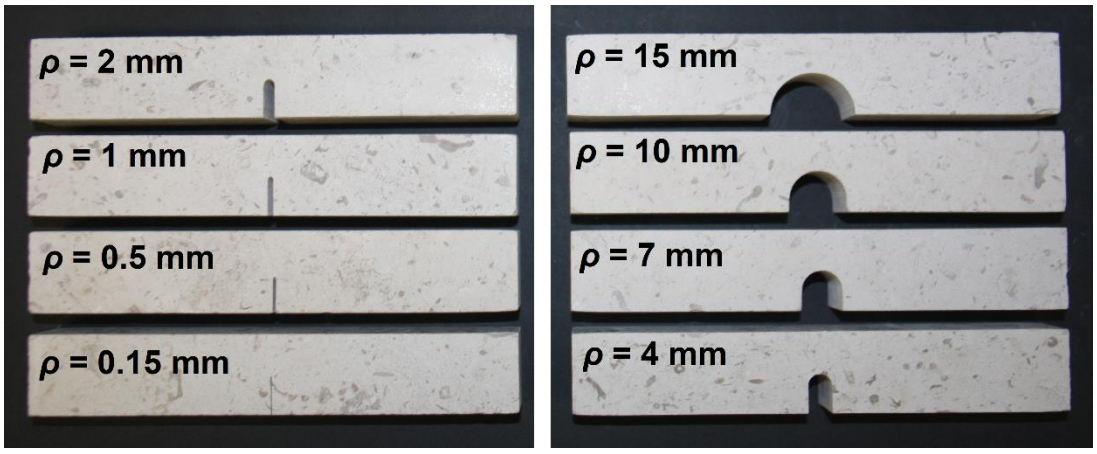

Figure III-31. SENB samples with different notch radii of the Moleanos limestone tested under three-point bending loading.

In this case, the used identification code consisted of a six-component name that indicates the type of test, the material, the notch radius (ρ),

the temperature, the loading position or distance from the notch bisector plane (m) and the repeated number of the test. For example, "3PBT-C2-7-T2-P3-6" indicates the sixth (6) three-point bending test (3PBT) of the Moleanos limestone (C2), with a notch radius of 7 mm (7), tested at 250ºC (T2) and with a loading position 8 mm away from the notch bisector plane (P3). *Table III-14* collects the possible variables considered for the identification code of the three-point bending test samples.

Table III-14. Variables of the SENB specimen codes for three-point bending tests.

TEST	MATERIAL	ρ (mm)	TEMP.	m (mm)	REPET.
3PBT	C2*	0.15	23ºC (T1)	0 (P1)	1
		0.5			2
		1		4 (P2)	3
		2	250ºC (T2)	8 (P3)	4
		4		12 (P4)	5
		7			6
		10			
		15			

*Moleanos limestone from a second delivery.

3.4.2 Test procedure

The followed three-point bending test procedure is based on the European standards EN 12372:2006. This procedure is in practice essentially the same as that of the four-point bending tests. The same SENB rock specimens and the same testing device used for the four-point bending tests is employed here, with the difference that, in this case, load is applied in a concentrated point. The loading position was varied in the tests for the assessment of mixed mode I+II loading conditions with predominant mode I influence. Four different loading positions were considered in the laboratory campaign, with a distance to the notch bisector plane (m) of 0, 4, 8 and 12 mm. Those tests with $m = 0$ provide pure mode I loading conditions. Thus, those results with the centred load are comparable to those of the four-point bending tests. However, as the loading position moves away from the bisector plane,

shear forces (mode II) get a higher influence. *Figure III-32* represents the three-point bending test configuration.

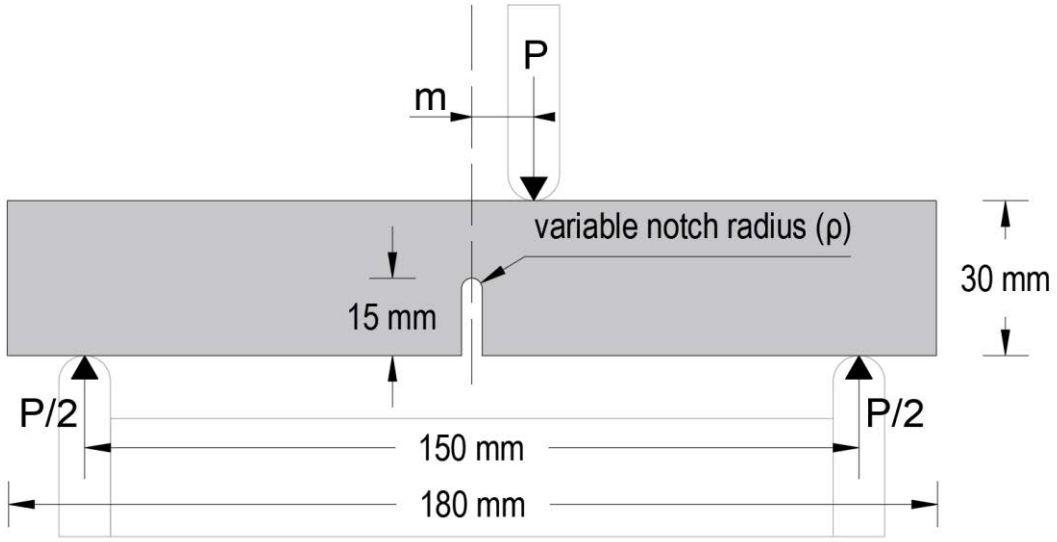

Figure III-32. Schematic representation of the performed three-point bending tests.

The experimental set-up shown in *Figure III-29* for the four-point bending tests can be extrapolated to these new tests. *Figure III-33* shows some pictures of the specific three-point bending device used in this case.

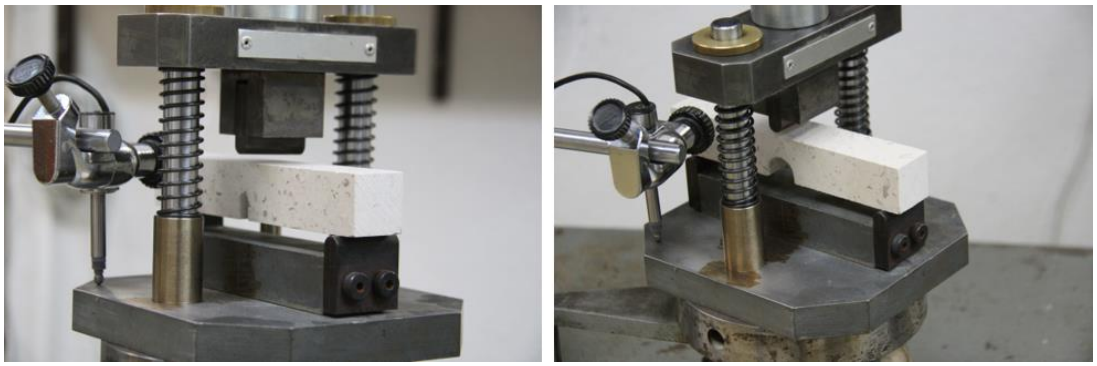

Figure III-33. Some pictures of the experimental set-up of the three-point bending tests.

Dealing first with centred load three-point bending tests and considering the same hypothesis as for the four-point bending tests, the smallest notches (i.e., $\rho = 0.15$ mm) are assumed to behave as crack-type defects, from which the fracture toughness (K_{IC}) is derived using

Equation (III-7). For the loading configuration depicted in *Figure III-32*, the parameter Y is calculated using *Equations (II-35)* and *(II-36)*, which were developed by Anderson (2005). For larger notches, the apparent fracture toughness (K_{IN}) is derived from the obtained failure loads (*Equation (III-8)*). On the other hand, due to the lack of analytical solutions for determining fracture toughness under mixed mode I+II loading conditions, the three-point bending tests with non-centred loads will be directly assessed through the application of the TCD and FEA in *Section 3* of Chapter IV.

With all this, 384 three-point bending tests have been performed in total, six per temperature, notch radius and loading position combination. In this case, two different temperature conditions were considered: 23ºC and 250ºC.

Additionally, taking advantage of the left over test specimens of the four-point bending tests, 11 extra three-point bending tests with a centred load were conducted on non-notched rock samples at room temperature, for determining the tensile strength of the four studied rocks and compare them with the four-point bending test and Brazilian test results. *Table III-15* summarises the variables considered for the identification code of the three-point bending tests with no notches.

Table III-15. Variables of the three-point bending (without notches) specimen codes.

TEST	MATERIAL	TEMPERATURE	REPETITIVENESS
3PBT	F	23ºC (T1)	1
	C		2
	M		3
	I		4

Analogously to *Equation (III-9)*, for the geometry depicted in *Figure III-32*, the tensile strength (σ_u) under three-point bending loading is calculated with the following expression:

$$\sigma_u = \frac{1.5 \cdot F \cdot L_o}{b \cdot h^2} \qquad \textit{(III-10)}$$

Again, F is the failure load, L_o the span between the supporting rollers, and b and h are the depth and the height of the specimen, respectively. All the individual results can be found in *Appendix A.4.* and are studied and interpreted in Chapter IV.

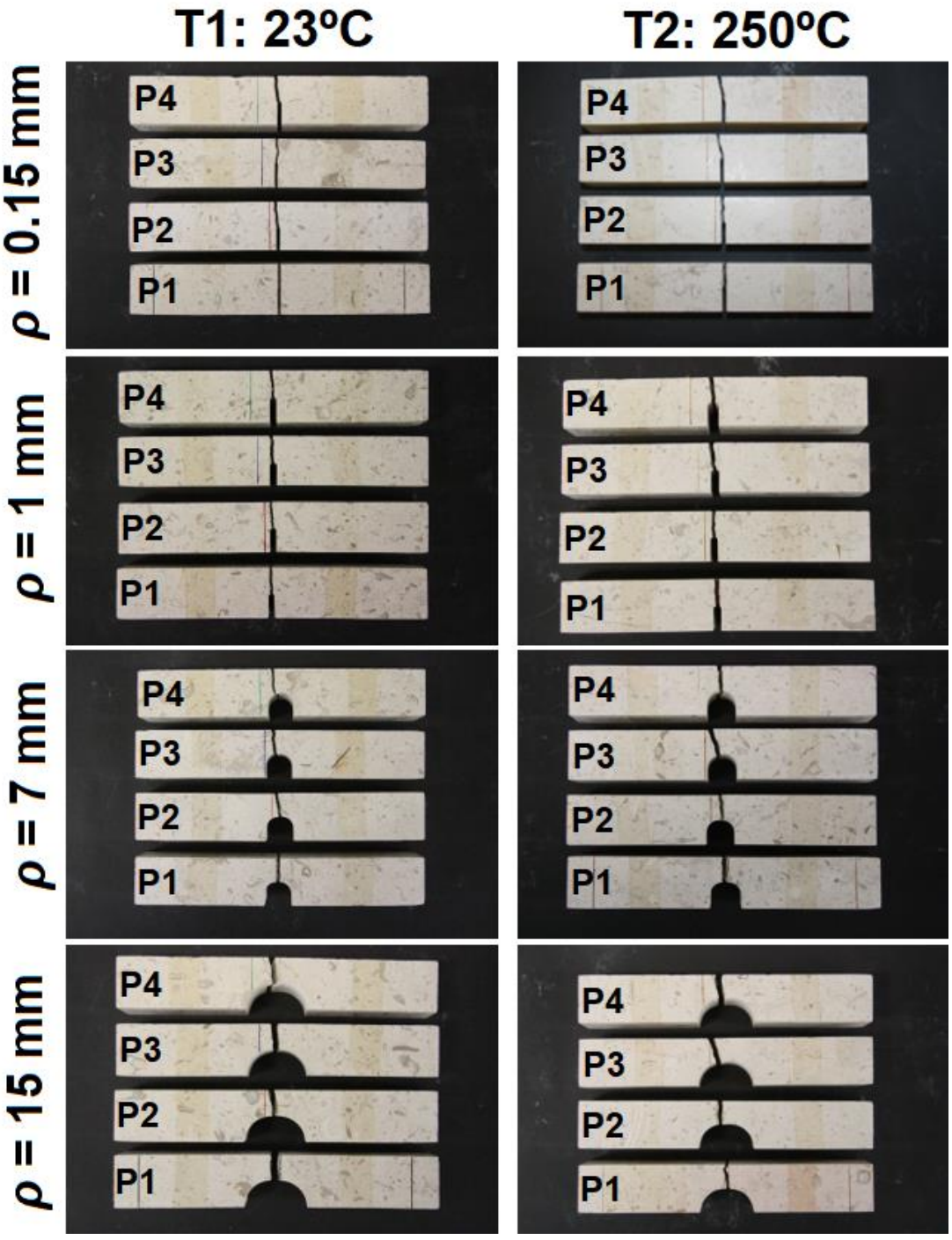

Figure III-34. Some representative fractured SENB specimens for each loading position and different notch radii, obtained from three-point bending tests at 23 and 250ºC.

Finally, *Figure III-34* provides some representative Moleanos limestone fractures specimens from the performed three-point bending tests, both at 23ºC and at 250ºC. As mode I is predominant in the studied loading configurations, the fracture planes are relatively vertical. However, it can be observed that fracture trajectories are somehow affected by the loading position. The fracture plane tends to incline as the loading position moves away from the notch bisector plane, or in other words, when mode II influence increases.

3.5 THERMAL EXPANSION TESTS

Although thermal expansion tests are not usual for rock characterisation, the thermal expansion curves of the four analysed rocks have been studied here in an attempt to distinguish different expansion patterns at the studied range of temperatures and to try to correlate tendencies with the variation of the mechanical rock properties with temperature. To do so, two different methodologies have been employed for thermal expansion measurements, namely by means of a digital comparator and by means of strain gauges.

3.5.1 Digital comparator

Firstly, thermal expansion was manually measured by means of digital comparator readings, with an accuracy of a hundredth of a millimetre. Parallelepiped 180x30x30 mm size rock samples without notches (as those used for determining the tensile strength through four- and three-point bending test) were employed. These samples were subjected to 10 progressive temperature steps up to 250ºC, in each of which the relative elongation with respect to the initial length of the sample was measured with the digital comparator. The readings were taken at five pre-marked points of the upper surface (*Figure III-35*) after staying 1 hour at the target temperature. These measurements were taken outside the oven, assuming a sufficiently fast reading procedure to avoid thermal recovery. *Figure III-35* shows some images of the digital comparator expansion measurements on a Moleanos limestone specimen. The position of the digital comparator was fixed and the surface over which the sample was located was completely flat to avoid misreadings. Likewise, the reading points (see *Figure III-35*) at which elongation was assessed were marked and named to ensure that relative measurements were always compared at the same points.

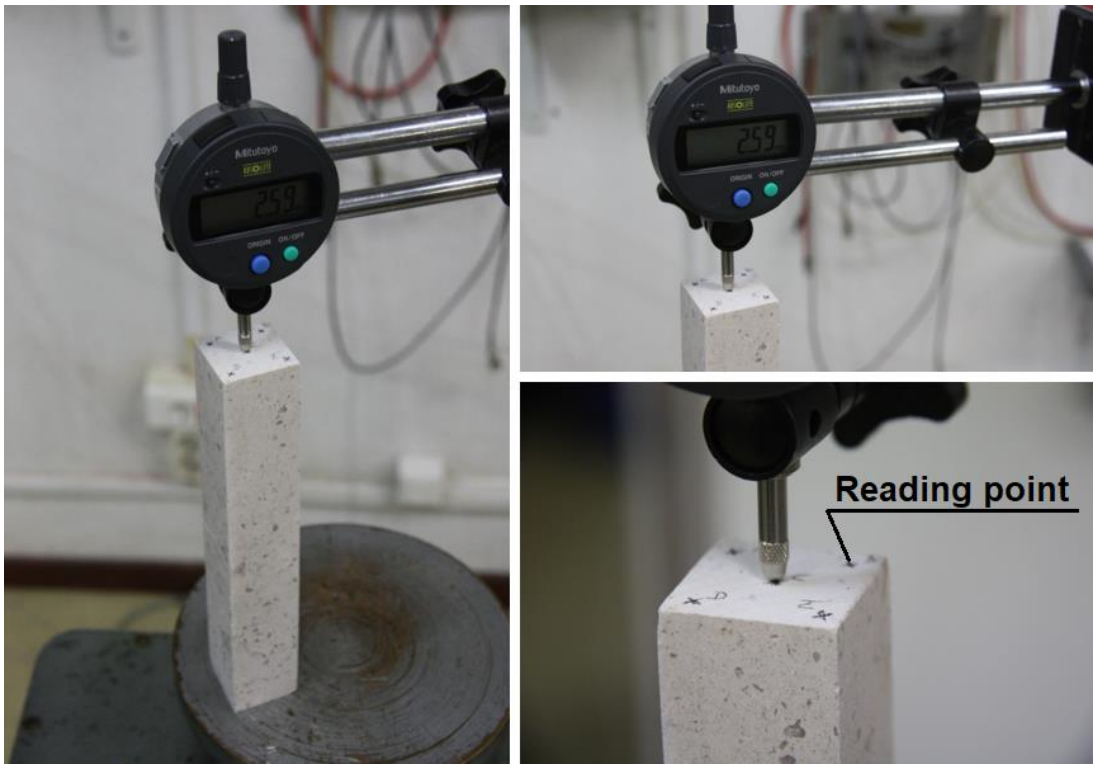

Figure III-35. Digital comparator expansion measurements.

The obtained thermal expansion measurements are collected in *Appendix A.5* and analysed in Chapter IV. Each reading is named after a code based on the variables collected in *Table III-16*. For example, "DCM-C-40-2-3" refers to the digital comparator measurement (DCM) of the second (2) Moleanos limestone (C) sample, at 40ºC (40) and corresponding to the marked point number 3 (3).

Table III-16. Variables of the digital comparator expansion measurement codes.

TEST	MATERIAL	TEMPERATURE	REPET.	POINT
DCM	F	23ºC 130ºC	1	1
	C	40ºC 150ºC	2	2
	M	50ºC 175ºC	3	3
	I	90ºC 225ºC	4	4
		110ºC 250ºC		5

3.5.2 Strain gauges

Secondly, as an alternative to the digital comparator expansion measurements, the longitudinal and diametric deformation of 50 mm diameter and 150 mm long cylindrical rock samples (as those used in uniaxial compression tests) were measured using strain gauges. The strain was measured by strain gauges exactly the same way as described in *Section 3.2.2* for determining stress-strain curves of uniaxial compression tests. However, in order to build the Wheatstone bridges with the strain gauges, a piece of Invar36 was used as the compensation sample instead of a rock sample (see *Figure III-36*). Invar36 is a nickel-iron alloy that exhibits an almost zero rate of thermal expansion (~10^{-6} mm/mm/ºC) from cryogenic temperatures to approximately 260ºC, which makes it suitable for this analysis. In this case, rock samples were not subjected to any loading during the duration of the tests. Strain readings were recorded as temperature was increased from room temperature up to 250ºC, considering 10 different temperature steps. At each temperature step, the specimen was left for 1 hour to ensure constant temperature conditions within the rock specimens.

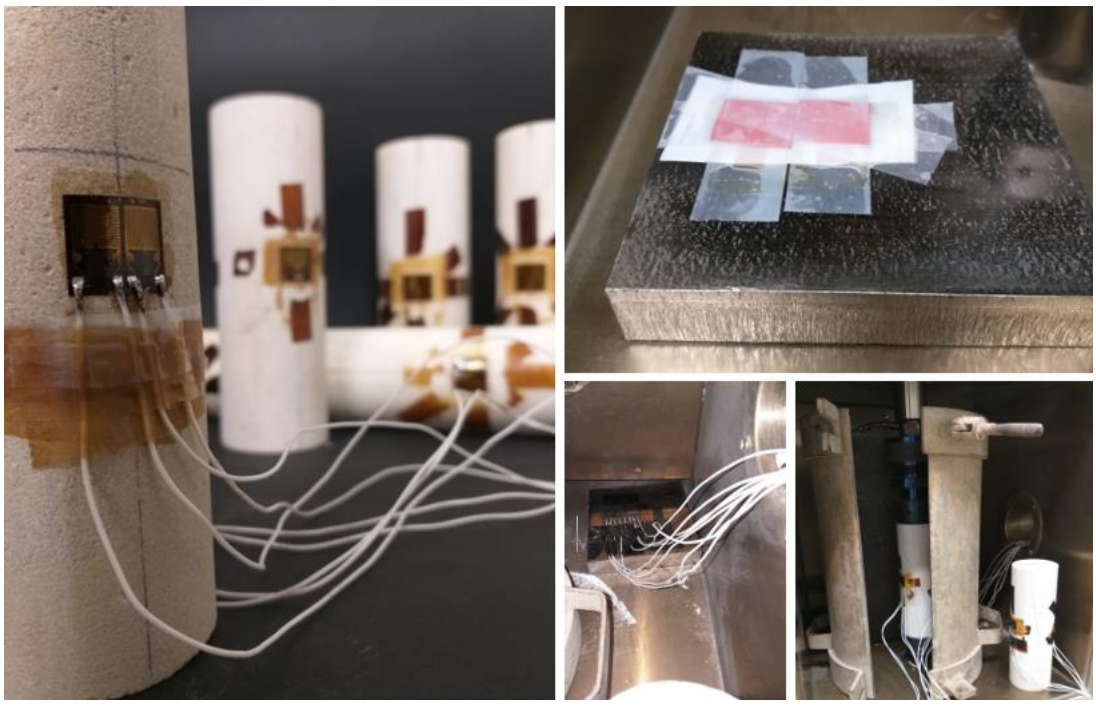

Figure III-36. Strain gauge expansion measurements (using invar36 as a compensation sample).

Together with the digital comparator expansion results, *Appendix A.5* collects the obtained thermal expansion measurements from the strain gauge readings. These measurements are then interpreted in Chapter IV. Each reading is named after a code based on the variables collected in *Table III-17*. As an example, "SGM-F-40-3" refers to the strain gauge measurement (SGM) of the third (3) Floresta sandstone (F) sample, at 40ºC (40).

Table III-17. Variables of the strain gauge expansion measurement codes.

TEST	MATERIAL	TEMPERATURE	REPET.
SGM	F	23ºC 150ºC	1
	C	40ºC 175ºC	2
	M	70ºC 200ºC	3
	I	100ºC 225ºC	4
		125ºC 250ºC	

3.6 PETROGRAPHIC CHARACTERIZATION

Finally, for a better understanding of the fracture processes and the microstructural definition of the studied rocks, several fractured SENB specimens tested under four-point bending conditions have been reconstructed and microstructurally analysed by means of thin-sections of rocks. The following sub-sections describe the sample reconstruction and thin-section preparation process and conducted microstructural analyses.

3.6.1 Sample preparation

The analysed thin-sections consist of approximately 30 μm (0.03 mm) thick rock sections of reconstructed SENB specimens broken under four-point bending conditions, for which the code criterion established in *Section 3.3.1* for the four-point bending test specimens (*Table III-12*) is maintained.

Among the tested samples, some representative specimens were selected for reconstruction and microstructural analyses. Approximately, 40 specimens were selected for each rock, including different notch radii as indicated in the tests summary of *Table III-8*. All the reconstructed samples correspond to four-point bending tests performed at room

temperature, except for those with $\rho = 0.15$ mm, in which the samples tested at 250ºC have been also reconstructed and studied aiming to check if there are appreciable microstructural changes as a consequence of the thermal treatment.

The sample reconstruction process is divided into three steps: First, as the analysis is focused on the notch region where fracture occurs, the central part of the samples is cut. Then, the two fractions of the broken specimens are manually reconstructed and located in a container to be preserved under vacuum during 24 hours. This allows to maintain the natural characteristics of the fractured specimen unaltered. Finally, impregnation takes place through the injection of synthetic resins (with blue ink). The blue ink is used to mark the areas of the sample where the resin penetrates, allowing to clearly identify the main crack, adjacent microcracks and pores of the rock in the microscopic analysis. After impregnation, it is necessary to wait 24 hours before proceeding with the roughing and polishing of the sample to obtain the 30 μm thick thin-sections. *Figure III-37* shows some pictures of the vacuum and impregnation equipment used for the reconstruction of the fractured rocks.

Figure III-37. Vacuum and impregnation equipment for rock reconstruction.

Prior to roughing and polishing of the reconstructed samples, the specimens are cut with an automated cutting saw to minimise the subsequent roughing works. A thickness of around 300-500 μm can be directly obtained with the automated cutting saw, which uses a vacuum retention system. *Figure III-38* shows some pictures of the cutting process.

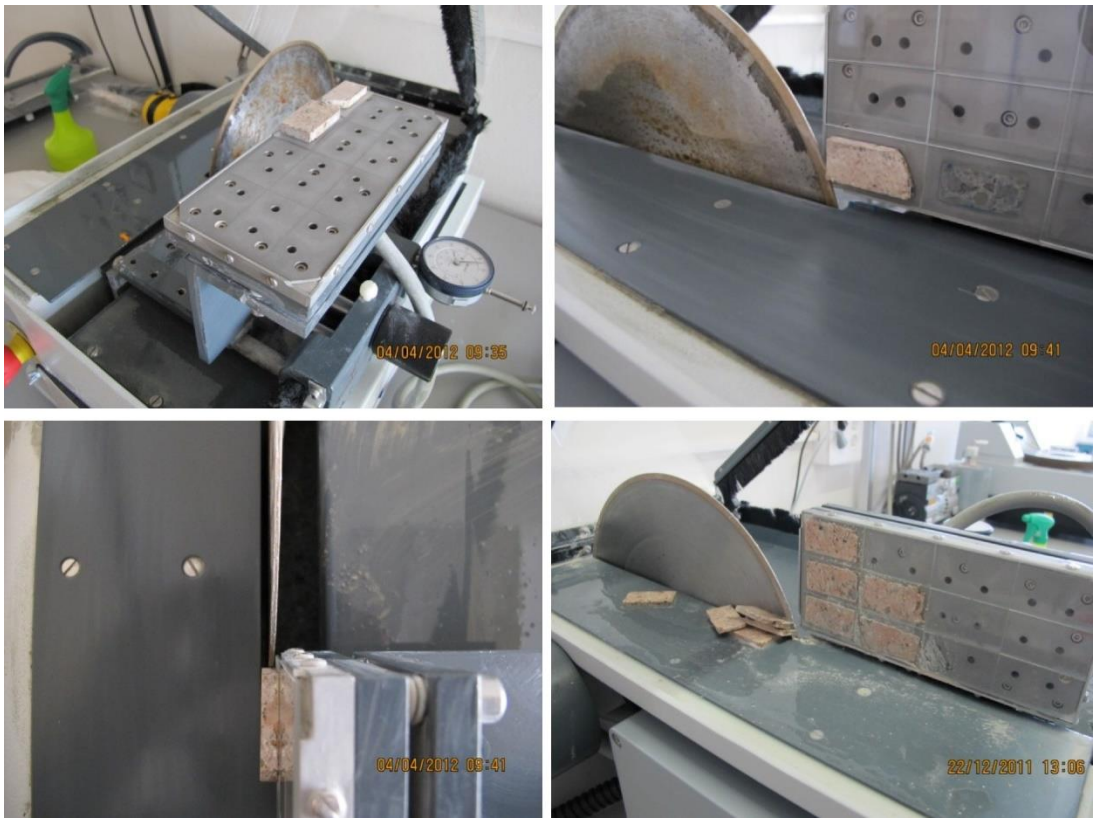

Figure III-38. Automated cutting saw equipment.

Ultimately, polishing of the reconstructed specimen sections is carried out until the desired thickness of 30 μm is reached. Polishing is done using silicon carbide as the abrasive material, and the rocks are retained in the polishing device by vacuum. The process is completely automatic, and the rotation speed and, therefore, the polishing speed, can be controlled. Once the desired level of roughing has been reached, the polishing of the samples is automatically interrupted, which guarantees thin-sections of the desired thickness. Finally, *Figure III-39* shows some pictures of the automated polishing equipment and process, and *Figure III-40* presents some pictures of the eventual thin-sections.

Figure III-39. Automated polishing equipment.

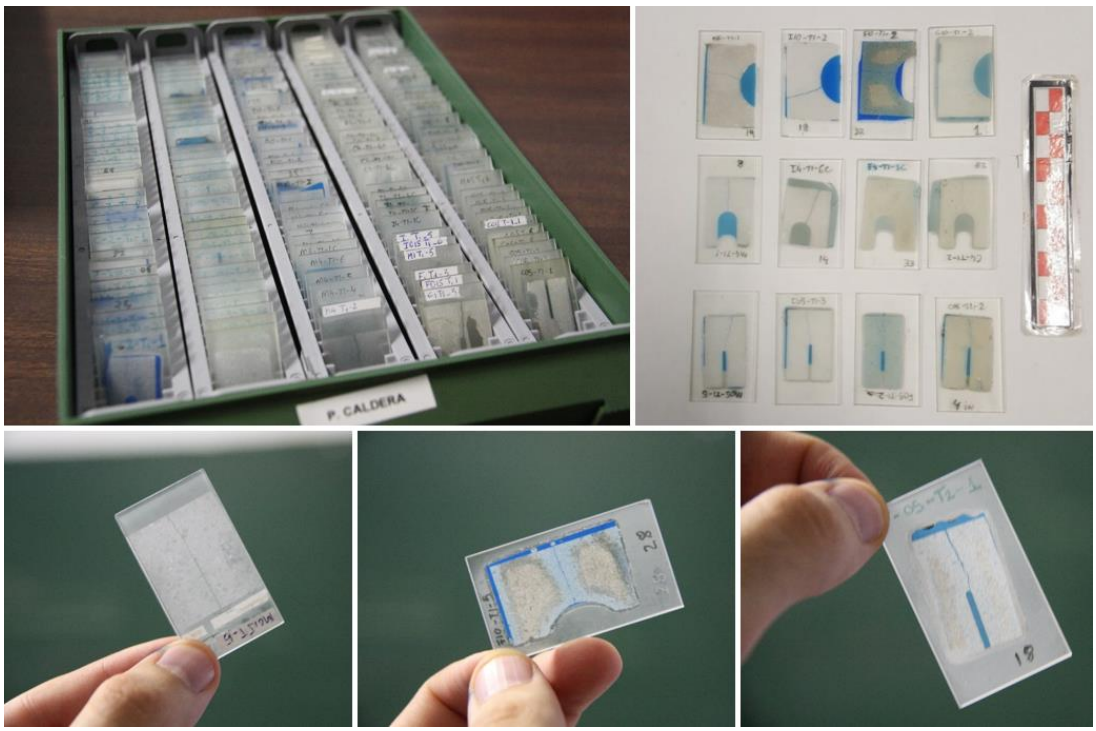

Figure III-40. Thin-sections from the reconstructed SENB specimens tested under four-point bending conditions.

3.6.2 Analysis procedure

With all this, 158 thin-sections have been prepared and studied, as those displayed in *Figure III-40*. The observation and analyses of the thin-sections are carried out with a petrographic microscope of transmitted and polarized light, which allows to identify the properties of the minerals when light passes through them. That is why the thin-sections are limited to a thickness of 30 μm. This type of petrographic analyses by means of optical microscopy allow to identify the different constituents of the analysed material, as well as to study the spatial relationship existing between them and the degree of physical and chemical alteration.

This study has been carried out using the NIS-Elements BR software, which allows the image to be examined in real time as it is directly linked to the optical microscope. Likewise, a small amount of liquid paraffin has been applied to each sample before starting the analysis, which facilitates distinguishing the different components. *Figure III-41* shows some images of the thin-section analyses using the optical microscope.

Figure III-41. Thin-section analyses using an optical microscope.

One of the main objectives of the performed microstructural analyses was the petrographic characterization of the four studied rocks, namely the Floresta sandstone, the Moleanos limestone, the Macael marble and the Carrara marble. Different characteristics obtained from the thin-section analyses such as the microstructural composition, the grain size distribution of the components or porosity have been already provided in *Section 2*, for the definition of these rocks.

On the other hand, it was also intended to rule out any possible microstructural change as a consequence of the thermal treatments to which the rocks samples were subjected during testing. As expected, no apparent microstructural alterations were observed at the studied range of temperatures when comparing the thin-sections of the samples tested at 23ºC and at 250ºC.

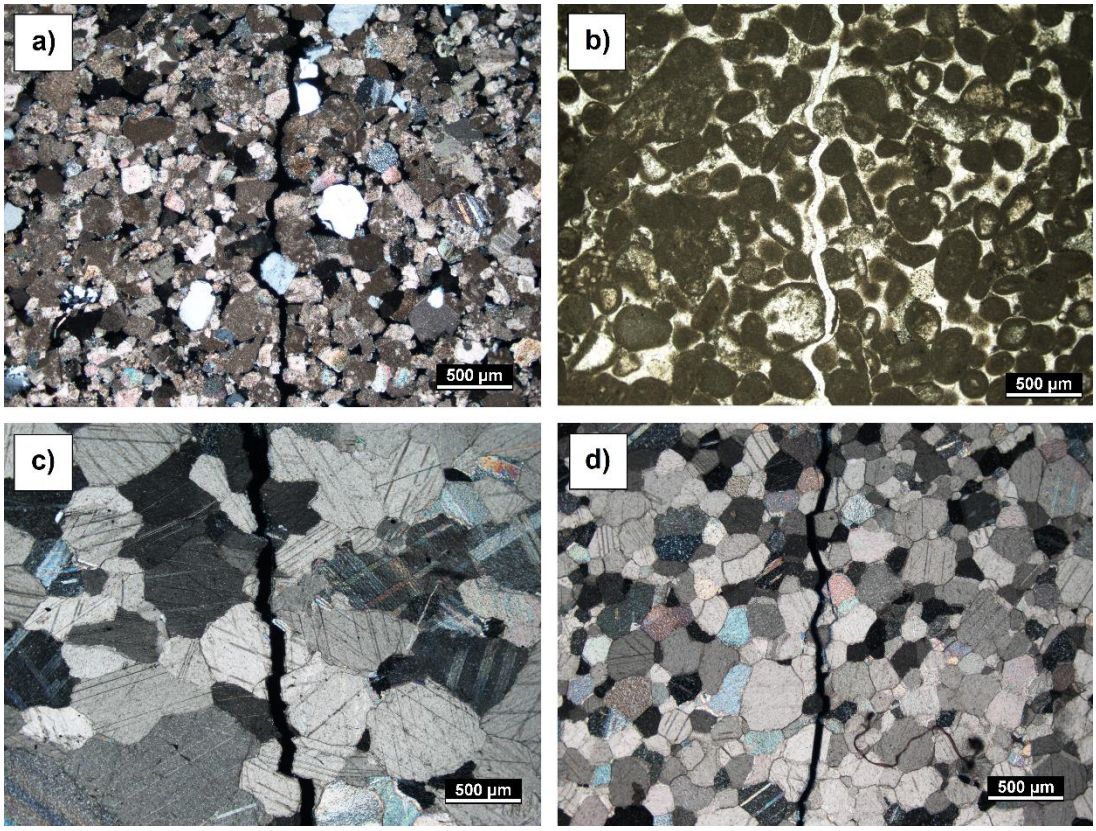

Figure III-42. Optical images of main cracks in the selected rocks: (a) Floresta Sandstone, (b) Moleanos limestone, (c) Macael marble, (d) Carrara marble.

Finally, the focus was placed on the fracture of the notched specimens. *Figure III-42* presents some pictures of the main cracks generated during the four-point bending tests for each of the four analysed rocks. Different aspects such as the initial type of fracture (i.e., transgranular or interganular) at the notch tip, the initial deviation of the cracks with respect to the theoretical notch bisector plane, the type of fractures along a distance equal to two times the critical distance ($2L$) of each rock, the sinuosity of the cracks, etc. has been studied aiming to relate them with the experimentally obtained fracture results. *Section 3.1.6* of Chapter IV provides the corresponding microstructural analysis and the studied correlations with the fracture results.

- Chapter IV -
Results and discussion

1 INTRODUCTION

The obtained results and their interpretation are presented, analysed and discussed in this section. First, the direct experimental results are addressed and the basic mechanical properties of the studied rocks are defined (*Section 2*), namely the tensile strength (σ_u), the compressive strength (σ_c), the Young's modulus (E), the Poisson's ratio (ν), the fracture toughness (K_{IC}), and the apparent fracture toughness (K_{IN}). With them, the mechanical behaviour of the rocks is characterised at a range of temperatures varying from 23 to 250ºC, including thermal expansion and petrographic analyses.

Based on the obtained experimental results, different rock fracture assessments are performed based on the TCD (*Section 3*) and the SED criterion (*Section 4*). In the first case, the critical distance of each of the analysed rocks is defined under different temperature conditions. This parameter is then used for the interpretation and prediction of the fracture behaviour of the analysed notched rocks under mode I and mixed mode I+II loading conditions at different temperatures, considering, in turn, the influence of the notch effect. The influence and the physical meaning of the critical distance is also discussed in this

section, which is a widely debated issue. Secondly, the fracture assessment of those same notched rocks is performed using the energy-based approach known as the SED criterion. The notch effect is also captured with this method and fracture load predictions are provided for mode I loading and different thermal conditions. The influence and size of the control volume over which the strain energy density is averaged is discussed here. Finally, a comparison between the two proposed methodologies and some comments on their advantages and limitations are provided.

Ultimately, as a continuation of Chapter IV, Chapter V will focus on the numerical study of the influence of grain size on several rock properties (i.e., $\sigma_u, \sigma_c, K_{IC}, E, \nu, L$) and the notch effect by means of discrete numerical analyses

2 EXPERIMENTAL RESULTS

2.1 TENSILE STRENGTH

The tensile strength results used in this work for the fracture assessments correspond to those obtained from the Brazilian tests, because they are widely accepted among the scientific community and have proven to offer similar results to those of direct tensile tests as indicated in *Section 1.4.1.1* of Chapter II. However, these results will be compared here with those obtained from four-point bending and three-point bending tests of non-notched samples, aiming to identify the extent of the differences in the results when using these methods.

Figure IV-1 shows the individual tensile strength (σ_u) results obtained from Brazilian tests (BT), four-point bending tests (4PB) and three-point bending tests (3PB) for the four selected rocks, all of them at room temperature (23ºC). It is generally observed that BT offer lower values of the tensile strength compared to the 4PB and the 3PB tests, as expected. 4PB and 3PB results are similar in the case of the Floresta sandstone and Moleanos limestone, while in the marbles 3PB results are slightly lower than 4PB ones, even of the order of the BT results in the case of the Carrara marble. In relative terms, 4PB and 3PB test results provide tensile strength values almost twice larger than those obtained from BT, somewhat lower in the Carrara marble.

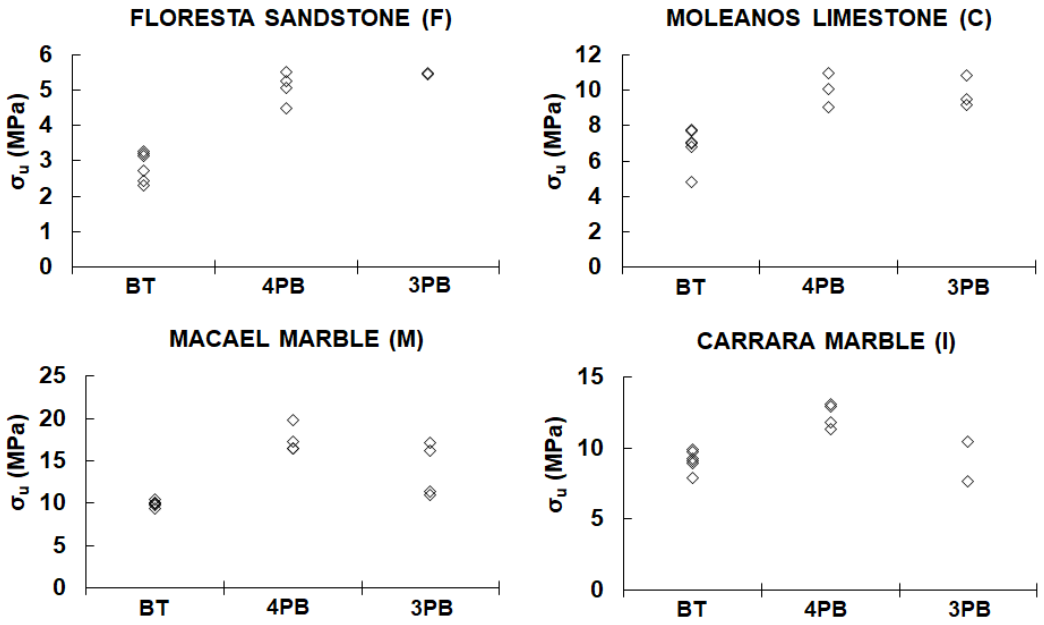

Figure IV-1. Tensile strength (σ_u) results obtained from Brazilian tests (BT), four-point bending tests (4PB) and three-point bending tests (3PB) at room temperature (23ºC).

Likewise, *Table IV-1* gathers the mean tensile strength and standard deviation results for each rock and testing method. The individual test results have not been included here for the sake of brevity and are, instead, collected in *Appendixes A.1, A.3* and *A.4*.

Table IV-1. Mean tensile strength (σ_u) and standard deviation results obtained from Brazilian tests (BT), four-point bending tests (4PB) and three-point bending tests (3PB) at room temperature (23ºC). Units in MPa.

TEST	(F)	(C)	(M)	(I)
BT	2.84 ± 0.42	6.86 ± 1.08	9.97 ± 0.33	9.16 ± 0.71
4PB	5.06 ± 0.43	10.05 ± 0.97	17.53 ± 1.59	12.31 ± 0.86
3PB	5.47 ± 0.03	9.85 ± 0.87	13.94 ± 3.21	9.06 ± 1.98

Focusing now on the BT results, which are the ones that will be used for the fracture assessments, marbles present the highest tensile strengths of almost 10 MPa, followed by the Moleanos limestone with less than 7 MPa and, eventually, by the Floresta sandstone with nearly 3 MPa. With regards to the Oolitic limestone and Biotite granite, Cicero et al. (2014) also provided the mean tensile strength and standard

deviation values obtained from Brazilian tests. These values are collected in *Table IV-2*. The granite presents a tensile strength slightly lower than the marbles, while the Oolitic limestone is 14% stronger than the Moleanos limestone.

Table IV-2. Mean tensile strength (σ_u) and standard deviation results obtained from Brazilian tests (BT) by Cicero et al. (2014). Units in MPa.

TEST	(O)	(G)
BT	7.8 ± 1.1	9.0 ± 1.3

2.1.1 Influence of temperature on tensile strength

The influence of temperature on the tensile strength of the tested rocks is irretrievably linked to their microstructure. The differential thermal expansion of adjacent mineral particles subjected to changes in temperature, and the presence of pores, microcracks or cavities allowing (or avoiding) that expansion define the thermal behaviour of rocks (e.g., Rao et al., 2007; Dwivedi et al., 2008; Yin et al., 2015). Thus, as a consequence of the existing heterogeneity in rock composition, different responses can be distinguished among the wide casuistic of the considered rocks.

Figure IV-2 represents the variation curves of the tensile strength (σ_u) of the four studied rocks with temperature at a range of 23 to 250ºC. The black solid line and black full symbols stand for the Brazilian tests performed under constant temperature conditions inside the oven (NC), while the grey solid line and grey full symbols correspond to the Brazilian tests performed after a thermal cycle (WC) at room temperature. By contrast, the black dashed line and empty symbols indicate the four-point bending test results that have been performed at the same temperatures as the Brazilian tests, in this case, only at the target temperature with no cooling before and during testing. Dots represent the individual test results (tabulated in *Appendixes A.1* and *A.3*) and the lines correspond to average value trends.

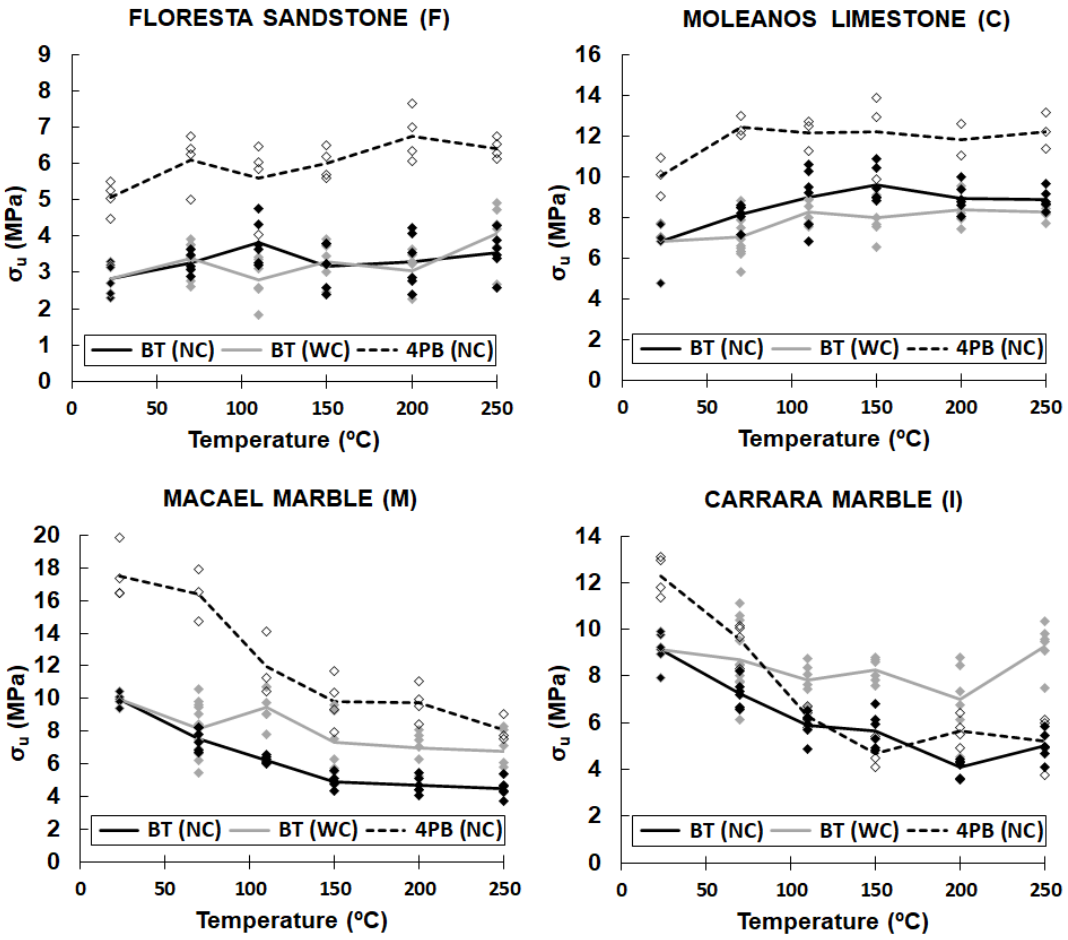

Figure IV-2. Variation of the tensile strength (σ_u) with temperature based on the Brazilian test (BT) and four-point bending (4PB) test results.

Similar tendencies with temperature are captured both with Brazilian tests and four-point bending tests. In absolute terms 4PB results keep presenting higher tensile strength values for the whole range of analysed temperatures, with the exception of the Carrara marble, at which 4PB tests and Brazilian tests provide similar results from approximately 110ºC onwards.

In general, two main trends are distinguished in *Figure IV-2*. The Floresta sandstone and the Moleanos limestone, those rocks presenting certain porosity, experiment a slight increase of the tensile strength at the onset of the heating process, no matter whether Brazilian tests o four-point bending test results are analysed. This increase is attributed to the closure of the preexisting pores and microcracks up to a certain critical temperature. However, the critical temperature after which the tensile strength reduces is not clearly captured at the studied range of

temperatures, which indicates that this critical temperature is probably above 250ºC. In the particular case of the Moleanos limestone, although a general increase is shown, a roughly horizontal region is observed from 70ºC according to the 4PB tests, and from 150ºC if Brazilian tests are considered.

By contrast, in the case of the marbles a clear tensile strength reduction is observed from the onset of heating, showing a more pronounced reduction in the four-point bending tests. These rocks do not present initial porosity and, therefore, thermally induced microcracks arise because of the lack of internal space for the uneven dilation of crystals when temperature increases.

It is also notorious that those results corresponding to the Brazilian tests performed at room temperature conditions after a heating and cooling cycle (grey solid lines) present a gentler trend compared to those performed at moderate temperature conditions (black solid lines), even though the general increase and decrease patterns are maintained in both cases. The smoothing of the curves seems to indicate a partial recovery of the inner microstructural conditions of the specimens after cooling. However, this behaviour is not that clear in the case of the Floresta sandstone, in which those tests with (WC) and without (NC) cooling before testing provide relatively similar results.

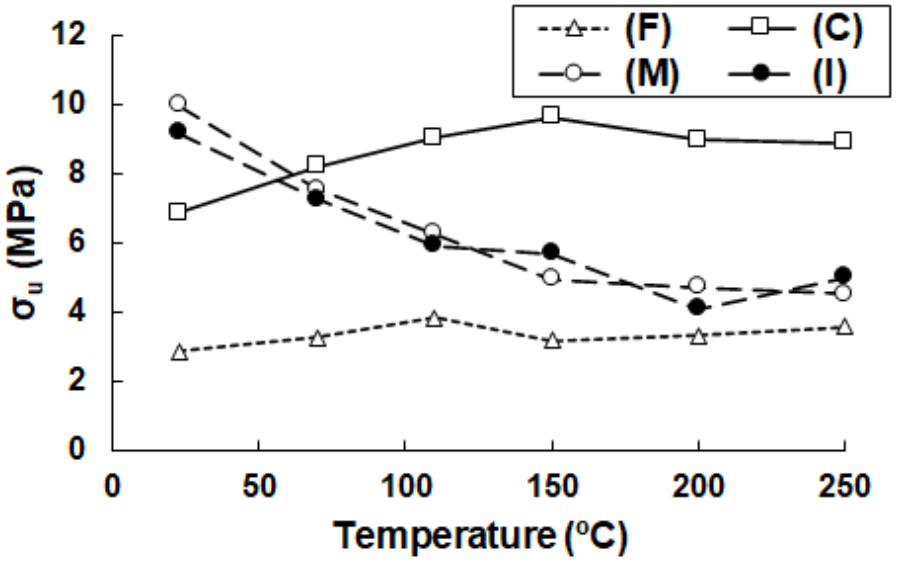

Figure IV-3. Summary of the tensile strength-temperature variation curves for each of the analysed rocks, obtained from BT (NC).

For a clearer comparison of the results, *Figure IV-3* summarises in a single plot the mean variation curves of the tensile strength with temperature for each of the analysed rocks depicted in *Figure IV-2* and corresponding to the Brazilian tests performed at high temperatures (BT(NC)). Both marbles develop a relatively similar behaviour and present similar tensile strengths at the studied range of temperatures up to 250ºC. The Moleanos limestone shows a significant tensile strength increase up to 150ºC, while in the Floresta sandstone, the increase is much softer both in relative and absolute terms.

Finally, *Table IV-3* gathers the mean tensile strength and standard deviation results for each of the six studied temperature steps and four selected rocks, obtained from Brazilian tests subjected to a thermal cycle (WC), performed in the oven (NC), and four-point bending tests in the oven.

Table IV-3. Mean tensile strength (σ_u) and standard deviation results obtained from Brazilian tests (BT) with (WC) and without (NC) cooling, and four-point bending tests (4PB) at different temperatures. Units in MPa.

TEST		(F)	(C)	(M)	(I)
23ºC	BT	2.84 ± 0.42	6.86 ± 1.08	9.97 ± 0.33	9.16 ± 0.71
	4PB	5.06 ± 0.43	10.05 ± 0.97	17.53 ± 1.59	12.31 ± 0.86
70ºC	BT(WC)	3.38 ± 0.40	7.08 ± 1.05	8.15 ± 1.61	8.70 ± 1.56
	BT(NC)	3.25 ± 0.30	8.18 ± 0.53	7.52 ± 0.67	7.26 ± 0.61
	4PB	6.10 ± 0.77	12.45 ± 0.48	16.41 ± 1.60	9.56 ± 0.84
110ºC	BT(WC)	2.80 ± 0.61	8.28 ± 0.59	9.50 ± 1.13	7.82 ± 0.74
	BT(NC)	3.82 ± 0.62	9.02 ± 1.49	6.25 ± 0.22	5.90 ± 0.58
	4PB	5.59 ± 1.06	12.19 ± 0.78	11.93 ± 1.94	6.26 ± 0.38
150ºC	BT(WC)	3.29 ± 0.52	7.99 ± 0.95	7.33 ± 1.78	8.26 ± 0.51
	BT(NC)	3.17 ± 0.59	9.62 ± 0.87	4.92 ± 0.41	5.67 ± 0.77
	4PB	6.00 ± 0.43	12.26 ± 2.09	9.84 ± 1.60	4.66 ± 0.66
200ºC	BT(WC)	3.04 ± 0.58	8.39 ± 0.73	6.99 ± 1.04	7.01 ± 1.57
	BT(NC)	3.30 ± 0.76	8.96 ± 0.68	4.70 ± 0.51	4.08 ± 0.39
	4PB	6.76 ± 0.72	11.83 ± 1.11	9.74 ± 1.07	5.67 ± 0.63
250ºC	BT(WC)	4.09 ± 0.82	8.32 ± 0.33	6.80 ± 1.23	9.30 ± 0.97
	BT(NC)	3.55 ± 0.58	8.88 ± 0.50	4.50 ± 0.55	5.00 ± 0.60
	4PB	6.41 ± 0.27	12.26 ± 0.89	8.11 ± 0.84	5.20 ± 1.09

2.2 COMPRESSIVE STRENGTH

The compressive strength (σ_c) is directly obtained from the failure load of the uniaxial compression tests, in which stresses are assumed to uniformly distribute throughout the specimen section. *Table IV-4* collects the mean compressive strength and standard deviation values obtained from the samples tested at room temperature conditions. The individual results are included in *Appendix A.2*. Likewise, *Table IV-5* gathers the results obtained by Cicero et al. (2014) for the Oolitic limestone and the Biotite granite.

Table IV-4. Mean compressive strength (σ_c) and standard deviation results at room temperature.

	(F)	(C)	(M)	(I)
σ_c (MPa)	50.4 ± 2.6	78.8 ± 8.1	86.6 ± 8.8	97.8 ± 4.5

Table IV-5. Mean compressive strength (σ_c) and standard deviation results at room temperature obtained by Cicero et al. (2014).

	(O)	(G)
σ_c (MPa)	135.7 ± 12.7	122.5 ± 4.8

The Floresta sandstone presents, as in the case of the tensile results, a significant lower strength, probably due to the scarce presence of cement and high porosity as indicated in the microstructural description provided in *Section 2.1* of Chapter III.

Table IV-6 shows the relation between the compressive strength and the tensile strength of those six rocks, calculated as the ratio between the mean strength values (σ_c/σ_u). As reported in *Section 1.4.1.1* of Chapter II, it is usually considered that tensile strength is approximately 10% of the uniaxial compression strength as a rough approximation. According to the obtained results in *Table IV-6*, the expected order of magnitude is generally fulfilled in the case of the six studied rocks, although the Floresta sandstone and the Oolitic limestone present relatively higher σ_c/σ_u values of around 17.

Table IV-6. Relation between compressive and tensile strength (σ_c/σ_u) at room temperature.

	(F)	(C)	(M)	(I)	(O)	(G)
σ_c/σ_u	17.8	11.5	8.7	10.7	17.4	13.6

2.2.1 Influence of temperature on compressive strength

The compressive strength, like the tensile strength, also depends on rock microstructural aspects that are certainly affected by temperature. Thus, significant variation of compressive strength with temperature is expected. *Figure IV-4* represents the variation of the average uniaxial compressive strength of the selected rocks with temperature at a range of 23 to 250ºC.

The Floresta sandstone develops a slight decrease of the compressive strength when temperature increases. The observed almost horizontal trend indicates low influence of temperature at least up to 250ºC in the case of the Floresta sandstone. On the other hand, both marbles present a more pronounced decreasing tendency from the onset of heating, very similar in both cases although in absolute values the Carrara marble shows a higher compressive strength. Finally, in the Moleanos limestone, a continuous and reasonably linear increase of the compressive strength is appreciated up to 250ºC.

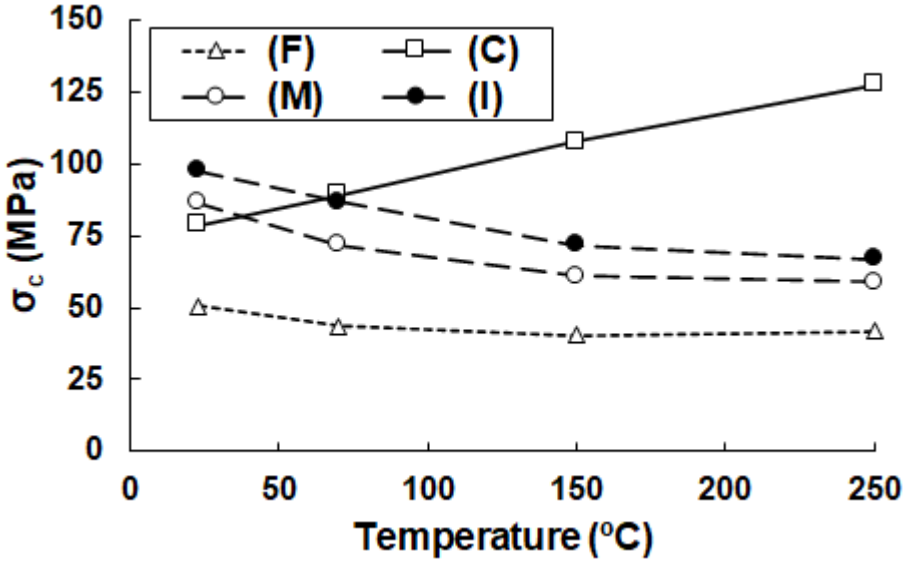

Figure IV-4. Variation of the compressive strength (σ_c) with temperature.

The observed phenomena are related to thermally induced micromechanisms that cause the closure or opening of microcracks as a consequence of thermal expansion of grains together with the applied stresses. Hoek (1965) stated than even in compression, the damage mechanisms of crack initiation is the result of tensile stresses at those microcracks or flaws. Thus, the appearance of new microcracks because of the thermal expansion of adjacent grains with no space for growth or the closure of preexisting pores and flaws will facilitate or hinder the coalescence of those microcracks and, therefore, will affect the compressive strength of the rocks as observed in *Figure IV-4*.

Table IV-7 summarises the obtained mean compressive strength values and the standard deviation at four different temperature steps: 23, 70, 150 and 250ºC. The individual results can be found in *Appendix A.2*.

Table IV-7. Mean compressive strength (σ_c) and standard deviation results at different temperatures. Units in MPa.

TEMP.	(F)	(C)	(M)	(I)
23ºC	50.4 ± 2.6	78.8 ± 8.1	86.6 ± 8.8	97.8 ± 4.5
70ºC	43.8 ± 4.4	89.3 ± 8.8	71.8 ± 5.3	86.9 ± 5.7
150ºC	40.6 ± 6.1	107.8 ± 21.6	61.1 ± 5.5	71.9 ± 3.3
250ºC	41.7 ± 6.9	127.5 ± 17.2	59.0 ± 4.6	67.0 ± 3.9

Proceeding as before, the ratio between the mean compressive strength and tensile strength of the rocks with temperature is now analysed in *Figure IV-5*. Both marbles and the limestone present a slight increase of σ_c/σ_u with temperature, while the sandstone reveals a significant drop from 23ºC to 70ºC and a successive slight decrease for higher temperatures up to 250ºC. The same results are also represented in a numeric form in *Table IV-8*, calculated from the mean strength values collected in *Table IV-3* and *Table IV-7*.

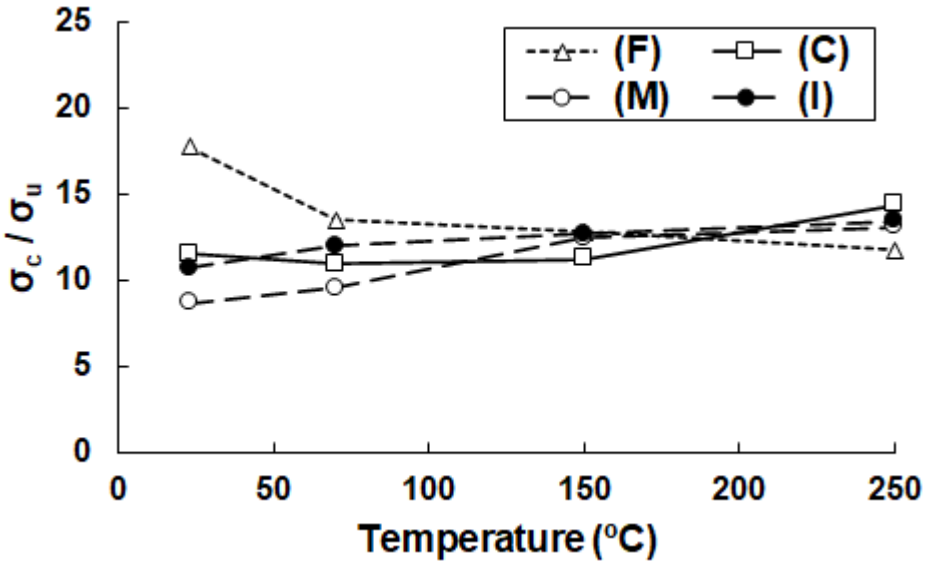

Figure IV-5. Variation of the σ_c/σ_u ratio with temperature.

Table IV-8. Relation between compressive and tensile strength (σ_c/σ_u) at different temperatures.

	(F)	(C)	(M)	(I)
σ_c/σ_u (23°C)	17.8	11.5	8.7	10.7
σ_c/σ_u (70°C)	13.5	10.9	9.5	12.0
σ_c/σ_u (150°C)	12.8	11.2	12.4	12.7
σ_c/σ_u (250°C)	11.8	14.4	13.1	13.4

2.3 YOUNG'S MODULUS AND POISSON'S RATIO

During uniaxial compression tests, the deformations of the rock specimens were measured in the longitudinal (or vertical, ε_V) and circumferential (or horizontal, ε_H) directions using strain gauges, as explained in *Section 3.2* of Chapter III. These measurements, together with the loading records, allow drawing the stress-strain curves for each specimen, from which the deformational parameters (i.e., Young's modulus and Poisson's ratio) are derived. *Figure IV-6* shows some representative stress-strain curves of each of the four selected rocks at room temperature. During uniaxial compression loading, longitudinal dimension reduces while circumferential dimension increases and, consequently, horizontal and vertical strains have opposite signs, positive and negative, respectively, according to the used convention.

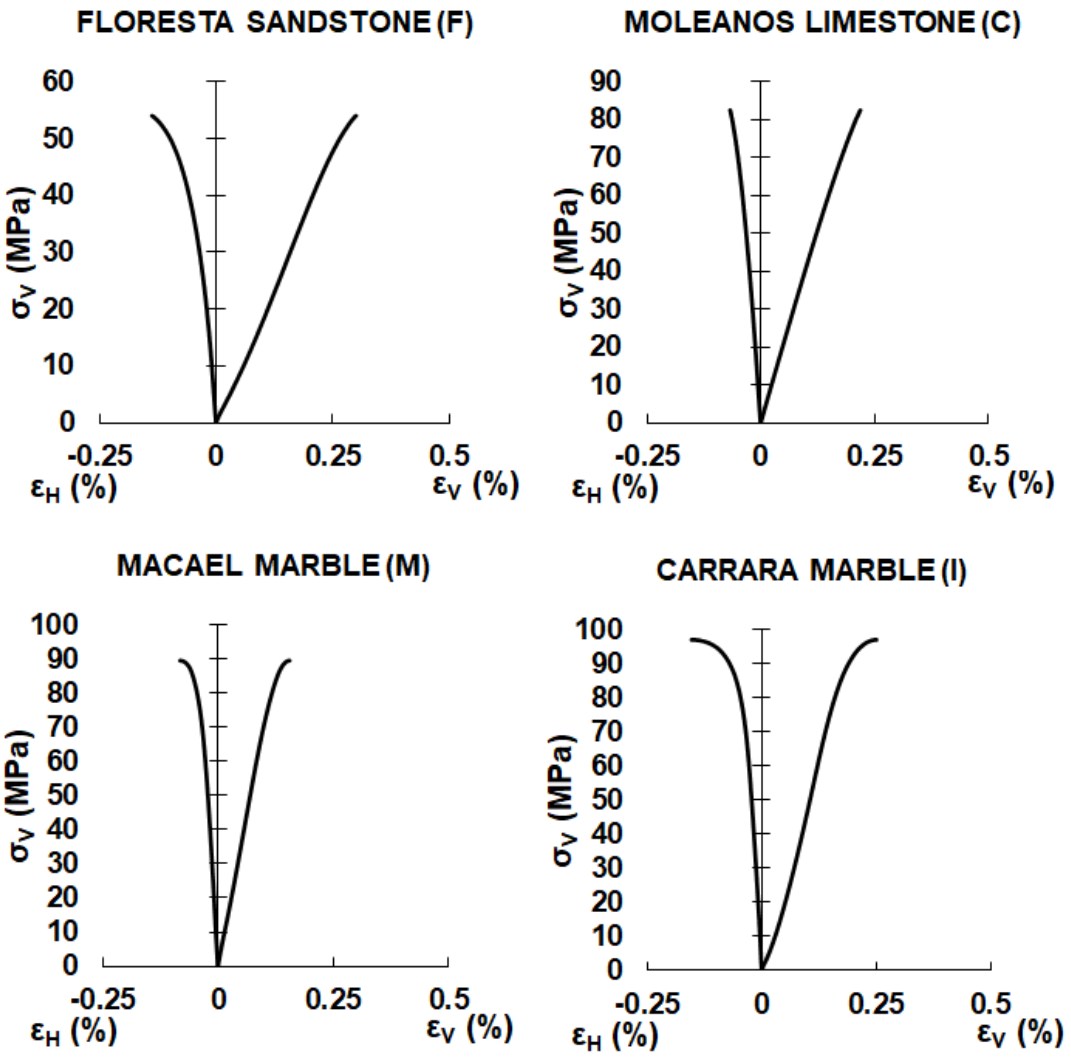

Figure IV-6. Some representative stress-strain curves of the four selected rocks at room temperature.

In general terms, all the studied rocks present a roughly linear elastic behaviour at room temperature, although the marbles show certain non-linearities close to the peak load, specially the Carrara marble. These stress-strain curves are consistent with those used by Miller (1965) for the classification of the typical stress-strain curves of rocks (see *Figure II-20*). Both marbles could be classified as Type IV, with a plasto-elasto-plastic behaviour, or at least as elasto-plastic (Type II) in the case of the Macael marble. Likewise, the Moleanos limestone shows a clear linear elastic behaviour till failure (Type I), and the Floresta sandstone responds to a plasto-elastic curve (Type III). In any case, based on these stress-strain curves, the use of LEFM is considered to be valid for the

fracture assessment of the four rocks, although a better agreement is expected for the Moleanos limestone.

Both the Young's modulus and the Poisson's ratio are calculated in this work considering the tangent slope at 50% of the peak load. Under these considerations, *Table IV-9* shows the obtained mean and standard deviation values of the Young's modulus and Poisson's ratio for each of the four selected rocks, obtained from the uniaxial compression tests at room temperature. Likewise, *Table IV-10* presents the same deformational parameters of the other two studied rocks (i.e., Oolitic limestone and Biotite granite) obtained by Cicero et al. (2014) by means of the same type of tests and calculated for 50% of the peak load as well.

Table IV-9. Mean Young's modulus (E_{50}), Poisson's ratio (ν_{50}) and standard deviation results at room temperature.

	(F)	(C)	(M)	(I)
E_{50} (GPa)	19.5 ± 2.0	38.4 ± 4.7	73.4 ± 7.1	57.1 ± 3.7
ν_{50}	0.36 ± 0.04	0.31 ± 0.05	0.35 ± 0.06	0.35 ± 0.04

Table IV-10. Mean Young's modulus (E_{50}), Poisson's ratio (ν) and standard deviation results at room temperature obtained by Cicero et al. (2014).

	(O)	(G)
E_{50} (GPa)	64.1 ± 2.2	45.6 ± 7.9
ν_{50}	0.33 ± 0.03	0.17 ± 0.03

Finally, the relation between the Young's modulus and the compressive strength of the rocks is analysed in *Table IV-11*. This ratio provides an overview of the relative deformability of the rocks under compressive loads. Both limestones present a similar E_{50}/σ_c ratio of almost 500. The granite and the Floresta sandstone show a lower value under 400 and marbles present the highest values with almost 600 and 850 for Carrara and Macael marbles, respectively.

Table IV-11. Relation between Young's modulus and compressive strength (E_{50}/σ_c) at room temperature.

	(F)	(C)	(M)	(I)	(O)	(G)
E_{50}/σ_c	387.0	487.6	847.4	584.1	472.4	372.2

Once the Young's modulus and the compressive strength of the rocks are defined, the studied rocks can be classified according to Deere & Miller's (1966) engineering classification system, as explained in *Section 1.3.1.2* in Chapter II.

First, *Figure IV-7* represents the particular values of the analysed sedimentary rocks (i.e., Floresta sandstone, Moleanos limestone and Oolitic limestone) on Deere & Miller's graph depicted in *Figure II-4*. It is observed that they all fall within the corresponding envelope defined for rocks with the same geological classification. The Floresta sandstone can be classified as a low strength rock with average modulus ratio (DM), with a relatively high modulus ratio within the envelope of sandstones. The Moleanos limestone corresponds to a medium strength with average modulus ratio rock (CM) and, finally, the Oolitic limestone also presents an average modulus ratio but a high strength instead (BM).

Proceeding in the same way, according to the results depicted in *Figure IV-8* (metamorphic rocks), both marbles are classified as medium strength high modulus ratio rocks (CH). These rocks do not fall strictly within region 3 corresponding to marbles. However, this region was defined in origin with only a few number of marble samples (22 specimens). Therefore, the obtained results suggest that region 3 should be extended.

Finally, *Figure IV-9* shows Deere & Miller's rock engineering classification graph for igneous rocks with the Biotite granite results represented on it. As most of the granites according to region 2, the studied granite is classified as a high strength and average modulus ratio rock (BM).

In general, comparing the obtained engineering classification results with those summarised by Deere & Miller (1966) for different rock families, it is observed that the analysed rocks in this work fall within the expected range for the corresponding rock types. Leaving aside the particular case of the sandstones that present a particularly broad casuistic of compressive strength and Young modulus values, the rest of analysed rocks offer roughly representative mean results within the corresponding rock families.

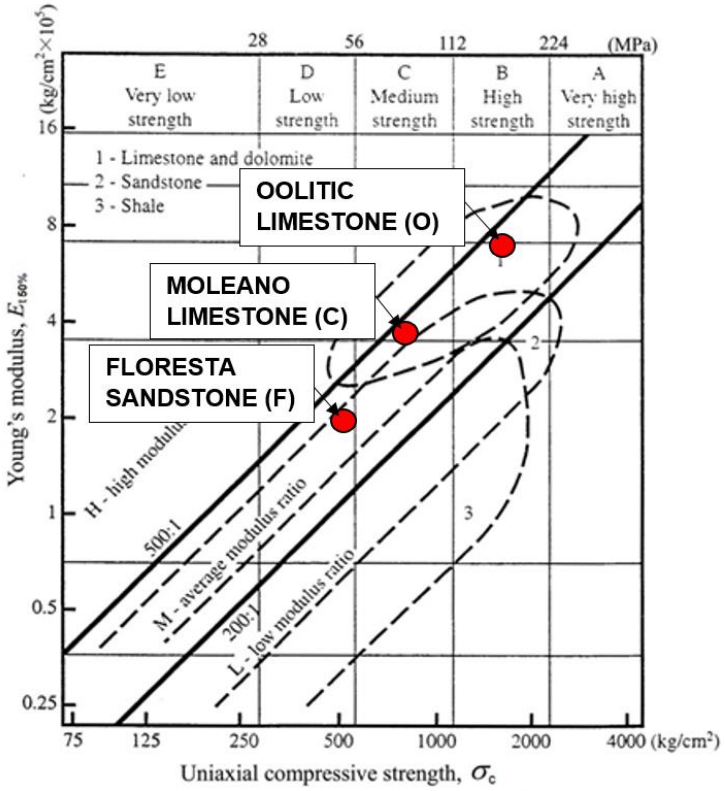

Figure IV-7. Classification of the Floresta sandstone, Moleanos limestone and Oolitic limestone according to Deere & Miller's (1966) engineering classification system.

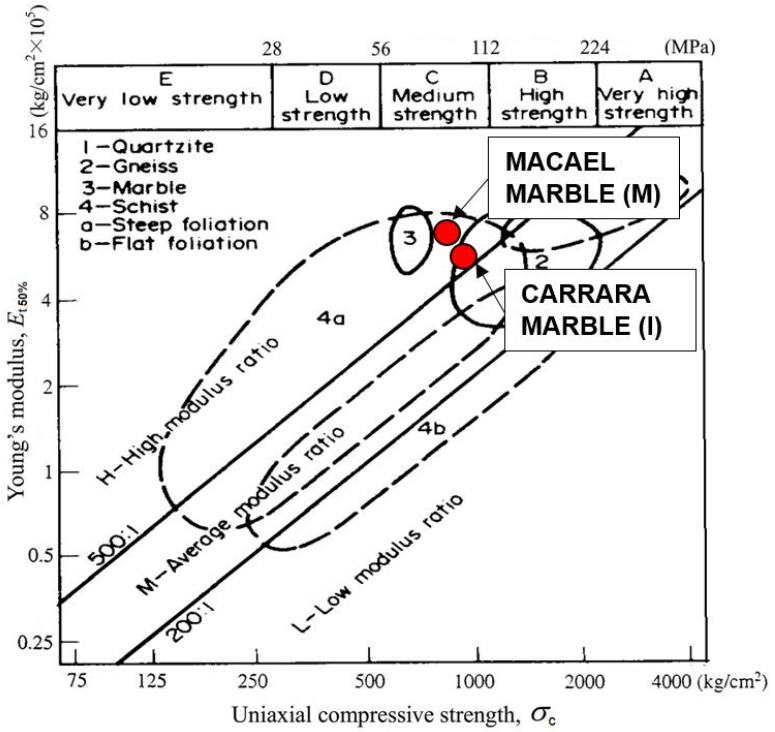

Figure IV-8. Classification of the Macael and Carrara marbles according to Deere & Miller's (1966) engineering classification system.

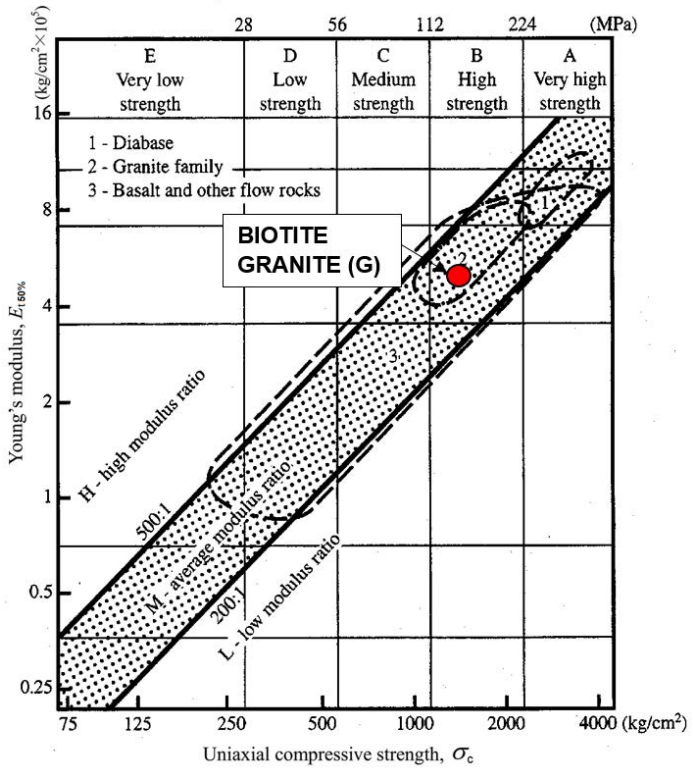

Figure IV-9. Classification of the studied granite according to Deere & Miller's (1966) engineering classification system.

2.3.1 Influence of temperature on Young's modulus and Poisson's ratio

As in the case of the strength parameters, the Young's modulus and the Poisson's ratio are also certainly affected by temperature. The extent of that influence can be appreciated in *Figure IV-10*, where some representative stress-strain curves are shown for different temperatures up to 250ºC. The linearity of the curves prior to the peaks reveals a predominantly quasi-brittle behaviour of the Floresta sandstone and the Moleanos limestone in the entire range of temperatures considered in this work. By contrast, the influence of temperature on the linear elastic behaviour of the marbles is more significant, especially in the Carrara marble. Both marbles show a certain degree of ductility in relative terms, which seems to be more noticeable as temperature increases. In the case of the Macael marble, reasonable linear behaviour is observed at 23ºC and 70ºC, but a certain non-linearity is noticed for higher temperatures. In the case of the Carrara marble, however, even those tests performed at room temperature display a not completely linear behaviour.

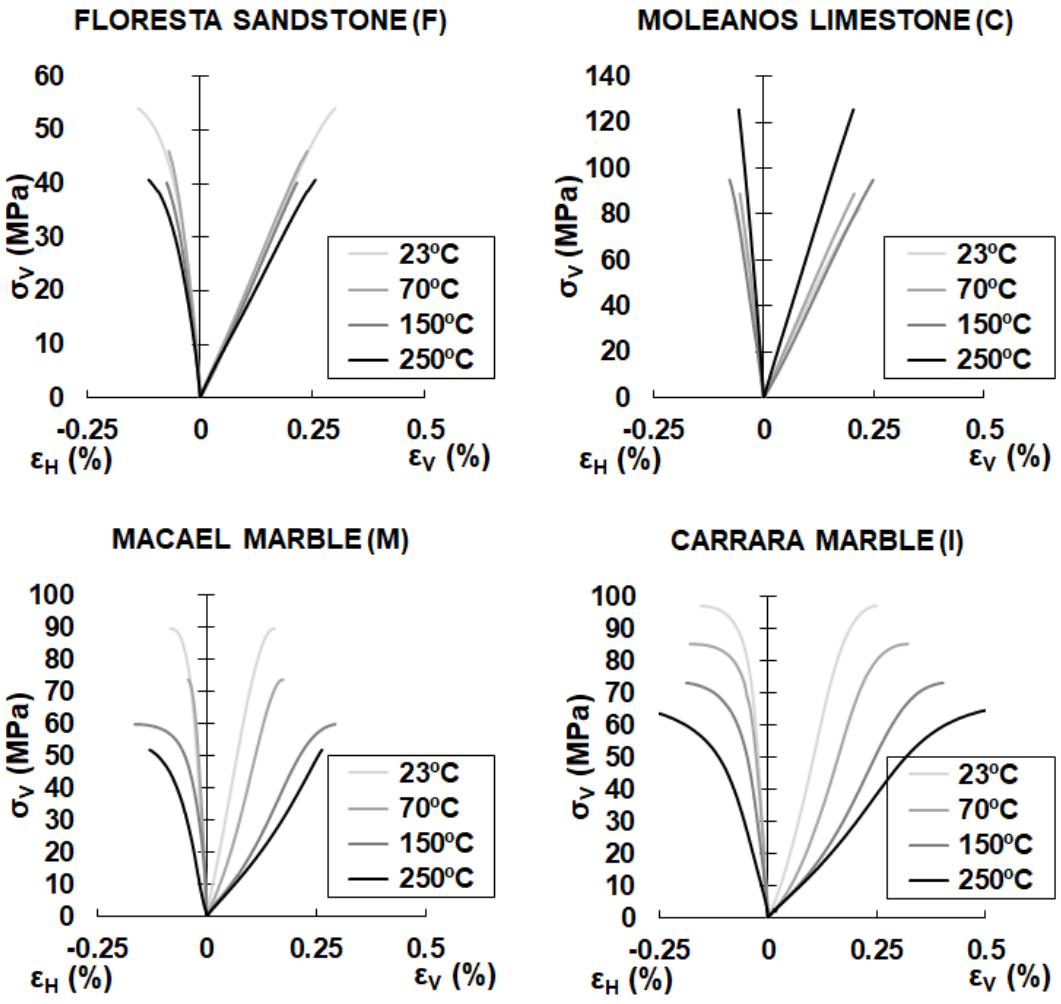

Figure IV-10. Some representative stress-strain curves of the four selected rocks at different temperatures.

The use of the TCD and the SED criterion, the two proposed methodologies, assumes that the studied rocks behave as roughly linear elastic materials at the considered range of temperatures (up to 250ºC). Both methodologies are based on LEFM and, therefore, worse fracture load predictions should be expected as non-linear behaviour becomes more significant. The extent of the influence of the observed non-linearities in rock fracture assessments will be addressed when interpreting the fracture results according to both the TCD and the SED criterion in *Sections 3* and *4*.

Analysing in detail the stress-strain curves depicted in *Figure IV-10* from which the Young's modulus and Poisson's ratio are calculated, several conclusions can be highlighted: First, the uniaxial compressive

strength (peak values) shows a clear decrease in the studied marbles, a less categorical decreasing trend in the case of the Floresta Sandstone, and an increasing tendency in the Moleanos limestone, as already indicated in *Figure IV-4*. Second, the variation of the stress-strain curve slopes with temperature suggests a strong decreasing trend in the case of the two marbles and a slightly increasing trend in the Moleanos limestone. By contrast, in the case of the Floresta sandstone, the influence of temperature on the Young's modulus seems to be small. *Figure IV-11* shows the resultant mean variation of the tangent Young's modulus with temperature calculated at 50% of the peak load for each of the four studied rocks. The Floresta sandstone presents a roughly constant or slightly decreasing tendency up to 250ºC. The Macael marble and the Carrara marble offer similar trends. They both reveal a clear reduction of the Young's modulus with temperature from the onset of heating, although the Macael marble provides slightly higher values of the Young's modulus in absolute terms. Finally, the Moleanos limestone shows a significant increment of E_{50} with temperature, although the growth is gentler, in relative terms, than that observed in *Figure IV-4* for the compressive strength. In the third place, the Poisson's ratio relates the vertical and horizontal strains of the rock samples subjected to uniaxial loading. Thus, its variation with temperature from the direct observation of the stress-strain curves is not as intuitive as that of the Young's modulus. Analogously to the determination of E, the Poisson's ratio is also calculated from the tangent slope of the axial and diametric stress-strain curves at 50% of the peak loads, following the ISRM (1979) recommendations. *Figure IV-12* represents the mean variation of the Poisson's ratio with temperature for each of the studied rocks. The four analysed rocks suggest a modest reduction of the Poisson's ratio up to approximately 70ºC. Then, both the Floresta sandstone and the Moleanos limestone show a roughly constant value of around 0.3 up to 250ºC, while the marbles present a clear and relatively steep increment. The high values approaching 0.5 for 250ºC are attributable to the lack of linear elastic behaviour of the marbles at that temperature, especially in the Carrara marble. It is also worth noting that ν_{50} (obtained in a consistent way with E_{50}) is higher than ν_0 for example, which considers the initial slope of the stress-strain curves instead.

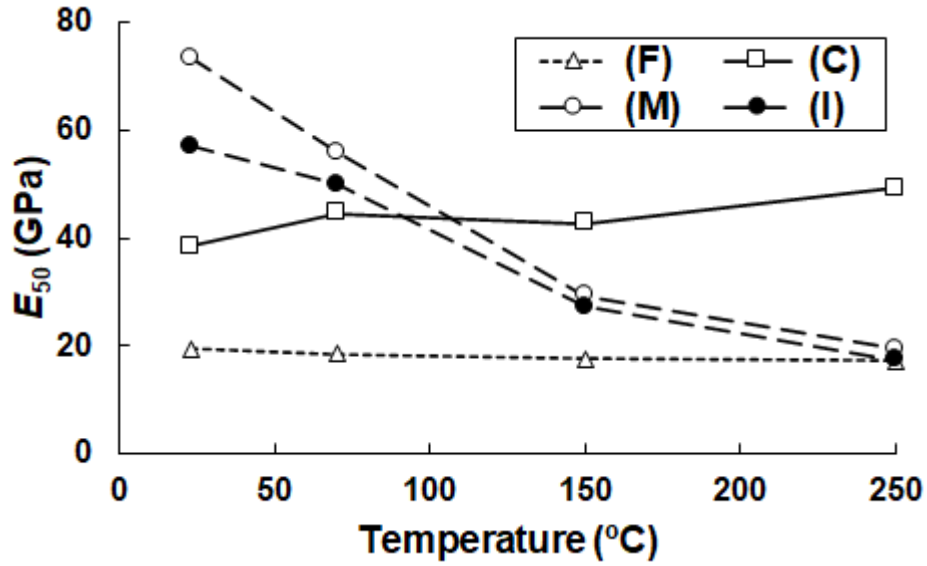

Figure IV-11. Variation of the Young's modulus (E_{50}) with temperature based on the uniaxial compression test results.

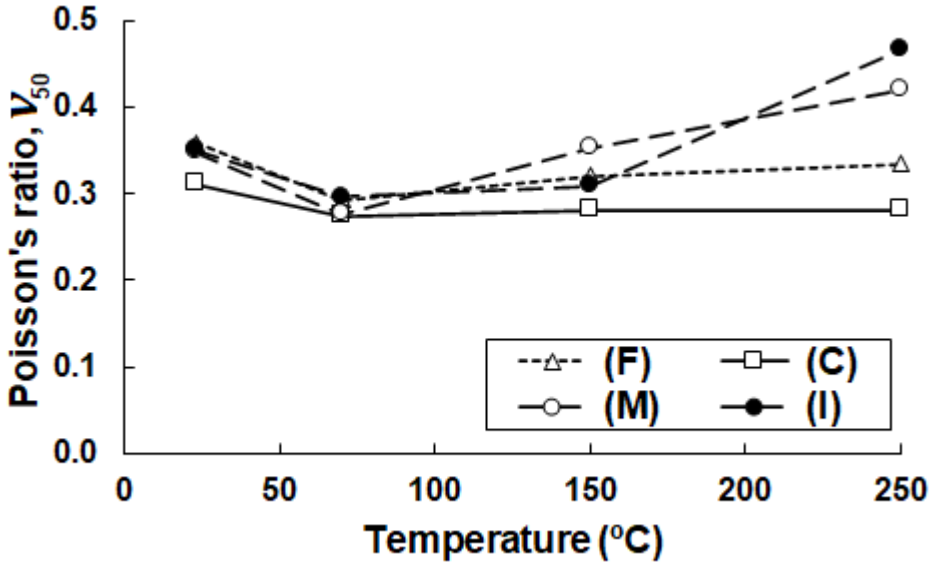

Figure IV-12. Variation of the Poisson's ratio (ν_{50}) with temperature based on the uniaxial compression test results.

The mean Young's modulus (E_{50}) and Poisson's ratio (ν_{50}) values represented in *Figure IV-11* and *Figure IV-12*, together with the standard deviation values, are summarised in *Table IV-12* for each of the considered four temperatures: 23, 70, 150 and 250ºC. The individual test results can be found in *Appendix A.2*.

Table IV-12. Mean Young's modulus (E_{50}), Poisson's ratio (v_{50}) and standard deviation results at different temperatures.

		(F)	(C)	(M)	(I)
23ºC	E_{50} (GPa)	19.5 ± 2.0	38.4 ± 4.7	73.4 ± 7.1	57.1 ± 3.7
	v_{50}	0.36 ± 0.04	0.31 ± 0.05	0.35 ± 0.06	0.35 ± 0.04
70ºC	E_{50} (GPa)	18.5 ± 1.2	44.6 ± 2.2	55.9 ± 6.6	50.1 ± 2.8
	v_{50}	0.29 ± 0.05	0.27 ± 0.01	0.28 ± 0.04	0.30 ± 0.05
150ºC	E_{50} (GPa)	17.6 ± 2.3	42.7 ± 9.4	29.4 ± 4.9	27.4 ± 3.1
	v_{50}	0.32 ± 0.02	0.28 ± 0.02	0.35 ± 0.07	0.31 ± 0.03
250ºC	E_{50} (GPa)	17.2 ± 2.1	49.2 ± 15.9	19.4 ± 3.1	17.4 ± 1.4
	v_{50}	0.34 ± 0.04	0.28 ± 0.05	0.42 ± 0.14	0.47 ± 0.08

Finally, aiming to determine the relative influence of temperature on the Young's modulus and compressive strength of rocks, *Figure IV-13* represents the ratio between the Young's modulus and the compressive strength (E_{50}/σ_c) against temperature.

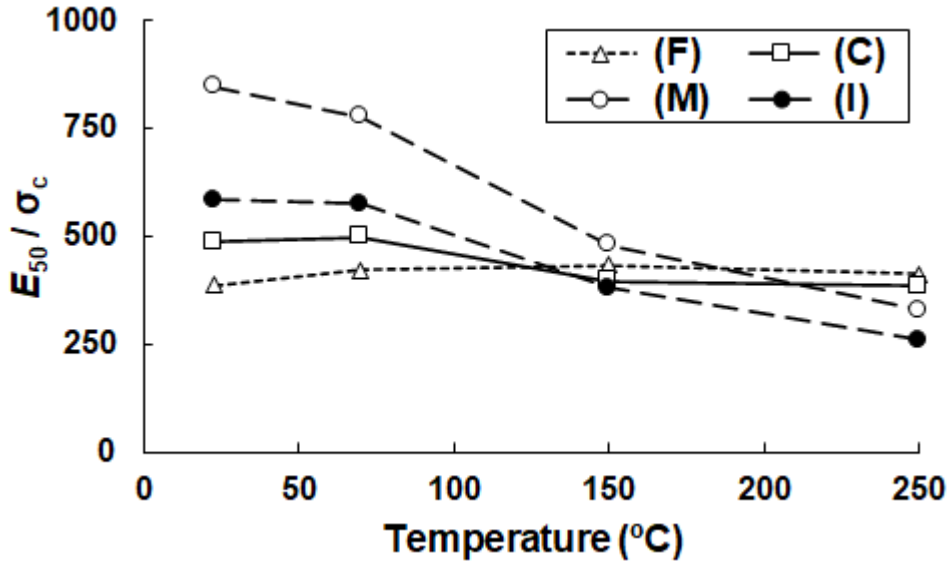

Figure IV-13. Variation of the E_{50}/σ_c ratio with temperature.

The Floresta sandstone (F) and the Moleanos limestone (C) show an approximately constant ratio with temperature. Thus, the variation of the Young's modulus and the compressive strength is proportional as temperature increases. However, the Macael marble (M) and the Carrara marble (I) display a significant reduction of E_{50}/σ_c with temperature.

This involves a relatively higher decrease of E_{50} with temperature compared to the decrease of σ_c. These conclusions are consistent with the stress-strain curves shown in *Figure IV-10*. In fact, the observed strains for 50% of the compressive strength are roughly constant in the case of the Floresta sandstone and the Moleanos limestone, which could explain the slight variations of E_{50}/σ_c with temperature. However, in the case of the Macael marble and the Carrara marble, those same strains corresponding to 50% of the compressive strength increase with temperature. Therefore, it could be concluded that E_{50}/σ_c decreases as temperature gets higher because of the non-linearities of these rocks.

The same results depicted in *Figure IV-13* are also represented numerically in *Table IV-13*. The indicated values are calculated from the ratio between the mean Young's modulus and compressive strength values collected, respectively, in *Table IV-12* and *Table IV-7*.

Table IV-13. Relation between Young's modulus and compressive strength (E_{50}/σ_c) at different temperature.

	(F)	(C)	(M)	(I)
E_{50}/σ_c (23ºC)	387.0	487.6	847.4	584.1
E_{50}/σ_c (70ºC)	422.9	499.6	778.7	576.3
E_{50}/σ_c (150ºC)	432.9	396.6	480.5	380.6
E_{50}/σ_c (250ºC)	413.1	385.9	329.1	260.2

2.4 FRACTURE TOUGHNESS

From a strict point of view, the fracture toughness corresponds to a cracked situation with a notch radius (ρ) equal to zero. However, when the notch radius is sufficiently small, the notch effect can be considered to be negligible. Here, those SENB samples with the smallest notch radius ($\rho = 0.15$ mm) have been assumed to behave as crack-type defects, and therefore, the obtained K_{IC} values under this configuration are assumed to be equal to those corresponding to a real crack ($\rho = 0$). This hypothesis will be validated when analysing the notch effect.

Thus, the fracture toughness is calculated in this work from the four-point bending tests of those samples with $\rho = 0.15$ mm, as indicated in *Section 3.3* of Chapter III. *Table IV-14* gathers the mean fracture

toughness and standard deviation values obtained from those tests at room temperature, for each of the analysed rocks. Likewise, *Table IV-15* includes the same results obtained by Cicero et al. (2014) from similar four-point bending tests with a slightly different specimen geometry (see *Section 3.3* of Chapter III).

Table IV-14. Mean fracture toughness (K_{IC}) and standard deviation results at room temperature, obtained from four-point bending tests.

	(F)	(C)	(M)	(I)
K_{IC} (MPa · m$^{1/2}$)	0.37 ± 0.06	0.73 ± 0.11	1.14 ± 0.13	0.74 ± 0.13

Table IV-15. Mean fracture toughness (K_{IC}) and standard deviation results at room temperature, obtained from four-point bending tests by Cicero et al. (2014).

	(O)	(G)
K_{IC} (MPa · m$^{1/2}$)	0.72 ± 0.02	1.24 ± 0.09

Additionally to the performance of the four-point bending tests, several three-point bending tests with different loading positions have been carried out on the Moleanos limestone to study mixed mode loading conditions, as indicated in *Section 3.4* of Chapter III. From those three-point bending tests with a centred loading configuration (mode I loading), the fracture toughness can be derived analogously to the four-point bending tests, considering the same hypothesis in which notches with $\rho = 0.15$ mm are assumed to behave as crack-type defects. The individual test results are included in *Appendix A.4*, but for comparison purposes, *Table IV-16* indicates the mean fracture toughness and standard deviation obtained at room temperature for the Moleanos limestone (C).

Table IV-16. Mean fracture toughness (K_{IC}) and standard deviation results of the Moleanos limestone at room temperature, obtained from three-point bending tests.

	(C)
K_{IC} (MPa · m$^{1/2}$) - 3PB	0.77 ± 0.05

Figure IV-14 compares the individual fracture toughness results of the Moleanos limestone obtained from both types of tests, that is, four-point bending (4PB) and three-point bending (3PB) tests. Relatively similar results are obtained from both methods, which indicates consistency between the four-point bending and three-point bending fracture results.

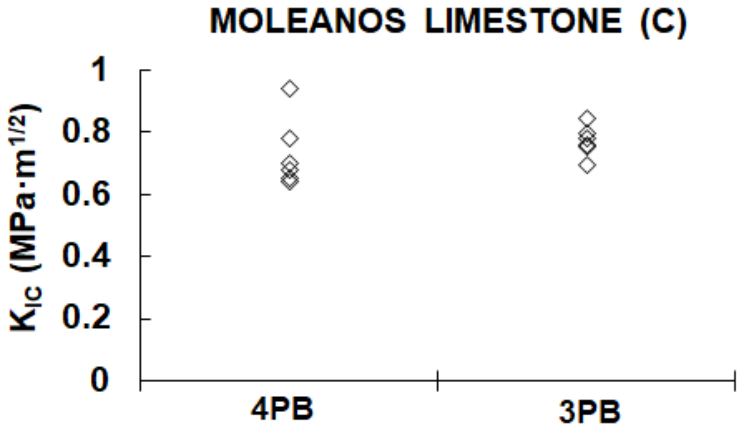

Figure IV-14. Fracture toughness (K_{IC}) results obtained from four-point bending tests (4PB) and three-point bending tests (3PB) at room temperature for the Moleanos limestone.

2.4.1 Influence of temperature on fracture toughness

The fracture toughness (K_{IC}) represents the resistance to propagation of a cracked component, that is, the fracture energy consumption rate required to generate new surfaces along the crack. For this reason, the variation of K_{IC} with temperature is also deeply related to the microstructure of the analysed material, since the required fracture energy for the creation of new surfaces is reduced in the presence of thermally induced microcracks, which facilitate crack propagation especially under mode I loading conditions (opening case). The opposite situation may also occur, as the fracture toughness could increase with the closure of pores or pre-existing microcracks, similarly to the case of the tensile strength. Both situations are observed in *Figure IV-15*, where the variation with temperature of the mean fracture toughness is represented for each of the studied rocks.

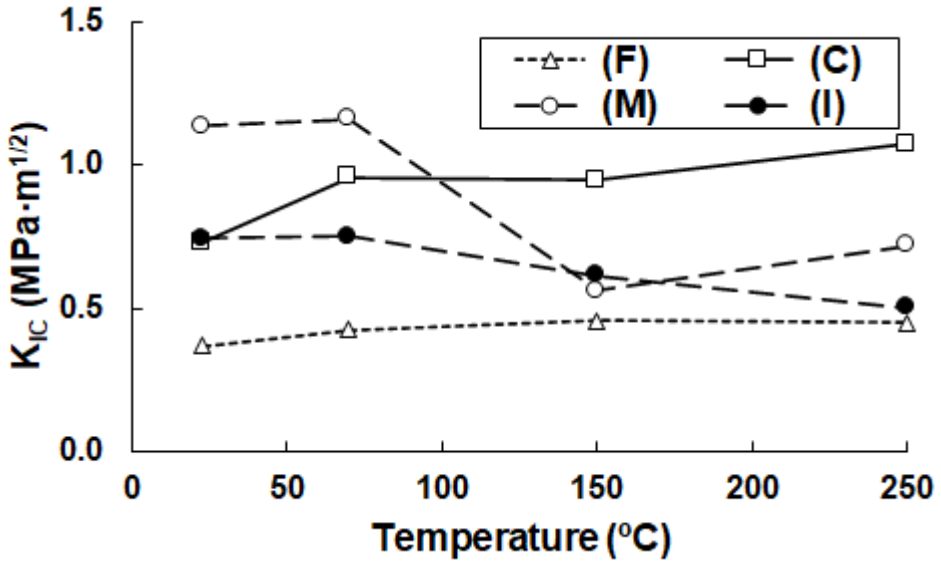

Figure IV-15. Variation of the fracture toughness (K_{IC}) with temperature based on the four-point bending test (with ρ = 0.15 mm) results.

Both the Floresta sandstone and the Moleanos limestone (C) show a continuous increment of the fracture toughness from the onset of the temperature growth, although in relative terms, the observed increase is somewhat less pronounced in the sandstone (F). As in the case of the tensile strength, this increasing tendency should be limited by a critical temperature. However, the temperature after which the fracture toughness decreases for these particular rocks seems to be beyond the studied range of temperatures. On the other hand, both marbles show no significant variation of K_{IC} in the increment step up to 70ºC. Then, an important drop of the fracture toughness is observed. The comments on the reasons explaining the observed tendencies in the tensile strength (*Section 2.1.1*) with temperature are also applicable to the fracture toughness.

Table IV-17. Mean fracture toughness (K_{IC}) and standard deviation results at different temperatures. Units in MPa · m$^{1/2}$.

TEMP.	(F)	(C)	(M)	(I)
23ºC	0.37 ± 0.06	0.73 ± 0.11	1.14 ± 0.13	0.74 ± 0.13
70ºC	0.43 ± 0.07	0.96 ± 0.06	1.16 ± 0.24	0.75 ± 0.14
150ºC	0.46 ± 0.08	0.95 ± 0.11	0.57 ± 0.07	0.62 ± 0.08
250ºC	0.45 ± 0.08	1.07 ± 0.17	0.72 ± 0.12	0.50 ± 0.17

Table IV-17 gathers the mean fracture toughness values depicted in *Figure IV-15* and the standard deviations for each of the considered rocks and temperatures, obtained from the four-point bending tests with the smallest notch radius ($\rho = 0.15$ mm). Likewise, *Table IV-18* presents the mean fracture toughness and standard deviation values of the Moleanos limestone at 23 and 250ºC, obtained in this case from the three-point bending tests with the smallest notch radius and with the centred load. *Appendixes A.3* and *A.4* collect the individual four-point bending and three-point bending test results, respectively.

Table IV-18. Mean fracture toughness (K_{IC}) and standard deviation results of the Moleanos limestone at different temperatures, obtained from three-point bending tests. Units in MPa · $m^{1/2}$.

TEMP.	(C)
23ºC	0.77 ± 0.05
250ºC	1.02 ± 0.15

Figure IV-16 summarises the individual fracture toughness results of the Moleanos limestone. At 250ºC, the obtained fracture toughness with the three-point bending tests is again similar in average terms to that of the four-point bending configuration. Thus, the consistency between both types of methods is reaffirmed.

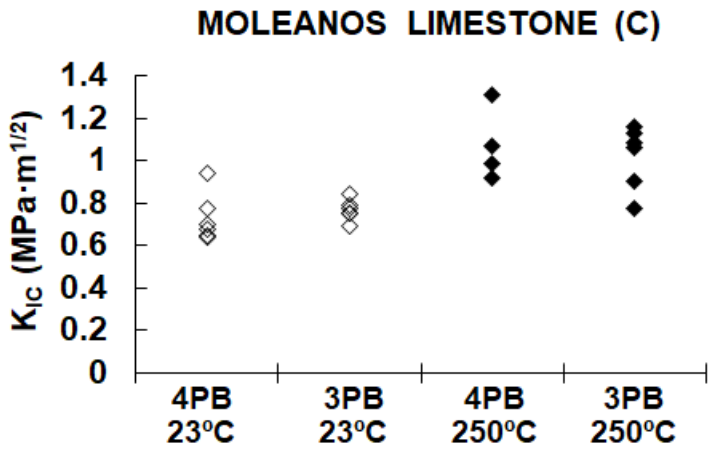

Figure IV-16. Fracture toughness (K_{IC}) results obtained from four-point bending tests (4PB) and three-point bending tests (3PB) at 23ºC and 250ºC for the Moleanos limestone.

2.5 FRACTURE LOAD RESULTS

This section provides the direct fracture results of the four-point bending and three-point bending tests on notched rock specimens. As indicated in *Sections 3.3* and *3.4* of Chapter III, the applied load and the displacements were recorded throughout the tests. Here, this directly acquired information is analysed in detail.

2.5.1 Four-point bending tests

Figure IV-17 gathers the experimentally obtained mean failure loads (F_{EXP}) of the four-point bending tests for each of the analysed rocks, temperatures and notch radii. The horizontal axis represents the square root of the notch radius ($\rho^{0.5}$) for a clearer visualization of the fracture load results of the notched specimens with small notch radii.

In general terms, the failure load seems to increase with temperature in the case of the porous rocks (i.e., Floresta sandstone and Moleanos limestone) and decreases in the case of the non-porous marbles (i.e., Macael marble and Carrara marble). These trends are consistent with those observed when analysing in *Sections 2.1.1* the influence of temperature on the tensile strength of those same rocks. This makes sense since fracture under four-point bending tests is mode I dominated, that is, the notches are subjected to opening and the main failure mechanisms is associated to the tensile strength of the rocks.

Likewise, the resultant failure loads (F_{EXP}) also show a generalised growing trend with the notch radius, confirming the notch effect. This statement is logical, because, as expected from LEFM, notches with large radii develop smaller stress concentrations at the notch tip than those with a small radius. However, this generality is not reflected so clearly in the case of the Carrara marble, probably because this rock does not behave as a linear elastic material (specially at high temperatures), as observed in the stress-strain curves of the uniaxial compression tests performed at different thermal conditions and depicted in *Figure IV-10*.

In absolute terms, the Macael marble presents the highest fracture resistance, followed by the Moleanos limestone, the Carrara marble and, eventually, the Floresta sandstone. The individual test results are collected in *Appendix A.3*, while the mean and standard deviation F_{EXP} values are summarised in *Table IV-19*.

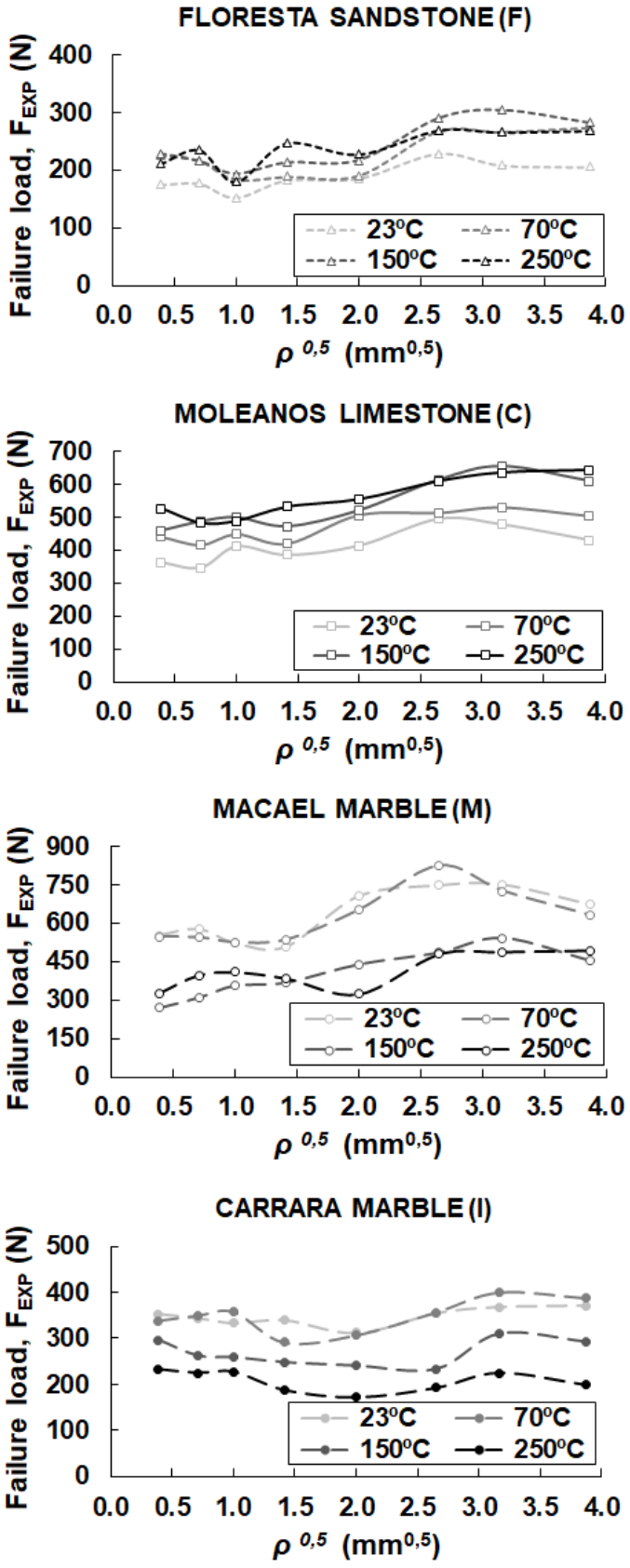

Figure IV-17. Experimentally obtained mean failure loads (F_{EXP}) of the four-point bending tests for each rock, notch radius and temperature.

Table IV-19. Mean failure loads (F_{EXP}) and standard deviation obtained from the four-point bending tests at different temperatures. Units in N.

TEMP.	ρ (mm)	(F)	(C)	(M)	(I)
23ºC	0.15	175 ± 56	363 ± 66	552 ± 79	353 ± 65
	0.50	177 ± 18	347 ± 44	577 ± 53	345 ± 71
	1	153 ± 21	411 ± 50	522 ± 58	334 ± 57
	2	183 ± 24	385 ± 35	507 ± 122	340 ± 36
	4	186 ± 23	414 ± 84	706 ± 101	313 ± 42
	7	229 ± 15	494 ± 46	749 ± 115	355 ± 60
	10	209 ± 14	477 ± 85	751 ± 54	368 ± 64
	15	206 ± 14	430 ± 60	673 ± 179	372 ± 49
70ºC	0.15	226 ± 36	440 ± 24	546 ± 138	339 ± 70
	0.50	217 ± 21	416 ± 68	544 ± 99	349 ± 53
	1	184 ± 34	448 ± 44	525 ± 60	357 ± 72
	2	189 ± 19	420 ± 31	535 ± 112	291 ± 36
	4	191 ± 30	506 ± 38	651 ± 75	308 ± 71
	7	268 ± 25	513 ± 29	824 ± 31	357 ± 39
	10	267 ± 22	529 ± 75	726 ± 81	399 ± 40
	15	274 ± 16	503 ± 59	630 ± 126	387 ± 95
150ºC	0.15	229 ± 47	459 ± 107	269 ± 40	296 ± 38
	0.50	216 ± 23	487 ± 63	309 ± 75	262 ± 58
	1	194 ± 20	499 ± 37	356 ± 64	259 ± 30
	2	213 ± 19	472 ± 29	368 ± 111	248 ± 16
	4	217 ± 10	521 ± 69	439 ± 61	240 ± 25
	7	290 ± 23	613 ± 54	484 ± 101	233 ± 19
	10	305 ± 43	654 ± 87	541 ± 38	310 ± 66
	15	283 ± 37	609 ± 109	453 ± 89	292 ± 35
250ºC	0.15	211 ± 31	527 ± 84	327 ± 52	232 ± 61
	0.50	236 ± 16	482 ± 66	398 ± 121	225 ± 76
	1	180 ± 17	488 ± 43	409 ± 66	227 ± 59
	2	247 ± 24	531 ± 54	386 ± 73	188 ± 32
	4	228 ± 8	554 ± 106	324 ± 57	173 ± 51
	7	269 ± 23	609 ± 52	479 ± 109	193 ± 62
	10	266 ± 23	636 ± 49	488 ± 81	225 ± 44
	15	269 ± 35	643 ± 17	494 ± 100	199 ± 41

In the case of an ideally linear-elastic material subjected to pure mode I loading conditions, the fracture load is expected to increase with the notch radius because the stress concentration at the tip reduces according to LEFM theory. However, when analysing the fracture loads of the studied rocks (see *Table IV-19*), although the general trend indicates an increase of F_{EXP} with the notch radius, significant variations are observed.

Apart from the own variability of rocks that irretrievably produces certain degree of scatter on the fracture load results due to their heterogeneous nature, the actual geometry of the specimens has turned out to be an important factor when comparing the obtained fracture loads. As indicated in *Section 3.3* of Chapter III, each rock sample has been checked and measure individually (the geometry specifications are gathered in *Appendix A.3*) to determine the slight oscillations from the theoretical geometry caused by precision of the cutting processes. Based on the theoretical 180x30x30 mm size SENB specimens with notch lengths (a) of 15 mm regardless the notch radius, the resistant section in the bisector plane of notches is supposed to be 15 mm length. However, according to the real measurements this is not strictly true.

Figure IV-18 compares, as an example, the obtained failure loads of the four-point bending tests (for 23ºC and 250ºC) with the real resistant section length for each of the studied rocks. Each dot corresponds to an individual test and the black solid line indicates the best-fit trend line. As expected, it can be observed at a glance that the failure load increases with the resistant section length in all the studied rocks, although in the Carrara marble the influence is much slighter.

Aiming to determine the extent of the notch effect on the analysed rocks without blurring the fracture results as a consequence of geometric inaccuracies, it is better to represent the results based on the apparent fracture toughness (K_{IN}) instead of the failure load (F_{EXP}). According to *Equation (III-8)* provided in *Section 3.3* of Chapter III, K_{IN} considers the geometry of the notch and the specimen and, therefore, should not be affected by those inaccuracies. Anticipating to the apparent fracture toughness results that will be provided below, *Figure IV-19* shows that, in general terms, K_{IN} is not significantly affected by the length of the resistant section, although the trend line in both marbles at 23ºC is not

completely horizontal probably as a consequence of the relatively high scatter of the results and non-linearities.

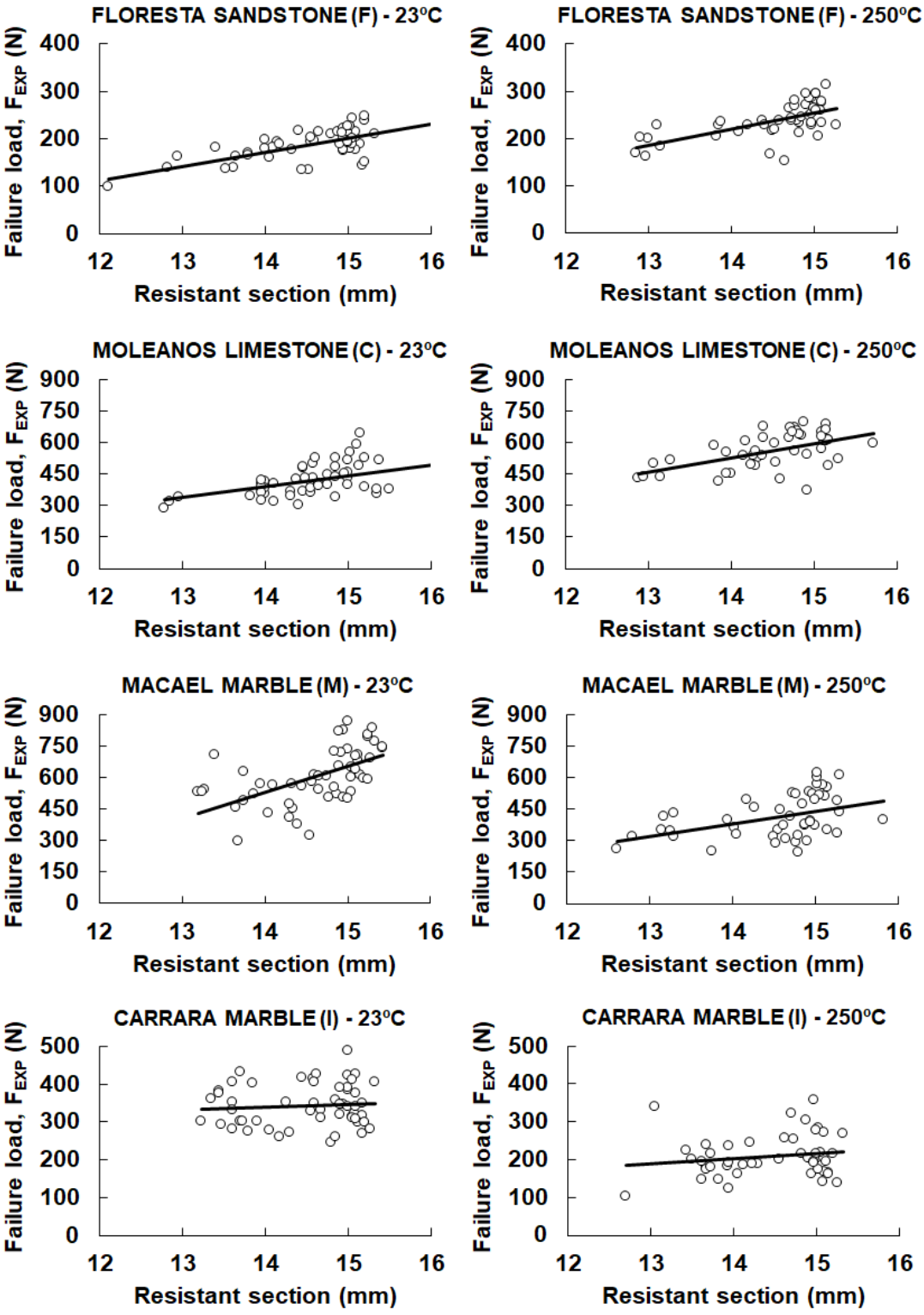

Figure IV-18. Relation between failure load (F_{EXP}) and real resistant section at the notch bisector plane in four-point bending tests.

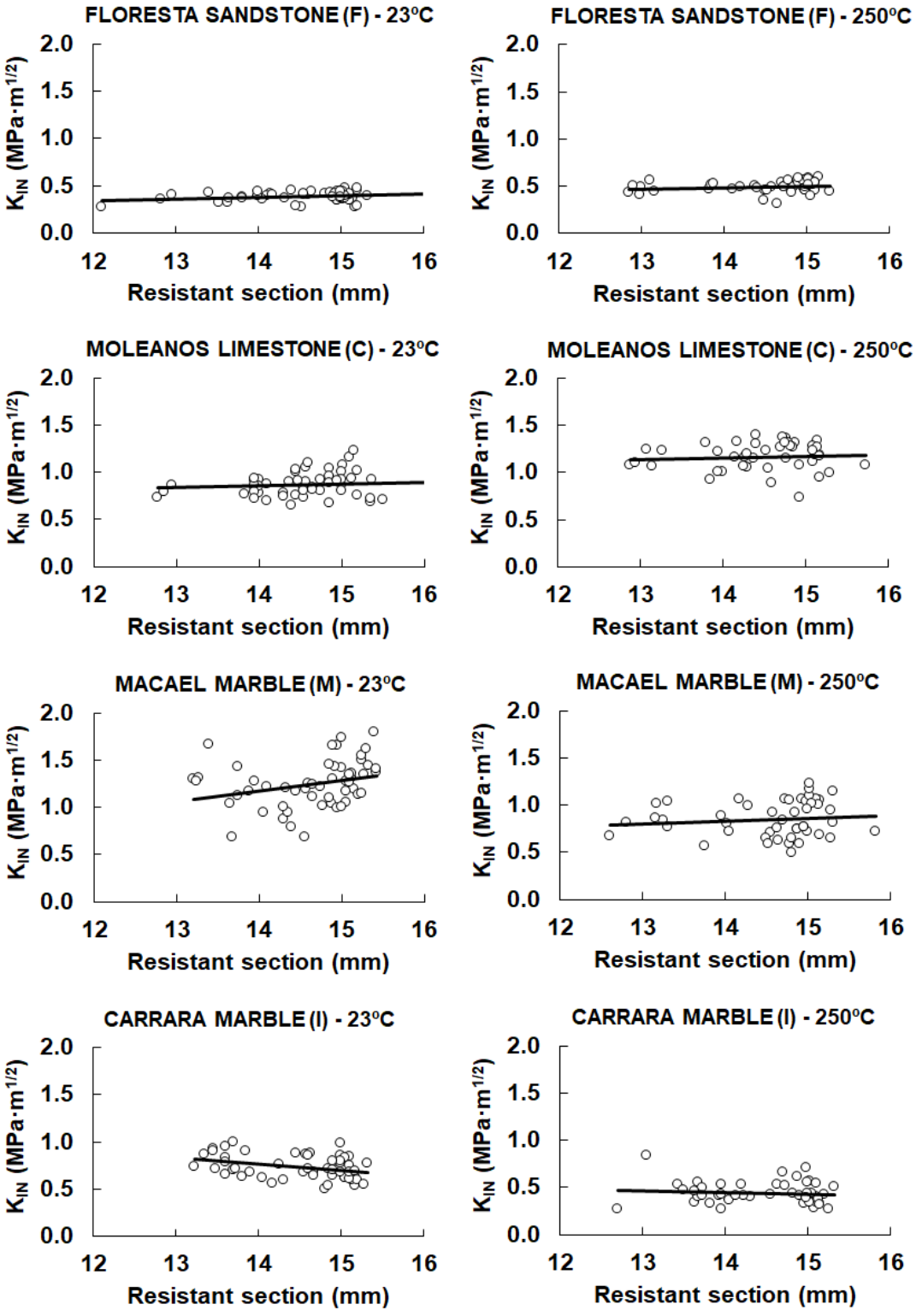

Figure IV-19. Relation between apparent fracture toughness (K_{IN}) and real resistant section at the notch bisector plane in four-point bending tests.

Thus, *Figure IV-19* represents the same individual fracture results as *Figure IV-18* but in terms of the apparent fracture toughness. This

parameter seems to somehow correct the influence of the notch length and specimen geometry and, therefore, the notch effect can be directly interpreted.

Figure IV-20 shows the variation of the apparent fracture toughness (K_{IN}) with the notch radius for each rock and temperature. The horizontal axis is represented as the square root of the notch radius for a better visualization of the fracture results corresponding to the smallest notch radii. The same conclusions derived from *Figure IV-17* are now reaffirmed in *Figure IV-20*. The fracture resistance increases with temperature in the case of the Floresta sandstone and Moleanos limestone at the studied range of temperatures. By contrast, it reduces in the case of the Macael and Carrara marbles. Likewise, a general increasing trend of the fracture resistance is observed when the notch radius increases, except for the Carrara marble in which no clear notch effect is appreciated.

Although curves in *Figure IV-17* and *Figure IV-20* might look similar at first sight, it is important to remark that the influence of resistant section length is corrected in *Figure IV-20* by analysing K_{IN} instead of F_{EXP}. Taking as an example the particular case of the Floresta sandstone at 250ºC, a significant fracture resistance drop is observed for $\rho = 1$ mm in *Figure IV-17*. Comparing the results with those of the apparent fracture toughness (*Figure IV-20*) for the same case, it seems that the mentioned drop for $\rho = 1$ mm was caused by geometric inaccuracies (i.e., smaller resistant section than expected from the theoretical geometry) and is corrected to a certain extent.

It is also observed that the apparent fracture toughness shows an initial roughly horizontal region after which the notch effect becomes more appreciable. This indicates that the previous assumption in which notches with $\rho = 0.15$ mm are supposed to behave as crack-type defects is valid. This issue will be discussed again when interpreting the notch effect according to the TCD.

Finally, *Table IV-20* gathers the mean apparent fracture toughness and standard deviation values obtained from the four-point bending tests for each rock, notch radius and temperature.

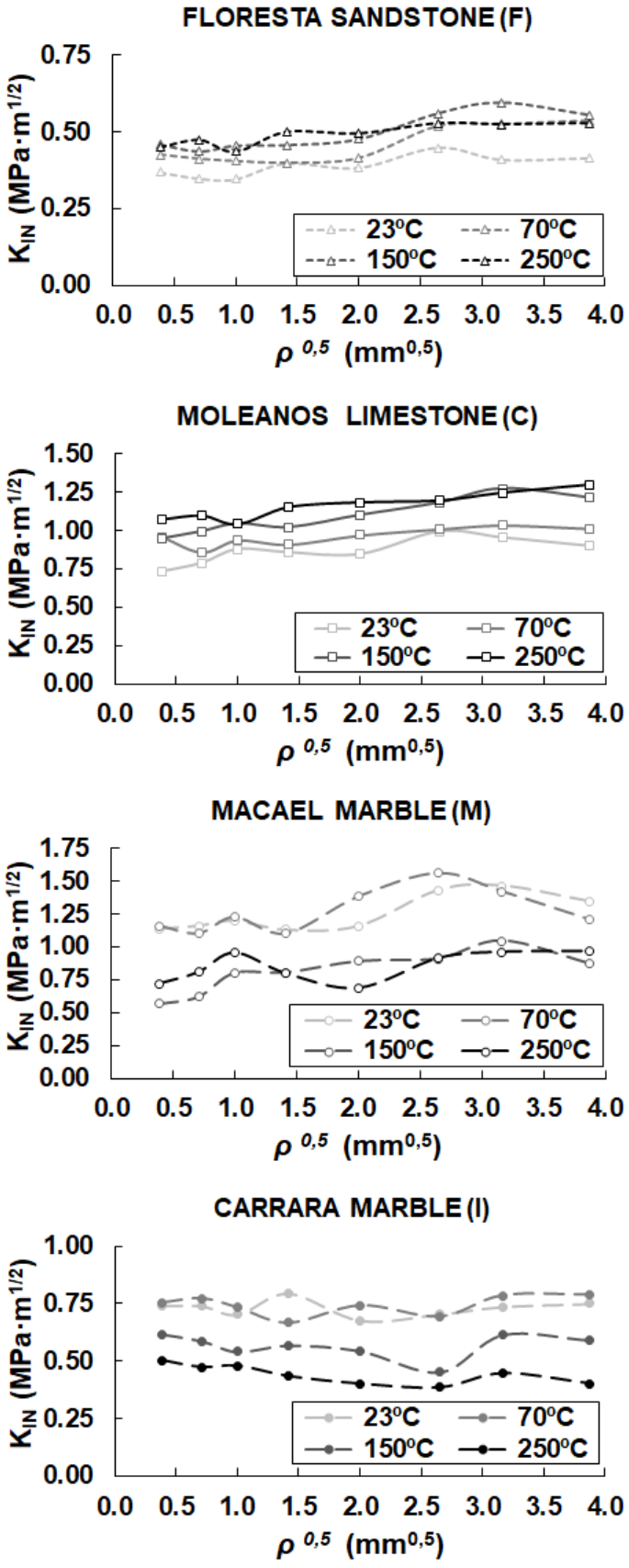

Figure IV-20. Mean apparent fracture toughness (K_{IN}) of the four-point bending tests for each rock, notch radius and temperature.

Table IV-20. Mean apparent fracture toughness (K_{IN}) and standard deviation values obtained from the four-point bending tests at different temperatures. Units in MPa · m$^{1/2}$.

TEMP.	ρ (mm)	(F)	(C)	(M)	(I)
23ºC	0.15	0.37 ± 0.06	0.73 ± 0.11	1.14 ± 0.13	0.74 ± 0.13
	0.50	0.35 ± 0.04	0.79 ± 0.06	1.16 ± 0.10	0.74 ± 0.17
	1	0.35 ± 0.06	0.88 ± 0.09	1.20 ± 0.17	0.70 ± 0.10
	2	0.40 ± 0.03	0.86 ± 0.08	1.13 ± 0.26	0.80 ± 0.11
	4	0.38 ± 0.05	0.84 ± 0.14	1.16 ± 0.28	0.68 ± 0.12
	7	0.45 ± 0.02	0.99 ± 0.08	1.43 ± 0.21	0.71 ± 0.12
	10	0.41 ± 0.03	0.95 ± 0.15	1.46 ± 0.10	0.74 ± 0.13
	15	0.41 ± 0.03	0.90 ± 0.13	1.35 ± 0.37	0.75 ± 0.11
70ºC	0.15	0.43 ± 0.07	0.96 ± 0.05	1.16 ± 0.24	0.75 ± 0.14
	0.50	0.41 ± 0.04	0.86 ± 0.07	1.10 ± 0.20	0.77 ± 0.13
	1	0.40 ± 0.06	0.94 ± 0.09	1.22 ± 0.15	0.73 ± 0.13
	2	0.40 ± 0.04	0.91 ± 0.07	1.10 ± 0.22	0.67 ± 0.08
	4	0.41 ± 0.07	0.97 ± 0.08	1.38 ± 0.14	0.74 ± 0.17
	7	0.52 ± 0.04	1.01 ± 0.07	1.56 ± 0.07	0.69 ± 0.08
	10	0.53 ± 0.05	1.03 ± 0.14	1.42 ± 0.16	0.78 ± 0.06
	15	0.54 ± 0.03	1.01 ± 0.10	1.21 ± 0.23	0.79 ± 0.19
150ºC	0.15	0.46 ± 0.08	0.95 ± 0.10	0.56 ± 0.07	0.62 ± 0.08
	0.50	0.44 ± 0.05	0.99 ± 0.05	0.62 ± 0.15	0.59 ± 0.11
	1	0.45 ± 0.05	1.05 ± 0.08	0.80 ± 0.15	0.54 ± 0.08
	2	0.46 ± 0.03	1.02 ± 0.06	0.80 ± 0.23	0.57 ± 0.04
	4	0.48 ± 0.02	1.10 ± 0.12	0.89 ± 0.13	0.54 ± 0.06
	7	0.56 ± 0.04	1.18 ± 0.08	0.91 ± 0.19	0.45 ± 0.05
	10	0.60 ± 0.08	1.27 ± 0.14	1.04 ± 0.07	0.61 ± 0.13
	15	0.56 ± 0.07	1.21 ± 0.23	0.87 ± 0.17	0.59 ± 0.07
250ºC	0.15	0.45 ± 0.08	1.07 ± 0.17	0.72 ± 0.12	0.50 ± 0.17
	0.50	0.47 ± 0.04	1.10 ± 0.10	0.81 ± 0.25	0.47 ± 0.15
	1	0.44 ± 0.06	1.04 ± 0.09	0.95 ± 0.12	0.48 ± 0.11
	2	0.50 ± 0.05	1.15 ± 0.11	0.80 ± 0.15	0.43 ± 0.08
	4	0.50 ± 0.02	1.18 ± 0.23	0.69 ± 0.09	0.40 ± 0.11
	7	0.53 ± 0.04	1.20 ± 0.10	0.91 ± 0.20	0.38 ± 0.13
	10	0.52 ± 0.04	1.25 ± 0.08	0.96 ± 0.16	0.45 ± 0.09
	15	0.53 ± 0.07	1.30 ± 0.04	0.97 ± 0.20	0.40 ± 0.08

Table IV-21. Mean apparent fracture toughness (K_{IN}) and standard deviation values obtained by Cicero et al. (2014) from four-point bending tests. Units in $MPa \cdot m^{1/2}$.

TEMP.	ρ (mm)	(O)	(G)
23ºC	0.15	0.72 ± 0.02	1.24 ± 0.09
	0.50	0.76 ± 0.05	1.24 ± 0.10
	1	0.78 ± 0.03	1.17 ± 0.10
	2	0.77 ± 0.02	1.26 ± 0.13
	4	0.81 ± 0.14	1.23 ± 0.13
	7	0.91 ± 0.04	1.38 ± 0.06
	10	0.93 ± 0.05	1.20 ± 0.15

Likewise, *Table IV-21* collects the mean apparent fracture toughness and standard deviation results of the Oolitic limestone (O) and Biotite granite (G) obtained by Cicero et al. (2014) from similar four-point bending tests at room temperature. The notch effect is evident for the Oolitic limestone, while no clear trend is observed for the Biotite granite. These results will be analysed together with those obtained in the performed laboratory campaign.

Finally, *Figure IV-21* displays the load-displacement curves obtained from the four-point bending tests. Each row corresponds to a different rock and, for the sake of simplicity, only some representative results of the specimens with 0.15 mm and 15 mm notch radii have been included in the first and second column, respectively. The solid curves stand for the room temperature case, while the dashed lines correspond to 250ºC. The initial nonlinear part of the curves is bounded to the test procedure, caused by the initial adjustment of the testing device on the specimen. Thus, it should be ignored in terms of deformations, but not in terms of load. Observing the linearity of the curves prior to the peaks, the brittle characteristics of the Floresta sandstone and the Moleanos limestone are evident even at high temperatures up to 250ºC. In the case of the Macael marble, the linear elastic behaviour is also clear generally speaking, although a slight influence of temperature can be observed on the brittleness of the rock at 250ºC. Finally, the Carrara marble shows the highest ductility in relative terms. Even the curves at room temperature are not completely linear (especially close to the peaks), which could explain the lack of the notch effect observed above in this rock.

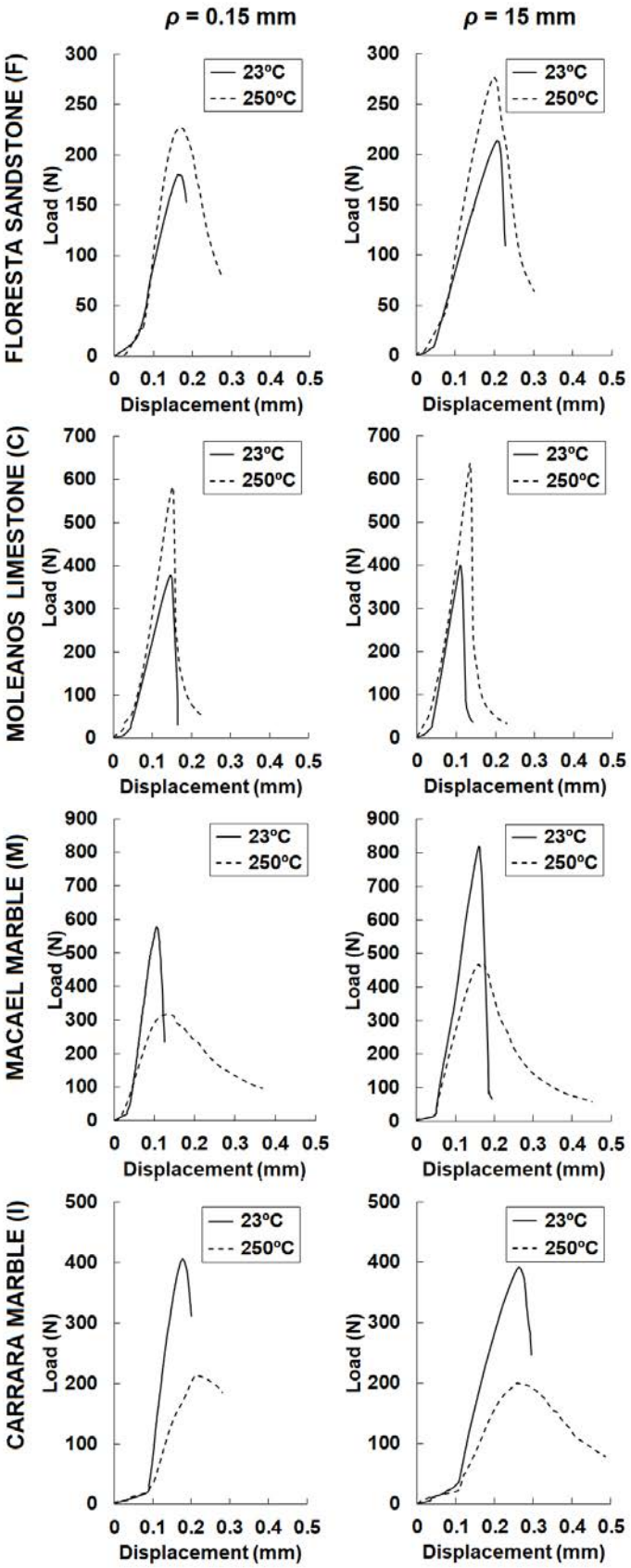

Figure IV-21. Load-displacement curves of the four-point bending tests at different temperatures.

From the interpretation of the load-displacement curves in *Figure IV-21* it can be affirmed that fracture resistance increases with temperature from 23ºC to 250ºC in the Floresta sandstone and the Moleanos limestone, while it drastically decreases in the case of the Macael and Carrara marbles. It is also observed that, as a general rule, larger notch radii develop higher load-bearing capacity. However, this is not accomplished in the case of the Carrara marble as a consequence of the observed non-linear behaviour. Besides, the non-linear behaviour seems to be more significant as temperature and the notch radius increase.

2.5.2 Three-point bending tests

Proceeding in the same way as for the four-point bending tests, the fracture results of the three-point bending tests are presented in this section. As indicated in *Section 3.4* of Chapter III, among the studied rocks, only the Moleanos limestone has been tested under three-point bending configurations, with a variable loading position in order to assess mixed-mode loading conditions, both at room temperature and at 250ºC. Accordingly, *Figure IV-22* displays the mean fracture loads obtained from the three-point bending tests of the Moleanos limestone, for each loading position (i.e., P1, P2, P3 and P4), notch radius and temperature. In parallel, *Table IV-22* collects the mean failure loads and the standard deviation values.

Loading position 1 (P1) stands for the centred load ($m = 0$, see *Section 3.4* of Chapter III), which implies pure mode I loading conditions. Thus, these results are comparable to those of the four-point bending tests that also correspond to mode I. Under this configuration, the notch effect can be directly assessed as before, by means of the apparent fracture toughness variation with the notch radius. However, the notch effect interpretation is not straightforward for the rest loading configurations in which the load is not centred (i.e., P2, P3 and P4). Non-centred loading generates mixed mode I+II loading conditions in which the analytical expression of the apparent fracture toughness (*Equation (III-8)* in the case of three-point bending tests) is no longer valid. For this reason, the notch effect under mixed mode I+II will be addressed when interpreting the results according to the TCD.

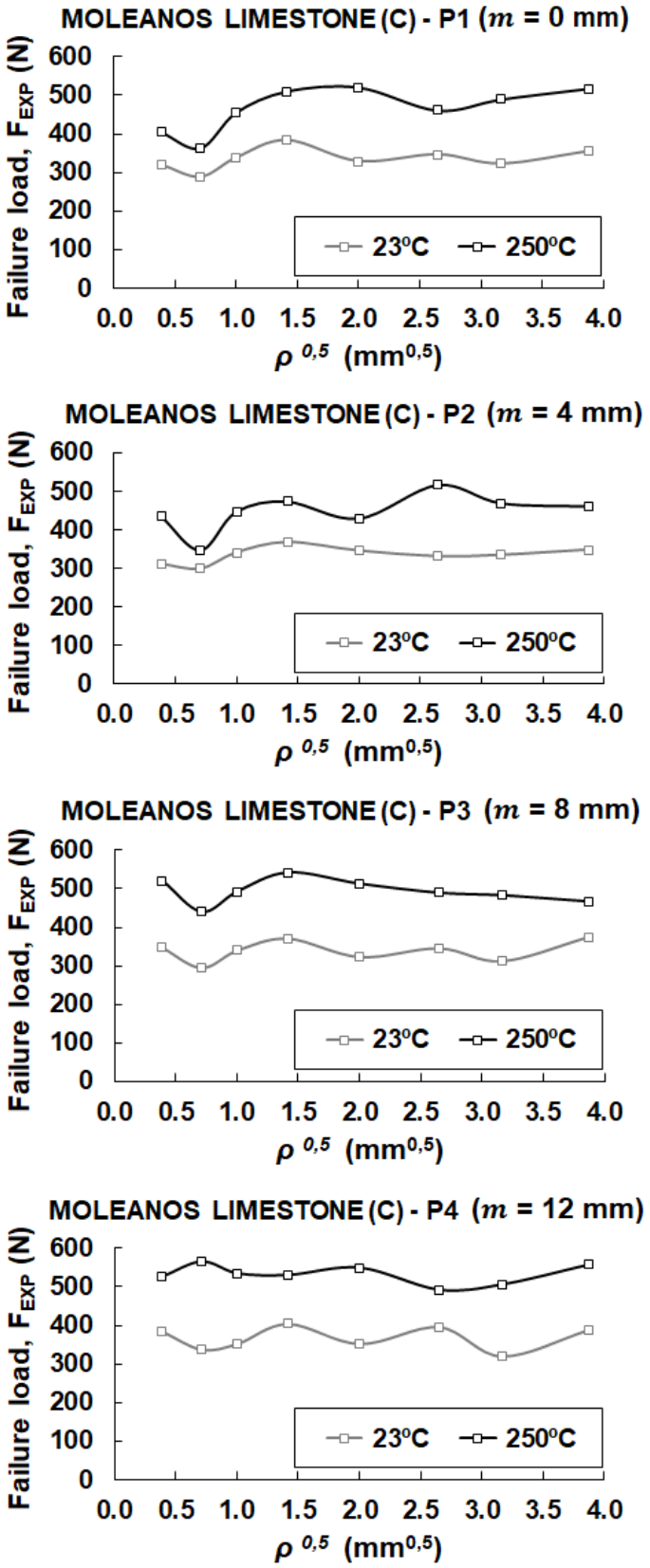

Figure IV-22. Experimentally obtained mean failure loads (F_{EXP}) of the three-point bending tests of the Moleanos limestone for each loading position, notch radius and temperature.

Table IV-22. Mean failure loads (F_{EXP}) and standard deviation obtained from three-point bending tests at different temperatures and loading positions. Units in N.

TEMP.	ρ (mm)	P1	P2	P3	P4
23ºC	0.15	320 ± 29	311 ± 29	347 ± 49	385 ± 22
	0.50	289 ± 21	299 ± 10	295 ± 7	337 ± 35
	1	338 ± 29	341 ± 23	340 ± 52	352 ± 75
	2	383 ± 29	368 ± 21	371 ± 16	405 ± 41
	4	329 ± 32	346 ± 22	323 ± 16	352 ± 24
	7	346 ± 14	332 ± 38	346 ± 44	396 ± 44
	10	323 ± 24	335 ± 29	313 ± 24	319 ± 28
	15	355 ± 8	348 ± 45	375 ± 17	389 ± 7
250ºC	0.15	406 ± 58	435 ± 45	521 ± 44	526 ± 69
	0.50	364 ± 80	346 ± 81	440 ± 50	565 ± 57
	1	456 ± 72	447 ± 49	493 ± 27	535 ± 36
	2	511 ± 43	474 ± 45	542 ± 95	530 ± 37
	4	521 ± 84	429 ± 126	513 ± 53	549 ± 38
	7	461 ± 60	517 ± 71	489 ± 86	492 ± 16
	10	490 ± 100	470 ± 79	482 ± 70	506 ± 88
	15	518 ± 72	461 ± 67	467 ± 69	557 ± 121

The results are consistent with those obtained for the Moleanos limestone from the four-point bending tests. The fracture resistance shows a clear increasing trend from 23ºC to 250ºC regardless the loading position or, in other words, regardless the mode mixity. The mixicity varies not only with the loading position, but also with the notch radius.

The obtained results are again influenced by the actual geometry of the specimens as observed in *Figure IV-23* for each temperature and loading position. Analogously to the four-point bending test results depicted in *Figure IV-18*, each dot in *Figure IV-23* represents an individual three-point bending test. It is remarkable the relatively higher scatter of the results obtained in those tests performed at 250ºC. Despite this, the trend lines show in all cases a clear increase of the failure load as the resistant section increases.

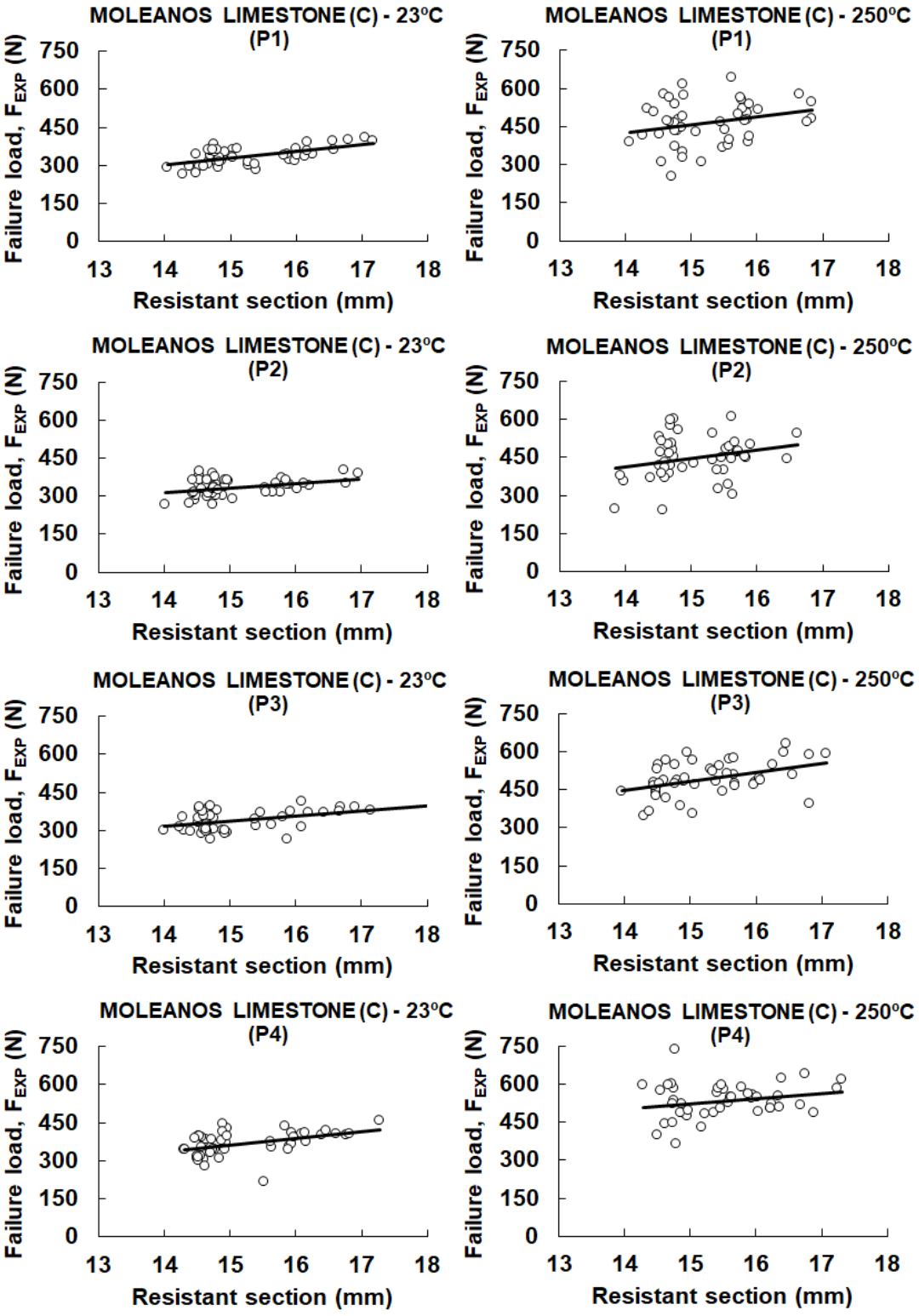

Figure IV-23. Relation between failure load (F_{EXP}) and real resistant section at the notch bisector plane in three-point bending tests.

In those three-point bending tests with the centred load (P1), the influence of the geometric inaccuracies can be again corrected by using

the actual notch and specimen dimensions when calculating the apparent fracture toughness with the analytical expression (*Equation (III-8)* in the particular case of three-point bending tests). *Figure IV-24* shows the resultant apparent fracture toughness values against the resistant section and, although the observed trend lines are not strictly horizontal (especially in those tests at 250ºC with a relatively high scatter of the results), the influence of the geometric inaccuracies is somehow mitigated.

By contrast, under mixed mode loading conditions the analytical expression cannot be applied. Consequently, the actual geometric measurements gathered in *Appendix A.4* will be considered in the numerical models when performing mixed mode I+II fracture assessments in *Section 3*.

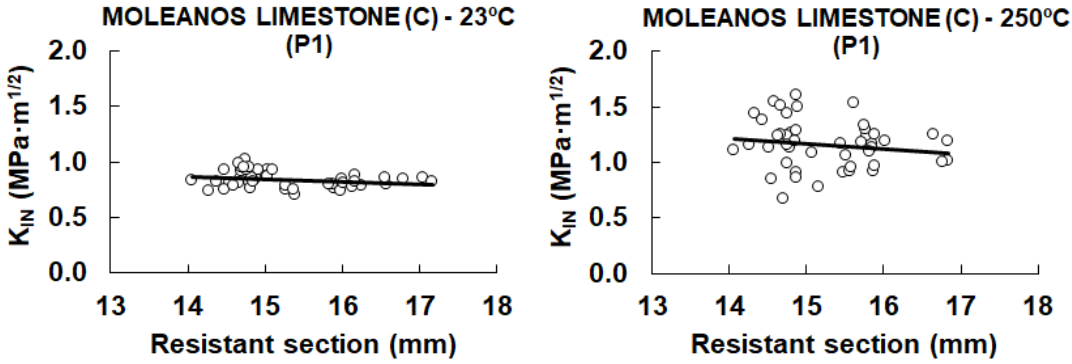

Figure IV-24. Relation between apparent fracture toughness (K_{IN}) and real resistant section at the notch bisector plane in three-point bending tests.

Focusing on the three-point bending tests with centred loads (i.e., pure mode I loading conditions), *Figure IV-25* presents the mean apparent fracture toughness (K_{IN}) results against notch radii, both at 23ºC and 250ºC. Comparing this plot with that of the mean failure load (F_{EXP}) depicted in *Figure IV-22* for the Moleanos limestone subjected to three-point loading (P1), it is observed that the geometric influence has been corrected. Likewise, the notch effect seems to be clear in *Figure IV-25*, since K_{IN} increases with the notch radius at the two studied temperatures.

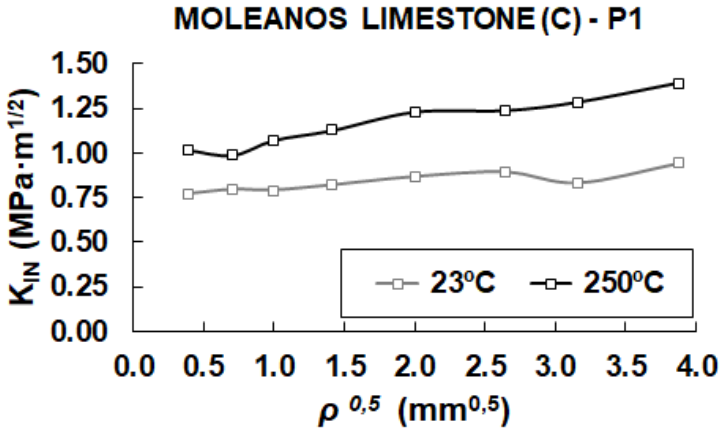

Figure IV-25. Mean apparent fracture toughness (K_{IN}) of three-point bending tests with centred load (P1) for each notch radius and temperature.

The numerical values of the mean apparent fracture toughness results are collected, together with the standard deviation values, in *Table IV-23*. The individual results are, in turn, available in *Appendix A.4*.

Table IV-23. Mean apparent fracture toughness (K_{IN}) and standard deviation values obtained from three-point bending tests with centred load at different temperatures. Units in MPa · m$^{1/2}$.

TEMP.	ρ (mm)	P1
23ºC	0.15	0.77 ± 0.05
	0.50	0.80 ± 0.04
	1	0.79 ± 0.05
	2	0.82 ± 0.03
	4	0.87 ± 0.09
	7	0.90 ± 0.03
	10	0.83 ± 0.05
	15	0.94 ± 0.02
250ºC	0.15	1.02 ± 0.15
	0.50	0.99 ± 0.22
	1	1.07 ± 0.16
	2	1.13 ± 0.10
	4	1.23 ± 0.20
	7	1.24 ± 0.17
	10	1.29 ± 0.25
	15	1.39 ± 0.19

All these apparent fracture toughness results corresponding to mode I loading conditions can be compared with those of the four-point bending tests. *Figure IV-26* displays, together in the same plot, the K_{IN} values for each notch radius at 23ºC and 250ºC, for both three-point bending tests with centred load and four-point bending tests. It is directly observed that both methods provide a very good agreement at the two considered temperatures.

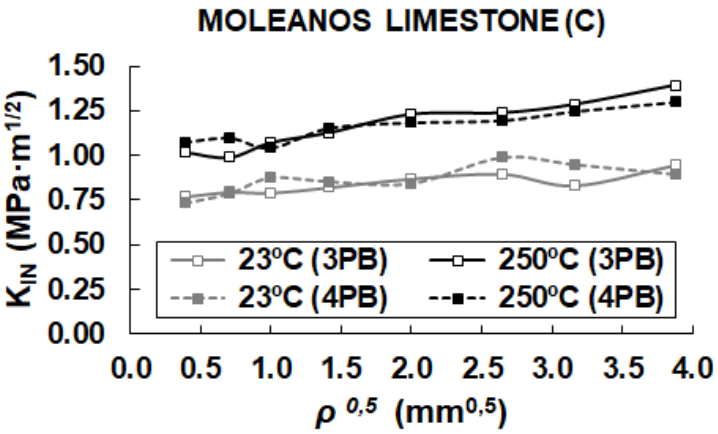

Figure IV-26. Comparison between mean apparent fracture toughness (K_{IN}) results of the Moleanos limestone obtained from three-point bending (3PB) tests with centred load (P1) and four-point bending tests, both at 23ºC and 250ºC.

Finally, some representative load-displacement curves of the three-point bending tests are provided in *Figure IV-27*. Each row corresponds to a particular notch radius (ρ = 0.15, 2, 7 and 15 mm), while each column corresponds to the two extreme loading positions, namely m = 0 (P1) and 12 mm (P4). The solid and dashed curves stand for room temperature and 250ºC results, respectively. The initial non-linear part of the curves that is observed in some cases up to approximately a load of 20 N is associated to the test procedure itself, caused by the initial adjustment of the testing device on the specimen. Consequently, this region should be ignored in terms of deformation but not in terms of load. In general, the tested Moleanos limestone shows a linear elastic behaviour up to the peaks, revealing mostly brittle characteristics even at 250ºC. These load-displacement curves will be commented in more detail in *Section 3*.

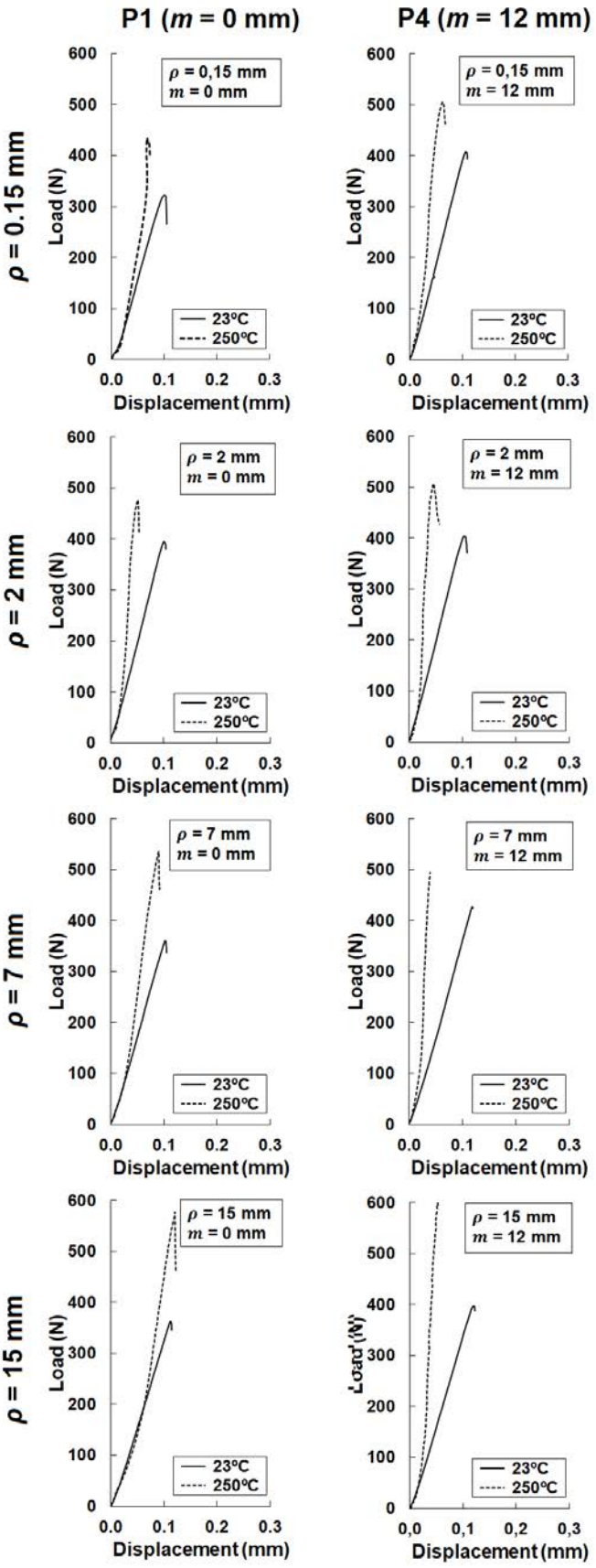

Figure IV-27. Load-displacement curves of the three-point bending tests at different temperatures and loading positions.

2.6 THERMAL EXPANSION

As emphasised in previous comments, the differential thermal expansion of adjacent grains and their constraint conditions (i.e., the presence or lack of internal space such as pores for grain expansion) can define to a great extent the thermal damage and the mechanical behaviour of rocks under different thermal conditions. For this reason, the thermal expansion curves of the four analysed rocks have been studied here in an attempt to distinguish different expansion patterns. To this end, as indicated in *Section 3.5* of Chapter III, the thermal expansion has been measured using two different methods. First, the longitudinal deformation of prismatic (180x30x30 mm) rock samples has been checked at different temperature steps by means of a digital comparator. Likewise, the longitudinal and diametric strains of cylindrical (50 mm diameter and 150 mm length) rock samples have been measured using strain gauges.

Figure IV-28 compares the obtained thermal expansion measurements (in percentage) for each of the analysed rocks and methods. In all the cases, the noted expansion readings are relative to the prior temperature steps. Analysing the curves, it is complicated to obtain clear and generalizable conclusions. However, several observations are worth being highlighted. Firstly, the two measurement methods offer similar results in the case of the Floresta sandstone and the Macael marble, but present significant differences in the Moleanos limestone and the Carrara marble. Secondly, both marbles, specially Macael marble, reveal the largest scatter of the results, regardless of the measuring method. On average, the Floresta sandstone shows a thermal expansion coefficient (α_{temp}) of $8.2 \cdot 10^{-6}$ ºC^{-1}, no matter either strain gauges or digital comparator are used for the measurements. In the case of the Moleanos limestone, α_{temp} varies from $6.8 \cdot 10^{-6}$ ºC^{-1} for strain gauge measurements to $7.4 \cdot 10^{-6}$ ºC^{-1} for digital comparator measurements. The Macael marble presents a significantly higher scatter of the thermal expansion curves regardless the method used, α_{temp} oscillating from $1.6 \cdot 10^{-5}$ ºC^{-1} to $7.7 \cdot 10^{-6}$ ºC^{-1}. Finally, the Carrara marble shows a higher thermal expansion coefficient when digital comparator is used, of approximately $1.7 \cdot 10^{-5}$ ºC^{-1}, comparing with strain gauge measurements that provide a value of $9.8 \cdot 10^{-6}$ ºC^{-1}.

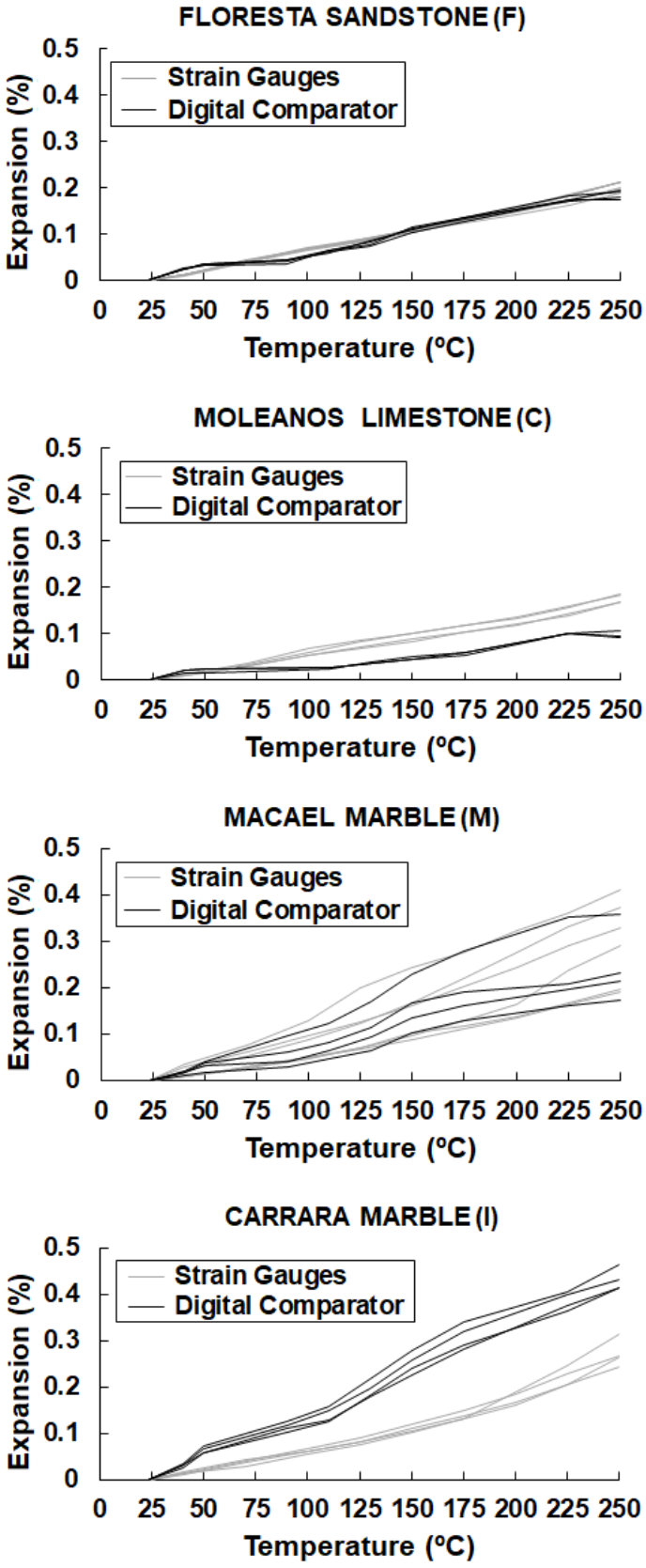

Figure IV-28. Thermal expansion measurements of the analysed rocks using strain gauges and a digital comparator.

It can also be concluded that the thermal expansion coefficient in the marbles is much higher than in the Floresta sandstone and the Moleanos limestone, which could facilitate the appearance of microcracks and, thus, reduce their resistance when temperature increases. It is important to take into account that the expansion values are given as a percentage. However, the digital comparator readings correspond to the elongation of the whole specimen in the longitudinal dimension (i.e., 180 mm), while the strain gauges are measuring deformations within a representative surface covered by the electrical resistor, which is 6 mm long, more than ten times larger than the mean grain size of the rocks, as required by standards (EN 14580:2006).

Analysing the digital comparator curves of the Floresta sandstone and the Moleanos limestone, a quasi-horizontal zone can be distinguished in the slopes from approximately 50ºC to around 90ºC in the case of the sandstone and 110ºC in the limestone. These regions, which are only appreciated in the porous rocks, could entail no significant external expansion of the samples. Thus, they could be governed by the inner expansion where the pre-existing pores, cavities or microcracks get closed. This phenomenon is obviously limited and after reaching a critical temperature, the mechanism changes and external expansion seems to be dominant. By contrast, both marbles show significant external expansion from the onset of heating, which agrees with their null porosity and the damage induced by differential thermal expansion. However, the mentioned horizontal region captured by the digital comparator is not appreciable when using strain gauges. This could be explained by the size of the measured expansion surface which, in the case of the strain gauges, is limited to the electrical resistor as stated above. In any case, more robust assertions would require further research focused on microstructural thermal changes, which is beyond the scope of this work.

3 APPLICATION OF THE TCD

The fracture results of the four-point bending and the three-point bending tests, which are addressed in *Sections 2.5.1* and *2.5.2,* are interpreted in this section using the TCD. First, mode I loading

conditions are studied and then, the focus is placed on the application of the TCD under mixed mode I+II loading conditions.

3.1 MODE I ANALYSIS

As stated above, the performed four-point bending tests and three-point bending tests with the centred load fulfil pure mode I loading conditions (opening case), as no shear stresses arise in the theoretical fracture plane (see *Figure II-31*).

The application of both the PM and the LM for those notched samples subjected to pure mode I loading conditions is relatively easy, since the stresses are directly analysed along the bisector plane of the notch. The stress field can be obtained either analytically, using existing analytical expressions for mode I loading conditions, or numerically. In fact, the analytical solutions for the apparent fracture toughness proposed by the PM in *Equation (II-75)* and by the LM in *Equation (II-80)* are based on the stress distribution function proposed by Creager & Paris (1967) and defined in *Equation (II-72)*.

Table IV-24. Mean critical distance (L) and standard deviation results at different temperatures calculated from Equation (II-70). Units in mm.

TEMP.	(F)	(C)	(M)	(I)
23ºC	5.82 ± 2.42	4.02 ± 2.10	4.20 ± 0.90	2.19 ± 0.79
70ºC	5.66 ± 1.84	4.43 ± 0.76	8.00 ± 3.26	3.59 ± 1.33
150ºC	7.52 ± 3.72	3.19 ± 0.83	4.33 ± 1.23	3.99 ± 1.36
250ºC	5.73 ± 2.81	4.77 ± 1.46	8.62 ± 3.16	3.65 ± 2.83

The analytical solutions of the apparent fracture toughness (K_{IN}) provided by the TCD depend on the fracture toughness (K_{IC}), already defined in *Section 2.4*, the notch radius (ρ), and the critical distance (L). The critical distance can be calculated applying *Equation (II-70)*, using the tensile strength (σ_u) and fracture toughness (K_{IC}) values determined in *Sections 2.1* and *2.4*. *Table IV-24* collects the different critical distance results for each of the analysed rocks and temperatures, indicating both the mean values and the corresponding standard deviation calculated from all the possible combinations of σ_u and K_{IC}. In particular, the values in *Table IV-24* are calculated using the K_{IC} values

obtained from the four-point bending tests. In any case and as observed in *Figure IV-16*, really similar K_{IC} values of the Moleanos limestone were obtained from the three-point bending tests.

Analysing the mean values of the critical distance shown in *Table IV-24* for the different rocks, the values of L vary with temperature from 5.66 to 7.52 mm in the case of the Floresta sandstone, from 3.19 to 4.77 mm in the Moleanos limestone, from 4.20 to 8.62 mm in the Macael marble and from 2.19 to 3.99 mm in the Carrara marble. Aliha & Ayatollahi (2008, 2013) gathered some data on the FPZ (which is related to the critical distance as indicated in *Section 2.4* of Chapter II) for a variety of similar rocks. They reported the cases of three different marbles with L values varying from 1.20 to 6.40 mm, two types of limestones with L = 4.60 - 10.40 mm and a sandstone with L = 2.90 mm, among others. The order of magnitude is reasonably in the same range in all the cases and the differences are caused by the different petrographic properties.

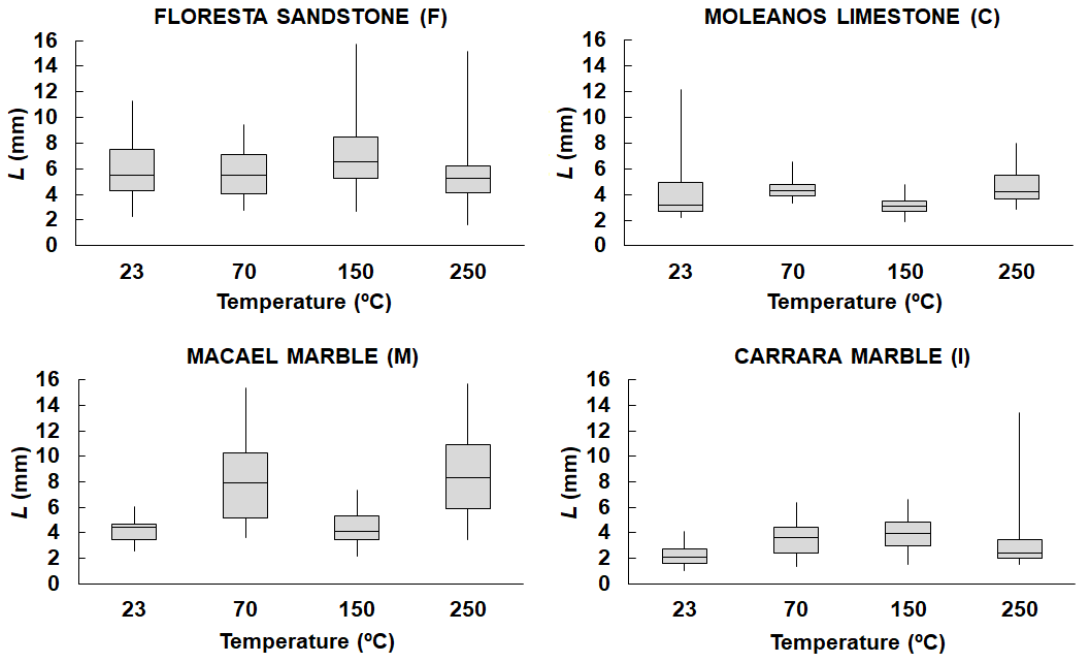

Figure IV-29. Variation of the critical distance (L) with temperature for each rock.

Likewise, *Figure IV-29* displays the variation of the critical distance (L) with temperature for each rock. In this case, the figure is composed

of box-and-whisker plots representing, from top to bottom, the maximum value, the third quartile, the median, the first quartile and the minimum value of the obtained results for L. These statistical values are derived, as in the case of the values in *Table IV-24*, from the calculation of L (*Equation (II-70)*) with all the possible combinations of the individual test results of σ_u and K_{IC}. At first sight, there are no clear tendencies of the variation of L with temperature according to the plots in *Figure IV-29*.

3.1.1 Interpretation of the notch effect

The notch effect can be interpreted from the mean apparent fracture toughness (K_{IN}) results depicted in *Figure IV-20* and *Figure IV-25*, corresponding, respectively, to the four-point bending tests and three-point bending tests (with centred load) results. Firstly, taking as a basis the four-point bending test results, *Figure IV-30* is constructed. Again, the apparent fracture toughness (K_{IN}) is represented against the square root of the notch radius ($\rho^{1/2}$), but it this case, the dots correspond to the experimental results of every individual test according to *Equation (III-8)*, in which the apparent fracture toughness (K_{IN}) is considered instead of the real fracture toughness (K_{IC}). The dashed lines represent the calculated curves according to the Line Method of the TCD (*Equation (II-80)*), using the mean values of the fracture toughness and the critical distance gathered in *Table IV-17* and *Table IV-24*, respectively. By contrast, the solid lines correspond to the best-fit curves according once again to *Equation (II-80)* of the LM, in which the value of the fracture toughness is fixed leaving the critical distance L as the only free variable.

Secondly, dealing with the three-point bending test results performed on the Moleanos limestone with the centred load, the notch effect is interpreted in the same way, based on *Equation (III-8)* and the Y factor corresponding to the three-point bending configuration (*Equation (II-35)*). Thus, *Figure IV-31* shows the same information as *Figure IV-30*, but for the Moleanos limestone subjected to three-point bending conditions in this case. It is observed that the notch effect assessed either by four-point bending or three-point bending tests show similar results for the Moleanos limestone, as expected from *Figure IV-26*.

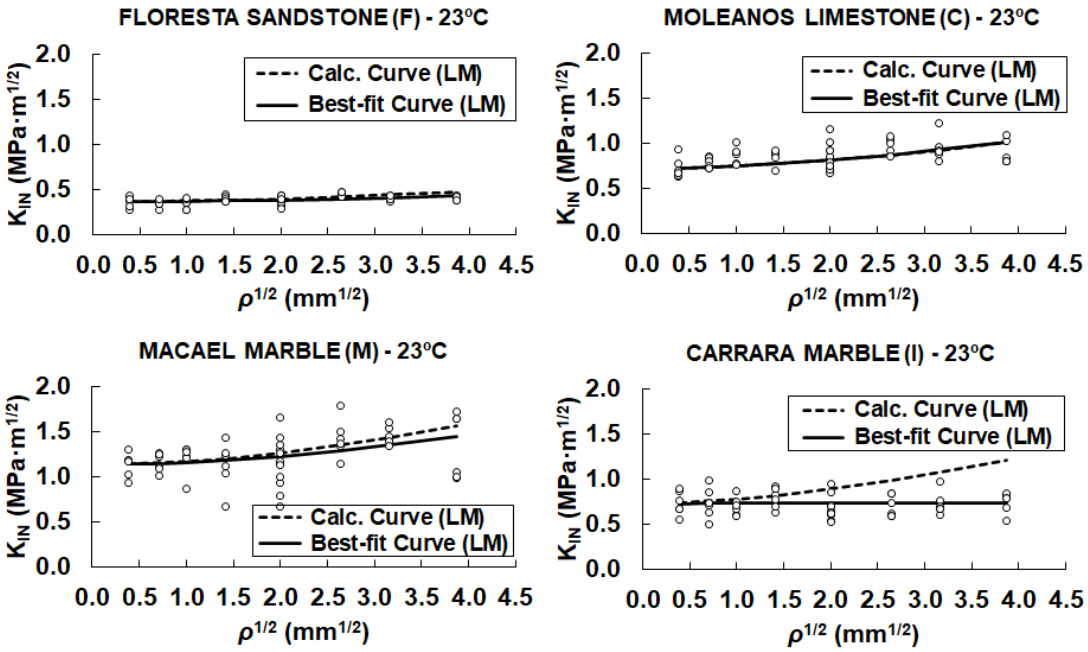

Figure IV-30. Test results of the apparent fracture toughness (K_{IN}) of each rock tested under four-point bending conditions and comparison with the LM of the TCD at room temperature.

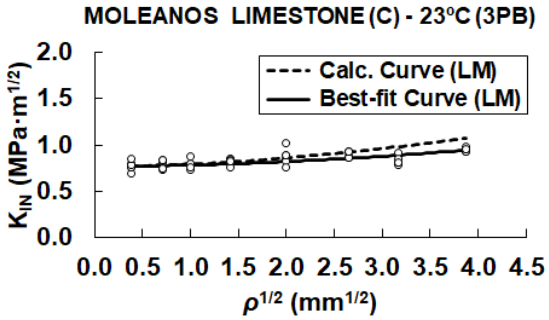

Figure IV-31. Test results of the apparent fracture toughness (K_{IN}) of the Moleanos limestone tested under three-point bending conditions (with centred load) and comparison with the LM of the TCD at room temperature.

Both *Figure IV-30* and *Figure IV-31* show a clear notch effect in all the cases except for the Carrara marble, since the apparent fracture toughness varies with the considered notch radius. According to Taylor (2007), when the notch radius is smaller than the critical distance of a certain material ($\rho/L < 1$), the notch will behave as a crack of the same length ($K_{IN} = K_{IC}$). This means that the notch effect can be neglected and that ordinary fracture mechanics can be used to analyse notches with a radius smaller than a few millimetres in the case of rocks (see

Table IV-24). In the Moleanos limestone, for example, it can be observed that the notch effect is almost negligible up to $\rho \approx 4$ mm, which agrees well with the expression of the normalised notch radius ($\rho/L < 1$).

In general, a reasonable good agreement between TCD predictions and laboratory results is obtained in most of the cases except for the Carrara Marble. This rock does not show a clear trend and the notch effect is not appreciated. Larger radii should be tested to try to identify the notch effect. As observed in *Figure IV-10* and *Figure IV-21*, the Carrara marble does not show a linear behaviour even at room temperature, which explains the bad agreement between the best-fit and calculated curves in *Figure IV-30* that are based on LEFM.

For the sake of clarity, the results corresponding to the Point Method (*Equation (II-75)*) of the TCD are not included in *Figure IV-30* and *Figure IV-31* but have been collected in *Appendix B*. In any case, *Table IV-25* collects the mean values of the critical distances obtained from the direct calculation using *Equation (II-70)*, and from the best-fit curves for both the Point Method (PM) and the Line Method (LM), keeping the fracture toughness as a fixed variable (*Table IV-17*).

Table IV-25. Summary of the mean critical distance values obtained at room temperature.

	(F)	(C)	(C2)*	(M)	(I)
Calculated L (mm)	5.82	4.02	3.97	4.20	2.19
Best-fit L (mm) - PM	3.66	2.29	3.40	2.85	8.62
Best-fit L (mm) - LM	9.94	3.96	7.41	6.02	-

*From Moleanos limestone under three-point bending (*Figure IV-31*).

As a general rule, the adjustment between calculated and best-fit curves becomes less accurate as the notch radius gets larger. This is because the range of application of *Equation (II-80)* corresponding to the LM (or *Equations (II-75)* in the case of the PM) is limited by the stress distribution function of Creager & Paris (1967), which is theoretically only valid for long and narrow notches. However, despite this limitation, the results have proved to be reasonable even when this hypothesis is not totally fulfilled. This inaccuracy is assumed to be the

main factor responsible for the differences between the calculated and best-fit values of L (*Table IV-25*). In any case, consequences due to moderate variations in L are rather limited, since this variable is square rooted both in *Equations (II-75)* (PM) and *(II-80)* (LM).

3.1.2 Influence of temperature on the notch effect

The same analysis is performed now considering temperature as a new variable. *Figure IV-32* represents again the variation of the apparent fracture toughness with the square root of the notch radius obtained from the four-point bending tests, including the calculated (dashed lines) and best-fit curves (solid lines) according to the LM of the TCD. Each individual plot corresponds to a certain rock and temperature, so that the influence of temperature on the notch effect can be assessed. The scale of the vertical axis of the plots have been set equal in all the cases for a direct comparison of the results, and figures corresponding to room temperature (*Figure IV-30*) are repeated here for the sake of comparison.

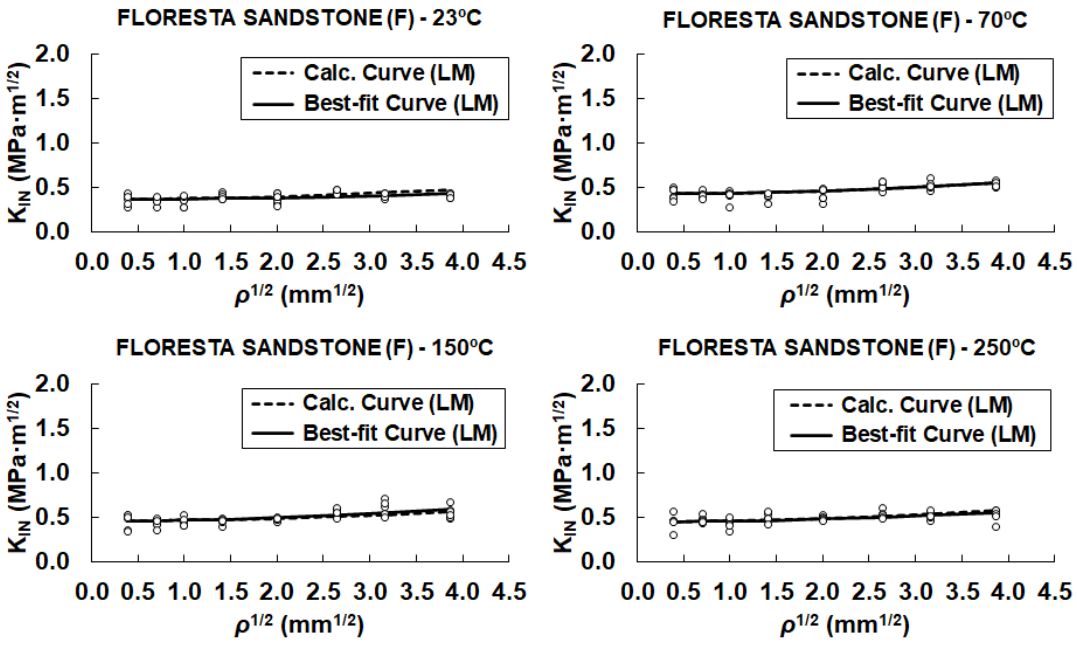

Figure IV-32. Test results of the apparent fracture toughness (K_{IN}) of each rock tested under four-point bending conditions and comparison with the LM of the TCD at different temperatures.

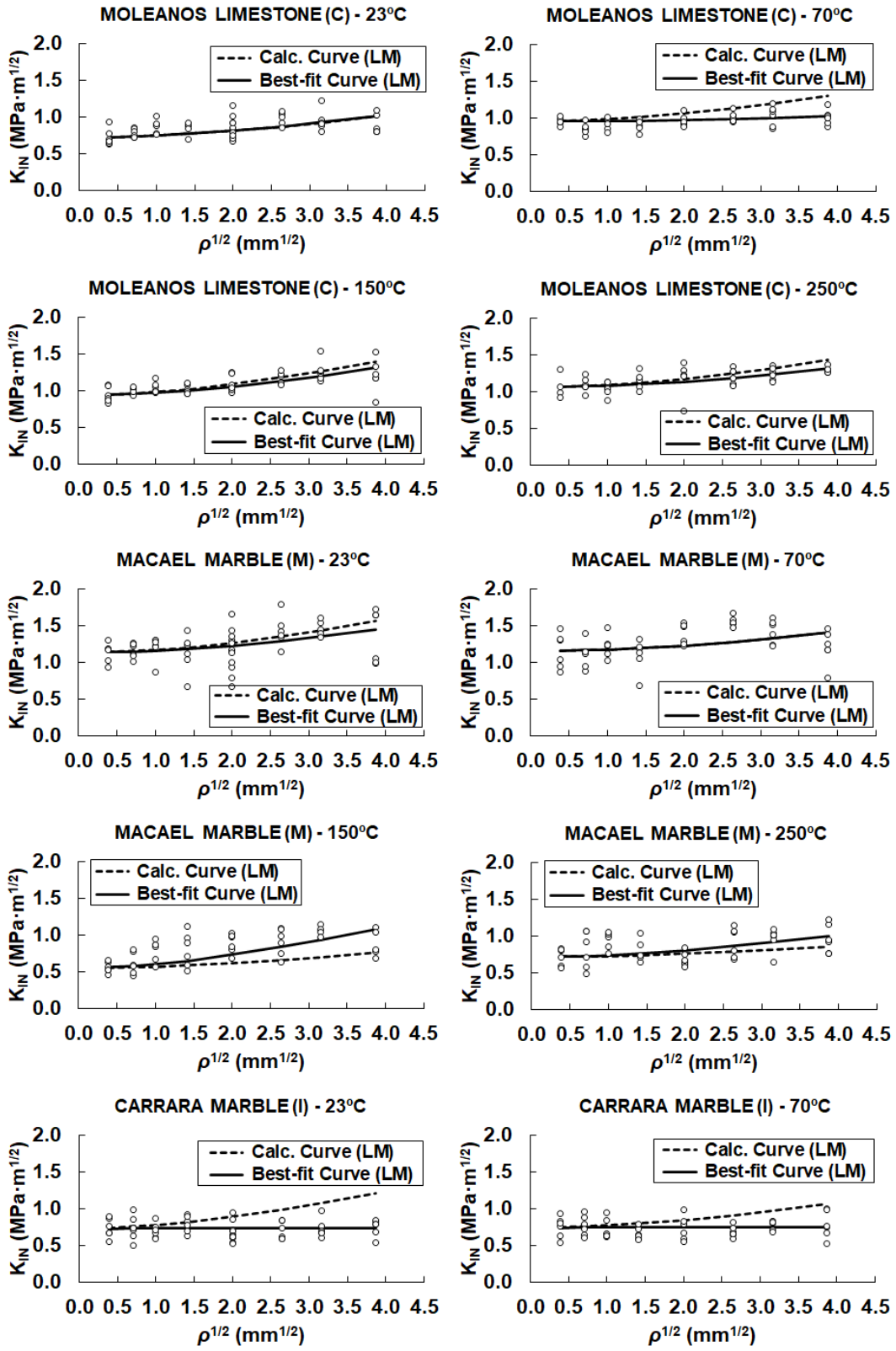

Figure IV-32. (Continued).

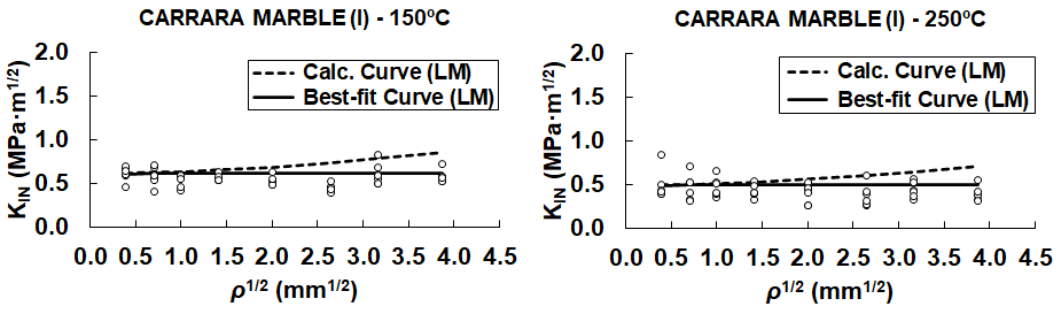

Figure IV-32. (Continued).

The same results obtained from the three-point bending tests (with centred load) for the Moleanos limestone at room temperature and at 250ºC are depicted in *Figure IV-33*, offering roughly equal results as the four-point bending tests.

As indicated for room temperature results, it can be confirmed based on *Figure IV-32* and *Figure IV-33* that for the largest notch radii, the adjustment between the calculated curves (dashed lines) and the best-fit curves (solid lines) becomes less accurate regardless temperature. Apart from the already mentioned use of Creager & Paris (1967) stress distribution function, another reason explaining this tendency is the fact that the value of K_{IC} is fixed for the best-fit curves. Therefore, both the dashed and solid lines start at the same point and the differences are more evident for the largest radii. However, it has been checked that leaving K_{IC} as a free variable for the best-fit curves provides similar results in most of the cases.

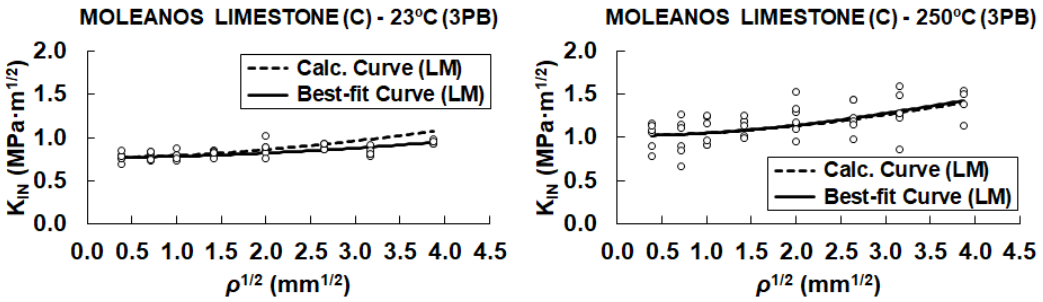

Figure IV-33. Test results of the apparent fracture toughness (K_{IN}) of the Moleanos limestone tested under three-point bending conditions (with centred load) and comparison with the LM of the TCD at different temperature.

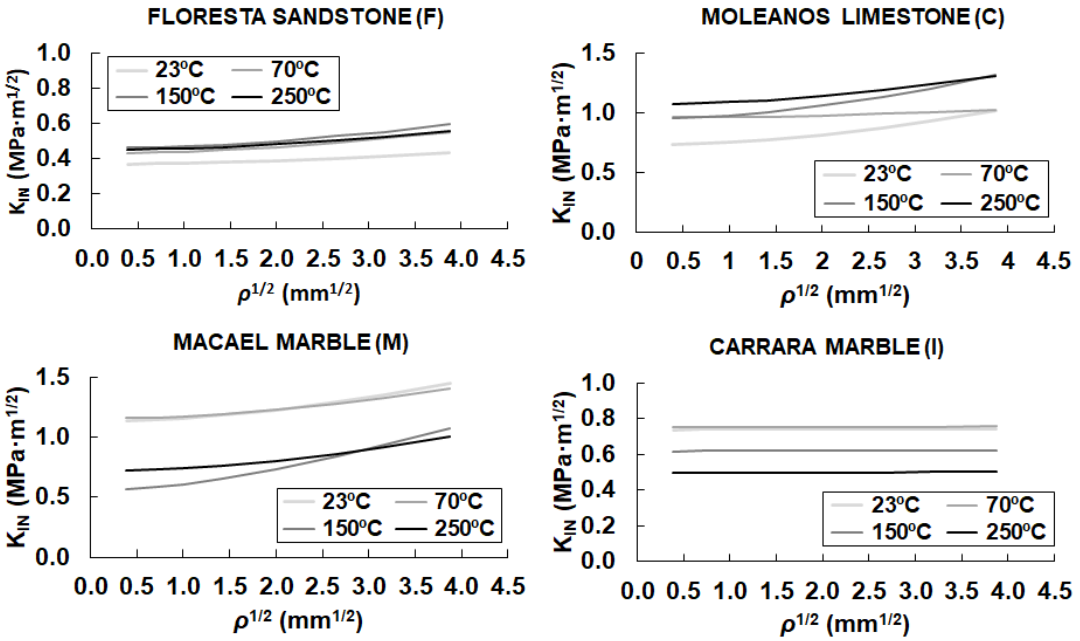

Figure IV-34. Summary of the best-fit apparent fracture toughness curves for each rock and temperature.

Figure IV-34 summarises the best-fit curves from *Figure IV-32*, representing, together for each rock, the results corresponding to the four considered temperatures. As expected from the analysis of the influence of temperature on the fracture toughness of the rocks (*Figure IV-15*), in the case of the Moleanos limestone and the Floresta sandstone the curves move upwards with temperature, while for the marbles the curves move down. However, the changes in the slopes of the curves are very limited, suggesting that temperature does not have a strong influence on the notch effect. In the particular case of the quasi horizontal curve corresponding to the Moleanos limestone at 70ºC, the curve would be approximately parallel to the rest of temperature cases if K_{IC} was left as a free variable, or in other words, the best-fit curve (solid line) would start with a lower apparent fracture toughness (K_{IN}) for $\rho = 0.15$ mm if K_{IN} was set free. This could indicate that the experimental tests may have not properly defined the fracture toughness value for the Moleanos limestone at 70ºC. In any case, the fracture toughness obtention methodology used in this work is fully validated and widely accepted among the scientific community, for this reason, it is justified to set this parameter as a known fixed value.

Again, *Figure IV-32*, *Figure IV-33* and *Figure IV-34* provide the results corresponding to the LM of the TCD, while those apparent fracture toughness curves obtained from the PM have been gathered in *Appendix B*. Likewise, *Table IV-26* collects the calculated values of the critical distance (*Equation (II-70)*) and those obtained from the best-fit of the PM (*Equation (II-75)*) and the LM (*Equation (II-80)*), for each rock and temperature, and considering the four-point bending test results. All the results in *Table IV-26* are consistent with those indicated in *Figure IV-29* and do not show any clear tendency with temperature either. It is noteworthy that, as a general rule, the critical distance values obtained from the best-fit of the LM are relatively higher than those derived from the PM. In this regard, comparing the best-fit and calculated apparent fracture toughness curves of the PM collected in *Appendix B* with those of the LM, relatively similar adjustments are obtained with slight slope variations characteristic to the chosen method.

Table IV-26. Summary of the mean critical distance values obtained at different temperatures from the four-point bending tests.

TEMP.	PARAMETER	(F)	(C)	(M)	(I)
23ºC	Calculated L (mm)	5.82	4.02	4.20	2.19
	Best-fit L (mm) - PM	3.66	2.29	2.85	8.62
	Best-fit L (mm) - LM	9.94	3.96	6.02	-
70ºC	Calculated L (mm)	5.66	4.43	8.00	3.59
	Best-fit L (mm) - PM	2.78	5.13	3.41	6.60
	Best-fit L (mm) - LM	5.86	-	7.74	-
150ºC	Calculated L (mm)	7.52	3.19	4.33	3.99
	Best-fit L (mm) - PM	2.79	2.40	1.06	10.52
	Best-fit L (mm) - LM	5.63	4.12	1.37	-
250ºC	Calculated L (mm)	5.73	4.77	8.62	3.65
	Best-fit L (mm) - PM	3.39	3.35	2.38	16.28
	Best-fit L (mm) - LM	7.45	7.43	3.91	-

Proceeding along the same way, *Table IV-27* collects the calculated values of the critical distance (*Equation (II-70)*) and those obtained from the best-fit of the PM (*Equation (II-75)*) and the LM (*Equation (II-80)*)

for the case of the Moleanos limestone subjected to three-point bending conditions (*Figure IV-33*) and both at 23ºC and at 250ºC. It is observed that the obtained results are relatively similar to those of the same material subjected to four-point bending conditions (*Table IV-26*).

Table IV-27. Summary of the mean critical distance values obtained at different temperatures for the Moleanos limestone from the three-point bending tests.

TEMP.	PARAMETER	(C2)*
23ºC	Calculated L (mm)	3.97
	Best-fit L (mm) - PM	3.40
	Best-fit L (mm) - LM	7.41
250ºC	Calculated L (mm)	4.20
	Best-fit L (mm) - PM	2.21
	Best-fit L (mm) - LM	3.86

*From Moleanos limestone under three-point bending (*Figure IV-33*).

The values of L corresponding to the LM and the Carrara marble are out of order due to the almost null slope of the best-fit curves (see the Carrara marble curves in *Figure IV-34*), which leads to extremely high values of the critical distance. The same occurs for the Moleanos limestone at 70ºC as indicated above. For this reason, these values have not been included in the table. In the case of the Moleanos limestone, the outlier value is associated to the fact that the fracture toughness (K_{IC}) is fixed when obtaining the best-fit curve. However, the Carrara marble does not show any appreciable notch effect at the studied range of notch radii, presenting a roughly constant apparent fracture toughness with ρ. This is caused by the non-linear behaviour of the Carrara marble interpreted from the stress-strain curves of the uniaxial compression tests (*Figure IV-10*), and from the load-displacement curves of the four-point bending (*Figure IV-21*) and three-point bending tests (*Figure IV-27*).

The consequences of the observed L variations are rather limited from the point of view of the apparent fracture toughness predictions obtained through *Equation (II-75)* (PM) and *Equation (II-80)* (LM), given that in such expressions the critical distance is square rooted, and moderate

variations of this parameter cause small variations in the resulting predictions.

3.1.3 Numerical determination of the critical distance

One of the main advantages of the TCD is the possibility of using analytical solutions avoiding the use of numerical analyses, which facilitates to a great extent the fracture assessments. However, as an alternative to the stress distribution function proposed by Creager & Paris (1967) in *Equation (II-72)*, numerically obtained stress fields can also be used in the analysis, applying either the PM or the LM.

As indicated above, the detected differences between the calculated and best-fit apparent fracture toughness curves for the largest notch radii can be caused by the fact that the largest notches studied are beyond the application range of the stress distribution of Creager & Paris (1967), in which *Equation (II-75)* (PM) and *Equation (II-80)* (LM) are based. For this reason, differences between numerically obtained stress field and that proposed by Creager & Paris (1967) will be compared here for the particular case of the Moleanos limestone, aiming to define the limitations of the analytical solution.

Thus, *Figure IV-35* represents, for the Moleanos limestone, the stress distribution along the notch bisector plane starting from the notch tip, both for three-point bending (3PBT) and four-point bending (4PBT) loading conditions with a unity load. The stress-distance curves represented by the solid lines stand for the Creager & Paris' (1967) analytical solution according to *Equation (II-72)*, in which the stress intensity factor (K_I) varies for each loading configuration based on *Equation (III-7)* (when a unity load $P = 1$ N is applied instead of the failure load F, the stress intensity factor K_I is obtained instead of the critical value of the fracture toughness K_{IC}). By contrast, the dashed curves indicate the stress distribution from the notch tip obtained from linear-elastic finite element analyses (FEM), using PLAXIS 2D (2017) and considering plane strain conditions. The results corresponding to notch radii of 0.15, 1, 4, 7 and 15 mm have been included in *Figure IV-35*. The plots in the left column correspond to the three-point bending configuration while the right column stands for the four-point bending loading cases.

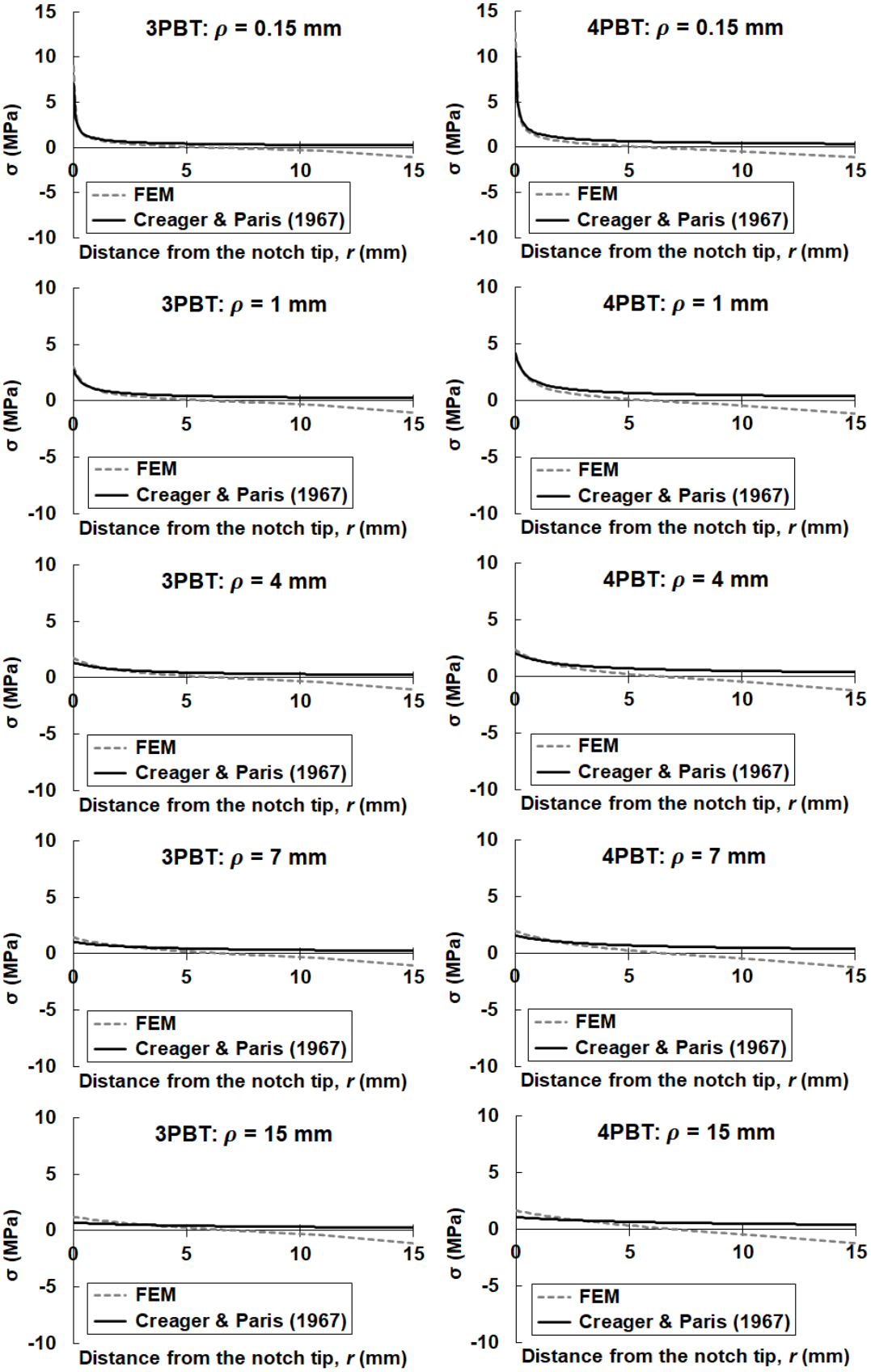

Figure IV-35. Comparison between FEM and Creager & Paris (1967) stress distribution function along the notch bisector plane for different notch radii.

The numerical models were constructed using the same geometry as the original rock samples tested in the laboratory (see *Figure III-28* or *Figure III-32*). As a consequence, a clear influence of the boundary is observed close to the border opposite to the notch, in which certain compression stresses arise. However, Creager & Paris (1967) stress distribution function considers semi-infinite body dimensions and, therefore, no boundary influence is observed.

In general, both curves show a good agreement in the surroundings of the notches and the agreement gets poorer as the influence of the front boundary becomes noticeable. This boundary influence explains the gradual difference between numerical and analytical stress fields as distance from the notch tip increases. Additionally, as expected from Creager & Paris (1967) stress distribution limitation, which is supposed to be only valid for long and narrow notches ($a \gg \rho$), it is observed that the largest notch radii (e.g., $\rho = 0.15$ mm) show a poorer agreement even close to the notch tip. Thus, it can be concluded that the largest notches are on the limit of the application range of Creager & Paris (1967).

With all this, although the largest notches are on the limit of the application range of Creager & Paris (1967), the analytical solution seems to provide a sufficiently accurate stress field in the first few millimetres (depending on the critical distance of each rock) from the notch tip where stresses are assessed both by the PM and the LM of the TCD.

Thus, as an alternative to the analytical approach for assessing mode I fracture conditions, the values of the critical distance (L) can be also calculated from the numerically obtained stress distribution curves along the notch bisector plane. FEM stress field is a priori a better approximation to the actual stress field of the tested rock samples. However, this solution involves a significant workload increase, since a numerical model is needed for each material and notch radius, and the stress-distance curves are evaluated one by one. Unlike the analytical approach in which a single value of L is derived from the direct calculation with *Equation (II-70)* or from the best-fit of the apparent fracture toughness values (using either *Equation (II-75)* for the PM or *Equation (II-80)* for the LM), in the case of the numerical approach, one

value of L can be derived from each notch and, therefore, from each model, by just finding the distance at which the failure criterion defined by the PM (*Equation (II-66)*) or LM (*Equation (II-77)*) is fulfilled.

As an example, *Table IV-28* shows the numerically obtained values of L for the Moleanos limestone at 23ºC and at 250ºC, derived by means of the three-point bending test models and using both the PM (*Equation (II-66)*) and the LM (*Equation (II-77)*). This table collects the values of L for each of the studied notch radii (each one corresponding to a single numerical model), and the average critical distance is indicated at the end. The mean critical distance for the Moleanos limestone at 23ºC is 4.2 mm while at 250ºC L increases to 4.7 mm in the case of using the PM. By contrast, when using the LM, L = 2.8 mm at 23ºC and slightly increases to 3.0 mm at 250ºC. Comparing the resulting values of L from the PM, the numerically obtained values are higher than those obtained analytically for the same mode I loading conditions collected in *Table IV-26*. By contrast, in the case of the LM results, lower values of L are obtained with the numerical approach. This is caused by the influence of the boundary when using the numerically obtained stress field instead of the Creager & Paris (1967) stress distribution function. Under these circumstances, the distance assessed with the LM, that is, $2L$, is limited by the compressed region (see *Figure IV-35*).

Table IV-28. Numerically obtained critical distances (L) for the Moleanos limestone using the three-point bending test models.

ρ (mm)	Point Method (PM)		Line Method (LM)	
	23ºC	250ºC	23ºC	250ºC
0.15	2.9 mm	3.0 mm	2.5 mm	2.6 mm
0.50	3.2 mm	3.1 mm	2.5 mm	2.4 mm
1	3.5 mm	3.7 mm	2.6 mm	2.8 mm
2	4.1 mm	4.4 mm	2.8 mm	3.0 mm
4	4.6 mm	5.2 mm	2.8 mm	3.2 mm
7	5.1 mm	5.5 mm	3.0 mm	3.2 mm
10	4.8 mm	5.9 mm	2.7 mm	3.3 mm
15	5.7 mm	6.5 mm	3.1 mm	3.6 mm
Mean:	**4.2 mm**	**4.7 mm**	**2.8 mm**	**3.0 mm**

Finally, in order to evaluate the influence of the observed critical distance variations, failure load predictions are assessed and discussed in the following *Section 3.1.4*. As highlighted above, the consequences of the observed critical distance differences are expected to be limited when performing fracture assessments with the TCD, since the value of L is square rooted both in the case of the PM (*Equation (II-75)*) and the LM (*Equation (II-80)*) expressions.

3.1.4 Fracture load predictions

Once the value of the critical distance (L) is defined for a certain material, it is straightforward to perform fracture predictions based on the analytical approach, by simply reversing *Equation (III-8)* and applying the apparent fracture toughness expression of the PM (*Equation (II-75)*) or the LM (*Equation (II-80)*). Thus, the expression for the predicted failure load according to the TCD (F_{TCD}) is as follows:

$$F_{TCD} = \frac{b\sqrt{h}}{Y} \cdot K_{IC} \frac{(1+\rho/L)^{3/2}}{1+2\rho/L} \qquad (PM) \qquad (IV\text{-}1)$$

$$F_{TCD} = \frac{b\sqrt{h}}{Y} \cdot K_{IC} \sqrt{\frac{\rho}{4L}+1} \qquad (LM) \qquad (IV\text{-}2)$$

By contrast, when using the numerical approach, the estimation of the failure load (F_{TCD}) is not so straightforward. The constructed numerical models consider a unity load and, therefore, the numerically obtained stress law at the notch bisector plane will correspond to that load. As a consequence of the considered linear-elastic constitutive model, the response is proportional to the applied load. Thus, the initial stress field can be rescaled so that the PM (*Equation (II-66)*) or LM (*Equation (II-77)*) failure criteria are fulfilled for a certain value of the critical distance (L). *Figure IV-36* represents the rescaling process both for the PM and the LM. The dashed curves indicate the initial stress law corresponding to the unity load, and the rescale factor will directly correspond to the value of the failure load (F_{TCD}).

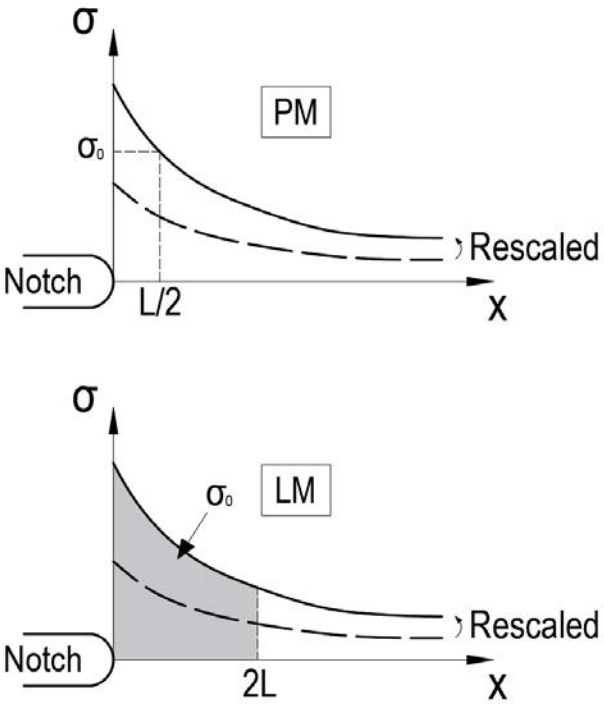

Figure IV-36. Schematic representation of the rescaling process for the determination of the failure load (F_{TCD}) based on the PM and LM.

Based on the above described methodologies for the determination of the failure loads, the fracture load predictions of analytically obtained results and numerically obtained results will be compared first. Following the example of the Moleanos limestone indicated in *Section 3.1.3*, *Figure IV-37* represents the ratio between the predicted and the experimentally obtained failure load (F_{TCD}/F_{EXP}) against the notch radii for the particular case of the Moleanos limestone subjected to three-point bending conditions, both at 23ºC and at 250ºC.

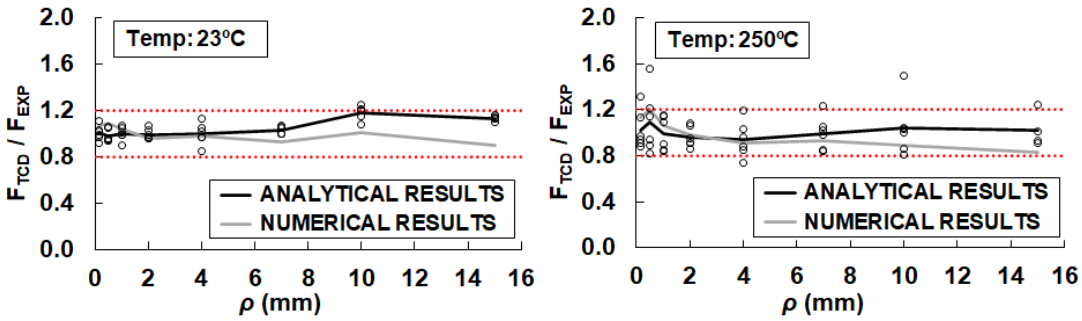

Figure IV-37. Load fracture predictions of the mode I loaded three-point bending tests of the Moleanos limestone at 23ºC and 250ºC, obtained from the analytical and the numerical analyses according to the LM of the TCD.

The dots correspond to the failure load prediction of each of the individual tests according to *Equation (IV-2)* (LM) and the black solid line represents the mean predictions considering the same criterion. These analytical results were obtained using the calculated value of L collected in *Table IV-27*, corresponding to the three-point bending tests. By contrast, the grey solid line stands for the numerically obtained fracture predictions, for which the mean value of L (*Table IV-28*) has been considered at each temperature. Differences would be small if L values of *Table IV-27* were used. The horizontal red dotted lines define an error interval of ±20%, which is a common range in fracture mechanics to define a boundary of good accuracy predictions. Systematic applications of the TCD were seen to return predictions typically falling within an error interval of ±20% (Taylor, 2007). This strip tries to encompass the intrinsic uncertainties of the performed laboratory tests and, especially, the variability of the fracture results due to the heterogeneous nature of the studied materials. It is observed in *Figure IV-37* that, in general terms, the obtained predictions fall within the error interval of ±20%, although the individual test results performed at 250ºC show a significant higher scatter compared to those at 23ºC.

Both the represented analytical and the numerical results are based on the application of the LM failure criterion defined by *Equation (II-77)* along the bisector of the notches. However, it can be observed that despite the differences in the values of L in both approaches, the failure load predictions are relatively similar. This is caused by the fact that different stress distributions are being considered in each case. The analytical approach considers the stress distribution of Creager & Paris (1967) while the numerical approach considers the stresses of the performed linear-elastic analyses. As expected from the conclusion derived from *Figure IV-35*, in the case of the smallest notch radii, differences between analytical and numerical fracture load predictions are relatively small and become more evident for the largest notches. This is because the theoretical application range of Creager & Paris' (1967) stress distribution function is limited for long and narrow notches ($a \gg \rho$) and, therefore, the agreement between the numerically obtained stress field and that defined by Creager & Paris (1967) close to the notch tip is significantly poorer for the largest notches (see *Figure IV-35*). In any case, both approaches have been shown to be valid providing

reasonable fracture load predictions within a reasonable interval of ±20%, even with the analytical approach beyond the theoretical application range of Creager & Paris (1967).

Based on the relatively similar results obtained from the analytical and numerical approaches and the accuracy level of both methodologies, the applicability of *Equations (IV-1)* (PM) and *(IV-2)* (LM) is justified for determining F_{TCD}, keeping in mind that the largest notches of the studied range are somehow on the limit.

Hereafter, the fracture load predictions of each of the studied rocks and temperatures will be assessed using the analytical approach, that with a far simpler application. In particular, the predictions corresponding to the LM of the TCD will be plotted. Those corresponding to the PM are collected in *Apprendix B*. To do so, the experimental results of the performed four-point bending tests and the predicted failure loads (F_{TCD}) calculated with *Equation (IV-2)* are compared in *Figure IV-38*.

The plots of *Figure IV-38* represent the ratio between the predicted failure load (F_{TCD}) and the experimental failure load (F_{EXP}) obtained from the four-point bending tests, against the notch radii (ρ). The dots correspond once again to the individual test results, while the solid line indicates the average fracture prediction for each notch. $F_{TCD}/F_{EXP} = 1$ stands for the exact prediction. Thus, the values below unity are underestimating and the values above are overestimating the failure load.

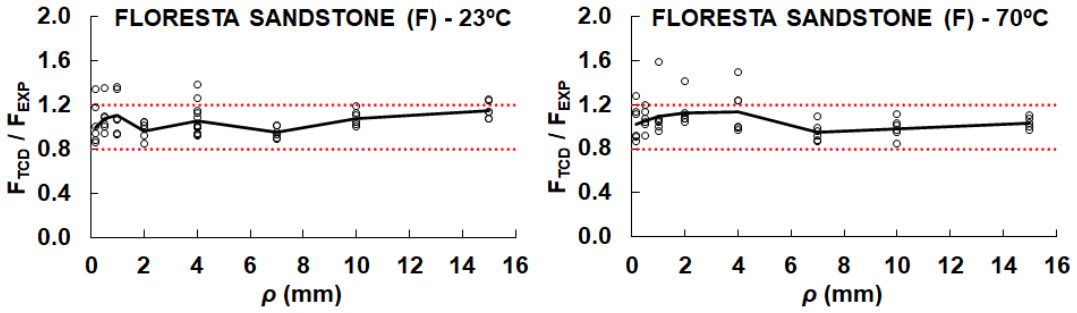

Figure IV-38. Fracture load predictions according to the LM of the TCD for each rock and temperature.

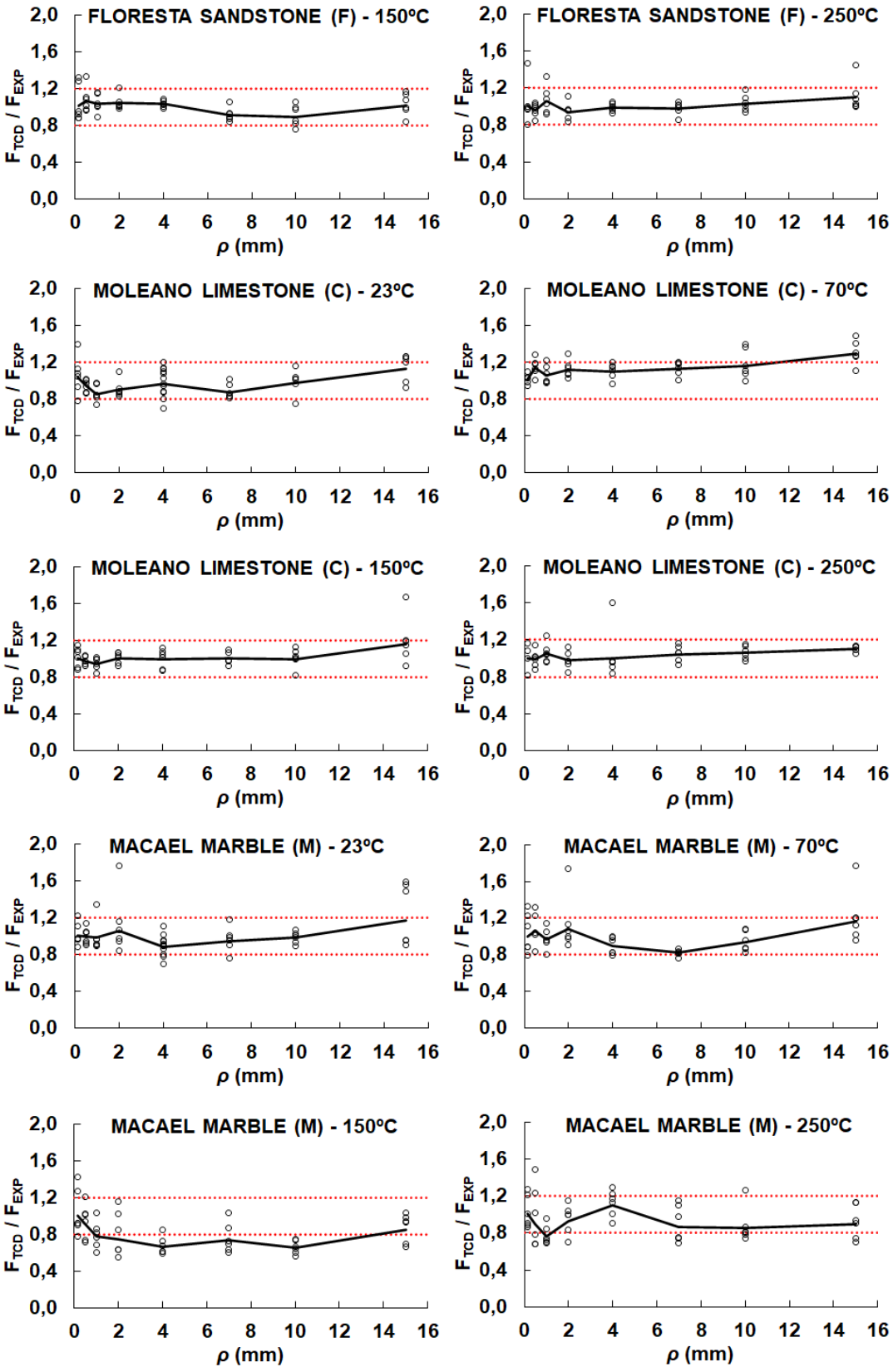

Figure IV-38. (Continued).

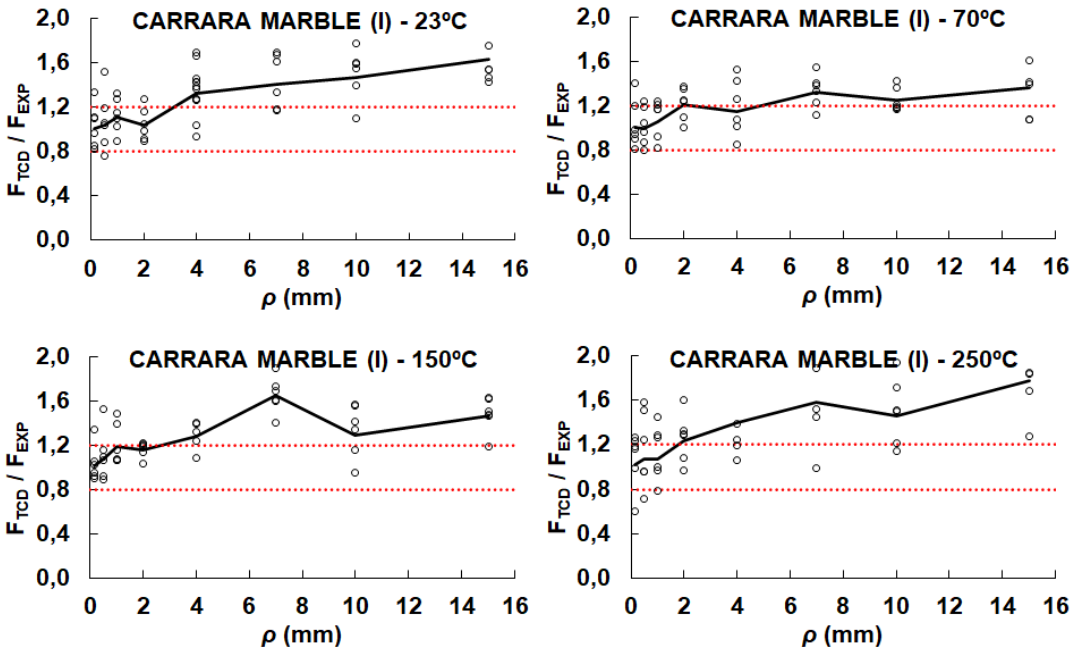

Figure IV-38. (Continued).

Good predictions are generally obtained even for the largest notches beyond the application range of the Creager & Paris' (1967) equation, except for the case of the Carrara marble. Comparing *Figure IV-32* and *Figure IV-38*, in those cases in which the calculated apparent fracture toughness curves are below the best-fit curves (e.g. Macael marble at 150ºC), the fracture predictions tend to underestimate the failure loads and vice versa. As expected, the Carrara Marble does not offer such good predictions as the rest of the rocks, especially for the largest notches. This worsening of failure load predictions is explained by the lower degree of linearity shown in the load-displacement curves in *Figure IV-21*, which is not necessarily associated to the high temperatures, as similar results are also observed at room temperature. Moreover, comparing the load-displacement curves of the Carrara marble for $\rho =$ 0.15 mm and 15 mm (*Figure IV-21*), there seems to be a slightly higher degree of non-linearity for the largest notches, which could explain, together with the limitation of Creager & Paris' (1967) stress distribution function, the worsening of the fracture load predictions as the notch radius increases. In any case, it can be concluded that the TCD provides an accurate fracture assessment tool for the assessment of notched rocks at different temperatures, as long as predominantly linear behaviour is guaranteed.

Relatively similar fracture load predictions are obtained by means of the PM (*Apprendix B*), also providing predictions within the interval of ±20%. However, it is clearly observed that the PM tends to slightly underestimate the fracture load compared with the results of the LM shown in *Figure IV-38*.

3.1.5 Relation between critical distance and grain size

The actual physical meaning of the critical distance (L) is still under discussion among the scientific community. However, it is widely accepted that it seems to be related to the corresponding material microstructure (Taylor, 2007). Taylor (2017) analysed the relation of the critical distance (L) with clearly identifiable microstructural distances (d) such as the grain size of different materials, and concluded that in most of the cases, L is found to lie between d and $10d$, as depicted in *Figure IV-39*.

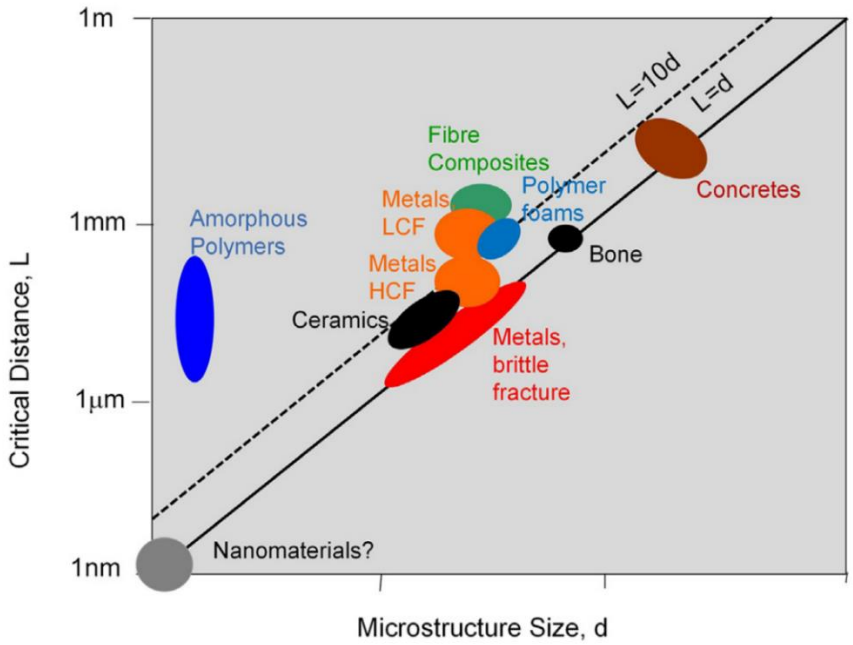

Figure IV-39. An overview of values of L found in different materials, plotted as a function of microstructure size d (Taylor, 2017).

In the particular case of the studied rocks, the correlation between the mean grain size and the critical distance is checked in *Figure IV-40*. No data on the variation of the grain size with temperature is available. Thus, only the results corresponding to room temperature are included.

First, the black vertical range of L values depicted in *Figure IV-40* for the Floresta sandstone, Moleanon limestone, Macael marble and Carrara marble correspond to those calculated values (with *Equation (II-70)*) represented in *Figure IV-29* for 23ºC. These ranges indicate, from top to bottom, the maximum value, the third quartile, the median, the first quartile and the minimum value of the obtained results for L. On the other hand, the empty diamond symbols indicate the values of L obtained from the best-fit of the PM (*Equation (II-75)*), while the filled diamond symbols correspond to the best-fit of the LM (*Equation (II-80)*). The L values of the Oolitic limestone and granite studied by Cicero et al. (2014) have also been included in *Figure IV-40*. In this case, the empty triangular symbols correspond to the calculated mean values of L according to *Equation (II-70)*. The red dashed lines indicate the expected correlation strip defined by Taylor (2017), in which the critical distance is supposed to lie between d and $10d$.

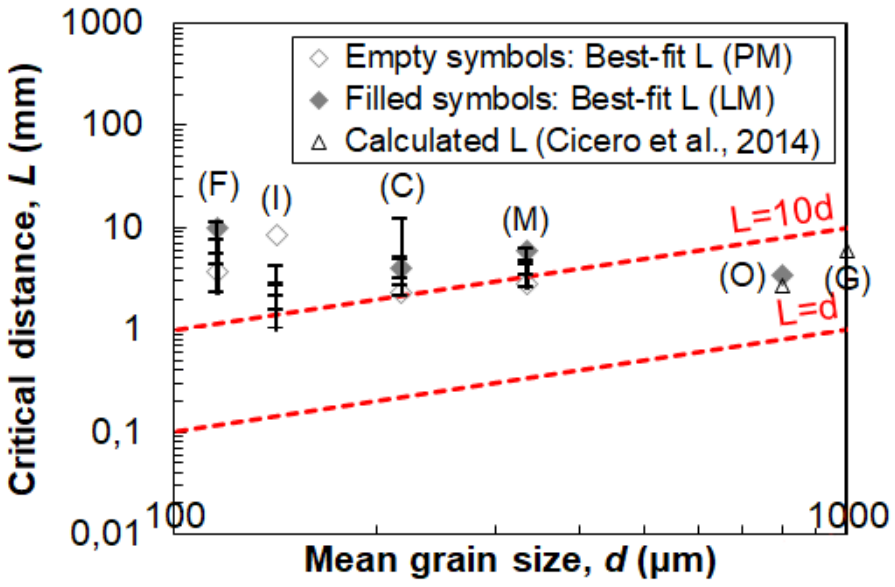

Figure IV-40. Correlation between grain size and critical distance of the studied rocks.

With all this, the obtained results are located slightly above of the scatter band defined by Taylor (2017). The obtained values of L are close to those depicted in *Figure IV-39* for concrete materials, presenting similar values of L but with slightly lower mean grain sizes.

3.1.6 Microstructural analysis

Trying to correlate the obtained fracture results with the microstructure of the studied rocks, several thin-sections of reconstructed four-point bending test specimens have been analysed with an optic microscope, as indicated in *Section 3.6* of Chapter III. It should be noted that crack propagation is a three-dimensional process, while thin-section analyses simplify the problem to a single plane (2D). Here, the thin-sections correspond to the middle plane of the specimens, assuming that, from an statistical point of view, the measured data is representative enough.

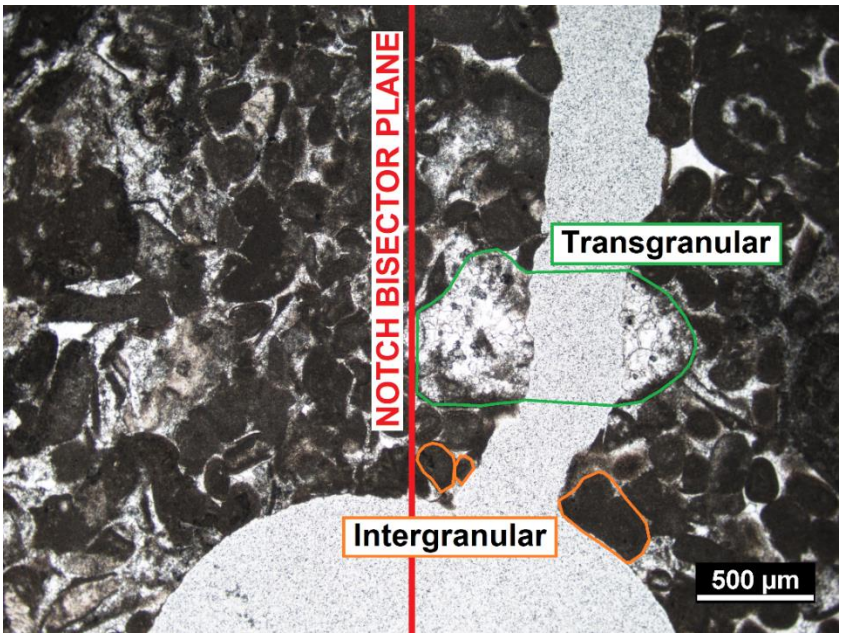

Figure IV-41. Crack initiation at the notch tip of a Moleanos limestone sample.

From a strict point of view, under mode I loading, crack should start and propagate through the notch bisector plane. However, as a consequence of the heterogeneous nature of rocks, small deviations may appear as that depicted in *Figure IV-41*. Many different factors may affect the crack propagation process, which makes detailed analysis difficult. The strength of the individual grains, their size, distribution and orientation, the presence (if any) of cement matrix, its strength, etc. highly influence the crack propagation trajectory, leading to intergranular (through grain boundaries) or transgranular (through

grains) fractures as crack progresses (see *Figure IV-41*). For this reason, intergranular and transgranular fracture is analysed in this section and compared with the obtained fracture results.

First, the focus is placed on the crack initiation point. Under pure mode I loading conditions, stress concentration occurs at the notch tip, where crack initiation is expected to take place. Thus, for each of the analysed thin-sections, the initial fracture type (intergranular or transgranular) have been checked. *Table IV-29* indicates the percentage of cases with integranular and transgranular fractures at the notch tip, just at the crack initiation region. Likewise, the percentage of deviated cracks (compared to the vertical notch bisector plane) and the mean angle for those deviated cracks have also been measured.

Table IV-29. Crack initiation data from thin-sections analyses.

	(F)	(C)	(M)	(I)
Intergranular cracks (%)	51.3	40.0	21.0	55.0
Transgranular cracks (%)	48.7	60.0	79.0	45.0
Deviated cracks (%)	37.5	29.2	50.0	37.5
Mean deviation angle (º)	9.7	13.1	16.0	13.6

Both the Floresta sandstone and the Carrara marble, those with the smallest mean grain sizes, offer a relatively similar number of intergranular and transgranular fractures at the crack tip, presenting both of them around 37.5% of deviated cracks. This could indicate that grain and boundary resistance are roughly the same, as the initial crack propagation does not show any clear preference in the type of fracture. However, in the Moleanos limestone and specially in the Macael marble, the percentage of transgranular crack initiation is significantly higher than intergranular crack initiation, which seems to indicate that grain resistance is somehow lower than that of the cement matrix or grain boundaries.

Generally speaking, the cracking process starts at the notch tip and propagates vertically as expected from pure bending moment (see *Figure III-31*). However, as the notch radius gets larger, the stress concentration at the notch tip gets smaller. Thus, other aspects as the presence of grain boundaries, the statistical distribution of the grains

and pores or weaker zones close to the notch tip may have an influence on the starting point of the crack propagation in the case of the largest notches. This also causes a scatter of the failure load results (*Table IV-19*). It is noteworthy the high percentage of initially deviated cracks (50%) in the case of the Macael marble, which seems to indicate that crack initiation is especially sensitive to the presence of weaker zones close to the notch tip where stresses concentrate.

After analysing the crack initiation region, the fracture type (intergranular or transgranular) along a distance equal to two times the critical distance ($2L$) was assessed, measured as a straight distance from the notch tip along the notch bisector plane. This distance is related with the so called FPZ as indicated in *Section 2.4* of Chapter II. *Table IV-30* gathers the average percentage of intergranular and transgranular fractures along $2L$ for each of the analysed rocks. Likewise, the sinuosity or roughness of the crack is also indicated in *Table IV-30*, measured as the ratio between the real crack length along the straight $2L$ distance and the actual $2L$ distance.

Table IV-30. Fracture data along a distance of $2L$ *from the notch tip, obtained from the thin-sections observation.*

	(F)	(C)	(M)	(I)
Intergranular cracks (%)	59.0	41.8	22.0	52.3
Transgranular cracks (%)	41.0	58.2	78.0	47.7
Roughness*	1.39	1.16	1.23	1.14

*Measured as the ratio between the real crack length and the theoretical $2L$ distance.

It is observed that the percentage of intergranular and transgranular fractures along the measured distance roughly coincides with that obtained in *Table IV-29* and corresponding to the initial fracture type. Moreover, in the case of the Floresta sandstone (F) and Moleanos limestone (C), this fracture data is individually analysed for each component in *Table IV-31*.

Table IV-31. Fracture data (particularised by components) along a distance of 2L from the notch tip, obtained from the thin-sections observation.

	(F)			(C)	
	[Sp]	[C]	[Q]	[Pel]	[Intra]
Intergranular cracks (%)	34.3	75.0	25.0	50.0	32.0
Transgranular cracks (%)	65.7	25.0	75.0	50.0	68.0

According to these individualised results, in the case of the Floresta sandstone, sparitic crystals [Sp] and quartzes [Q] show a transgranular fracture preference, while carbonates [C] (specially micritic crystals) show a predominant intergranular cracking. By contrast, in the case of the Moleanos limestone, pellets [Pel] do not show any fracture preference while intraclasts [Intra] mainly present transgranular cracking.

On the other hand, the relation between the fracture results, in particular the apparent fracture toughness (K_{IN}), and the fracture type have been studied trying to corroborate if there is any relation between fracture resistance and intergranular or transgranular cracking.

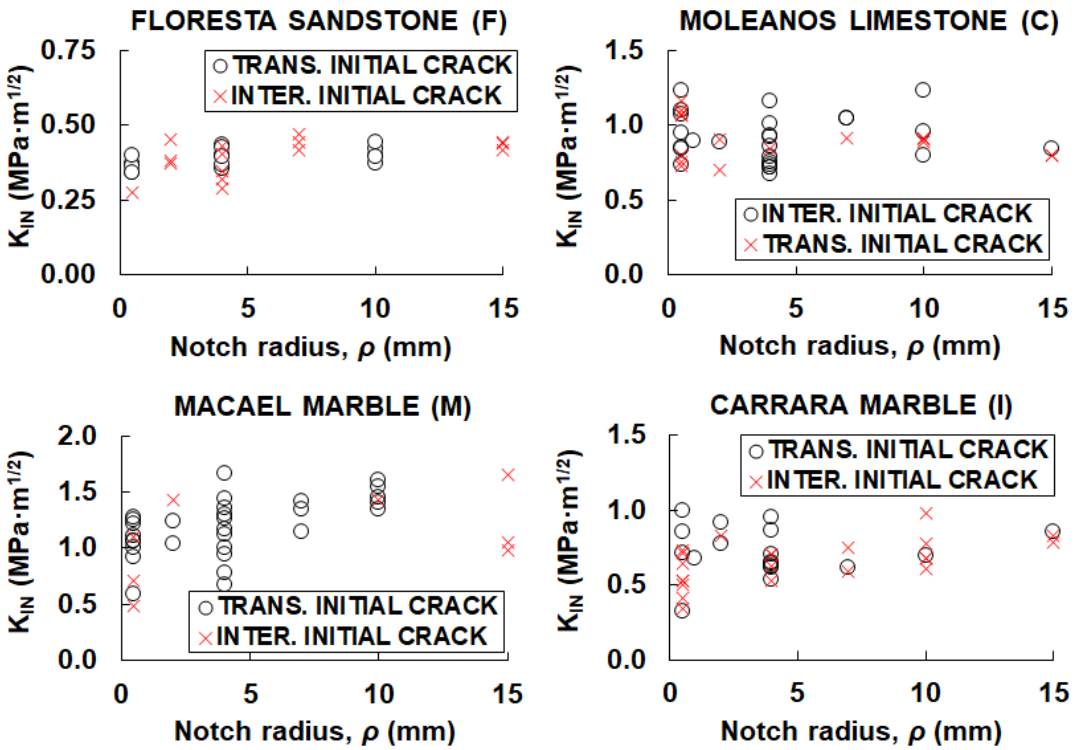

Figure IV-42. Apparent fracture toughness against notch radius for each of the analysed rocks, indicating those with an initial transgranular or intergranular crack.

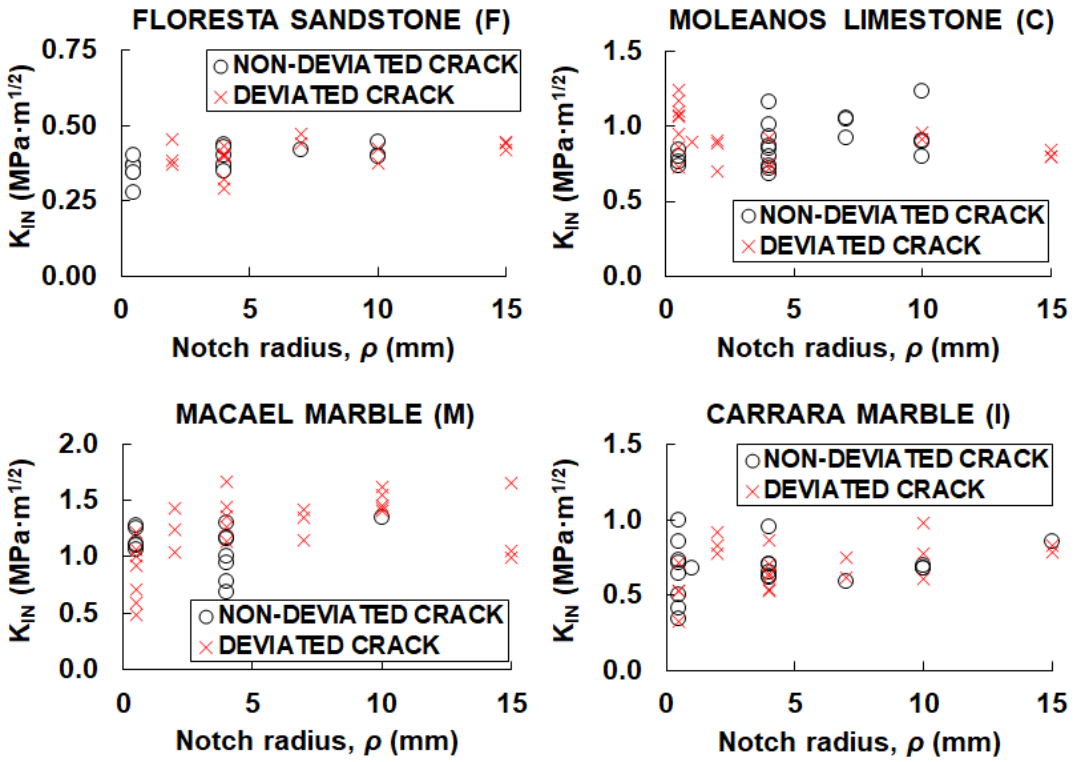

Figure IV-43. Apparent fracture toughness against notch radius for each of the analysed rocks, indicating those with an initially deviated and non-deviated crack.

Firstly, *Figure IV-42* represents the variation of the apparent fracture toughness against the notch radius for each of the analysed rocks. Each dot corresponds to an individual thin-section analysis, or in other words, to a single reconstructed four-point bending sample. The results are represented according to the initial fracture type, which can be intergranular (black circles) or transgranular (red crosses). At first sight, the observed results do not show a clear trend and general conclusions cannot be derived from this analysis. This indicates that the fracture resistance of the notched rock samples is not highly influenced by the grain resistance, showing no clear preference between intergranular or transgranular initial cracking. However, on average, transgranular cracking imply higher values of fracture toughness (K_{IC}) in the four studied rocks. For example, in the particular case of the Macael marble, transgranular cracks involve a clear higher resistance, probably as a consequence of the grain size, which is relatively larger than in the rest of analysed rocks. This could force the crack to cross

over a certain grain when bordering it is more difficult, leading to a higher value of the fracture resistance.

Proceeding along a similar track, *Figure IV-43* provides the same results as *Figure IV-42*, but in this case the results are distinguished between those with an initially deviated crack (red crosses) and non-deviated crack (black circles). Those samples with a deviated initial crack tentatively show a higher fracture resistance (i.e., higher apparent fracture toughness), as for example in the case of the Macael marble. However, this conclusion is not robust enough and more research is needed on this issue.

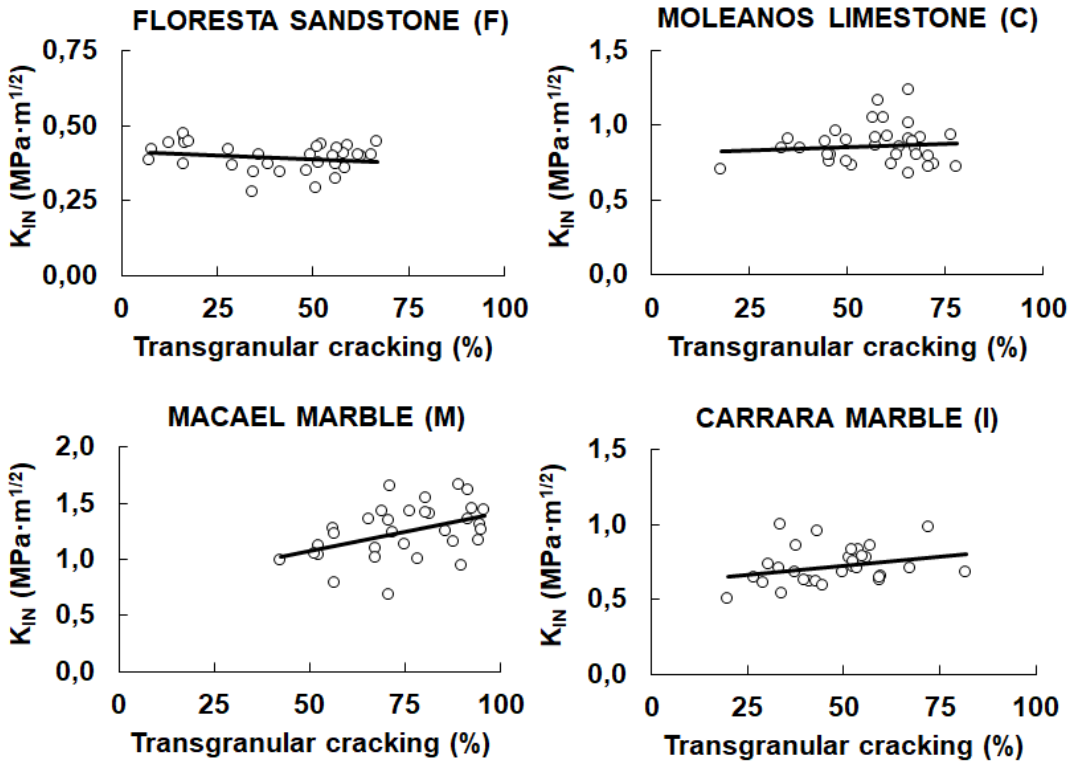

Figure IV-44. Apparent fracture toughness against the percentage of transgranular cracking over a distance equal to $2L$ *from the notch tip.*

Finally, instead of focusing on the initial crack type at the notch tip, *Figure IV-44* analyses the variation of the apparent fracture toughness with the percentage of transgranular fractures over a distance equal to two times the critical distance of each rock ($2L$), starting from the notch tip. Each dot represents an individual fractured rock sample and the solid line stands for the best-bit trend line.

Both the Floresta sandstone and the Moleanos limestone show a roughly constant trend, or even slightly decreasing tendency in the case of the Floresta sandstone. In any case, the apparent fracture toughness does not show an important correlation with the fracture type in the case of the two porous rocks, which indicates that grain resistance to being divided, compared to bond resistance, does not condition the global fracture resistance. Porosity also plays a key role in the cracking process and could somehow affect the observed trends, as voids facilitate crack propagation and could even define its path in such a way that the crack sews different pores together. By contrast, in the case of the two marbles, the results show a clear increase of the apparent fracture toughness with the percentage of transgranular fractures over a distance equal to $2L$, specially for the Macael marble. This increasing tendency seems to indicate that grains offer a higher fracture resistance than the bonds, leading to a higher apparent fracture toughness of the specimen.

3.2 MIXED MODE I+II ANALYSIS

Section 3.1 was focused on the fracture assessment of rocks subjected to pure mode I loading conditions. It is generally accepted that crack propagation phenomena in rocks are mode I dominated due to the relatively small tensile resistance of rocks that makes them highly sensitive to opening loading (mode I). However, rock masses are usually subjected to complex loading conditions and the defects within the rock are randomly orientated. For this reason, in many practical situations the influence of combined opening-sliding shear deformations (i.e., mixed mode I+II) has to be studied. Here, the fracture of U-notched Moleanos limestone samples subjected to mixed mode I+II loading conditions (with a predominant mode I influence) will be assessed, based on the fracture results of the performed three-point bending tests with variable loading position.

To the best of the author's knowledge, the TCD has not been applied yet in the field of rock fracture mechanics under mixed mode loading conditions. Thus, the applicability of the TCD, which was already validated for mode I in *Section 3.1*, is extended here to mixed mode I+II loading conditions. In particular, the LM of the TCD will be used for mixed mode fracture assessment. *Section 2.7.5* of Chapter II provides a

detailed description of the TCD-based analysis methodology under mixed mode loading conditions, which is taken as a basis in this analysis.

3.2.1 Mode Mixity

The application of the LM of the TCD is somehow more complicated for mixed mode loading conditions than for mode I loading conditions, because of the general lack of analytical solutions for mixed mode problems. However, these problems can be studied numerically as in the case of mode I loading (see *Section 3.1.3*), but with certain differences.

The opening-sliding shear mixed mode (I+II) fracture investigation on notched specimens requires the characterization of the mode mixity (M_e). $M_e = 1$ stands for pure mode I loading conditions while $M_e = 0$ corresponds to pure mode II. This dimensionless parameter is calculated with *Equation (II-87)*, for which mode I and mode II Notch Stress Intensity Factors ($NSIFs$) must be defined. These parameters are calculated, respectively, with *Equations (II-88)* and *(II-89)*, and they evaluate the stresses (σ_θ, $\tau_{r\theta}$) along the notch bisector plane ($\theta = 0$).

The stress distributions (σ_θ and $\tau_{r\theta}$) along the bisector of the notch are derived from linear elastic finite element analyses under plane strain conditions, using the software PLAXIS 2D (2017). One model has been constructed for each notch radius and loading position, using triangular 15-node finite elements for the meshing criterion, with a refined region around the notch tip as shown in *Figure IV-45*. Aiming to minimise the influence of the notch length (or resistant section) observed in *Figure IV-23*, each model has been constructed using the average value of the actual measured notch lengths for each notch radius and loading position.

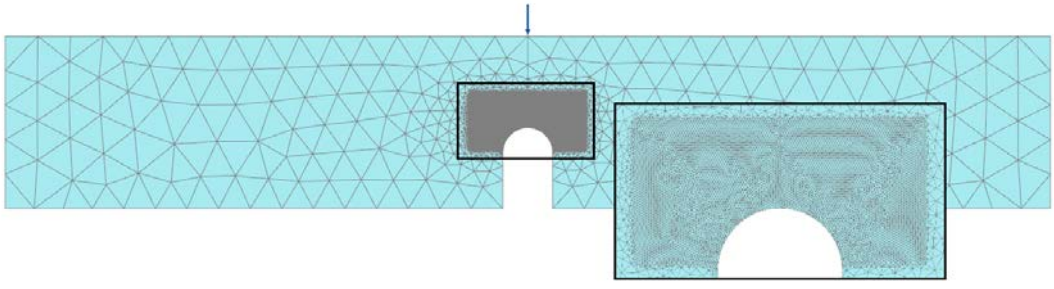

Figure IV-45. Representation of the simulated three-point bending test finite numerical models with the refined region.

The linear-elastic models are defined by only two parameters: the Young's modulus (E_{50}) and the Poisson's ratio (ν_{50}). The used parameters correspond to those obtained experimentally from uniaxial compression tests for the Moleanos limestone, both at room temperature and at 250ºC (*Table IV-12*). These parameters are summarised in *Table IV-32*.

Table IV-32. Mean values of the Young's modulus and Poisson's ratio of the Moleanos limestone at room temperature and at 250ºC.

	23ºC	250ºC
Young's modulus, E_{50} (GPa)	38.4	49.2
Poisson's ratio, ν_{50}	0.31	0.28

The values of the Young's moduli do not affect the obtained stress fields, but the Poisson's ratio does have an influence on them. Due to the linear elastic behaviour, the stress response is proportional to the load, and for simplicity, a unity load of 1 N/m has been introduced in all the models for each loading position, as represented in *Figure III-32*. Then, the stresses can be rescaled according to the obtained failure loads.

Once σ_θ and $\tau_{r\theta}$ are numerically obtained, the NSIFs (K_I^u and K_{II}^u) are assessed along the bisector notch plane. As indicated in *Section 2.7.5* of Chapter II, K_I^u and K_{II}^u show an oscillating value ahead of the notch tip. Lazzarin & Filippi (2006) recommended computing the mean values of K_I^u and K_{II}^u over a distance of 0.4 times the notch radius from the notch tip along the bisector plane, in which K_I^u and K_{II}^u are assumed to be roughly constant. However, for the notch radii considered in the present work (up to 15 mm), the previous approach does not provide representative K^u values, given that at a distance of 0.4 times the notch radius, the NSIF field is far from being sensibly constant, as shown in *Figure IV-46*. *Figure IV-46* represents, as an example, the variation of the NSIFs (both K_I^u and K_{II}^u) versus the distance from the notch tip for different notch radii (ρ = 1, 4 and 15 mm) and loading configurations (m = 0 and 12 mm). The black dots correspond to K_I^u values, while grey dots stand for K_{II}^u values. In this work the following expression is proposed to determine the distance (x) at which the NSIFs must be computed, which is represented in *Figure IV-46* by vertical red dashed lines:

$$x = 0.4\rho\left(1 - \frac{0.4\rho}{0.4\rho + 0.8\,mm}\right) \qquad (IV\text{-}3)$$

This equation provides values very close to 0.4 times the notch radius for notch radii below 2.5 mm, in agreement with Lazzarin & Filippi's (2006) proposal, and generates assessment limits located within the nearly constant NSIF field for larger radii.

So, in short, both *Equations (II-88)* and *(II-89)* are evaluated from the notch tip to a distance defined by *Equation (IV-3)* and the mode mixity M_e is subsequently calculated with *Equation (II-87)*. It can be concluded from *Figure IV-46* that M_e depends on the loading position and on the notch radius for those cases in which the load is not centred. By contrast, for those cases with the centred load ($m = 0$), $K_{II}^u = 0$ and, therefore, pure mode I loading conditions ($M_e = 1$) are fulfilled.

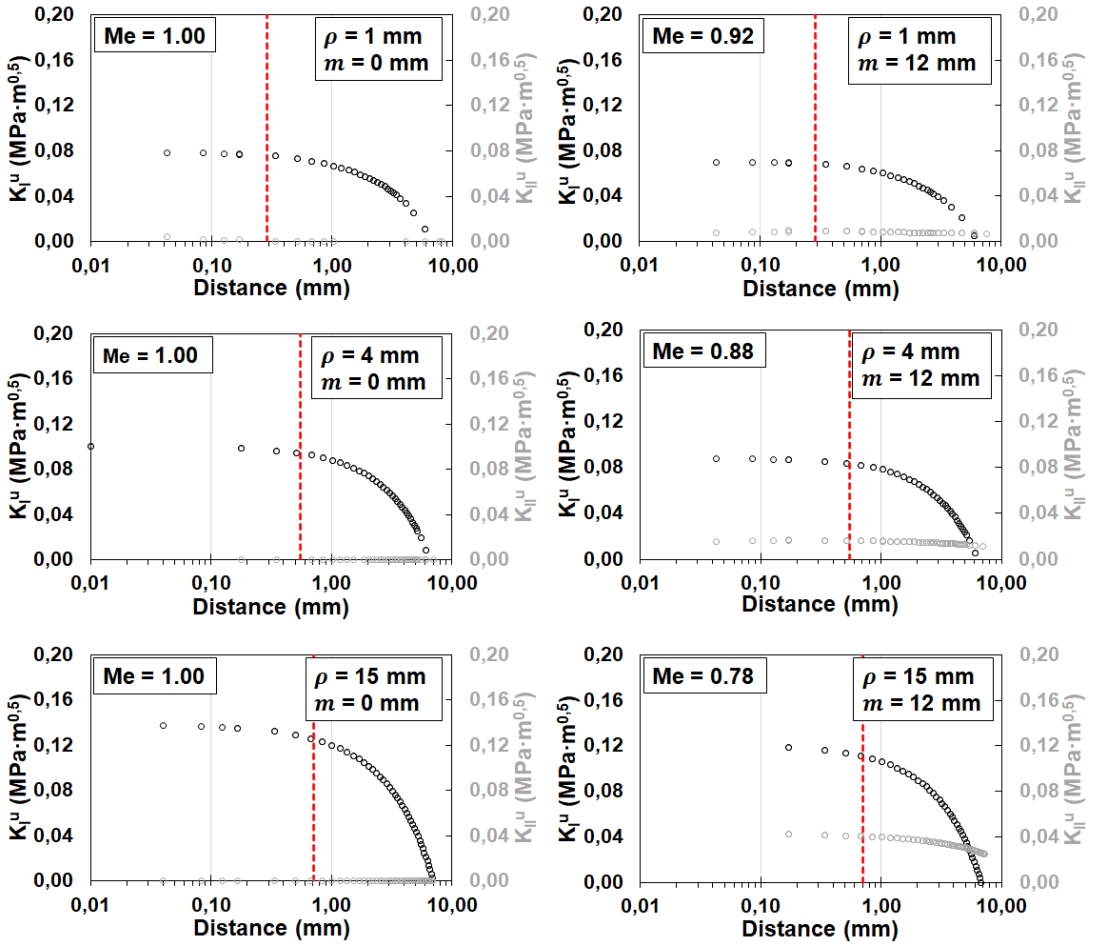

Figure IV-46. NSIFs versus distance for different notch radii (ρ = 1, 4 and 15 mm) and loading positions (m = 0 and 12 mm) at room temperature.

Table IV-33. Calculated values of the mode mixity (M_e) for each numerical model according to Equation (II-87).

TEMP.	ρ (mm)	P1	P2	P3	P4
23ºC	0.15	1.000	0.955	0.945	0.928
	0.50	1.000	0.972	0.935	0.923
	1	1.000	0.965	0.937	0.922
	2	1.000	0.953	0.921	0.904
	4	1.000	0.930	0.890	0.881
	7	1.000	0.911	0.866	0.853
	10	1.000	0.890	0.837	0.827
	15	1.000	0.856	0.792	0.781
250ºC	0.15	1.000	0.967	0.948	0.892
	0.50	1.000	0.960	0.935	0.934
	1	1.000	0.957	0.928	0.913
	2	1.000	0.952	0.920	0.904
	4	1.000	0.934	0.894	0.880
	7	1.000	0.911	0.850	0.853
	10	1.000	0.890	0.837	0.827
	15	1.000	0.856	0.792	0.783

Table IV-33 gathers the calculated values of the mode mixity (M_e) for each of the numerical models according to *Equation (II-87)*. It is observed that M_e reduces or, in other words, the mode II influence gets more evident as the loading position moves away from the centre and as the notch radius is larger. The small discrepancies that contradict these trends are caused by the sensitivity of the smallest notches when calculating the NSIFs (*Equations (II-88)* and *(II-89)*), as the number of calculation points along the assessed distance from the notch tip (*Equation (IV-3)* is relatively small in the case of the smallest notches (see *Figure IV-46*).

3.2.2 Interpretation of mixed mode I+II results

The fracture results of the three-point bending tests with the centred load (corresponding to mode I loading conditions) were already addressed both analytically and numerically in *Section 3.1*. In particular, the obtained fracture load predictions by means of the LM of the TCD provided relatively similar results for the Moleanos limestone, both at

room temperature and at 250ºC (*Figure IV-37*). With regards to the mixed mode I+II results, the performed numerical analyses follow the same procedure as that described for mode I loading conditions, with the only difference that the critical plane over which *Equation (II-77)* (LM) is assessed changes. Thus, finite element analyses are performed under the same conditions, with the only difference that the bisector of the notch is no longer the critical plane for mixed mode (I+II) loading conditions.

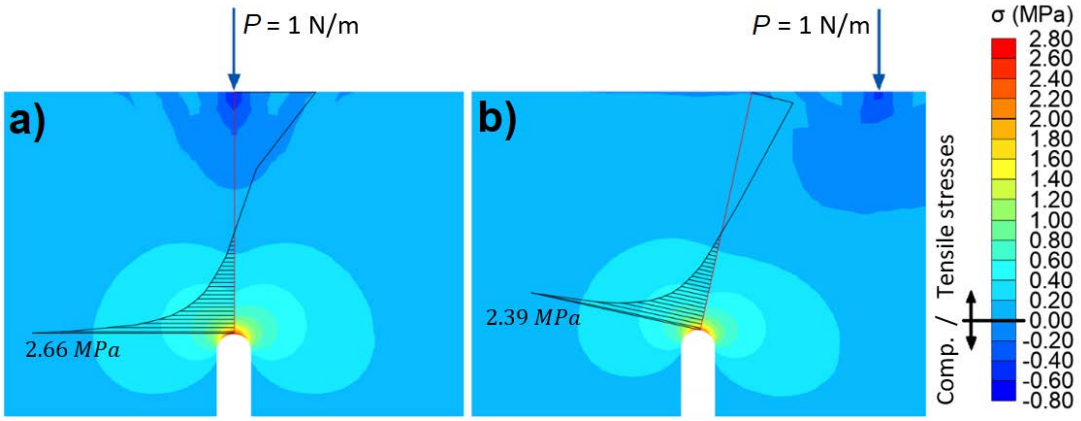

Figure IV-47. Numerically obtained critical planes and stress-distance curves for two different models with $\rho = 1$ *mm and (a)* $m = 0$ *mm and (b)* $m = 12$ *mm, both of them at room temperature.*

As indicated in *Section 2.7.5* of Chapter II, the main problem to be addressed is the definition of the plane where the stress field must be evaluated under mixed mode loading, for which the origin (hot spot) and the orientation of the focus path must be specified. It is generally accepted that the static fracture processes take place in highly stressed regions, as those generated by the notches. Accordingly, the superficial point experiencing the largest stress is usually taken as the starting point of the critical plane, which continues perpendicular to the maximum principal stress (tensile stress). Thus, the hot spot is characterized as the point on the circumference of the U-notch with the highest maximum principal stress (corresponding to the notch tip for mode I loading conditions). Starting from this point, the stress versus distance curve in which *Equation (II-77)* of the LM is assessed is plotted along the plane normal to the maximum principal stress. This plane goes along the centre of the semicircular U-notch. *Figure IV-47* shows, as an example,

the critical planes obtained from the numerical models for two particular cases with $\rho = 1$ mm and different loading positions ($m = 0$ and $m = 12$ mm). The numerically obtained stress-distance curves correspond to a unity load ($P = 1$ N/m). However, the curves derived can be rescaled according to the experimentally obtained failure load in order to obtain the stress-distance curve corresponding to failure situation. With this, the value of the critical distance (L) can be found by simply applying either the PM or the LM of the TCD at failure conditions. That is, the value of L satisfying *Equation (II-66)* (PM) or *Equation (II-77)* (LM) is to be found.

Here, for mixed mode (I+II) loading analyses, only the LM will be applied based on the obtained accurate results under mode I loading conditions (*Section 3.1*). Following the above mentioned methodology, a value of L is obtained for each notch radius and loading position. These individual values of L are represented by dots in *Figure IV-48*, against the corresponding mode mixity (M_e) indicated in *Table IV-33*.

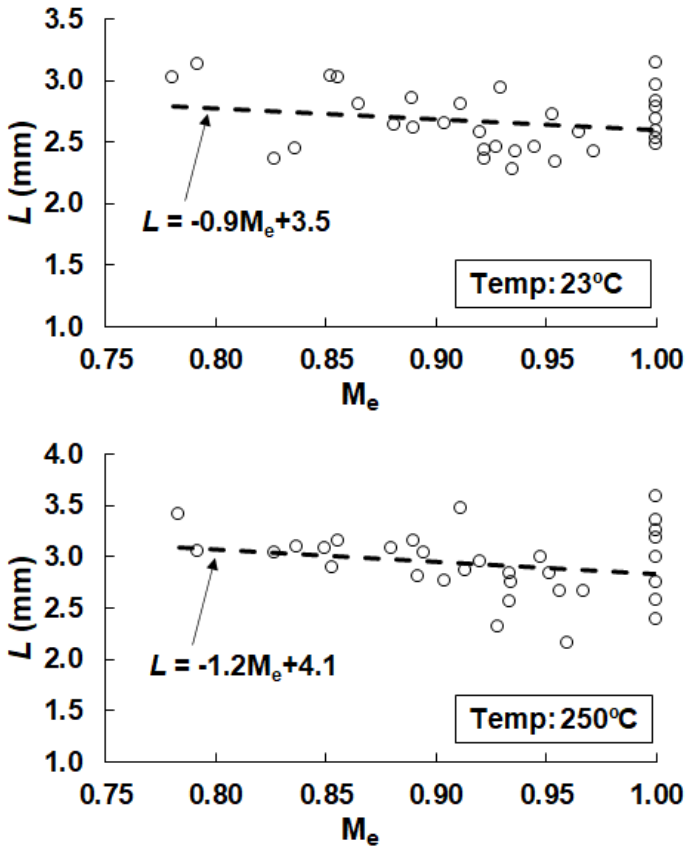

Figure IV-48. Variation of the critical distance (L) of the Moleanos limestone with the mode mixity (M_e) at 23ºC and 250ºC.

According to *Equation (II-86)* proposed by Negru et al. (2015) to link the critical distance with the mode mixity, L is linearly correlated with M_e. This linear correlation is indicated in *Figure IV-48* by the dashed lines, including the equations with the obtained material constants both at 23ºC and at 250ºC. Similar trends are observed in both cases, although the critical distance values are slightly higher at 250ºC. It is observed that L decreases with M_e at the studied range of mode mixities with predominant mode I influence.

In order to study the observed tendency more in detail, *Figure IV-49* represents the same results depicted in *Figure IV-48* but distinguishing the values according to the notch radii (ρ), using a different symbol for each one.

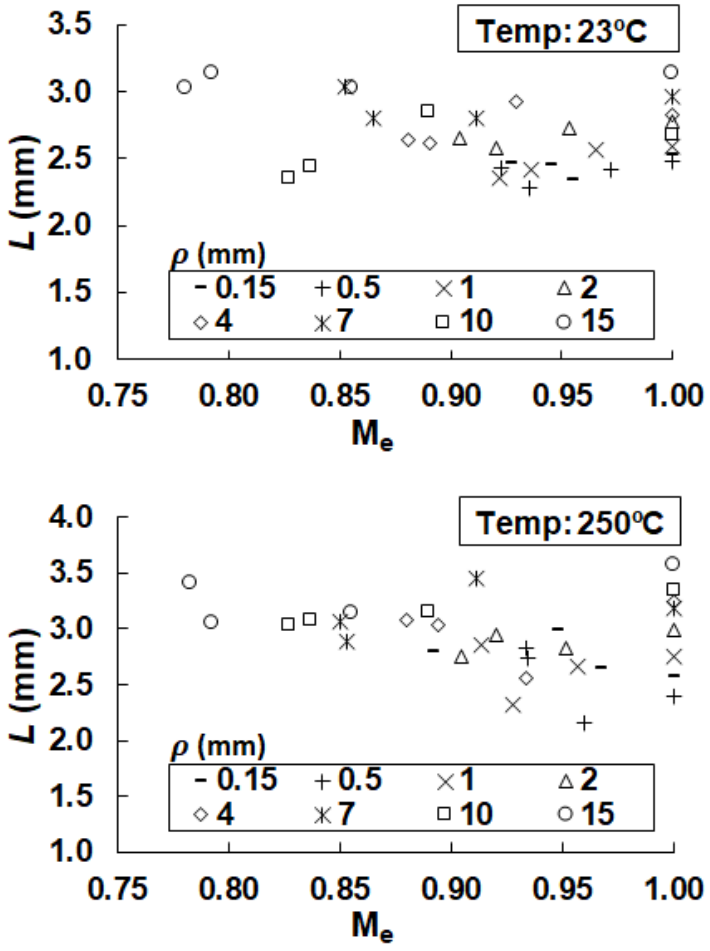

Figure IV-49. Variation of the critical distance (L) with the mode mixity (M_e) at 23ºC and 250ºC, represented with a different symbol for each notch radius.

When the results of each notch radius are analysed separately, it seems that the values of the critical distance are roughly constant for each notch radius or, at least, no clear decreasing or increasing tendencies are observed. In general terms, L seems to increase with the notch radius both at 23ºC and at 250ºC. This generality can also be observed in those L values collected in *Table IV-28* for those models subjected to mode I loading ($M_e = 1$).

The variation of the critical distance with the notch radius is clearly depicted in *Figure IV-50*. The horizontal axis represents the square root of ρ for the sake of clarity of the results. In any case, the increasing trend of L with notch radius seems to be clear both at 23ºC and at 250ºC.

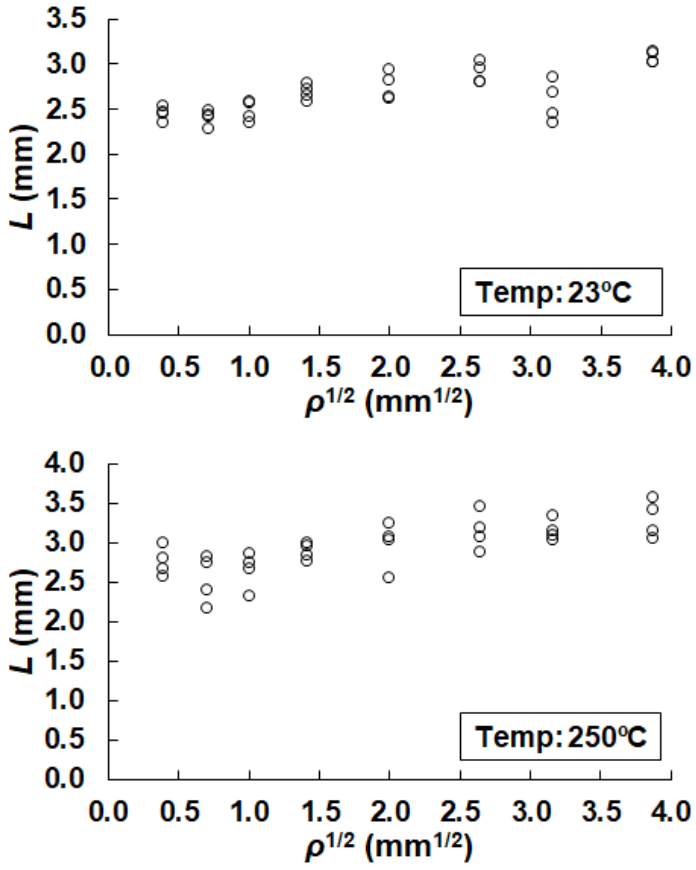

Figure IV-50. Variation of the critical distance (L) with the square root of the notch radius ($\rho^{1/2}$) at 23ºC and 250ºC.

The observed results indicate that L somehow increases with the notch radius rather than decreasing with M_e (as thought from *Figure*

IV-48) for the cases studied here. However, further research is needed for other cases. Establishing a real definition of the physical meaning of the critical distance is still a fundamental challenge among researchers (Taylor, 2017). L is supposed to be an intrinsic parameter of the material and has been related by different authors to clearly identifiable microstructural distances such as the grain size in the case of rocks. The analytical expressions corresponding to TCD do not consider the possible influence of the notch radius on the critical distance, assuming it is a material property (*Equation (II-70)*). However, the results shown in *Figure IV-50* seem to show certain influence on ρ. Dealing with this topic, Pluvinage & Capelle (2014) studied several characteristic length parameters generally used in different notch fracture criteria and stated that the scale length of the fracture volume process is not intrinsic to material but depends on the notch geometry, loading mode, constraints, etc. Here, the variations of L with ρ could be caused by the limited specimen dimensions or, in other words, due to the influence of boundary conditions. All this being said, it should be kept in mind that the observed variations of L do not have significant effects when performing predictions of critical loads as demonstrated in *Section 3.1.4* (see *Figure IV-38*).

In this *Section 3.2* an study of the critical distance under mixed mode (I+II) loading conditions has been presented. To do so, the experimentally obtained failure loads have been used to calculate a value of L for each notch radius and loading position, or in other words, for each mode mixity (M_e). Consequently, it does not make sense to provide fracture load predictions based on those values of L (as in *Section 3.1.4*), since they have been obtained from the same failure loads that are intended to be predicted. In general, the values of L are only obtained from experimentally obtained failure loads for a couple of extreme mode mixity values, from which the material constant parameters A and B of *Equation (II-86)* are derived. Once A and B are known, the value of L for any M_e value can be calculated and, eventually, used for fracture load assessments.

The methodology for the calculation of the predicted failure loads from L was already described in section *Section 3.1.4* for the particular case of mode I loading conditions (see *Section 3.1.3* for the description

of the numerical determination of the critical distance). The process is exactly the same with the only difference that the critical plane over which the PM or LM are applied rotates from the notch bisector plane under mixed mode I+II loading conditions (see *Figure IV-47*). However, in this section, the analysis of the variation of the critical distance with the mode mixity was considered to be more interesting.

4 APPLICATION OF THE SED CRITERION

As an alternative to the use of the TCD, the applicability of the SED criterion on the fracture assessment of U-notched rock samples is studied in this section. This energy-based analysis will be based on the fracture results of the performed four-point bending tests (both at room temperature and at higher temperatures up to 250ºC) described in *Section 3.3* of Chapter III, and on those four-point bending tests performed by Cicero et al. (2014), all of them under pure mode I loading conditions. Cicero et al. (2014) interpreted the test results using only the TCD.

4.1 MODE I ANALYSIS

A detailed description of the analytical frame of the SED criterion is provided in *Section 2.8.3* of Chapter II, and specifically in *Section 2.8.3.2*, the procedure for the application of the average SED criterion is explained. Basically, this approach states that the average strain energy density over a certain control volume (or control area under plane strain conditions) is limited by a material dependent critical value (W_c). Thus, failure occurs when the average strain energy density ($\overline{W}$) reaches W_c. Assuming linear elastic behaviour of rocks, W_c is calculated with *Equation (II-98)*, which only depends on the tensile strength (σ_u) and Young's modulus (E) of the material.

Berto et al. (2007) provided *Equation (II-130)* to define the average value of the strain energy density for the case of blunt V-notches, which simplifies to a great extent the fracture analysis of notched components. Considering the above mentioned failure criterion (defined by *Equation (II-97)*) and for the particular case of U-shaped notched components subjected to mode I loading conditions, *Equation (II-130)* can be rewritten as follows to express failure situation:

$$W_c = 0.785 \cdot H\left(\nu, \frac{R_0}{\rho}\right) \cdot \frac{\sigma_{max}^2}{E} \qquad \textit{(IV-4)}$$

σ_{max} is the maximum stress at the notch tip at failure, and E is the Young's modulus of the analysed material. The function H, on the other hand, depends on the ratio R_0/ρ and on the Poisson's ratio ν for U-shaped notches.

Table IV-34 collects the values of W_c for each of the six studied rocks, calculated with *Equation (II-98)* based on the tensile strength values obtained from Brazilian tests and gathered in *Table IV-1* and *Table IV-2*, and the Young's moduli derived from the uniaxial compression tests and collected in *Table IV-9* and *Table IV-10*.

Table IV-34. Critical SED values (W_c) of each rock at room temperature.

	(F)	(C)	(M)	(I)	(O)	(G)
W_c (kPa)	0.2066	0.6128	0.6770	0.7344	0.4746	0.8882

On the other hand, the radius (R_0) defining the control area (Ω) over which the strain energy is averaged (see *Figure II-66*) is calculated with *Equation (II-108)* when plane strain conditions are considered. The corresponding results of R_0 are collected in *Table IV-35* for each rock.

Table IV-35. Values of R_0 of each rock at room temperature.

	(F)	(C)	(M)	(I)	(O)	(G)
R_0 (mm)	3.905	2.964	3.101	1.538	2.128	6.433

The obtained R_0 values are of the order of millimetres due to the relatively low values of the tensile strength (σ_u) of rocks, which appear dividing in *Equation (II-108)*. As a consequence, the size of Ω will be relatively large in the case of rocks compared to other materials such as steels or polymers, for example.

Fracture load predictions can be easily performed from the direct application of *Equation (IV-4)*, by simply inverting that expression to obtain the maximum stress at failure (σ_{max}) and calculating the load generating that σ_{max} at the notch tip. Thus, once all the material

dependent parameters of *Equation (IV-4)* have been defined, the only issue is how to obtain the H function. Here, three different methodologies are proposed and compared based on the direct use of *Equation (IV-4)*. The first method (Method A) directly applies existing tabulated values of H (as those collected in *Table II-10*, which correspond to U-notches) and some extrapolations when necessary, avoiding the use of numerical modelling. By contrast, the other two methods are based on the numerical evaluation of the H function (Method B) and $\overline{W}$ (Method C), respectively.

With all this, an individual and detailed description is given below for each of the proposed methodologies, focusing on the particularities as well as on the associated advantages and limitations.

4.1.1 Method A: Published values of H

This first technique constitutes the simplest and most straightforward methodology, as the use of numerical modelling is avoided. Method A deals with analytical solutions based on the direct application of *Equation (IV-4)* through already tabulated values of the H function, as those proposed by Lazzarin & Berto (2005) and shown in *Table II-10*.

The range of values of R_0/ρ of *Table II-10* vary from 0.0005 up to 1, which may be sufficient for materials such as steels or polymers (e.g., Berto & Lazzarin, 2014; Cicero et al., 2017), but falls short for rocks where that ratio reaches much higher values. In the case of the studied granite, for instance, $R_0 = 6.43$ mm and considering the smallest analysed notch radius ($\rho = 0.15$ mm) R_0/ρ reaches a value of almost 43. For this reason, this first method proposes a double extrapolation, considering a second order polynomial function to extend the Poisson's ratio values and a first order rational function for larger ratios of R_0/ρ.

First, in order to expand the H values for higher Poisson's ratios, second order polynomial trendlines have been considered, since they offer a good agreement. *Figure IV-51* represents, as an example, the individual values of H for each ν (for the case of $R_0/\rho = 0.05$) and the corresponding trendline. The extrapolated values of H are calculated by the obtained second order polynomial function in each case. The obtained relative error of those values calculated by the polynomial

function compared to those in *Table II-10* is less than 0.02% in all the cases.

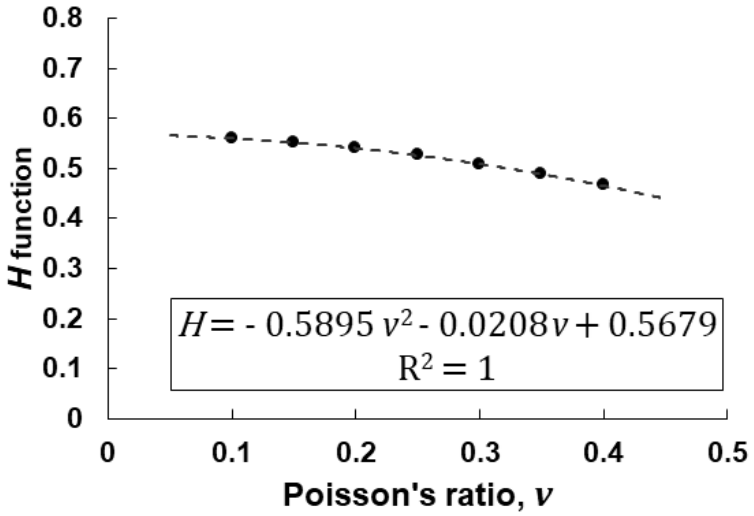

Figure IV-51. Second order polynomial adjustment for $R_0/\rho = 0.05$.

For the extrapolation of the H values for higher R_0/ρ ratios, some considerations must be taken into account. In the extreme case of analysing a crack with a radius equal to zero ($\rho = 0$), both R_0/ρ and the maximum stress at the tip tend to infinite. In this situation H should be zero in order to accomplish *Equation (IV-4)*. In the opposite case of an infinite notch radius ($\rho = \infty$), the specimen would develop a certain resistance and the maximum stress would have a finite value. Thus, H should also have a finite value according to *Equation (IV-4)*. These conditions imply that the best-fit equation must have a horizontal asymptote for $H = 0$ and must cut the vertical axis for $R_0/\rho = 0$ in a certain finite value.

Among all the possible equations meeting these conditions, a rational equation of order 1 has the simplest form, since only two parameters are required:

$$H = \frac{a'}{R_0/\rho + b'} \qquad (IV\text{-}5)$$

a' and b' are obtained for each value of the Poisson's ratio from the best adjustment of the rational function shown in *Equation (IV-5)*. The

specific case of the rational best-fit curve for $v = 0.25$ is represented in *Figure IV-52* as an example. A good agreement is observed between the tabulated H values (the dots) and the best-fit rational curve (the dotted line).

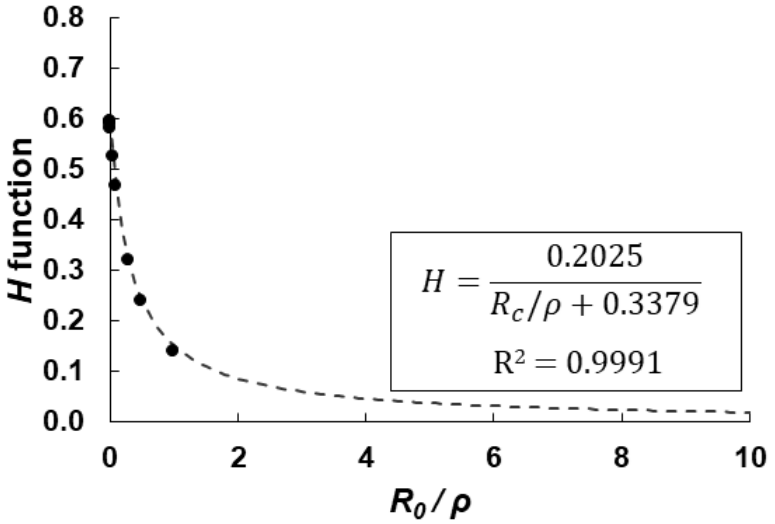

Figure IV-52. First order rational adjustment for $v = 0.25$.

The best-fit parameters a' and b' have been obtained for the particular values of v corresponding to each of the analysed rocks (*Table IV-9* and *Table IV-10*). These parameters, which allow the required H function to be calculated for any R_0/ρ ratio, have been collected in *Table IV-36* together with the coefficient of determination (R-square, R^2) of each adjustment.

Table IV-36. Obtained best-fit parameters from Equation (IV-5) and the corresponding coefficient of determination (R^2) for each rock.

	(F)	(C)	(M)	(I)	(O)	(G)
v	0.36	0.31	0.35	0.35	0.33	0.17
a'	0.1727	0.1864	0.1758	0.1751	0.1811	0.2199
b'	0.3100	0.3229	0.3129	0.3123	0.3181	0.3546
R^2	0.9989	0.9990	0.9989	0.9989	0.9990	0.9990

With all this, *Table IV-37* extends those H values collected in *Table II-10* (indicated in grey) for a broader range of R_0/ρ and v values

(indicated in black). This new table is suitable for geomaterials like rocks where the critical length (R_0) values are relatively high.

Table IV-37. Extrapolated values of the H function for U-notched specimens.

R_0/ρ	Poisson's ratio, v							
	0.10	0.15	0.20	0.25	0.30	0.35	0.40	0.45
0.0005	0.6294	0.6215	0.6104	0.5960	0.5785	0.5577	0.5337	0.5065
0.001	0.6286	0.6207	0.6095	0.5952	0.5777	0.5571	0.5332	0.5061
0.005	0.6225	0.6145	0.6033	0.5889	0.5714	0.5506	0.5268	0.4997
0.01	0.6149	0.6068	0.5956	0.5813	0.5638	0.5432	0.5194	0.4925
0.05	0.5599	0.5515	0.5401	0.5258	0.5086	0.4884	0.4652	0.4392
0.1	0.5028	0.4942	0.4828	0.4687	0.4518	0.4322	0.4099	0.3848
0.3	0.3528	0.3445	0.3341	0.3216	0.3069	0.2902	0.2713	0.2503
0.5	0.2672	0.2599	0.2508	0.2401	0.2276	0.2135	0.1976	0.1801
1	0.1590	0.1537	0.1473	0.1399	0.1314	0.1217	0.1110	0.0992
2	0.0982	0.0950	0.0911	0.0866	0.0815	0.0758	0.0696	0.0629
5	0.0433	0.0418	0.0400	0.0379	0.0356	0.0330	0.0302	0.0272
10	0.0224	0.0216	0.0207	0.0196	0.0184	0.0170	0.0155	0.0140
20	0.0114	0.0110	0.0105	0.0100	0.0093	0.0086	0.0079	0.0071
30	0.0077	0.0074	0.0070	0.0067	0.0062	0.0058	0.0053	0.0047
40	0.0058	0.0056	0.0053	0.0050	0.0047	0.0044	0.0040	0.0036
50	0.0046	0.0044	0.0042	0.0040	0.0038	0.0035	0.0032	0.0029

Once the H function is known from the tabulated values, the maximum stress at the notch tip (σ_{max}) corresponding to the failure situation becomes the only unknown and, therefore, can be calculated using *Equation (IV-4)*. The resultant σ_{max} value should be consistent with the expression proposed by Creager & Paris (1967), which defines, for long and narrow notches, the stress distribution as a function of distance from the notch tip (*Equation (II-72)*). The stress will be maximum at the tip, for $x = 0$. Thus:

$$\sigma_{max} = \sigma(x = 0) = \frac{2K_I}{\sqrt{\pi\rho}} \qquad (IV\text{-}6)$$

where K_I is the stress intensity factor of a crack with the same dimensions of the notch being analysed. At failure, K_I reaches a critical

value (K_{IC}) that can be analytically calculated with *Equation (II-32)*, F being the pursued failure load.

Thus, considering the energy-based failure criterion established by *Equation (IV-4)*, the maximum stress at the notch tip defined in *Equation (IV-6)* and the analytical expressions for defining the stress intensity factor for the particular case of SENB specimens subjected to four-point bending conditions (*Equations (II-32)*, *(II-33)* and *(II-34)*), the predicted failure load (here referred to as F_{SED}) can be directly calculated. The resulting expression is:

$$F_{SED} = \frac{b}{2Y}\sqrt{\frac{W_c \cdot E \cdot \rho \cdot \pi \cdot h}{0.785 \cdot H}} \qquad (IV\text{-}7)$$

b, h and ρ are previously defined geometrical parameters (*Figure III-28*), Y is the non-dimensional factor defined in *Equation (II-33)*, which also depends on geometrical aspects, and E is the Young's modulus. The critical strain energy (W_c) and the H function are also known variables collected, respectively, in *Table IV-34* and *Table IV-37*.

With all this, based on the application of *Equation (IV-7)*, *Figure IV-53* gathers the fracture load predictions for the six analysed rocks, representing, as in the case of the TCD results (*Section 3.1.4*), the ratio of the predicted failure load (F_{SED}) and the experimental failure load (F_{EXP}), against the notch radius (ρ). The dots correspond to the individual results for each of the four-point bending test specimens, while the solid line represents the mean values for the different notch radii. Again, $F_{SED}/F_{EXP} = 1$ stands for the exact prediction, and an envelope of ±20% have been defined with horizontal red dashed lines. This strip delimited by the dashed lines will be considered as representative of the accuracy of the predictions for mean values.

Based on the results depicted in *Figure IV-53*, it can be generally observed that Method A offers reasonable results even for the largest notches beyond the application range of Creager & Paris (1967). The Carrara Marble shows the worst predictions with almost 50% of the individual results outside the established limits, especially those with the largest notch radii. This is probably a consequence of the non-linear

behaviour observed for the Carrara marble even at room temperature (*Figure IV-10*) while, for the calculation of W_c, linear-elastic behaviour is being assumed. Besides, the application of Creager & Paris' (1967) formulation for the definition of the σ_{max} at the notch tip (*Equation (IV-6)*) could also explain the worsening of the results as notch radius gets larger. The results for the rest of the rocks, which roughly present linear behaviour till failure according to *Figure IV-10* and *Figure IV-21*, fall acceptably within the upper and lower bands, with more than 70% of the dots inside these limits in the case of the Macael Marble and more than 80% for the remaining rocks. Finally, the predictions tend to be more conservative for the smaller notch radii, where Creager & Paris' (1967) stress distribution function better matches the real stress distribution along the notch bisector plane (*Figure IV-35*).

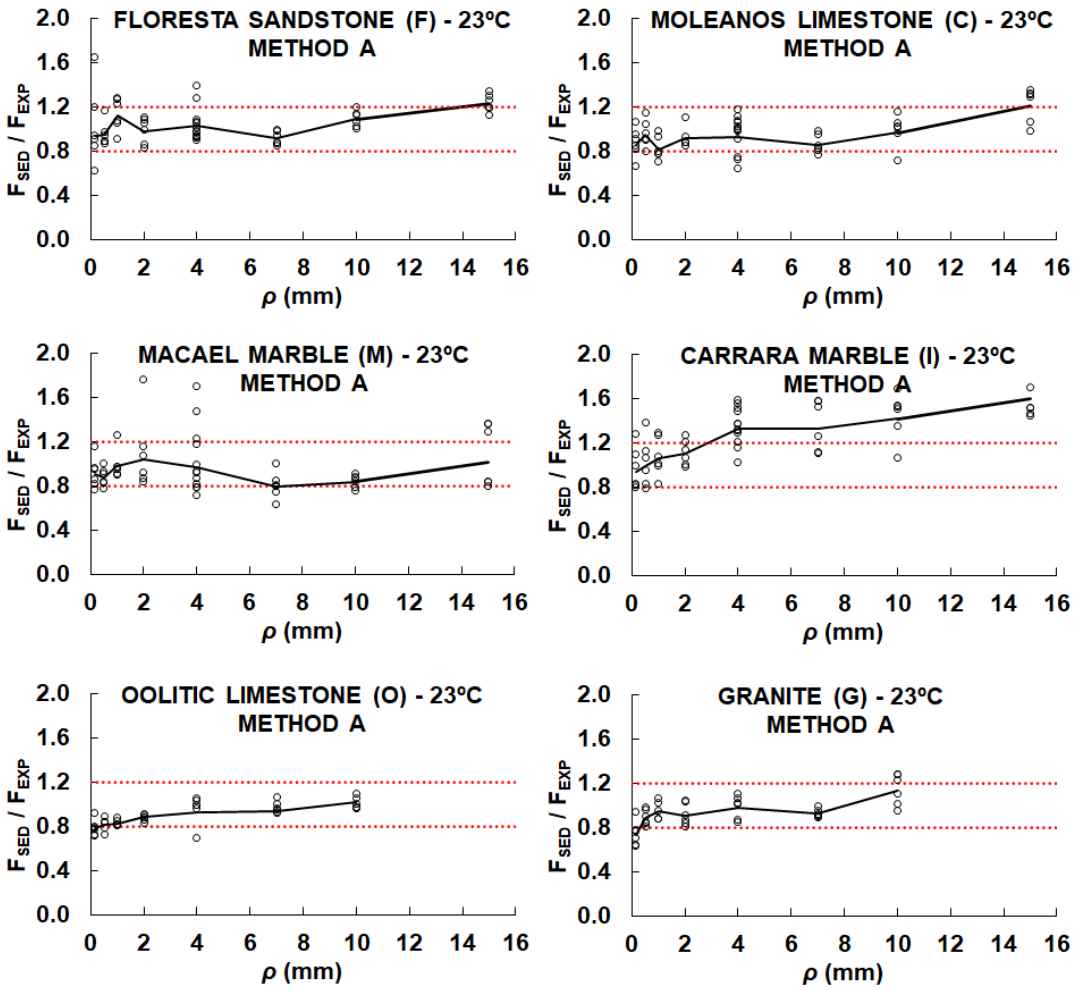

Figure IV-53. SED predictions (Method A) of the failure load for each rock at room temperature.

4.1.2 Method B: Numerical evaluation of H function

The second proposed method deals with numerical modelling in order to generate a new table for the H function, adapted to the range of R_0/ρ values appropriate for the analysed rocks. The H function is theoretically independent of the notch radius considered in the calculation model (ρ_{fem}), only depending on ν and on the ratio R_0/ρ as long as U-shaped notches ($2\alpha = 0$) are considered. For this reason, from a strict point of view, it is necessary to conduct a single numerical model for each material with a specific notch radius. With this unique model per material, the values of H that correspond to any R_0/ρ can be obtained by simply rescaling the control area (Ω, defined by R_0). Theoretically, for a given value of R_0/ρ and for each ν, only one value of H is possible. Consequently, any combination of R_0 and ρ offering the same ratio will also provide the same H for a certain material. However, this statement is rather limited because of the influence of boundary conditions, since the bigger the notch radius (ρ) the larger the control area (defined by R_0) for a given value of R_0/ρ, and the other way around.

Figure IV-54 shows, as an example, the case of the Moleanos limestone. It is observed how, for a certain value of R_0/ρ, the size of the control area increases with the size of the modelled notch, representing the cases of ρ_{fem} = 1, 2 and 4 mm, respectively.

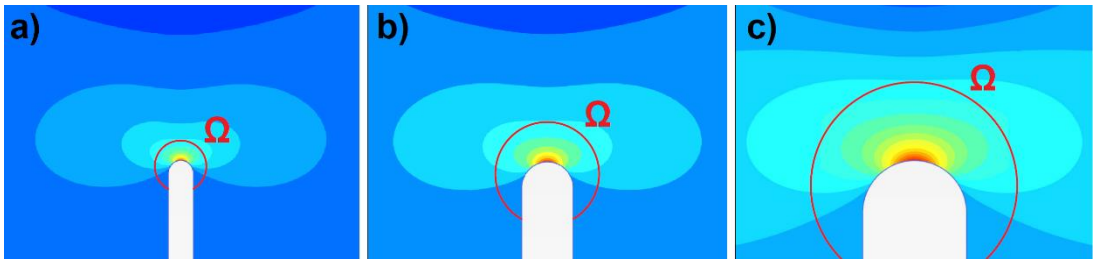

Figure IV-54. Control areas (Ω) of the Moleanos limestone (C) for R_0/ρ = 1.4819 (corresponding to R_0 = 2.9638 mm and ρ = 2 mm) and for a numerical model with (a) ρ_{fem} = 1, (b) 2 and (c) 4 mm.

Thus, the chosen notch radius for the numerical model will influence the dimensions of the control area (Ω) over which the strain energy is averaged. The lower bound of this area is delimited by the refinement of the mesh, while the upper bound has a double limitation. First, the geometry of the numerical model physically limits the maximum size of

that area and, second, the closed form expressions of the SED criterion (see *Section 2.8.3* of Chapter II) are only valid in the vicinity of the notch. In fact, the applied methodology assumes that the local stress field assessed from the notch tip to a distance R_0 is governed by the Generalised Notch Stress Intensity Factor, which is true up to a distance where the influence of the outer limit of the specimen is negligible, but is no longer valid for large values of R_0 where the influence of the boundary becomes noticeable.

The critical radius (R_0) is unique for each rock, as it only depends on the material through the Poisson's ratio (ν), the fracture toughness (K_{IC}) and the tensile strength (σ_u). *Table IV-35* gathers the corresponding values for each of the six analysed rocks. However, in order to use a single numerical model for each of the rocks with a single notch radius (ρ_{fem}), the considered critical radius R_{0_fem} in the calculation will vary so as to maintain the R_0/ρ ratio. Thus, R_{0_fem} will have to fulfil the following expression:

$$\frac{R_0}{\rho} = \frac{R_{0\_fem}}{\rho_{fem}} \quad \rightarrow \quad R_{0\_fem} = R_0 \frac{\rho_{fem}}{\rho} \qquad \textit{(IV-8)}$$

According to this expression, when the notch radius that is implemented in the model (ρ_{fem}) is larger than the notch radius that is being assessed in the fracture prediction (ρ), the value of R_{0_fem} considered in the calculation will be larger than the critical radius (R_0) corresponding to the rock. Therefore, it can be concluded that the larger ρ_{fem} is selected for the model, the larger the required control areas (Ω). By contrast, the control area will get smaller as lower values of ρ_{fem} are considered in the model. This tendency can be clearly seen, for example, in *Figure IV-55*, corresponding to the Moleanos limestone, and in *Figure IV-56*, corresponding to the Macael marble. These figures represent a matrix with all the range of possibilities. The columns correspond to the different notch radii that have been implemented in the numerical model (ρ_{fem}), starting from 0.15 mm up to 15 mm. On the other hand, the rows indicate the notch radii for which the fracture is assessed (ρ).

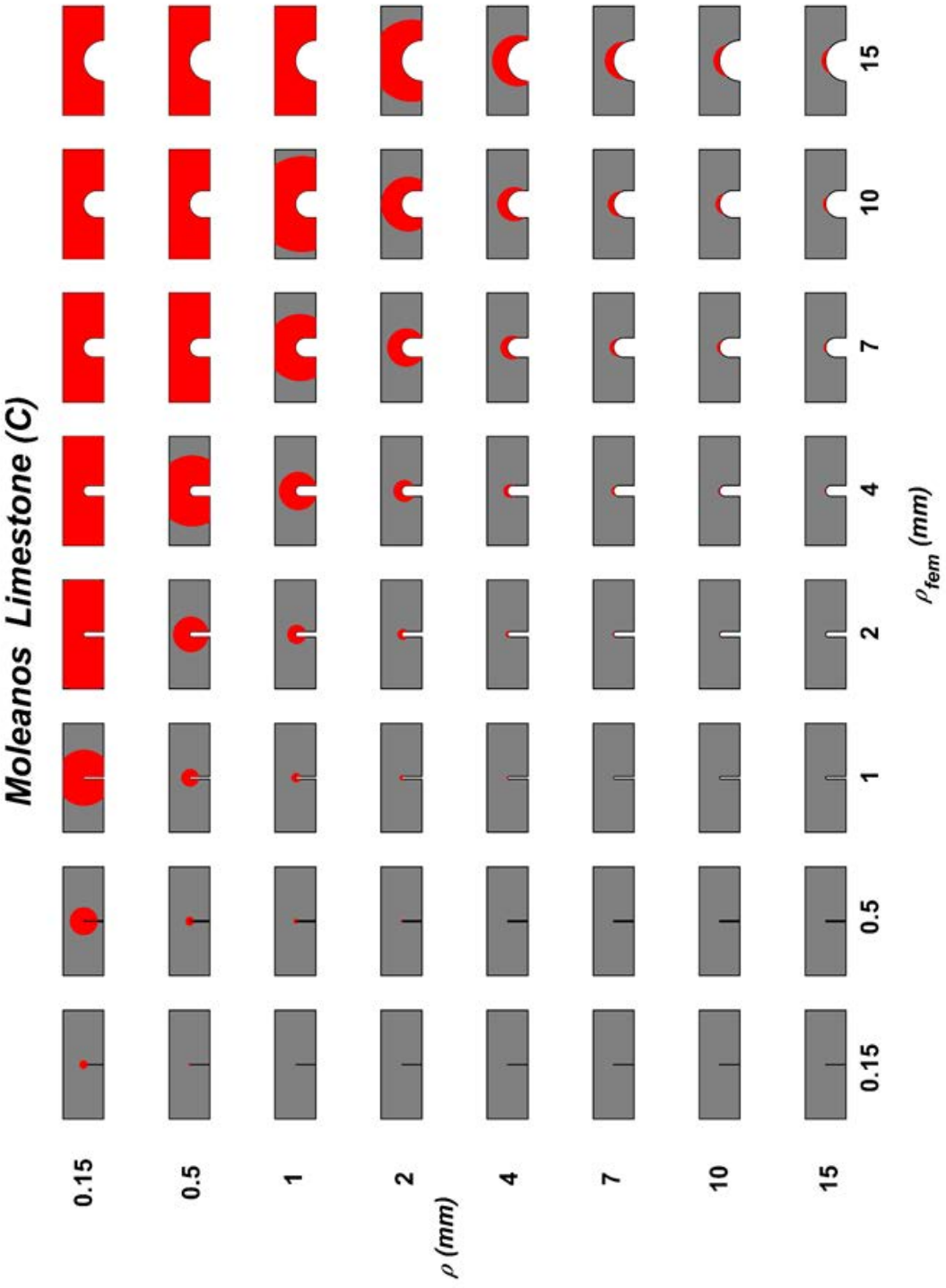

Figure IV-55. Size of the control area (Ω) for each notch radius used in the numerical model (ρ_{fem}) and studied notch radius (ρ) combination, corresponding to the particular case of the Moleanos limestone.

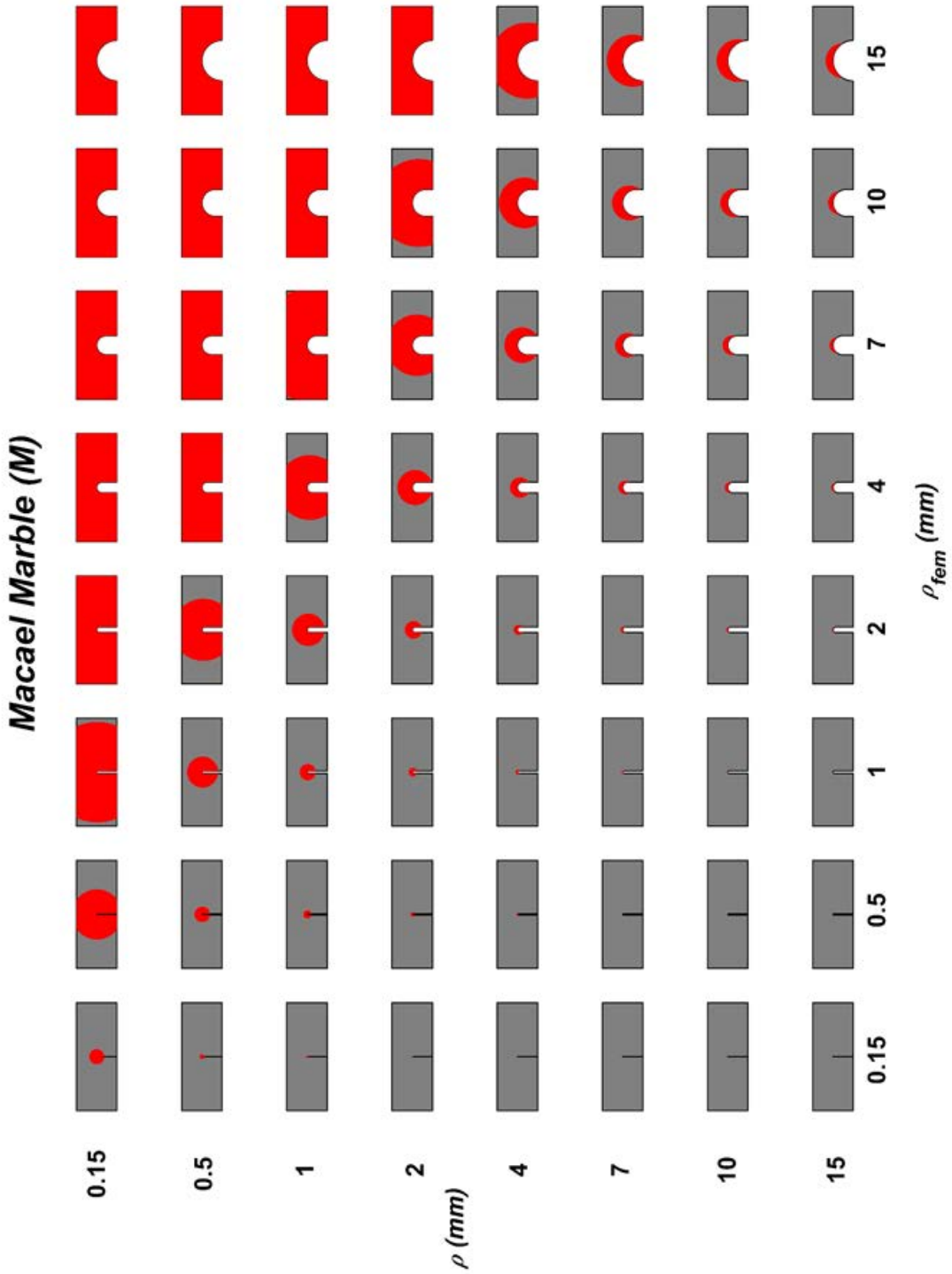

Figure IV-56. Size of the control area (Ω) for each notch radius used in the numerical model (ρ_{fem}) and studied notch radius (ρ) combination, corresponding to the particular case of the Macael marble.

All the possibilities within a row should provide the same value of H, since R_0 is a constant for the material and, therefore, correspond to the same ratio R_0/ρ. It can be directly observed that as smaller notch radii (ρ) are beeing evaluated larger control areas are required. Likewise, as we move towards greater values of ρ_{fem} the control areas become larger, even exceeding the geometric boundaries of the model in many cases.

These matrixes offer a very valuable information for the selection of the most suitable notch for the numerical model (ρ_{fem}). A sensitivity analysis has been carried out in order to determine the most suitable notch radius to be implemented. First of all, a notch with $\rho_{fem} = 1$ mm has been considered, obtaining the corresponding values of H. These values have proven to be very similar to those proposed by Lazzarin & Berto (2005) and shown in *Table II-10*, which were, in origin, obtained numerically for $\rho_{fem} = 1$ mm. The numerical models made with the rest of the notch sizes have also been checked, and it was observed that the best results correspond to the model with the smallest notch radius, $\rho_{fem} = 0.15$ mm, while the largest radii offer the poorest results. This generality makes sense, since the control area (Ω) becomes larger as higher values of ρ_{fem} are implemented in the model, even exceeding its geometric limits (see *Figure IV-55* and *Figure IV-56*). For these reasons and for the sake of simplicity, only the results for $\rho_{fem} = 0.15$ mm and $\rho_{fem} = 1$ mm are presented here.

In this work, a finite element code PLAXIS 2D (2017) has been used to model the test specimens. A linear elastic model is used to simulate the rocks, as in the case of the numerical analysis of the TCD. The applied load in the models is not determinant, since H is independent of the maximum stress at the notch tip (σ_{max}) and proportional to the mean strain energy density ($\overline{W}$), which are the only required outputs of the numerical models. Both *Table IV-38* and *Table IV-39* gather the H values for the different notch radii. These values are directly obtained by inverting *Equation (II-130)*, both for the results of the model with $\rho_{fem} = 1$ mm and $\rho_{fem} = 0.15$ mm, respectively. All the values in *Table II-10* and *Table IV-38* are obtained numerically with a notch radius $\rho_{fem} = 1$ mm (with slightly different boundary conditions), but only those indicated in grey are comparable with the values proposed by Lazzarin & Berto (2005) in *Table II-10*, since the corresponding R_0/ρ

ratios are in the same range. By contrast, the remaining values are outside that range and must therefore be compared with the extrapolated values of the first methodology (Method A).

Table IV-38. H function obtained numerically from the model with $\rho_{fem} = 1$ mm (Method B).

ρ (mm)	(F)	(C)	(M)	(I)	(O)	(G)
0.15	0.0032	0.0037	0.0027	0.0051	0.0049	0.0032
0.5	0.0130	0.0155	0.0072	0.0236	0.0191	0.0058
1	0.0295	0.0344	0.0174	0.0509	0.0420	0.0135
2	0.0629	0.0726	0.0379	0.1066	0.0907	0.0328
4	0.1311	0.1524	0.0797	0.2186	0.1910	0.0719
7	0.2281	0.2570	0.1456	0.3290	0.2939	0.1318
10	0.3018	0.3264	0.2091	0.3929	0.3564	0.1909
15	0.3762	0.3955	0.2889	0.4593	-	-

Table IV-39. H function obtained numerically from the model with $\rho_{fem} = 0.15$ mm (Method B).

ρ (mm)	(F)	(C)	(M)	(I)	(O)	(G)
0.15	0.0059	0.0069	0.0035	0.0102	0.0077	0.0025
0.5	0.0214	0.0243	0.0131	0.0354	0.0270	0.0110
1	0.0428	0.0482	0.0266	0.0699	0.0542	0.0231
2	0.0848	0.0948	0.0529	0.1348	0.1101	0.0472
4	0.1663	0.1939	0.1022	0.2940	0.2373	0.0937
7	0.3121	0.3340	0.1796	0.4539	0.3375	0.1614
10	0.4087	0.4391	0.2886	0.5148	0.4242	0.2269
15	0.5113	0.5001	0.3937	0.5495	-	-

Once the H function is known, the predicted failure load (F_{SED}) is calculated proceeding in the same way as in Method A, applying *Equation (IV-7)*. The obtained predictions are shown in *Figure IV-57* and *Figure IV-58*.

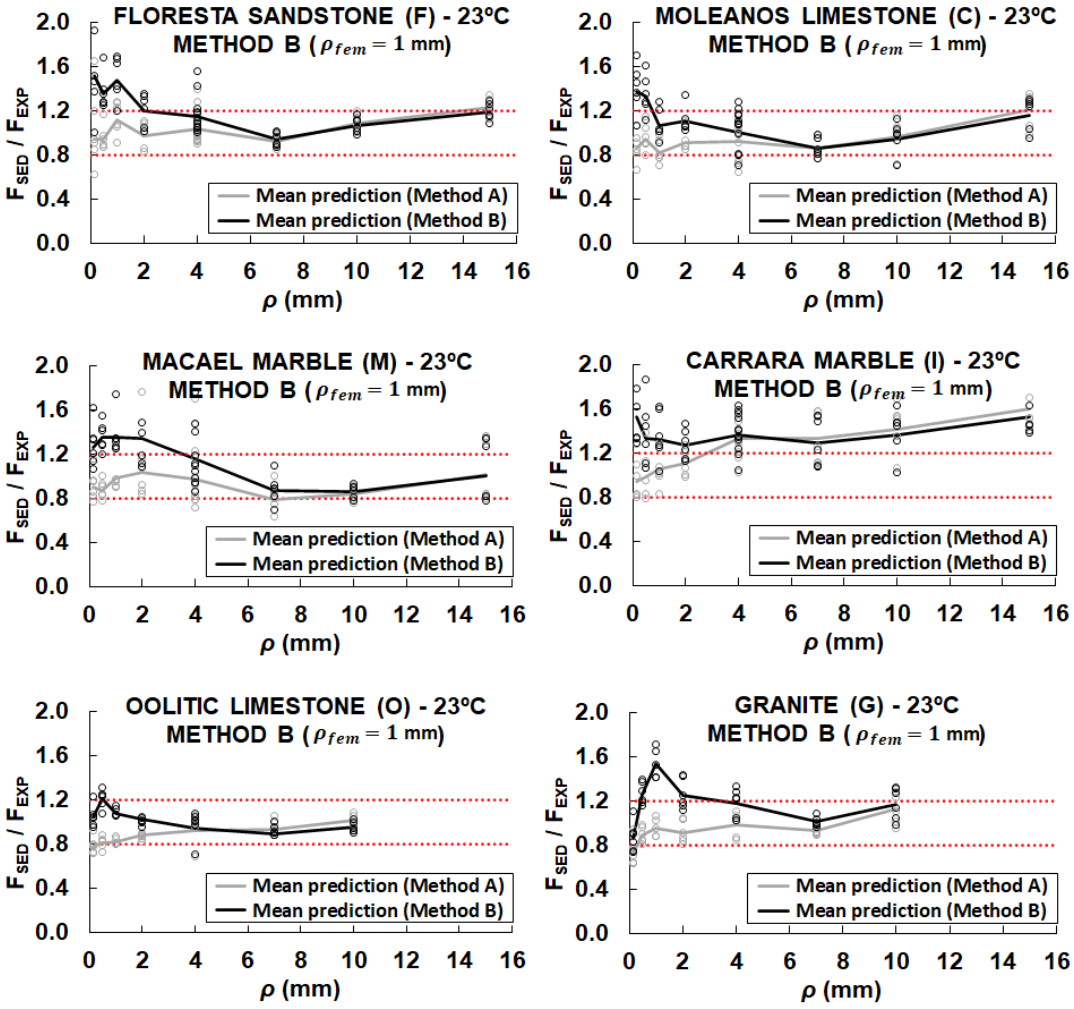

Figure IV-57. SED predictions (Method B: $\rho_{fem} = 1$ mm) of the failure load for each rock at room temperature.

Figure IV-57 shows the results obtained using the H values from the numerical model with $\rho_{fem} = 1$ mm superposed on the previous results depicted in *Figure IV-53* (Method A). For the range of comparable R_0/ρ values, that is, the non-extrapolated part but the overlapping one, the coincidence should be reflected in the last segment of the plotted curves, from $\rho = 4$ mm onwards for the Oolitic limestone, Moleanos limestone, Floresta sandstone and Carrara marble, and from $\rho = 7$ mm on for the granite and Macael marble. All the curves reveal a clear similarity in this range of values, except the granite that shows some differences. On the contrary, the initial part of the curves is to be compared with the extrapolated values of Method A. It can be observed that the adjustment between both curves is somewhat worse in this zone. A generalized overestimation using Method B is observed in *Figure IV-57* for the

smallest notch radii in all the analysed rocks. The control area over which the strain energy density is averaged exceeds the boundary condition in these cases (see for example $\rho_{fem} = 1$ mm column in *Figure IV-55* and *Figure IV-56*), which explains the observed overestimations. However, the predictions for the biggest notches (corresponding to the relatively small control areas) offer more accurate predictions according to *Figure IV-57*. Thus, it can be concluded that the numerical model with $\rho_{fem} = 1$ mm might be sufficient to obtain the H for R_0/ρ ratios common in materials like steels or polymers with lower critical radii (R_0), as done by Lazzarin & Berto (2005), but falls short in materials like rocks where R_0 is of the order of several millimeters, specially in the case of evaluating the fracture of small notches.

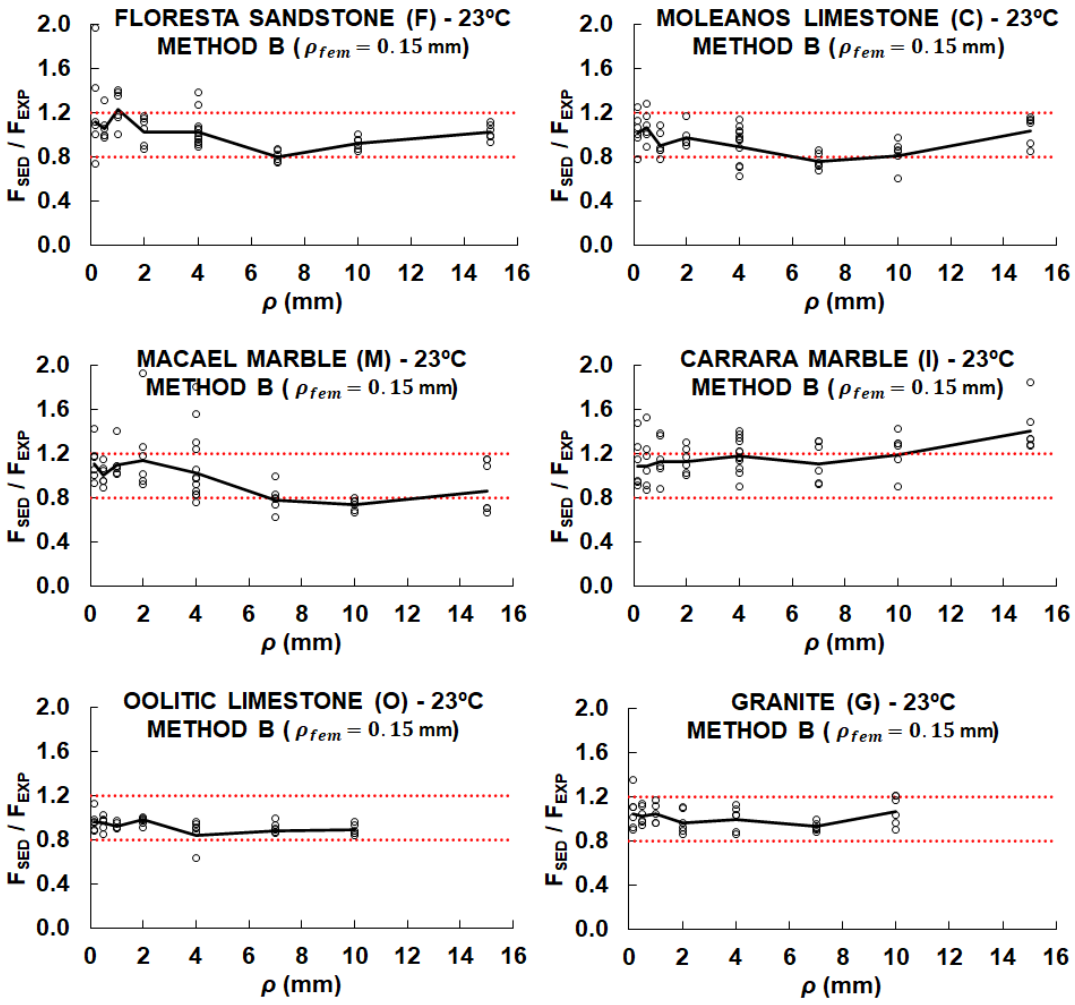

Figure IV-58. SED predictions (Method B: $\rho_{fem} = 0.15$ mm) of the failure load for each rock at room temperature.

Finally, the results obtained using H values from the numerical model with $\rho_{fem} = 0.15$ mm are shown in *Figure IV-58*. The accuracy of the predicted failure loads (F_{SED}) is reasonable in all the studied rocks, even for the Carrara marble which offered the worst results in the previous cases. More than 80% of the individual results fall, on average, within the ±20% strip defined by the dashed lines, except the Carrara marble, where the percentage is considerably lower despite the improvement in the mean results. Moreover, the tendency observed when applying the extrapolation (Method A), in which less conservative results were obtained when increasing the notch radius, is not perceived here (neither in *Figure IV-57* nor in *Figure IV-58*).

4.1.3 Method C: Numerical evaluation of $\overline{W}$

The two previous methods are based on Creager & Paris (1967) to define the stress distribution at the notch tip (*Equation (II-72)*), since *Equation (IV-7)* is used for fracture load predictions. However, as highlighted in numerous occasions, *Equation (II-72)* is theoretically valid only for long and narrow notches ($a \gg \rho$), so the largest analysed radii are outside its application range, despite having proven to offer reasonable results. This third methodology aims to avoid the use of *Equation (II-72)*, directly relating the applied load (P) in the numerical model with the obtained strain energy density. In fact, it is based on the existing proportionality relation between P and the mean strain energy density corresponding to a given control area ($\overline{W}$). This proportionality is squared (see *Equation (II-130)*), so that twice the applied load ($2P$) involves four times the average strain energy density ($4\overline{W}$).

On this basis, Method C calculates, using finite element analyses, the necessary load for the mean strain energy density ($\overline{W}$) to be equal to the critical strain energy density (W_c). This load defines the failure condition and will therefore be equal to the predicted failure load (F_{SED}).

The results of this last proposed methodology are depicted in *Figure IV-59*. It is generally observed that the accuracy of the predictions is quite reasonable for the largest notch radii, where the use of *Equation (II-72)* was theoretically out of application. However, the predicted failure loads for the smallest notch radii do not provide such good results and there is a clear and general tendency to overestimate them. Finally, the results corresponding to the granite are noticeably above the

theoretical failure line, which implies an overestimation factor of around 1.4 on average. Among all the studied rocks, the granite is the one with the largest critical radius and with the smallest specimen height. For this reason, the influence of the boundary is more noticeable than in the rest of rocks. Besides, Method C directly applies *Equation (II-130)* for the fracture assessment, which is theoretically only valid when the control area embraces the semi-circular edge of the notch and not its rectilinear flanks according to Lazzarin & Berto (2005). This statement justifies the worsening of the results in Method C, especially in the case of the granite and in the case of evaluating the failure of the smallest notch radii. However, this effect is somehow smoothened when applying Method B, where the fracture is assessed according to Creager & Paris (1967) through the application of *Equation (II-72)*.

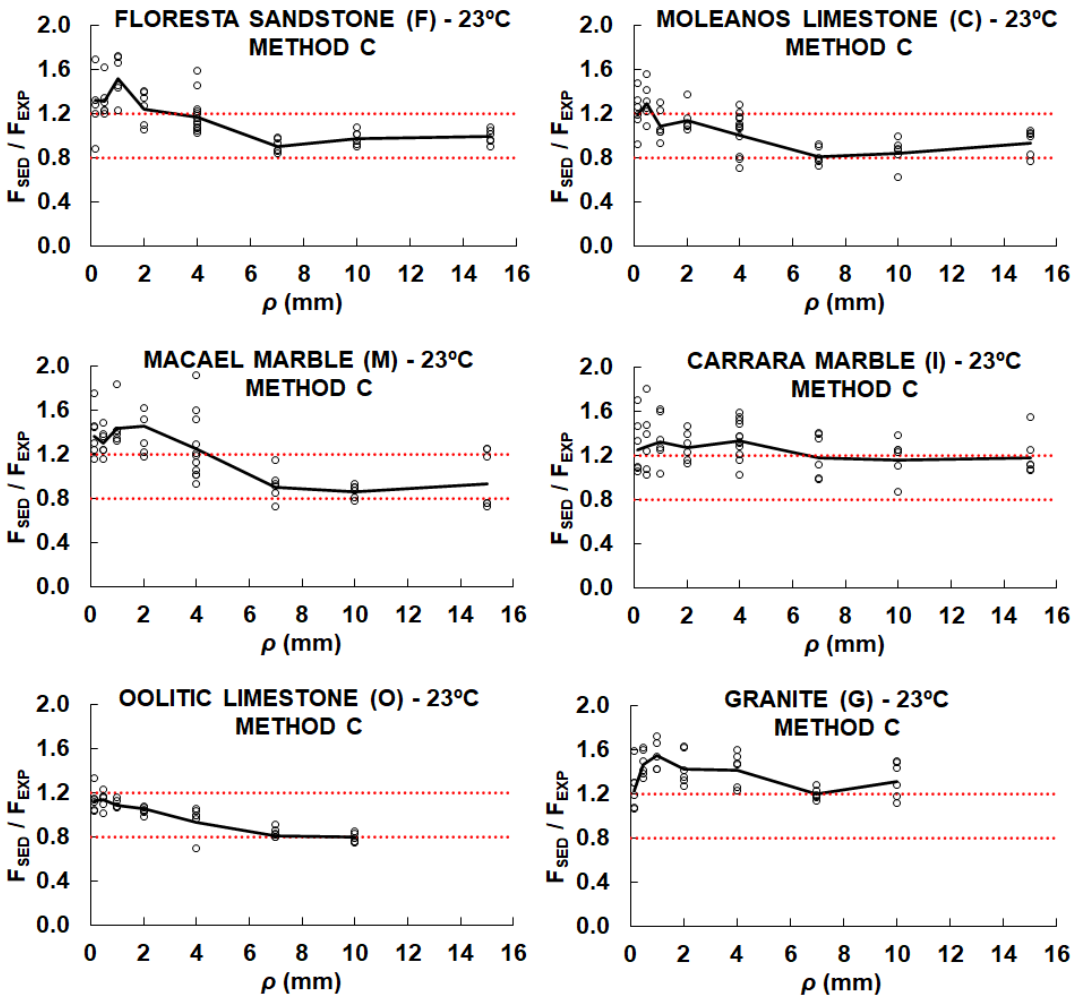

Figure IV-59. SED predictions (Method C) of the failure load for each rock at room temperature.

Finally, it should be pointed out that although Method C avoids the use of *Equation (II-72)* of Creager & Paris (1967), it requires the construction of a specific numerical model for each test condition, that is, one for each material type and notch radius. This implies an important drawback, as the required workload for the fracture assessment increases considerably.

4.2 MODE I ANALYSIS UNDER DIFFERENT THERMAL CONDITIONS

The energy-based methodology used in the previous *Section 4.1* for the fracture assessment of rocks at room temperature is now extended to apply the SED criterion up to temperatures of 250ºC. The focus is placed on the results of the Floresta sandstone (F), Moleanos limestone (C), Macael marble (M) and Carrara marble (I) subjected to four-point bending conditions at four different temperatures up to 250ºC. In this case, the Oolitic limestone and the Biotite granite are not considered since the four-point bending tests performed by Cicero et al. (2014) were only executed at room temperature. The considered failure criterion is exactly the same as before, in which the average strain energy density ($\overline{W}$) over a certain control area (Ω) is limited by a critical value (W_c). The critical strain energy (W_c) has been assumed to be constant for each rock and temperature, presuming that the analysed rocks behave as linear-elastic materials at the studied range of temperatures (see *Figure IV-10*). Under this hypothesis, *Equation (IV-4)* proposed by Lazzarin & Berto (2005) for the fracture assessment of notched components is still valid for the evaluation of the U-notched rocks at high temperatures, just varying the material dependent parameters accordingly with temperature. *Table IV-40* and *Table IV-41* contains the calculated values of W_c and R_0 of each of the analysed rocks and considered temperatures.

Table IV-40. Critical SED values (W_c) of each rock at different temperatures.

	(F)	(C)	(M)	(I)
W_c (kPa) – 23ºC	0.2066	0.6128	0.6770	0.7344
W_c (kPa) – 70ºC	0.2852	0.7501	0.5058	0.5265
W_c (kPa) – 150ºC	0.2858	1.0828	0.4121	0.5877
W_c (kPa) – 250ºC	0.3656	0.8011	0.5215	0.7170

Table IV-41. Values of R_0 of each rock at different temperatures.

	(F)	(C)	(M)	(I)
R_0 (mm) – 23ºC	3.905	2.964	3.101	1.538
R_0 (mm) – 70ºC	4.781	3.916	6.736	2.889
R_0 (mm) – 150ºC	5.383	2.732	3.133	3.141
R_0 (mm) – 250ºC	3.956	4.065	4.730	1.469

In general terms, among the three methods proposed in *Section 4.1* for the adaptation of the SED approach to the required R_0/ρ ratios of rocks, the fracture load predictions provided by the first and simplest method (Method A) were accurate enough, and the theoretical improvement offered by the other methods based on numerical analyses did not justify the significant increase of the workload.

Thus, the most straightforward and simplest method will be applied here for the fracture assessment of the analysed rocks at different temperatures; that is, tabulated values of H will be directly used (Method A), as those presented in *Table IV-37* as an extension to those of *Table II-10*. *Section 4.1.1* provides a detailed description and justification of the extrapolation methods for the definition of the H function outside the values defined by Lazzarin & Berto (2005) in *Table II-10*.

In order to obtain the particular H values corresponding to each of the analysed rocks and temperatures with *Equation (IV-5)*, the best-fit parameters a' and b' have been obtained for the particular values of v corresponding to each rock and temperature, exactly in the same way as done in *Table IV-36* for room temperature cases. These new parameters are collected in *Table IV-42*, together with the coefficient of determination (R^2) of each adjustment.

The obtained values of a' and b' allow to calculate H for any R_0/ρ ratio, and once the pursued H is known, the failure load can be directly calculated again by means of *Equation (IV-7)*, considering the variation with temperature of the material dependent parameters (i.e., W_c, E and R_0).

Table IV-42. Obtained best-fit parameters from Equation (IV-5) and the corresponding coefficient of determination (R^2) for each rock at different temperatures.

TEMP.		(F)	(C)	(M)	(I)
23ºC	v	0.36	0.31	0.35	0.35
	a'	0.1727	0.1864	0.1758	0.1751
	b'	0.3100	0.3229	0.3129	0.3123
	R^2	0.9989	0.9990	0.9989	0.9989
70ºC	v	0.29	0.28	0.28	0.30
	a'	0.1914	0.1963	0.1957	0.1904
	b'	0.3275	0.3321	0.3316	0.3266
	R^2	0.9990	0.9991	0.9991	0.9990
150ºC	v	0.32	0.28	0.35	0.31
	a'	0.1838	0.1945	0.1742	0.1869
	b'	0.3204	0.3304	0.3113	0.3233
	R^2	0.9990	0.9990	0.9989	0.9990
250ºC	v	0.34	0.28	0.42	0.47
	a'	0.1797	0.1944	0.1533	0.1375
	b'	0.3166	0.3303	0.2911	0.2748
	R^2	0.9989	0.9990	0.9986	0.9983

Figure IV-60 illustrates the obtained failure load predictions for each rock and temperature according to the SED criterion, and, in particular, the proposed Method A. The dots correspond to each of the individual results and the solid line represents the mean failure load predictions. Again, the vertical axis indicates the ratio between the predicted failure load (F_{SED}) calculated with *Equation (IV-7)* and the experimentally obtained failure load (F_{EXP}) from the four-point bending tests at different temperature conditions. Likewise, in the horizontal axis, the notch radius (ρ) is represented. The horizontal red dotted lines define an error band of ±20%, which is a common practice in fracture mechanics to define a region of reasonable accuracy. This envelope aims to somehow comprise the intrinsic uncertainties of the performed laboratory tests as well as the variability of the fracture results due to the heterogeneous nature of the rocks.

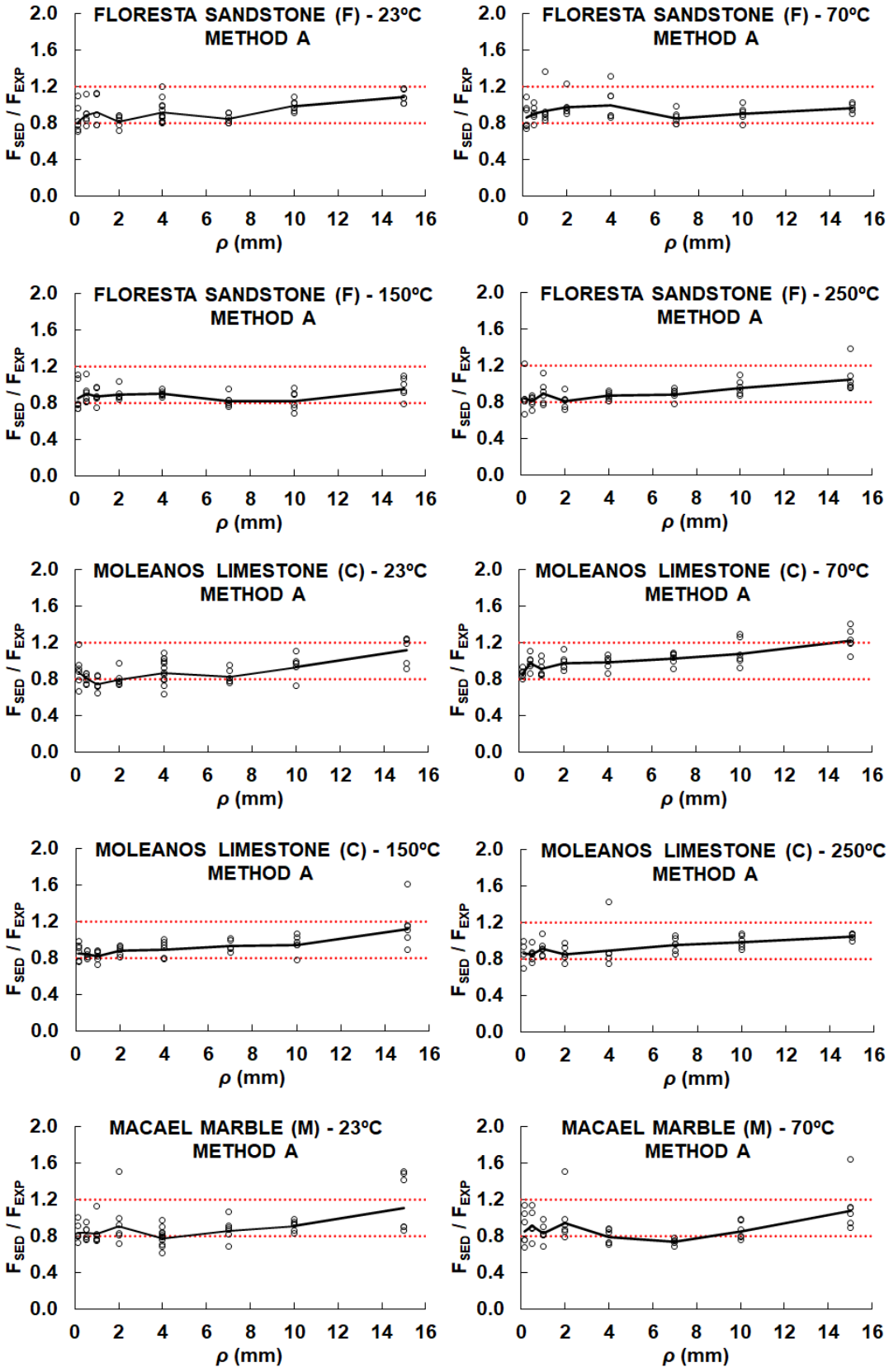

Figure IV-60. SED predictions (Method A) of the failure load for each rock at different temperatures.

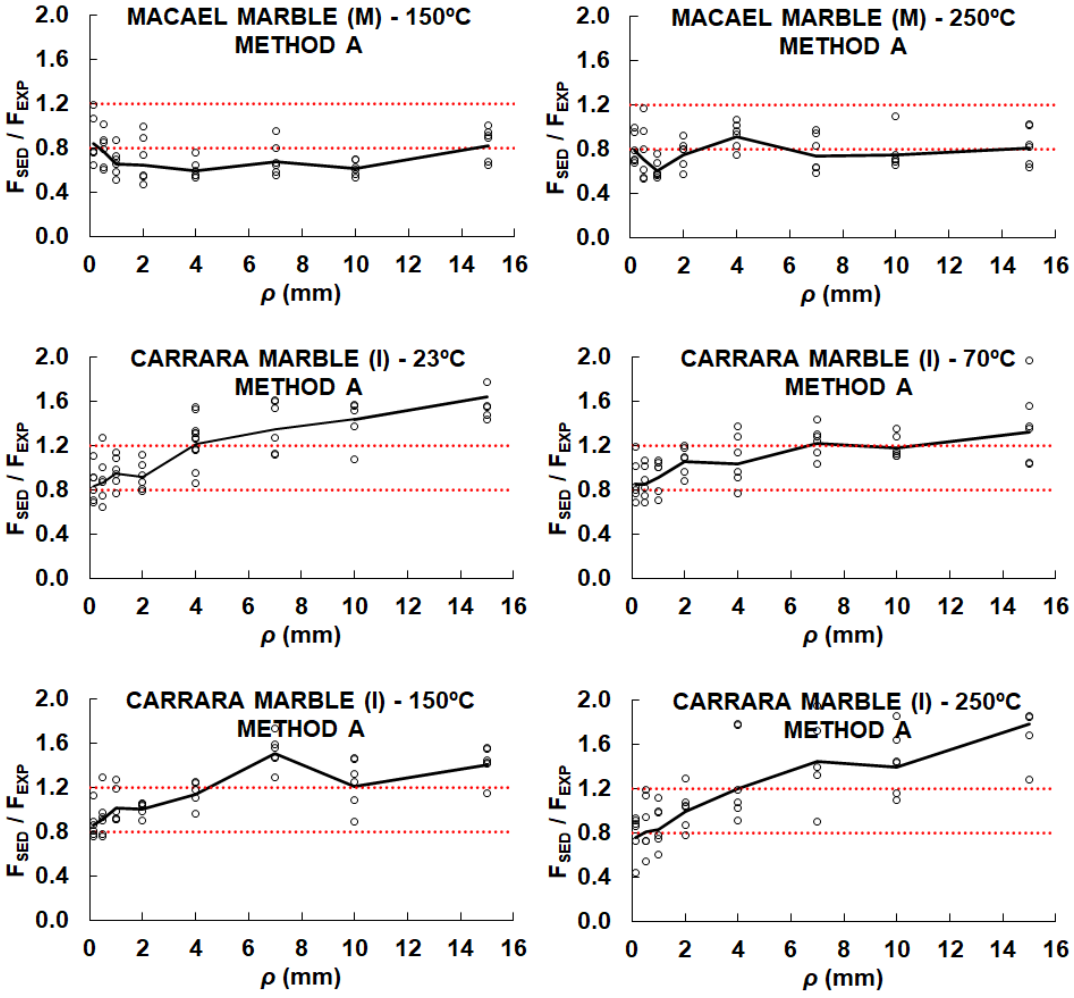

Figure IV-60. (Continued).

Several observations should be highlighted from the analysis of the results in *Figure IV-60*. Both the Floresta sandstone and the Moleanos limestone, those rocks with the most evident linear-elastic behaviour (*Figure IV-10*), offer relatively good failure predictions for the whole range of analysed temperatures. Similarly, the mean fracture prediction curves of the Macael marble at 23ºC and at 70ºC also fall significantly within the defined ±20% band. However, the results for 150ºC and 250ºC indicate a generalised underestimation. The stress-strain curves of the uniaxial compression tests for the Macael marble at 150ºC and 250ºC (*Figure IV-10*) suggest a not so linear behaviour at these temperatures, which could explain the worsening of the prediction shown in these two particular cases. The same argument could be attributed to the Carrara marble, the rock presenting the highest non-linearity in relative terms both at room and at higher temperatures (*Figure IV-10*).

Besides, the stress field at the notch tip is defined by Creager & Paris' (1967) stress distribution function with this method, which is theoretically only valid for long and narrow notches. This could also affect the worsening of the failure predictions in the case of the largest notches, as in the case of the Carrara marble for example. Despite this, relatively good failure predictions (within a ±20% range) were obtained in the rest of the rocks even for the largest notches, although a general upward trend of F_{SED}/F_{EXP} is observed in many cases as the notches get larger.

4.3 COMPARISON BETWEEN SED AND TCD PREDICTIONS

Figure IV-61 compares, for each of the analysed rocks and temperatures, the predicted mean failure loads (F_{PRED}/F_{EXP}) obtained from the SED approach (Method A), which are depicted in *Figure IV-60* (black curves), and those of the TCD (LM) shown in *Figure IV-38* (grey curves), all of them corresponding to pure mode I loading conditions.

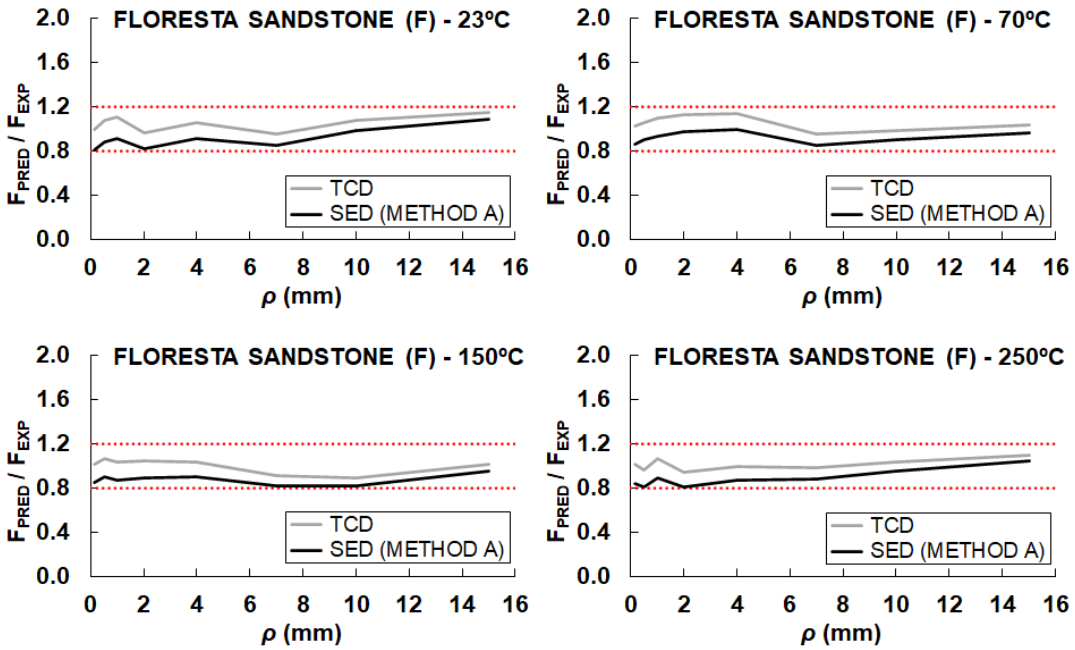

Figure IV-61. Comparison between the mean failure load predictions according to the SED criterion (Method A) and the TCD (LM).

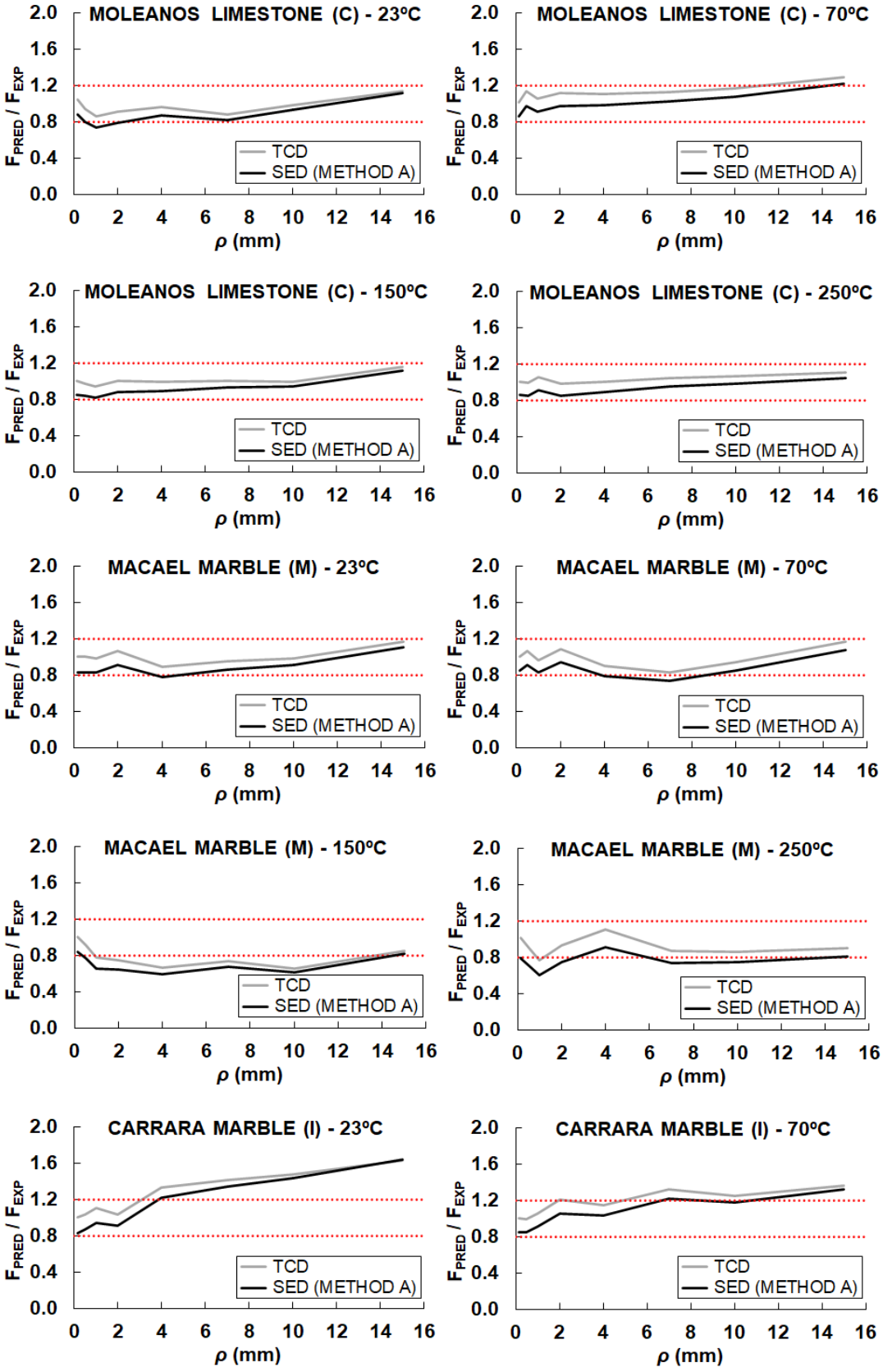

Figure IV-61. (Continued).

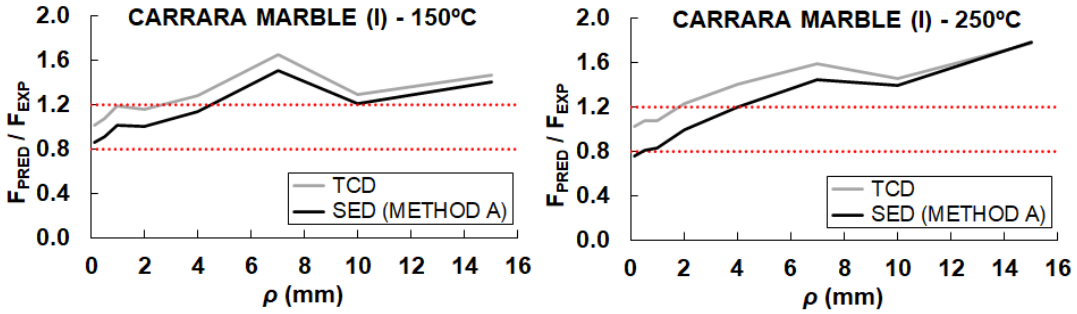

Figure IV-61. (Continued).

In general terms, both the TCD and the SED criterion offer relatively similar and accurate failure load predictions, although certain differences are clearly observed. The SED criterion provides lower failure load predictions than the TCD in all the studied cases. This difference is more notorious in the case of the smallest notches and tends to reduce as the notch radius gets larger. In this regard, it is important to remark that the represented SED failure predictions are calculated using the critical strain energy density value (W_c) according to *Equation (II-98)*. Thus, this value corresponds to the theoretical area under a tensile test stress-strain curve assuming a strict linear behaviour till failure, as indicated in *Figure IV-62a*.

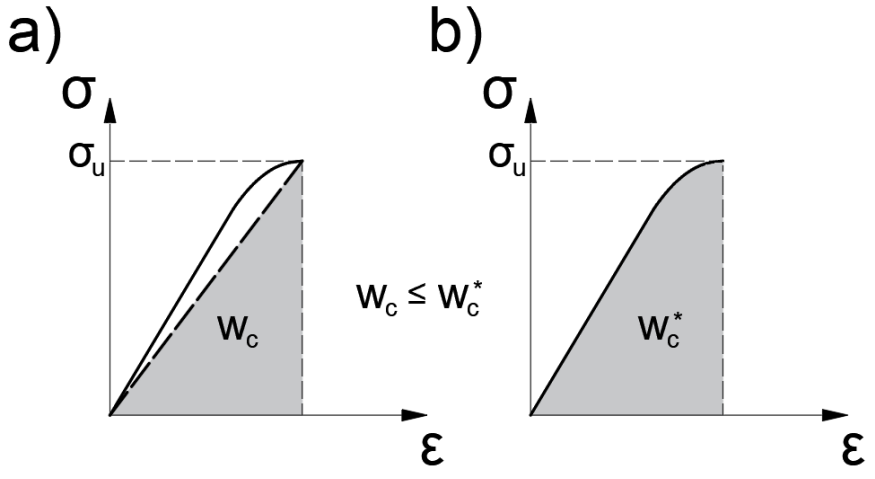

Figure IV-62. Critical strain energy density calculated for (a) a theoretical linear behaviour (W_c) or (b) for a non-linear behaviour (W_c^*).

However, based on *Figure IV-10*, certain subcritical crack growth prior to final failure can be expected, particularly at high temperatures.

This leads to a non-perfectly linear behaviour as that indicated in *Figure IV-62b*. The critical strain energy density corresponding to the area under the real non-linear stress-strain curve (W_c^*) is larger than the calculated W_c value. Thus, W_c^* will provide higher load fracture predictions than W_c. The tensile stress-strain curves are not available in this work and are difficult to be obtained in rocks. As a simple approach to consider the material non-linearity in the estimation of W_c^*, its value can be calibrated for a particular notch radius and then be used for the failure load predictions of the rest of notch radii, since W_c^* is a material parameter. By just inverting *Equation (IV-7)* and leaving the critical strain energy density as the only unknown, W_c^* can be calibrated. Here, for example, W_c^* has been calculated from the experimental failure load of the samples with $\rho = 0.15$ mm. Accordingly, *Figure IV-63* represents, together with the TCD and SED load failure predictions depicted in *Figure IV-61*, black dashed curves with the new SED predictions based on the calibrated value of W_c^*.

In general, the three methods (i.e., SED criterion, calibrated SED criterion and the TCD) provide relatively similar failure load estimations. It is observed that the calibrated SED failure predictions offer slightly higher estimations of the failure load than those with the original Method A (closer to $F_{PRED}/F_{EXP} = 1$ in many cases) providing, in general terms, similar results to those offered by the TCD. This calibration process can be applied in those cases in which non-linearities are not excessively large. However, when non-linear behaviour is important, the SED criterion can no longer be applied as it is based on LEFM. For example, for the Carrara marble at 250ºC, it is observed that methods based on LEFM, like SED criterion or TCD, do not provide satisfactory predictions.

Therefore, the TCD and the SED provide similar failure load predictions, especially when the critical strain energy density is calibrated to consider the small non-linearities of the tensile stress-strain curves. One of the main advantages of the SED criterion is that the strain energy density can be easily evaluated numerically through finite element analyses by using coarse meshes, and, although it is not the purpose of this work, it permits to take into account higher order terms and three-dimensional effects (e.g., Campagnolo et al., 2015). Besides,

once the H function is tabulated numerical analyses are no longer required and failure load predictions can be directly performed. By contrast, the main disadvantage compared to the TCD is that additional tests are required (i.e., uniaxial compression tests with strain gauge measurements), since the deformational parameters are needed.

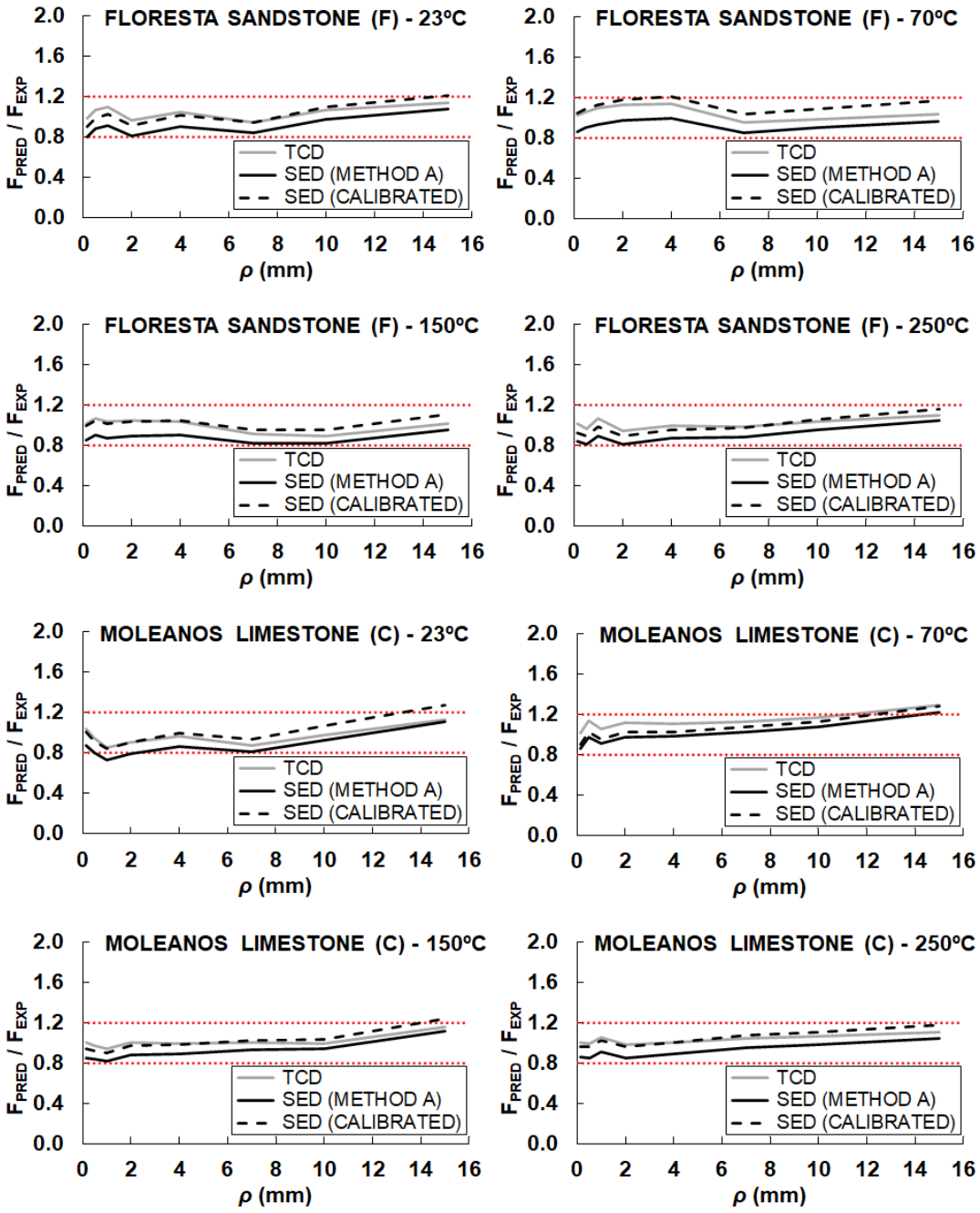

Figure IV-63. Comparison between the mean failure load predictions according to the SED criterion, both using the calculated values of W_c (Method A) and the calibrated values of W_c^*, and the TCD (LM).

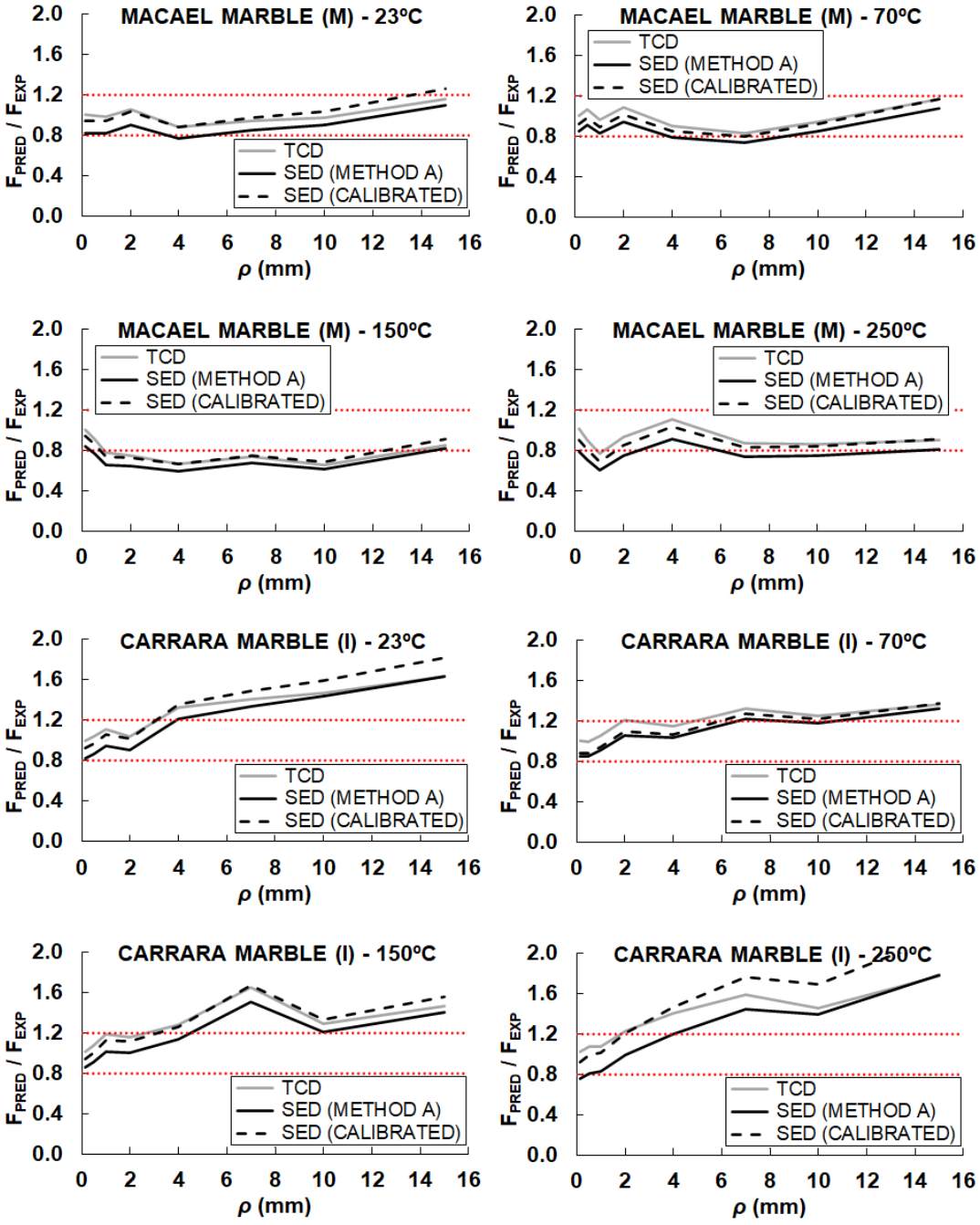

Figure IV-63. (Continued).

Based on the results, differences in the fracture load predictions obtained by the SED criterion and the TCD do not justify the additional workload involved by the SED approach. Indeed, the workload and cost of measuring the Young's modulus and the Poisson's ratio at temperatures above approximately 70ºC is substantial because special (and significantly more expensive) strain gauges, adhesives and cables are required. As an order of magnitude, the economic cost of performing

a uniaxial compression test at high temperatures (up to 250ºC) compared to a traditional uniaxial compression test at room temperature is approximately 4 or 5 times more expensive. Additionally, the complexity of performing the uniaxial compression tests at high temperatures compared to those at room temperature is also noteworthy.

With all this, the applicability of both the TCD and the SED criterion in the particular field of rock fracture mechanics has been validated, and the particularities and limitations of these methodologies for the fracture assessment of such complex and heterogeneous materials like rocks have been identified.

- Chapter V -
Discrete element analyses

1 NUMERICAL ANALYSIS: DISCRETE ELEMENT METHOD

After validating in *Sections 3* and *4* of Chapter IV the applicability of the TCD and the SED criterion for the fracture assessment of U-notched rocks under different loading and temperature conditions, Chapter V aims to complete those analyses by studying the influence of grain size in the fracture of notched rock samples. To this end, numerical analyses provide a suitable tool and, in particular, block-based methods such as the Discrete Element Method (DEM) allow to model rocks as an assemblage of grains with different boundary conditions.

Here, the influence of the grain size on the fracture behaviour of U-shaped notched rock beams under mode I loading conditions is studied. Particularly, the focus is placed on the analysis of the notch effect through the variation of the apparent fracture toughness and the correlation between the grain size and the critical distance of the material, which is a key parameter for fracture assessments according to the TCD. Thus, the influence of the grain size on the notch effect is analysed. Additionally, the effect of the grain size on several macroscopic properties of the analysed rock is also investigated, such as Young's modulus, Poisson's ratio, tensile strength and fracture toughness.

Many real rock features make detailed analyses difficult, such as inhomogeneities, grain size distribution, grain aspect ratio, porosity, etc. Consequently, in order to obtain conclusions as clear as possible and to avoid the influence of other possible factors other than grain size, the performed analyses have been simplified by modelling ideal rock materials with non-porous crystalline structure (only grains, without matrix), similar to the metamorphic marbles analysed in this work. More specifically, an ideal rock material that somehow resembles the analysed Macael marble tested is studied and 5 different grain sizes are considered to facilitate the analyses and the interpretation of the results.

1.1 NUMERICAL MODELS

Among the existing block-based approaches for the fracture analyses of rocks the DEM is used in this work. The DEM is a numerical technique to simulate the behaviour of a population of independent particles (Cundall & Strack, 1979). Each particle is represented numerically and is identified with its specific properties (e.g., shape, size, material properties). The DEM describes the material behaviour as the interaction of rigid or deformable bodies of arbitrary shape (i.e., grains), where the contact laws govern the macroscopic response of the material according to normal and tangential behaviour in the interfaces, as represented in *Figure V-1.*

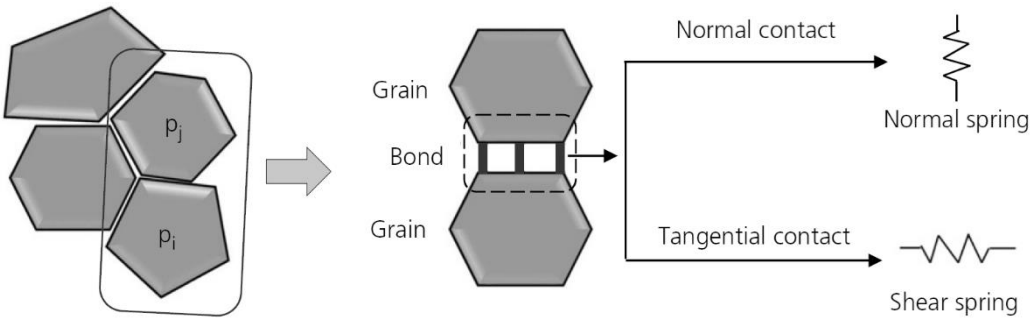

Figure V-1. Illustration of the assemblage of irregularly shaped grains and their bonding model (Gui et al., 2016).

The DEM allows finite displacements and rotations of the discrete particles as a consequence of the interaction through their contacts, including complete detachment, and recognizes new contacts

automatically as the calculation progresses. Here, UDEC v6.00 (Itasca, 2010) is used for the construction and analyses of the different numerical models.

The grains are represented by deformable blocks that are subdivided into finite-difference elements (zones), and each element responds according to a prescribed stress-strain law. Likewise, the discontinuities stand for the boundaries (joints) between the grains (blocks), and their relative motion is governed by force–displacement relations for movement both in the normal and shear directions. Subsequently, the characteristics of the constructed numerical models are described.

1.1.1 Geometry

In order to represent the grains of the rocks in the numerical models, Voronoi tessellation is used to create randomly sized polygonal blocks. These Voronoi polygons are defined by an average edge length (l), which is varied in this work to analyse the effect of the grain size on the fracture of the rocks. On the other hand, the size homogeneity of the Voronoi polygons is defined by the number of iterations (n) in the relaxation process during the generation of the mesh. The more iterations, the more homogeneous the polygons will be in terms of size. In this work, the number of iterations (n) has been set equal to 30 in all the simulations, which has been considered as an appropriate value for a uniform distribution of the grain size. The considered values for l are 1, 1.5, 2, 2.5 and 3 mm, as depicted in *Figure V-2*.

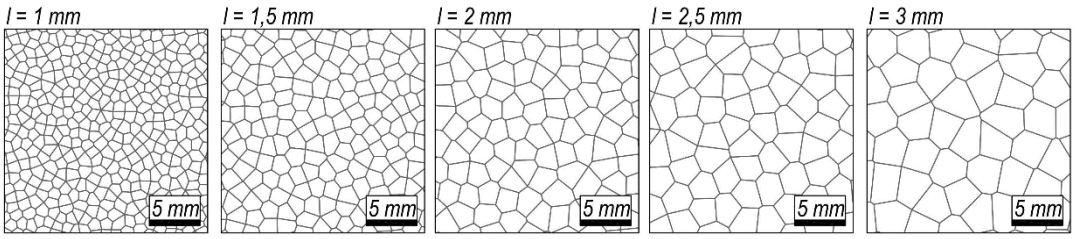

Figure V-2. Representation of the Voronoi tessellations with different average edge length (l).

The modelled grains are relatively large compared to those of the Macael marble due to computational capacity limitations and present a highly uniform distribution. *Figure V-3* provides the size distribution curves of modelled grains. Both, frequency and cumulative frequency are

represented in percentage. Grain diameter corresponds to the diameter of ideally circular grains with the same area as the actual modelled grains.

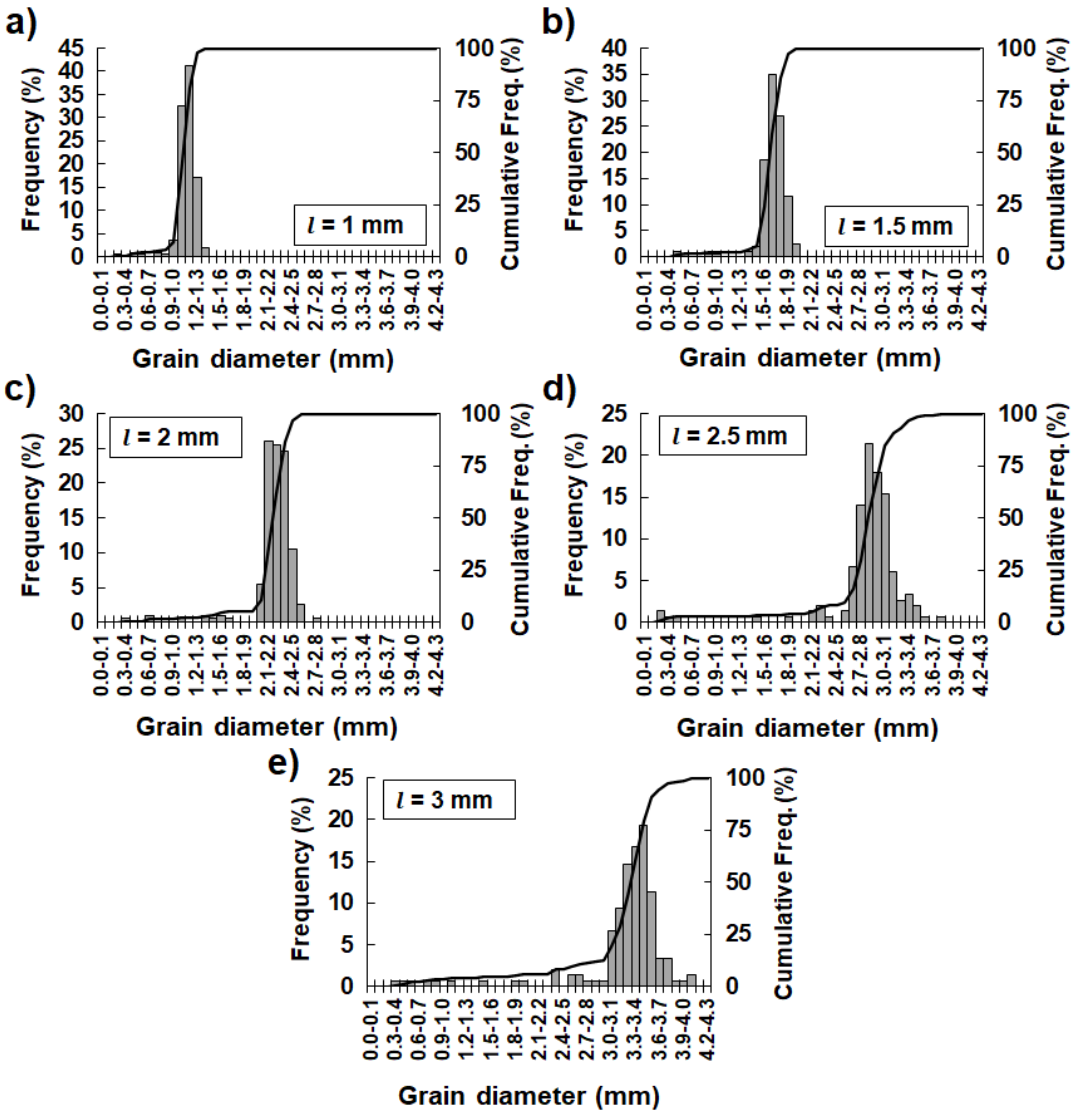

Figure V-3. Size distribution curves of the grains defined by an average length l of (a) 1 mm, (b) 1.5 mm, (c) 2 mm, (d) 2.5 mm and (e) 3 mm.

The observed outlier values below the average grain diameter correspond to grains located at the outer boundaries of the region defined by the Voronoi tessellation and, therefore, do not affect the crack propagation. *Table V-1* gathers some statistical values of the grains, namely the mean grain diameters, the standard deviations and the sorting coefficients defined as the ratio between the first and third

quartiles (Q1 and Q3, respectively). This latter parameter indicates that the size distribution is notably uniform as the coefficient is close to 1 in all the cases.

Table V-1. Statistical parameters of the modelled grain sizes.

	Average edge length (l)				
	1 mm	1.5 mm	2 mm	2.5 mm	3 mm
Mean grain diameter (mm)	1.109	1.659	2.213	2.829	3.187
Standard deviation (mm)	0.132	0.194	0.290	0.505	0.631
Sorting coef. (Q1/Q3)	1.110	1.092	1.083	1.096	1.095

The blocks are discretized into constant-strain finite-difference triangular zones, as shown in *Figure V-4*. The zones are defined by the maximum edge length (e) of the triangles composing the mesh, which has been set to the same value as the average block edge length. In this way, the proportion of zones within the blocks remains roughly constant.

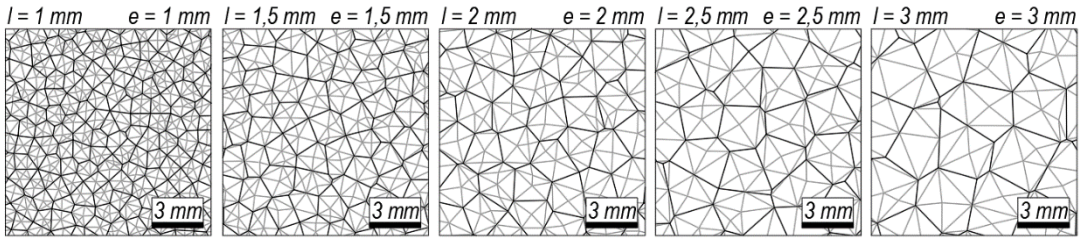

Figure V-4. Representation of the zones within the Voronoi polygons.

Different numerical models have been constructed with the same geometry as those performed laboratory tests of the described experimental campaign. These models consist of 60 tensile splitting (Brazilian) tests (*Figure V-5a*), 30 uniaxial compression tests (*Figure V-5b*) and 300 four-point bending tests (*Figure V-5c*), all of them under plane strain conditions. Compression models are not strictly necessary for the performed fracture analyses based on the TCD, but they are also studied for a better characterisation of the simulated materials through the Young's modulus and to determine the influence of the grain size on the elastic parameters. *Table V-2* summarises the number of analysed models, indicating the number of grain sizes and the repetitiveness.

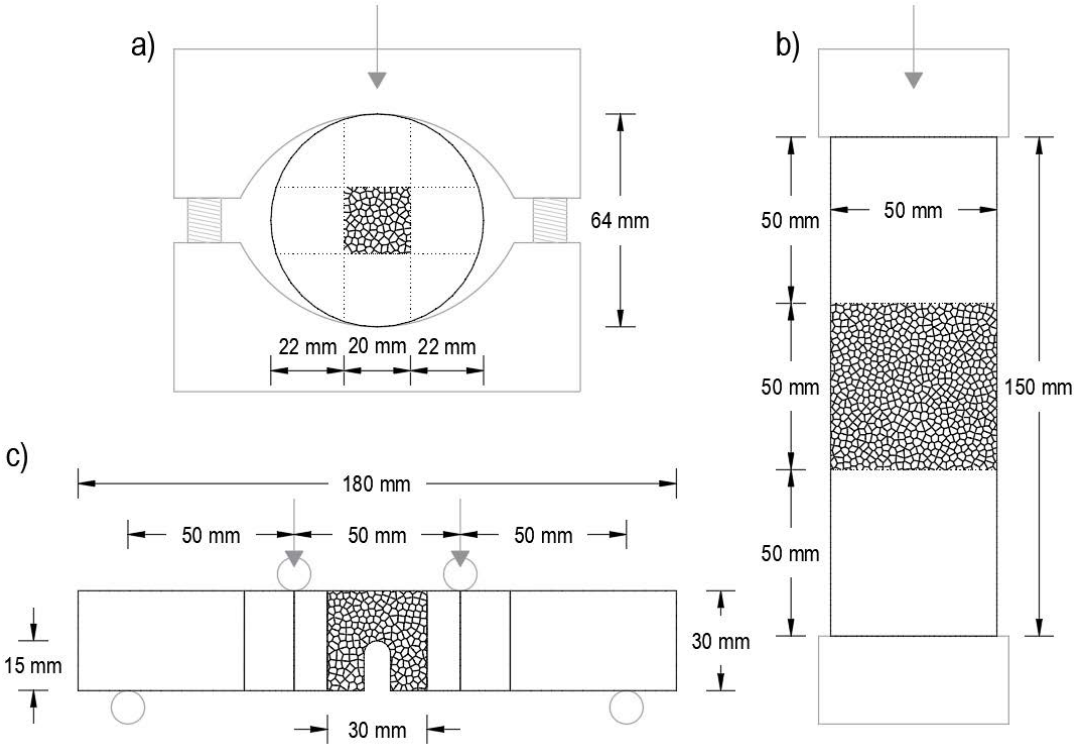

Figure V-5. Representation of the simulated numerical models corresponding to (a) tensile splitting (Brazilian) tests, (b) simple plain strain compression tests and (c) four-point bending tests.

Table V-2. Summary of the analysed discrete numerical models.

MODELS	Nº grain sizes	Repet.	**Total**
Brazilian test models	5	12	**60**
Uniaxial compression test models	5	6	**30**
Four-point bending test models			**300**
with $\rho = 1$ mm	1	6	6
with $\rho = 1.5$ mm	2	6	12
with $\rho = 2$ mm	3	6	18
with $\rho = 2.5$ mm	4	6	24
with $\rho = 3$ mm	5	6	30
with $\rho = 4$ mm	5	6	30
with $\rho = 5.5$ mm	5	6	30
with $\rho = 7$ mm	5	6	30
with $\rho = 8.5$ mm	5	6	30
with $\rho = 10$ mm	5	6	30
with $\rho = 12.5$ mm	5	6	30
with $\rho = 15$ mm	5	6	30

In compression models, the crack initiation is not necessarily associated with failure (e.g., Nicksiar & Martin, 2014), since scattered microcracks may arise before reaching the compression strength of the material. In fact, crack initiation and peak load are very different (e.g., Yue et al., 2017). This is due to the fact that, at low load levels, a lot of microcracks start to develop in a diffuse manner, but later coalescence takes place and leads to a macroscopic crack and final failure (see *Section 1.4.1.2* in Chapter II). According to Hoek (1965), the damage mechanisms of crack initiation is the result of tensile stresses at microcracks or contacts between grains, even under compressive forces. As shown in *Figure V-6*, the compressive force can be resolved into tensile and shear stresses acting on the boundaries between the grains. However, compression-induced tensile microcracks do not necessarily propagate immediately after being created as a consequence of the interaction between grains, and it is not till coalescence takes place that final failure occurs.

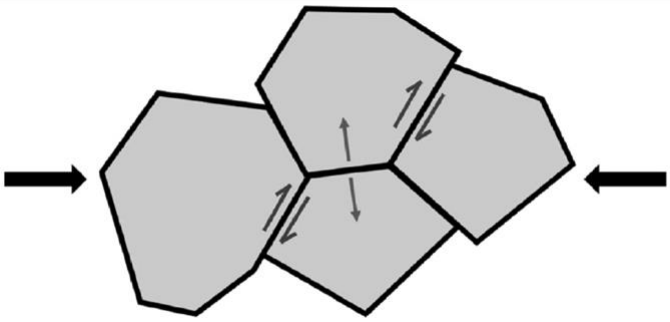

Figure V-6. Micromechanisms for compression-induced tensile stress at the contacts between the particles in DEM (Ghazvinian et al., 2014).

This is different when dominant tensile failure is analysed. Whenever a tensile crack of a certain size has been created, critical crack growth starts and failure follows immediately. Under these circumstances crack initiation and peak loads are very close. This statement is relative to the analysed scale, since when moving deeper into the microscale (e.g., μm, nm, etc.) the difference between crack initiation and peak load will increase.

With all this, the estimated Young's modulus and Poisson's ratio values in this analysis correspond to the secant slopes at 50% of the peak

strength (E_{50}). Besides, based on the scale of the modelled grains (i.e., of the order of millimetres), the crack initiation load has been, in a first approximation, set equal to the peak load to define the tensile strength (σ_u) obtained from Brazilian test models (*Figure V-5a*) and to analyse the notch effect from the four-point bending models (*Figure V-5c*). In this sense, different authors (e.g., Dan & Konietzky, 2014) have shown Brazilian test simulations where crack initiation and peak strength are very close to each other. Hoek & Martin (2014) have also shown that, when dominant tensile failure occurs, as in the case of Brazilian and four-point bending tests, crack initiation and peak strength are very close.

As the results might depend on the specific distribution of the Voronoi blocks representing the grains of each individual model, the meshes have been randomly generated and a minimum repetitiveness of 6 Voronoi tessellations have been used for each case. Besides, the symmetry with respect to the bisector plane of the notches (see *Figure V-5*) has not been considered when constructing the four-point bending test models because the distribution of the Voronoi blocks (grains) is not symmetric, as in reality.

The actual arrangement of the Voronoi polygons (or grains) produces a scatter of the results even when keeping the average grain size constant. For the particular case of the Brazilian tests and the four-point bending tests, the results show a visible scatter (mesh dependency) because the orientation of the grain contacts at the zone where the fracture starts notably influences the results.

1.1.2 Materials

For the intact blocks, an isotropic linearly elastic behaviour has been assumed in this work, which only requires two parameters: the bulk modulus (K_0) and the shear modulus (G_0). This means that the grains are supposed to be homogeneous, isotropic and exhibit a linear stress-strain behaviour with no hysteresis on unloading. The rock is idealized as an assembly of unbreakable grains. Thus, cracks can only propagate along the boundaries.

On the other hand, the Coulomb slip model with residual strength is considered to model the interaction between grains. This model provides a linear representation of joint stiffness and yield limit, and is based

upon elastic stiffness, frictional, cohesive and tensile strength properties, and dilation characteristics common to rock joints (Itasca, 2010). Here, the term joint refers to the contact between grains. The residual strength simulates displacement-weakening of the joint by loss of frictional, cohesive and/or tensile strength at the onset of shear or tensile failure. That is, an internal fracture flag is set for each joint segment when the tensile or shear strength is exceeded. Thus, when a joint is fractured, the joint tensile strength, the joint friction angle and the joint cohesion are set to residual values.

In order to make the models more computationally efficient and less time-consuming, the Voronoi tessellation has only been generated in the vicinity of the notch (as shown in *Figure V-5*) where the fracture is starting. The remaining parts of the model are also composed by deformable blocks with the same constitutive properties as the intact blocks but different internal meshing. To ensure that no sliding or opening is occurring in the contact between these blocks and the region with Voronoi polygons, these contacts are defined as "joined" contacts with high values of the joint cohesion and tensile strength.

The calibration process of the required parameters is based on the experimental results obtained for the Macael marble, which presents low porosity, isotropic, uniform and relatively homogeneous distribution of the grain size, with a crystalline structure and no matrix around the grains. *Table V-3* summarises the mechanical properties of the Macael marble obtained in the laboratory and analysed in Chapter IV.

Table V-3. Mechanical properties of the Macael marble.

Parameter	Value
Bulk density (kg/m^3)	2715
Young's modulus, E_{50} (GPa)	73.4
Poisson's ratio, ν	0.28
Tensile strength, σ_u (MPa)	9.97
Fracture toughness, K_{IC} (MPa $\cdot$ m$^{1/2}$)	1.14

However, it is important to remark that it is not the purpose of this analysis to simulate the exact behaviour of the Macael, but to model rock-like materials with comparable properties and within a realistic

order of magnitude. Indeed, relatively large grain sizes are studied compared to those of the marble due to computational capacity limitations.

All the parameters in *Table V-3* correspond to the rock behaviour at the macro-scale. The properties of the individual grains do not have to be strictly the same, but in this case, considering the homogeneity of the studied rock, the values in *Table V-3* have been taken as the basis for the calculation of the bulk (K_0) and shear (G_0) modulus of the grains:

$$K_0 = \frac{E}{3(1-2v)} \qquad (V\text{-}1)$$

$$G_0 = \frac{E}{2(1+v)} \qquad (V\text{-}2)$$

With this, *Table V-4* gathers the parameters of the material constitutive model used for the definition of the isotropic linear elastic behaviour of the rock grains, derived from the values in *Table V-3*.

Table V-4. Parameters for the isotropic linear elastic constitutive model of the grains.

Parameter	Value
Bulk density (kg/m^3)	2715
Bulk modulus, K_0 (GPa)	56
Shear modulus, G_0 (GPa)	29

Table V-5. Parameters for the Coulomb slip constitutive model with residual strength.

Parameter	Value
Joint cohesion, *jc* (MPa)	24.5
Joint dilatation angle, *jd* (º)	5
Joint friction angle, *jf* (º)	35
Joint tensile strength, *jt* (MPa)	49.0
Joint residual cohesion, *jresc* (MPa)	0
Joint residual friction angle, *jrf* (º)	25
Joint residual tensile strength, *jrt* (MPa)	0

Table V-6. Zone size dependent stiffnesses for the Coulomb slip constitutive model with residual strength.

Parameter	Value
Joint normal stiffness, jkn (GPa/mm) - $l = 1$ mm	1880
Joint shear stiffness, jks (GPa/mm) - $l = 1$ mm	938
Joint normal stiffness, jkn (GPa/mm) - $l = 1.5$ mm	1250
Joint shear stiffness, jks (GPa/mm) - $l = 1.5$ mm	626
Joint normal stiffness, jkn (GPa/mm) - $l = 2$ mm	938
Joint shear stiffness, jks (GPa/mm) - $l = 2$ mm	469
Joint normal stiffness, jkn (GPa/mm) $l = 2.5$ mm	751
Joint shear stiffness, jks (GPa/mm) - $l = 2.5$ mm	375
Joint normal stiffness, jkn (GPa/mm) - $l = 3$ mm	626
Joint shear stiffness, jks (GPa/mm) - $l = 3$ mm	313

These parameters define the behaviour of the grains. However, their contact conditions must be adjusted to obtain the desired behaviour at the macro-scale. As a result of the calibration process, the parameters of the considered joint constitutive model, namely the Coulomb slip model with residual strength, are summarised in *Table V-5* and *Table V-6*. The former includes the joint cohesion, dilatation, friction and tensile properties and their residual values, while the latter gathers the zone size dependent parameters (i.e., normal and shear stiffnesses of the joints).

Very high values for the joint stiffnesses lead to a slow response and a slow solution convergence of the models without a significant change in the behaviour of the system, as the timestep calculation is based upon stiffnesses. For this reason, both the joint normal stiffness (jkn) and the shear stiffness (jks) should be kept smaller than a factor times (usually 10) the equivalent stiffness of the stiffest neighbouring zone in blocks adjoining the joint (Itasca, 2010):

$$jkn \,\&\, jks \;\leq 10\left[\max\left(\frac{K_0 + 4/3G_0}{\Delta z_{min}}\right)\right] \qquad (V\text{-}3)$$

where K and G_0 are those of the block material, and z_{min} is the smallest width of the zone adjacent to the joint in the normal direction. As a

general criterion in the performed simulations, z_{min} has been set to half of the maximum edge length established for the zones. There may also be problems with block interpenetration if the normal stiffness is very low, as the contact overlap between blocks can be excessively large. On this basis, the normal stiffness (jkn) has been set to the limit value defined by *Equation (V-3)*.

Furthermore, the ratio of the normal to shear stiffness (jkn/jks) dramatically affects the Poisson response of a rock mass (Itasca, 2010). When the shear stiffness is equal to the normal stiffness ($jkn = jks$) the Poisson's effect is zero. Thus, for a more realistic representation of the Poisson's ratio, the ratio jkn/jks must be larger than unity. Several articles can be found in the literature dealing with this topic (e.g., Asadi & Barla, 2012; Nassir et al., 2013). Here, $jkn/jks = 2$ has been adopted, which is assumed to be a reasonable ratio (see *Table V-6*).

Anticipating to the results presented in *Section 1.2*, the parameters used in the numerical models (*Table V-5* and *Table V-6*) lead to a relatively similar macro-scale response as that obtained experimentally for the Macael marble in terms of tensile strength and elastic parameters such as the Young's modulus and the Poisson's ratio (*Table V-3* summarises the macroscopic parameters of the Macael marble). In general, the numerically obtained macroscopic parameters are slightly higher (around 20% in the case of the tensile strength and the Poisson's ratio). The obtained macroscopic properties from the numerical models are summarised and discussed below in *Section 1.2*.

1.1.3 Boundary conditions

With regards to the model boundary conditions, a constant loading velocity has been applied in all the cases (*Figure V-5*) to simulate the real laboratory test conditions that are performed under displacement control. The applied velocity is sufficiently small to ensure quasi-static responses of the numerical models.

The user-specified velocity is input to the model as an exterior boundary condition and viscous damping is specified for the blocks to avoid dynamic effects. The specified damping conditions cause the vibrational energy to be absorbed in proportion to the rate of change of the kinetic energy. Here, the ratio of damping dissipation to kinetic

energy change has been set equal to 0.5, which gives a relatively fast convergence and ensures that no dynamic effects will affect the results.

1.2 INTERPRETATION OF THE RESULTS

First, the results dealing with the influence of the grain size on the elastic macroscopic properties (i.e., Young's modulus and Poisson's ratio) are presented. These results have no specific relation to the subsequent discussion on the fracture behaviour of the notched specimens but do provide important information on the characterization of the analysed rock. The obtained elastic macroscopic properties are compared to those obtained in the experimental campaign for Macael marble. The objective of these first results is to define and delimit the characteristics of the rock-like material being analysed, in order to know to which real cases the results could be related.

Subsequently, the influence of the grain size on the fracture properties (i.e., tensile strength and fracture toughness) is analysed in more detail. In this case, in addition to comparing these properties with those of the Macael marble, their study is of special interest for the analysis of the notch effect through the TCD and, in particular, through the LM. According to the definition of the critical distance provided by *Equation (II-70)*, the grain size dependence of both tensile strength (σ_u) and fracture toughness (K_{IC}) will define the variation of L with the grain size. Besides, the failure criterion defined by the LM of the TCD (*Equation (II-77)*) limits the average stress over a distance $2L$ from the notch tip to σ_u. Thus, the interpretation of the notch effect that, based on the TCD, arises from this failure criterion, is influenced by the proper characterization of these properties and, consequently, by the grain size.

1.2.1 Influence of grain size on elastic parameters

Firstly, six compression test models were carried out for each of the considered grain sizes (*Figure V-5b*), only varying the distribution of the grains. The performed models correspond to plane strain conditions. Thus, the obtained moduli stand for the plane strain situation ($E_{50,PSM}$), different from those obtained in the laboratory for cylindrical specimens (E_{50}). Both moduli are related through the Poisson's ratio (ν) by means of the following expression:

$$E_{50,PSM} = \frac{E_{50}}{1 - \nu^2} \qquad (V\text{-}4)$$

As a result, *Figure V-7* gathers three different curves. The plane strain modulus ($E_{50,PSM}$) and the Poisson's ratio (ν) are obtained directly from the compression test models for each of the grain sizes, considering the deformations within a 25x25 mm square in the middle of the specimens. The obtained results are slightly sensitive to the size of this area (Ghazvinian et al., 2014). The numerically obtained $E_{50,PSM}$ values are corrected with *Equation (V-4)* to get E_{50}. The latter values of E_{50} are comparable to those obtained in the laboratory and correspond, as mentioned above, to the secant Young's modulus at 50% of the peak strength. The open symbols represent the individual values and the full symbols and solid lines represent mean values of the Young's moduli ($E_{50,PSM}$ & E_{50}) and Poisson's ratio (ν). Comparing the emergent macroscopic values of E_{50} and ν with those of the Macael marble (*Table V-3*), slightly lower values of the Young's modulus and higher values of the Poisson's ratio are obtained.

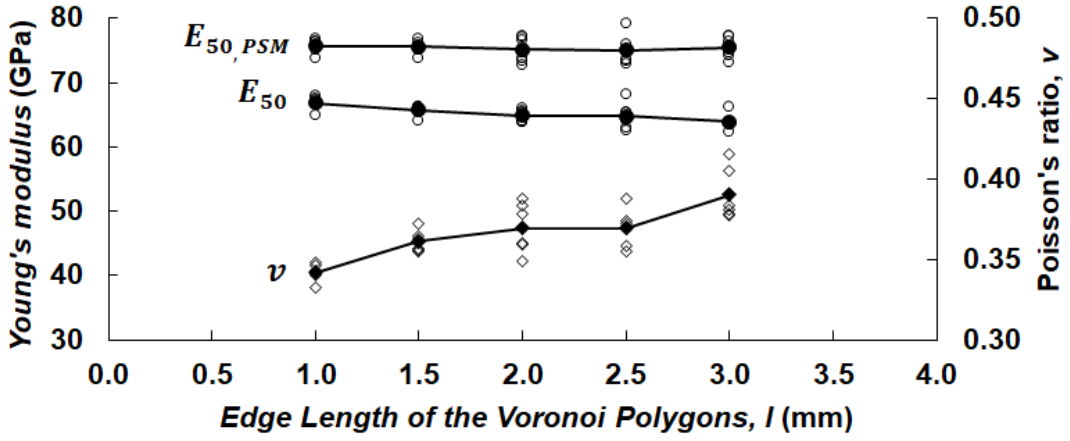

Figure V-7. Variation of the Young's modulus ($E_{50,PSM}$ & E_{50}) and Poisson's ratio (ν) with the grain size.

According to *Figure V-7*, in general terms, an increasing tendency with the grain size is observed in the case of the Poisson's ratio, which depends on the jkn/jks relation (Ghazvinian et al., 2014). Gui et al. (2016) reported a similar increase in the Poisson's ratio with the grain

size. By contrast, $E_{50,PSM}$ seems roughly constant with the grain size, which might be attributed to the variation of jkn for each of the grain sizes in accordance with *Equation (V-3)*. Gui et al. (2016), for example, reported an increase of the Young's modulus with the grain size because they kept jkn constant in their simulations.

1.2.2 Influence of grain size on tensile strength

Twelve Brazilian test models have been run for each of the analysed grain sizes. As an example, *Figure V-8* shows the obtained horizontal stresses (σ_{xx}) in a Brazilian test model at the onset of cracking, from which the tensile strength of the material (σ_u) has been derived, and a picture of the generation of the first cracks in the middle of the specimen. As mentioned above, the peak load and the crack initiation load have been assumed to roughly coincide under this loading configuration. Thus, the tensile strength is calculated from the crack initiation load.

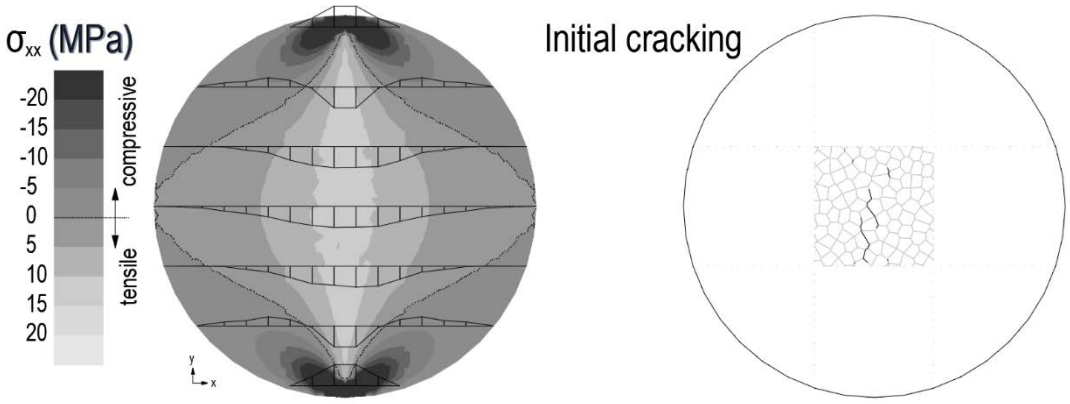

Figure V-8. Example (l = 2 mm) of the horizontal stresses of a Brazilian test model at the onset of cracking ($F_{failure}$ = 11.37 kN/mm) and generated cracks once the strength is exceeded. Tensile stresses are positive.

The variation of the tensile strength with grain size is represented in *Figure V-9*. A continuous increase of the tensile strength is observed, which is in accordance with the results obtained by other authors (e.g., Gui et al., 2016). More specifically, a proportional variation of σ_u with the square root of the edge length (l) is observed, which has been adjusted by a linear law (grey solid line) that roughly coincides with the average values (black dashed line).

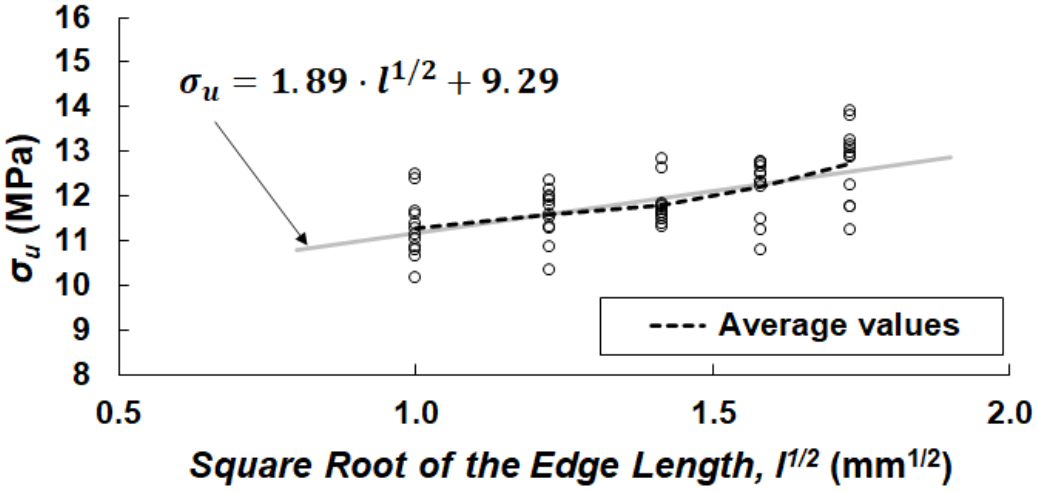

Figure V-9. Variation of the tensile strength (σ_u) with the grain size.

Gui et al. (2016), for example, simulated six different Brazilian tests with Voronoi tessellation grains ranging from 1 to 6 mm and concluded that the tensile strength increases with the grain size of the models. They stated that this could be caused by the fact that with an increase in the grain size, less potential fractures are included in the numerical models and, therefore, the characteristics of the models will be closer to intact rock.

1.2.3 Influence of grain size on notch effect

300 four-point bending tests have been modelled in total with a repetitiveness of 6 models per notch radius and grain size combination, only varying the randomly generated Voronoi mesh (see *Table V-2*). In order to consider the notch effect, several notch radii have been incorporated in the four-point bending models, with radii (ρ) ranging from 1 mm to 15 mm. In this analysis, only intergranular failure is being considered. Thus, the cracks can only propagate along the boundaries of the grains. Consequently, the minimum radius of the aforementioned notches has been limited to the grain size in each case (l), in such a way that, for example, in those models with a grain size of 3 mm the minimum modelled notch radius is also of 3 mm. This restriction intends to avoid the possibility of a notch not having at least one grain boundary at the tip, which could cause the breakdown of the calculation model due to the intergranular failure assumption. With all this, *Table V-7* indicates the number of four-point bending test models analysed per

notch radius and grain size combination in correspondence the above mentioned criteria.

Table V-7. Summary of the performed four-point bending test models.

		Grain size (l) of the model				
		1 mm	1.5 mm	2 mm	2.5 mm	3 mm
Notch radius (ρ) of the model	1 mm	6	-	-	-	-
	1.5 mm	6	6	-	-	-
	2 mm	6	6	6	-	-
	2.5 mm	6	6	6	6	-
	3 mm	6	6	6	6	6
	4 mm	6	6	6	6	6
	5.5 mm	6	6	6	6	6
	7 mm	6	6	6	6	6
	8.5 mm	6	6	6	6	6
	10 mm	6	6	6	6	6
	12.5 mm	6	6	6	6	6
	15 mm	6	6	6	6	6

For each of the individual numerical models of the four-point bending tests, the crack initiation load (F_i) has been calculated at the onset of cracking, just at the moment prior to the appearance of the first crack. As shown in *Figure V-10*, the bending moment between the loading points is constant in a four-point bending configuration ($M_b = F \cdot L_o/6$). At the same time, the horizontal stress (σ_{xx}) at the bisector of the notch can be equated to a bending moment (M_b) defined by a pair of forces (P^*) with a lever arm (z), where $M_b = P^* \cdot z$. Thus, the crack initiation load F_i (with force/depth length units) can be obtained equating both expressions:

$$F_i = \frac{6 \cdot P^* \cdot z}{L_o} \qquad (V\text{-}5)$$

where L_o is defined in *Figure V-5c* (150 mm), and P^* and z are derived from the stress field obtained along the bisector of the notch just in the calculation step prior to the development of the first crack.

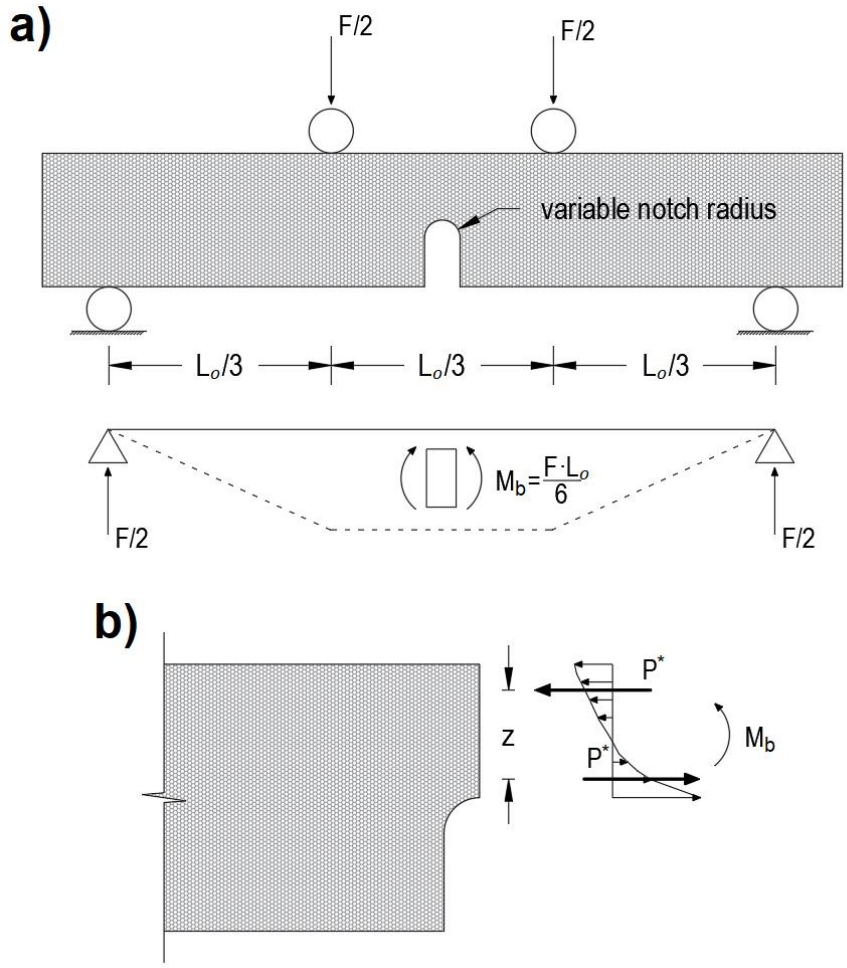

Figure V-10. Scheme to illustrate (a) the bending moment in the rock beam and (b) the stress field in the bisector of the notch.

Once the crack initiation load (F_i) is obtained, which can be assumed to roughly coincide with the failure load ($F_i \approx F_{failure}$), K_{IN} may be determined using the formulation proposed by Srawley & Gross (1976) in *Equations (III-8)*, *(II-33)* and *(II-34)* (*Section 0* of Chapter III and *Section 2.5.1.1* of Chapter II) for Single Edge Notched Bend (SENB) specimens as those simulated in this work (*Figure V-5c*). S and s_i in *Equation (II-33)* represent the spans between the outer supporting rollers and the inner loading points, respectively, and α_0 is the relative crack length defined as the ratio between the initial notch length (15 mm) and the total height (30 mm) of the specimen ($\alpha_0 = 0.5$) (see *Figure V-5c*). *Figure V-11* represents the stresses in the surrounding of the notch at the onset of cracking, from which the crack initiation load (F_i) is derived in each case. Likewise, *Figure V-12* shows, as an example,

some representative numerical four-point bending test models for grain sizes of 1, 2 and 3 mm after the appearance of the cracks at the notch tip, once the crack initiation load has been exceeded. As expected, cracks initiate at the notch tip where maximum stress concentration occurs and propagate upwards as a consequence of pure mode I loading conditions.

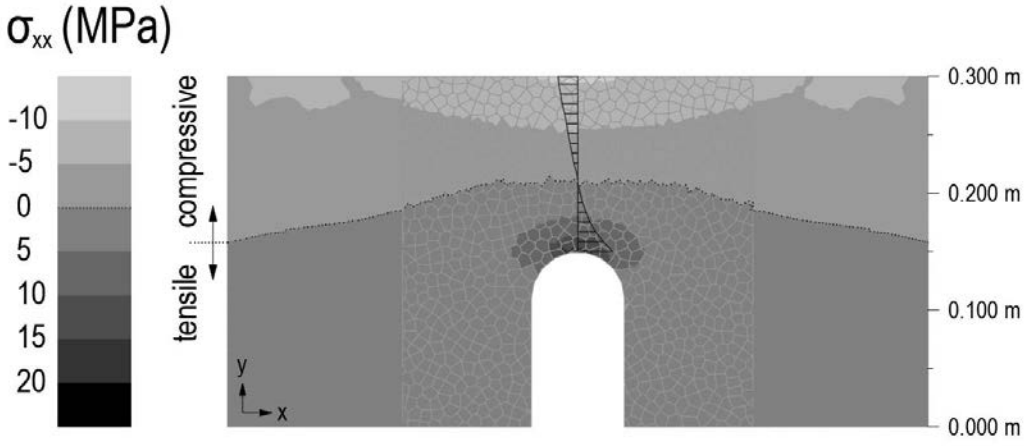

Figure V-11. Example (l = 1 mm; ρ = 4 mm) of the horizontal stresses (σ_{xx}) of the four-point bending test models at the onset of cracking. Tensile stresses are positive.

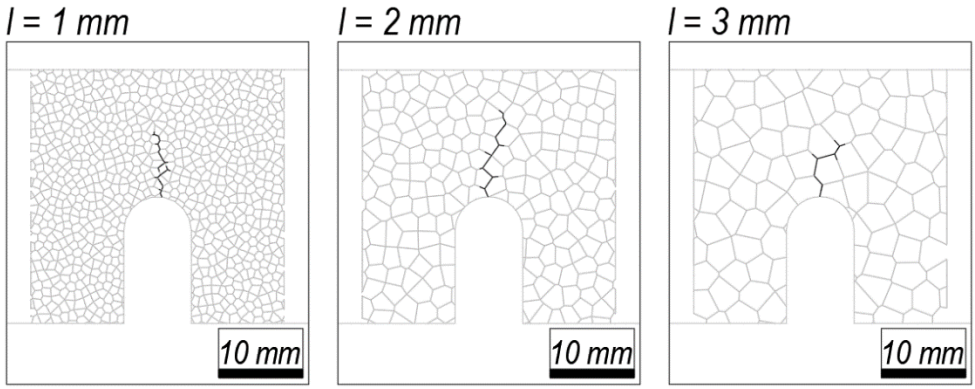

Figure V-12. Examples of formed cracks in DEM four-point bending models (with ρ = 4 mm) for grain sizes of 1, 2 and 3 mm.

Appendix C gathers in *Table C-1* the individual K_{IN} results of the four-point bending test models for each notch radii (ρ) and Voronoi edge lengths (l) that define the different grain sizes (*Figure V-2*).

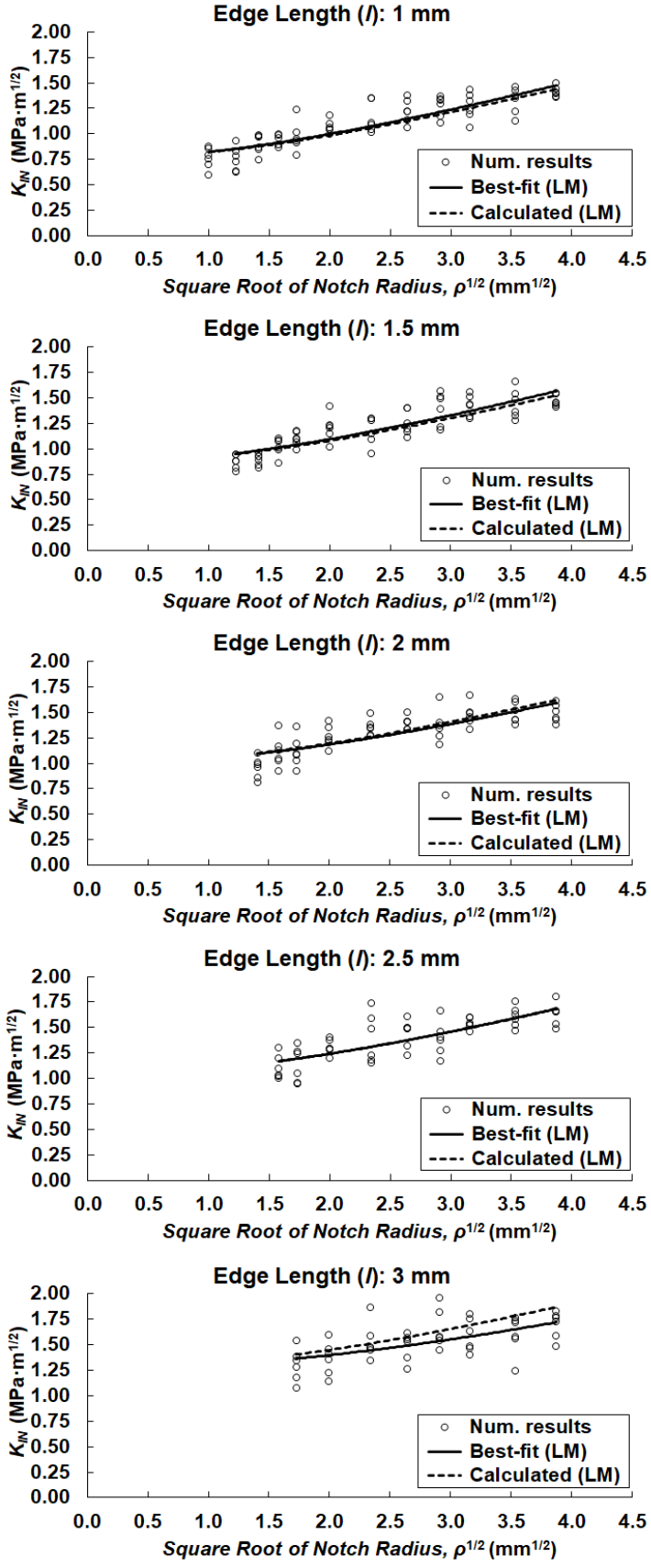

Figure V-13. Variation of the apparent fracture toughness (K_{IN}) with the notch radius for each Voronoi edge length (l).

To portray the notch effect, the results of the four-point bending models are graphically depicted in *Figure V-13*. The followed procedure is the same as that considered in *Section 3* of Chapter IV to define the notch effect through the TCD from the experimentally obtained failure loads, but using the numerically obtained failure loads instead. The individual results of the apparent fracture toughness are represented by dots in *Figure V-13*. K_{IN} increases gradually with the notch radius, so the notch effect is clear. The solid lines of the plots represent the best-fit curves according to *Equation (II-80)* (corresponding to the LM of the TCD), leaving K_{IC} and L as free variables for the adjustment. By contrast, the dashed lines stand for the calculated curves, based once again on *Equation (II-80)* but using K_{IC} from the best-fit solution and L from *Equation (II-70)*. A good agreement between both curves is observed in general terms. However, in the case of $l = 3$ mm the adjustment between the two curves is slightly worse, which could be caused by the relatively large grain size with respect to the specimen geometry.

Figure V-14 summarises in a single plot the best-fit curves represented in *Figure V-13*. It is observed that, in general terms, the curves flatten and move upwards as the grain size increases. This means, respectively, a decrease in the notch effect and an increase in the fracture toughness with the grain size.

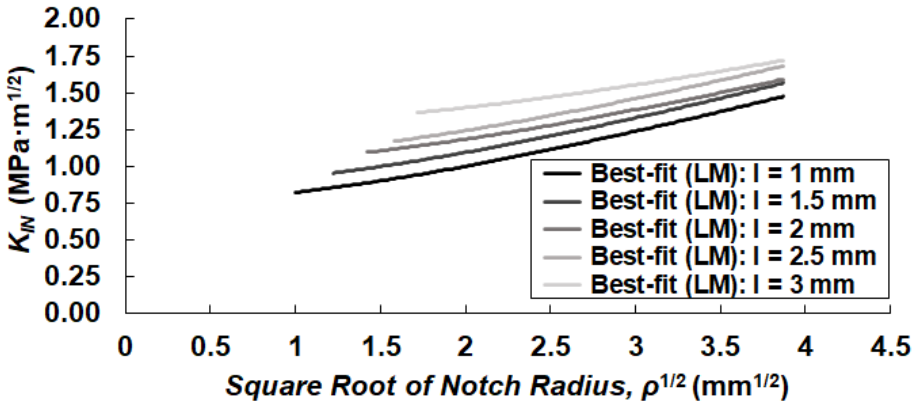

Figure V-14. Summary of the best-fit curves of Figure V-13.

1.2.4 Influence of grain size on fracture toughness

As mentioned above, the observed translation of the curves in *Figure V-14* indicates an increment of the fracture toughness of the rock specimens with the grain size. This effect was first discussed by Potyondy & Cundall (2004) and by many other authors since then (e.g., Moosavi et al., 2018). The fracture toughness reflects the residual strength of a component to crack propagation. Thus, considering the intergranular failure assumption, the larger the grains the less potential grain boundaries for crack propagation and, therefore, K_{IC} will increase because higher fracture energy is required to generate new cracking surfaces. *Figure V-15* represents the variation of the fracture toughness with the grain size. The represented values are obtained from the best-fit curve adjustment of *Equation (II-80)* for each analysed grain size.

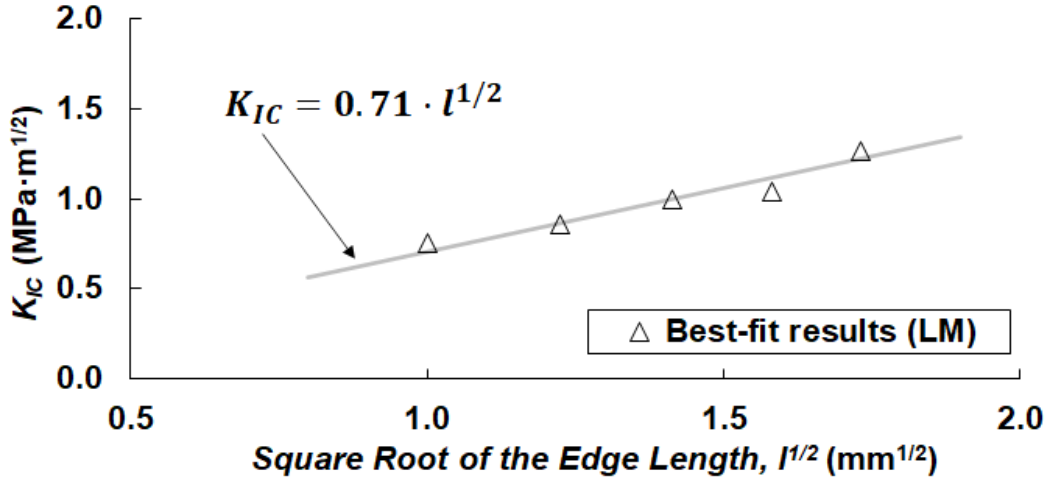

Figure V-15. Variation of the fracture toughness (K_{IC}) with the grain size.

It is clearly observed that K_{IC} depends on the size of the grains. This is not surprising, as the concept of fracture toughness implies an internal length scale, whereby the ratio of fracture toughness to material strength has the dimensions of square root of length (Potyondy & Cundall, 2004). In fact, *Figure V-15* shows that K_{IC} is proportional to the square root of the edge length (l) of the grain, which has also been suggested in previous studies (e.g., Duriez et al., 2016; Moosavi et al., 2018). Comparing these results with those depicted in *Figure V-9*, the proportional increase of K_{IC} with l is notably larger than that of σ_u.

Thus, according to *Equation (II-70)*, which defines the critical distance as a function of the ratio K_{IC}/σ_u, certain dependency of L on the grain size is expected.

1.2.5 Influence of grain size on critical distance

Proceeding in a similar way, the critical distance can also be derived from the adjustment of the best-fit curves according to *Equation (II-80)* of the LM. These best-fit results are compared in *Figure V-16* to those calculated from *Equation (II-70)*. The latter are calculated using the mean tensile strength obtained from the numerical models (*Figure V-9*) and the fracture toughness from the best-fit curves (*Figure V-15*). A good agreement is observed between the best-fit and the calculated results of L in all the cases except for the largest grain size.

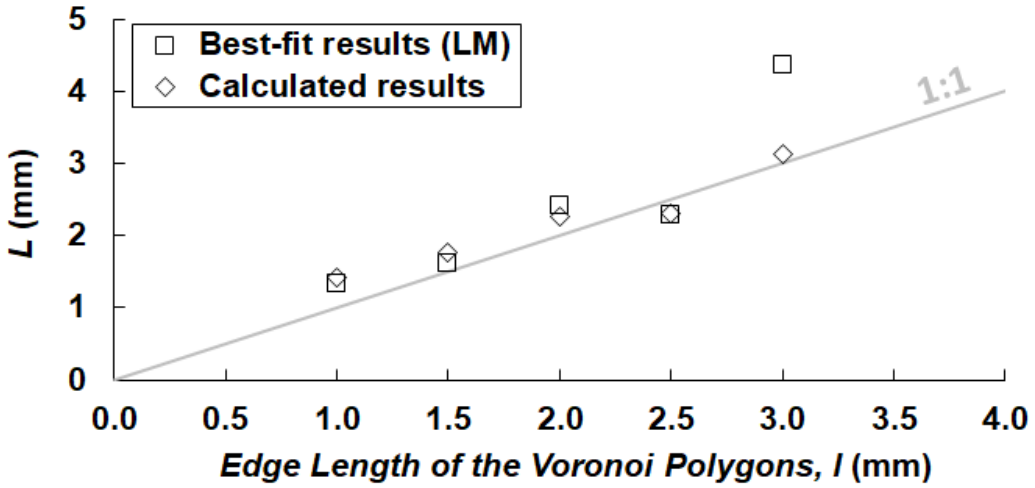

Figure V-16. Variation of the critical distance (L) with the grain size.

All in all, a 1:1 linear relation is observed between the critical distance L and the grain size, L being of the order of the average edge length of the Voronoi polygons ($L \approx l$). This linear relation makes sense according to the definition of L provided by *Equation (II-70)* and considering the dependency of both K_{IC} and σ_u on the grain size. Taylor (2017) analysed the relation of the critical distance (L) with clearly identifiable microstructural distances (d) such as the grain size of different materials, and concluded that in most of the cases, L is found to lie between d and $10d$. Thus, the obtained results are located towards the bottom of the scatter band defined by Taylor (2017). However, this

correlation between the critical distance and the grain size must be understood only in qualitative terms because the numerical simulations are simply an idealization of the real problem (2D grains, only intergranular fractures) of an already highly idealised rock (non-porous, isotropic, very uniform grains with 1:1 aspect ratio). Consequently, the obtained values are not compared with those obtained experimentally and discussed in *Section 3.1.5* of Chapter IV (see *Figure IV-40*).

Finally, *Table V-8* summarises the parameters derived from the performed numerical analyses for each of the considered grain sizes, including the mean tensile strength, the fracture toughness and the critical distance from the best-fit and from the calculated case, all of them being key parameters for the fracture assessment according to the TCD.

Table V-8. Summary of the emergent macroscopic properties derived from the numerical analyses of each grain size.

	Average edge length (l)				
	1 mm	1.5 mm	2 mm	2.5 mm	3 mm
E_{50} (GPa)	66.8	65.7	64.8	64.8	64.0
v	0.34	0.36	0.37	0.37	0.39
σ_u (MPa)	11.29	11.59	11.79	12.20	12.74
K_{IC} (MPa · m$^{1/2}$)	0.76	0.86	1.00	1.04	1.26
L (mm) – Best-fit	1.33	1.63	2.41	2.29	4.37
L (mm) – Calculated	1.43	1.76	2.27	2.30	3.13

1.3 DIFFERENCE BETWEEN CONTINUOUS AND DISCRETE STRESS FIELDS

Despite the generally accepted condition that rocks are heterogeneous and discontinuous materials, it is a common practice to consider the rock as a continuum in order to simplify the rock mechanics analyses, especially when global responses are of interest. However, a continuous approach might not be appropriate for more accurate assessments in which detailed information is required or when discontinuities cannot be neglected. For this reason, Chapter V takes advantage of the use of discrete numerical tools for the analysis of the influence of the grain size on the fracture behaviour of rocks.

On the other hand, those fracture analyses presented in *Sections 3* and *4* of Chapter IV where, respectively, the TCD and the SED criterion are applied, are based on the analysis of the continuous stress fields close to the notches. In the case of the SED criterion, the stresses are evaluated within a control area at the notch tip, in order to define the strain energy density. By contrast, in the case of the TCD, the stresses are assessed along a certain plane starting at the notch surface, which coincides with the bisector plane under mode I loading conditions. Specifically, when using the PM, the stresses are evaluated at a distance ($L/2$) from the tip, while for the LM, the stresses are averaged over a distance ($2L$) starting at the notch tip.

In any case, the considered stress fields in the performed fracture assessments are based on the traditional continuous approach. Therefore, the tested rock samples have been studied as continuous materials. Aiming to determine the extent of the differences between discrete and continuous analyses, the stress fields along the bisector plane obtained by both methods have been compared here. *Figure V-17* gathers, as an example, some representative stress-distance curves obtained from DEM (using UDEC v6.00) and FEM (using PLAXIS 2D 2017) analyses, corresponding to $\rho = 3$ mm (*Figure V-17a*), $\rho = 7$ mm (*Figure V-17b*) and $\rho = 15$ mm (*Figure V-17c*), all of them for a mean grain size of 1 and 3 mm. The represented stresses are the normal stresses to the notch bisector plane.

In general terms, good agreement is observed between the solid curves corresponding to the continuous approach and the dotted curves corresponding to the discrete approach. The illustrated DEM curves correspond to a particular random case and can vary in each model depending on the actual position of the grains.

If the stresses of FEM and DEM results are compared for $r = 0$, in general, the maximum stress at the notch tip seems to be slightly higher when FEM is used, although the difference is practically negligible when the grain size is sufficiently small. Besides, the stepped appearance of the dotted curves softens as the grain size decreases. In fact, in those curves corresponding to the models with a grain size of 1 mm (*Figure V-17a1, b1, c1*), the differences between the DEM and FEM curves are insignificant.

Finally, the consequences of the notch effect can be directly observed in the plots of *Figure V-17*. The stress concentrations around the notch tip are relatively higher for the smallest notch radii, as expected. When the notch radius is sufficiently large (e.g., $\rho = 15$ mm) the notch effect tends to vanish and the stresses approximate to those corresponding to a simple section reduction with no appreciable stress intensification.

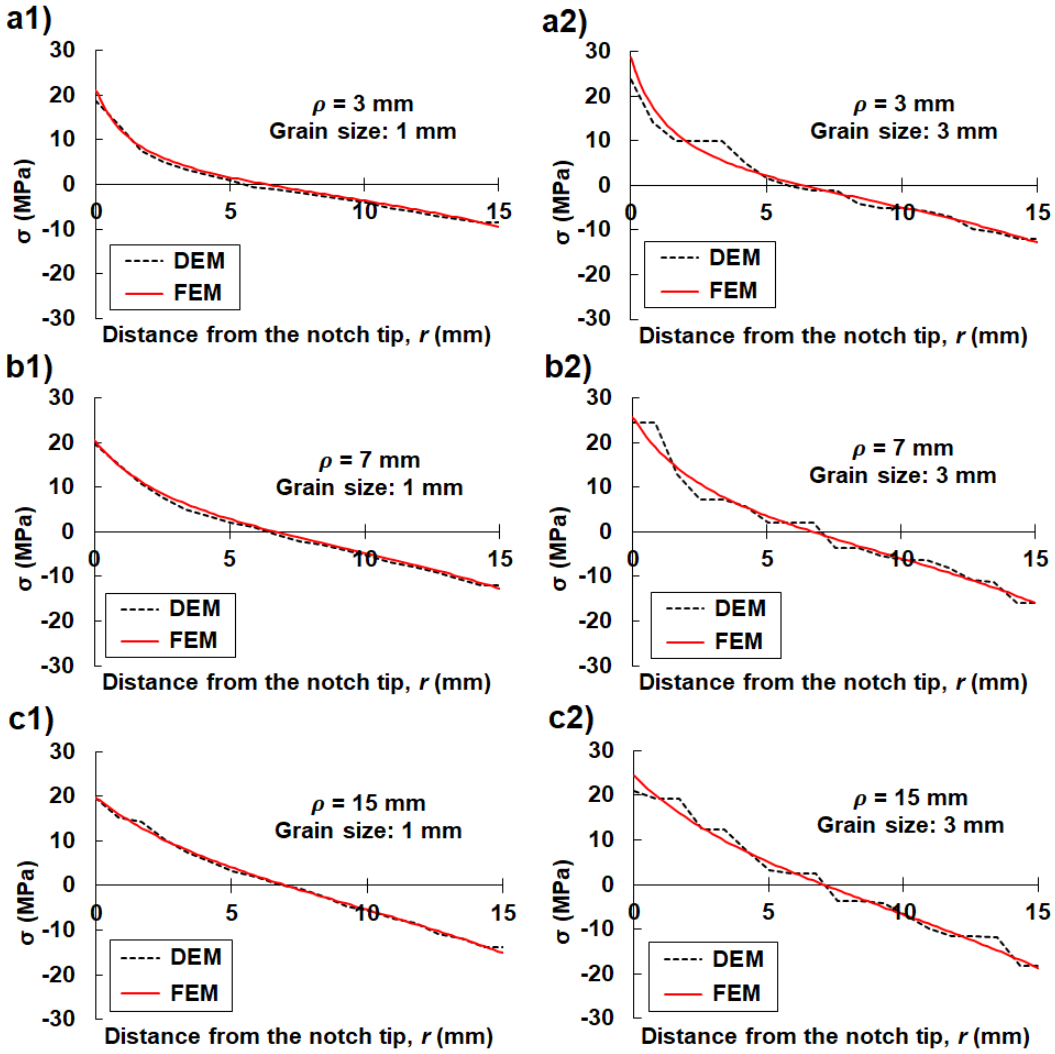

Figure V-17. Comparison of the numerically obtained stress laws in the bisector of the notch tip for (a) $\rho = 3$ mm, (b) $\rho = 7$ mm and (c) $\rho = 15$ mm, both for grain sizes of 1 mm and 3 mm.

The studied DEM models from which the dotted curves are derived correspond to those described in *Section 1.1* and depicted in *Figure V-5c*. The represented stresses are defined at the moment prior to the appearance of the first cracks at the notch tip, which is assumed to

roughly coincide with the failure load as justified above. However, the failure criterion established by the discrete numerical models in which a crack initiates and propagates when the shear or tensile strength of the grain contacts is reached, cannot be imposed in a continuous approach. For this reason, in order to represent comparable curves in *Figure V-17*, the FEM solid curves are obtained from finite element models in which the failure load derived from the DEM models is applied. In this case, a finite element code called PLAXIS 2D has been used to model the test specimens. The simulated rock samples correspond to the same geometry as that shown in *Figure V-5c*, including the same notch radii. The finite element mesh has been refined in the region surrounding the notches as depicted in *Figure V-18*, trying to avoid any possible influence of the mesh. For this reason, no repetitiveness of the models has been considered in this case, as the influence of the mesh is considered to be negligible.

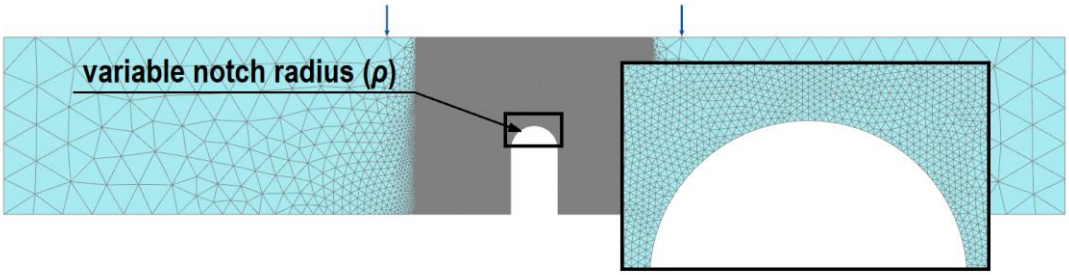

Figure V-18. Representation of the simulated four-point bending test finite numerical models.

For FEM analyses, a linear elastic constitutive model has been used to simulate the rock and, therefore, only two parameters are required: The Young's modulus (E) and the Poisson's ratio (v). These deformational parameters correspond to the macro-scale behavior of the rocks. Thus, they cannot be derived from the parameters in *Table V-4* that define the behaviour of the grains. The used elastic parameters have been obtained from the simulated uniaxial compression tests (*Figure V-5b*), which are provided in *Table V-8*.

With regard to the boundary conditions of the models, all the contours have been set free except for the supporting points. In this case, the simulations are not performed under displacement control. Instead,

the failure loads obtained from the DEM analyses have been directly introduced in the four-point bending test models, as stated above.

With all this, bearing in mind the differences between FEM and DEM results depicted in *Figure V-17*, it is worth highlighting that the fracture analyses performed by means of the TCD and the SED criterion consider continuous stress fields. Indeed, what both the TCD and the SED criterion do is to evaluate stresses at a certain distance or within a control volume (or area) so that differences between continuous and discontinuous stresses are somehow absorbed or compensated in this region, as characterised in *Figure V-19*.

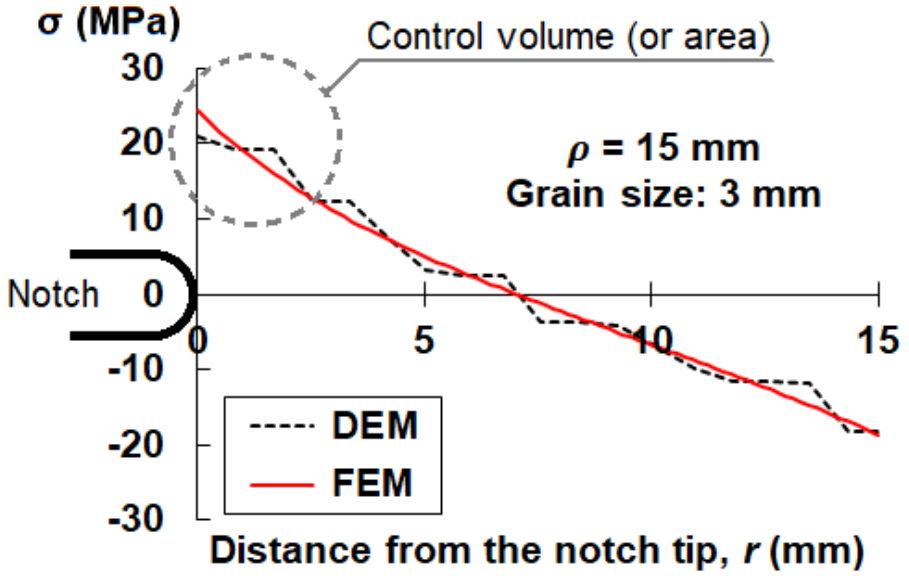

Figure V-19. Conceptual representation of the control volume (or area) over which continuous and discontinuous stresses are somehow compensated.

- Chapter VI -
Conclusions and future research

1 CONCLUSIONS

The main objective of this doctoral work was to deepen into the knowledge of rock fracture behaviour by studying the applicability and limitations of two different failure criteria (i.e., the TCD and the SED criterion) in the field of rock mechanics. In particular, the focus is placed on the fracture behaviour of six different rocks, namely a Floresta sandstone, Moleanos limestone, Macael marble, Carrara marble, Oolitic limestone and Biotite granite, under the presence of U-notch type defects and under different loading and temperature conditions. The first four rocks on the list were tested in the laboratory campaign performed within the framework of this doctoral thesis, while the last two rocks correspond to a previous work carried out by Cicero et al. (2014), from which the fracture data has been reused. In any case, the six studied rocks comprise a wide casuistic of rock lithologies that enable to obtain robust conclusions about the applicability and limitations of both the TCD and the SED criterion.

The TCD is a local failure criterion based on the stress field around the defect and on the concept of the critical distance (L), while the SED criterion is an energy-based approach that evaluates the strain energy

density within a control volume around the defect. Although both methodologies are widely used at present in the field of fracture mechanics and their applicability has been validated for different materials like steels or polymers, for example, its use on the particular field of rocks still requires further research. Thus, this work aims to respond to the general demand for specific tools and methodologies for assessment of rock fracture of notched components, leaving aside the over-conservative application of ordinary fracture mechanics that have been traditionally used to deal with this problem.

It is generally accepted that crack propagation phenomena in rocks are mode I dominated as a consequence of the relatively small tensile resistance of rocks that makes them highly sensitive to opening loading (mode I) conditions. For this reason, the applicability of the TCD and the SED criterion under mode I loading condition was studied first in this work. However, as rock masses are usually subjected to complex loading conditions and the defects within rocks are randomly orientated, in many practical situations the influence of combined opening-sliding shear deformations (i.e., mixed mode I+II) needs to be studied. Consequently, after validating the use of the TCD and the SED criterion for mode I loading, the extension of the TCD to mixed mode I+II was also analysed.

Additionally, the influence of temperature was considered as a variable in this research, aiming to validate the applicability of the proposed methodologies under high temperature conditions up to 250ºC, which is an expected range for conventional high-level radioactive waste disposal and for conventional or hot fracture rock geothermal energy systems, for example. To do so, the influence of temperature on the main rock parameters was studied trying to explore the prospective extrapolation of the TCD and the SED criterion to high temperature conditions. In particular, the tensile strength (σ_u), the fracture toughness (K_{IC}), the compressive strength (σ_c), the Young's modulus (E), the Poisson's ratio (ν) and the thermal expansion were analysed in this work.

Both the TCD and the SED criterion only require basic rock parameters for the assessment of rock fracture predictions, which can be easily determined in the laboratory from simple and standardized tests

(somehow less usual under high temperature conditions). This greatly facilitates the application and validation of both methodologies, since complex parameters that might be difficult or expensive to be obtained or that could lead to important sources of uncertainty are not required.

Accordingly, the performed fracture assessments are based on an exhaustive and systematic laboratory campaign, which offers a new valuable database on the fracture properties of a sandstone, a limestone and two different marbles at different temperatures up to 250ºC. *Table III-8* summarises the performed laboratory tests, which include 300 Brazilian tests, 120 uniaxial compression tests, 882 four-point bending tests on SENB specimens with variable notch radii, 395 three-point bending tests with variable notch radii and loading positions, 290 thermal expansion measurements, and 158 thin-section analyses.

With all this, several conclusions should be highlighted from the obtained results, which have been classified by topics:

A. Regarding the test types for determining the tensile strength and the fracture toughness of the studied rock:

- The tensile strength (σ_u) results obtained from Brazilian tests (BT), four-point bending tests (4PB) and three-point bending tests (3PB) have been compared. It was observed that BT offer lower values of the tensile strength compared to the 4PB and the 3PB tests, which tend to overestimate σ_u. However, dealing with the fracture toughness, similar results are obtained both from 3PB and 4PB tests.

B. Regarding the influence of temperature on the studied rock parameters:

- The Floresta sandstone and the Moleanos limestone, those with significant porosity, develop an increment of the tensile strength (σ_u) and the fracture toughness (K_{IC}) up to a certain critical temperature. This increment is related to the closure of the existing pores or microcracks during the initial heating stages. However, when a certain critical temperature is reached, the main mechanism changes and a decrease of the

tensile strength and the fracture toughness occurs. The critical temperature after which the fracture toughness decreases in the case of the Floresta sandstone and the Moleanos limestone has not been clearly captured for the studied range of temperatures. However, a subsequent reduction of K_{IC} is expected as observed in the literature for different rocks. This strength reduction is caused by the appearance of new thermally induced microcracks as a consequence of a differential expansion between adjacent internal particles of rocks.

- In the case of the Macael marble and the Carrara marble, those rocks with null porosity and, therefore, no space for internal expansion of grains, only this second mechanism (i.e., the appearance of microcracks) is shown. In these cases, a decrease in the tensile strength and fracture toughness is appreciated practically from the onset of the thermal increment.
- The compressive strength (σ_c) shows a generalised decrease with temperature in all the studied rocks except for the Moleanos limestone, which displays a completely opposite behaviour up to 250ºC. Similarly, homologous trends are observed in the influence of temperature on the Young's moduli of the rocks. However, the E values of the marbles present a relatively marked drop while the reduction of the E of the sandstone is almost negligible. In general, a roughly constant evolution of σ_c/σ_u is interpreted from the results, which implies that both the compressive and the tensile strength of the studied rocks vary more or less proportionally with temperature.
- With regard to the Poisson's ratio (ν), the four rocks show a decrement up to approximately 70ºC. Then, both marbles present a significant rise up to 250ºC (probably because of the observed non-linearities), while the Poisson's ratio values of the sandstone and the limestone remain roughly constant.
- In order to verify whether or not the use of Linear Elastic Fracture Mechanics (LEFM), in which the TCD and the SED are based, is valid up to 250ºC, the stress-strain curves derived from the uniaxial compression tests have been studied. The

linearity of the curves prior to the peaks reveals a predominantly quasi-brittle behaviour of the Floresta sandstone and the Moleanos limestone in the entire range of temperatures considered in this work. By contrast, the influence of temperature on the linear elastic behaviour of the marbles is more significant, especially in the Carrara marble. Both marbles show a certain degree of ductility in relative terms, which appears to be more noticeable as temperature increases. In the case of the Macael marble, reasonable brittle behaviour is observed at 23ºC and 70ºC, but certain non-linearity is noticed for higher temperatures. In the case of the Carrara marble, however, even those tests performed at room temperature display a not completely linear behaviour. Regardless of these comments, all the studied rocks have been assumed to behave as quasi-brittle materials and both the TCD and the SED criterion have been applied in all the cases, expecting worse fracture load predictions as non-linear behaviour becomes more significant.

C. Regarding the notch effect:

- The notch effect has proven to be evident and substantial in all the studied rocks except for the Carrara marble, since the apparent fracture toughness (K_{IN}) of rocks increases with the notch radius. However, the apparent fracture toughness shows an initial roughly horizontal region in which the notch effect is almost negligible. This indicates that the assumption for determining the fracture toughness of the rocks in which notches with $\rho = 015$ mm are supposed to behave as crack-type defects is valid. It is generally accepted that the notch effect if no longer negligible when the notch radius is larger than the critical distance of a certain material ($\rho > L$).
- On the other hand, there does not seem to be any change in the notch effect of the rocks with temperature, as the tendencies of the apparent fracture toughness against notch radius curves remain approximately parallel and only the

absolute values change according to the real fracture toughness (K_{IC}) variations with temperature.

D. Regarding the application of the fracture criteria:

D.1. Regarding the application of the TCD under mode I loading conditions:

- Under mode I loading conditions, the TCD, and in particular the LM, has provided reasonable fracture load predictions within a strip of ±20% with respect to the mean experimental failure loads, except for the Carrara marble, which shows a non-linear behaviour even at room temperature. In this work, the analytical stress distribution function defined by Creager & Paris (1967) was used to apply the TCD, which is theoretically only valid for long and narrow notches ($a \gg \rho$). However, reasonable results were obtained even beyond the application range of Creager & Paris (1967). In order to analyse the extent of the influence of the analytical approach, the analytically obtained fracture load predictions were compared with those from numerically obtained stress fields. In general, the improvement of the prediction results does not justify the increased workload of the numerical analyses. Both the analytical and numerical stress fields show a good agreement in the surroundings of the notches and get poorer as the influence of the boundary becomes noticeable. This boundary influence explains the gradual difference between numerical and analytical stress fields as distance from the notch tip increases. Additionally, it is observed that the largest notch radii (e.g., $\rho = 15$ mm) show a poorer agreement even close to the notch tip. Thus, it can be concluded that the largest notches analysed in this work are on the limit of the application range of Creager & Paris (1967).
- The critical distance is of the order of a few millimetres in the case of the analysed rocks. Although slight variations are observed in the values of L depending on the used method for its calculation (i.e., direct calculation with the analytical expression, best adjustment of the PM, best adjustment of the

LM, numerical approach), the consequences of those differences are rather limited when performing fracture load predictions, as L is square rooted in the analytical solutions of both the PM and the LM.

D.2. Regarding the application of the TCD under mixed mode I+II loading conditions:

- The application of TCD has also been validated to perform fracture assessments of U-notched rock components under mixed mode (I+II) loading conditions, even at high temperatures as long as linear elastic conditions are guaranteed.
- The interpretation of the mixed mode (I+II) results by means of the TCD allows the critical distance for different mode mixities (M_e) to be characterised using the stress field at the corresponding critical plane, which is derived from numerical models. When analysing the obtained values of L against M_e, a linear relation can be interpreted. However, if these results are observed separately for each notch radius, a certain influence of the notch radius on the critical distance is shown. This influence seems to indicate that, for the studied cases, L is relatively constant with M_e for each notch radius.

D.3. Regarding the application of the SED criterion under mode I loading conditions:

- Similarly to the TCD, the SED criterion has also provided reasonable fracture load predictions at different temperatures under mode I loading conditions, within a range of ±20% with respect to the average experimental failure loads. Again, the results of the Carrara Marble offer the poorest fracture load predictions as a consequence of the observed non-linear behaviour.
- Three different methodologies have been proposed for the application of the SED criterion on rocks. Method A provides a good agreement between the predicted and the experimental failure loads, avoiding the use of numerical analyses and using

tabulated values of the H function (and, when necessary, their corresponding extrapolation). By contrast, Method B requires simple numerical analyses in order to calculate the H function. In this case, the best results correspond to the numerical model with the smallest notch radius ($\rho_{fem} = 0.15$ mm), and it has been demonstrated that the results of Method B, derived from the numerical model with $\rho_{fem} = 1$ mm, and those of Method A (whose tabulated values, in origin, were also numerically obtained for $\rho_{fem} = 1$ mm) are quite similar in the comparable range of values. Both Method A and B provide reasonable results even beyond the application range of the Creager & Paris' (1967) stress distribution in which both methods are based. Finally, Method C requires a more laborious numerical modelling analysis than Method B, but avoids the use of the Creager & Paris' (1967) stress distribution. Satisfactory fracture load predictions are obtained for the largest notch radii with this third method, while for the smallest notches significant overestimations are generated because of the relatively large size of the control volume, which reaches or is affected by the boundary conditions in these cases. It must be highlighted that, in the case of rocks, the sizes of the control areas over which the strain energy density is averaged are relatively large. Thus, especial care must be taken in order to ensure that the influence of the boundary can really be neglected. Possible approximate solutions to this problem are applying the Method A or the Method B with a sufficiently small ρ_{fem} value that guarantees tiny critical radii. In this way, the local stress field evaluated from the notch tip to a radial distance R_0 will still be governed by the Generalised Notch Stress Intensity Factor and the assumed hypotheses will be valid.

- The energy-based approach calculates the critical strain energy density (W_c) assuming a perfectly linear elastic behaviour of the rocks. However, as concluded from the stress-strain curves of the uniaxial compression tests, this is not completely true and certain subcritical crack growth prior to final failure can be expected, especially at high temperatures. For this reason,

as a simple approach to consider the material non-linearity in the estimation of W_c, it was proposed to calibrate W_c for a particular notch radius and then be used for the failure load predictions of the rest of notch radii, since W_c is a material parameter. The calibrated SED failure predictions offer slightly higher and more accurate estimations of the failure load providing, in general terms, similar results to those offered by the TCD. This calibration process can be applied in those cases in which non-linearities are not excessively large. However, when non-linear behaviour is important, the SED criterion can no longer be applied as it is based on LEFM. For example, for the Carrara marble at 250ºC, it is observed that methods based on LEFM, like SED criterion or TCD, do not provide satisfactory predictions, especially for the largest notches.

D.4. Regarding the comparison between the TCD and the SED criterion:

- In general, the TCD and the SED provide similar failure load predictions, especially when the critical strain energy density is calibrated. One of the main advantages of the SED criterion is that the strain energy density can be easily evaluated numerically through finite element analyses by using coarse meshes, and, although it is not the purpose of this work, it permits to take into account higher order terms and three-dimensional effects. Besides, once the H function is tabulated numerical analyses are no longer required and failure load predictions can be directly performed. By contrast, the main disadvantage compared to the TCD is that additional tests are required (i.e., uniaxial compression tests with strain gauge measurements), since the deformational parameters are needed. Based on the results, differences in the fracture load predictions obtained by the SED criterion and the TCD do not justify the additional workload involved by the SED approach. Indeed, the workload and cost of measuring the Young's modulus and the Poisson's ratio at temperatures above approximately 70ºC is substantial because special (and more

expensive) strain gauges, adhesives and wires are required. Additionally, the complexity of performing the uniaxial compression tests at high temperatures compared to those at room temperature is also remarkable. With regards to the TCD, once the critical distance (L) of a certain material is defined, it is straightforward to perform fracture assessments of any component made of that material.

E. Regarding the influence of grain size:

- The actual physical definition of the critical distance is still a matter of debate among the scientific community. However, L seems to be linearly related to the grain size of the rock. In particular, the studied rocks show a linear relation between the critical distance and the mean grain size of a factor above 10. That is, the critical distance of the rocks seems to be slightly higher than ten times the mean grain size.
- Aiming to go deeper into the study of rock fracture initiation and the physical meaning of the critical distance, the influence of grain size has been numerically studied by means of Discrete Element Method (DEM). The observed variation of the apparent fracture toughness with the notch radii shows a slight decrease when the rock grain size increases, which seems to indicate that the notch effect softens with the increase of the grain size. This variation also implies an increase of the critical distance with the grain size, which can be derived both from the best-fit adjustment of the apparent fracture toughness results and from the analytical calculation of L using the numerically obtained values of the tensile strength and the fracture toughness. The interpretation of the four-point bending test models using the TCD provided satisfactory results and values of the critical distance that corresponded to the grain size in a nearly 1:1 linear proportion. This correlation between the critical distance and the grain size must be understood only in qualitative terms because the numerical simulations are simply an idealization of the real problem (2D grains, only intergranular fractures) of an already highly

idealised rock (non-porous, isotropic, very uniform grains with 1:1 aspect ratio). To allow for an interpretation of the notch effect with the TCD, splitting (Brazilian) tests were also numerically simulated to obtain the tensile strength. It is observed that the tensile strength increases with the grain size but, proportionally, less than the fracture toughness. Additionally, simple compression tests were numerically simulated and an increase in the Young's moduli and Poisson's ratios with the grain size was found.

2 FUTURE RESEARCH

Rock fracture mechanics is a relatively recent and active brunch of mechanics that is in continuous development. Below, some possible future research topics are outlined as a follow-up to the doctoral work presented here:

- In this work, Brazilian tests are used for the indirect determination of the tensile strength of the studied rocks. The execution of direct tensile tests is generally difficult and requires special care to ensure that failure occurs due to uniform tensile stresses. However, performing direct tensile tests at the same range of temperatures as the Brazilian tests would provide more accurate tensile strength results and, consequently, fracture load predictions. Additionally, tensile stress-strain curves would provide interesting information on the linear behaviour of the rocks when subjected to direct tensile loading conditions and would allow a more realistic determination of the critical strain energy density (W_c) and a more detailed comparison between testing methods to get the tensile strength.
- Although the applicability of the TCD under mixed mode I+II has been studied in this work. It would be interesting to deepen into this analysis and study further mode mixities, as for example pure mode II loading conditions or even mixed mode I+III loading conditions.
- The applicability of the SED criterion to mixed mode loading conditions could be extended. To do so, simple numerical

analyses are needed similar to those performed for mode I loading conditions. In essence, changes in the control area under mixed mode loading conditions are to be determined.

- In this work, plane strain conditions are considered for the fracture analysis of the SENB specimens. However, a detailed analysis of three-dimensional effects (whose influence is especially important close to the borders) would provide an added value to the research.
- Despite the involved computational cost and workload, DEM analyses have a huge potential for the fracture analyses of rocks. They provide a suitable tool to study the physical meaning of the critical distance. For this reason, the performed numerical analyses could be extended to consider, for example, porosity or intergranular cracking, as well as the influence of different components within the rock microstructure.
- In the performed fracture assessments, the boundary conditions of the rock beams seem to play a role. Therefore, sensitivity analyses on the influence of specimen size would be of interest, comparing, for example, the results with thicknesses of 30, 70 and 100 mm.
- Based on the importance of the fracture toughness (K_{IC}) as a parameter for the fracture assessment of any cracked and notched component, a collaboration with the University of A Coruña (Spain) has arisen aiming to compare different rock fracture toughness testing methods (under mode I loading conditions). In particular, four-point bending tests and pseudo-compact tension (pCT) tests will be compared for a more detailed characterization of K_{IC} of different rocks (see Muñoz-Ibañez, 2020).
- Aiming to deepen into the physical meaning of the critical distance, a proper characterization of the Fracture Process Zone (FPZ) by means of digital image correlation (DIC) and X-ray computed microtomography (micro-CT) would be of a great interest.

- Chapter VII -
Bibliography

Akbardoost, J., Ayatollahi, M.R., Aliha, M.R.M., Pavier, M.J. & Smith, D.J., 2014. Size-dependent fracture behavior of Guiting limestone under mixed mode loading. *Int J Rock Mech Min Sci,* Vol. 71, pp. 369-380.

Albrecht, P. & Yamada, K., 1977. Rapid calculation of stress intensity factors. *J Struct Div,* Vol. 103, pp. 377-389.

Aliha, M. & Ayatollahi, M., 2009. Brittle fracture evaluation of a fine grain cement mortar in combined tensile-shear deformation. *Fatigue Fract Eng Mater Struct,* Vol. 32, pp. 987-994.

Aliha, M. & Ayatollahi, M., 2013. Two-parameter fracture analysis of SCB rock specimen under mixed mode loading. *Eng Fract Mech,* Vol. 103, pp. 115-123.

Aliha, M., Ayatollahi, M. & Pakzad, R., 2008. Brittle fracture analysis using a ring-shape specimen containing two angled cracks. *Int J Fract,* Vol. 153, pp. 63-68.

Aliha, M., Bahmani, A. & Akhondi, S., 2015. Determination of mode III fracture toughness for different materials using a new designed test configuration. *Mater Des,* Vol. 86, pp. 863-871.

Aliha, M., Berto, F., Mousavi, A. & Razavi, S., 2017. On the applicability of ASED criterion for predicting mixed mode I+II fracture toughness results of a rock material. *Theor Appl Fract Mech,* Vol. 92, pp. 198-204.

Aliha, M., Hosseinpour, G. & Ayatollahi, M., 2013. Application of cracked triangular specimen subjected to three-point bending for investigating fracture behavior of rock materials. *Rock Mech Rock Eng,* Vol. 46(5), pp. 1023-1034.

Aliha, M., Mahdavi, E. & Ayatollahi, M., 2017. The influence of specimen type on tensile fracture toughness of rock materials. *Pure Appl Geophys,* Vol. 174, pp. 1237-1253.

Al-Shayea, N., Khan, K. & Abduljauwad, S., 2000. Effects of confining pressure and temperature on mixed-mode (I-II) fracture toughness of a limestone rock. *Int J Rock Mech Min Sci,* Vol. 37, pp. 629-643.

Amaral, P., Guerra Rosa, L. & Cruz Fernandes, J., 2008. Assessment of fracture toughness in ornamental stones. *Int J Rock Mech Min Sci,* Vol. 45, pp. 554-563.

Amrollahi, H., Baghbanan, A. & Hashemolhosseini, H., 2011. Measuring fracture toughness of crystalline marbles under modes I and II and mixed mode I-II loading conditions using CCNBD and HCCD specimens. *Int J Rock Mech Min Sci,* Vol. 48(7), pp. 1123-1134.

Anderson, T., 2005. *Fracture mechanics. Fundamentals and Applications.* Boca Ratón: Taylor & Francis Group.

Anon, 1977. The description of rock masses for engineering purposes. *Q J Eng Geol Hydroge,* Vol. 10(4), pp. 355-388.

Araújo, R., Sousa, J. & Bloch, M., 1997. Experimental investigation on the influence of temperature on the mechanical properties of reservoir rocks. *Int J Rock Mech Min Sci,* Vol. 34, pp. 298.e1-298.e16.

Asadi, M. & Barla, G., 2012. A bonded particle model simulation of shear strength and asperity segradation for rough rock fractures. *Rock Mech Rock Eng,* Vol. 45, pp. 649-675.

ASTM C880, 2018. Standard Test Method for Flexural Strength of Dimension Stone. *ASTM International, West Conshohocken, USA.*

ASTM C99, 2018. Standard Test Method for Modulus of Rupture of Dimension Stone. *ASTM International, West Conshohocken, USA.*

ASTM D2936, 2020. Standard test method for direct tensile strength of intact rock core specimens. *ASTM International, West Conshohocken, USA.*

ASTM D3967, 2008b. Standard test method for splitting tensile strength of intact rock core specimens. *ASTM International, West Conshohocken, USA.*

ASTM E-1820-09e1, 2009. Standard Test Method for Measurement of Fracture Toughness. *Philadelphia: American Society for Testing and Materials.*

ASTM E-399-09e2, 2009. Standard Test Method for Linear-Elastic Plane-Strain Fracture Toughness KIc of Metallic Materials. *Philadelphia: American Society for Testing and Materials.*

Atkinson, B., MacDonald, D. & Meredith, P., 1984. Acoustic response and fracture mechanics of granite subjected to thermal and stress cycling experiments. *Zurich: Clausthal, W. (ed.) Proceedings of the 3rd International Conference on Crack Growth. Technical Report in Geological Structures and Materials.*

Atzori, B., Zappalorto, M. & Berto, F., 2010. A theoretical treatise for notch and defect sensitivity under torsion. *Mech Res Commun,* Vol. 37(2), pp. 173-176.

Ayatollahi, M., Akbardoost, J. & Berto, F., 2016. Size effects on mixed-mode fracture behavior of polygranular graphite. *Carbon,* Vol. 103, pp. 394-403.

Ayatollahi, M., Bahrami, B., Mirzaei, A. & Yazid Yahya, M., 2019. Effect of support friction on mode I stress intensity factor and fracture toughness in SENB testing. *Theor Appl Fract Mech*, Vol. 103, pp.102288.

Ayatollahi, M. & Aliha, M., 2008. On the use of Brazilian disc specimen for calculating mixed mode I-II fracture toughness of rock materials. *Eng Fract Mech,* Vol. 75, pp. 4631-4641.

Ayatollahi, M. & Torabi, A., 2009. A criterion for brittle fracture in U-notched components under mixed mode loading. *Eng Fract Mech,* Vol. 76, pp. 1883-1896.

Backers, T., Stanchits, S. & Dresen, G., 2005. Tensile fracture propagation and acoustic emission activity in sandstone. *In J Rock Mech Min Sci,* Vol. 42(7-8), pp. 1094-1101.

Bahrami, B., Ayatollahi, M., Mirzaei, A. & Yazid Yahya, M., 2020. Support type influence on rock fracture toughness measurement using semi-circular bending specimen. *Rock Mech Rock Eng*, Vol. 53, pp. 2175-2183.

Balme, M., Rocchi, V., Jones, C., Sammonds, P., Meredith, P. & Boon, S., 2004. Fracture toughness measurements on igneous rocks using high-pressure, high-temperature rock fracture mechanics cell. *J Volcanol Geotherm Res,* Vol. 132, pp. 159-172.

Bao, Y. & Jin, Z., 1993. Size effects and mean strength criterion for ceramics. *Fatigue Fract Eng Mater Struct,* Vol. 16, pp. 829-835.

Barenblatt, G., 1959. The formation of equilibrium cracks during brittle fracture. General ideas and hypotheses. Axially symmetric cracks.. *J Appl Math Mech,* Vol. 23(3), pp. 434-444.

Barton, N., Lien, R. & Lunde, J., 1974. Engineering classification of rock masses for the design of rock support. *Rock Mech,* Vol. 6, pp. 189-236.

Bellett, D., Taylor, D., Marco, S., Mazzeo, E. & Pircher, T., 2005. The fatigue behaviour of three-dimensional stress concentration. *Int J Fatigue*, Vol. 27, pp. 207-221.

Beltrami, E., 1885. Sulle condizioni di resistenza dei corpi elastici. *Il Nuovo Cimento (1877-1894),* Vol. 18, pp. 145-155.

Belytschko, T. & Black, T., 1999. Elastic crack growth in finite elements with minimal remeshing. *Int J Num Method Eng,* Vol. 45(5), pp. 601-620.

Belytschko, T., Fish, J. & Engelmann, B., 1988. A finite element with embedded localization zones. *Comput Method Appl Mech Eng,* Vol. 70, pp. 59-89.

Belytschko, T. & Lin, J., 1987. A three-dimensional impact-penetration algorithm with erosion. *Comput Struct,* Vol. 25, pp. 95-104.

Belytschko, T., Lu, Y. & Gu, L., 1994. Element-free galerkin methods. *Int J Num Method Eng,* 37(2), pp. 229-256.

Berto, F. & Lazzarin, P., 2009. A review of the volume-based strain energy density approach applied to V-notches and welded structures. *Theor Appl Fract Mech,* Vol. 52(3), pp. 183-194.

Berto, F. & Lazzarin, P., 2014. Recent developments in brittle and quasi-brittle failure assessment of engineering materials by means of local approaches. *Mater Sci Eng R Rep,* Vol. 75, pp. 1-48.

Berto, F., Lazzarin, P., Gómez, F. & Elices, M., 2007. Fracture assessment of U-notches under mixed mode loading: two procedures based on the “equivalent local mode I” concept. *Int J Fract,* Vol. 148(4), pp. 415-433.

Bhattacharya, S. & Kumar, A., 1995. Rotational factor using bending moment approach under elasto-plastic situation—I. Notch 3PB geometry. *Eng Fract Mech,* Vol. 50(4), pp. 493-505.

Bieniawski, Z., 1973. Engineering classification of jointed rock masses. *Trans S African Instn Civ Eng,* Vol. 15(12), pp. 335-344.

Bieniawski, Z., 1984. Rock mechanics design in mining and tunneling. *Rotterdam: A.A. Balkmea.*

Brace, W., 1964. Brittle fracture of rocks. *Proceedings of the International Conference on State of Stress in the Earth's Crust,* pp. 111-174.

Brace, W., B.W., P. & Scholz, C., 1966. Dilatancy in the fracture of crystalline rocks. *J Geophys Res,* Vol. 71(16), pp. 3939-3953.

Brebbia, C. & Walker, S., 2016. Boundary element techniques in engineering. *Elsevier.*

Broek, D., 1982. Elementary engineering fracture mechanics. *The Hague: Springer.*

Brown, W. J. & Srawley, J., 1966. Plane strain crack toughness testing of high strength metallic materials. *Philadelphia: ASTM STP 410, American Society for Testing and Materials.*

BS7910, 2005. Guide to methods for assessing the acceptability of flaws in metallic structures. *London: British Standards Institution.*

Bunger, A., Lakirouhani, A. & Detournay, E., 2010. Modelling the effect of injection system compressibility and viscous fluid flow on hydraulic fracture breakdown pressure. *Rock Stress and Earthquakes-Proc 5th International Symposium on In-situ Rock Stress,* pp. 56-67.

Campagnolo, A., Berto, F. & Lazzarin, P., 2015. The effects of different boundary conditions on three-dimensional cracked discs under anti-plane loading. *Eur J Mech A-Solid,* Vol. 50, pp. 76-86.

Cardani, G. & Meda, A., 2004. Marble behaviour under monotonic and cyclic loading in tension. *Constru Build Mater,* Vol. 18, pp. 419-424.

Carpinteri, A. y otros, 2008. A finite fracture mechanics approach to structures with sharp V-notches. *Eng Fract Mech,* Vol. 75(7), pp. 1736-1752.

CEN/TS 14425-1, 2003. Advanced Technical Ceramics - Test Methods for Determination of Fracture Toughness of Monolithic Ceramics - Part 1: Guide to Test Method Selection. *European: Committee for Standarization.*

Chandler, M., Meredith, P., Brantut, N. & Crawford, B.R., 2017. Effect of temperature on the fracture toughness of anisotropic shale and other rocks. *Geological Society London Special Publications.*

Chang, K., 1981. On the maximum strain criterion - a new approach to the angled crack problem. *Eng Fract Mech,* Vol. 14, pp. 107-124.

Chang, S., Lee, C. & Jeon, S., 2002. Measurement of rock fracture toughness under modes I and II and mixed-mode conditions by using disc-type specimens. *Eng Geol,* Vol. 66, pp. 79-97.

Chen, C. & Pan, H., 1978. Collection of Papers on Fracture of Metals. *Beijing: Metallurgy Industry Press.*

Chen, D. & Chen, L., 2018. The admissible range of notch root radius for applying the singular stress field to its fracture analysis. *Eng Fract Mech,* Vol. 202, pp. 202-213.

Chengyong, W., Peide, L., Rongsheng, H. & Xiutang, S., 1990. Study of the fracture process zone in rock by laser speckle interferometry. *In J Rock Mech Min Sci Geomech Abs,* Vol. 27, pp. 65-69.

Chen, Y., Ni, J., Shao, W. & Azzam, R., 2012. An experimental study on the influence of temperature on the mechanical properties of granite under a uni-axial compression and fatigue loading. *Int J Rock Mech Min Sci,* Vol. 56, pp. 62-66.

Cicero, S., Berto, F., Ibánez Gutiérrez, F.T., Procopio, I. & Madrazo, V., 2017. SED criterion estimations of fracture loads in structural steels operating at lower shlef temperatures and containing U-notches. *Theor Appl Fract Mech,* Vol. 90, pp. 234-243.

Cicero, S., García, T., Castro, J., Madrazo, V. & Andrés, D., 2014. Analysis of notch effect on the fracture behaviour of granite and limestone: An approach from the Theory of Critical Distances. *Eng Geol,* Vol. 177, pp. 1-9.

Coates, D., 1964. Classification of rocks for rock mechanics. *Int J Rock Mech Min Sci,* Vol. 1, pp. 421-429.

Coates, D. & Parsons, R., 1966. Experimental criteria for classification of rock substances. *Int J Rock Mech Min Sci,* Vol. 3, pp. 181-189.

Colback, P., 1966. An analysis of brittle fracture initiation and propagation in the Brazilian test. *Proc 1st Congr Int Soc Rock Mech, Lisbon,* pp. 385-391.

Coviello, A., Lagioia, R. & Nova, R., 2005. On the Measurement of the Tensile Strength of Soft Rocks. *Rock Mech Rock Eng,* Vol. 38(4), pp. 251-273.

Creager, M. & Paris, C., 1967. Elastic field equations for blunt cracks with reference to stress corrosion cracking. *Int J Fract,* Vol. 3, pp. 247-252.

Cundall, P., 1971. A computer model for simulating progressive large scale movements in blocky rock systems. *Proc Symp Rock Fracture (ISRM), Nancy.*

Cundall, P., 1988. Formulation of a three-dimensional distinct element modelpart i. a scheme to detect and represent contacts in a system composed of many polyhedral blocks. *Int J Rock Mech Min Sci Geomech Abstr,* Vol. 25, pp. 107-116.

Cundall, P. & Strack, O., 1979. A Discrete Numerical Model for granular assemblies. *Geotechnique,* Vol. 29, pp. 47-65.

Dan, D. & Konietzky, H., 2014. Numerical simulations and interpretations of Brazilian tensile tests on transversely isotropic rocks. *Int J Rock Mech Min Sci,* Vol. 71, pp. 53-63.

Deere, D. & Miller, R., 1966. Engineering classification and index properties for intact rock. *Nuevo Méjico: Tech Rept No. AFWL-TR-65-116, Air Force Weapons Lab., Kirtland Air Force Base.*

Deere, D., Peck, R., Monsees, J. & Schmidt, B., 1969. Design of tunnel liners and support system. *Office of high speed ground transportation, U.S. Department of transportation. PB 183799.*

Dengina, N., Kazak, V. & Pristash, V., 1993. Changes in Rocks at High Temperatures. *Fiziko-Techniczeskie Problemy Razrabotki Poleznych Iskopaemych,* pp. 96-103.

Diederichs, M., 2003. Rock fracture and collapse under low confinement conditions. *Rock Mech Rock Eng,* Vol. 36(5), pp. 339-381.

Diederichs, M. & Kaiser, P., 1999. Tensile strength and abutment relaxation as failure control mechanics in underground excavations. *Int J Rock Mech Min Sci,* Vol. 36, pp. 69-96.

Dimitriyev, A., Kusyayev, L., Protasov, Y. & Yamschichikov, V., 1969. Physical Properties of Rocks at High Temperature. *Moscow: Nedra.*

Dolbow, J. & Belytschko, T., 1999. A finite element method for crack growth without remeshing. *Int J Num Method Eng,* Vol. 46, pp. 131-150.

Dongming, Z. & Yushun, Y., 2018. The effect of high temperature on tensile strength and damage characteristics of limestone. *Geotech Geol Eng,* Vol. 36, pp. 3527-3535.

Duclos, R. & Paquet, J., 1991. High-temperature behaviour of basalts - role of temperature and strain rate on compressive strength and Kic toughness of partially glassy basalts at atmospheric pressure. *Int J Rock Mech Min Sci Geomech Abstr,* Vol. 28, pp. 71-76.

Dugdale, D., 1960. Yielding of steel sheets containing slits. *J Mech Phys Solids,* Vol. 8, pp. 100-104.

Duncan, N., 1969. *Engineering Geology and Rock Mechanics, Vol. 1.* London: Leonard Hill.

Dunham, R., 1962. Classification of carbonate rocks according to depositional textures. *Am Assoc Petrol Geol Mem,* Vol. 1, pp. 108-121.

Duriez, J., Scholtès, L. & Donzè, F., 2016. Micromechanics of wing crack propagation for different flaw properties. *Eng Fract Mech,* Vol. 153, pp. 378-398.

Dvorkin, E., Cuitio, A. & Gioia, G., 1990. Finite elements with displacement interpolated embedded localization lines insensitive to mesh size and distortions. *Int J Num Method Eng,* Vol. 30(3), pp. 541-564.

Dwivedi, R., Goel, R., Prasad, V. & Sinha, A., 2008. Thermomechanical properties of Indian and other granites. *Int J Rock Mech Min Sci,* Vol. 45, pp. 303-315.

Einstein, H. & Baecher, G., 1982. Probabilistic and statistical methods in engineering geology. I. Problem statement and introduction to solution. *Rock Mech,* Vol. 12, pp. 47-61.

Elayachi, I., Pluvinage, G., Bensalah, M.O., Lebienvenu, M. & Dlouhy, I., 2005. To Joint Effect of Temperature and Notch Root Radius on Fracture Toughness. *Eng Mech,* Vol. 12, pp. 11-22.

Ellyin, F., 1997. Fatigue Damage, Crack Growth and Life Prediction. *London: Chapman & Hall.*

EN 12372, 2006. Natural stone test methods - Determination of flexural strength under concentrated load. *European: Committee for Standarization.*

EN 13161, 2008. Natural stone test methods - Determination of flexural strength under constant moment. *European: Committee for Standarization.*

EN 1341, 2013. Slabs of natural stone for external paving - Requirements and test methods.

EN 13755, 2008. Natural stone test methods - Determination of water absorption at atmospheric pressure. *European: Committee for Standarization.*

EN 14580, 2006. Natural Stone Test Methods – Determination of Static Elastic Modulus. *European: Committee for Standarization.*

EN 1926, 2007. Natural Stone Test Methods - Determination of Uniaxial Compressive Strength. *European: Committee for Standarization.*

EN 1936, 2007. Natural stone test methods - Determination of real density and apparent density, and of total and open porosity. *European: Committee for Standarization.*

Erdogan, F. & Sih, C., 1963. On the crack extension in plates under plane loading and transverse shear. *J Basic Eng,* Vol. 85, pp. 519-525.

Ewalds, H. & Wanhill, R., 1984. Fracture mechanics. *London: Edward Arnold.*

Fakhri, M., Amoosoltani, E. & Aliha, M., 2017. Crack behavior analysis of roller compacted concrete mixtures containing reclaimed asphalt pavement and crumb rubber. *Eng Fract Mech,* Vol. 180, pp. 43-59.

Feng, G. y otros, 2018. The influence of temperatures on mixed-mode (I + II) and mode II fracture toughness of sandstone. *Eng Fract Mech,* Vol. 189, pp. 51-63.

Feng, G. y otros, 2017. The influence of temperature on Mode I fracture toughness and fracture characteristics of sandstone. *Rock Mech Rock Eng,* Vol. 50, pp. 2007-2019.

Fenghui., E., 2000. Prediction of intrinsic fracture toughness for brittle materials from the apparent toughness of notched-crack specimen. *J Mater Sci,* Vol. 35, pp. 2543-2546.

Filippi, S., Lazzarin, P. & Tovo, R., 2002. Developments of some explicit formulas useful to describe elastic stress field ahead of the notches. *Int J Solids Struct,* Vol. 39, pp. 4543-4565.

Filon, L., 1900. On the resistance to torsion of certain forms of shafting, with special reference to the effect of keyways.. *Trans Roy Soc London,* Vol. 193, pp. 309-352.

FITNET FFS Procedure, 2008. *Fitness-for-Service (FFS) Proceure, vol. 1.,* GKSS, Geesthacht.

Folk, R., 1959. Practical petrographic classification of limestones. *Bull Am Assoc Petrol Geol,* Vol. 43, pp. 1-38.

Fowell, R.J., Hudson, J.A., Xu, C., Chen, J.F. & X., Zhao, 1995. Suggested Methodfor Determining Mode I Fracture Toughness Using Cracked Chevron Notched Brazilian Disc (CCNBD) Specimens. *International Society for Rock Mechanics Commission on Testing Methods,* pp. 259-268.

Franklin, J., 1975. Safety and economy of tunneling. *Proc 10th Canadian Rock Mech Symp, Kingstone,* pp. 27-53.

Franklin, J. & Dusseault, M., 1989. Rock Engineering. *New York: McGraw-Hill.*

Funatsu, T., Seto, M., Shimada, H., Matsui, K. & Kuruppu, M., 2004. Combined effects of increasing temperature and confining pressure on the fracture toughness of clay bearing rocks. *Int J Rock Mech Min Sci,* Vol. 41, pp. 927-938.

Funatsu, T., Shimizu, N., Kuruppu, M. & Matsui, K., 2015. Evaluation of mode I fracture toughness assisted by the numerical determination of K-resistance. *Rock Mech Rock Eng,* Vol. 48, pp. 143-157.

Galouei, M. & Fakhimi, A., 2015. Size effect, material ductility and shape of fracture process zone in quasi-brittle materials. *Comput Geomech,* Vol. 65, pp. 126-135.

Gdoutos, E., 1990. Fracture Mechanics Criteria and Applications. *Dordrecht/Boston/London: Kluwer Academic Publisher.*

Ghazvinian, E., Diederichs, M. & Quey, R., 2014. 3D random Voronoi grain-based models for simulation of brittle rock damage and fabric-guided micro-fracturing. *J Rock Mech Geotech Eng,* Vol. 6, pp. 506-521.

Gillemot, L., 1965. Brittle fracture of welded materials. *Commonwealth Welding Conference, Vol. C.7,* pp. 353-358.

Gillemot, L., 1976. Criterion of crack initiation and spreading. *Eng Fract Mech,* Vol. 8, pp. 239-253.

Gillemot, L., Czoboly, E. & Havas, I., 1985. Fracture mechanics applications of absorbed specific fracture energy: notch and unnotched specimens. *Theor Appl Fract Mech,* Vol. 4, pp. 39-45.

Glinka, G., 1985. Energy density approach to calculation of inelastic strain–stress near notches and cracks. *Eng Fract Mech,* Vol. 22, pp. 485-508.

Glinka, G. & Newport, A., 1987. Universal features of elastic notch tip stress fields. *Int J Fatigue,* Vol. 9, pp. 143-150.

Gómez, F. & Elices, M., 2004. A fracture criterion for blunted V-notched samples. *Int J Fract,* Vol. 127, pp. 239-264.

Gómez, F., Elices, M., Berto, F. & Lazzarin, P., 2007. Local strain energy to assess the static failure of U-notches in plates under mixed mode loading. *Int J Fract,* Vol. 145, pp. 29-45.

Gómez, F., Elices, M., Berto, F. & Lazzarin, P., 2008. A generalised notch stress intensity factor for U-notched components loaded under mixed mode. *Eng Fract Mech,* Vol. 75(16), pp. 4819-4833.

Gómez, F., Elices, M., Berto, F. & Lazzarin, P., 2009. Fracture of U-notched specimens under mixed mode: Experimental results and numerical predictions. *Eng Fract Mech,* Vol. 76(2), pp. 236-249.

Gómez, F., Elices, M. & Valiente, A., 2000. Cracking in PMMA containing U-shaped notches. *Fatigue Fract Eng Mater Struct,* Vol. 23, pp. 795-803.

Gómez, F. & Torabi, A., 2018. Application of the equivalent material concept to fracture of U-notched solids under small scale yielding. *Proc Struct Int*, Vol. 13, pp. 267-272.

Gorski, B., 1993. Tensile testing apparatus. *United States Patent, Patente nº 5193396.*

Griffith, A., 1921. The phenomena of rupture and flow in solids. *Philosophical transactions of the Royal Society of London,* Vol. 221, pp. 163-198.

Gross, R. & Mendelson, A., 1972. Plane elastostatic analysis of V-notched plates. *Int J Fract Mech,* Vol. 8, pp. 267-276.

Gui, Y.L., Zhao, Z.Y., Ji, J., Wang, X.M., Zhou, K.P. & Ma, S.Q., 2016. The grain effect of intact rock modelling using discrete element method with Voronoi grains. *Geotch Lett,* Vol. 6, pp. 1-8.

Guo, L.L., Zhang, Y.B., Zhang, Y.J., Yu, Z.W. & Zhang, J.N., 2018. Experimental investigation of granite properties under different temperatures and pressures and numerical analysis of damage effect in enhanced geothermal system. *Renew Energy,* Vol. 126, pp. 107-125.

Haddad, M., K.N., S. & Topper, T., 1979. Fatigue crack propagation of short cracks. *J Eng Mater Technol Trans ASME,* Vol. 101, pp. 42-46.

Harrison, J. & Hudson, J., 2000. Engineering Rock Mechanics Part II: Illustrative worked examples. *Oxford: Pergamon.*

Hawkes, I. & Mellor, M., 1970. Uniaxial testing in rock mechanics laboratories. *Eng Geol,* Vol. 4(3), pp. 117-285.

Heap, M., Baud, P. & Meredith, P., 2009. Influence of temperature on brittle creep in sandstones. *Geophys Res,* Vol. 36, p. L19305.

Hedner, G., 1987. Brittle fracture initiation from a blunting crack. *Eng Fract Mech,* Vol. 28, pp. 115-125.

Heuze, F., 1983. High-temperature mechanical, physical and thermal properties of granitic rocks—a review. *Int J Rock Mech Min Sci Geomech Abstr,* Vol. 20, pp. 3-10.

Hoek, E., 1964. Rock fracture around mining excavations. *Proc 4th Int Conf on Strata Control and Rock Mech, New York.*

Hoek, E., 1965. Rock fracture under static stress conditions. *University of Cape Town, South Africa: PhD Thesis.*

Hoek, E., 1983. Strength of jointed rock masses. *Geotechnique,* Vol. 3, pp. 187-223.

Hoek, E., 1986. Practical rock mechanics - development over the past 25 years. *Keynote address delivered 24.2.1986.*

Hoek, E. & Brown, E., 1980. Underground excavations in rock. *London: Institution of Mining and Metallurgy.*

Hoek, E. & Martin, C., 2014. Fracture initiation and propagation in intact rock – a review. *J Rock Mech Geotech Eng,* Vol. 6, pp. 287-300.

Homand-Etienne, F. & Houpert, R., 1989. Thermally induced microcracking in granites: characterization and analysis. *Int J Rock Mech Min Sci,* Vol. 26, pp. 125-134.

Hondros, G., 1959. The evaluation of Poisson's ratio and the modulus of materials of a low tensile resistance by the Brazilian (indirect tensile) test with particular reference to concrete. *Aust J Appl Sci,* Vol. 10, pp. 243-268.

Hudson, A. & Harrison, J., 1997. Engineering rock mechanics, an introduction to the principles. *Oxford: Elsevier.*

Hudson, J., 1969. Tensile strength and the ring test. *Int J Rock Mech Min Sci,* Vol. 6, pp. 91-97.

Hussain, M., Pu, S. & Underwood, J., 1974. Strain Energy Release Rate for a Crack under Combined Mode I and Mode II, Fracture Analysis. *Philadelphia: ASTM STP 560.*

Inglis, C., 1913. Stresses in a plate due to the presence of cracks and sharp corners. *Spring Meetings of the Fifty-fourth Session of the Institution of Naval Architects, King's College, Cambridge, England, U.K.,* Vol. 55, pp. 219-230.

Iqbal, M. & Mohanty, B., 2006. Experimental calibration of stress intensity factors of the ISRM suggested cracked chevron-notched Brazilian disc specimen used for determination of mode-I fracture toughness. *Int J Rock Mech Min Sci,* Vol. 43, pp. 1270-1276.

Irwin, G., 1948. Fracture dynamics. *American Society of Metals, Cleveland,* pp. 147-166.

Irwin, G., 1957. Analysis of stresses and strains near the end of a crack traversing a plate. *J Appl Mech,* Vol. 24, pp. 361-364.

Irwin, G., 1960. Plastic zone near a crack and fracture toughness. *Proceedings of the 7th Sagamore Ordnance Materials Research Conference: Mechanical and Metallurgical Behavior of Sheet Materials,* pp. 63-78.

ISRM, 1978. Suggested methods for the quantitative description of discontinuities in rock masses: International Society for Rock Mechanics.. *Int J Rock Mech Min Sci Geomech Abs,* Vol. 15, pp. 319-368.

ISRM, 1979. Suggested methods for determining the uniaxial compressive strength and deformability of rock materials: Part 1. Suggested method for determining deformability of

rock materials in uniaxial compression. *Int J Rock Mech Min Sci Geomech Abstr,* Vol. 16(2), pp. 137-138.

ISRM, 1979. Suggested Methods for Determining the Uniaxial Compressive Strength and Deformability of Rock Materials: Part 2. Suggestes method for determining deformability of rock materials in uniaxial compreesion. *Int J Rock Mech Min Sci Geomech Abstr,* Vol. 16(2), pp. 138-140.

ISRM, 1981. Suggested methods for determining the uniaxial compressive strength and deformability of rock. *In Soc Rock Mech, secretary, Lisbon.*

Itasca, 2010. Itasca Consulting Group, Inc. UDEC v6.00 Manual.

Ito, T., 2008. Effect of pore pressure gradient on fracture initiation in fluid saturated porous media: rock. *Eng Fract Mech,* Vol. 75, pp. 1753-1762.

Ito, T. & Hayasi, K., 1991. Physical background to the breakdown pressure in hydraulic fracturing tectonic stress measurements. *Int J Rock Mech Min Sci Geomech Abstr,* Vol. 28, pp. 285-293.

Jaeger, J., 1967. Failure of rocks under tensile conditions. *Int J Rock Mech Min Sci Geomech Abstr*, Vol. 4(2), pp. 219-227.

Jaeger, J., Cook, N. & Zimmermann, R., 2007. Fundamentals of rock mechanics. *Malden: Blackwell Publishing.*

Jaeger, J. & Hoskins, E., 1966. Rock failure under the confined Brazilian test. *J Geophys Res*, Vol. 71, pp. 2651-2659.

Janelid, I., 1965. Rock mechanics and its significance in mine and rock excavation design. *Royal Acad Eng Sci,* Vol. 142, pp. 7-12.

Janssen, M., Zuidema, J. & Wanhill, R., 2002. Fracture Mechanics. *London: Spon.*

Jenabidehkordi, A., 2019. Computational methods for fracture in rock: a review and recent advances. *Front Struct Civ Eng,* Vol. 13, pp. 273-287.

Judd, W., 1964. Rock stress, rock mechanics and research, in State of Stress in the Earth's Crust. *New York: Elsevier.*

Keles, C. & Tutluoglu, L., 2011. Investigation of proper specimen geometry for mode I fracture toughness testing with flattened Brazilian disc method. *Int J Fract,* Vol. 169, pp. 61-75.

Kim, J., Kim, D. & Moon, S., 2004. Evaluation of Static and Dynamic Fracture Toughness Using Apparent Fracture Toughness of Notched Specimens. *Mater Sci Eng,* Vol. 387, pp. 381-384.

Kinloch, A. & Williams, J., 1980. Crack blunting mechanisms in polymers. *J Mater Sci,* Vol. 15, pp. 987-996.

Kipp, M. & Sih, G., 1975. The strain energy density failure criterion applied to notched elastic solids. *Int J Solids Struct,* Vol. 11(2), pp. 153-173.

Korzeniowski, W. & Skrzypkowski, K., 2012. Investigations of influence of temperature up to 1100°C in the aspect of potential possibilities of the process of underground coal gasification. *Przegląd Górniczy,* Vol. 68(5), pp. 44-53.

Krynine, P., 1948. The megascopic study and field classificaion of sedimentary rocks. *J Geol,* Vol. 56(2), pp. 130-165.

Kujawski, D., 1991. Estimations of stress intensity factors for small cracks at notches. *Fatigue Fract Eng Mat Struct,* Vol. 14(10), pp. 953-965.

Kuruppu, M., 1997. Fracture toughness measurement using chevron notched semi-circular bend specimen. *Int J Fract,* Vol. 86(4), pp. 33-38.

Kuruppu, M., Obara, Y., Ayatollahi, M.R., Chong, K.P. & Funatsu, T., 2014. ISRM-Suggested method for determining the mode I static fracture toughness using semicircular bend specimen. *Rock Mech Rock Eng,* Vol. 47, pp. 267-274.

Labuz, J., Shah, S. & Dowding, C., 1983. Post peak tensile load-displacement response and the fracture process zone in rock. *24th U.S. Symposium on Rock Mechanics,* pp. 421-428.

Labuz, J., Shah, S. & Dowding, C., 1985. Experimental analysis of crack propagation in granite. *Int J Rock Mech Min Sci Geomech Abs,* Vol. 22(2), pp. 85-98.

Labuz, J., Shah, S. & Dowding, C., 1987. The fracture process zone in granite: evidence and effect. *Int J Rock Mech Min Sci Geomech Abs,* Vol. 24(4), pp. 235-246.

Lama, R. & Vutukuri, V., 1978. Handbook on mechanical properties of rocks. *Clausthal, Germany: Trans Tech Publications.*

Lataji, E., 1972. Effect of tensile stress gradient on brittle fracture initiation. *Int J Rock Mech Min Sci Geomech Abstr,* Vol. 9, pp. 569-578.

Lauffer, H., 1958. Classification for tunnel construction (in German). *Beologie und Bauwesen,* Vol. 24, pp. 46-51.

Lazzarin, P. & Berto, F., 2005. Some expressions for the strain energy in a finite colime surrounding the root of blunt V-notches. *Int J Fract,* Vol. 135, pp. 161-185.

Lazzarin, P. & Berto, F., 2008. Control volumes and strain energy density under small and large scale yielding due to tensile and torsion loading. *Fatigue Fract Eng Mater Struct,* Vol. 31, pp. 95-107.

Lazzarin, P., Berto, F. & Ayatollahi, M., 2013. Brittle failure of inclined key-hole notches in isostatic graphite under in-plane mixed mode loading. *Fatigue Fracture Eng Mater Struct,* Vol. 36(9), pp. 942-955.

Lazzarin, P., Berto, F., Elices, M. & Gómez, J., 2009. Brittle failures from U- and V-notches in mode I and mixed, I + II, mode: a synthesis based on the strain energy density averaged on finite-size volumes. *Fatigue Fract Eng Mater Struct,* Vol. 32(8), pp. 671-684.

Lazzarin, P. & Filippi, S., 2006. A generalized stress intensity factor to be applied to rounded V-shaped notches. *Int J Solids Struct,* Vol. 43, pp. 2461-2478.

Lazzarin, P., Livieri, P., Berto, F. & Zappalorto, M., 2008. Local strain energy density and fatigue strength of welded joints under uniaxial and multiaxial loading. *Eng Fract mech,* Vol. 75, pp. 1875-1889.

Lazzarin, P. & Zambardi, R., 2001. A finite-volume-energy based approach to predict the static and fatigue behavior of components with sharp V-shaped notches. *Int J Fract,* Vol. 112(3), pp. 275-298.

Lazzarin, P. & Zambardi, R., 2002. The Equivalent Strain Energy Density approach re-formulated and applied to sharp V-shaped notches under localized and generalized plasticity. *Fatigue Fract Eng Mater Struct,* Vol. 25(10), pp. 917-928.

Lazzarin, P., Zappalorto, M. & Yates, J., 2007. Analytical study of stress distributions due to semi-elliptic notches in shafts under torsion loading. *Int J Eng Sci,* Vol. 45, pp. 308-328.

Li, H., Bai, Y., Xia, M., Ke, F. & Yin, X., 2000. Damage localization as a possible precursor of earthquake rupture. *Microscopic and Macroscopic Simulation: Towards Predictive Modelling of the Earthquake Process,* pp. 1929-1943.

Lin, Q., Fakhimi, A., Haggerty, M. & Labuz, J., 2009. Initiation of tensile and mixed-mode fracture in sandstone. *Int J Rock Mech Min Sci,* Vol. 46(3), pp. 489-497.

Livieri, P. & Lazzarin, P., 2005. Fatigue strength of steel and aluminium welded joints based on generalised stress intensity factors and local strain energy values. *Int J Fract,* Vol. 133, pp. 247-276.

Lockner, D.A., Byerlee, J.D., Kuksenko, V., Ponomarev, A. & Sidorin, A., 1991. Quasi-static fault growth and shear fracture energy in granite. *Nature,* Vol. 350, pp. 39-42.

Love, A., 1906. A Treatise on the Mathematical Theory of Elasticity. *London: Cambridge University Press.*

Lukas, P. & Klesnil, M., 1978. Fatigue limit of notched bodies. *Mater Sci Eng,* Vol. 34, pp. 61-66.

Luong, M., 1990. Tensile and shear strengths of concrete and rock. *Eng Fract Mecg,* Vol. 35, pp. 127-135.

Madrazo, V., 2013. Análisis, desarrollo y aplicación de la Teoría de las Distancias Críticas en la evaluación en rotura de componentes estructurales. *Santander: Universidad de Cantabria, PhD Thesis (Spanish).*

Madrazo, V., Cicero, S. & Carrascal, I., 2012. On the Point Method and the Line Method notch effect predictions in Al7075-T651. *Eng Fract Mech,* Vol. 79, pp. 363-379.

Ma, G., An, X. & He, L., 2010. The numerical manifold method: a review. *Int J Comput Method,* Vol. 7, pp. 1-32.

Mahanta, B., Singh, T. & Ranjith, P., 2016. Influence of thermal treatment on mode I fracture toughness of certain Indian rocks. *Eng Geol,* Vol. 210, pp. 103-114.

Mao, X., Zhang, L., Li, T. & Li, H., 2009. Properties of Failure Mode and Thermal Damage for Limestone at High Temperature. *Min Sci Technol,* Vol. 19, pp. 290-294.

Matula, M. & Holzer, R., 1978. Engineering topology of rock masses. *Proc of Felsmekanik Kolloquium , Grundlagen ung Andwendung der Felsmekanik, Karlsruhe, Germany,* pp. 107-121.

McClintock, F. & Irwin, G., 1965. Plasticity aspects of fracture mechanics. *ASTM STP 381 Fracture Toughness Testing and its Applications. Philadelphia,* pp. 84-113.

McClintock, F. & Walsh, J., 1962. Friction on Griffith's cracks in rock under pressure. *Proc 4th US Nat Congr Appl Mech,* pp. 1015-1021.

McClure, S. & Horn, R., 2014. An investigation of stimulation mechanisms in enhanced geothermal systems. *Int J Rock Mech Min Sci,* Vol. 72, pp. 242-260.

Meredith, P., 1983. A fracture mechanics study of experimentally deformed crystal rocks. *University of London: PhD Thesis.*

Meredith, P. & Atkinson, B., 1985. Fracture toughness and subcritical crack growth during high-temperature tensile deformation of Westerly granite and Black gabbro. *Phys Earth Planet Inter,* Vol. 39, pp. 33-51.

Miller, R., 1965. Engineering classification and index properties for intact rock. *Univ. Illinois: PhD Thesis.*

Mirsayar, M., 2015. Mixed mode fracture analysis using extended maximum tangential strain criterion. *Mater Des*, Vol. 86, pp. 941-947.

Mirsayar, M., Razmi, A., Aliha, M. & Berto, F., 2018. EMTSN criterion for evaluating mixed mode I/II crack propagation in rock materials. *Eng Fract Mech*, Vol. 190, pp. 186-197.

Molski, K. & Glinka, G., 1981. A method of elastic-plastic stress and strain calculation at a notch root. *Mater Sci Eng,* Vol. 50, pp. 93-100.

Moosavi, S., Scholtès, L. & Giot, R., 2018. Influence of stress induced microcracks on the tensile fracture behavior of rocks. *Comput Geotech,* Vol. 104, pp. 81-95.

Mühlhaus, H., Sakaguchi, H. & Wei, Y., 1997. Particle based modelling of dynamic fracture in jointed rock. *Procedings of the 9th international conference of the international association of computer methods and advances in geomechanics–IACMAG,* Vol. 97, pp. 207-216.

Müller, L., 1963. Rock construction (in German). *Stuttgart: Ferdinand-Enke-Verlag.*

Muñoz-Ibáñez, A., 2020. Experimental investigation of mode I fracture toughness. *University of A Coruña: PhD Thesis.*

Muñoz-Ibáñez, A., Delgado-Martín, J., Costas, M., Rabuñal-Dopico, J., Alvarellos-Iglesias, J. & Canal-Vila, J., 2020. Mode I fracture toughness determination in rocks using a Pseudo-Compact Tension (pCT) test approach. *Rock Mech Rock Eng*, Vol. 53(7), pp. 3267-3285.

Murakami, Y., 1987. Stress Intensity Factors Handbook. *New York: Pergamon Press.*

Murrell, S., 1963. A criterion for brittle fracture of rocks and concrete under triaxial stress and the effect of pore pressure on the criterion. *Proc of the 5th Rock Mechanics Symposium, University of Minnesota,* pp. 563-577.

Nassir, M., Settari, A. & Wan, R., 2013. Joint stiffness and deformation behaviour of discontinuous rock. *J Can Petrol Technol,* Vol. 49(9), pp. 78-85.

Negru, R., Marsavina, L., Voiconi, Y., Linul, E. Filipescu, H. & Belgiu, G., 2015. Application of TCD for brittle fracture of notched PUR materials. *Theor Appl Fract Mech,* Vol. 80, pp. 87-95.

Neuber, H., 1936. Kerbspannungslehre. *Ing - Wes,* Vol. 7, pp. 271-281.

Neuber, H., 1958. Theory of Notch Stresses: Principles for exact calculation of strength with reference to structural form and material. *Berlin: Springer-Verlag.*

Neuber, N. & Weiss, V., 1962. Application of Weibull's Statistical Theory of Fracture to Sheet Specimen. *ASME paper,* pp. 62-WA-270.

Nicksiar, M. & Martin, C., 2014. Factors affecting crack initiation in low porosity crystalline rocks. *Rock Mech Rock Eng,* Vol. 47, pp. 1165-1181.

Novozhilov, V., 1969. On a necessary and sufficient criterion for brittle strength. *Appl Math Mech,* Vol. 33(2), pp. 201-210.

Ouchterlony, F., 1988. ISRM suggested methods for determining the fracture-toughness of rock. *Int J Rock Mech Min Sci Geomech Abstr,* Vol. 25, pp. 71-96.

Pacher, F., 1975. The development of the New Austrian Tunnelling Method and the main features in design work and construction. *16th Symp on Rock Mechanics, Minneapolis,* pp. 223-232.

Palmström, A., 1995. RMi – a rock mass characterization system for rock engineering purposes. *University of Oslo: PhD Thesis.*

Parisio, F., Tarokh, A., Makhnenko, R., Naumov, D., Miao, X.Y., Kolditz, O. & Nagel, T., 2019. Experimental characterization and numerical modelling of fracture processes in granite. *Int J Solids Struct,* Vol. 163, pp. 102-116.

Perras, M. & Diederichs, M., 2014. A Review of the Tensile Strength of Rock: Concepts and Testing. *Geotch Geol Eng,* Vol. 32, pp. 525-546.

Patching, T. & Coates, D., 1968. A recommended rock classification for rock mechanics purposes. *CIM Bull,* pp. 1195-1197.

Paterson, M. & Wong, T., 2005. Experimental rock deformation - the brittle field. *New York: Springer.*

Pelekis, I. & Susmel, L., 2016. The Theory of Critical Distances to estimate static and dynamic strength of notched plain concrete. *21st European Conference of Fracture, ECF21, Catania, Italy,* Vol. 2, pp. 2006-2013.

Peng, W., 1988. The damage mechanics model for jointed rock mass and its nonlinear fem analysis. *Chin J Rock Mech Eng,* Vol. 7(3), pp. 193-202.

Peterson, R., 1938. Methods of correlating data from fatigue test of stress concentration specimens. *New York: Stephen Timoshenko Anniversary Volume.*

Peterson, R., 1959. Notch Sensitivity. *New York: McGraw Hill.*

Pettijohn, F., 1948. A preface to the classification of the Sedimentary rocks. *J Geol,* Vol. 56(2), pp. 112-117.

Picart, P., Diouf, B., Lolive, E. & J.M., B., 2004. Investigation of fracture mechanisms in resin concrete using spatially multiplexed digital fresnel holograms. *Opt Eng,* Vol. 43, pp. 1169-1176.

Pinińska, J., 2007. The effect of an Increased Temperature on the Mechanical Properties of Rocks. *Prace Naukowe Instytutu Geotechniki i Hydrotechniki Politechniki,* pp. 527-534.

Pirsson, L.V., 1908. Rocks and rock minerals. *New York: John Wiley & Sons.*

Plaxis bv., 2017. Plaxis 2D Manual 2017. *The Netherlands.*

Pluvinage, G., 1998. Fatigue and fracture emanating from notch; the use of the notch stress intensity factor. *Nucl Eng Des,* Vol. 185, pp. 173-184.

Pluvinage, G., Azari, Z., Kadi, N., Dlouhý, I. & Kozák, V., 1999. Effect of ferritic microstructure on local damage zone distance associated with fracture near notch. *Theor Appl Fract Mech,* Vol. 31(2), pp. 149-156.

Pluvinage, G. & Capelle, J., 2014. On characteristic lengths used in notch fracture mechanics. *Int J Fract,* Vol. 187, pp. 187-197.

Pollard, D. & Fletcher, R., 2005. Fundamentals of Structural Geology. *Cambridge and New York: Cambridge University Press.*

Potyondy, D. & Cundall, P., 2004. A bonded-particle model for rock. *Int J rock Mech Min Sci,* Vol. 41, pp. 1329-1364.

Proctor, R., 1971. Mapping geological conditions in tunnels. *Bull Ass Eng Geol,* Vol. 8, pp. 1-31.

Pusch, R. & Morfeldt, C., 1993. Characterization of rock masses for construction of underground openings from numeric calculation of stresses, deformations and ground water flow. *Väg och vattenbyggaren,* Vol. 93(4), pp. 13-18.

R6, 2001. Assessment of the integrity of structures containing defects. *British Energy Generation.*

Rabcewicz, L., 1964. The new Austrian tunnelling method. *Water Power,* pp. 511-515.

Rabczuk, T. & Zi, G., 2007. A meshfree method based on the local partition of unity for cohesive cracks. *Comput Mech,* Vol. 39(6), pp. 743-760.

Ramspott, L.D., Ballou, L.B., Carlson, R.C., Montan, D.N., Butkovich, T.R., Duncan, J.E., Patrick, W.C., Wilder, D.G., Brough, W.G. & Mayr, M.C., 1979. Technical concept for a test of geologic storage of spent reactor fuel in the climax granite, Nevada Test Site. *California Univ., Livermore, CA (United States), Lawrence Livermore Lab.*

Ranjith, P., Viete, D., Chen, B. & Perera, M., 2012. Transformation plasticity and the effect of temperature on the mechanical behaviour of hawkesbury sandstone at atmospheric pressure. *Eng Geol,* Vol. 151, pp. 120-127.

Rao, Q., Wang, Z., Xie, H. & Xie, Q., 2007. Experimental study of mechanical properties of sandstone at high temperature. *J Cent South Univ Technol,* Vol. 14, pp. 478-483.

Razavi, S., Aliha, M. & Berto, F., 2018. Application of an average strain energy density criterion to obtain the mixed mode fracture load of granite rock tested with the cracked asymmetric four-point bend specimens. *Theor Appli Fract Mech,* Vol. 97, pp. 419-425.

Razumek, D. & Faszynka, S., 2017. Influence of the notch radius on fatigue crack propagation in beam specimens of 2017A-T4 alloy. *Mat Sci, Vol.* 53(3), pp. 112-117.

Rooke, D. & Cartwright, D., 1976. Compendium of Stress Intensity Factors. *London: Her Majesty's Stationary Office.*

Selmin, V., 1993. The node-centred finite volume approach: bridge between finite differences. *Comput Method Appl Mech Eng,* Vol. 102, pp. 107-138.

Seweryn, A. & Lukaszewicz, A., 2002. Verification of brittle fracture criteria for elements with V-shaped notches. *Eng Fract Mech,* Vol. 69, pp. 1487-1510.

Shahri, M. & Sandström, R., 2010. Fatigue analysis of friction stir welded aluminium profile using critical distance. *Int J Fatigue*, Vol. 32, pp. 302-309.

Shangyi, Z., Yingren, Z. & Weidong, D., 2003. Stability analysis on jointed rock slope by strength reduction fem. *Chin J Rock Mech Eng,* Vol. 2, p. 020.

Shi, G., 1977. Stereographic method for the stability analysis of the discontinuous rocks. *Scintia Sin,* Vol. 3, pp. 260-271.

Shi, G., 1992. Manifold method of material analysis. *Tech Rep, DTIC Document.*

Shi, G. & Goodman, R., 1985. Two dimensional discontinuous deformation analysis. *Int J Num Anal Method Geomech,* Vol. 9(6), pp. 541-556.

Shimizu, H., Murata, S. & Ishida, T., 2011. The distinct element analysis for hydraulic fracturing in hard rock considering fluid viscosity and particle size distribution. *Int J Rock Mech Min Sci,* Vol. 48, pp. 712-727.

Shrock, R., 1948. A classification of sedimentary rocks. *J Geol,* Vol. 56(2), pp. 118-129.

Siggins, A., 1993. Rock testing and site characterization. Principles, practice and projects. pp. 601-618.

Sih, G., 1973. A Special Theory of Crack Propagation: Methods of Analysis and Solutions of Crack Problems. *Mechanics of Fracture, Noordhoff, International Publishing, Leyden,* pp. 21-45.

Sih, G., 1974. Strain-energy-density factor applied to mixed mode crack problems. *Int J Fract,* Vol. 10(3), pp. 305-321.

Sih, G., 1991. Mechanics of Fracture Initiation and Propagation: Surface and Volume Energy Density Applied as Failure Criterion. *Dordrecht: Kluwer Academic Publisher.*

Sih, G., Czoboly, E. & Gillemot, L., 1982. Absorbed Specific Energy and Strain Energy Density Criterion, Proceedings of an International Symposium on Absorbed Specific Energy and Strain Energy Density Criterion. *The Netherlands: Martinus Nijhoff Publishers.*

Sih, G. & Ho, J., 1991. Sharp notch fracture strength characterized by critical energy density. *Theor Appl Fract Mech,* Vol. 16(3), pp. 179-214.

Sih, G., van Elst, H. & Broek, D., 1974. Surface Layer Energy and Strain Energy Density for a Blunted Crack or Notch. *Prospect of Fracture Mechanics, Noordhoff International Publishing, Leyden,* pp. 85-102.

Silling, S., 2000. Reformulation of elasticity theory for discontinuities and long-range forces. *J Mech Phys Solids,* Vol. 48, pp. 175-209.

Simpson, R., Bordas, S., Trevelyan, J. & Rabczuk, T., 2012. A two-dimensional isogeometric boundary element method for elastostatic analysis. *Comput Method Appl Mech Eng,* Vol. 209, pp. 87-100.

Sirdesai, N., Singh, T., Ranjith, P. & Singh, R., 2017. Effect of varied durations of thermal treatment on the tensile strength of red sandstone. *Rock Mech Rock Eng,* Vol. 50, pp. 205-213.

Smith, D., Ayatollahi, M. & Pavier, M., 2001. The role of T-stress in brittle fracture for linear elastic materials under mixed-mode loading. *Fatigue Fract Eng Mater Struct*, Vol. 24, pp. 137-150.

Smith, E., 2004. The elastic stress distribution near the root of an elliptically cylindrical notch subjected to mode III loadings. *Int J Eng Sci,* Vol. 42, pp. 1831-1839.

Smith, R. & Miller, K., 1977. Fatigue cracks at notches. *Int J Mech Sci,* Vol. 19, pp. 11-22.

Srawley, J. & Gross, B., 1976. Cracks and fracture. *ASTM Spec Tech Publ,* Vol. 601, pp. 559-579.

Susmel, L. & Taylor, D., 2008. The theory of critical distances to predict static strength of notched brittle components subjected to mixed-mode loading. *Eng Fract Mech,* Vol. 75, pp. 534-550.

Susmel, L. & Taylor, D., 2010. An elasto-plastic reformulation of the Theory of Critical Distances to estimate lifetime of notched components failing in the low/medium cycle fatigue regime. *J Eng Mater Technol Trans,* Vol. 132, pp. 0210021-0210028.

Sygala, A., Bukowska, M. & Janoszek, T., 2013. High temperature versus geomechanical parameters of selected rocks - the present state of research. *J Sust Min,* 12(4), pp. 45-51.

Tada, H., Paris, P. & Irwin, G., 1985. The Stress Analysis of Cracks Handbook. *2 ed. St. Louis: Paris Productions.*

Tarokh, A. & Fakhimi, A., 2014. Discrete element simulation of the effect of particle size on the size of fracture process zone in quasi-brittle materials. *Comput Geotch,* Vol. 62, pp. 51-60.

Taylor, D., 2004. Predicting the fracture strength of ceramic materials using the Theory of Critical Distances. *Eng Fract Mech,* Vol. 71, pp. 2407-2416.

Taylor, D., 2007. The Theory of Critical Distances: A New Perspective in Fracture Mechanics. *London: Elsevier.*

Taylor, D., 2017. The Theory of Critical Distances: a link to micromechanisms. *Theor Appl Fract Mech,* Vol. 90, pp. 228-233.

Taylor, D., Cornetti, P. & Pugno, N., 2005. The fracture mechanics of finite crack extension. *Eng Fract Mech,* Vol. 72, pp. 1021-1038.

Taylor, D. & Kasiri, S., 2008. A comparison of critical distance methods for fracture prediction. *Int J Mech Sci,* Vol. 50, pp. 1075-1081.

Terzaghi, K., 1946. Introduction to tunnel geology. *In Rock tunnelling with steel supports, by Proctor and White.*

Timoshenko, S. & Goodier, J., 1951. Theory of elasticity. *New York: McGraw-Hill.*

TML Manual, 2017. Tokyo Measuring Instruments Laboratory Co., Ltd. Pam E-1007E.

Torabi, A., Berto, F., Campagnolo, A. & Akbardoost, J., 2017. Averaged strain energy density criterion to predict ductile failure of U-notched Al 6061-T6 plates under mixed mode loading. *Theor Appl Fract Mech,* Vol. 91, pp. 86-93.

Tullis, J. & Yund, R., 1977. Experimental deformation of dry Westerly granite. *J Geophys Res,* Vol. 82, pp. 5705-5718.

Tutluoglu, L. & Keles, C., 2011. Mode I fracture toughness determination with straight notched disk bending method. *Int J Rock Mech Min Sci,* Vol. 48(8), pp. 1248-1261.

Tutluoglu, L. & Keles, C., 2012. Effects of geometric factors on mode I fracture toughness for modified ring tests. *Int J Rock Mech Min Sci,* Vol. 51, pp. 149-161.

Usami, S., Tanaka, M., Jono, M. & Komai, K., 1985. Current research on fatigue cracks. *Kyoto: The Society of Materials Science.*

Vishal, V., Pradhan, S. & Singh, T., 2011. Tensile strength of rock under elevated temperatures. *Geotech Geol Eng,* Vol. 29, pp. 1127-1133.

Waddoups, M., Eisenmann, J. & Kaminski, B., 1971. Macroscopic Fracture Mechanics of Advanced Composite Materials. *J Compos Mater,* Vol. 5, pp. 446-454.

Wei, M., Dai, F., Xu, N. & Zhao, T., 2016. Stress intensity factors and fracture process zones of ISRM-suggested chevron notched specimens for mode I fracture toughness testing of rocks. *Eng Fract Mech,* Vol. 168, pp. 174-189.

Westergaard, H., 1939. Bearing pressures and cracks. *J Appl Mech,* Vol. 61, pp. 49-53.

Wheel, M., 1996. A geometrically versatile finite volume formulation for plane elastostatic stress. *J Strain Anal Eng,* 31(2), pp. 111-116.

Whitney, J. & Nuismer, R., 1974. Stress fracture criteria for laminated composites containing stress concentrations. *J Compos Mater,* Vol. 8, pp. 253-265.

Wickham, G., Tiedeman, H. & Skinner, E., 1972. Support determinationd based on geologic predictions. *Proc Rapid Exc & Tunn Conf,* pp. 43-64.

Wigglesworth, L. & Stevenson, A., 1939. Flexure and torsion of cylinders with cross-sections bounded by orthogonal circular arcs. *Proc Roy Soc London,* Vol. 184, pp. 391-414.

Williams, M., 1952. Stress singularities resulting from various boundary conditions in angular corners of plates in extension. *J Appl Mech,* Vol. 19, pp. 526-528.

Williams, M., 1957. On the stress distribution at the base of stationary crack. *J Appl Mech,* Vol. 24, pp. 109-114.

Williamson, 1980. Uniform rock classification for geotechnical engineering purposes. *Transportation Research Record 783, National Academy of Sciences, Washington D.C,* pp. 9-14.

Wu, C. & Tsai, H., 2017. Effect of notch radius on nanocrystalline Au under tensile deformation at low temperature. *J Comput Theor Nanosci,* Vol. 14(10), pp. 4669-4673.

Wu, G., Wang, Y., Swift, G. & Chen, J., 2013. Laboratory Investigation of the Effects of Temperature on the Mechanical Properties of Sandstone. *Geotech Geol Eng,* Vol. 31, pp. 809-816.

Wu, Z., Qin, B., Chen, L. & Luo, Y., 2005. Experimental study on mechanical character of sandstone of the upper plank of coal bed under high temperature. *Chin J Rock Mech Eng,* Vol. 24, pp. 1863-1867.

Xu, X., Gao, F., Shen, X. & Xie, H., 2008. Mechanical characteristics and microcosmic mechanisms of granite under temperature loads. *J Chin Univ Min Technol,* Vol. 18, pp. 413-417.

Xu, X. y otros, 2009. Research of microcosmic mechanism of brittle-plastic transition for granite under high temperature. *Proc Earth Planet Sci,* Vol. 1, pp. 432-437.

Xu, X. & Liu, Q., 2000. A preliminary study on basic mechanical properties for granite at high temperature. *Chin J Geotch Eng,* Vol. 22(3), pp. 332-335.

Yang, S.Q., Ranjith, P.G., Jing, H.W., Tian, W.L. & Ju, Y., 2017. An experimental investigation on thermal damage and failure mechanical behavior of granite after exposure to different high temperature treatments. *Geothermics,* Vol. 65, pp. 180-197.

Yin, T., Li, X., Cao, W. & Xia, K., 2015. Effects of thermal treatment on tensile strength of Laurentian granite using Brazilian test. *Rock Mech Rock Eng,* Vol. 48, pp. 2213-2223.

Yosibash, Z., Bussiba, A. & Gilad, I., 2004. Failure criteria for brittle elastic materials. *Int J Fract,* Vol. 125, pp. 307-333.

Yu, C. & Kobayashi, A., 1994. Fracture process zone associated with mixed mode fracture of sicw/al2o3.. *J Non-Cryst Solids,* Vol. 177, pp. 26-35.

Yue, L., Sun, S., Liu, J., Wei, J. & Wu, J., 2017. Research on crack initiation mechanism and fracture criterion of rock-type materials under compression-shear stress. *Adv Mech Eng,* Vol. 9(10), pp. 1-13.

Zang, A., Wagner, F.C., Stanchits, S., Janssen, C. & Dresen, G., 2000. Fracture process zone in granite. *J Geophys Res,* Vol. 105, pp. 23651-23662.

Zappalorto, M. & Lazzarin, P., 2007. Analytical study of the elastic–plastic stress fields ahead of parabolic notches under antiplane shear loading. *Int J Fract,* Vol. 148(2), pp. 139-154.

Zappalorto, M. & Lazzarin, P., 2009. A new version of the Neuber rule accounting for the influence of the notch opening angle for out-of-plane shear loads. *Int J Solids Struct,* Vol. 46(9), pp. 1901-1910.

Zappalorto, M. & Lazzarin, P., 2010. A unified approach to the analysis of nonlinear stress and strain fields ahead of mode III-loaded notches and cracks. *Int J Solids Struct,* Vol. 47(6), pp. 851-864.

Zappalorto, M. & Lazzarin, P., 2011. Strain energy-based evaluations of plastic notch stress intensity factors at pointed V-notches under tension. *Eng Fract Mech,* Vol. 78(15), pp. 2691-2706.

Zhang, L., Mao, X., Liu, R., Guo, X. & Ma, D., 2013. The Mechanical Properties of Mudstone at High Temperatures: an Experimental Study. *Rock Mech Rock Eng,* Vol. 47, pp. 1479-1484.

Zhang, L., Mao, X. & Lu, A., 2009. Experimental study of on the mechanical properties of rocks at high temperature. *Sci China Ser E,* Vol. 52, pp. 641-646.

Zhi-jun, W., Yang-Sheng, Z., Yuan, Z. & Chong, W., 2009. Research Status Quo and Prospection of Mechanical Characteristics of Rock under High Temperature and High Pressure. *Proc Earth Planet Sci,* pp. 565-570.

Zietlow, W. & Labuz, J., 1998. Measurement of the intrinsic process zone in rock using acoustic emission. *Int J Rock Mech Min Sci,* Vol. 39(3), pp. 291-299.

Zoback, M., 2007. Reservoir Geomechanics. *New York: Cambridge University Press.*

Zuo, J., Xie, H., Dai, F. & Ju, Y., 2014. Three-point bending test investigation of the fracture behavior of siltstone after thermal treatment. *Int J Rock Mech Min Sci,* Vol. 70, pp. 133-143.

- Appendix A -
Experimental results

- Appendix A.1. -
Brazilian test results

Table A.1.-1. Individual tensile strength (σ_u) values obtained from Brazilian tests for the Floresta sandstone (F).

CODE	σ_u (MPa)	CODE	σ_u (MPa)
BT-F-T1-1	2.72	BT-F-T4(NC)-1	2.38
BT-F-T1-2	3.28	BT-F-T4(NC)-2	3.24
BT-F-T1-3	3.20	BT-F-T4(NC)-3	2.58
BT-F-T1-4	2.31	BT-F-T4(NC)-4	3.79
BT-F-T1-5	3.13	BT-F-T4(NC)-5	3.80
BT-F-T1-6	2.42	BT-F-T4(NC)-6	3.23
BT-F-T3(NC)-1	3.18	BT-F-T4(WC)-1	3.19
BT-F-T3(NC)-2	2.90	BT-F-T4(WC)-2	3.46
BT-F-T3(NC)-3	3.62	BT-F-T4(WC)-3	3.72
BT-F-T3(NC)-4	3.08	BT-F-T4(WC)-4	3.90
BT-F-T3(NC)-5	3.50	BT-F-T4(WC)-5	2.46
BT-F-T3(NC)-6	-	BT-F-T4(WC)-6	3.02
BT-F-T3(WC)-1	3.44	BT-F-T6(NC)-1	4.21
BT-F-T3(WC)-2	3.40	BT-F-T6(NC)-2	2.38
BT-F-T3(WC)-3	3.93	BT-F-T6(NC)-3	2.85
BT-F-T3(WC)-4	3.10	BT-F-T6(NC)-4	4.08
BT-F-T3(WC)-5	3.75	BT-F-T6(NC)-5	3.54
BT-F-T3(WC)-6	3.62	BT-F-T6(NC)-6	2.75
BT-F-T3(WC)-7	2.78	BT-F-T6(WC)-1	3.24
BT-F-T3(WC)-8	3.44	BT-F-T6(WC)-2	3.63
BT-F-T3(WC)-9	3.34	BT-F-T6(WC)-3	2.38
BT-F-T3(WC)-10	3.77	BT-F-T6(WC)-4	2.26
BT-F-T3(WC)-11	3.34	BT-F-T6(WC)-5	3.29
BT-F-T3(WC)-12	2.60	BT-F-T6(WC)-6	3.47
BT-F-T5(NC)-1	4.32	BT-F-T2(NC)-1	2.58
BT-F-T5(NC)-2	4.77	BT-F-T2(NC)-2	3.38
BT-F-T5(NC)-3	3.25	BT-F-T2(NC)-3	3.88
BT-F-T5(NC)-4	3.75	BT-F-T2(NC)-4	3.47
BT-F-T5(NC)-5	3.19	BT-F-T2(NC)-5	3.66
BT-F-T5(NC)-6	3.64	BT-F-T2(NC)-6	4.30
BT-F-T5(WC)-1	2.57	BT-F-T2(WC)-1	4.19
BT-F-T5(WC)-2	3.41	BT-F-T2(WC)-2	3.69
BT-F-T5(WC)-3	2.53	BT-F-T2(WC)-3	4.33
BT-F-T5(WC)-4	3.12	BT-F-T2(WC)-4	2.67
BT-F-T5(WC)-5	3.36	BT-F-T2(WC)-5	4.72
BT-F-T5(WC)-6	1.82	BT-F-T2(WC)-6	4.92

Table A.1.-2. Individual tensile strength (σ_u) values obtained from Brazilian tests for the Moleanos limestone (C).

CODE	σ_u (MPa)	CODE	σ_u (MPa)
BT-C-T1-1	6.82	BT-C-T4(NC)-1	9.45
BT-C-T1-2	7.75	BT-C-T4(NC)-2	10.92
BT-C-T1-3	7.08	BT-C-T4(NC)-3	9.00
BT-C-T1-4	7.69	BT-C-T4(NC)-4	8.86
BT-C-T1-5	7.00	BT-C-T4(NC)-5	9.01
BT-C-T1-6	4.80	BT-C-T4(NC)-6	10.46
BT-C-T3(NC)-1	7.17	BT-C-T4(WC)-1	9.13
BT-C-T3(NC)-2	8.06	BT-C-T4(WC)-2	7.70
BT-C-T3(NC)-3	8.61	BT-C-T4(WC)-3	7.99
BT-C-T3(NC)-4	8.49	BT-C-T4(WC)-4	7.59
BT-C-T3(NC)-5	8.22	BT-C-T4(WC)-5	8.95
BT-C-T3(NC)-6	8.50	BT-C-T4(WC)-6	6.56
BT-C-T3(WC)-1	6.51	BT-C-T6(NC)-1	8.81
BT-C-T3(WC)-2	6.23	BT-C-T6(NC)-2	8.04
BT-C-T3(WC)-3	8.49	BT-C-T6(NC)-3	10.01
BT-C-T3(WC)-4	8.86	BT-C-T6(NC)-4	9.41
BT-C-T3(WC)-5	5.34	BT-C-T6(NC)-5	8.60
BT-C-T3(WC)-6	7.51	BT-C-T6(NC)-6	8.92
BT-C-T3(WC)-7	6.97	BT-C-T6(WC)-1	9.56
BT-C-T3(WC)-8	7.88	BT-C-T6(WC)-2	8.39
BT-C-T3(WC)-9	6.62	BT-C-T6(WC)-3	7.43
BT-C-T3(WC)-10	6.32	BT-C-T6(WC)-4	7.96
BT-C-T3(WC)-11	6.36	BT-C-T6(WC)-5	8.77
BT-C-T3(WC)-12	7.88	BT-C-T6(WC)-6	8.21
BT-C-T5(NC)-1	10.61	BT-C-T2(NC)-1	8.27
BT-C-T5(NC)-2	7.65	BT-C-T2(NC)-2	9.70
BT-C-T5(NC)-3	9.50	BT-C-T2(NC)-3	8.67
BT-C-T5(NC)-4	6.85	BT-C-T2(NC)-4	9.21
BT-C-T5(NC)-5	10.31	BT-C-T2(NC)-5	8.80
BT-C-T5(NC)-6	9.23	BT-C-T2(NC)-6	8.66
BT-C-T5(WC)-1	7.75	BT-C-T2(WC)-1	8.19
BT-C-T5(WC)-2	8.90	BT-C-T2(WC)-2	8.24
BT-C-T5(WC)-3	8.56	BT-C-T2(WC)-3	8.46
BT-C-T5(WC)-4	8.93	BT-C-T2(WC)-4	8.62
BT-C-T5(WC)-5	7.55	BT-C-T2(WC)-5	7.76
BT-C-T5(WC)-6	8.00	BT-C-T2(WC)-6	8.64

Table A.1.-3. Individual tensile strength (σ_u) values obtained from Brazilian tests for the Macael marble (M).

CODE	σ_u (MPa)	CODE	σ_u (MPa)
BT-M-T1-1	10.07	BT-M-T4(NC)-1	4.90
BT-M-T1-2	9.94	BT-M-T4(NC)-2	5.57
BT-M-T1-3	10.09	BT-M-T4(NC)-3	4.32
BT-M-T1-4	9.85	BT-M-T4(NC)-4	4.73
BT-M-T1-5	9.42	BT-M-T4(NC)-5	5.09
BT-M-T1-6	10.44	BT-M-T4(NC)-6	4.90
BT-M-T3(NC)-1	7.31	BT-M-T4(WC)-1	5.73
BT-M-T3(NC)-2	7.82	BT-M-T4(WC)-2	7.57
BT-M-T3(NC)-3	8.22	BT-M-T4(WC)-3	5.54
BT-M-T3(NC)-4	8.23	BT-M-T4(WC)-4	9.58
BT-M-T3(NC)-5	6.87	BT-M-T4(WC)-5	6.27
BT-M-T3(NC)-6	6.69	BT-M-T4(WC)-6	9.29
BT-M-T3(WC)-1	9.03	BT-M-T6(NC)-1	4.43
BT-M-T3(WC)-2	8.36	BT-M-T6(NC)-2	4.08
BT-M-T3(WC)-3	9.78	BT-M-T6(NC)-3	4.44
BT-M-T3(WC)-4	8.42	BT-M-T6(NC)-4	4.66
BT-M-T3(WC)-5	9.58	BT-M-T6(NC)-5	5.48
BT-M-T3(WC)-6	10.57	BT-M-T6(NC)-6	5.12
BT-M-T3(WC)-7	6.62	BT-M-T6(WC)-1	7.48
BT-M-T3(WC)-8	7.43	BT-M-T6(WC)-2	6.30
BT-M-T3(WC)-9	6.22	BT-M-T6(WC)-3	7.77
BT-M-T3(WC)-10	6.88	BT-M-T6(WC)-4	7.03
BT-M-T3(WC)-11	5.46	BT-M-T6(WC)-5	8.05
BT-M-T3(WC)-12	9.44	BT-M-T6(WC)-6	5.28
BT-M-T5(NC)-1	6.16	BT-M-T2(NC)-1	4.34
BT-M-T5(NC)-2	6.26	BT-M-T2(NC)-2	4.68
BT-M-T5(NC)-3	5.98	BT-M-T2(NC)-3	4.59
BT-M-T5(NC)-4	6.08	BT-M-T2(NC)-4	5.41
BT-M-T5(NC)-5	6.56	BT-M-T2(NC)-5	4.25
BT-M-T5(NC)-6	6.45	BT-M-T2(NC)-6	3.74
BT-M-T5(WC)-1	9.03	BT-M-T2(WC)-1	7.15
BT-M-T5(WC)-2	10.69	BT-M-T2(WC)-2	8.08
BT-M-T5(WC)-3	9.75	BT-M-T2(WC)-3	6.09
BT-M-T5(WC)-4	9.06	BT-M-T2(WC)-4	8.31
BT-M-T5(WC)-5	10.71	BT-M-T2(WC)-5	5.36
BT-M-T5(WC)-6	7.77	BT-M-T2(WC)-6	5.82

Table A.1.-4. Individual tensile strength (σ_u) values obtained from Brazilian tests for the Carrara marble (I).

CODE	σ_u (MPa)	CODE	σ_u (MPa)
BT-I-T1-1	9.13	BT-I-T4(NC)-1	6.13
BT-I-T1-2	8.94	BT-I-T4(NC)-2	5.32
BT-I-T1-3	9.76	BT-I-T4(NC)-3	4.84
BT-I-T1-4	9.93	BT-I-T4(NC)-4	6.83
BT-I-T1-5	7.93	BT-I-T4(NC)-5	5.96
BT-I-T1-6	9.25	BT-I-T4(NC)-6	4.95
BT-I-T3(NC)-1	7.20	BT-I-T4(WC)-1	7.60
BT-I-T3(NC)-2	7.53	BT-I-T4(WC)-2	8.79
BT-I-T3(NC)-3	7.36	BT-I-T4(WC)-3	8.03
BT-I-T3(NC)-4	6.59	BT-I-T4(WC)-4	8.59
BT-I-T3(NC)-5	8.23	BT-I-T4(WC)-5	8.72
BT-I-T3(NC)-6	6.65	BT-I-T4(WC)-6	7.81
BT-I-T3(WC)-1	10.57	BT-I-T6(NC)-1	3.58
BT-I-T3(WC)-2	11.14	BT-I-T6(NC)-2	4.31
BT-I-T3(WC)-3	9.51	BT-I-T6(NC)-3	4.45
BT-I-T3(WC)-4	8.49	BT-I-T6(NC)-4	4.36
BT-I-T3(WC)-5	10.38	BT-I-T6(NC)-5	3.60
BT-I-T3(WC)-6	9.50	BT-I-T6(NC)-6	4.19
BT-I-T3(WC)-7	8.04	BT-I-T6(WC)-1	6.78
BT-I-T3(WC)-8	8.48	BT-I-T6(WC)-2	7.36
BT-I-T3(WC)-9	7.73	BT-I-T6(WC)-3	4.54
BT-I-T3(WC)-10	6.62	BT-I-T6(WC)-4	8.81
BT-I-T3(WC)-11	6.13	BT-I-T6(WC)-5	8.45
BT-I-T3(WC)-12	7.77	BT-I-T6(WC)-6	6.14
BT-I-T5(NC)-1	5.69	BT-I-T2(NC)-1	4.10
BT-I-T5(NC)-2	6.20	BT-I-T2(NC)-2	4.98
BT-I-T5(NC)-3	4.86	BT-I-T2(NC)-3	4.67
BT-I-T5(NC)-4	6.22	BT-I-T2(NC)-4	4.98
BT-I-T5(NC)-5	5.93	BT-I-T2(NC)-5	5.83
BT-I-T5(NC)-6	6.51	BT-I-T2(NC)-6	5.44
BT-I-T5(WC)-1	8.75	BT-I-T2(WC)-1	9.82
BT-I-T5(WC)-2	7.63	BT-I-T2(WC)-2	9.56
BT-I-T5(WC)-3	7.44	BT-I-T2(WC)-3	9.09
BT-I-T5(WC)-4	8.06	BT-I-T2(WC)-4	9.48
BT-I-T5(WC)-5	6.66	BT-I-T2(WC)-5	10.34
BT-I-T5(WC)-6	8.37	BT-I-T2(WC)-6	7.52

Table A.1.-5. Individual tensile strength (σ_u) values obtained from Brazilian tests for the Moleanos limestone coming from a second delivery (C2).

CODE	σ_u (MPa)	CODE	σ_u (MPa)
BT-C2-T1-1	4.61	BT-C2-T1-7	6.48
BT-C2-T1-2	7.69	BT-C2-T1-8	5.99
BT-C2-T1-3	5.92	BT-C2-T1-9	5.68
BT-C2-T1-4	8.79	BT-C2-T1-10	8.50
BT-C2-T1-5	6.12	BT-C2-T1-11	4.83
BT-C2-T1-6	8.48	BT-C2-T1-12	7.42

- Appendix A.2. -
Uniaxial compression test results

Table A.2.-1. Individual compressive strength (σ_c), Young's modulus (E) and Poisson's ratio (v) values obtained from uniaxial compression tests for the Floresta sandstone (F).

CODE	σ_c (MPa)	E_{50} (GPa)	v
UCT-F-T1-1	50.71	20.70	0.30
UCT-F-T1-2	50.53	20.90	0.40
UCT-F-T1-3	48.40	18.80	0.36
UCT-F-T1-4	51.06	19.90	0.35
UCT-F-T1-5	55.61	22.80	0.42
UCT-F-T1-6	-	-	-
UCT-F-T1-7	51.31	19.30	0.41
UCT-F-T1-8	54.02	21.30	0.35
UCT-F-T1-9	49.54	20.20	0.32
UCT-F-T1-10	47.05	16.70	0.34
UCT-F-T1-11	47.99	16.50	0.37
UCT-F-T1-12	48.63	17.60	0.32
UCT-F-T3-1	48.10	17.50	0.28
UCT-F-T3-2	37.31	17.90	0.32
UCT-F-T3-3	46.02	20.30	0.25
UCT-F-T3-4	48.07	18.80	0.34
UCT-F-T3-5	42.67	19.50	0.35
UCT-F-T3-6	40.54	17.10	0.23
UCT-F-T4-1	43.62	18.90	0.33
UCT-F-T4-2	-	-	-
UCT-F-T4-3	37.04	14.00	0.31
UCT-F-T4-4	40.13	19.20	0.31
UCT-F-T4-5	49.08	16.60	0.34
UCT-F-T4-6	33.20	19.20	0.30
UCT-F-T2-1	40.68	16.50	0.34
UCT-F-T2-2	35.64	14.40	0.36
UCT-F-T2-3	41.54	18.00	0.30
UCT-F-T2-4	36.03	16.50	0.37
UCT-F-T2-5	41.73	17.40	0.28
UCT-F-T2-6	54.67	20.60	0.35

Table A.2.-2. Individual compressive strength (σ_c), Young's modulus (E) and Poisson's ratio (v) values obtained from uniaxial compression tests for the Moleanos limestone (C).

CODE	σ_c (MPa)	E_{50} (GPa)	v
UCT-C-T1-1	60.51	42.80	0.41
UCT-C-T1-2	77.40	40.30	0.25
UCT-C-T1-3	-	-	-
UCT-C-T1-4	82.09	40.00	0.31
UCT-C-T1-5	82.88	37.10	0.27
UCT-C-T1-6	65.85	37.90	0.33
UCT-C-T1-7	82.49	38.80	0.24
UCT-C-T1-8	85.65	34.80	0.33
UCT-C-T1-9	79.48	26.20	0.26
UCT-C-T1-10	83.89	43.30	0.33
UCT-C-T1-11	81.85	39.70	0.36
UCT-C-T1-12	84.17	41.50	0.33
UCT-C-T3-1	-	-	-
UCT-C-T3-2	93.77	45.40	0.28
UCT-C-T3-3	88.91	44.90	0.25
UCT-C-T3-4	100.59	47.40	0.29
UCT-C-T3-5	86.27	43.90	0.29
UCT-C-T3-6	76.83	41.40	0.27
UCT-C-T4-1	107.54	39.50	0.26
UCT-C-T4-2	95.14	43.20	0.32
UCT-C-T4-3	148.99	61.20	0.30
UCT-C-T4-4	101.26	35.80	0.28
UCT-C-T4-5	106.63	38.80	0.25
UCT-C-T4-6	86.96	37.90	0.29
UCT-C-T2-1	141.13	66.00	0.36
UCT-C-T2-2	154.54	61.70	0.32
UCT-C-T2-3	110.83	35.70	0.29
UCT-C-T2-4	120.80	33.10	0.27
UCT-C-T2-5	112.45	35.60	0.22
UCT-C-T2-6	125.49	63.20	0.23

Table A.2.-3. Individual compressive strength (σ_c), Young's modulus (E) and Poisson's ratio (v) values obtained from uniaxial compression tests for the Macael marble (M).

CODE	σ_c (MPa)	E_{50} (GPa)	v
UCT-M-T1-1	-	-	-
UCT-M-T1-2	90.22	70.70	0.35
UCT-M-T1-3	91.86	88.00	0.29
UCT-M-T1-4	69.84	63.30	0.48
UCT-M-T1-5	93.90	70.10	0.33
UCT-M-T1-6	85.47	70.90	0.35
UCT-M-T1-7	88.42	68.10	0.29
UCT-M-T1-8	69.46	70.50	0.27
UCT-M-T1-9	87.86	78.70	0.33
UCT-M-T1-10	94.83	70.50	0.45
UCT-M-T1-11	89.61	73.70	0.35
UCT-M-T1-12	91.47	83.00	0.34
UCT-M-T3-1	72.03	65.10	0.31
UCT-M-T3-2	64.14	47.40	0.26
UCT-M-T3-3	76.55	54.90	0.33
UCT-M-T3-4	67.00	50.20	0.29
UCT-M-T3-5	73.68	56.80	0.22
UCT-M-T3-6	77.34	61.00	0.25
UCT-M-T4-1	59.85	28.40	0.28
UCT-M-T4-2	70.55	37.80	0.33
UCT-M-T4-3	58.04	25.20	0.43
UCT-M-T4-4	63.94	32.40	0.26
UCT-M-T4-5	59.39	26.50	0.43
UCT-M-T4-6	54.92	25.90	0.39
UCT-M-T2-1	60.10	20.00	0.53
UCT-M-T2-2	57.32	15.20	0.50
UCT-M-T2-3	51.87	20.50	0.35
UCT-M-T2-4	65.86	23.50	0.28
UCT-M-T2-5	60.75	20.90	0.27
UCT-M-T2-6	58.09	16.40	0.59

Table A.2.-4. Individual compressive strength (σ_c), Young's modulus (E) and Poisson's ratio (v) values obtained from uniaxial compression tests for the Carrara marble (I).

CODE	σ_c (MPa)	E_{50} (GPa)	v
UCT-I-T1-1	91.33	50.60	0.39
UCT-I-T1-2	101.08	57.80	0.30
UCT-I-T1-3	97.07	59.90	0.30
UCT-I-T1-4	94.18	51.90	0.36
UCT-I-T1-5	97.86	51.60	0.33
UCT-I-T1-6	105.97	62.30	0.41
UCT-I-T1-7	98.31	59.20	0.35
UCT-I-T1-8	92.38	57.60	0.36
UCT-I-T1-9	102.90	59.40	0.35
UCT-I-T1-10	101.06	59.30	0.34
UCT-I-T1-11	93.54	56.90	0.40
UCT-I-T1-12	97.87	59.00	0.33
UCT-I-T3-1	85.26	44.80	0.30
UCT-I-T3-2	85.10	53.10	0.34
UCT-I-T3-3	77.39	50.60	0.31
UCT-I-T3-4	88.69	50.20	0.36
UCT-I-T3-5	93.83	50.50	0.24
UCT-I-T3-6	90.82	51.10	0.25
UCT-I-T4-1	76.22	30.80	0.34
UCT-I-T4-2	65.95	23.40	0.29
UCT-I-T4-3	73.15	27.00	0.28
UCT-I-T4-4	72.78	28.20	0.33
UCT-I-T4-5	73.39	-	-
UCT-I-T4-6	71.99	-	-
UCT-I-T4-7	69.61	-	-
UCT-I-T2-1	71.41	17.70	0.49
UCT-I-T2-2	66.37	18.10	0.41
UCT-I-T2-3	63.18	15.50	0.42
UCT-I-T2-4	64.20	15.90	0.62
UCT-I-T2-5	64.54	18.20	0.49
UCT-I-T2-6	72.34	19.20	0.39

- Appendix A.3. -
Four-point bending test results

Table A.3.-1. Mean geometric measurements (b: depth; h: height; a: notch length), failure load ($F_{failure}$) and fracture toughness (K_{IC}) results obtained from the four-point bending tests for the Floresta sandstone (F) specimens with the smallest notch radius (ρ = 0.15 mm).

CODE	b (mm)	h (mm)	a (mm)	$F_{failure}$ (N)	K_{IC} (MPa · m$^{1/2}$)
4PBT-F-015-T1-1	29.74	29.81	15.66	194	0.42
4PBT-F-015-T1-2	29.77	29.66	15.34	175	0.37
4PBT-F-015-T1-3	29.79	29.92	17.82	99	0.28
4PBT-F-015-T1-4	29.85	29.73	16.11	137	0.32
4PBT-F-015-T1-5	29.77	29.75	13.05	265	0.43
4PBT-F-015-T1-6	29.79	29.79	15.69	181	0.39
4PBT-F-015-T3-1	29.71	29.89	14.01	217	0.39
4PBT-F-015-T3-2	29.78	29.87	14.66	198	0.38
4PBT-F-015-T3-3	30.02	29.85	15.71	232	0.50
4PBT-F-015-T3-4	29.81	29.75	14.22	182	0.34
4PBT-F-015-T3-5	29.80	29.92	13.35	282	0.47
4PBT-F-015-T3-6	29.76	29.86	14.73	245	0.48
4PBT-F-015-T4-1	29.78	29.54	13.93	197	0.36
4PBT-F-015-T4-2	29.79	29.89	16.59	203	0.49
4PBT-F-015-T4-3	29.87	29.81	13.14	320	0.52
4PBT-F-015-T4-4	29.90	29.85	15.93	238	0.53
4PBT-F-015-T4-5	29.76	29.75	13.87	195	0.35
4PBT-F-015-T4-6	29.77	29.77	15.95	222	0.50
4PBT-F-015-T2-1	29.86	29.74	15.09	151	0.31
4PBT-F-015-T2-2	29.48	29.66	15.84	205	0.46
4PBT-F-015-T2-3	29.69	29.96	16.86	228	0.56
4PBT-F-015-T2-4	29.8	29.77	14.95	232	0.47
4PBT-F-015-T2-5	29.78	29.69	14.59	234	0.45
4PBT-F-015-T2-6	29.75	29.71	15.21	217	0.45

Table A.3.-2. Mean geometric measurements (b: depth; h: height; a: notch length), failure load ($F_{failure}$) and fracture toughness (K_{IC}) results obtained from the four-point bending tests for the Moleanos limestone (C) specimens with the smallest notch radius (ρ = 0.15 mm).

CODE	b (mm)	h (mm)	a (mm)	$F_{failure}$ (N)	K_{IC} (MPa · m$^{1/2}$)
4PBT-C-015-T1-1	29.91	29.97	14.47	378	0.70
4PBT-C-015-T1-2	29.26	29.46	12.61	319	0.64

4PBT-C-015-T1-3	30.00	29.88	14.76	486	0.94
4PBT-C-015-T1-4	29.34	29.27	14.87	303	0.65
4PBT-C-015-T1-5	29.71	29.74	14.89	337	0.68
4PBT-C-015-T1-6	29.86	30.01	16.01	355	0.78
4PBT-C-015-T3-1	30.08	30.01	15.75	466	0.99
4PBT-C-015-T3-2	30.12	30.16	16.08	433	0.94
4PBT-C-015-T3-3	29.63	29.73	15.02	433	0.88
4PBT-C-015-T3-4	29.74	29.62	15.95	-	-
4PBT-C-015-T3-5	29.56	29.68	16.02	409	0.95
4PBT-C-015-T3-6	29.86	30.28	16.37	462	1.03
4PBT-C-015-T4-1	29.59	29.62	14.46	558	1.08
4PBT-C-015-T4-2	29.74	29.63	15.19	448	0.94
4PBT-C-015-T4-3	29.76	29.71	16.52	343	0.83
4PBT-C-015-T4-4	29.89	29.65	16.06	386	0.89
4PBT-C-015-T4-5	29.46	29.46	15.28	401	0.87
4PBT-C-015-T4-6	29.82	29.94	13.76	616	1.07
4PBT-C-015-T2-1	29.87	29.83	14.11	593	1.07
4PBT-C-015-T2-2	29.79	29.61	14.31	520	0.99
4PBT-C-015-T2-3	30.05	29.79	15.72	-	-
4PBT-C-015-T2-4	29.81	29.76	15.91	411	0.92
4PBT-C-015-T2-5	29.88	29.92	15.10	-	-
4PBT-C-015-T2-6	29.94	29.77	15.97	583	1.31

Table A.3.-3. Mean geometric measurements (b: depth; h: height; a: notch length), failure load ($F_{failure}$) and fracture toughness (K_{IC}) results obtained from the four-point bending tests for the Macael marble (M) specimens with the smallest notch radius (ρ = 0.15 mm).

CODE	b (mm)	h (mm)	a (mm)	$F_{failure}$ (N)	K_{IC} (MPa · m$^{1/2}$)
4PBT-M-015-T1-1	29.57	29.69	14.54	611	1.19
4PBT-M-015-T1-2	29.85	29.59	15.54	430	0.94
4PBT-M-015-T1-3	29.93	29.95	15.38	577	1.19
4PBT-M-015-T1-4	29.80	29.80	14.90	654	1.30
4PBT-M-015-T1-5	29.56	29.57	15.70	519	1.17
4PBT-M-015-T1-6	29.99	29.96	15.09	522	1.03
4PBT-M-015-T3-1	29.40	29.68	15.35	487	1.05
4PBT-M-015-T3-2	29.98	29.94	14.89	755	1.47
4PBT-M-015-T3-3	30.11	30.05	14.99	676	1.31
4PBT-M-015-T3-4	29.52	29.50	15.14	447	0.95

4PBT-M-015-T3-5	29.92	30.00	15.87	403	0.87
4PBT-M-015-T3-6	29.68	29.89	17.16	509	1.31
4PBT-M-015-T4-1	29.79	29.91	16.06	206	0.46
4PBT-M-015-T4-2	29.58	29.42	15.15	296	0.64
4PBT-M-015-T4-3	29.96	30.01	16.21	256	0.57
4PBT-M-015-T4-4	30.11	30.17	13.63	321	0.53
4PBT-M-015-T4-5	29.54	29.82	16.14	284	0.66
4PBT-M-015-T4-6	29.68	29.69	15.19	254	0.53
4PBT-M-015-T2-1	29.63	29.51	15.24	293	0.59
4PBT-M-015-T2-2	29.61	29.95	15.38	361	0.80
4PBT-M-015-T2-3	29.81	29.82	14.38	345	0.83
4PBT-M-015-T2-4	29.84	29.70	15.55	250	0.57
4PBT-M-015-T2-5	29.85	29.83	15.15	398	0.71
4PBT-M-015-T2-6	29.64	29.59	15.31	318	0.82

Table A.3.-4. Mean geometric measurements (b: depth; h: height; a: notch length), failure load ($F_{failure}$) and fracture toughness (K_{IC}) results obtained from the four-point bending tests for the Carrara marble (I) specimens with the smallest notch radius (ρ = 0.15 mm).

CODE	b (mm)	h (mm)	a (mm)	$F_{failure}$ (N)	K_{IC} (MPa · m$^{1/2}$)
4PBT-I-015-T1-1	29.76	29.85	15.95	302	0.67
4PBT-I-015-T1-2	29.87	29.81	15.36	418	0.87
4PBT-I-015-T1-3	29.99	29.79	15.62	260	0.56
4PBT-I-015-T1-4	29.77	29.67	15.00	332	0.68
4PBT-I-015-T1-5	29.63	29.68	14.36	406	0.77
4PBT-I-015-T1-6	29.78	29.85	16.00	402	0.90
4PBT-I-015-T3-1	29.66	29.53	15.61	241	0.54
4PBT-I-015-T3-2	29.87	29.93	16.84	314	0.77
4PBT-I-015-T3-3	29.62	29.77	15.42	394	0.84
4PBT-I-015-T3-4	29.94	29.74	14.74	412	0.81
4PBT-I-015-T3-5	29.78	29.75	16.47	389	0.93
4PBT-I-015-T3-6	29.52	29.69	15.76	282	0.63
4PBT-I-015-T4-1	29.70	29.70	14.19	318	0.59
4PBT-I-015-T4-2	29.71	29.89	15.83	310	0.68
4PBT-I-015-T4-3	29.71	29.56	15.16	221	0.47
4PBT-I-015-T4-4	29.87	29.78	15.03	301	0.61
4PBT-I-015-T4-5	29.86	29.70	15.59	321	0.70
4PBT-I-015-T4-6	29.69	29.67	15.31	308	0.65

4PBT-I-015-T2-1	29.68	29.63	14.13	340	0.84
4PBT-I-015-T2-2	29.75	29.77	14.06	268	0.51
4PBT-I-015-T2-3	29.52	29.58	15.03	200	0.40
4PBT-I-015-T2-4	29.60	29.62	13.83	215	0.43
4PBT-I-015-T2-5	29.49	29.44	13.97	181	0.41
4PBT-I-015-T2-6	29.78	29.80	14.16	191	0.42

Table A.3.-5. Mean geometric measurements (b: depth; h: height; a: notch length), failure load ($F_{failure}$) and apparent fracture toughness (K_{IN}) results obtained from the four-point bending tests for the Floresta sandstone (F) specimens with different notch radii.

CODE	b (mm)	h (mm)	a (mm)	$F_{failure}$ (N)	K_{IN} (MPa · m$^{1/2}$)
4PBT-F-05-T1-1	29.83	29.74	14.77	189	0.37
4PBT-F-05-T1-2	29.75	29.67	14.72	173	0.34
4PBT-F-05-T1-3	29.67	29.65	14.48	143	0.28
4PBT-F-05-T1-4	29.74	29.74	14.59	188	0.36
4PBT-F-05-T1-5	29.86	29.62	14.52	177	0.34
4PBT-F-05-T1-6	29.63	29.61	15.06	193	0.4
4PBT-F-1-T1-1	29.68	29.61	15.09	134	0.28
4PBT-F-1-T1-2	29.94	29.81	15.36	135	0.28
4PBT-F-1-T1-3	29.14	29.4	15.35	159	0.36
4PBT-F-1-T1-4	29.71	29.79	16.97	139	0.35
4PBT-F-1-T1-5	29.82	29.56	16.61	161	0.4
4PBT-F-1-T1-6	29.69	29.64	15.47	188	0.41
4PBT-F-2-T1-1	29.79	29.67	16.02	162	0.37
4PBT-F-2-T1-2	29.81	29.55	15.75	169	0.38
4PBT-F-2-T1-3	29.77	29.65	15.25	216	0.45
4PBT-F-2-T1-4	29.76	29.74	14.94	208	0.42
4PBT-F-2-T1-5	29.8	29.63	15.63	179	0.39
4PBT-F-2-T1-6	29.69	29.69	15.89	164	0.37
4PBT-F-4-T1-1	29.84	29.83	16.31	137	0.32
4PBT-F-4-T1-2	29.74	29.65	15.65	198	0.44
4PBT-F-4-T1-3	29.68	29.57	16.17	182	0.43
4PBT-F-4-T1-4	29.54	29.74	14.72	180	0.36
4PBT-F-4-T1-5	29.64	29.71	14.66	188	0.37
4PBT-F-4-T1-6	29.73	29.63	14.68	176	0.35
4PBT-F-4-T1-7	29.64	29.57	14.57	205	0.4
4PBT-F-4-T1-8	29.64	29.53	14.93	194	0.4

4PBT-F-4-T1-9	29.48	29.65	14.55	203	0.4
4PBT-F-4-T1-10	29.8	29.91	15.04	213	0.43
4PBT-F-4-T1-11	29.61	29.68	14.48	150	0.29
4PBT-F-4-T1-12	29.79	29.78	14.46	209	0.4
4PBT-F-7-T1-1	29.68	29.86	14.86	224	0.44
4PBT-F-7-T1-2	29.86	29.81	14.76	242	0.47
4PBT-F-7-T1-3	29.65	29.47	14.47	211	0.42
4PBT-F-7-T1-4	29.88	29.84	14.64	238	0.46
4PBT-F-7-T1-5	29.83	29.83	14.73	214	0.42
4PBT-F-7-T1-6	29.87	29.67	14.47	247	0.47
4PBT-F-10-T1-1	29.64	29.55	14.60	202	0.4
4PBT-F-10-T1-2	29.82	29.5	14.50	190	0.37
4PBT-F-10-T1-3	29.59	29.66	14.66	214	0.42
4PBT-F-10-T1-4	29.76	29.66	14.64	226	0.44
4PBT-F-10-T1-5	29.62	29.76	14.71	201	0.39
4PBT-F-10-T1-6	30.01	29.88	14.93	221	0.43
4PBT-F-15-T1-1	29.82	29.58	14.66	211	0.42
4PBT-F-15-T1-2	29.72	29.63	14.63	226	0.44
4PBT-F-15-T1-3	29.59	29.7	15.05	214	0.44
4PBT-F-15-T1-4	29.48	29.62	14.72	189	0.38
4PBT-F-15-T1-5	29.67	29.62	15.07	202	0.42
4PBT-F-15-T1-6	29.59	29.7	14.70	194	0.38
4PBT-F-05-T3-1	29.74	29.86	14.30	256	0.47
4PBT-F-05-T3-2	29.81	29.79	14.80	216	0.42
4PBT-F-05-T3-3	29.74	29.72	14.86	209	0.42
4PBT-F-05-T3-4	29.79	29.67	14.22	206	0.39
4PBT-F-05-T3-5	29.76	29.77	14.23	219	0.41
4PBT-F-05-T3-6	29.66	29.66	14.15	194	0.36
4PBT-F-1-T3-1	29.74	29.76	15.25	220	0.46
4PBT-F-1-T3-2	29.77	29.75	15.27	211	0.44
4PBT-F-1-T3-3	29.74	29.81	16.75	166	0.41
4PBT-F-1-T3-4	29.95	29.86	16.87	169	0.42
4PBT-F-1-T3-5	29.93	29.87	15.41	133	0.28
4PBT-F-1-T3-6	29.76	29.78	15.17	206	0.42
4PBT-F-2-T3-1	29.88	29.94	16.03	180	0.40
4PBT-F-2-T3-2	29.81	29.78	15.77	190	0.42
4PBT-F-2-T3-3	29.62	29.47	14.52	211	0.42
4PBT-F-2-T3-4	29.81	29.85	15.06	201	0.41
4PBT-F-2-T3-5	29.78	29.81	15.80	197	0.43
4PBT-F-2-T3-6	29.90	29.84	15.10	157	0.32

4PBT-F-4-T3-1	29.77	29.91	15.84	213	0.47
4PBT-F-4-T3-2	29.87	29.80	15.57	224	0.48
4PBT-F-4-T3-3	29.86	29.73	15.54	145	0.31
4PBT-F-4-T3-4	29.93	29.81	15.45	179	0.38
4PBT-F-4-T3-5	29.90	29.76	15.85	212	0.47
4PBT-F-4-T3-6	29.76	29.76	15.61	174	0.38
4PBT-F-7-T3-1	29.90	29.89	14.81	275	0.53
4PBT-F-7-T3-2	29.87	29.92	14.75	265	0.51
4PBT-F-7-T3-3	29.72	29.72	14.78	227	0.45
4PBT-F-7-T3-4	29.74	29.76	14.64	255	0.50
4PBT-F-7-T3-5	29.97	29.92	14.87	290	0.56
4PBT-F-7-T3-6	29.99	29.81	14.55	296	0.56
4PBT-F-10-T3-1	29.74	29.87	15.04	302	0.61
4PBT-F-10-T3-2	29.79	29.77	14.73	272	0.53
4PBT-F-10-T3-3	29.74	29.79	14.79	276	0.54
4PBT-F-10-T3-4	29.83	29.80	14.73	238	0.46
4PBT-F-10-T3-5	29.77	29.71	14.65	256	0.50
4PBT-F-10-T3-6	29.90	29.69	14.85	257	0.51
4PBT-F-15-T3-1	29.91	29.81	14.70	297	0.57
4PBT-F-15-T3-2	29.68	29.76	14.87	270	0.54
4PBT-F-15-T3-3	29.82	29.75	14.65	285	0.55
4PBT-F-15-T3-4	29.65	29.75	14.62	259	0.50
4PBT-F-15-T3-5	29.76	29.81	14.83	261	0.52
4PBT-F-15-T3-6	29.97	29.84	14.92	-	-
4PBT-F-05-T4-1	29.76	29.78	14.73	243	0.48
4PBT-F-05-T4-2	29.71	29.76	14.73	213	0.42
4PBT-F-05-T4-3	29.78	29.79	15.33	231	0.48
4PBT-F-05-T4-4	29.63	29.74	14.86	213	0.43
4PBT-F-05-T4-5	29.81	29.72	15.20	221	0.46
4PBT-F-05-T4-6	29.75	29.65	14.80	175	0.35
4PBT-F-1-T4-1	29.80	29.76	15.29	217	0.45
4PBT-F-1-T4-2	29.79	29.73	16.77	185	0.46
4PBT-F-1-T4-3	29.84	30.08	15.64	196	0.41
4PBT-F-1-T4-4	29.73	29.81	16.70	215	0.53
4PBT-F-1-T4-5	29.73	29.84	16.92	186	0.47
4PBT-F-1-T4-6	29.78	29.89	16.84	164	0.41
4PBT-F-2-T4-1	29.80	29.80	15.87	214	0.48
4PBT-F-2-T4-2	29.92	30.03	16.06	179	0.39
4PBT-F-2-T4-3	29.77	29.71	15.78	217	0.48
4PBT-F-2-T4-4	29.88	29.78	15.74	207	0.45

4PBT-F-2-T4-5	29.76	29.83	15.08	232	0.47
4PBT-F-2-T4-6	29.74	29.79	15.02	231	0.47
4PBT-F-4-T4-1	29.85	29.82	15.42	220	0.46
4PBT-F-4-T4-2	29.80	29.68	15.49	231	0.50
4PBT-F-4-T4-3	29.71	29.73	15.56	208	0.45
4PBT-F-4-T4-4	29.70	29.84	15.75	220	0.48
4PBT-F-4-T4-5	29.79	29.75	16.23	203	0.47
4PBT-F-4-T4-6	29.99	29.99	15.99	223	0.49
4PBT-F-7-T4-1	29.70	29.55	14.36	285	0.55
4PBT-F-7-T4-2	29.79	29.72	14.53	299	0.58
4PBT-F-7-T4-3	29.83	29.83	14.64	306	0.59
4PBT-F-7-T4-4	29.81	29.77	14.61	315	0.61
4PBT-F-7-T4-5	29.85	29.62	14.49	250	0.48
4PBT-F-7-T4-6	29.89	29.79	14.65	288	0.55
4PBT-F-10-T4-1	29.90	29.82	14.69	366	0.71
4PBT-F-10-T4-2	29.85	29.78	14.73	280	0.55
4PBT-F-10-T4-3	29.62	29.79	14.84	313	0.62
4PBT-F-10-T4-4	29.69	29.97	15.02	270	0.54
4PBT-F-10-T4-5	29.83	29.71	14.51	341	0.65
4PBT-F-10-T4-6	29.84	29.83	14.76	259	0.50
4PBT-F-15-T4-1	29.83	29.97	14.90	247	0.48
4PBT-F-15-T4-2	29.89	30.02	14.94	298	0.58
4PBT-F-15-T4-3	29.70	29.73	14.81	250	0.50
4PBT-F-15-T4-4	29.91	29.96	14.94	346	0.68
4PBT-F-15-T4-5	29.68	29.54	14.47	292	0.57
4PBT-F-15-T4-6	29.73	29.48	14.64	263	0.53
4PBT-F-05-T2-1	29.68	29.67	15.10	237	0.49
4PBT-F-05-T2-2	29.74	29.79	15.09	264	0.54
4PBT-F-05-T2-3	29.73	29.73	14.93	236	0.48
4PBT-F-05-T2-4	29.75	29.73	14.46	229	0.44
4PBT-F-05-T2-5	29.70	29.60	15.08	219	0.46
4PBT-F-05-T2-6	29.79	29.70	14.73	228	0.45
4PBT-F-1-T2-1	29.71	29.78	16.63	183	0.45
4PBT-F-1-T2-2	29.92	29.68	16.68	199	0.49
4PBT-F-1-T2-3	29.72	29.78	16.93	168	0.43
4PBT-F-1-T2-4	29.90	29.81	16.91	201	0.50
4PBT-F-1-T2-5	29.92	29.91	15.44	167	0.35
4PBT-F-1-T2-6	29.76	29.68	16.71	161	0.40
4PBT-F-2-T2-1	29.49	29.09	14.37	238	0.49
4PBT-F-2-T2-2	29.75	29.90	15.13	267	0.54

4PBT-F-2-T2-3	29.71	29.74	14.89	246	0.49
4PBT-F-2-T2-4	29.81	29.81	15.09	242	0.49
4PBT-F-2-T2-5	29.70	29.64	14.82	211	0.42
4PBT-F-2-T2-6	29.75	29.72	14.95	280	0.57
4PBT-F-4-T2-1	29.78	29.68	15.83	228	0.51
4PBT-F-4-T2-2	29.64	29.68	15.81	236	0.53
4PBT-F-4-T2-3	29.79	29.76	15.39	236	0.50
4PBT-F-4-T2-4	29.75	29.68	15.48	227	0.49
4PBT-F-4-T2-5	29.79	29.70	15.30	227	0.48
4PBT-F-4-T2-6	29.79	29.78	15.68	213	0.46
4PBT-F-7-T2-1	29.94	29.97	14.82	312	0.60
4PBT-F-7-T2-2	29.85	29.75	14.65	276	0.54
4PBT-F-7-T2-3	29.58	29.70	14.63	260	0.51
4PBT-F-7-T2-4	29.60	29.73	14.73	265	0.52
4PBT-F-7-T2-5	29.79	29.80	14.80	257	0.51
4PBT-F-7-T2-6	29.78	29.70	14.75	247	0.49
4PBT-F-10-T2-1	29.88	29.92	15.02	271	0.54
4PBT-F-10-T2-2	29.90	29.91	14.94	285	0.56
4PBT-F-10-T2-3	29.72	29.74	14.72	295	0.58
4PBT-F-10-T2-4	29.77	29.76	14.79	232	0.46
4PBT-F-10-T2-5	29.75	29.84	14.87	250	0.49
4PBT-F-10-T2-6	29.80	29.69	14.69	264	0.52
4PBT-F-15-T2-1	29.84	29.81	14.86	284	0.56
4PBT-F-15-T2-2	29.80	29.78	14.76	295	0.58
4PBT-F-15-T2-3	29.83	29.81	14.91	294	0.58
4PBT-F-15-T2-4	29.58	29.70	14.65	203	0.40
4PBT-F-15-T2-5	29.70	29.75	14.65	277	0.54
4PBT-F-15-T2-6	29.68	29.61	14.59	259	0.51

Table A.3.-6. Mean geometric measurements (b: depth; h: height; a: notch length), failure load ($F_{failure}$) and apparent fracture toughness (K_{IN}) results obtained from the four-point bending tests for the Moleanos limestone (C) specimens with different notch radii.

CODE	b (mm)	h (mm)	a (mm)	$F_{failure}$ (N)	K_{IN} (MPa · m$^{1/2}$)
4PBT-C-05-T1-1	29.70	29.86	16.91	341	0.86
4PBT-C-05-T1-2	29.97	30.05	17.28	287	0.73
4PBT-C-05-T1-3	30.29	30.36	15.81	413	0.84
4PBT-C-05-T1-4	29.96	29.99	17.14	315	0.80

4PBT-C-05-T1-5	30.12	30.07	15.62	366	0.76
4PBT-C-05-T1-6	30.15	29.89	15.34	359	0.73
4PBT-C-1-T1-1	29.48	29.51	15.21	363	0.78
4PBT-C-1-T1-2	29.57	29.42	15.05	422	0.90
4PBT-C-1-T1-3	29.55	29.56	14.99	431	0.89
4PBT-C-1-T1-4	29.69	29.65	15.83	342	0.77
4PBT-C-1-T1-5	29.47	29.58	15.11	431	0.91
4PBT-C-1-T1-6	29.60	29.68	15.23	478	1.01
4PBT-C-2-T1-1	29.56	29.35	15.35	399	0.88
4PBT-C-2-T1-2	29.46	29.44	15.34	318	0.70
4PBT-C-2-T1-3	29.24	29.35	15.40	400	0.90
4PBT-C-2-T1-4	29.73	29.46	15.36	402	0.88
4PBT-C-2-T1-5	29.43	29.46	15.46	416	0.93
4PBT-C-2-T1-6	29.58	29.43	15.48	377	0.84
4PBT-C-4-T1-1	29.62	29.45	15.45	382	0.85
4PBT-C-4-T1-2	29.28	28.98	14.68	343	0.74
4PBT-C-4-T1-3	29.64	29.55	15.60	388	0.86
4PBT-C-4-T1-4	30.01	29.99	16.04	360	0.79
4PBT-C-4-T1-5	29.85	29.97	16.02	420	0.93
4PBT-C-4-T1-6	29.99	29.87	15.92	325	0.72
4PBT-C-4-T1-7	29.60	29.17	13.97	525	1.01
4PBT-C-4-T1-8	29.50	29.62	14.27	356	0.68
4PBT-C-4-T1-9	29.53	29.48	14.38	591	1.16
4PBT-C-4-T1-10	31.25	29.28	13.91	514	0.92
4PBT-C-4-T1-11	29.32	29.28	13.93	375	0.72
4PBT-C-4-T1-12	29.41	29.40	14.20	387	0.75
4PBT-C-7-T1-1	29.22	29.24	14.49	446	0.92
4PBT-C-7-T1-2	29.21	29.36	14.79	500	1.05
4PBT-C-7-T1-3	29.86	29.88	15.03	523	1.04
4PBT-C-7-T1-4	29.39	29.59	14.59	432	0.86
4PBT-C-7-T1-5	29.81	29.84	14.82	550	1.08
4PBT-C-7-T1-6	29.91	29.94	14.94	513	1.00
4PBT-C-10-T1-1	30.08	29.94	14.79	642	1.23
4PBT-C-10-T1-2	29.96	29.96	15.11	480	0.96
4PBT-C-10-T1-3	29.12	29.27	14.42	436	0.89
4PBT-C-10-T1-4	29.06	28.88	13.88	457	0.92
4PBT-C-10-T1-5	29.07	28.86	13.86	399	0.80
4PBT-C-10-T1-6	29.12	29.08	14.13	450	0.91
4PBT-C-15-T1-1	29.78	29.80	15.05	395	0.80
4PBT-C-15-T1-2	29.06	29.10	14.45	402	0.84

4PBT-C-15-T1-3	29.49	29.49	14.94	384	0.80
4PBT-C-15-T1-4	29.24	28.85	14.40	485	1.03
4PBT-C-15-T1-5	29.26	29.27	14.62	391	0.81
4PBT-C-15-T1-6	29.25	29.10	14.50	526	1.10
4PBT-C-05-T3-1	29.58	29.54	16.54	345	0.86
4PBT-C-05-T3-2	29.64	29.51	14.18	437	0.83
4PBT-C-05-T3-3	30.02	29.99	14.83	395	0.76
4PBT-C-05-T3-4	30.31	30.17	17.00	343	0.82
4PBT-C-05-T3-5	29.80	29.65	14.31	514	0.97
4PBT-C-05-T3-6	29.99	29.96	14.78	462	0.89
4PBT-C-1-T3-1	29.04	29.42	14.78	411	0.86
4PBT-C-1-T3-2	29.34	29.34	14.77	483	1.01
4PBT-C-1-T3-3	30.05	29.82	15.38	477	0.99
4PBT-C-1-T3-4	29.59	29.46	14.94	389	0.81
4PBT-C-1-T3-5	29.65	29.58	15.23	433	0.92
4PBT-C-1-T3-6	29.48	29.32	14.62	497	1.02
4PBT-C-2-T3-1	29.60	29.67	15.45	439	0.95
4PBT-C-2-T3-2	29.57	29.33	15.36	446	0.99
4PBT-C-2-T3-3	29.40	29.51	15.30	410	0.89
4PBT-C-2-T3-4	29.55	29.51	15.34	402	0.88
4PBT-C-2-T3-5	30.01	29.80	15.51	372	0.79
4PBT-C-2-T3-6	30.28	29.95	15.67	451	0.95
4PBT-C-4-T3-1	29.77	29.71	14.46	484	0.93
4PBT-C-4-T3-2	29.87	29.68	14.26	538	1.01
4PBT-C-4-T3-3	29.43	29.35	14.02	481	0.92
4PBT-C-4-T3-4	29.72	29.73	14.31	508	0.96
4PBT-C-4-T3-5	29.65	29.42	14.19	463	0.89
4PBT-C-4-T3-6	29.36	29.70	14.60	562	1.11
4PBT-C-7-T3-1	29.28	29.50	14.08	503	0.96
4PBT-C-7-T3-2	29.22	29.23	14.16	504	1.00
4PBT-C-7-T3-3	29.42	29.53	14.42	483	0.95
4PBT-C-7-T3-4	29.86	29.97	15.17	563	1.13
4PBT-C-7-T3-5	29.21	29.59	14.46	529	1.04
4PBT-C-7-T3-6	29.80	29.84	14.81	494	0.97
4PBT-C-10-T3-1	30.01	30.13	15.03	539	1.04
4PBT-C-10-T3-2	29.39	29.27	13.99	626	1.21
4PBT-C-10-T3-3	29.25	29.04	14.14	428	0.86
4PBT-C-10-T3-4	29.72	29.88	14.70	564	1.09
4PBT-C-10-T3-5	29.34	29.34	14.20	451	0.88
4PBT-C-10-T3-6	29.26	29.10	14.02	564	1.11

4PBT-C-15-T3-1	29.75	29.71	14.74	525	1.04
4PBT-C-15-T3-2	29.58	29.56	14.77	507	1.03
4PBT-C-15-T3-3	29.51	29.60	15.14	418	0.88
4PBT-C-15-T3-4	29.89	29.87	15.17	584	1.19
4PBT-C-15-T3-5	29.97	29.92	15.34	455	0.93
4PBT-C-15-T3-6	30.06	29.89	14.65	530	1.01
4PBT-C-05-T4-1	30.02	30.13	15.57	461	0.95
4PBT-C-05-T4-2	29.55	29.53	14.53	475	0.94
4PBT-C-05-T4-3	30.09	30.26	15.24	-	-
4PBT-C-05-T4-4	29.58	29.53	16.73	402	1.03
4PBT-C-05-T4-5	30.12	29.75	14.35	535	1.00
4PBT-C-05-T4-6	29.52	29.63	14.18	560	1.06
4PBT-C-1-T4-1	29.60	29.55	15.01	467	0.97
4PBT-C-1-T4-2	29.51	29.39	14.76	484	1.00
4PBT-C-1-T4-3	29.68	29.60	15.13	502	1.05
4PBT-C-1-T4-4	29.53	29.40	14.84	521	1.08
4PBT-C-1-T4-5	29.33	29.58	15.26	459	0.99
4PBT-C-1-T4-6	29.38	29.36	14.86	559	1.18
4PBT-C-2-T4-1	29.63	29.61	15.50	493	1.08
4PBT-C-2-T4-2	29.85	30.23	16.08	514	1.11
4PBT-C-2-T4-3	29.49	29.53	15.19	450	0.96
4PBT-C-2-T4-4	29.47	29.58	15.17	477	1.01
4PBT-C-2-T4-5	29.55	29.63	15.36	461	0.99
4PBT-C-2-T4-6	29.31	29.37	15.28	436	0.96
4PBT-C-4-T4-1	30.21	30.08	15.83	509	1.08
4PBT-C-4-T4-2	29.27	29.27	14.79	463	0.98
4PBT-C-4-T4-3	29.95	30.04	16.38	443	1.01
4PBT-C-4-T4-4	29.94	30.00	15.51	502	1.04
4PBT-C-4-T4-5	30.21	30.16	15.91	594	1.26
4PBT-C-4-T4-6	30.11	29.78	15.06	614	1.23
4PBT-C-7-T4-1	29.35	29.51	14.45	561	1.11
4PBT-C-7-T4-2	30.80	29.85	14.62	648	1.20
4PBT-C-7-T4-3	30.39	30.00	14.90	640	1.22
4PBT-C-7-T4-4	29.42	29.37	14.07	669	1.29
4PBT-C-7-T4-5	29.12	29.08	13.93	549	1.08
4PBT-C-7-T4-6	29.11	29.11	14.09	-	-
4PBT-C-10-T4-1	29.86	29.84	14.98	566	1.13
4PBT-C-10-T4-2	29.84	29.79	15.09	579	1.18
4PBT-C-10-T4-3	30.25	30.02	14.92	644	1.23
4PBT-C-10-T4-4	30.09	30.30	15.09	809	1.54

4PBT-C-10-T4-5	29.26	29.35	14.12	653	1.27
4PBT-C-10-T4-6	29.38	29.30	13.87	676	1.28
4PBT-C-15-T4-1	29.85	29.82	14.91	594	1.18
4PBT-C-15-T4-2	31.29	29.22	14.25	626	1.17
4PBT-C-15-T4-3	29.88	29.87	15.06	763	1.53
4PBT-C-15-T4-4	29.35	29.17	14.12	425	0.84
4PBT-C-15-T4-5	29.43	29.16	14.24	612	1.23
4PBT-C-15-T4-6	29.87	29.84	15.38	637	1.33
4PBT-C-05-T2-1	29.72	29.72	16.65	500	1.24
4PBT-C-05-T2-2	30.28	29.82	16.95	432	1.07
4PBT-C-05-T2-3	29.57	29.59	16.64	435	1.10
4PBT-C-05-T2-4	29.68	29.63	16.48	435	1.07
4PBT-C-05-T2-5	29.84	29.83	14.68	603	1.16
4PBT-C-05-T2-6	29.69	29.82	14.65	488	0.95
4PBT-C-1-T2-1	29.49	29.52	15.20	527	1.13
4PBT-C-1-T2-2	29.3	29.56	15.26	488	1.05
4PBT-C-1-T2-3	29.52	29.52	15.15	536	1.14
4PBT-C-1-T2-4	29.71	29.5	14.95	504	1.04
4PBT-C-1-T2-5	29.28	29.03	15.03	448	1.00
4PBT-C-1-T2-6	29.64	29.51	14.91	427	0.88
4PBT-C-2-T2-1	29.52	29.62	15.45	607	1.32
4PBT-C-2-T2-2	29.59	29.67	15.40	538	1.16
4PBT-C-2-T2-3	29.6	29.7	15.45	496	1.07
4PBT-C-2-T2-4	29.55	29.75	15.80	449	1.00
4PBT-C-2-T2-5	29.96	30.26	16.11	539	1.16
4PBT-C-2-T2-6	29.61	29.69	15.39	560	1.20
4PBT-C-4-T2-1	30.07	30.04	15.64	621	1.30
4PBT-C-4-T2-2	30.09	29.98	15.46	596	1.23
4PBT-C-4-T2-3	30.17	30.01	15.61	673	1.40
4PBT-C-4-T2-4	29.81	29.93	15.01	370	0.73
4PBT-C-4-T2-5	30.12	30.14	16.87	514	1.22
4PBT-C-4-T2-6	30.05	30.2	16.25	552	1.22
4PBT-C-7-T2-1	29.77	29.44	14.27	613	1.18
4PBT-C-7-T2-2	29.34	29.13	13.98	685	1.34
4PBT-C-7-T2-3	29.25	29.15	14.05	647	1.28
4PBT-C-7-T2-4	29.38	29.38	14.28	566	1.11
4PBT-C-7-T2-5	29.46	29.44	14.32	604	1.18
4PBT-C-7-T2-6	29.68	29.79	14.87	541	1.08
4PBT-C-10-T2-1	29.78	29.79	14.64	656	1.27
4PBT-C-10-T2-2	30.08	29.99	14.82	610	1.17

4PBT-C-10-T2-3	29.72	29.76	14.66	627	1.22
4PBT-C-10-T2-4	29.52	29.37	14.60	669	1.36
4PBT-C-10-T2-5	31.29	29.33	14.46	694	1.32
4PBT-C-10-T2-6	29.26	29.03	14.26	558	1.14
4PBT-C-15-T2-1	29.89	29.98	15.13	633	1.26
4PBT-C-15-T2-2	29.92	29.93	15.13	654	1.31
4PBT-C-15-T2-3	29.85	29.88	15.06	636	1.27
4PBT-C-15-T2-4	29.79	29.87	15.17	620	1.26
4PBT-C-15-T2-5	29.47	29.53	14.81	667	1.37
4PBT-C-15-T2-6	29.91	30.02	15.27	650	1.31

Table A.3.-7. Mean geometric measurements (b: depth; h: height; a: notch length), failure load ($F_{failure}$) and apparent fracture toughness (K_{IN}) results obtained from the four-point bending tests for the Macael marble (M) specimens with different notch radii.

CODE	b (mm)	h (mm)	a (mm)	$F_{failure}$ (N)	K_{IN} (MPa · m$^{1/2}$)
4PBT-M-05-T1-1	29.66	29.62	14.97	542	1.11
4PBT-M-05-T1-2	29.87	29.75	14.90	552	1.10
4PBT-M-05-T1-3	29.72	29.85	14.80	650	1.27
4PBT-M-05-T1-4	30.00	29.94	15.17	504	1.01
4PBT-M-05-T1-5	29.87	29.95	15.20	604	1.22
4PBT-M-05-T1-6	29.86	29.84	15.24	608	1.25
4PBT-M-1-T1-1	29.46	29.29	14.99	407	0.87
4PBT-M-1-T1-2	29.82	29.74	15.64	560	1.22
4PBT-M-1-T1-3	29.46	29.51	16.31	529	1.30
4PBT-M-1-T1-4	29.60	29.35	15.03	567	1.21
4PBT-M-1-T1-5	29.42	29.35	16.08	540	1.31
4PBT-M-1-T1-6	29.63	29.68	16.43	528	1.28
4PBT-M-2-T1-1	29.85	29.82	15.17	606	1.24
4PBT-M-2-T1-2	29.54	29.47	15.72	626	1.43
4PBT-M-2-T1-3	29.98	29.88	16.23	456	1.04
4PBT-M-2-T1-4	29.60	29.50	15.55	570	1.27
4PBT-M-2-T1-5	29.64	29.47	15.80	297	0.68
4PBT-M-2-T1-6	29.28	29.06	15.31	488	1.12
4PBT-M-4-T1-1	29.86	29.83	16.43	602	1.66
4PBT-M-4-T1-2	29.88	29.98	15.53	594	1.16
4PBT-M-4-T1-3	30.00	29.33	14.98	677	0.94
4PBT-M-4-T1-4	29.39	29.86	15.31	704	0.68

4PBT-M-4-T1-5	29.86	29.75	15.35	771	0.79
4PBT-M-4-T1-6	29.90	29.69	15.39	634	1.00
4PBT-M-4-T1-7	30.07	30.17	15.12	590	1.17
4PBT-M-4-T1-8	30.20	30.02	14.82	700	1.13
4PBT-M-4-T1-9	30.01	30.07	14.95	730	1.31
4PBT-M-4-T1-10	30.10	30.28	15.16	939	1.36
4PBT-M-4-T1-11	30.24	29.83	14.51	739	1.44
4PBT-M-4-T1-12	28.92	28.69	13.59	794	1.26
4PBT-M-7-T1-1	29.07	28.92	13.67	590	1.15
4PBT-M-7-T1-2	30.14	30.24	15.14	700	1.35
4PBT-M-7-T1-3	30.20	30.04	15.04	730	1.42
4PBT-M-7-T1-4	29.31	29.32	13.92	939	1.79
4PBT-M-7-T1-5	30.16	30.25	14.83	739	1.37
4PBT-M-7-T1-6	30.36	30.36	15.11	794	1.50
4PBT-M-10-T1-1	29.56	29.46	14.21	802	1.54
4PBT-M-10-T1-2	29.64	29.53	14.61	717	1.43
4PBT-M-10-T1-3	29.42	29.17	14.32	719	1.45
4PBT-M-10-T1-4	29.63	29.47	14.05	745	1.40
4PBT-M-10-T1-5	29.08	29.07	13.77	832	1.61
4PBT-M-10-T1-6	29.09	29.16	13.89	692	1.35
4PBT-M-15-T1-1	29.87	29.72	14.77	501	0.99
4PBT-M-15-T1-2	29.31	29.59	14.64	821	1.65
4PBT-M-15-T1-3	29.26	29.24	14.19	529	1.05
4PBT-M-15-T1-4	29.20	29.46	14.46	501	1.00
4PBT-M-15-T1-5	29.20	29.52	14.52	864	1.73
4PBT-M-15-T1-6	29.43	29.46	14.56	820	1.65
4PBT-M-05-T3-1	29.81	29.89	15.16	437	0.88
4PBT-M-05-T3-2	30.02	29.94	15.24	471	0.95
4PBT-M-05-T3-3	29.86	30.05	15.27	559	1.13
4PBT-M-05-T3-4	29.85	29.87	15.17	562	1.14
4PBT-M-05-T3-5	29.89	29.95	15.12	-	-
4PBT-M-05-T3-6	30.17	30.17	15.52	692	1.40
4PBT-M-1-T3-1	29.30	29.74	15.42	478	1.03
4PBT-M-1-T3-2	29.81	29.82	15.42	596	1.25
4PBT-M-1-T3-3	29.43	29.43	16.00	517	1.23
4PBT-M-1-T3-4	29.33	29.53	16.30	503	1.23
4PBT-M-1-T3-5	29.36	29.36	16.13	458	1.12
4PBT-M-1-T3-6	29.50	29.60	16.40	600	1.47
4PBT-M-2-T3-1	29.46	29.46	14.77	579	1.19
4PBT-M-2-T3-2	30.03	29.89	15.11	343	0.69

4PBT-M-2-T3-3	29.98	30.05	15.19	664	1.32
4PBT-M-2-T3-4	29.97	29.95	15.22	603	1.22
4PBT-M-2-T3-5	29.54	29.47	15.44	478	1.06
4PBT-M-2-T3-6	29.10	29.14	14.49	542	1.13
4PBT-M-4-T3-1	30.25	29.95	15.07	657	1.29
4PBT-M-4-T3-2	29.87	29.87	15.38	591	1.23
4PBT-M-4-T3-3	29.91	29.90	15.36	718	1.48
4PBT-M-4-T3-4	29.75	29.70	14.95	761	1.54
4PBT-M-4-T3-5	29.94	29.87	15.26	609	1.25
4PBT-M-4-T3-6	29.81	29.91	17.32	571	1.50
4PBT-M-7-T3-1	30.33	30.26	15.00	837	1.57
4PBT-M-7-T3-2	29.44	29.45	14.03	807	1.53
4PBT-M-7-T3-3	29.37	29.18	13.72	-	-
4PBT-M-7-T3-4	29.26	29.07	13.79	866	1.67
4PBT-M-7-T3-5	30.58	30.33	15.09	826	1.55
4PBT-M-7-T3-6	30.20	30.18	14.87	784	1.47
4PBT-M-10-T3-1	29.04	29.25	14.06	629	1.24
4PBT-M-10-T3-2	29.17	29.33	14.16	626	1.23
4PBT-M-10-T3-3	30.64	30.48	15.18	748	1.39
4PBT-M-10-T3-4	28.99	29.15	13.86	774	1.51
4PBT-M-10-T3-5	29.47	29.49	14.31	825	1.60
4PBT-M-10-T3-6	29.04	29.42	14.57	753	1.54
4PBT-M-15-T3-1	29.06	28.94	13.68	600	1.17
4PBT-M-15-T3-2	29.84	29.80	14.63	412	0.79
4PBT-M-15-T3-3	30.14	30.40	15.23	723	1.38
4PBT-M-15-T3-4	30.11	30.06	14.81	662	1.25
4PBT-M-15-T3-5	30.31	30.28	15.05	773	1.46
4PBT-M-15-T3-6	30.17	30.28	15.15	612	1.17
4PBT-M-05-T4-1	29.23	29.76	14.90	222	0.45
4PBT-M-05-T4-2	29.83	29.72	14.78	394	0.78
4PBT-M-05-T4-3	29.66	29.82	15.09	398	0.81
4PBT-M-05-T4-4	29.71	29.67	15.00	238	0.49
4PBT-M-05-T4-5	29.89	29.99	15.21	297	0.60
4PBT-M-05-T4-6	30.12	29.96	14.83	307	0.59
4PBT-M-1-T4-1	29.19	29.27	15.12	398	0.88
4PBT-M-1-T4-2	29.25	29.21	14.81	269	0.57
4PBT-M-1-T4-3	29.62	29.02	14.62	451	0.95
4PBT-M-1-T4-4	29.76	29.73	16.71	342	0.85
4PBT-M-1-T4-5	29.39	29.51	15.15	313	0.67
4PBT-M-1-T4-6	29.57	29.97	16.69	362	0.88

4PBT-M-2-T4-1	29.95	29.50	15.54	237	0.52
4PBT-M-2-T4-2	29.56	29.42	15.64	426	0.97
4PBT-M-2-T4-3	29.84	29.80	15.02	445	0.90
4PBT-M-2-T4-4	29.74	29.85	15.72	517	1.13
4PBT-M-2-T4-5	29.39	29.49	15.52	321	0.72
4PBT-M-2-T4-6	29.66	29.63	15.71	265	0.59
4PBT-M-4-T4-1	30.08	30.04	15.51	475	0.98
4PBT-M-4-T4-2	29.38	29.70	14.97	500	1.03
4PBT-M-4-T4-3	29.89	29.93	15.11	404	0.81
4PBT-M-4-T4-4	29.97	29.89	15.27	487	0.99
4PBT-M-4-T4-5	29.94	29.82	15.05	340	0.68
4PBT-M-4-T4-6	29.92	29.94	15.01	427	0.84
4PBT-M-7-T4-1	30.15	29.32	14.16	395	0.75
4PBT-M-7-T4-2	30.27	30.28	14.90	591	1.10
4PBT-M-7-T4-3	30.19	30.19	14.95	335	0.63
4PBT-M-7-T4-4	30.40	30.84	15.51	526	0.98
4PBT-M-7-T4-5	30.44	30.84	15.59	574	1.08
4PBT-M-7-T4-6	30.21	29.97	14.56	486	0.90
4PBT-M-10-T4-1	28.75	28.96	13.44	557	1.07
4PBT-M-10-T4-2	29.12	29.05	13.68	596	1.14
4PBT-M-10-T4-3	29.63	29.62	14.42	557	1.08
4PBT-M-10-T4-4	29.53	29.38	14.17	541	1.05
4PBT-M-10-T4-5	29.76	29.64	14.40	501	0.96
4PBT-M-10-T4-6	29.27	29.45	14.27	497	0.97
4PBT-M-15-T4-1	28.89	28.87	13.73	397	0.79
4PBT-M-15-T4-2	30.13	30.14	15.00	410	0.79
4PBT-M-15-T4-3	29.47	29.41	14.03	361	0.69
4PBT-M-15-T4-4	30.29	30.30	15.12	583	1.11
4PBT-M-15-T4-5	30.24	30.10	14.92	425	0.81
4PBT-M-15-T4-6	29.58	29.58	14.33	543	1.05
4PBT-M-05-T2-1	29.73	29.76	14.96	242	0.49
4PBT-M-05-T2-2	29.73	30.01	15.29	522	1.06
4PBT-M-05-T2-3	29.51	29.68	14.76	531	1.06
4PBT-M-05-T2-4	30.17	30.08	15.53	348	0.71
4PBT-M-05-T2-5	29.75	29.70	15.13	447	0.92
4PBT-M-05-T2-6	29.86	29.81	14.91	296	0.59
4PBT-M-1-T2-1	29.50	29.38	16.21	414	1.02
4PBT-M-1-T2-2	29.27	29.54	15.27	455	0.99
4PBT-M-1-T2-3	29.65	29.92	16.62	428	1.03
4PBT-M-1-T2-4	29.93	29.83	15.66	493	1.06

4PBT-M-1-T2-5	29.63	29.48	16.18	317	0.76
4PBT-M-1-T2-6	29.49	29.38	16.23	349	0.86
4PBT-M-2-T2-1	29.84	29.80	15.00	321	0.64
4PBT-M-2-T2-2	29.55	29.59	15.64	398	0.89
4PBT-M-2-T2-3	29.40	29.38	14.51	369	0.74
4PBT-M-2-T2-4	29.99	29.94	15.89	328	0.72
4PBT-M-2-T2-5	29.96	29.95	15.18	522	1.05
4PBT-M-2-T2-6	29.92	30.01	15.14	375	0.75
4PBT-M-4-T2-1	29.97	29.83	15.33	315	0.65
4PBT-M-4-T2-2	29.85	29.63	14.98	304	0.62
4PBT-M-4-T2-3	29.97	29.93	15.31	371	0.76
4PBT-M-4-T2-4	29.99	29.94	15.42	284	0.59
4PBT-M-4-T2-5	30.13	30.05	17.45	259	0.67
4PBT-M-4-T2-6	29.86	29.69	14.99	414	0.84
4PBT-M-7-T2-1	30.39	30.35	15.05	611	1.14
4PBT-M-7-T2-2	30.20	30.29	15.14	550	1.05
4PBT-M-7-T2-3	30.57	30.77	15.67	560	1.07
4PBT-M-7-T2-4	29.26	29.15	14.00	351	0.69
4PBT-M-7-T2-5	30.30	30.35	15.05	432	0.81
4PBT-M-7-T2-6	30.29	30.29	15.29	368	0.71
4PBT-M-10-T2-1	29.38	29.53	14.56	522	1.04
4PBT-M-10-T2-2	30.31	30.12	15.10	566	1.09
4PBT-M-10-T2-3	28.83	28.55	13.43	507	1.01
4PBT-M-10-T2-4	28.99	29.33	14.06	485	0.95
4PBT-M-10-T2-5	29.43	29.44	14.39	515	1.02
4PBT-M-10-T2-6	28.99	29.29	14.02	331	0.65
4PBT-M-15-T2-1	30.11	30.26	15.24	599	1.16
4PBT-M-15-T2-2	30.24	30.33	15.38	392	0.77
4PBT-M-15-T2-3	29.60	29.40	14.38	622	1.23
4PBT-M-15-T2-4	30.34	30.40	15.55	469	0.92
4PBT-M-15-T2-5	30.13	30.10	15.15	388	0.76
4PBT-M-15-T2-6	30.28	30.31	15.31	492	0.95

Table A.3.-8. Mean geometric measurements (b: depth; h: height; a: notch length), failure load ($F_{failure}$) and apparent fracture toughness (K_{IN}) results obtained from the four-point bending tests for the Carrara marble (I) specimens with different notch radii.

CODE	b (mm)	h (mm)	a (mm)	$F_{failure}$ (N)	K_{IN} (MPa · m$^{1/2}$)
4PBT-I-05-T1-1	29.30	29.27	14.47	246	0.50
4PBT-I-05-T1-2	29.56	29.58	15.88	432	0.99
4PBT-I-05-T1-3	29.86	29.70	14.85	358	0.71
4PBT-I-05-T1-4	29.54	29.61	15.04	413	0.86
4PBT-I-05-T1-5	29.42	29.29	14.39	318	0.64
4PBT-I-05-T1-6	29.46	29.34	16.12	301	0.74
4PBT-I-1-T1-1	29.77	29.40	15.15	353	0.76
4PBT-I-1-T1-2	29.36	29.62	15.57	277	0.61
4PBT-I-1-T1-3	29.34	29.50	15.20	272	0.59
4PBT-I-1-T1-4	29.82	29.79	15.17	426	0.87
4PBT-I-1-T1-5	29.78	29.72	15.17	328	0.68
4PBT-I-1-T1-6	29.87	29.68	15.08	347	0.71
4PBT-I-2-T1-1	29.16	29.19	15.59	351	0.83
4PBT-I-2-T1-2	29.11	29.23	15.63	330	0.78
4PBT-I-2-T1-3	29.08	29.24	15.79	382	0.92
4PBT-I-2-T1-4	29.04	29.29	14.62	309	0.64
4PBT-I-2-T1-5	29.14	29.21	15.76	375	0.90
4PBT-I-2-T1-6	29.06	29.06	15.59	294	0.70
4PBT-I-4-T1-1	29.45	29.54	15.94	406	0.95
4PBT-I-4-T1-2	29.54	29.61	16.01	280	0.65
4PBT-I-4-T1-3	29.19	28.99	15.29	302	0.70
4PBT-I-4-T1-4	29.47	29.40	15.60	274	0.62
4PBT-I-4-T1-5	28.94	28.94	15.22	302	0.71
4PBT-I-4-T1-6	29.55	29.64	16.29	360	0.86
4PBT-I-4-T1-7	28.84	28.70	13.85	261	0.54
4PBT-I-4-T1-8	28.84	29.03	14.08	345	0.70
4PBT-I-4-T1-9	29.80	29.36	14.31	314	0.61
4PBT-I-4-T1-10	28.97	29.03	13.96	323	0.64
4PBT-I-4-T1-11	29.06	29.05	13.88	317	0.62
4PBT-I-4-T1-12	29.02	28.97	13.80	268	0.53
4PBT-I-7-T1-1	29.00	28.88	13.78	375	0.74
4PBT-I-7-T1-2	29.25	29.50	14.45	309	0.62
4PBT-I-7-T1-3	29.02	28.93	13.81	298	0.59
4PBT-I-7-T1-4	29.12	29.14	13.94	299	0.59

4PBT-I-7-T1-5	28.97	28.98	13.98	422	0.85
4PBT-I-7-T1-6	29.20	29.23	14.13	426	0.84
4PBT-I-10-T1-1	29.10	29.49	14.49	489	0.98
4PBT-I-10-T1-2	29.07	29.23	14.23	384	0.77
4PBT-I-10-T1-3	29.28	29.26	14.16	309	0.61
4PBT-I-10-T1-4	29.26	29.15	14.25	347	0.70
4PBT-I-10-T1-5	29.14	29.03	14.03	340	0.68
4PBT-I-10-T1-6	29.01	29.03	13.93	340	0.68
4PBT-I-15-T1-1	28.77	29.38	14.33	410	0.83
4PBT-I-15-T1-2	29.06	28.94	14.34	405	0.85
4PBT-I-15-T1-3	28.96	28.99	13.99	391	0.79
4PBT-I-15-T1-4	28.90	28.94	13.77	350	0.69
4PBT-I-15-T1-5	29.19	28.81	13.91	391	0.79
4PBT-I-15-T1-6	29.11	29.04	13.77	282	0.55
4PBT-I-05-T3-1	29.24	29.28	15.88	268	0.65
4PBT-I-05-T3-2	29.28	29.33	15.80	405	0.96
4PBT-I-05-T3-3	29.56	29.46	16.05	370	0.88
4PBT-I-05-T3-4	29.48	29.50	14.76	390	0.80
4PBT-I-05-T3-5	29.94	29.58	14.94	302	0.61
4PBT-I-05-T3-6	29.82	29.80	15.07	362	0.73
4PBT-I-1-T3-1	30.44	29.95	15.21	336	0.67
4PBT-I-1-T3-2	30.09	30.09	15.37	470	0.95
4PBT-I-1-T3-3	29.90	29.80	15.07	419	0.85
4PBT-I-1-T3-4	29.79	29.80	14.94	332	0.66
4PBT-I-1-T3-5	29.49	29.37	15.14	290	0.63
4PBT-I-1-T3-6	29.52	29.46	15.25	296	0.64
4PBT-I-2-T3-1	29.39	29.46	15.72	318	0.73
4PBT-I-2-T3-2	29.58	29.63	15.87	283	0.65
4PBT-I-2-T3-3	29.58	29.63	15.86	261	0.59
4PBT-I-2-T3-4	29.38	29.41	15.70	278	0.64
4PBT-I-2-T3-5	29.68	29.74	16.02	350	0.80
4PBT-I-2-T3-6	29.36	29.40	15.55	258	0.59
4PBT-I-4-T3-1	29.40	29.17	16.64	223	0.60
4PBT-I-4-T3-2	29.46	29.65	15.38	312	0.67
4PBT-I-4-T3-3	29.10	27.11	14.21	218	0.55
4PBT-I-4-T3-4	29.78	29.75	16.11	344	0.79
4PBT-I-4-T3-5	29.22	29.43	16.79	376	1.00
4PBT-I-4-T3-6	29.53	29.51	15.61	372	0.84
4PBT-I-7-T3-1	28.93	29.15	13.81	353	0.69
4PBT-I-7-T3-2	29.27	29.38	14.13	337	0.65

4PBT-I-7-T3-3	29.71	29.91	14.76	304	0.59
4PBT-I-7-T3-4	29.08	29.16	13.97	417	0.82
4PBT-I-7-T3-5	29.09	29.22	13.87	343	0.66
4PBT-I-7-T3-6	29.60	29.38	14.21	385	0.75
4PBT-I-10-T3-1	29.02	29.35	14.13	367	0.72
4PBT-I-10-T3-2	29.81	30.16	14.88	437	0.83
4PBT-I-10-T3-3	29.92	29.86	14.56	441	0.84
4PBT-I-10-T3-4	29.22	29.55	14.24	417	0.81
4PBT-I-10-T3-5	28.96	28.95	14.34	391	0.82
4PBT-I-10-T3-6	29.42	29.31	14.41	341	0.69
4PBT-I-15-T3-1	28.84	28.83	14.43	351	0.76
4PBT-I-15-T3-2	28.95	28.89	13.97	494	1.00
4PBT-I-15-T3-3	29.28	29.33	14.57	326	0.67
4PBT-I-15-T3-4	29.19	29.07	13.99	503	1.00
4PBT-I-15-T3-5	29.22	29.58	14.56	265	0.53
4PBT-I-15-T3-6	28.93	28.88	13.94	381	0.77
4PBT-I-05-T4-1	29.54	29.53	16.02	245	0.58
4PBT-I-05-T4-2	29.76	29.75	15.86	185	0.41
4PBT-I-05-T4-3	29.60	29.51	16.62	216	0.55
4PBT-I-05-T4-4	29.76	29.69	14.85	341	0.68
4PBT-I-05-T4-5	29.26	29.27	15.87	294	0.71
4PBT-I-05-T4-6	29.84	29.87	15.16	292	0.59
4PBT-I-1-T4-1	29.47	29.61	15.40	277	0.60
4PBT-I-1-T4-2	29.60	29.48	14.74	212	0.43
4PBT-I-1-T4-3	29.90	29.58	14.81	228	0.46
4PBT-I-1-T4-4	29.66	30.66	16.31	278	0.59
4PBT-I-1-T4-5	29.90	29.84	15.59	281	0.60
4PBT-I-1-T4-6	29.82	29.77	14.98	276	0.55
4PBT-I-2-T4-1	29.73	29.59	15.77	246	0.56
4PBT-I-2-T4-2	29.29	29.39	15.62	277	0.64
4PBT-I-2-T4-3	29.38	29.37	15.45	242	0.55
4PBT-I-2-T4-4	29.43	29.37	15.69	237	0.55
4PBT-I-2-T4-5	29.32	29.27	15.45	254	0.58
4PBT-I-2-T4-6	29.23	29.23	15.53	233	0.54
4PBT-I-4-T4-1	29.18	29.23	15.27	284	0.64
4PBT-I-4-T4-2	29.30	29.27	15.52	228	0.53
4PBT-I-4-T4-3	29.65	29.63	15.58	225	0.49
4PBT-I-4-T4-4	29.63	29.74	15.57	229	0.50
4PBT-I-4-T4-5	29.49	29.52	15.22	-	-
4PBT-I-4-T4-6	29.21	29.29	15.76	236	0.56

4PBT-I-7-T4-1	29.62	29.51	14.18	225	0.43
4PBT-I-7-T4-2	29.46	29.66	14.31	242	0.46
4PBT-I-7-T4-3	29.41	29.29	13.91	206	0.39
4PBT-I-7-T4-4	29.31	29.30	14.20	236	0.47
4PBT-I-7-T4-5	28.96	28.92	13.90	264	0.53
4PBT-I-7-T4-6	29.53	29.21	14.07	226	0.44
4PBT-I-10-T4-1	29.79	29.58	14.57	257	0.51
4PBT-I-10-T4-2	29.60	29.78	14.72	424	0.83
4PBT-I-10-T4-3	29.06	29.06	14.23	274	0.56
4PBT-I-10-T4-4	29.19	29.26	14.06	302	0.59
4PBT-I-10-T4-5	29.14	29.07	13.82	350	0.68
4PBT-I-10-T4-6	29.13	29.19	14.23	253	0.51
4PBT-I-15-T4-1	28.89	29.11	14.14	358	0.73
4PBT-I-15-T4-2	28.88	28.83	13.92	261	0.53
4PBT-I-15-T4-3	29.17	29.20	14.26	266	0.54
4PBT-I-15-T4-4	29.02	29.07	14.13	289	0.59
4PBT-I-15-T4-5	29.48	29.19	14.15	299	0.59
4PBT-I-15-T4-6	29.11	29.13	14.29	282	0.58
4PBT-I-05-T2-1	29.37	29.45	14.48	357	0.71
4PBT-I-05-T2-2	29.73	29.85	15.23	257	0.53
4PBT-I-05-T2-3	29.90	30.01	16.39	147	0.34
4PBT-I-05-T2-4	29.51	29.58	14.68	204	0.41
4PBT-I-05-T2-5	29.32	29.37	14.42	161	0.32
4PBT-I-05-T2-6	29.71	29.65	16.23	224	0.53
4PBT-I-1-T2-1	29.68	29.74	15.04	322	0.66
4PBT-I-1-T2-2	29.60	29.39	15.34	162	0.36
4PBT-I-1-T2-3	29.60	29.59	15.39	246	0.53
4PBT-I-1-T2-4	29.88	30.44	15.72	254	0.52
4PBT-I-1-T2-5	29.93	29.71	15.41	189	0.40
4PBT-I-1-T2-6	29.61	29.68	15.46	189	0.41
4PBT-I-2-T2-1	29.48	29.38	15.71	238	0.55
4PBT-I-2-T2-2	29.66	29.62	15.90	215	0.49
4PBT-I-2-T2-3	29.72	29.71	15.89	148	0.33
4PBT-I-2-T2-4	29.19	29.51	15.84	178	0.42
4PBT-I-2-T2-5	29.38	29.45	15.78	173	0.40
4PBT-I-2-T2-6	29.25	29.19	15.47	179	0.41
4PBT-I-4-T2-1	29.19	29.18	15.23	236	0.53
4PBT-I-4-T2-2	29.30	29.34	15.72	193	0.45
4PBT-I-4-T2-3	29.25	29.16	15.21	122	0.27
4PBT-I-4-T2-4	29.60	29.78	16.28	200	0.47

4PBT-I-4-T2-5	29.57	29.58	15.46	186	0.41
4PBT-I-4-T2-6	29.10	29.13	16.43	103	0.27
4PBT-I-7-T2-1	29.06	28.79	13.69	202	0.40
4PBT-I-7-T2-2	28.92	28.97	13.72	136	0.27
4PBT-I-7-T2-3	28.95	28.86	13.66	213	0.42
4PBT-I-7-T2-4	29.15	29.21	14.34	303	0.61
4PBT-I-7-T2-5	28.72	28.82	13.75	142	0.29
4PBT-I-7-T2-6	28.92	28.83	13.68	163	0.32
4PBT-I-10-T2-1	29.01	29.10	14.00	168	0.34
4PBT-I-10-T2-2	29.05	29.10	14.05	217	0.43
4PBT-I-10-T2-3	28.97	28.90	13.90	214	0.43
4PBT-I-10-T2-4	29.17	29.19	14.17	284	0.57
4PBT-I-10-T2-5	29.08	29.04	13.94	270	0.54
4PBT-I-10-T2-6	29.82	30.07	14.95	195	0.38
4PBT-I-15-T2-1	29.10	29.10	14.13	193	0.39
4PBT-I-15-T2-2	29.00	29.06	14.06	277	0.56
4PBT-I-15-T2-3	29.77	30.05	15.03	172	0.34
4PBT-I-15-T2-4	28.85	28.80	13.83	190	0.38
4PBT-I-15-T2-5	29.07	29.12	13.97	163	0.32
4PBT-I-15-T2-6	28.98	28.71	14.16	200	0.42

Table A.3.-9. Mean geometric measurements (b: depth; h: height), failure load ($F_{failure}$) and tensile strength (σ_u) values obtained from the four-point bending tests for the Floresta sandstone (F) specimens without notches.

CODE	b (mm)	h (mm)	$F_{failure}$ (N)	σ_u (MPa)
4PBT-F-T1-1	29.61	29.69	878	5.04
4PBT-F-T1-2	29.67	29.53	772	4.48
4PBT-F-T1-3	30.18	29.70	976	5.50
4PBT-F-T1-4	29.86	29.72	921	5.24
4PBT-F-T3-1	29.77	29.78	1187	6.75
4PBT-F-T3-2	29.74	29.69	1120	6.41
4PBT-F-T3-3	29.61	29.69	868	4.99
4PBT-F-T3-4	29.72	29.69	1091	6.25
4PBT-F-T5-1	29.76	29.77	1059	6.02
4PBT-F-T5-2	29.82	29.78	1137	6.45
4PBT-F-T5-3	29.69	29.68	1020	5.85
4PBT-F-T5-4	29.69	29.67	706	4.05
4PBT-F-T4-1	29.74	29.72	982	5.61

4PBT-F-T4-2	29.71	29.67	1078	6.18
4PBT-F-T4-3	29.67	29.66	989	5.68
4PBT-F-T4-4	30.12	29.62	1147	6.51
4PBT-F-T6-1	29.73	29.72	1110	6.34
4PBT-F-T6-2	29.65	29.72	1058	6.06
4PBT-F-T6-3	29.73	29.68	1338	7.66
4PBT-F-T6-4	29.88	29.70	1228	6.99
4PBT-F-T2-1	29.71	29.65	1136	6.52
4PBT-F-T2-2	29.76	29.95	1118	6.28
4PBT-F-T2-3	29.79	29.82	1191	6.74
4PBT-F-T2-4	29.74	29.73	1072	6.11

Table A.3.-10. Mean geometric measurements (b: depth; h: height), failure load ($F_{failure}$) and tensile strength (σ_u) values obtained from the four-point bending tests for the Moleanos limestone (C) specimens without notches.

CODE	b (mm)	h (mm)	$F_{failure}$ (N)	σ_u (MPa)
4PBT-C-T1-1	30.23	30.05	1999	10.98
4PBT-C-T1-2	30.15	29.92	1629	9.05
4PBT-C-T1-3	29.67	29.54	1745	10.11
4PBT-C-T3-1	29.99	29.89	2155	12.07
4PBT-C-T3-2	30.07	29.92	2206	12.29
4PBT-C-T3-3	29.87	29.77	2293	12.99
4PBT-C-T5-1	30.07	29.90	2243	12.52
4PBT-C-T5-2	29.58	29.64	1957	11.30
4PBT-C-T5-3	30.19	29.91	2296	12.75
4PBT-C-T4-1	29.63	29.74	1731	9.90
4PBT-C-T4-2	29.75	29.66	2264	12.98
4PBT-C-T4-3	29.70	29.67	2422	13.89
4PBT-C-T6-1	29.54	29.68	-	-
4PBT-C-T6-2	29.85	29.84	2234	12.61
4PBT-C-T6-3	30.04	29.68	1949	11.04
4PBT-C-T2-1	29.94	30.27	2409	13.17
4PBT-C-T2-2	30.01	30.24	2234	12.21
4PBT-C-T2-3	29.63	29.62	1973	11.39

Table A.3.-11. Mean geometric measurements (b: depth; h: height), failure load ($F_{failure}$) and tensile strength (σ_u) values obtained from the four-point bending tests for the Macael marble (M) specimens without notches.

CODE	b (mm)	h (mm)	$F_{failure}$ (N)	σ_u (MPa)
4PBT-M-T1-1	30.00	29.54	2879	16.49
4PBT-M-T1-2	30.03	30.06	2976	16.45
4PBT-M-T1-3	30.01	29.96	3561	19.84
4PBT-M-T1-4	29.95	29.64	3040	17.33
4PBT-M-T3-1	29.93	29.93	3207	17.94
4PBT-M-T3-2	29.66	30.44	-	-
4PBT-M-T3-3	29.78	29.84	2606	14.74
4PBT-M-T3-4	29.85	29.86	2938	16.55
4PBT-M-T5-1	30.02	29.88	1864	10.43
4PBT-M-T5-2	29.75	29.83	1985	11.25
4PBT-M-T5-3	29.82	29.64	2466	14.12
4PBT-M-T5-4	29.38	29.86	1133	6.49
4PBT-M-T4-1	29.83	29.80	1397	7.91
4PBT-M-T4-2	29.75	29.82	1651	9.36
4PBT-M-T4-3	29.72	29.96	2082	11.70
4PBT-M-T4-4	29.89	29.91	1853	10.39
4PBT-M-T6-1	29.93	29.87	1769	9.94
4PBT-M-T6-2	29.73	29.75	1483	8.45
4PBT-M-T6-3	30.01	30.02	1989	11.03
4PBT-M-T6-4	29.94	29.95	1708	9.54
4PBT-M-T2-1	29.86	29.86	1376	7.75
4PBT-M-T2-2	29.85	29.95	1620	9.08
4PBT-M-T2-3	30.13	30.04	1360	7.50
4PBT-M-T2-4	29.87	29.73	-	-

Table A.3.-12. Mean geometric measurements (b: depth; h: height), failure load ($F_{failure}$) and tensile strength (σ_u) values obtained from the four-point bending tests for the Carrara marble (I) specimens without notches.

CODE	b (mm)	h (mm)	$F_{failure}$ (N)	σ_u (MPa)
4PBT-I-T1-1	29.94	29.70	2285	12.98
4PBT-I-T1-2	29.76	29.55	2268	13.09
4PBT-I-T1-3	29.47	29.52	1944	11.35
4PBT-I-T1-4	29.70	29.65	2058	11.82

4PBT-I-T3-1	29.59	29.66	1682	9.69
4PBT-I-T3-2	29.79	29.39	1746	10.18
4PBT-I-T3-3	29.95	29.65	1763	10.04
4PBT-I-T3-4	29.52	29.42	1420	8.33
4PBT-I-T5-1	29.29	29.18	1020	6.13
4PBT-I-T5-2	29.24	29.47	1085	6.41
4PBT-I-T5-3	29.24	29.49	1136	6.70
4PBT-I-T5-4	29.71	29.78	1021	5.81
4PBT-I-T4-1	29.93	30.10	743	4.11
4PBT-I-T4-2	30.16	29.63	-	-
4PBT-I-T4-3	29.69	29.50	929	5.39
4PBT-I-T4-4	29.70	29.44	771	4.50
4PBT-I-T6-1	29.78	29.89	875	4.93
4PBT-I-T6-2	29.71	29.75	1129	6.44
4PBT-I-T6-3	29.34	29.40	984	5.82
4PBT-I-T6-4	29.59	29.66	955	5.50
4PBT-I-T2-1	29.59	29.80	660	3.77
4PBT-I-T2-2	29.74	29.45	1028	5.98
4PBT-I-T2-3	30.03	29.76	875	4.94
4PBT-I-T2-4	29.52	29.61	1056	6.12

- Appendix A.4. -
Three-point bending test results

Appendix A.4.
Three-point bending test results

Table A.4.-1. Mean geometric measurements (b: depth; h: height; a: notch length), failure load ($F_{failure}$) and fracture toughness (K_{IC}) results obtained from the three-point bending tests with the centred load (P1) for the Moleanos limestone (C2) specimens (coming from a second delivery) with the smallest notch radius (ρ = 0.15 mm).

CODE	b (mm)	h (mm)	a (mm)	$F_{failure}$ (N)	K_{IC} (MPa · m$^{1/2}$)
3PBT-C2-015-T1-P1-1	29.90	30.55	14.65	322	0.76
3PBT-C2-015-T1-P1-2	29.85	29.82	14.42	282	0.70
3PBT-C2-015-T1-P1-3	30.28	29.81	13.93	342	0.79
3PBT-C2-015-T1-P1-4	29.78	29.97	14.70	300	0.75
3PBT-C2-015-T1-P1-5	29.82	30.30	15.03	311	0.78
3PBT-C2-015-T1-P1-6	29.93	30.50	14.49	364	0.84
3PBT-C2-015-T2-P1-1	29.76	29.60	14.44	307	0.78
3PBT-C2-015-T2-P1-2	29.82	29.54	14.02	435	1.06
3PBT-C2-015-T2-P1-3	29.89	29.91	14.83	426	1.09
3PBT-C2-015-T2-P1-4	29.52	29.34	13.88	469	1.16
3PBT-C2-015-T2-P1-5	29.86	29.25	14.45	431	1.13
3PBT-C2-015-T2-P1-6	29.62	29.67	14.18	368	0.91

Table A.4.-2. Mean geometric measurements (b: depth; h: height; a: notch length), failure load ($F_{failure}$) and apparent fracture toughness (K_{IN}) results obtained from the three-point bending tests with the centred load (P1) for the Moleanos limestone (C2) specimens (coming from a second delivery) with different notch radii.

CODE	b (mm)	h (mm)	a (mm)	$F_{failure}$ (N)	K_{IN} (MPa · m$^{1/2}$)
3PBT-C2-05-T1-P1-1	29.87	30.37	15.51	318	0.83
3PBT-C2-05-T1-P1-2	29.52	30.24	15.70	296	0.81
3PBT-C2-05-T1-P1-3	29.58	30.02	15.74	262	0.74
3PBT-C2-05-T1-P1-4	29.66	30.40	16.02	295	0.82
3PBT-C2-05-T1-P1-5	29.86	30.28	16.23	292	0.83
3PBT-C2-05-T1-P1-6	29.22	30.09	15.62	268	0.75
3PBT-C2-1-T1-P1-1	29.73	29.75	13.77	316	0.74
3PBT-C2-1-T1-P1-2	30.22	30.06	13.89	389	0.88
3PBT-C2-1-T1-P1-3	29.25	29.30	13.29	339	0.80
3PBT-C2-1-T1-P1-4	29.35	29.61	13.36	341	0.78
3PBT-C2-1-T1-P1-5	29.85	29.71	13.88	338	0.80
3PBT-C2-1-T1-P1-6	29.75	29.72	14.35	303	0.75

3PBT-C2-2-T1-P1-1	29.92	29.79	12.73	409	0.85
3PBT-C2-2-T1-P1-2	29.78	29.90	13.33	362	0.80
3PBT-C2-2-T1-P1-3	30.50	29.65	13.09	395	0.85
3PBT-C2-2-T1-P1-4	30.40	29.71	12.92	400	0.84
3PBT-C2-2-T1-P1-5	29.82	29.79	13.65	334	0.76
3PBT-C2-2-T1-P1-6	29.84	30.14	12.96	397	0.82
3PBT-C2-4-T1-P1-1	29.84	29.53	14.85	317	0.84
3PBT-C2-4-T1-P1-2	29.51	29.57	14.67	336	0.88
3PBT-C2-4-T1-P1-3	29.69	29.87	15.06	311	0.82
3PBT-C2-4-T1-P1-4	29.64	29.68	14.93	382	1.02
3PBT-C2-4-T1-P1-5	29.72	29.66	14.84	289	0.76
3PBT-C2-4-T1-P1-6	29.56	30.18	15.31	338	0.89
3PBT-C2-7-T1-P1-1	29.88	29.97	14.99	340	0.88
3PBT-C2-7-T1-P1-2	29.87	29.97	14.93	360	0.92
3PBT-C2-7-T1-P1-3	29.34	29.47	14.46	332	0.87
3PBT-C2-7-T1-P1-4	29.35	29.52	14.48	330	0.86
3PBT-C2-7-T1-P1-5	29.84	29.99	14.89	364	0.93
3PBT-C2-7-T1-P1-6	29.55	30.00	15.09	352	0.92
3PBT-C2-10-T1-P1-1	29.65	29.66	15.00	302	0.81
3PBT-C2-10-T1-P1-2	29.95	29.49	14.90	294	0.79
3PBT-C2-10-T1-P1-3	29.57	30.03	15.33	340	0.91
3PBT-C2-10-T1-P1-4	30.01	30.16	13.99	358	0.81
3PBT-C2-10-T1-P1-5	30.16	29.76	14.93	330	0.86
3PBT-C2-10-T1-P1-6	29.77	29.46	14.62	311	0.81
3PBT-C2-15-T1-P1-1	29.86	29.85	15.08	350	0.92
3PBT-C2-15-T1-P1-2	29.76	29.85	15.16	354	0.94
3PBT-C2-15-T1-P1-3	29.87	29.63	15.14	341	0.93
3PBT-C2-15-T1-P1-4	29.90	29.53	14.74	362	0.95
3PBT-C2-15-T1-P1-5	29.41	29.78	15.12	361	0.98
3PBT-C2-15-T1-P1-6	29.91	29.86	15.12	359	0.95
3PBT-C2-05-T2-P1-1	29.47	29.80	14.99	475	1.26
3PBT-C2-05-T2-P1-2	29.71	29.77	15.51	413	1.16
3PBT-C2-05-T2-P1-3	29.98	29.65	15.59	390	1.11
3PBT-C2-05-T2-P1-4	29.97	30.51	15.63	347	0.90
3PBT-C2-05-T2-P1-5	29.15	30.47	15.92	307	0.85
3PBT-C2-05-T2-P1-6	29.98	29.81	15.10	251	0.66
3PBT-C2-1-T2-P1-1	29.53	29.43	13.87	375	0.92
3PBT-C2-1-T2-P1-2	29.93	30.03	14.15	389	0.91
3PBT-C2-1-T2-P1-3	30.35	29.94	14.08	501	1.16
3PBT-C2-1-T2-P1-4	29.98	30.49	14.60	411	0.96

3PBT-C2-1-T2-P1-5	29.78	29.86	14.06	521	1.24
3PBT-C2-1-T2-P1-6	30.15	30.01	14.12	538	1.25
3PBT-C2-2-T2-P1-1	30.10	30.00	13.97	515	1.18
3PBT-C2-2-T2-P1-2	29.38	29.54	12.70	548	1.19
3PBT-C2-2-T2-P1-3	30.32	29.78	12.95	482	1.01
3PBT-C2-2-T2-P1-4	30.00	29.71	12.94	467	1.00
3PBT-C2-2-T2-P1-5	29.86	30.05	13.40	575	1.25
3PBT-C2-2-T2-P1-6	29.61	29.92	14.06	477	1.13
3PBT-C2-4-T2-P1-1	30.28	29.99	14.16	471	1.10
3PBT-C2-4-T2-P1-2	30.29	29.91	14.32	398	0.95
3PBT-C2-4-T2-P1-3	30.10	29.35	13.73	641	1.53
3PBT-C2-4-T2-P1-4	30.42	29.45	13.69	555	1.29
3PBT-C2-4-T2-P1-5	29.91	29.40	13.64	563	1.33
3PBT-C2-4-T2-P1-6	29.97	29.39	13.66	498	1.18
3PBT-C2-7-T2-P1-1	29.43	29.62	14.86	536	1.43
3PBT-C2-7-T2-P1-2	29.42	29.71	14.95	461	1.23
3PBT-C2-7-T2-P1-3	29.30	29.62	14.77	447	1.19
3PBT-C2-7-T2-P1-4	29.62	30.06	15.31	433	1.15
3PBT-C2-7-T2-P1-5	29.75	29.73	15.39	520	1.44
3PBT-C2-7-T2-P1-6	29.62	29.30	14.54	371	0.99
3PBT-C2-10-T2-P1-1	29.75	29.56	14.67	571	1.49
3PBT-C2-10-T2-P1-2	29.61	29.82	15.15	466	1.25
3PBT-C2-10-T2-P1-3	30.50	30.07	15.43	471	1.23
3PBT-C2-10-T2-P1-4	29.48	29.56	14.67	327	0.86
3PBT-C2-10-T2-P1-5	29.95	29.44	14.57	616	1.60
3PBT-C2-10-T2-P1-6	29.64	29.48	14.60	489	1.28
3PBT-C2-15-T2-P1-1	29.95	29.91	15.33	577	1.55
3PBT-C2-15-T2-P1-2	30.09	30.02	15.37	-	-
3PBT-C2-15-T2-P1-3	29.78	29.94	15.26	565	1.51
3PBT-C2-15-T2-P1-4	30.01	29.70	15.18	420	1.13
3PBT-C2-15-T2-P1-5	29.98	29.56	15.13	508	1.38
3PBT-C2-15-T2-P1-6	30.11	29.40	14.40	-	-

Table A.4.-3. Mean geometric measurements (b: depth; h: height; a: notch length) and failure load ($F_{failure}$) results obtained from the three-point bending tests with $m = 4$ mm (P2) for the Moleanos limestone (C2) specimens (coming from a second delivery) with different notch radii.

CODE	b (mm)	h (mm)	a (mm)	$F_{failure}$ (N)
3PBT-C2-015-T1-P2-1	29.41	29.64	13.61	328
3PBT-C2-015-T1-P2-2	29.47	29.68	14.62	290
3PBT-C2-015-T1-P2-3	29.56	29.67	13.89	313
3PBT-C2-015-T1-P2-4	29.71	29.69	14.15	333
3PBT-C2-015-T1-P2-5	30.26	30.06	16.04	264
3PBT-C2-015-T1-P2-6	30.26	29.70	13.48	340
3PBT-C2-05-T1-P2-1	29.84	29.30	14.65	298
3PBT-C2-05-T1-P2-2	30.01	29.37	14.89	282
3PBT-C2-05-T1-P2-3	29.75	29.65	15.15	300
3PBT-C2-05-T1-P2-4	30.07	29.76	15.31	311
3PBT-C2-05-T1-P2-5	29.81	29.01	14.11	300
3PBT-C2-05-T1-P2-6	30.22	29.74	14.94	303
3PBT-C2-1-T1-P2-1	29.77	29.85	14.05	372
3PBT-C2-1-T1-P2-2	29.94	29.98	14.06	346
3PBT-C2-1-T1-P2-3	29.95	30.14	14.25	347
3PBT-C2-1-T1-P2-4	29.16	29.26	13.13	351
3PBT-C2-1-T1-P2-5	29.39	29.81	14.16	314
3PBT-C2-1-T1-P2-6	29.44	29.58	14.02	314
3PBT-C2-2-T1-P2-1	29.66	29.48	12.51	387
3PBT-C2-2-T1-P2-2	29.78	29.80	13.03	349
3PBT-C2-2-T1-P2-3	29.74	29.31	13.44	364
3PBT-C2-2-T1-P2-4	30.17	29.77	13.03	400
3PBT-C2-2-T1-P2-5	29.84	29.76	14.79	356
3PBT-C2-2-T1-P2-6	30.31	30.04	14.33	351
3PBT-C2-4-T1-P2-1	29.74	29.57	14.86	314
3PBT-C2-4-T1-P2-2	30.01	29.71	15.06	347
3PBT-C2-4-T1-P2-3	29.91	30.07	15.28	345
3PBT-C2-4-T1-P2-4	30.14	29.61	14.69	337
3PBT-C2-4-T1-P2-5	29.76	29.88	15.35	350
3PBT-C2-4-T1-P2-6	29.74	29.58	15.04	382
3PBT-C2-7-T1-P2-1	29.76	30.06	15.49	327
3PBT-C2-7-T1-P2-2	29.89	30.06	15.31	309
3PBT-C2-7-T1-P2-3	29.71	30.06	15.32	268
3PBT-C2-7-T1-P2-4	29.83	30.04	15.49	363

3PBT-C2-7-T1-P2-5	29.51	29.91	14.98	361
3PBT-C2-7-T1-P2-6	29.61	29.78	14.82	361
3PBT-C2-10-T1-P2-1	29.73	29.97	15.29	308
3PBT-C2-10-T1-P2-2	29.92	29.76	15.30	316
3PBT-C2-10-T1-P2-3	29.84	29.94	15.20	326
3PBT-C2-10-T1-P2-4	29.95	29.88	15.12	335
3PBT-C2-10-T1-P2-5	29.68	29.69	14.94	333
3PBT-C2-10-T1-P2-6	29.87	29.81	15.06	390
3PBT-C2-15-T1-P2-1	29.43	29.83	15.38	361
3PBT-C2-15-T1-P2-2	30.15	29.38	14.84	398
3PBT-C2-15-T1-P2-3	29.62	29.85	15.07	375
3PBT-C2-15-T1-P2-4	30.35	29.88	15.49	270
3PBT-C2-15-T1-P2-5	30.12	29.60	14.77	323
3PBT-C2-15-T1-P2-6	29.53	29.59	14.92	362
3PBT-C2-015-T2-P2-1	29.72	29.26	14.73	416
3PBT-C2-015-T2-P2-2	29.95	30.26	16.27	357
3PBT-C2-015-T2-P2-3	29.64	29.56	13.09	441
3PBT-C2-015-T2-P2-4	29.52	29.67	13.97	469
3PBT-C2-015-T2-P2-5	29.76	30.59	14.75	446
3PBT-C2-015-T2-P2-6	30.03	29.81	14.27	483
3PBT-C2-05-T2-P2-1	29.84	29.75	15.08	384
3PBT-C2-05-T2-P2-2	30.60	29.68	15.74	376
3PBT-C2-05-T2-P2-3	29.56	29.46	15.62	247
3PBT-C2-05-T2-P2-4	30.06	29.75	15.18	240
3PBT-C2-05-T2-P2-5	29.33	29.70	15.02	418
3PBT-C2-05-T2-P2-6	29.77	30.15	15.27	408
3PBT-C2-1-T2-P2-1	29.80	29.81	14.23	-
3PBT-C2-1-T2-P2-2	30.31	29.19	13.61	491
3PBT-C2-1-T2-P2-3	30.04	29.56	14.05	399
3PBT-C2-1-T2-P2-4	29.51	29.38	13.48	501
3PBT-C2-1-T2-P2-5	29.40	29.50	14.10	398
3PBT-C2-1-T2-P2-6	29.47	29.35	13.74	444
3PBT-C2-2-T2-P2-1	29.63	29.66	14.61	427
3PBT-C2-2-T2-P2-2	29.81	29.89	14.07	451
3PBT-C2-2-T2-P2-3	29.62	30.04	14.71	438
3PBT-C2-2-T2-P2-4	30.38	29.31	12.69	545
3PBT-C2-2-T2-P2-5	30.41	29.58	13.91	508
3PBT-C2-2-T2-P2-6	30.06	30.01	14.29	474
3PBT-C2-4-T2-P2-1	29.87	29.64	14.08	344
3PBT-C2-4-T2-P2-2	29.66	30.00	14.58	325

3PBT-C2-4-T2-P2-3	30.05	30.27	14.93	542
3PBT-C2-4-T2-P2-4	29.37	29.89	14.42	449
3PBT-C2-4-T2-P2-5	30.89	29.82	14.20	610
3PBT-C2-4-T2-P2-6	30.25	29.85	14.20	304
3PBT-C2-7-T2-P2-1	29.85	29.54	14.72	556
3PBT-C2-7-T2-P2-2	29.67	29.91	15.17	450
3PBT-C2-7-T2-P2-3	29.63	30.05	15.31	602
3PBT-C2-7-T2-P2-4	30.02	29.60	14.91	576
3PBT-C2-7-T2-P2-5	29.91	29.70	15.09	430
3PBT-C2-7-T2-P2-6	29.88	29.61	14.90	490
3PBT-C2-10-T2-P2-1	29.91	29.65	14.92	477
3PBT-C2-10-T2-P2-2	29.96	29.55	14.85	504
3PBT-C2-10-T2-P2-3	29.88	29.48	14.79	596
3PBT-C2-10-T2-P2-4	29.89	29.62	15.01	369
3PBT-C2-10-T2-P2-5	29.87	29.84	15.23	409
3PBT-C2-10-T2-P2-6	29.85	29.62	14.94	463
3PBT-C2-15-T2-P2-1	29.26	30.13	15.57	387
3PBT-C2-15-T2-P2-2	29.74	29.98	15.32	500
3PBT-C2-15-T2-P2-3	29.96	30.37	15.99	369
3PBT-C2-15-T2-P2-4	29.40	29.90	15.36	468
3PBT-C2-15-T2-P2-5	30.29	29.43	14.91	529
3PBT-C2-15-T2-P2-6	30.19	29.46	14.90	512

Table A.4.-4. Mean geometric measurements (b: depth; h: height; a: notch length) and failure load ($F_{failure}$) results obtained from the three-point bending tests with $m = 8$ mm (P3) for the Moleanos limestone (C2) specimens (coming from a second delivery) with different notch radii.

CODE	b (mm)	h (mm)	a (mm)	$F_{failure}$ (N)
3PBT-C2-015-T1-P3-1	29.66	29.68	11.53	411
3PBT-C2-015-T1-P3-2	29.92	29.78	13.58	370
3PBT-C2-015-T1-P3-3	29.90	30.29	15.52	303
3PBT-C2-015-T1-P3-4	29.95	29.67	12.99	389
3PBT-C2-015-T1-P3-5	29.48	29.55	14.58	292
3PBT-C2-015-T1-P3-6	30.17	29.76	14.35	318
3PBT-C2-05-T1-P3-1	29.81	30.15	15.84	301
3PBT-C2-05-T1-P3-2	29.17	30.37	15.46	301
3PBT-C2-05-T1-P3-3	30.30	29.66	15.09	287
3PBT-C2-05-T1-P3-4	29.70	30.13	16.12	298

3PBT-C2-05-T1-P3-5	29.38	29.90	14.96	286
3PBT-C2-05-T1-P3-6	29.91	29.93	14.99	298
3PBT-C2-1-T1-P3-1	29.54	29.33	13.52	353
3PBT-C2-1-T1-P3-2	29.31	29.65	13.77	266
3PBT-C2-1-T1-P3-3	30.00	30.08	14.15	373
3PBT-C2-1-T1-P3-4	29.03	29.10	13.00	311
3PBT-C2-1-T1-P3-5	30.08	30.15	14.06	415
3PBT-C2-1-T1-P3-6	29.61	29.39	13.74	323
3PBT-C2-2-T1-P3-1	30.06	29.70	12.78	391
3PBT-C2-2-T1-P3-2	29.35	29.39	12.71	373
3PBT-C2-2-T1-P3-3	29.47	30.10	13.66	369
3PBT-C2-2-T1-P3-4	30.01	29.35	12.20	378
3PBT-C2-2-T1-P3-5	29.96	30.09	14.63	370
3PBT-C2-2-T1-P3-6	29.64	30.53	15.13	342
3PBT-C2-4-T1-P3-1	29.78	29.52	14.88	326
3PBT-C2-4-T1-P3-2	29.56	29.79	15.38	296
3PBT-C2-4-T1-P3-3	29.81	29.99	15.39	341
3PBT-C2-4-T1-P3-4	30.08	29.76	15.12	334
3PBT-C2-4-T1-P3-5	29.90	30.22	15.70	328
3PBT-C2-4-T1-P3-6	29.54	29.71	15.47	314
3PBT-C2-7-T1-P3-1	29.85	30.11	15.44	387
3PBT-C2-7-T1-P3-2	29.91	29.97	15.21	348
3PBT-C2-7-T1-P3-3	29.65	29.70	14.89	376
3PBT-C2-7-T1-P3-4	29.75	30.16	15.60	353
3PBT-C2-7-T1-P3-5	29.54	30.07	15.53	347
3PBT-C2-7-T1-P3-6	29.99	29.80	15.09	263
3PBT-C2-10-T1-P3-1	29.80	29.74	15.07	295
3PBT-C2-10-T1-P3-2	29.57	30.01	15.40	305
3PBT-C2-10-T1-P3-3	29.78	29.80	15.09	358
3PBT-C2-10-T1-P3-4	29.80	29.69	15.04	295
3PBT-C2-10-T1-P3-5	29.98	29.88	15.23	320
3PBT-C2-10-T1-P3-6	29.99	29.92	15.27	303
3PBT-C2-15-T1-P3-1	30.13	29.66	15.05	358
3PBT-C2-15-T1-P3-2	29.80	29.89	15.34	384
3PBT-C2-15-T1-P3-3	30.25	29.63	15.03	372
3PBT-C2-15-T1-P3-4	29.92	29.72	15.43	352
3PBT-C2-15-T1-P3-5	30.09	30.05	15.51	389
3PBT-C2-15-T1-P3-6	30.29	29.45	14.74	395
3PBT-C2-015-T2-P3-1	29.95	30.18	14.49	472
3PBT-C2-015-T2-P3-2	30.10	30.04	14.59	542

3PBT-C2-015-T2-P3-3	29.24	29.28	12.21	591
3PBT-C2-015-T2-P3-4	29.79	29.82	14.15	509
3PBT-C2-015-T2-P3-5	29.49	29.77	14.46	530
3PBT-C2-015-T2-P3-6	29.89	30.33	14.93	480
3PBT-C2-05-T2-P3-1	29.91	29.73	15.24	437
3PBT-C2-05-T2-P3-2	29.81	30.07	16.10	442
3PBT-C2-05-T2-P3-3	29.87	29.55	14.73	487
3PBT-C2-05-T2-P3-4	29.32	29.32	15.02	345
3PBT-C2-05-T2-P3-5	29.66	29.57	15.08	451
3PBT-C2-05-T2-P3-6	30.72	29.88	15.43	475
3PBT-C2-1-T2-P3-1	29.41	29.58	13.59	477
3PBT-C2-1-T2-P3-2	29.78	29.62	13.57	484
3PBT-C2-1-T2-P3-3	29.68	29.80	13.83	470
3PBT-C2-1-T2-P3-4	29.40	29.46	13.40	493
3PBT-C2-1-T2-P3-5	29.40	29.33	13.07	546
3PBT-C2-1-T2-P3-6	29.65	29.94	13.86	485
3PBT-C2-2-T2-P3-1	29.34	29.80	13.34	629
3PBT-C2-2-T2-P3-2	30.02	30.07	13.50	507
3PBT-C2-2-T2-P3-3	29.37	29.53	13.05	-
3PBT-C2-2-T2-P3-4	30.05	29.93	13.51	596
3PBT-C2-2-T2-P3-5	29.86	29.73	12.91	393
3PBT-C2-2-T2-P3-6	29.91	29.43	12.62	585
3PBT-C2-4-T2-P3-1	29.54	29.84	14.34	442
3PBT-C2-4-T2-P3-2	29.79	30.20	14.63	511
3PBT-C2-4-T2-P3-3	29.78	30.15	14.46	463
3PBT-C2-4-T2-P3-4	30.12	29.70	14.09	568
3PBT-C2-4-T2-P3-5	30.07	29.62	13.95	573
3PBT-C2-4-T2-P3-6	29.88	29.93	14.58	519
3PBT-C2-7-T2-P3-1	29.68	29.80	15.04	472
3PBT-C2-7-T2-P3-2	29.60	29.74	14.84	483
3PBT-C2-7-T2-P3-3	29.38	29.73	14.68	352
3PBT-C2-7-T2-P3-4	29.42	29.65	14.57	468
3PBT-C2-7-T2-P3-5	29.91	29.86	14.82	566
3PBT-C2-7-T2-P3-6	29.90	29.86	14.90	595
3PBT-C2-10-T2-P3-1	29.89	29.67	14.91	547
3PBT-C2-10-T2-P3-2	29.90	29.71	14.79	495
3PBT-C2-10-T2-P3-3	29.95	29.76	14.91	387
3PBT-C2-10-T2-P3-4	29.52	29.28	14.67	487
3PBT-C2-10-T2-P3-5	29.72	30.02	15.39	564
3PBT-C2-10-T2-P3-6	29.85	30.01	15.38	414

3PBT-C2-15-T2-P3-1	29.74	29.65	15.27	361
3PBT-C2-15-T2-P3-2	29.75	29.71	15.23	423
3PBT-C2-15-T2-P3-3	29.70	29.88	15.43	464
3PBT-C2-15-T2-P3-4	29.69	30.02	15.49	471
3PBT-C2-15-T2-P3-5	30.20	30.27	15.74	549
3PBT-C2-15-T2-P3-6	30.04	29.93	15.42	531

Table A.4.-5. Mean geometric measurements (b: depth; h: height; a: notch length) and failure load ($F_{failure}$) results obtained from the three-point bending tests with $m = 12$ mm (P4) for the Moleanos limestone (C2) specimens (coming from a second delivery) with different notch radii.

CODE	b (mm)	h (mm)	a (mm)	$F_{failure}$ (N)
3PBT-C2-015-T1-P4-1	30.15	29.66	12.89	400
3PBT-C2-015-T1-P4-2	29.65	29.70	13.79	356
3PBT-C2-015-T1-P4-3	29.82	29.85	13.91	365
3PBT-C2-015-T1-P4-4	30.95	29.56	13.47	404
3PBT-C2-015-T1-P4-5	30.77	29.58	13.63	407
3PBT-C2-015-T1-P4-6	30.01	29.52	13.36	375
3PBT-C2-05-T1-P4-1	29.54	29.76	13.37	400
3PBT-C2-05-T1-P4-2	29.57	29.46	14.62	309
3PBT-C2-05-T1-P4-3	29.94	29.34	14.57	345
3PBT-C2-05-T1-P4-4	29.47	29.51	14.90	305
3PBT-C2-05-T1-P4-5	29.84	29.45	14.89	318
3PBT-C2-05-T1-P4-6	29.74	29.52	15.21	343
3PBT-C2-1-T1-P4-1	29.73	30.39	14.75	353
3PBT-C2-1-T1-P4-2	29.88	30.43	14.91	214
3PBT-C2-1-T1-P4-3	29.31	30.39	14.50	345
3PBT-C2-1-T1-P4-4	29.79	29.88	14.04	434
3PBT-C2-1-T1-P4-5	30.05	30.31	14.33	392
3PBT-C2-1-T1-P4-6	29.74	29.43	13.82	372
3PBT-C2-2-T1-P4-1	29.97	29.64	14.93	333
3PBT-C2-2-T1-P4-2	30.01	29.81	13.19	403
3PBT-C2-2-T1-P4-3	30.21	29.97	13.82	410
3PBT-C2-2-T1-P4-4	29.92	30.38	13.10	458
3PBT-C2-2-T1-P4-5	29.66	29.93	13.11	404
3PBT-C2-2-T1-P4-6	30.26	29.86	13.39	419
3PBT-C2-4-T1-P4-1	29.83	29.59	14.89	368
3PBT-C2-4-T1-P4-2	29.71	29.65	14.91	345

3PBT-C2-4-T1-P4-3	29.62	30.30	15.36	370
3PBT-C2-4-T1-P4-4	29.76	29.63	14.71	343
3PBT-C2-4-T1-P4-5	29.40	29.60	15.10	310
3PBT-C2-4-T1-P4-6	30.23	29.87	15.24	373
3PBT-C2-7-T1-P4-1	30.11	29.72	15.22	319
3PBT-C2-7-T1-P4-2	29.55	30.06	15.09	426
3PBT-C2-7-T1-P4-3	29.88	29.93	15.04	443
3PBT-C2-7-T1-P4-4	29.68	30.05	15.16	415
3PBT-C2-7-T1-P4-5	29.67	29.83	14.96	377
3PBT-C2-7-T1-P4-6	29.51	29.52	14.56	396
3PBT-C2-10-T1-P4-1	29.51	29.70	15.18	299
3PBT-C2-10-T1-P4-2	29.59	29.71	15.14	350
3PBT-C2-10-T1-P4-3	29.76	29.62	15.00	276
3PBT-C2-10-T1-P4-4	29.96	29.93	15.22	331
3PBT-C2-10-T1-P4-5	29.54	29.77	15.45	343
3PBT-C2-10-T1-P4-6	29.60	29.71	15.18	313
3PBT-C2-15-T1-P4-1	30.17	29.02	14.50	395
3PBT-C2-15-T1-P4-2	30.29	29.24	14.61	381
3PBT-C2-15-T1-P4-3	30.04	29.42	14.85	391
3PBT-C2-15-T1-P4-4	30.22	29.41	14.68	383
3PBT-C2-15-T1-P4-5	30.15	29.39	14.84	397
3PBT-C2-15-T1-P4-6	30.09	29.17	14.69	385
3PBT-C2-015-T2-P4-1	29.68	29.41	13.18	505
3PBT-C2-015-T2-P4-2	29.95	30.57	15.15	566
3PBT-C2-015-T2-P4-3	83.98	29.74	13.78	555
3PBT-C2-015-T2-P4-4	29.75	30.43	14.02	622
3PBT-C2-015-T2-P4-5	29.50	29.77	14.60	427
3PBT-C2-015-T2-P4-6	29.92	29.89	14.67	480
3PBT-C2-05-T2-P4-1	30.09	30.38	13.63	637
3PBT-C2-05-T2-P4-2	29.28	29.85	12.54	615
3PBT-C2-05-T2-P4-3	29.61	29.91	12.66	581
3PBT-C2-05-T2-P4-4	29.51	29.76	12.87	487
3PBT-C2-05-T2-P4-5	29.66	30.10	13.86	520
3PBT-C2-05-T2-P4-6	29.72	30.20	13.85	551
3PBT-C2-1-T2-P4-1	29.72	30.04	14.68	484
3PBT-C2-1-T2-P4-2	29.69	29.92	13.99	541
3PBT-C2-1-T2-P4-3	29.84	29.86	14.25	546
3PBT-C2-1-T2-P4-4	30.04	30.06	14.27	587
3PBT-C2-1-T2-P4-5	30.47	29.99	13.77	503
3PBT-C2-1-T2-P4-6	29.25	30.42	14.40	547

3PBT-C2-2-T2-P4-1	29.27	29.70	13.02	516
3PBT-C2-2-T2-P4-2	29.68	29.31	12.94	507
3PBT-C2-2-T2-P4-3	29.67	29.54	12.74	-
3PBT-C2-2-T2-P4-4	29.89	29.90	14.02	562
3PBT-C2-2-T2-P4-5	29.97	29.83	13.79	491
3PBT-C2-2-T2-P4-6	30.39	29.68	14.16	576
3PBT-C2-4-T2-P4-1	30.07	29.77	14.19	523
3PBT-C2-4-T2-P4-2	29.81	30.03	14.59	582
3PBT-C2-4-T2-P4-3	29.73	29.93	14.33	-
3PBT-C2-4-T2-P4-4	29.80	29.84	14.20	545
3PBT-C2-4-T2-P4-5	29.66	29.73	14.25	593
3PBT-C2-4-T2-P4-6	29.61	29.69	14.22	503
3PBT-C2-7-T2-P4-1	29.69	29.72	14.79	483
3PBT-C2-7-T2-P4-2	29.59	29.83	14.88	498
3PBT-C2-7-T2-P4-3	29.79	29.88	14.92	474
3PBT-C2-7-T2-P4-4	29.46	29.77	14.92	484
3PBT-C2-7-T2-P4-5	29.95	29.78	14.90	519
3PBT-C2-7-T2-P4-6	30.00	30.05	15.08	495
3PBT-C2-10-T2-P4-1	30.15	30.07	15.79	594
3PBT-C2-10-T2-P4-2	29.98	29.99	15.19	365
3PBT-C2-10-T2-P4-3	30.07	30.03	15.28	534
3PBT-C2-10-T2-P4-4	30.21	30.04	15.28	582
3PBT-C2-10-T2-P4-5	30.33	29.81	15.07	521
3PBT-C2-10-T2-P4-6	29.87	29.96	15.33	440
3PBT-C2-15-T2-P4-1	29.88	29.48	14.74	446
3PBT-C2-15-T2-P4-2	29.86	29.90	15.13	735
3PBT-C2-15-T2-P4-3	30.18	29.51	14.78	599
3PBT-C2-15-T2-P4-4	30.21	29.61	15.05	573
3PBT-C2-15-T2-P4-5	29.64	29.88	15.38	397
3PBT-C2-15-T2-P4-6	29.94	29.98	15.30	594

Table A.4.-6. Mean geometric measurements (b: depth; h: height), failure load ($F_{failure}$) and tensile strength (σ_u) results obtained from the three-point bending tests for the Floresta sandstone (F) specimens without notches.

CODE	b (mm)	h (mm)	$F_{failure}$ (N)	σ_u (MPa)
3PBT-F-T1-1	29.81	29.76	639	5.44
3PBT-F-T1-2	29.70	29.75	641	5.49

Table A.4.-7. Mean geometric measurements (b: depth; h: height), failure load ($F_{failure}$) and tensile strength (σ_u) results obtained from the three-point bending tests for the Moleanos limestone (C) specimens without notches.

CODE	b (mm)	h (mm)	$F_{failure}$ (N)	σ_u (MPa)
3PBT-C-T1-1	29.82	30.28	1316	10.83
3PBT-C-T1-2	29.90	29.99	1098	9.18
3PBT-C-T1-3	29.91	30.15	1151	9.52

Table A.4.-8. Mean geometric measurements (b: depth; h: height), failure load ($F_{failure}$) and tensile strength (σ_u) results obtained from the three-point bending tests for the Macael marble (M) specimens without notches.

CODE	b (mm)	h (mm)	$F_{failure}$ (N)	σ_u (MPa)
3PBT-M-T1-1	29.87	29.78	1294	10.99
3PBT-M-T1-2	29.80	29.59	1886	16.26
3PBT-M-T1-3	30.04	30.01	2061	17.14
3PBT-M-T1-4	29.68	29.76	1329	11.37

Table A.4.-9. Mean geometric measurements (b: depth; h: height), failure load ($F_{failure}$) and tensile strength (σ_u) results obtained from the three-point bending tests for the Carrara marble (I) specimens without notches.

CODE	b (mm)	h (mm)	$F_{failure}$ (N)	σ_u (MPa)
3PBT-I-T1-1	29.46	29.40	866	7.66
3PBT-I-T1-2	29.77	29.77	1227	10.46

- Appendix A.5. -
Thermal expansion measurements

Table A.5.-1. Digital comparator readings of the Floresta sandstone (F): Sample nº1.

CODE	Length (mm)	CODE	Length (mm)
DCM-F-23-1-1	7.87	DCM-F-130-1-1	8.03
DCM-F-23-1-2	8.00	DCM-F-130-1-2	8.16
DCM-F-23-1-3	8.01	DCM-F-130-1-3	8.16
DCM-F-23-1-4	7.88	DCM-F-130-1-4	8.02
DCM-F-23-1-5	7.95	DCM-F-130-1-5	8.10
DCM-F-40-1-1	7.91	DCM-F-150-1-1	8.07
DCM-F-40-1-2	8.05	DCM-F-150-1-2	8.21
DCM-F-40-1-3	8.05	DCM-F-150-1-3	8.20
DCM-F-40-1-4	7.93	DCM-F-150-1-4	8.07
DCM-F-40-1-5	7.99	DCM-F-150-1-5	8.14
DCM-F-50-1-1	7.96	DCM-F-175-1-1	8.12
DCM-F-50-1-2	8.06	DCM-F-175-1-2	8.24
DCM-F-50-1-3	8.06	DCM-F-175-1-3	8.25
DCM-F-50-1-4	7.94	DCM-F-175-1-4	8.12
DCM-F-50-1-5	8.01	DCM-F-175-1-5	8.19
DCM-F-90-1-1	7.97	DCM-F-225-1-1	8.18
DCM-F-90-1-2	8.09	DCM-F-225-1-2	8.32
DCM-F-90-1-3	8.09	DCM-F-225-1-3	8.32
DCM-F-90-1-4	7.95	DCM-F-225-1-4	8.17
DCM-F-90-1-5	8.02	DCM-F-225-1-5	8.26
DCM-F-110-1-1	7.98	DCM-F-250-1-1	8.17
DCM-F-110-1-2	8.11	DCM-F-250-1-2	8.32
DCM-F-110-1-3	8.12	DCM-F-250-1-3	8.35
DCM-F-110-1-4	7.99	DCM-F-250-1-4	8.19
DCM-F-110-1-5	8.05	DCM-F-250-1-5	8.3

Table A.5.-2. Digital comparator readings of the Floresta sandstone (F): Sample nº2.

CODE	Length (mm)	CODE	Length (mm)
DCM-F-23-2-1	7.77	DCM-F-130-2-1	7.93
DCM-F-23-2-2	7.76	DCM-F-130-2-2	7.91
DCM-F-23-2-3	7.89	DCM-F-130-2-3	8.03
DCM-F-23-2-4	7.91	DCM-F-130-2-4	8.05
DCM-F-23-2-5	7.82	DCM-F-130-2-5	7.97
DCM-F-40-2-1	7.82	DCM-F-150-2-1	7.98
DCM-F-40-2-2	7.81	DCM-F-150-2-2	7.97

DCM-F-40-2-3	7.93	DCM-F-150-2-3	8.08
DCM-F-40-2-4	7.95	DCM-F-150-2-4	8.11
DCM-F-40-2-5	7.87	DCM-F-150-2-5	8.01
DCM-F-50-2-1	7.84	DCM-F-175-2-1	8.03
DCM-F-50-2-2	7.81	DCM-F-175-2-2	8.01
DCM-F-50-2-3	7.94	DCM-F-175-2-3	8.12
DCM-F-50-2-4	7.97	DCM-F-175-2-4	8.13
DCM-F-50-2-5	7.88	DCM-F-175-2-5	8.05
DCM-F-90-2-1	7.86	DCM-F-225-2-1	8.09
DCM-F-90-2-2	7.84	DCM-F-225-2-2	8.08
DCM-F-90-2-3	7.96	DCM-F-225-2-3	8.20
DCM-F-90-2-4	7.93	DCM-F-225-2-4	8.22
DCM-F-90-2-5	7.89	DCM-F-225-2-5	8.11
DCM-F-110-2-1	7.90	DCM-F-250-2-1	8.15
DCM-F-110-2-2	7.88	DCM-F-250-2-2	8.14
DCM-F-110-2-3	7.99	DCM-F-250-2-3	8.22
DCM-F-110-2-4	8.02	DCM-F-250-2-4	8.24
DCM-F-110-2-5	7.94	DCM-F-250-2-5	8.16

Table A.5.-3. Digital comparator readings of the Floresta sandstone (F): Sample nº3.

CODE	Length (mm)	CODE	Length (mm)
DCM-F-23-3-1	7.82	DCM-F-130-3-1	7.98
DCM-F-23-3-2	7.96	DCM-F-130-3-2	8.09
DCM-F-23-3-3	7.96	DCM-F-130-3-3	8.07
DCM-F-23-3-4	7.80	DCM-F-130-3-4	7.93
DCM-F-23-3-5	7.91	DCM-F-130-3-5	8.05
DCM-F-40-3-1	7.88	DCM-F-150-3-1	8.03
DCM-F-40-3-2	7.99	DCM-F-150-3-2	8.14
DCM-F-40-3-3	7.99	DCM-F-150-3-3	8.14
DCM-F-40-3-4	7.86	DCM-F-150-3-4	7.99
DCM-F-40-3-5	7.95	DCM-F-150-3-5	8.09
DCM-F-50-3-1	7.92	DCM-F-175-3-1	8.07
DCM-F-50-3-2	8.01	DCM-F-175-3-2	8.19
DCM-F-50-3-3	8.00	DCM-F-175-3-3	8.17
DCM-F-50-3-4	7.88	DCM-F-175-3-4	8.03
DCM-F-50-3-5	7.97	DCM-F-175-3-5	8.12
DCM-F-90-3-1	7.91	DCM-F-225-3-1	8.14
DCM-F-90-3-2	8.03	DCM-F-225-3-2	8.27

DCM-F-90-3-3	8.03	DCM-F-225-3-3	8.27
DCM-F-90-3-4	7.87	DCM-F-225-3-4	8.13
DCM-F-90-3-5	7.99	DCM-F-225-3-5	8.20
DCM-F-110-3-1	7.95	DCM-F-250-3-1	8.15
DCM-F-110-3-2	8.06	DCM-F-250-3-2	8.25
DCM-F-110-3-3	8.05	DCM-F-250-3-3	8.26
DCM-F-110-3-4	7.92	DCM-F-250-3-4	8.15
DCM-F-110-3-5	8.02	DCM-F-250-3-5	8.20

Table A.5.-4. Digital comparator readings of the Floresta sandstone (F): Sample nº4.

CODE	Length (mm)	CODE	Length (mm)
DCM-F-23-4-1	7.67	DCM-F-130-4-1	7.81
DCM-F-23-4-2	7.64	DCM-F-130-4-2	7.79
DCM-F-23-4-3	7.69	DCM-F-130-4-3	7.81
DCM-F-23-4-4	7.75	DCM-F-130-4-4	7.88
DCM-F-23-4-5	7.64	DCM-F-130-4-5	7.80
DCM-F-40-4-1	7.72	DCM-F-150-4-1	7.87
DCM-F-40-4-2	7.68	DCM-F-150-4-2	7.83
DCM-F-40-4-3	7.71	DCM-F-150-4-3	7.87
DCM-F-40-4-4	7.79	DCM-F-150-4-4	7.93
DCM-F-40-4-5	7.71	DCM-F-150-4-5	7.93
DCM-F-50-4-1	7.73	DCM-F-175-4-1	7.92
DCM-F-50-4-2	7.69	DCM-F-175-4-2	7.90
DCM-F-50-4-3	7.73	DCM-F-175-4-3	7.92
DCM-F-50-4-4	7.80	DCM-F-175-4-4	7.98
DCM-F-50-4-5	7.72	DCM-F-175-4-5	7.89
DCM-F-90-4-1	7.77	DCM-F-225-4-1	8.02
DCM-F-90-4-2	7.71	DCM-F-225-4-2	7.98
DCM-F-90-4-3	7.76	DCM-F-225-4-3	7.99
DCM-F-90-4-4	7.83	DCM-F-225-4-4	8.07
DCM-F-90-4-5	7.71	DCM-F-225-4-5	7.97
DCM-F-110-4-1	7.80	DCM-F-250-4-1	8.04
DCM-F-110-4-2	7.76	DCM-F-250-4-2	8.00
DCM-F-110-4-3	7.78	DCM-F-250-4-3	8.01
DCM-F-110-4-4	7.86	DCM-F-250-4-4	8.06
DCM-F-110-4-5	7.77	DCM-F-250-4-5	7.99

Table A.5.-5. Digital comparator readings of the Moleanos limestone (C): Sample nº1.

CODE	Length (mm)	CODE	Length (mm)
DCM-C-23-1-1	8.07	DCM-C-130-1-1	8.15
DCM-C-23-1-2	8.08	DCM-C-130-1-2	8.16
DCM-C-23-1-3	7.77	DCM-C-130-1-3	7.83
DCM-C-23-1-4	7.77	DCM-C-130-1-4	7.83
DCM-C-23-1-5	7.96	DCM-C-130-1-5	8.04
DCM-C-40-1-1	8.10	DCM-C-150-1-1	8.17
DCM-C-40-1-2	8.11	DCM-C-150-1-2	8.20
DCM-C-40-1-3	7.79	DCM-C-150-1-3	7.84
DCM-C-40-1-4	7.80	DCM-C-150-1-4	7.85
DCM-C-40-1-5	7.99	DCM-C-150-1-5	8.04
DCM-C-50-1-1	8.09	DCM-C-175-1-1	8.19
DCM-C-50-1-2	8.13	DCM-C-175-1-2	8.23
DCM-C-50-1-3	7.79	DCM-C-175-1-3	7.87
DCM-C-50-1-4	7.80	DCM-C-175-1-4	7.85
DCM-C-50-1-5	7.99	DCM-C-175-1-5	8.06
DCM-C-90-1-1	-	DCM-C-225-1-1	8.27
DCM-C-90-1-2	-	DCM-C-225-1-2	8.29
DCM-C-90-1-3	-	DCM-C-225-1-3	7.93
DCM-C-90-1-4	-	DCM-C-225-1-4	7.92
DCM-C-90-1-5	-	DCM-C-225-1-5	8.15
DCM-C-110-1-1	8.11	DCM-C-250-1-1	8.25
DCM-C-110-1-2	8.19	DCM-C-250-1-2	8.29
DCM-C-110-1-3	7.80	DCM-C-250-1-3	7.97
DCM-C-110-1-4	7.78	DCM-C-250-1-4	7.97
DCM-C-110-1-5	8.00	DCM-C-250-1-5	8.13

Table A.5.-6. Digital comparator readings of the Moleanos limestone (C): Sample nº2.

CODE	Length (mm)	CODE	Length (mm)
DCM-C-23-2-1	8.25	DCM-C-130-2-1	7.96
DCM-C-23-2-2	8.29	DCM-C-130-2-2	8.05
DCM-C-23-2-3	7.97	DCM-C-130-2-3	8.04
DCM-C-23-2-4	7.97	DCM-C-130-2-4	7.96
DCM-C-23-2-5	8.13	DCM-C-130-2-5	8.01
DCM-C-40-2-1	7.94	DCM-C-150-2-1	7.98
DCM-C-40-2-2	8.02	DCM-C-150-2-2	8.06

DCM-C-40-2-3	8.02	DCM-C-150-2-3	8.07
DCM-C-40-2-4	7.93	DCM-C-150-2-4	7.97
DCM-C-40-2-5	7.98	DCM-C-150-2-5	8.03
DCM-C-50-2-1	7.94	DCM-C-175-2-1	8.01
DCM-C-50-2-2	8.03	DCM-C-175-2-2	8.08
DCM-C-50-2-3	8.02	DCM-C-175-2-3	8.08
DCM-C-50-2-4	7.95	DCM-C-175-2-4	8.00
DCM-C-50-2-5	7.99	DCM-C-175-2-5	8.06
DCM-C-90-2-1	-	DCM-C-225-2-1	8.09
DCM-C-90-2-2	-	DCM-C-225-2-2	8.17
DCM-C-90-2-3	-	DCM-C-225-2-3	8.16
DCM-C-90-2-4	-	DCM-C-225-2-4	8.06
DCM-C-90-2-5	-	DCM-C-225-2-5	8.12
DCM-C-110-2-1	7.95	DCM-C-250-2-1	8.08
DCM-C-110-2-2	8.04	DCM-C-250-2-2	8.16
DCM-C-110-2-3	8.03	DCM-C-250-2-3	8.14
DCM-C-110-2-4	7.94	DCM-C-250-2-4	8.04
DCM-C-110-2-5	7.99	DCM-C-250-2-5	8.11

Table A.5.-7. Digital comparator readings of the Moleanos limestone (C): Sample nº3.

CODE	Length (mm)	CODE	Length (mm)
DCM-C-23-3-1	7.93	DCM-C-130-3-1	7.99
DCM-C-23-3-2	7.81	DCM-C-130-3-2	7.89
DCM-C-23-3-3	7.84	DCM-C-130-3-3	7.91
DCM-C-23-3-4	7.96	DCM-C-130-3-4	8.02
DCM-C-23-3-5	7.88	DCM-C-130-3-5	7.94
DCM-C-40-3-1	7.96	DCM-C-150-3-1	8.00
DCM-C-40-3-2	7.85	DCM-C-150-3-2	7.90
DCM-C-40-3-3	7.88	DCM-C-150-3-3	7.92
DCM-C-40-3-4	8.00	DCM-C-150-3-4	8.04
DCM-C-40-3-5	7.92	DCM-C-150-3-5	7.96
DCM-C-50-3-1	7.97	DCM-C-175-3-1	8.03
DCM-C-50-3-2	7.87	DCM-C-175-3-2	7.91
DCM-C-50-3-3	7.88	DCM-C-175-3-3	7.94
DCM-C-50-3-4	8.01	DCM-C-175-3-4	8.05
DCM-C-50-3-5	7.92	DCM-C-175-3-5	7.98
DCM-C-90-3-1	-	DCM-C-225-3-1	8.10
DCM-C-90-3-2	-	DCM-C-225-3-2	7.99

DCM-C-90-3-3	-	DCM-C-225-3-3	8.02
DCM-C-90-3-4	-	DCM-C-225-3-4	8.18
DCM-C-90-3-5	-	DCM-C-225-3-5	8.05
DCM-C-110-3-1	7.97	DCM-C-250-3-1	8.10
DCM-C-110-3-2	7.86	DCM-C-250-3-2	7.98
DCM-C-110-3-3	7.88	DCM-C-250-3-3	8.02
DCM-C-110-3-4	8.03	DCM-C-250-3-4	8.12
DCM-C-110-3-5	7.93	DCM-C-250-3-5	8.05

Table A.5.-8. Digital comparator readings of the Macael marble (M): Sample nº1.

CODE	Length (mm)	CODE	Length (mm)
DCM-M-23-1-1	6.91	DCM-M-130-1-1	7.11
DCM-M-23-1-2	6.93	DCM-M-130-1-2	7.14
DCM-M-23-1-3	6.76	DCM-M-130-1-3	6.97
DCM-M-23-1-4	6.78	DCM-M-130-1-4	6.99
DCM-M-23-1-5	6.94	DCM-M-130-1-5	7.14
DCM-M-40-1-1	6.93	DCM-M-150-1-1	7.18
DCM-M-40-1-2	6.95	DCM-M-150-1-2	7.26
DCM-M-40-1-3	6.79	DCM-M-150-1-3	7.05
DCM-M-40-1-4	6.83	DCM-M-150-1-4	7.11
DCM-M-40-1-5	6.97	DCM-M-150-1-5	7.22
DCM-M-50-1-1	6.97	DCM-M-175-1-1	7.24
DCM-M-50-1-2	7.00	DCM-M-175-1-2	7.28
DCM-M-50-1-3	6.82	DCM-M-175-1-3	7.10
DCM-M-50-1-4	6.86	DCM-M-175-1-4	7.14
DCM-M-50-1-5	7.00	DCM-M-175-1-5	7.27
DCM-M-90-1-1	6.99	DCM-M-225-1-1	7.27
DCM-M-90-1-2	7.04	DCM-M-225-1-2	7.31
DCM-M-90-1-3	6.87	DCM-M-225-1-3	7.14
DCM-M-90-1-4	6.91	DCM-M-225-1-4	7.18
DCM-M-90-1-5	7.05	DCM-M-225-1-5	7.30
DCM-M-110-1-1	7.04	DCM-M-250-1-1	7.32
DCM-M-110-1-2	7.08	DCM-M-250-1-2	7.33
DCM-M-110-1-3	6.92	DCM-M-250-1-3	7.18
DCM-M-110-1-4	6.93	DCM-M-250-1-4	7.22
DCM-M-110-1-5	7.09	DCM-M-250-1-5	7.35

Table A.5.-9. Digital comparator readings of the Macael marble (M): Sample nº2.

CODE	Length (mm)	CODE	Length (mm)
DCM-M-23-2-1	7.80	DCM-M-130-2-1	7.91
DCM-M-23-2-2	7.93	DCM-M-130-2-2	8.06
DCM-M-23-2-3	8.22	DCM-M-130-2-3	8.34
DCM-M-23-2-4	8.04	DCM-M-130-2-4	8.14
DCM-M-23-2-5	7.95	DCM-M-130-2-5	8.08
DCM-M-40-2-1	7.81	DCM-M-150-2-1	7.97
DCM-M-40-2-2	7.95	DCM-M-150-2-2	8.14
DCM-M-40-2-3	8.26	DCM-M-150-2-3	8.39
DCM-M-40-2-4	8.05	DCM-M-150-2-4	8.21
DCM-M-40-2-5	7.98	DCM-M-150-2-5	8.16
DCM-M-50-2-1	7.82	DCM-M-175-2-1	8.03
DCM-M-50-2-2	7.97	DCM-M-175-2-2	8.19
DCM-M-50-2-3	8.26	DCM-M-175-2-3	8.44
DCM-M-50-2-4	8.06	DCM-M-175-2-4	8.23
DCM-M-50-2-5	7.99	DCM-M-175-2-5	8.20
DCM-M-90-2-1	7.83	DCM-M-225-2-1	8.08
DCM-M-90-2-2	7.99	DCM-M-225-2-2	8.24
DCM-M-90-2-3	8.27	DCM-M-225-2-3	8.51
DCM-M-90-2-4	8.08	DCM-M-225-2-4	8.32
DCM-M-90-2-5	8.02	DCM-M-225-2-5	8.25
DCM-M-110-2-1	7.86	DCM-M-250-2-1	8.11
DCM-M-110-2-2	8.02	DCM-M-250-2-2	8.27
DCM-M-110-2-3	8.31	DCM-M-250-2-3	8.53
DCM-M-110-2-4	8.12	DCM-M-250-2-4	8.32
DCM-M-110-2-5	8.04	DCM-M-250-2-5	8.27

Table A.5.-10. Digital comparator readings of the Macael marble (M): Sample nº3.

CODE	Length (mm)	CODE	Length (mm)
DCM-M-23-3-1	8.00	DCM-M-130-3-1	8.20
DCM-M-23-3-2	7.87	DCM-M-130-3-2	8.04
DCM-M-23-3-3	7.99	DCM-M-130-3-3	8.15
DCM-M-23-3-4	8.25	DCM-M-130-3-4	8.41
DCM-M-23-3-5	8.06	DCM-M-130-3-5	8.22
DCM-M-40-3-1	8.05	DCM-M-150-3-1	8.27
DCM-M-40-3-2	7.89	DCM-M-150-3-2	8.12

DCM-M-40-3-3	8.02	DCM-M-150-3-3	8.23
DCM-M-40-3-4	8.28	DCM-M-150-3-4	8.47
DCM-M-40-3-5	8.09	DCM-M-150-3-5	8.29
DCM-M-50-3-1	8.08	DCM-M-175-3-1	8.31
DCM-M-50-3-2	7.92	DCM-M-175-3-2	8.15
DCM-M-50-3-3	8.05	DCM-M-175-3-3	8.28
DCM-M-50-3-4	8.30	DCM-M-175-3-4	8.52
DCM-M-50-3-5	8.11	DCM-M-175-3-5	8.35
DCM-M-90-3-1	8.10	DCM-M-225-3-1	8.39
DCM-M-90-3-2	7.95	DCM-M-225-3-2	8.22
DCM-M-90-3-3	8.07	DCM-M-225-3-3	8.34
DCM-M-90-3-4	8.29	DCM-M-225-3-4	8.58
DCM-M-90-3-5	8.14	DCM-M-225-3-5	8.41
DCM-M-110-3-1	8.13	DCM-M-250-3-1	8.41
DCM-M-110-3-2	7.99	DCM-M-250-3-2	8.25
DCM-M-110-3-3	8.11	DCM-M-250-3-3	8.40
DCM-M-110-3-4	8.34	DCM-M-250-3-4	8.60
DCM-M-110-3-5	8.18	DCM-M-250-3-5	8.43

Table A.5.-11. Digital comparator readings of the Macael marble (M): Sample nº4.

CODE	Length (mm)	CODE	Length (mm)
DCM-M-23-4-1	8.20	DCM-M-130-4-1	8.50
DCM-M-23-4-2	8.45	DCM-M-130-4-2	8.78
DCM-M-23-4-3	8.30	DCM-M-130-4-3	8.58
DCM-M-23-4-4	7.94	DCM-M-130-4-4	8.25
DCM-M-23-4-5	8.24	DCM-M-130-4-5	8.55
DCM-M-40-4-1	8.22	DCM-M-150-4-1	8.60
DCM-M-40-4-2	8.50	DCM-M-150-4-2	8.88
DCM-M-40-4-3	8.33	DCM-M-150-4-3	8.70
DCM-M-40-4-4	7.99	DCM-M-150-4-4	8.36
DCM-M-40-4-5	8.28	DCM-M-150-4-5	8.65
DCM-M-50-4-1	8.28	DCM-M-175-4-1	8.69
DCM-M-50-4-2	8.54	DCM-M-175-4-2	8.98
DCM-M-50-4-3	8.36	DCM-M-175-4-3	8.80
DCM-M-50-4-4	8.00	DCM-M-175-4-4	8.41
DCM-M-50-4-5	8.32	DCM-M-175-4-5	8.75
DCM-M-90-4-1	8.38	DCM-M-225-4-1	8.83
DCM-M-90-4-2	8.63	DCM-M-225-4-2	9.10

DCM-M-90-4-3	8.48	DCM-M-225-4-3	8.93
DCM-M-90-4-4	8.10	DCM-M-225-4-4	8.56
DCM-M-90-4-5	8.41	DCM-M-225-4-5	8.89
DCM-M-110-4-1	8.40	DCM-M-250-4-1	8.84
DCM-M-110-4-2	8.69	DCM-M-250-4-2	9.10
DCM-M-110-4-3	8.53	DCM-M-250-4-3	8.93
DCM-M-110-4-4	8.14	DCM-M-250-4-4	8.59
DCM-M-110-4-5	8.47	DCM-M-250-4-5	8.89

Table A.5.-12. Digital comparator readings of the Carrara marble (I): Sample nº1.

CODE	Length (mm)	CODE	Length (mm)
DCM-I-23-1-1	7.50	DCM-I-130-1-1	7.89
DCM-I-23-1-2	7.63	DCM-I-130-1-2	8.03
DCM-I-23-1-3	7.57	DCM-I-130-1-3	7.97
DCM-I-23-1-4	7.35	DCM-I-130-1-4	7.73
DCM-I-23-1-5	7.54	DCM-I-130-1-5	7.93
DCM-I-40-1-1	7.55	DCM-I-150-1-1	8.00
DCM-I-40-1-2	7.70	DCM-I-150-1-2	8.14
DCM-I-40-1-3	7.64	DCM-I-150-1-3	8.08
DCM-I-40-1-4	7.42	DCM-I-150-1-4	7.84
DCM-I-40-1-5	7.60	DCM-I-150-1-5	8.04
DCM-I-50-1-1	7.61	DCM-I-175-1-1	8.13
DCM-I-50-1-2	7.76	DCM-I-175-1-2	8.24
DCM-I-50-1-3	7.71	DCM-I-175-1-3	8.19
DCM-I-50-1-4	7.48	DCM-I-175-1-4	7.95
DCM-I-50-1-5	7.67	DCM-I-175-1-5	8.15
DCM-I-90-1-1	7.72	DCM-I-225-1-1	8.22
DCM-I-90-1-2	7.86	DCM-I-225-1-2	8.37
DCM-I-90-1-3	7.81	DCM-I-225-1-3	8.31
DCM-I-90-1-4	7.57	DCM-I-225-1-4	8.07
DCM-I-90-1-5	7.77	DCM-I-225-1-5	8.27
DCM-I-110-1-1	7.77	DCM-I-250-1-1	8.31
DCM-I-110-1-2	7.93	DCM-I-250-1-2	8.43
DCM-I-110-1-3	7.85	DCM-I-250-1-3	8.44
DCM-I-110-1-4	7.63	DCM-I-250-1-4	8.23
DCM-I-110-1-5	7.82	DCM-I-250-1-5	8.36

Table A.5.-13. Digital comparator readings of the Carrara marble (I): Sample nº2.

CODE	Length (mm)	CODE	Length (mm)
DCM-I-23-2-1	7.85	DCM-I-130-2-1	8.16
DCM-I-23-2-2	8.02	DCM-I-130-2-2	8.30
DCM-I-23-2-3	7.95	DCM-I-130-2-3	8.30
DCM-I-23-2-4	7.80	DCM-I-130-2-4	8.16
DCM-I-23-2-5	7.97	DCM-I-130-2-5	8.29
DCM-I-40-2-1	7.89	DCM-I-150-2-1	8.26
DCM-I-40-2-2	8.08	DCM-I-150-2-2	8.41
DCM-I-40-2-3	8.02	DCM-I-150-2-3	8.40
DCM-I-40-2-4	7.85	DCM-I-150-2-4	8.28
DCM-I-40-2-5	8.03	DCM-I-150-2-5	8.39
DCM-I-50-2-1	7.94	DCM-I-175-2-1	8.39
DCM-I-50-2-2	8.12	DCM-I-175-2-2	8.50
DCM-I-50-2-3	8.08	DCM-I-175-2-3	8.48
DCM-I-50-2-4	7.91	DCM-I-175-2-4	8.36
DCM-I-50-2-5	8.07	DCM-I-175-2-5	8.46
DCM-I-90-2-1	8.02	DCM-I-225-2-1	8.47
DCM-I-90-2-2	8.19	DCM-I-225-2-2	8.62
DCM-I-90-2-3	8.15	DCM-I-225-2-3	8.63
DCM-I-90-2-4	8.00	DCM-I-225-2-4	8.52
DCM-I-90-2-5	8.15	DCM-I-225-2-5	8.62
DCM-I-110-2-1	8.06	DCM-I-250-2-1	8.54
DCM-I-110-2-2	8.20	DCM-I-250-2-2	8.69
DCM-I-110-2-3	8.20	DCM-I-250-2-3	8.74
DCM-I-110-2-4	8.05	DCM-I-250-2-4	8.64
DCM-I-110-2-5	8.21	DCM-I-250-2-5	8.71

Table A.5.-14. Digital comparator readings of the Carrara marble (I): Sample nº3.

CODE	Length (mm)	CODE	Length (mm)
DCM-I-23-3-1	7.24	DCM-I-130-3-1	7.59
DCM-I-23-3-2	7.15	DCM-I-130-3-2	7.52
DCM-I-23-3-3	7.30	DCM-I-130-3-3	7.66
DCM-I-23-3-4	7.42	DCM-I-130-3-4	7.74
DCM-I-23-3-5	7.29	DCM-I-130-3-5	7.65
DCM-I-40-3-1	7.31	DCM-I-150-3-1	7.70
DCM-I-40-3-2	7.19	DCM-I-150-3-2	7.62

DCM-I-40-3-3	7.35	DCM-I-150-3-3	7.77
DCM-I-40-3-4	7.48	DCM-I-150-3-4	7.87
DCM-I-40-3-5	7.35	DCM-I-150-3-5	7.75
DCM-I-50-3-1	7.36	DCM-I-175-3-1	7.80
DCM-I-50-3-2	7.28	DCM-I-175-3-2	7.75
DCM-I-50-3-3	7.42	DCM-I-175-3-3	7.89
DCM-I-50-3-4	7.53	DCM-I-175-3-4	7.98
DCM-I-50-3-5	7.41	DCM-I-175-3-5	7.86
DCM-I-90-3-1	7.44	DCM-I-225-3-1	7.95
DCM-I-90-3-2	7.37	DCM-I-225-3-2	7.87
DCM-I-90-3-3	7.50	DCM-I-225-3-3	8.00
DCM-I-90-3-4	7.64	DCM-I-225-3-4	8.15
DCM-I-90-3-5	7.51	DCM-I-225-3-5	8.01
DCM-I-110-3-1	7.54	DCM-I-250-3-1	8.01
DCM-I-110-3-2	7.41	DCM-I-250-3-2	7.96
DCM-I-110-3-3	7.57	DCM-I-250-3-3	8.10
DCM-I-110-3-4	7.68	DCM-I-250-3-4	8.16
DCM-I-110-3-5	7.55	DCM-I-250-3-5	8.06

Table A.5.-15. Digital comparator readings of the Carrara marble (I): Sample nº4.

CODE	Length (mm)	CODE	Length (mm)
DCM-I-23-4-1	8.08	DCM-I-130-4-1	8.37
DCM-I-23-4-2	7.95	DCM-I-130-4-2	8.30
DCM-I-23-4-3	8.08	DCM-I-130-4-3	8.40
DCM-I-23-4-4	8.24	DCM-I-130-4-4	8.56
DCM-I-23-4-5	8.09	DCM-I-130-4-5	8.41
DCM-I-40-4-1	8.10	DCM-I-150-4-1	8.46
DCM-I-40-4-2	8.01	DCM-I-150-4-2	8.38
DCM-I-40-4-3	8.13	DCM-I-150-4-3	8.48
DCM-I-40-4-4	8.29	DCM-I-150-4-4	8.63
DCM-I-40-4-5	8.15	DCM-I-150-4-5	8.51
DCM-I-50-4-1	8.16	DCM-I-175-4-1	8.56
DCM-I-50-4-2	8.06	DCM-I-175-4-2	8.49
DCM-I-50-4-3	8.19	DCM-I-175-4-3	8.59
DCM-I-50-4-4	8.33	DCM-I-175-4-4	8.72
DCM-I-50-4-5	8.21	DCM-I-175-4-5	8.61
DCM-I-90-4-1	8.24	DCM-I-225-4-1	8.71
DCM-I-90-4-2	8.18	DCM-I-225-4-2	8.66

DCM-I-90-4-3	8.28	DCM-I-225-4-3	8.77
DCM-I-90-4-4	8.43	DCM-I-225-4-4	8.89
DCM-I-90-4-5	8.30	DCM-I-225-4-5	8.78
DCM-I-110-4-1	8.28	DCM-I-250-4-1	8.76
DCM-I-110-4-2	8.21	DCM-I-250-4-2	8.72
DCM-I-110-4-3	8.32	DCM-I-250-4-3	8.88
DCM-I-110-4-4	8.45	DCM-I-250-4-4	8.97
DCM-I-110-4-5	8.33	DCM-I-250-4-5	8.82

Table A.5.-16. Strain gauge readings of the Floresta sandstone (F).

CODE	Expansion (%)		CODE	Expansion (%)	
	Vert.	Horiz.		Vert.	Horiz.
SGM-F-23-1	-	0.0000	SGM-F-23-3	0.0000	0.0000
SGM-F-40-1	-	0.0098	SGM-F-40-3	0.0121	0.0117
SGM-F-70-1	-	0.0388	SGM-F-70-3	0.0429	0.0423
SGM-F-100-1	-	0.0635	SGM-F-100-3	0.0669	0.0665
SGM-F-125-1	-	0.0813	SGM-F-125-3	0.0860	0.0854
SGM-F-150-1	-	0.1028	SGM-F-150-3	0.1086	0.1084
SGM-F-175-1	-	0.1254	SGM-F-175-3	0.1312	0.1309
SGM-F-200-1	-	0.1475	SGM-F-200-3	0.1544	0.1543
SGM-F-225-1	-	0.1711	SGM-F-225-3	0.1830	0.1822
SGM-F-250-1	-	0.1994	SGM-F-250-3	0.2129	0.2116
SGM-F-23-2	0.0000	0.0000	SGM-F-23-4	0.0000	0.0000
SGM-F-40-2	0.0107	0.0115	SGM-F-40-4	0.0120	0.0125
SGM-F-70-2	0.0420	0.0414	SGM-F-70-4	0.0404	0.0413
SGM-F-100-2	0.0699	0.0686	SGM-F-100-4	0.0665	0.0672
SGM-F-125-2	0.0893	0.0862	SGM-F-125-4	0.0865	0.0870
SGM-F-150-2	0.1093	0.1050	SGM-F-150-4	0.1092	0.1099
SGM-F-175-2	0.1294	0.1235	SGM-F-175-4	0.1313	0.1318
SGM-F-200-2	0.1486	0.1412	SGM-F-200-4	0.1547	0.1554
SGM-F-225-2	0.1717	0.1632	SGM-F-225-4	0.1835	0.1841
SGM-F-250-2	0.1967	0.1881	SGM-F-250-4	0.2107	0.2110

Table A.5.-17. Strain gauge readings of the Moleanos limestone (C).

CODE	Expansion (%)		CODE	Expansion (%)	
	Vert.	Horiz.		Vert.	Horiz.
SGM-C-23-1	0.0000	0.0000	SGM-C-23-3	0.0000	0.0000
SGM-C-40-1	0.0096	0.0115	SGM-C-40-3	0.0128	0.0104
SGM-C-70-1	0.0318	0.0341	SGM-C-70-3	0.0355	0.0314

SGM-C-100-1	0.0537	0.0561	SGM-C-100-3	0.0699	0.0531
SGM-C-125-1	0.0712	0.0732	SGM-C-125-3	0.0852	0.0684
SGM-C-150-1	0.0882	0.0900	SGM-C-150-3	0.1012	0.0850
SGM-C-175-1	0.1043	0.1061	SGM-C-175-3	0.1183	0.1027
SGM-C-200-1	-	-	SGM-C-200-3	0.1349	0.1196
SGM-C-225-1	0.1402	0.1217	SGM-C-225-3	0.1583	-
SGM-C-250-1	0.1696	0.1457	SGM-C-250-3	0.1854	0.1677
SGM-C-23-2	-	0.0000			
SGM-C-40-2	-	0.0118			
SGM-C-70-2	-	0.0348			
SGM-C-100-2	-	0.0609			
SGM-C-125-2	-	0.0844			
SGM-C-150-2	-	0.1022			
SGM-C-175-2	-	0.1195			
SGM-C-200-2	-	0.1360			
SGM-C-225-2	-	0.1599			
SGM-C-250-2	-	0.1848			

Table A.5.-18. Strain gauge readings of the Macael marble (M).

CODE	Expansion (%)		CODE	Expansion (%)	
	Vert.	Horiz.		Vert.	Horiz.
SGM-M-23-1	0.0000	0.0000	SGM-M-23-3	0.0000	0.0000
SGM-M-40-1	0.0086	0.0194	SGM-M-40-3	0.0340	0.0082
SGM-M-70-1	0.0301	0.0521	SGM-M-70-3	0.0758	0.0262
SGM-M-100-1	0.0508	0.0875	SGM-M-100-3	0.1285	0.0462
SGM-M-125-1	0.0704	0.1232	SGM-M-125-3	0.1984	0.0706
SGM-M-150-1	0.0963	0.1660	SGM-M-150-3	0.2450	0.1027
SGM-M-175-1	0.1286	0.2196	SGM-M-175-3	0.2746	0.1180
SGM-M-200-1	0.1640	0.2758	SGM-M-200-3	0.3226	0.1389
SGM-M-225-1	0.2371	0.3305	SGM-M-225-3	0.3625	0.1681
SGM-M-250-1	0.2911	0.3738	SGM-M-250-3	0.4100	0.1953
SGM-M-23-2	0.0000	0.0000			
SGM-M-40-2	0.0297	0.0096			
SGM-M-70-2	0.0610	0.0293			
SGM-M-100-2	0.0970	0.0492			
SGM-M-125-2	0.1248	0.0668			
SGM-M-150-2	0.1609	0.0887			
SGM-M-175-2	0.2028	0.1116			
SGM-M-200-2	0.2434	0.1348			

SGM-M-225-2	0.2899	0.1641
SGM-M-250-2	0.3285	0.1914

Table A.5.-19. Strain gauge readings of the Carrara marble (I).

CODE	Expansion (%)		CODE	Expansion (%)	
	Vert.	Horiz.		Vert.	Horiz.
SGM-I-23-1	0.0000	0.0000	SGM-I-23-3	0.0000	-
SGM-I-40-1	0.0171	0.0126	SGM-I-40-3	0.0129	-
SGM-I-70-1	0.0426	0.0401	SGM-I-70-3	0.0292	-
SGM-I-100-1	0.0610	0.0657	SGM-I-100-3	0.0546	-
SGM-I-125-1	0.0823	0.0905	SGM-I-125-3	0.0762	-
SGM-I-150-1	0.1115	0.1191	SGM-I-150-3	0.1012	-
SGM-I-175-1	0.1373	0.1492	SGM-I-175-3	0.1303	-
SGM-I-200-1	0.1657	0.1851	SGM-I-200-3	-	-
SGM-I-225-1	0.2062	0.2280	SGM-I-225-3	0.2473	-
SGM-I-250-1	0.2634	0.2676	SGM-I-250-3	0.3136	-
SGM-I-23-2	0.0000	0.0000			
SGM-I-40-2	0.0116	0.0111			
SGM-I-70-2	0.0371	0.0357			
SGM-I-100-2	0.0611	0.0584			
SGM-I-125-2	0.0814	0.0781			
SGM-I-150-2	0.1050	0.1022			
SGM-I-175-2	0.1326	0.1309			
SGM-I-200-2	0.1620	0.1625			
SGM-I-225-2	0.2055	0.2077			
SGM-I-250-2	0.2436	0.2479			

- Appendix B -
Apparent fracture toughness and fracture predictions with the PM

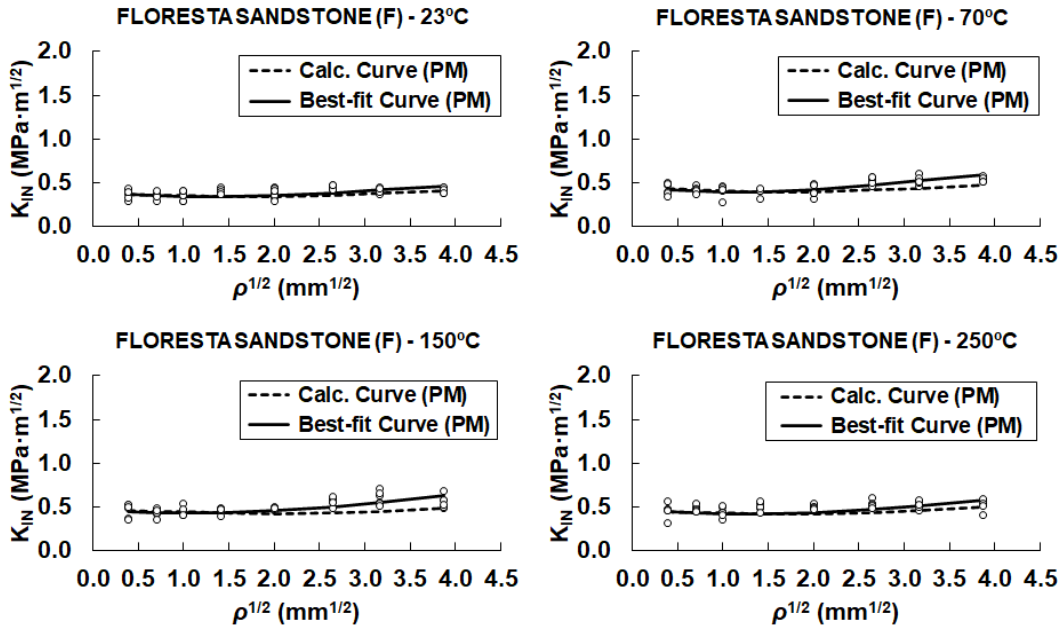

Figure B.1. Test results of the apparent fracture toughness (K_{IN}) of the Floresta sandstone (F) under four-point bending conditions and comparison with the PM of the TCD at different temperatures.

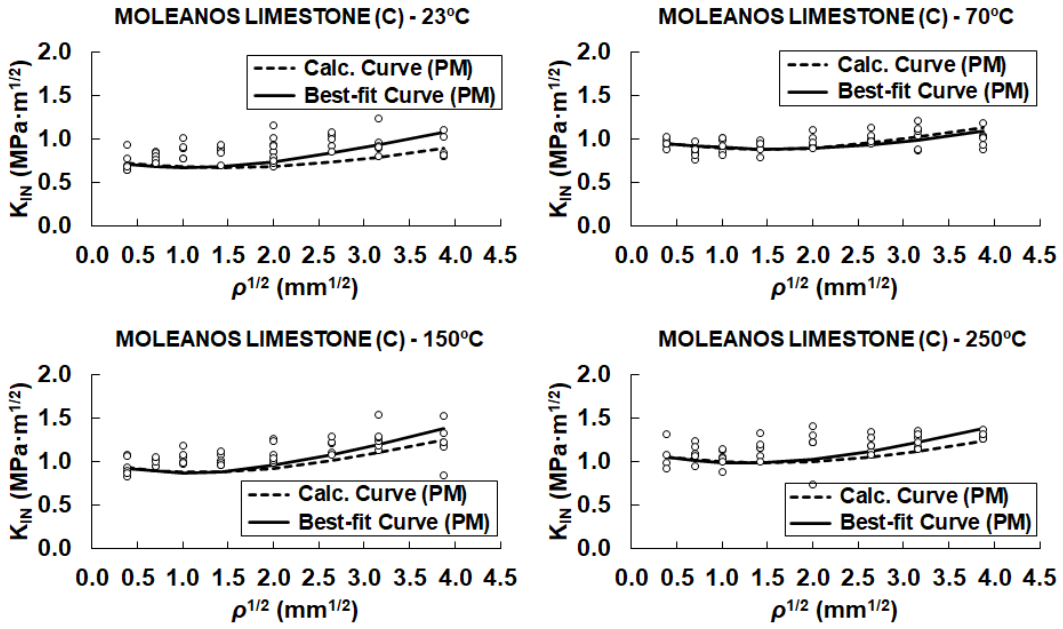

Figure B.2. Test results of the apparent fracture toughness (K_{IN}) of the Moleanos limestone (C) under four-point bending conditions and comparison with the PM of the TCD at different temperatures.

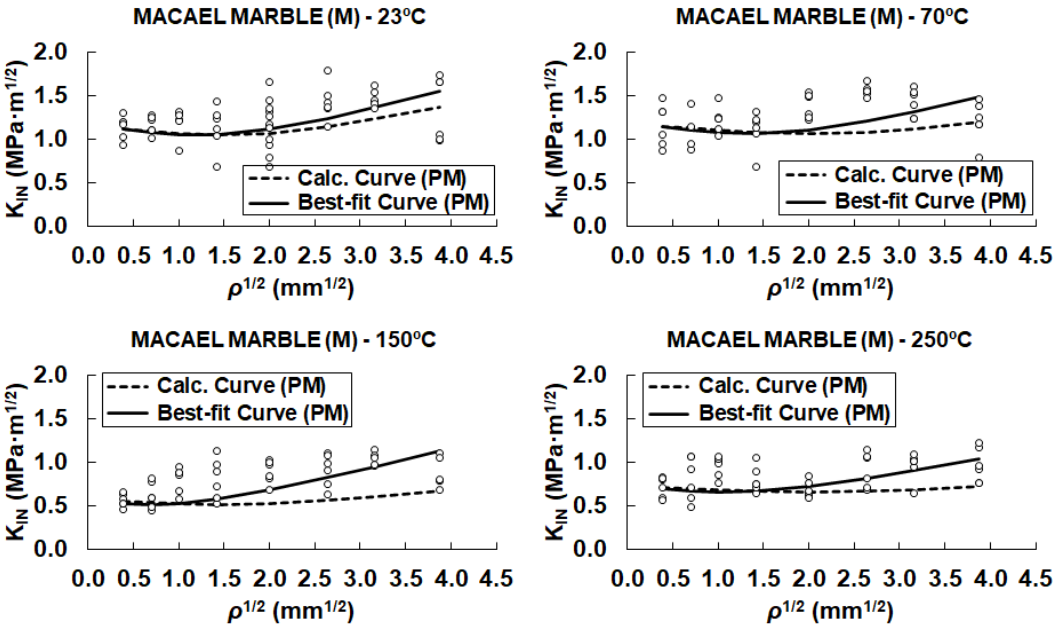

Figure B.3. Test results of the apparent fracture toughness (K_{IN}) of the Macael marble (M) under four-point bending conditions and comparison with the PM of the TCD at different temperatures.

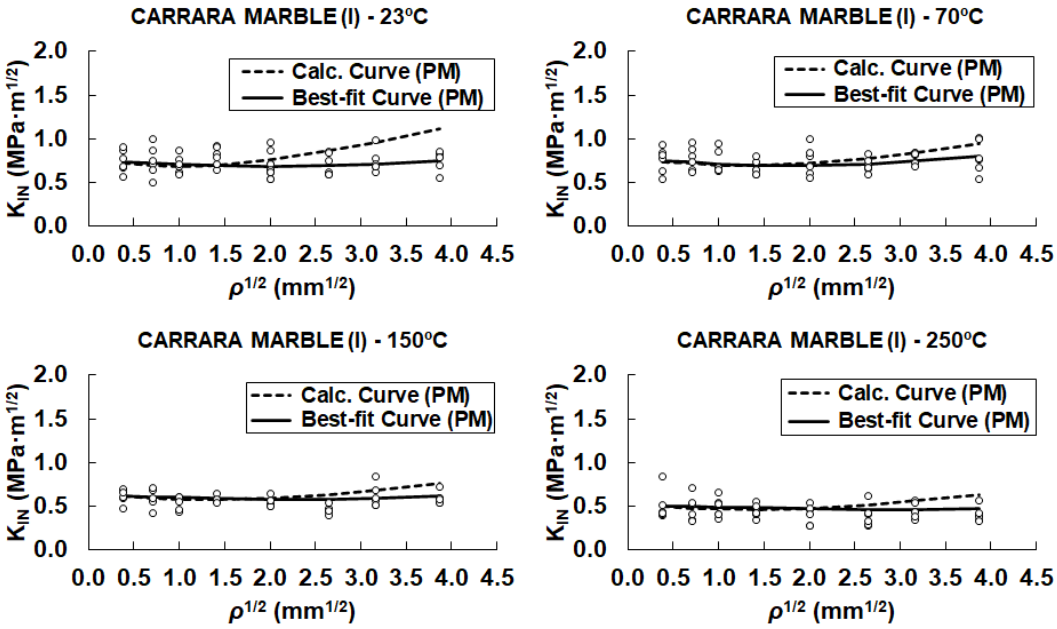

Figure B.4. Test results of the apparent fracture toughness (K_{IN}) of the Carrara marble (I) under four-point bending conditions and comparison with the PM of the TCD at different temperatures.

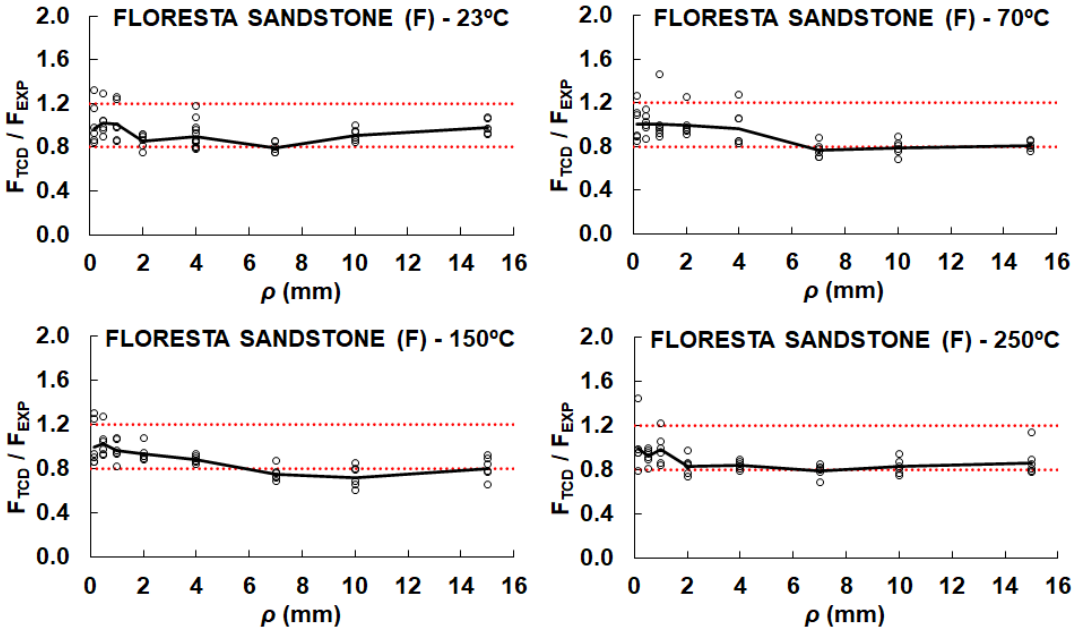

Figure B.5. Fracture load predictions according to the PM of the TCD for the Floresta sandstone (F) at different temperatures.

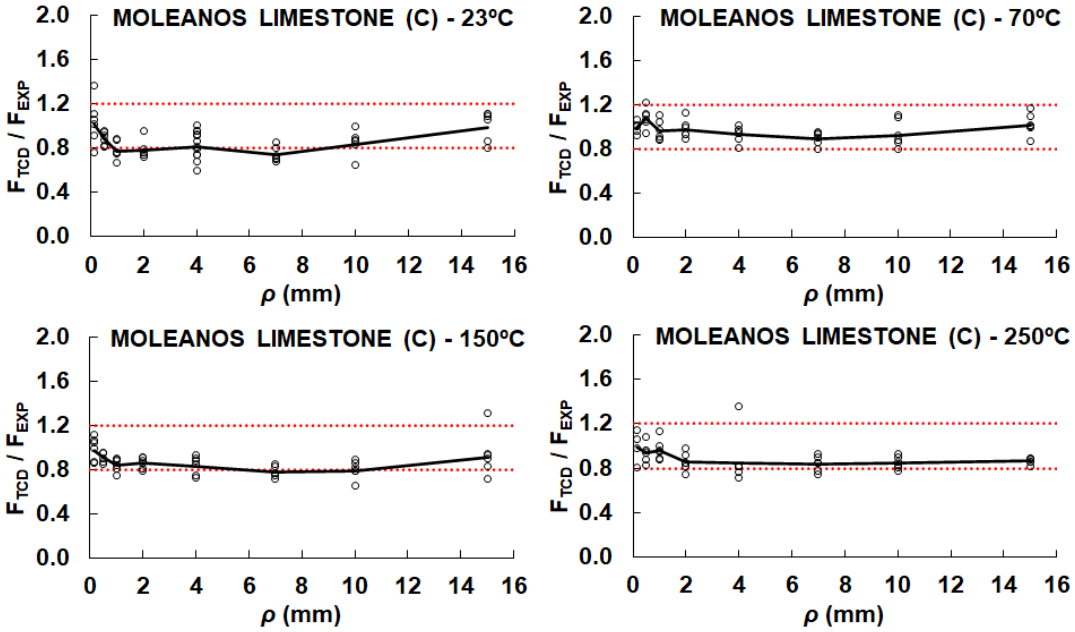

Figure B.6. Fracture load predictions according to the PM of the TCD for the Moleanos limestone (C) at different temperatures.

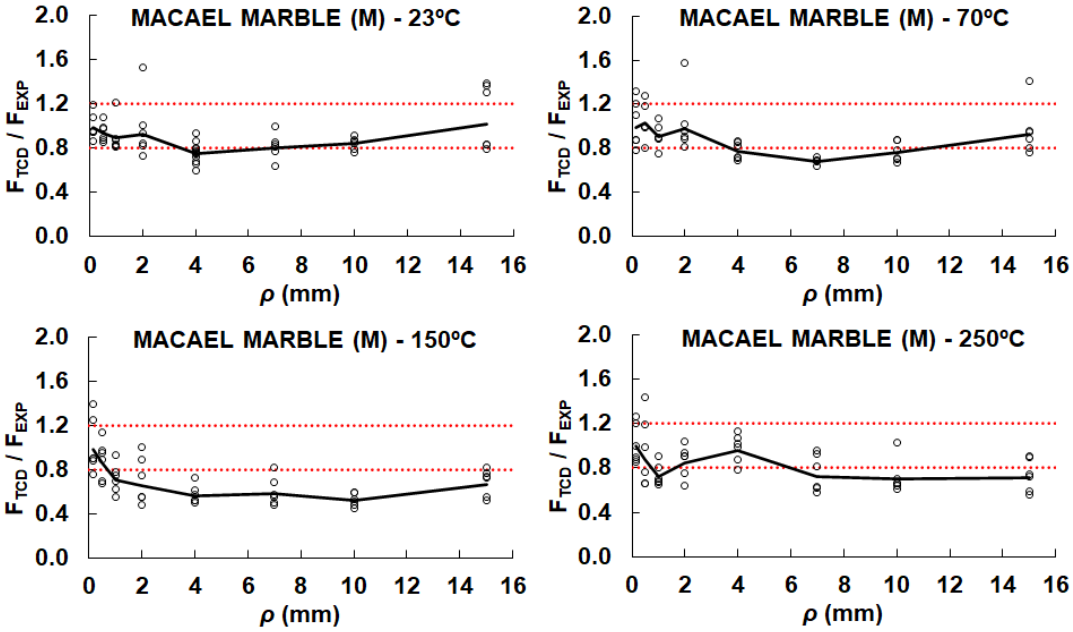

Figure B.7. Fracture load predictions according to the PM of the TCD for the Macael marble (M) at different temperatures.

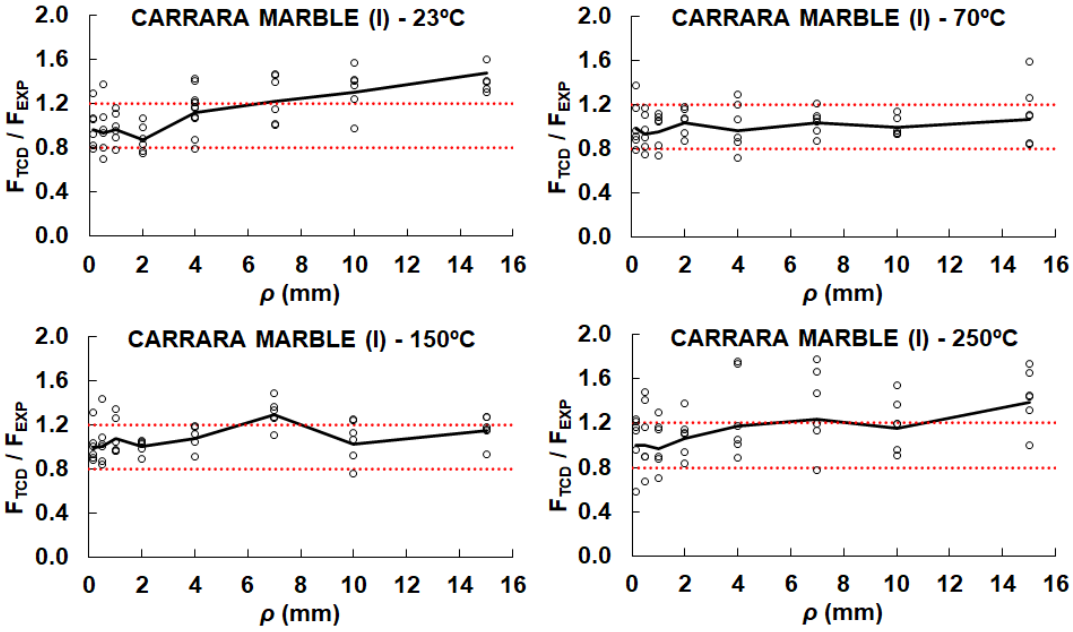

Figure B.8. Fracture load predictions according to the PM of the TCD for the Carrara marble (I) at different temperatures.

- Appendix C -
Results of the four-point bending test numerical models

Table C-1. Apparent fracture toughness (K_{IN}) results obtained from numerical four-point bending test models for each notch radius (ρ) and grain size (l) combination. Units in MPa · m$^{1/2}$.

ρ (mm)	l = 1 mm	l = 1.5 mm	l = 2 mm	l = 2.5 mm	l = 3 mm
1	0.85				
1	0.79				
1	0.59				
1	0.76				
1	0.88				
1	0.70				
1.5	0.93	0.88			
1.5	0.72	0.77			
1.5	0.78	0.81			
1.5	0.63	0.94			
1.5	0.62	0.94			
1.5	0.83	0.88			
2	0.87	0.92	0.99		
2	0.97	0.96	0.86		
2	0.85	0.93	1.01		
2	0.97	0.89	0.96		
2	0.99	0.81	1.09		
2	0.74	0.84	0.81		
2.5	0.87	1.08	1.16	1.03	
2.5	0.96	1.07	1.03	1.09	
2.5	0.99	1.01	0.93	1.00	
2.5	0.89	1.10	1.04	1.19	
2.5	0.99	0.99	1.12	1.02	
2.5	0.89	0.85	1.37	1.30	
3	0.92	1.06	1.02	1.05	1.54
3	0.79	0.99	0.93	0.95	1.07
3	1.23	1.09	1.35	0.95	1.35
3	0.91	1.16	1.08	1.26	1.28
3	0.94	1.18	1.19	1.24	1.17
3	1.01	1.10	1.09	1.35	1.38
4	1.04	1.42	1.23	1.29	1.22
4	1.18	1.22	1.26	1.28	1.59
4	1.04	1.02	1.21	1.20	1.14
4	1.10	1.15	1.42	1.40	1.36
4	1.00	1.23	1.12	1.28	1.41

4	1.06	1.20	1.34	1.37	1.45
5.5	1.10	1.14	1.34	1.22	1.47
5.5	1.35	1.29	1.37	1.48	1.59
5.5	1.01	1.27	1.27	1.59	1.44
5.5	1.35	0.95	1.35	1.15	1.47
5.5	1.09	1.29	1.28	1.18	1.35
5.5	1.04	1.09	1.49	1.73	1.87
7	1.22	1.10	1.41	1.49	1.55
7	1.32	1.19	1.49	1.48	1.37
7	1.22	1.40	1.33	1.49	1.61
7	1.06	1.40	1.41	1.60	1.57
7	1.13	1.16	1.40	1.23	1.53
7	1.37	1.25	1.33	1.31	1.26
8.5	1.34	1.57	1.39	1.17	1.82
8.5	1.11	1.49	1.18	1.46	1.45
8.5	1.17	1.18	1.64	1.66	1.57
8.5	1.37	1.51	1.26	1.40	1.57
8.5	1.29	1.21	1.34	1.37	1.54
8.5	1.33	1.38	1.36	1.27	1.96
10	1.06	1.56	1.45	1.60	1.49
10	1.37	1.44	1.50	1.54	1.47
10	1.22	1.43	1.67	1.59	1.63
10	1.19	1.31	1.49	1.52	1.80
10	1.43	1.50	1.33	1.52	1.75
10	1.32	1.30	1.42	1.45	1.40
12.5	1.22	1.32	1.51	1.58	1.24
12.5	1.46	1.36	1.42	1.46	1.71
12.5	1.42	1.66	1.63	1.66	1.74
12.5	1.37	1.54	1.60	1.52	1.58
12.5	1.12	1.48	1.37	1.76	1.76
12.5	1.35	1.27	1.42	1.62	1.56
15	1.40	1.54	1.61	1.54	1.48
15	1.44	1.46	1.44	1.65	1.76
15	1.37	1.54	1.42	1.66	1.58
15	1.49	1.44	1.57	1.48	1.83
15	1.36	1.41	1.50	1.65	1.73
15	1.40	1.42	1.37	1.80	1.78